

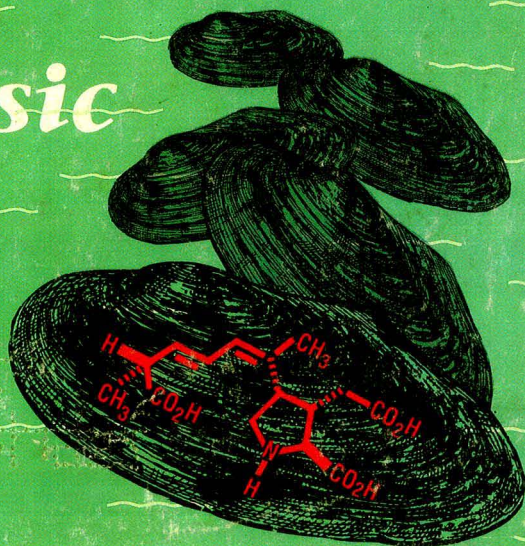
SEPTEMBER 15, 1989

Analytical CHEMISTRY



The Amnesic Shellfish Poisoning Mystery

1053 A



LISTEN TO THE QUIET

and have your
very own gnome.

Vacuum pumps in general are a noisy sort of lab hardware. Especially during the roughing stage. But at working pressure you want quiet.

At Precision we do something about noise.

We put a unique flutter valve in our pump to help reduce irritating clatter. Less noise means less fatigue on you.

The flutter valve is just one step in our effort to remove problems. Problems with noise, vibration level, internal leakage, improper gas flow, wear on parts, and oil breakdown.

Things that reduce performance.

Because that's our business. We worry about building the pump so you can concentrate on getting good results. Accurate results. Scientific results.

So don't worry. Be precise. Pump with Precision.

The gnome is to remind you of the features of our pump—small, fast, hard working, quiet as the night.

Send for the Precision belt drive bulletin. You'll receive your very own gnome when you return the warranty registration card that comes with the purchase of a Precision pump.



Write Precision Scientific, P.O. Box 10066, Rochester, NY 14610. Or call 800-621-8820.

MEMBER
SAMA
SCIENTIFIC APPARATUS
MAKERS ASSOCIATION

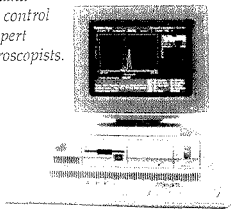
*Your Performance Demands
Precision®*

Precision Scientific

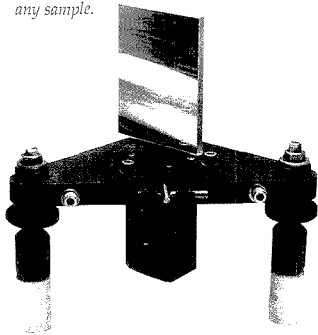
CIRCLE 129 ON READER SERVICE CARD



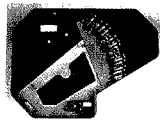
Easy-to-use data system. The entire spectrometer is operated from one IBM Personal System/2 Model 50 with color graphics. Our ThermoSPEC™ software offers multi-level operation including menu-driven control for novices and occasional users, and command mode control for expert spectroscopists.



Flexibility of a sequential ICP. Correct wavelengths may be identified and conditions optimized for any element in any sample.

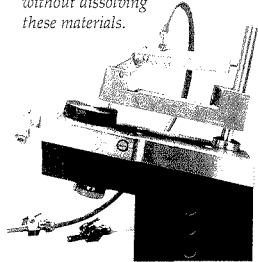


Economy from selectable low argon flow. High flow provides extra sensitivity for low concentrations or difficult samples, but low flow saves argon on routine samples.

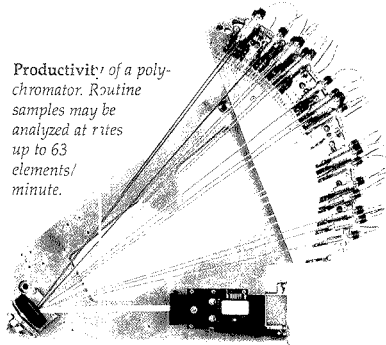


Vacuum option for P and S detection. Both the mono- and the polychromator can be outfitted for vacuum UV determinations.

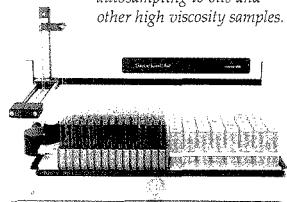
No metal prep with an optional solid sampling accessory. Spark ablation of metals and briquetted powders into the argon stream makes it possible to do "direct reading" measurements without dissolving these materials.



Productivity of a polychromator. Routine samples may be analyzed at rates up to 63 elements/minute.



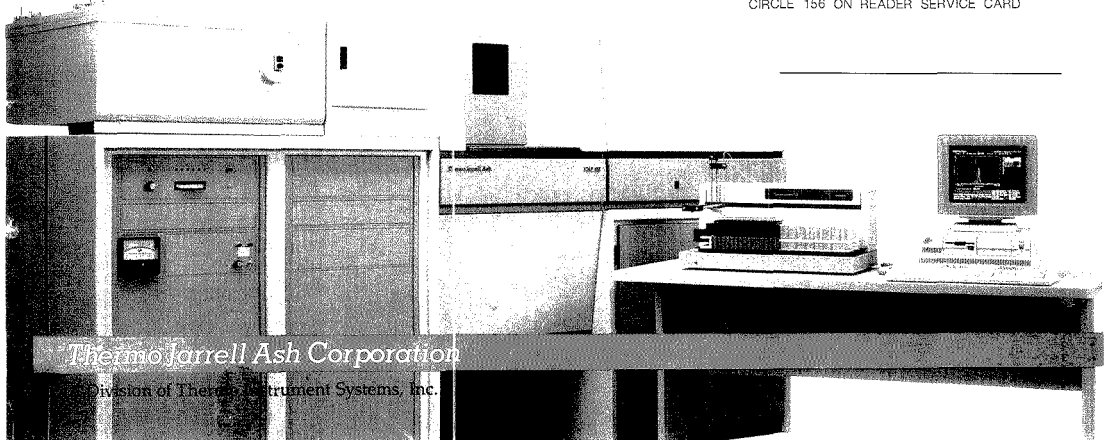
Unattended operation. With the microprocessor controlled TJA-300™ Autosampler, the PolyScan can do automatic profiling, automatic standardization, limit and other quality control checks on all samples in full compliance with CLP requirements. An optional autodilutor extends autosampling to oils and other high viscosity samples.



These Critical Details Make the PolyScan 61E The World's Most Advanced ICP

For literature or a demonstration, call (508) 520-1880. Or write Thermo Jarrell Ash, Inc., 8 East Forge Parkway, Franklin, MA 02038-9101.

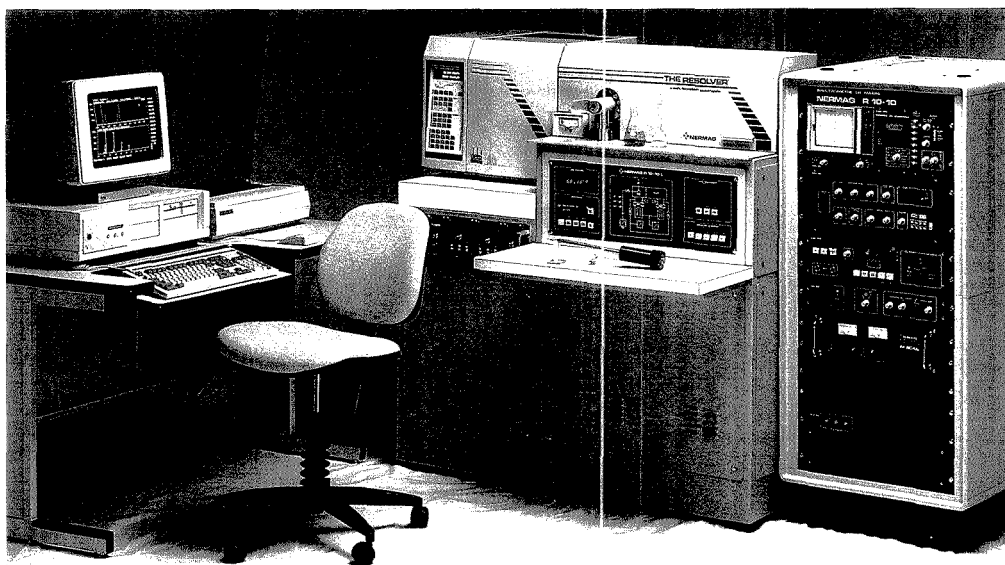
CIRCLE 156 ON READER SERVICE CARD



Thermo Jarrell Ash Corporation

Division of Thermo Instrument Systems, Inc.

You said you needed positive and negative ions, EI/CI, DCI, FAB, Thermospray ionization, a color data system, 4,000 dalton mass range, variable resolution up to 6,000, and you wanted all that in a quadrupole mass spectrometer?



We responded.

Now you don't have to play the "assemble a mass-spec" game when you need a new ionization technique in a hurry.

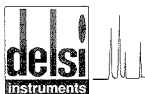
The Resolver allows you to use any method by simply plugging in the appropriate source.

But more importantly, The Resolver offers the ability to obtain spectra in which the reported isotopic ratio is meaningful, while detecting even smaller quantities of the analyte.

Finally, with the power of our Spectral 30 color data system you obtain a reduced entry fee into the high performance club. . .

. . . at a quadrupole price.

THE RESOLVER™



Delsi Inc., 15701 West Hardy Road, Houston, Texas 77060. FAX (713) 591-2132 Tel (713) 847-0811
NERMAG 49 Quai du Halage 92500 RUEIL-MALMAISON France Tel.: (1) 47.32.92.35 Telex: Rlormag 204 029 F

 NERMAG

CIRCLE 32 ON READER SERVICE CARD

SEPTEMBER 15, 1989
VOLUME 18
NUMBER 18

ANCIAM
 The Audit Bureau
 61(18) 1009A-1064A/2001-2128 (1989)
 ISSN 0003-2700

Registered in U.S. Patent and Trademark Office; Copyright 1989 by the American Chemical Society
 ANALYTICAL CHEMISTRY (ISSN 0003-2700) is published semimonthly by the American Chemical Society at 1155 16th St., N.W., Washington, DC 20036. Editorial offices are located at the same ACS address (202-872-4570; FAX 202-872-6325; TDD 202-872-8733). Second-class postage paid at Washington, DC, and additional mailing offices. Postmaster: Send address changes to ANALYTICAL CHEMISTRY Member & Subscriber Services, P.O. Box 3337, Columbus, OH 43210.

Claims for missing numbers will not be allowed if loss was due to failure of notice of change of address to be received in the time specified; if claim is dated (a) North America: more than 90 days beyond issue date, (b) all other foreign: more than one year beyond issue date, or if the reason given is "missing from files."

Copyright Permission: An individual may make a single reprographic copy of an article in this publication for personal use. Reprographic copying beyond that permitted by Section 107 or 108 of the U.S. Copyright Law is allowed, provided that the appropriate per-copy fee is paid through the Copyright Clearance Center, Inc., 27 Congress St., Salem, MA 01970. For reprint permission, write Copyright Administrator, Publications Division, ACS, 1155 16th St., N.W., Washington, DC 20036.

Registered names and trademarks, etc., used in this publication, even without specific indication thereof, are not to be considered unprotected by law.

Advertising Management: Centcom, Ltd., 500 Post Rd. East, Westport, CT 06880 (203-226-7131)

1989 subscription rates include air delivery outside the U.S., Canada, and Mexico

	1 yr	2 yr
Members		
Domestic	\$ 27	\$ 45
Canada and Mexico	56	103
Europe	83	157
All Other Countries	120	231
Nonmembers		
Domestic	49	83
Canada and Mexico	78	141
Europe	155	280
All Other Countries	192	354

Three-year and other rates contact: Member & Subscriber Services, ACS, P.O. Box 3337, Columbus, OH 43210 (614-447-3776 or 800-333-9511).

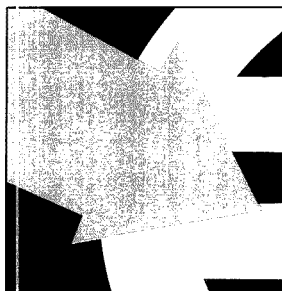
Subscription orders by phone may be charged to VISA, MasterCard, Barclay card, Access, or American Express. Call toll free 800-ACS-5558 in the continental United States; in the Washington, DC, metropolitan area and outside the continental United States, call 202-872-8065. Mail orders for new and renewal subscriptions should be sent with payment to the Business Management Division, ACS, P.O. Box 57136, West End Station, Washington, DC 20037.

Subscription service inquiries and changes of address (Include both old and new addresses with ZIP code and recent mailing label) should be directed to the ACS Columbus address noted above. Please allow six weeks for change of address to become effective.

ACS membership information: Lorraine Bowlin (202-872-4567)

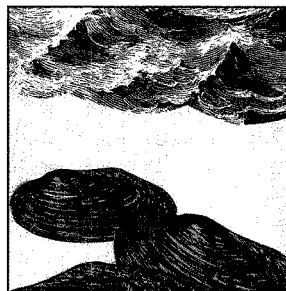
Single issues, current year, \$7.00 except review issue and LabGuide, \$12.00; back issues and volumes and microform editions available by single volume or back issue collection. For information or to order, call 800-ACS-5558 or write the Microform & Back Issues Office at the Washington address.

Nonmembers rates in Japan: Rates above do not apply to nonmember subscribers in Japan, who must enter subscription orders with Maruzen Company Ltd., 3-10 Nihonbashi 2-chome, Chuo-ku, Tokyo 103, Japan. Tel: (03) 272-7211.



REPORT 1023 A

Fluorescence line-narrowing spectroscopy can be used to obtain high-resolution optical spectra of molecules for which conventional low-temperature absorption spectra yield broad vibronic bands. Gerald J. Small and Ryszard Jankowiak of Iowa State University discuss the instrumentation involved in FLNS and its application to the study of chemical carcinogenesis



ANALYTICAL APPROACH 1053 A

On the cover. The amnesic shellfish poisoning mystery. In 1987 Canadian newspapers were filled with headlines reporting a life-threatening outbreak of food poisoning. Michael A. Quilliam and Jeffrey L. C. Wright of the National Research Council of Canada's Atlantic Research Laboratory describe the analytical methods used to isolate the toxin responsible

BRIEFS 1014 A

NEWS 1021 A

A ANALYTICAL CHEMISTRY given to undergraduates. ▶ Bright Source lasers gain in power by pulsing

BOOKS 1037 A

Critical reviews. Recently released books on NMR, electrochemistry, surface spectroscopy, gas and liquid chromatography, ion-molecule reactions, and chemometrics are reviewed

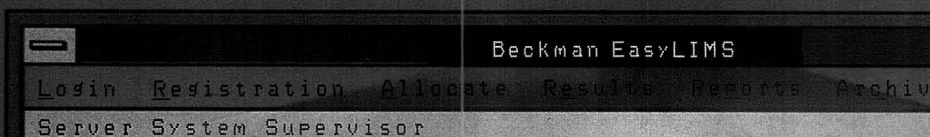
FOCUS 1047 A

Looking at the environment. Two recent meetings, the 19th International Symposium on Environmental Analytical Chemistry and the Fifth Annual Waste Testing and Quality Assurance Symposium, sparked the interest of both analytical and environmental scientists

NEW PRODUCTS & MANUFACTURERS' LITERATURE 1050 A

AUTHOR INDEX 2001

The power of LIMS for the



Create "presentation-quality" reports and diagrams with EasyLIMS 3-D graphics package.



EasyLIMS login screen couples power and flexibility with easy-to-use Windows to handle virtually any laboratory application.

Beckman EasyLIMS

Login Registration Allocate Results Reports Archive Utilities Help

Registration

Work Registration

Request No. 00532 5/6/88

Substances

Product ABC Stage 1
Test Class 1 Group
Soil Matrix
Stage 1 Polymer Precursor
Research Catalyst 987
V-1002 Test Group
Water Matrix
Product XYZ Stage 2

Labels: 1 per test 1 per sample

Options: Don't print Print

No. in group: 3

TESTS

- Water Content
- Appearance
- Monomer Analysis
- HPLC Analysis
- Loss on Drying
- Alkalinity
- Metals Analysis

Buttons: Notes, Register, Exit

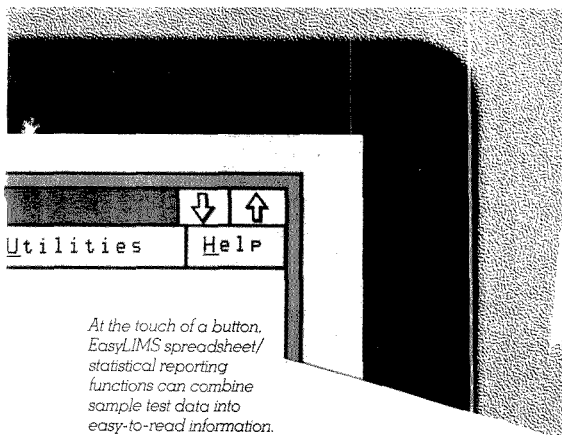
Search: []

Keys: Code Description

Buttons: OK, Cancel

growing lab: EasyLIMS™

Announcing a major innovation in data management for the growing laboratory: PC-based EasyLIMS from Beckman. LIMS is not just for the large lab anymore. Now everyone can enjoy the benefits of increased productivity and faster, more accurate data management. And we've made it easy...



At the touch of a button, EasyLIMS spreadsheet/statistical reporting functions can combine sample test data into easy-to-read information.



Easy to afford

From single-user software and documentation to a completely networked or turnkey system, there's a Beckman EasyLIMS package to suit your needs and your budget.

Easy to install

EasyLIMS is PC-based so it can operate on suitable IBM® PC or PS/2® systems. And our unique QuickStart™ package comes with software preloaded and tested so all you do is take it out of the box, plug it in and flick the 'on' switch.

Easy to start-up

EasyLIMS regional user training courses are conducted regularly to ensure quick, easy start-up. And should you need any additional assistance, our worldwide technical support team is just a phone call away.

Easy to use

EasyLIMS is the only LIMS based on Microsoft® Windows, making data

management effortless. A simple click of the mouse lets you move from screen to screen and tailor reports to your liking.

Easy to upgrade

EasyLIMS runs on the popular Novell® network making modular expandability simple. So as you grow and your needs change, affordable EasyLIMS grows with you every step of the way.

Easy to order

Get the power of EasyLIMS for your lab. On your next coffee break call us for a demonstration at 201-444-8900. In the time it takes to enjoy a cup of coffee you can see how EasyLIMS can increase the productivity of your lab ten fold. The decision is easy, call now.

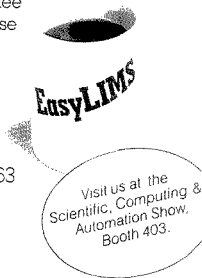
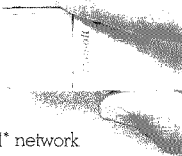
EasyLIMS for the growing lab that thinks big!

Beckman Instruments, Inc.
160 Hopper Avenue, Waldwick, NJ 07463

BECKMAN

IBM and PS/2 are trademarks of the International Business Machines Corporation. Microsoft is a trademark of Microsoft Corporation. Novell is a trademark of Novell, Inc. EasyLIMS and QuickStart are trademarks of Beckman Instruments, Inc.

CIRCLE 20 ON READER SERVICE CARD



Articles**Signal Fluctuations Due to Individual Droplets in Inductively Coupled Plasma Atomic Emission Spectrometry 2002**

Large fluctuations in ICP emission intensities are caused by individual aerosol droplets. Time- and space-resolved emission and laser light scattering experiments are described.

John W. Olesik*, Lisa J. Smith, and Eric J. Williamsen, Department of Chemistry, Venable and Kenan Laboratories, CB 3290, University of North Carolina, Chapel Hill, NC 27599-3290

Multivariate Determination of Glucose in Whole Blood by Attenuated Total Reflection Infrared Spectroscopy 2009

Multivariate calibration with the PLS algorithm is performed on spectral data in the range of 1500–750 cm^{-1} . On the basis of 127 standards, an average prediction error of 19.8 mg/dL is achieved.

H. M. Heise* and Ralf Marbach, Institut für Spektrochemie und angewandte Spektroskopie, Bunsen-Kirchhoff-Strasse 11, D-4600 Dortmund 1, FRG and **Günter Janatsch** and **J. D. Kruse-Jarres**, Institut für Klinische Chemie und Laboratoriumsmedizin, Katharinenhospital, Kriegsbergstrasse 60, D-7000 Stuttgart 1, FRG

Multivariate Calibration for Assays in Clinical Chemistry Using Attenuated Total Reflection Infrared Spectra of Human Blood Plasma 2016

The quantitative multivariate determination of protein, glucose, triglycerides, cholesterol, urea, and uric acid in blood plasma using the PLS algorithm is described. Relative prediction errors based on the square root of the prediction error sum of squares and the population average concentrations vary between 3% and 30%.

Günter Janatsch and **J. D. Kruse-Jarres**, Institut für Klinische Chemie und Laboratoriumsmedizin, Katharinenhospital, Kriegsbergstrasse 60, D-7000 Stuttgart 1, FRG and **Ralf Marbach** and **H. M. Heise***, Institut für Spektrochemie und angewandte Spektroskopie, Bunsen-Kirchhoff-Strasse 11, D-4600 Dortmund 1, FRG

Global Optimization by Simulated Annealing with Wavelength Selection for Ultraviolet-Visible Spectrophotometry 2024

Generalized simulated annealing is demonstrated as a method of global optimization. The procedure is compared with simplex using mathematical functions containing many local optima and is also applied to wavelength selection.

John H. Kalivas*, Nancy Roberts, and Jon M. Sutter, Department of Chemistry, Idaho State University, Pocatello, ID 83209

Multivariate Calibration in Inductively Coupled Plasma Mass Spectrometry 2031

Molecular ion interferences in ICP/MS are circumvented using multiple linear regression and principle components regression. The methods are applied to the Mo–Cd and Zr–Mo–Ru–Cd–In–Sn systems.

Michael E. Ketterer* and **John J. Reschl**, United States Environmental Protection Agency, National Enforcement Investigations Center, Box 25227, Building 53, Denver Federal Center, Denver, CO 80225 and **Michael J. Peters**, ICF Technology, Inc., 165 South Union Boulevard, Suite 802, Lakewood, CO 80228

Ion Detection by Fourier Transform Ion Cyclotron Resonance: The Effect of Initial Radial Velocity on the Coherent Ion Packet 2040

Excitation of the ion ensemble in FT-ICR is strongly phase-angle-dependent. Ions that have significant initial radial velocities produce a poorly defined ion packet following excitation.

Curtiss D. Hanson, Eric L. Kerley, Mauro E. Castro, and David H. Russell*, Department of Chemistry, Texas A&M University, College Station, TX 77843

Comparison of Sample Preparation Methods for the Fourier Transform Infrared Analysis of an Organo-Clay Mineral Sorption Mechanism 2047

In a comparison of spectra from five FT-IR techniques, the interpretation of an organo-mineral sorption interaction is found not to be affected by the preparation methods or techniques.

John M. Bowen*, Senja V. Compton, and M. Sterling Blanche, Western Research Institute, P.O. Box 3395, University Station, Laramie, WY 82070

Enhanced Analysis of Poly(ethylene glycols) and Peptides Using Thermo Spray Mass Spectrometry 2050

The amount of peptide sample needed for direct injection is decreased by 1–2 orders of magnitude by using an ion source with both a needle-tip repeller electrode and a restricted vaporizer probe tip.

Saul W. Fink and **Royal B. Freas***, Department of Chemistry, University of Houston, Houston, TX 77204-5641

* Corresponding author

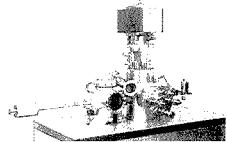
Ruled and Holographic Diffraction Gratings

Instruments SA provides a wide variety of high performance diffraction gratings. Among the many standard types available are aberration corrected blazed and ion etched concave monochromator gratings, flat field gratings for use with diode array detectors, toroidal gratings for use in the VUV and classically ruled as well as holographic plane gratings. Applications range from upper atmosphere ozone monitoring by satellite to bio testing and emission spectrometers. For further information contact Jobin Yvon, Instruments SA (201) 494-8660. CIRCLE 80



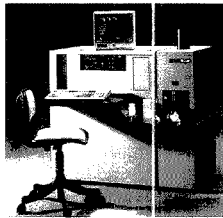
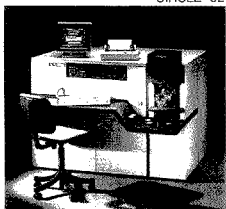
Nanoscan 50 The Field Emission Auger Microprobe

Low energy, high brightness field emission source guarantees high signal and excellent spatial resolution in SEM and SAM. Other features include video-rate SEM/SAM image accumulation, full automation, and high constant energy resolution. For further information, contact the Riber Division of Instruments SA, Inc. at (201) 494-8660. CIRCLE 81



Glow Discharge Spectroanalyzer

The GDL Excitation Source for direct solid sample analysis, uses the principle of cathodic sputtering. The conducting sample forms the cathode which is bombarded with positive argon ions to excite the sample atoms. The GDL is used for both elemental and surface analysis of metals including ferrous and non-ferrous alloys, noble metals and ceramics. For further information contact Jobin Yvon, Instruments SA (201) 494-8660. CIRCLE 82

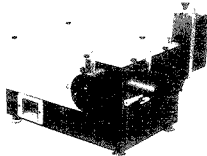


Compact Sequential ICP Spectrometer

The JY 24 has the advantages of a full featured ICP spectrometer in a single, compact, space-saving unit. By using a large surface area and high groove density holographic grating, the resolution and light gathering power of the JY 24 are unequalled for its size. For further information contact Jobin Yvon, Instruments SA (201) 494-8660. CIRCLE 83

Spectrometers

With a line of single and double spectrometers which spans from 100 to 1500 mm in focal length, Instruments SA/Jobin Yvon can furnish the ideal spectrometer for any UV, Visible or IR application. This broad range of instruments significantly reduces the need for compromise in coverage, stray light rejection or resolution when specifying a system. Each spectrometer can be automated for integration into a spectroanalytical system. For further information contact Instruments SA/Jobin Yvon (201) 494-8660. CIRCLE 84



Simultaneous and Sequential ICP Spectrometers

The JY 70 Plus consists of an integrated direct reading double polychromator — sequential spectrometer. This ICP system combines the speed of simultaneous, multi-element analysis with the versatility and flexibility of the sequential system. For further information on the JY 70 Plus or JY 38 Plus contact Jobin Yvon, Instruments SA (201) 494-8660. CIRCLE 85

INTRODUCING THE NEW JY 50 POLYSCAN FROM A WORLD LEADER IN ICP SYSTEMS

The JY 50 PolyScan not only provides all the advantages inherent in a simultaneous multi-element Spectroanalyzer but also offers spectral line selection flexibility which previously was found only in sequential ICP systems. Jobin Yvon has developed a new scanning entrance slit which furnishes 2.2 nm wavelength displacement from any of the preselected fixed analytical channels.

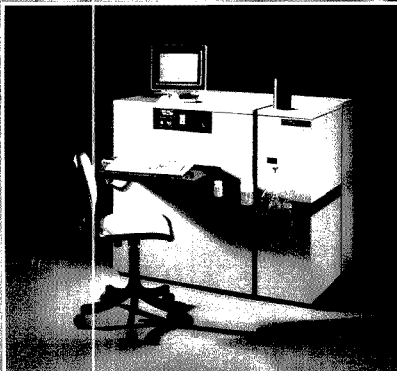
For more information on the JY 50 PolyScan and the complete spectrum of JY instruments, use the reader service card, or write or call today.

CIRCLE 86 ON READER SERVICE CARD

JOBIN YVON  **J-Y DIVISION**
Instruments SA, Inc.

6 Olsen Avenue, Edison, NJ 08820-2419
Tel. (201) 494-8660, Telex 844516
FAX (201) 494-8796

In Europe: Jobin Yvon, 16-18 Rue du
Canal 91163 Longjumeau, France
Tel. (33) 1.69.09.34.93
Telex JOBYVON 692882F
FAX 011-331-6909-0721



Enhanced Analysis of Sulfonated Azo Dyes Using Liquid Chromatography/Thermospray Mass Spectrometry 2054

Modifications to a thermospray vaporizer probe and ion source are made that enhance ion evaporation, resulting in increased sample ion current. The interaction and effect of probe-tip size, repeller voltage, and flow rate on sulfonated azo dye detection are reported.

Matthew A. McLean and Royal B. Freas*, Department of Chemistry, University of Houston, Houston, TX 77204-5641

Single Amino Acid Contributions to Protein Retention in Cation-Exchange Chromatography: Resolution of Genetically Engineered Subtilisin Variants 2059

Neutral and charged amino acids substituted into the contact region between the protein surface and the sorbent are shown to affect the chromatographic behavior of proteins.

Roman M. Chicz and Fred E. Regnier*, Department of Biochemistry, Purdue University, West Lafayette, IN 47907

Synthesis and Characterization of a Hydride-Modified Porous Silica Material as an Intermediate in the Preparation of Chemically Bonded Chromatographic Stationary Phases 2067

The sequential chlorination reduction of native silica results in a support containing fairly stable surface Si-H groups, as indicated by spectroscopic, hydrolytic, and thermal evidence. Its use for the formation of direct Si-C surface bonds is proposed.

Junior E. Sandoval* and Joseph J. Pesek, Department of Chemistry, San Jose State University, San Jose, CA 95192

Supercritical Fluid Chromatographic Determination of Fatty Acids and Their Esters on an ODS-Silica Gel Column 2076

Free fatty acids and their esters are separated on an inert ODS-silica gel column using CO₂ as the mobile phase (without a modifier) with FID and UV detection.

Akira Nomura*, Joseph Yamada, Kin-ichi Tsunoda, Keiji Sakaki, and Toshihiro Yokochi, National Chemical Laboratory for Industry, Tsukuba, Ibaraki 305, Japan

Polymer-Bound Tetrahydroborate for Arsine Generation in a Flow Injection System 2079

An anion-exchange resin serves as a carrier for tetrahydroborate ion in a flow system for the determination of As. Tolerance toward metal ion interference is improved as compared with conventional methods of reagent administration.

Solomon Tesfaldet and Knut Irgum*, Department of Analytical Chemistry, University of Umeå, S-901 87 Umeå, Sweden

Characterization of the Nitrogen and Phosphorus Thermionic Detector Response in Capillary Supercritical Fluid Chromatography 2082

Response of the thermionic detector is characterized with respect to various detector parameters and mobile-phase composition. Mobile phases modified with 10 mol % of an organic modifier can be used without affecting detector sensitivity.

P. A. David and M. Novotny*, Department of Chemistry, Indiana University, Bloomington, IN 47405

Square Wave Voltammetry at a Mercury Film Electrode: Experimental Results 2086

Previous theoretical predictions for square wave voltammetry at a film electrode are confirmed experimentally for Pb(II)/Pb(Hg) at a Ag-based Hg film electrode.

Kazimierz Wkiel and Janet Osteryoung*, Department of Chemistry, State University of New York at Buffalo, Buffalo, NY 14214

Square Wave and Linear Scan Anodic Stripping Voltammetry at Iridium-Based Mercury Film Electrodes 2092

The Ir-based Hg film electrode is characterized for direct and anodic stripping square wave voltammetry. The experimental response for Pb is compared with the theoretical model for square wave and linear scan voltammetry.

Carolyn Wechter and Janet Osteryoung*, Department of Chemistry, State University of New York at Buffalo, Buffalo, NY 14214

Application of the Three-Distance Clustering Method in Analytical Chemistry 2098

Automatic prediction of properties or classification based on hierarchical multilevel clustering of multivariate analytical data can be successfully applied to a large number of objects.

Jure Zupan* and Desire L. Massart, Farmaceutisch Instituut, Vrije Universiteit Brussel, Larbeeklaan 103, Brussels, Belgium

Automated Segmented Flow Electrochemical Analyzer 2102

The instrument can analyze 100 samples per hour using pulse techniques. It has a detection limit of about 5×10^{-8} M for reversible species, a linear range of over 10⁴, and a precision of 0.5%.

Palitha Jayaweera and Louis Ramaley*, Trace Analysis Research Centre, Department of Chemistry, Dalhousie University, Halifax, Nova Scotia, Canada B3H 4J3

Automated Titrations Using a Discontinuous Programmed Flow Analyzer 2109

The automatic generation of analytical cycles for titrations in flowing streams is described. Argentometric potentiometric titrations of Cl⁻ in water using discontinuous programmed flow are demonstrated.

Dennis P. Arnold*, Centre for Analytical Science, Department of Chemistry, Queensland University of Technology, G.P.O. Box 2434, Brisbane, Queensland 4001, Australia and Russell M. Peachey, John D. Petty, and Denis R. Sweatman, Ionode Pty. Ltd., P.O. Box 52, Holland Park, Queensland 4121, Australia

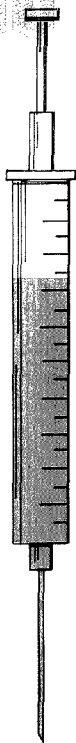
NITROGEN AND SULFUR

ONE INJECTION TWO RESULTS

Need Nitrogen and Sulfur on the same sample? Now you can do it! Couple the Antek Pyro-fluorescent™ Sulfur Detector with our Antek Pyro-chemiluminescent™ Nitrogen System.

Autosamplers and data acquisition/control systems are available for automated operation.

Chromatography detectors available:
Nitrogen Specific
Sulfur Specific



Features

- common pyroreactor for sample combustion and oxidation
- analyze gases, liquids or solids
- ppb to % range
- analysis time 30 seconds for gases and liquids. Up to 10 minutes for solids

Reduces the amount of sample prep required, the analysis time, and sample introduction by half. And, cut your instrument costs at the same time. Systems available for laboratory or process/online.

Applications

- petroleum liquids
- greases or residuals
- polymers
- biomedical samples
- high purity gases (for semi-conductors, etc.)
- LPG or other hydrocarbon gases
- atmospheric gases
- coal
- foods
- engine exhaust
- water/waste water

Typical Results

28.1ppm ±0.3	Water	148ppm±1
0.50ppm ±0.01	Naphtha	0.30ppm ±0.01
346ppm ±1.0	Diesel	48ppm±0.5
1.0ppm ±0.1	Butane	3.0ppm ±0.1
3.1ppm ±0.1	Propylene	1.8ppm ±0.1
0.9ppm ±0.1	Polyethylene	1.6ppm ±0.4
872ppm ±14	Coke	846ppm ±4
1.8ppm ±0.01	Fish Oil	4.1ppm ±0.4

For more information on your application or for a price quote, contact us in Houston or Dusseldorf.
In the USA, call toll free, (800) 365-2143

Patent Pending



ANTEK[®] INSTRUMENTS, INC.

Antek Instruments, Inc.
6005 North Freeway
Houston, Texas 77076-3998
Tel: 713/691-2265

TW X: 910-881-1792
Toll Free: 800/365-2143
FAX: 713-691-5606

Antek Instruments, GmbH
Wacholderstrasse 7
4000 Dusseldorf Angermund 31
Federal Republic of Germany

Tel: (0203) 74325/6
TLX: 8551136 ANDU D
FAX: (0203) 741545

CIRC_E 1 ON READER SERVICE CARD

ANALYTICAL CHEMISTRY, VOL. 61, NO. 18, SEPTEMBER 15, 1989 • 1017 A

Unlock Improved Performance and Value for Ion Chromatography

Simultaneous Analysis of Anions & Cations

6 Anions & 3 Cations

Temperature Control Eliminates Drift

0.25 μ S-cm

2 hours

PPB Detection of Anions

Inorganic Anions 50 PPB



ALLTECH

2051 Waukegan Rd • Deerfield, IL 60015
Phone: 312-948-8600

CIRCLE 5 ON READER SERVICE CARD

Good Laboratory Practices An Agrochemical Perspective

Requirements for good laboratory practices (GLP) are here to stay! This new book will teach you how to implement a GLP program that meets federal standards. You'll get an overview of good laboratory practices from EPA, academic, and industrial perspectives. You'll become more familiar with current practices, probable changes, what needs to be done, why, and how to do it. You'll read case histories from experts describing implementation of standards in their own laboratories. Also, you'll examine the nonscientific aspects of implementation, ranging from the role of management to financial considerations. With 19 chapters, this book provides a better understanding of GLP standards with regard to **compliance** **quality assurance** **standard operating procedures**. Also included is the text of the proposed FIFRA Generic Good Laboratory Practices Standards.

If you are a chemist, quality assurance manager, or are involved in the implementation of a GLP program, you'll find that *Good Laboratory Practices: An Agrochemical Perspective* is an excellent guide for conducting chemical studies that comply with GLP standards.

Willa Y. Garner, *Editor, U.S. Environmental Protection Agency*

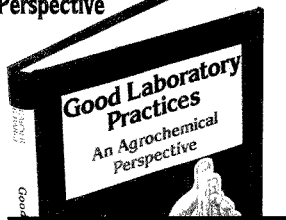
Maureen Barge, *Editor, FMC Corporation*

Developed from a symposium sponsored by the Division of Agrochemicals of the American Chemical Society

ACS Symposium Series No. 369 168 pages (1988) Clothbound
ISBN 0-8412-1480-8 LC 88-6330 US & Canada \$39.95 Export \$47.95

Order from: American Chemical Society, Distribution Office Dept. 87
1155 Sixteenth St., N.W., Washington, DC 20036

or CALL TOLL FREE **800-227-5558** and use your credit card!



BRIEFS

Correspondence

Exchange of Comments on Identification and Quantitation of Arsenic Species in a Dogfish Muscle Reference Material for Trace Elements 2116

Yasuyuki Shibata* and Masatoshi Morita, Chemistry and Physics Division, National Institute for Environmental Studies, 16-2 Onogawa, Tsukuba, Ibaraki 305, Japan and K.W.M. Siu*, R. E. Sturgeon, J. W. McLaren, and S. S. Berman, Division of Chemistry, National Research Council of Canada, Montreal Road, Ottawa, Ontario, Canada K1A 0R9

Complex Mixture Analysis Using Differential Gas Chromatographic Mass Spectrometry 2118

Amit Ghosh and Robert J. Anderegg*, Department of Chemistry, University of Maine, Orono, ME 04469

Technical Notes

Chiral Polysiloxanes Derived from (*R,R*)-Tartramide for the Gas Chromatographic Separation of Enantiomers 2121

Kouji Nakamura*, Tanabe Seiyaku, 16-89, Kashima 3-chome, Yodogawa-ku, Osaka 532, Japan and Shoji Hara and Yasuo Dobashi, Tokyo College of Pharmacy, 1432-1 Horinouchi, Hachioji, Tokyo 192-03, Japan

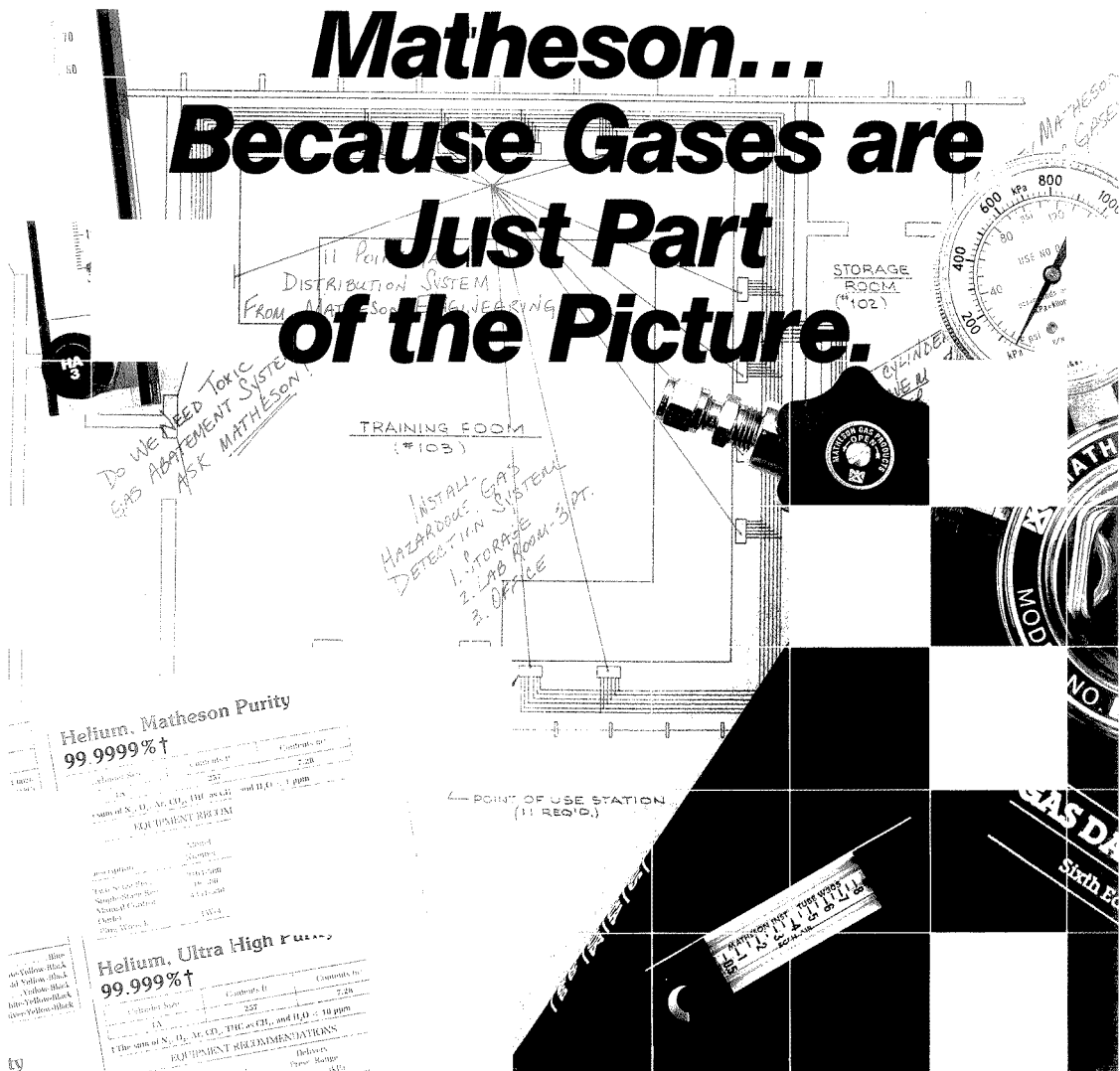
Fabrication and Characterization of Glassy Carbon Linear Array Electrode: 2124

L. Joseph Magee, Jr., and Janet Osteryoung*, Department of Chemistry, State University of New York at Buffalo, Buffalo, NY 14214

Tuning and Calibration in Thermospray Liquid Chromatography/Mass Spectrometry Using Trifluoroacetic Acid Cluster Ions 2126

Steven J. Stout* and Adrian R. daCunha, American Cyanamid Company, Agricultural Research Division, P.O. Box 400, Princeton, NJ 08540

Matheson... Because Gases are Just Part of the Picture.



You know Matheson as the pioneer in specialty gases; the reliable supplier of over 90 different gases in a variety of purities and sizes to suit your application.

But, did you know that Matheson offers you much more to meet today's laboratory requirements for increased efficiency and safety? Matheson engineers can provide you with gas distribution systems, hazardous gas detection instrumentation and toxic waste abatement systems customized to meet your lab's need.

Gases cannot be used alone. You need the right

Gas Distribution Systems,
select Reader Service No. 100
Toxic Waste Abatement,
select Reader Service No. 101

Gas Detection,
select Reader Service No. 102
Gases,
select Reader Service No. 103

regulators, flowmeters and other equipment to handle them properly. To select or install the right equipment to achieve maximum effectiveness, the exclusive full service back-up of Matheson is required.

Get the whole picture. Contact your Matheson office or use the Reader Service Numbers below.

Matheson®
Gas Products
World Leader in Specialty Gases & Equipment
30 Seaview Drive, Secaucus, NJ 07096-1587

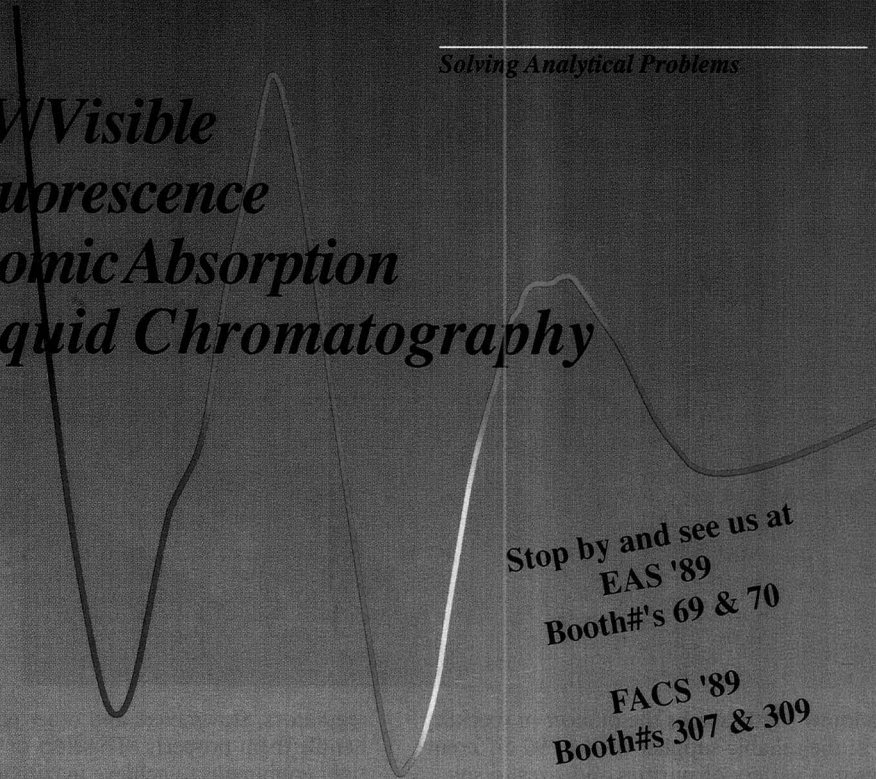
Regulators,
select Reader Service No. 104
Flowmeters,
select Reader Service No. 105

Gas Handling Equipment,
select Reader Service No. 106
Publications,
select Reader Service No. 107

**Put 80 Years of Experience
and 161,000 People
to Work for You.**

Solving Analytical Problems

*UV/Visible
Fluorescence
Atomic Absorption
Liquid Chromatography*



**Stop by and see us at
EAS '89
Booth#'s 69 & 70**

**FACS '89
Booth#s 307 & 309**

**See what our experience and resources can do for you.
Compare the value of our spectroscopy systems before
you purchase.**

Call us toll-free at 800-548-9001 or write:
Hitachi Instruments, Inc.
15 Miry Brook Road, Danbury CT 06810



Hitachi Instruments, Inc.

CIRCLE 63 ON READER SERVICE CARD

Instrumental Analysis Enhancement Program

The 1989-90 academic year is the seventh year that the Society for Analytical Chemists of Pittsburgh (SACP) has sponsored a program to provide copies of ANALYTICAL CHEMISTRY to undergraduate students enrolled in instrumental analysis courses in U.S. colleges and universities. This year 1133 subscriptions will go to 359 academic institutions participating in the Enhancement Program for Students in Instrumental Analysis Courses.

The subscriptions are intended to enrich course content and to encourage students to continue studying analytical chemistry at the graduate level. Professors participating in the program ensure that the issues are available to students in the laboratory, and some of them assign student projects based on the material in the JOURNAL. A guide is also provided that contains suggestions for the JOURNAL's use as a supplemental teaching tool.

The program begins this month and will continue through February. Originating at the Allerton Conference in 1981, the program was funded in its first year (1982) by the ACS Corporation Associates. Since 1983 the program has been partially supported by a \$5000 grant from SACP.

Pulsing for Power

By concentrating the output of a relatively low-energy chemical laser into a fast, tightly focused, repeating pulse of light, researchers at Los Alamos National Laboratory have been able to generate enough power to strip away eight of neon's 10 electrons. Eventually, this type of pulsed laser could become the basis for an even more powerful laboratory X-ray laser.

Two lasers capable of these fast pulses, named Bright Source I and II, are now in operation at Los Alamos. Bright Source I, which began operation about three years ago, is a KrF laser producing 248-nm light with an energy output of only 20 mJ. However, says Bright Source project director Gottfried Schappert, that output is squeezed into a 0.5-ps pulse focused onto just 5-10 μm^2 . This intensely

bright pulse of light corresponds to an irradiance of over 10^{17} W/cm². Furthermore, pulses can be repeated at a rate of up to 5 Hz.

Recently, a second Bright Source laser began operation (see photo). Costing \$2.5 million, this XeCl laser emits light at 308 nm and produces an energy output of about 300 mJ. Jamming that energy into a fast pulse increases the irradiance tenfold over Bright Source I. Eventually, says Schappert, Bright Source II could reach an output of 1 J, producing an irradiance of $\sim 10^{20}$ W/cm².

These high-power pulses can force an atom to absorb several hundred photons. To remove the eight Ne electrons, says Schappert, required ~ 1 kV of energy corresponding to 250 photons. In addition, Bright Source lasers can heat a target to temperatures high enough that the atoms produce X-rays. Although these X-rays are incoherent, they could, like a flashlamp in a ruby laser, pump an X-ray laser. Says Schappert, "Scientists, for a long time, have sought a laboratory X-ray laser that could unlock the mysteries of atomic structure similar to the way X-rays are now used in the medical field."

For Your Information

The Ronald Belcher Memorial Award provides a \$1000 travel grant to a promising analytical researcher 30 years of age or younger and who has no more than one year of post-doctoral experience. Applications are due December 31. More information is available from R. Chalmers, Department of Chemistry, University of Aberdeen, Old Aberdeen, Scotland, or James Winefordner, Department of Chemistry, University of Florida, Gainesville, FL 32611.

The National Science Foundation (NSF) is again requesting nominations of outstanding American researchers 35 or younger, or not more than 5 years beyond receipt of their Ph.D.s, for the **Alan T. Waterman Award**. Nominations, which must be received by December 31, should be sent to the Waterman Award Committee, NSF, 1800 G St., N.W., Room 545, Washington, DC 20550.

The 1988 American Type Culture Collection (ATCC) Fungi/Yeast Update lists 1150 new strains representing 600 species that have been added to ATCC's collection. For more information, contact ATCC/MKTING NR24, 12301 Parklawn Dr., Rockville, MD 20852.

Nippon Sanso K.K. has become the sole owner of Matheson Gas Products, the first commercial producer and supplier of specialty gases. The Japanese firm, which owned 50% of the company, acquired the remaining portion of Matheson from AmeriGas.

The National Institute of Standards and Technology (NIST) developed two new standards for the detection of **sulfur emission by pulp and paper industries**. Hydrogen sulfide in 5- and 20-ppm concentrations is available from Standard Reference Materials, NIST, B311 Chemistry Bldg., Gaithersburg, MD 20899 (301-975-6776).

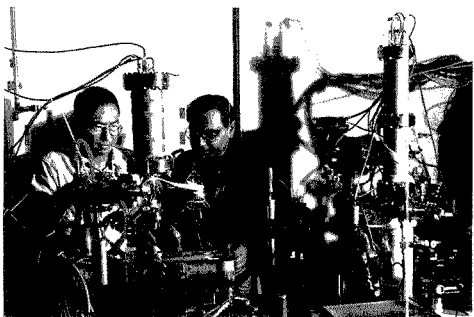
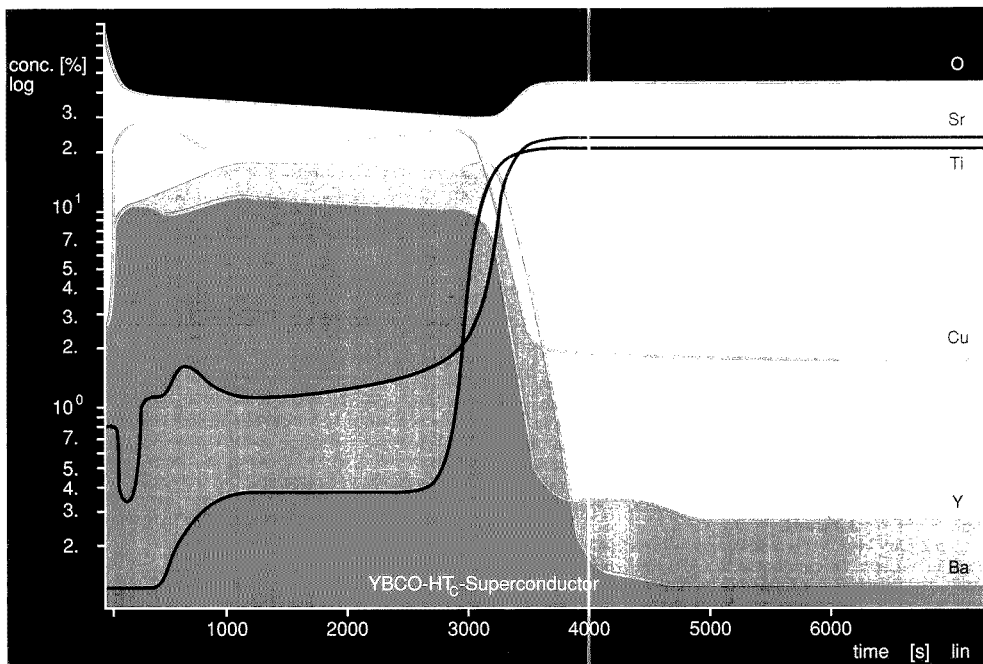
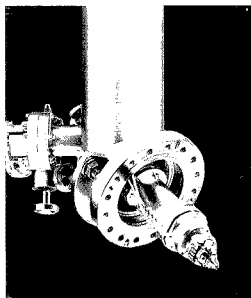


PHOTO COURTESY OF LOS ALAMOS NATIONAL LABORATORY

REVEALING THE TRUE CHARACTER...



Sputtered Neutrals Mass Spectrometry (SNMS) – a New Method for Quantitative Depth-Profile Analysis



Homogeneity and chemical composition of different layers determine the quality of the new high-temperature superconductors. Accurate quantification of each individual layer is crucial. One by one, atomic layers are stripped away by ion bombardment. The resultant neutral particles can then be analyzed by the SSM 200 detection system.

Only now is the true character revealed!

In other words, the depth profile. Quantitatively!

All made possible by the SSM 200, whose modular construction can be adapted to both Leybold surface analysis or any other UHV system.

Interested? Call: PA (412) 327-5700

■ LEYBOLD VACUUM PRODUCTS INC.
LAS GROUP
5700 Mellon Road, Export, PA 15632

■ LEYBOLD AG
Bonner Strasse 498 D-5000 Cologne 51



Innovative Vacuum Technology

CIRCLE 92 ON READER SERVICE CARD

A Degussa Company

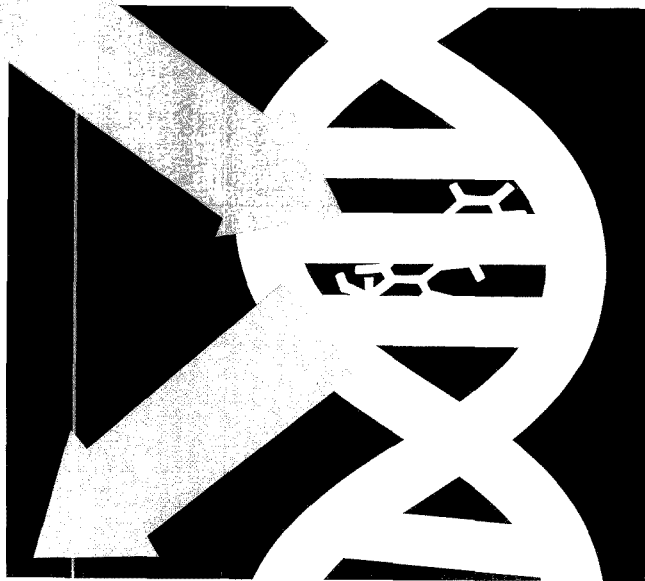
Fluorescence Line-Narrowing Spectroscopy

in the Study of Chemical Carcinogenesis

Ryszard Jankowiak and Gerald J. Small

Ames Laboratory—USDOE and Department of Chemistry
Iowa State University
Ames, IA 50011

Fluorescence line-narrowing spectroscopy (FLNS) is useful for obtaining high-resolution optical spectra of molecules or atomic ions imbedded in amorphous solids for which conventional low-temperature absorption spectra yield broad vibronic bands. The potential of FLNS as a direct analysis methodology was first explored in our laboratory for determination of polycyclic aromatic hydrocarbons (PAHs) in complex samples such as solvent-re-



REPORT

fined coal (1). This work yielded encouraging results, but we were also interested in biomolecular problems, which FLNS can solve more readily than other high-resolution techniques such as GC/MS. FLNS has been applied to a wide variety of biomolecules and biomolecular systems including photosynthetic pigments (2, 3), antenna protein-pigment complexes (4), and proteins (5). In this REPORT, we will discuss the principles and instrumentation involved in fluorescence line-narrowing spectroscopy and the application of FLNS to the study of cellular macromolecular damage and chemical carcinogenesis.

Principles of FLNS

In conventional low-temperature solid-state absorption spectra, the linewidth attributable to site heterogeneity, Γ_{inh} , is commonly referred to as inhomogeneous line broadening, whereas thermal broadening of a single vibronic transition is considered a homogeneous broadening mechanism. Because the homogeneous broadening contribution to the linewidth is approximately equal to kT , it can be effectively eliminated by a sufficient reduction in sample temperature. For example, the pure dephasing contribution from analyte-host interactions to Γ_{hom} is typically $< 0.1 \text{ cm}^{-1}$ at 4.2 K. Even at liquid helium temperatures, however, the band-broadening contribution of Γ_{inh} is still $\sim 300 \text{ cm}^{-1}$.

(For pure vibrational transitions, Γ_{inh} is reduced from this value by about 1 order of magnitude.) Figure 1 depicts the contributions from both homogeneous and inhomogeneous broadening. By definition, line-narrowing spectroscopies can "get under the skin" of the inhomogeneously broadened profile and, in the process, significantly reduce the inhomogeneous line-broadening contribution to the linewidth.

The extent to which broadening from Γ_{inh} can be "narrowed out" depends on the type of transition being probed and the state of the analyte initially prepared by the light field. If the inhomogeneous contributions to band broadening are much less than the homogeneous contributions, however, the inhomogeneous contributions are ef-

fectively eliminated.

FLNS is a relatively simple technique (6). In Figure 1, a narrow-frequency laser whose width, ω_L , is much less than Γ_{inh} excites only a narrow

isochromat (the signal from a small-volume element of the sample) of an inhomogeneously broadened absorption band associated with the fluorescent state (usually S_1). The sharp un-

derlying absorption profiles with width Γ_{hom} indicate the zero-phonon lines (ZPLs) of different analyte sites in the host. If the absorption corresponds to the origin, or (0,0) band, Γ_{hom} is $< 0.1 \text{ cm}^{-1}$ at 4 K for compounds that have moderately strong fluorescence. For analytical applications, $\Delta\omega_L$ need not be less than 1 cm^{-1} .

Initially the laser only excites the ZPLs of sites within the isochromat defined by the laser. At sufficiently low analyte concentrations ($< 10^{-3} \text{ M}$), intermolecular energy transfer—which can lead to site randomization—does not compete with fluorescence so that the fluorescence spectrum is a structured, line-narrowed array of ZPLs associated with the excited isochromat. For (0,0) band excitation the ZPLs correspond to transitions originating from the zero-point vibrational S_1 level and terminating at the zero-point and vibrational sublevels of S_0 . The former transition is of the resonant type degenerate with ω_L .

Although one could try to excite electronic states lying higher in energy than S_1 (e.g., S_2) to generate FLN spectra for the $S_1 \rightarrow S_0$ transition, this strategy would not be successful because the isochromat selected by the laser for the $S_2 \leftarrow S_0$ transition generally maps onto a broad "polychromat" of S_1 following internal conversion. That is, the site excitation energy distributions for $S_1 \leftarrow S_0$ transitions are not correlated. As shown in Figure 1, the FLN spectrum will shift as ω_L is tuned across the inhomogeneous profile.

Fortunately, the site excitation energy distributions of different vibrational levels of the S_1 state generally are highly correlated. This means that excitation of a vibronic band, (1,0), of S_1 can still yield an FLN spectrum that originates from the zero-point level of S_1 . The use of vibronic excitation offers several advantages over origin band excitation, including improved selectivity and the ability to determine both the ground- and excited-state vibrational frequencies of the chromophore. The improved selectivity is attributable to the vibronic features in the $S_1 \leftarrow S_0$ absorption spectrum, which are often more sensitive to structural perturbations than the $S_1 \rightarrow S_0$ fluorescence spectrum (7).

Figure 2 shows a vibronic excitation scheme in which ω_L excites two overlapping one-quantum vibronic transitions $(1_{\alpha,0})$ and $(1_{\beta,0})$, which will not be resolved in the absorption spectrum. The laser excites two different isochromats, one for α and one for β , and because of the correlation, the two isochromats undergo vibrational relaxation (wiggly arrows) to two different points in the zero-point distribution of

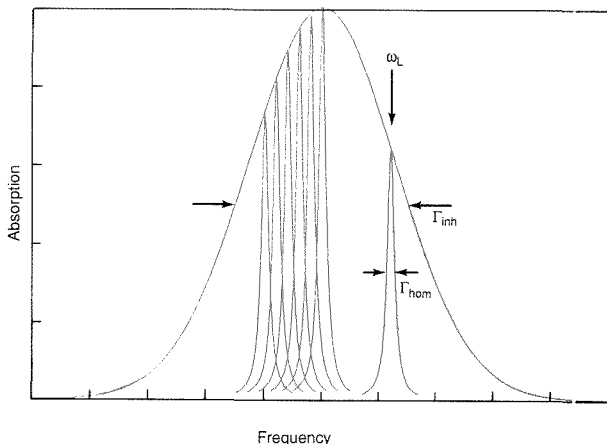


Figure 1. Schematic of an inhomogeneously broadened absorption profile of width Γ_{inh} in solid matrices.

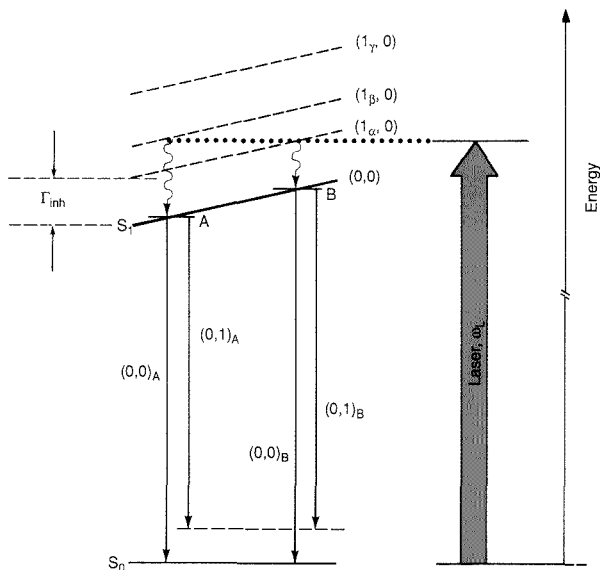



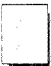
Figure 2. Schematic of laser site selection in FLNS.

The slope of excited-state levels represents the variation of their energies as a function of the site. Γ_{inh} denotes the inhomogeneous broadening of the (0,0) transition. Using the laser excitation, ω_L , two subsets of molecules within Γ_{inh} are selectively excited.

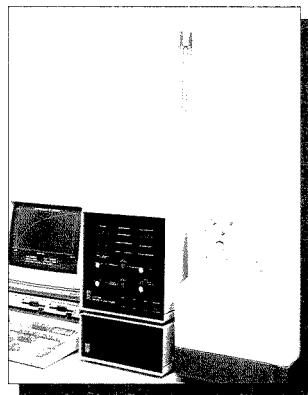
How to succeed in SFC without overspending

Here are two practical alternatives to spending \$30,000 to \$50,000 for a supercritical fluid chromatograph, and both use Isco lab-proven syringe pumps.

 Adapt your GC for SFC with programmable fluid delivery. An Isco SFC-500 pump with PC-based controller gives you pulseless flow, menu-driven software for pressure and density gradients, and unlimited method storage on computer disks. It installs as a "front end" on practically any GC, using the existing column oven and detector(s). And it offers a uniquely flexible way to apply SFC methodology to your difficult GC separations.

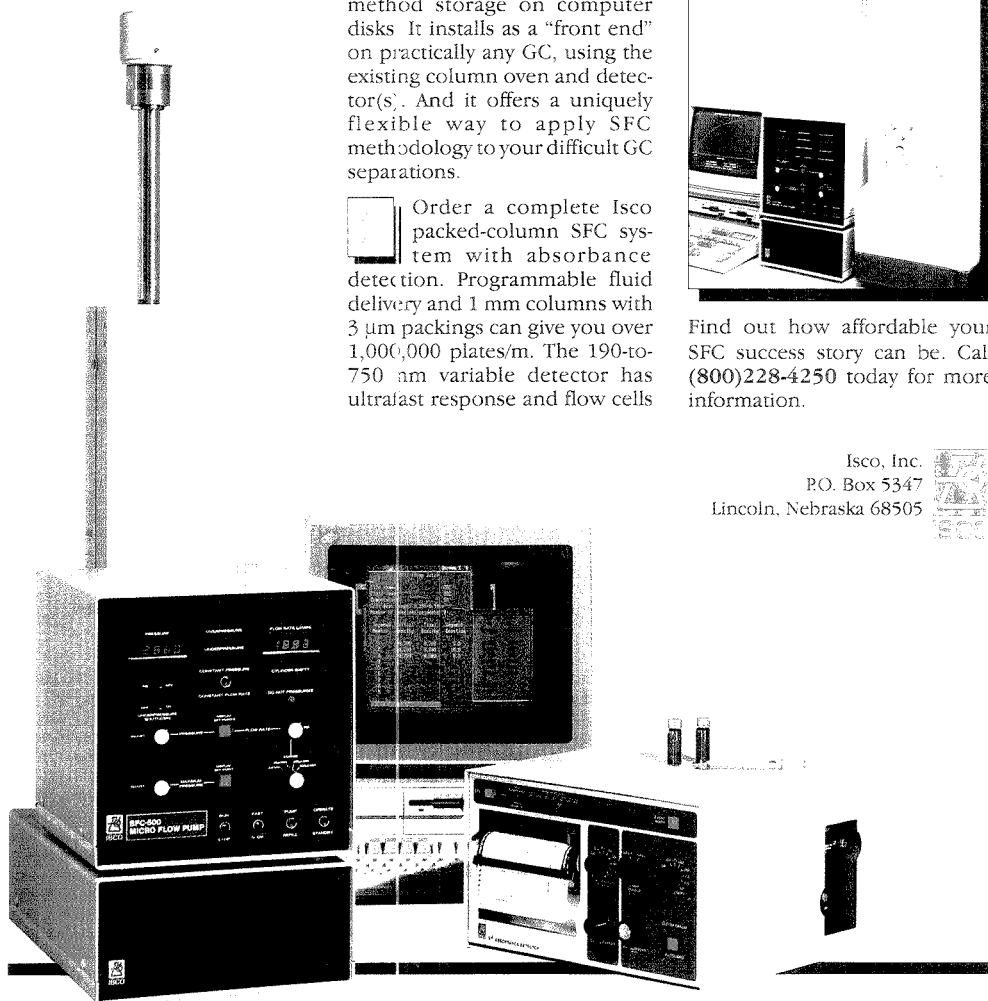
 Order a complete Isco packed-column SFC system with absorbance detection. Programmable fluid delivery and 1 mm columns with 3 μm packings can give you over 1,000,000 plates/m. The 190-to-750 nm variable detector has ultrafast response and flow cells

down to 0.12 μl to let you see your peaks as the column resolves them.



Find out how affordable your SFC success story can be. Call (800)228-4250 today for more information.

Isco, Inc.
P.O. Box 5347
Lincoln, Nebraska 68505



CIRCLE 77 ON READER SERVICE CARD

ANALYTICAL CHEMISTRY, VOL. 61, NO. 18, SEPTEMBER 15, 1989 • 1025 A

the S_1 state. Following population of the zero-point level, fluorescence occurs from these two energetically distinct transition isochromats and produces a "doubling" of every line in the FLN spectrum. The displacements between ω_L and the doublet components of the origin transition yield the excited-state vibrational frequencies $\omega_{\alpha'}$ and $\omega_{\beta'}$, and the displacements between the origin doublet and lower energy doublets in the FLN spectrum yield the ground-state frequencies ω_{α} and ω_{β} . By measuring the FLN spectrum as a function of ω_L located within the $S_1 \leftarrow S_0$ absorption spectrum one can, in principle, determine the frequencies of all modes active in the absorption spectrum. Each ω_L value yields a distinct fingerprint for the analyte, and the ω_L variable can be used to unravel spectral interferences for mixtures.

Instrumentation

The FLNS system employed in our laboratory (see Figure 3) was designed to provide a spectral resolution of $\sim 3 \text{ cm}^{-1}$ at 400 nm with photon-counting sensitivity. Because PAH metabolites and DNA adducts absorb in the 340–450-nm region, an excimer (XeCl gas) pumped dye laser with a 20-ns pulse width provides a convenient excitation source. Average power densities typically range from 5 to 100 mW/cm^2 at a pulse repetition rate of $\sim 30 \text{ Hz}$. A 1-m focal length McPherson 2061 monochromator ($f/10$) with a reciprocal linear dispersion of 0.42 nm/mm (2400 groove/mm grating) is used to disperse the fluorescence. Optimum resolution is determined by an intensified blue-enhanced gateable photodiode array (PDA). The PDA and monochromator provide a $\sim 7.0\text{-nm}$ segment of the fluorescence spectrum for a given monochromator setting. (For survey studies of uncharacterized samples, it is best to use a monochromator with higher reciprocal linear dispersion, which gives lower resolution. Fruitful studies could even be conducted at 77 K, followed by higher resolution studies at 4.2 K once a qualitative assessment of the types of fluorescent chromophores present has been made.) A double-nested glass liquid helium Dewar (with fused-quartz optical windows) was designed to eliminate liquid nitrogen from the optical pathways.

A glass-forming solvent of 50% glycerol, 40% water, and 10% ethanol by volume is most often employed for macromolecular DNA and globin adducts, nucleoside adducts, and the PAH metabolites themselves. Quartz tubing (3 mm o.d. \times 2 mm i.d. \times 1 cm) is used to contain the solvent ($\sim 30 \mu\text{L}$ total volume). For metabolites and ad-

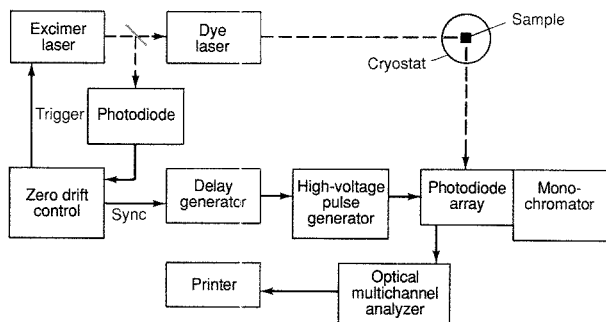


Figure 3. Block diagram of the F_{NS} instrumentation.

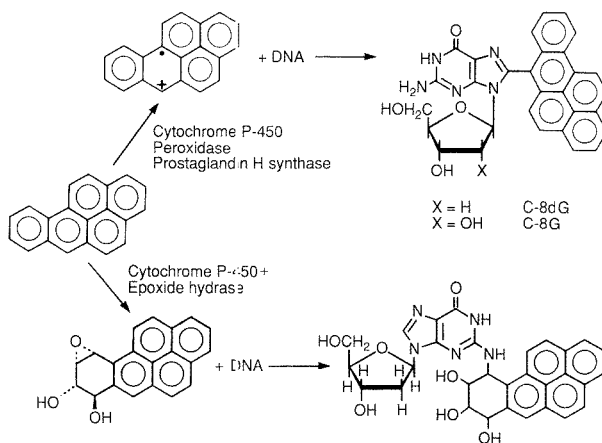


Figure 4. One-electron oxidation and mono-oxygenation in the metabolic activation of BP.

Two different types of adducts are formed with the DNA base guanine acting as the nucleophile.

ducts prone to facile photooxidation, the sample is subjected to several freeze-pump-thaw cycles and sealed under vacuum. Samples are held vertically by an aluminum sample holder designed to occlude laser light scatter from the sample tube edges. They can be cooled from 300 K to 4.2 K in about 2 min by direct immersion in boiling helium.

Mechanisms of carcinogenesis

Most carcinogens require metabolic activation; covalent binding of metabolites to DNA, RNA, and protein is generally believed to be the first critical step in the multistage process that leads to tumor formation (7, 8). PAHs

rank second to mycotoxin mold metabolites in carcinogenic potency (8). The principal events in chemical carcinogenesis are strongly influenced and often determined by host-dependent factors that may vary according to cell type, tissue, individual, strain, and species.

The current view for PAHs is that metabolic activation to electrophilic intermediates can occur by two pathways: mono-oxygenation to yield diol epoxides (9, 10) and one-electron oxidation to produce radical cations (11). Figure 4 shows these two pathways for benzo[*a*]pyrene (BP). The top of the figure shows a radical cation-type adduct in which BP is bound at its C-6

In Search of Mass Spectrometer Excellence?

ANNOUNCEMENT

**Kratos and Shimadzu
join forces.**

*A combination of skills that will
bring unprecedented technological
advancement and customer support.*

KRATOS/SHIMADZU HAS THE ANSWER!

If these are your mass spectrometer requirements, in a range of instrumentation from high resolution/high mass sector or time of flight (TOF) systems to dedicated bench top quadrupoles, Kratos/Shimadzu is your obvious choice.

For more information on the complete line of Kratos mass spectrometry systems, write or call us today.

 **KRATOS**
ANALYTICAL

U.K. Barton Dock Road, Urmston, Manchester M31 2LD. Tel: 061 865 4466. Fax: 668482.
Fax: 061 865 0707

U.S.A. 535 East Crescent Avenue, Ramsey, NJ 07446. Tel: (201) 825-7500. Fax: (201) 825-8659
West Germany, Karlsburgstrasse 6, D7500 Karlsruhe-41. Tel: (0721) 404091. Fax: 782-5928
Fax: 0721 404094

France, Les Bureaux de Sevres 72-78, Grande Rue 92310 Sevres. Tel: (1) 4 53 1010. Tx: 631606
Fax: (1) 4 534 0109

Netherlands, P.O. Box 16, 7750AA, Dalfen. Tel: (0) 5241-2780. Fax: (0) 5241-2753
Canada, 12 Bal Harbour Drive, Grimsby, Ontario L3M 4P7. Tel: (416) 945-9262

CIRCLE 88 ON READER SERVICE CARD

position to the C-8 of guanine. One-electron oxidation can occur through cellular peroxidases, prostaglandin H synthase, or cytochrome P-450 catalysis of the one-electron oxidation.

The microsomal enzyme systems present in cells (including cytochrome P-450 and aryl hydrocarbon hydroxylase) catalyze the monooxygenation of PAH to more water-soluble oxygenated derivatives. Arene oxides (epoxides) are the likely precursors of numerous PAH metabolites, including phenols, dihydrodiols, diol epoxides, tetrols, and conjugation products. Considerable support for this mechanism has come from the determination of the structure of a major adduct formed between BP and DNA in numerous *in vitro* and *in vivo* experiments. The structure of the adduct at the bottom of Figure 4 involves covalent binding of the (+) enantiomer of the metabolite *trans*-7,8-dihydroxy-*anti*-9,10-epoxy-7,8,9,10-tetrahydrobenzo[*a*]pyrene [(+)-*anti*-BPDE] through its 10-position to the exocyclic nitrogen (N-2) of guanine. The diol epoxide and radical

cation pathways for PAH lead to parent fluorescent chromophores that are distinctly different, such as the pyrene and BP derivatives in Figure 4.

Our understanding of the initial phases of chemical carcinogenesis has been hampered by the unavailability of practical high-resolution and sensitive bioanalytical techniques for the determination and characterization of both cellular macromolecular (i.e., intact DNA) adducts and nucleotide adducts. The problem is difficult; one needs to detect a DNA damage level of ~ 1 base pair in 10^8 in $\sim 100 \mu\text{g}$ of DNA for *in vivo* studies at a sufficiently good resolution to distinguish between structurally similar adducts. Distinction between stereoisomers of a given metabolite bound to a particular nucleic acid base is a good example of the necessary selectivity.

In vitro FLNS of DNA and nucleoside adducts

FLNS can be applied to macromolecular DNA, globin, and nucleoside adducts (6, 12, 13) and polar metabolites

(14). Figure 5 shows one of the first FLN spectra obtained for a macromolecular DNA-carcinogen adduct formed from a highly reactive diol epoxide of BP. The vibronic bands in the structured spectrum are limited to a width of 10 cm^{-1} by the monochromator. Prior to this work (14) it was not clear whether interactions between DNA and the fluorescent chromophore would render FLN inoperative, that is, produce a large homogeneous broadening that no amount of magic could circumvent.

The stereoisomers of BPDE exhibit remarkably different tumorigenic and mutagenic activities (15). Adduct formation with DNA appears to occur primarily at guanine, and the relative yields from the *anti*-BPDE and *syn*-BPDE isomers are dependent on the species under study (16, 17). In the *anti*-diastereomer (*anti*-BPDE) the benzylic hydroxyl group and the epoxide oxygen atom are on opposite faces of the molecule, whereas in the *syn*-isomer (*syn*-BPDE) these groups are on the same face. Because each diastereomer may exist as a pair of enantiomers, four stereoisomers of BPDE are possible (in Figure 4, the structure of (+)-*anti*-BPDE is shown).

FLN spectra for native DNA adducts derived from (+) and (-)-*anti*-BPDE and *syn*-BPDE (18) along with a spectrum of the tetraol of BPDE (BPT) are shown in Figure 6. (BPDE-DNA adducts are known to be unstable and dissociate to the tetraol, particularly in the presence of light.) These spectra were obtained using an excitation wavelength of 371.6 nm (vibronic excitation), and the bands in each spectrum represent the multiplet origin structure. Not only is the tetraol distinguished from the adducts; the adducts themselves can be distinguished primarily by vibronic intensity distributions.

Interpretation of the vibronically excited FLN spectra indicates that the S_1 state energy increases in going from the *syn*-BPDE adduct to the (-)-*anti*-BPDE to the (+)-*anti*-BPDE adduct to the tetraol. The ability of FLNS to resolve different stereoisomeric adducts appears to result from DNA-metabolite intermolecular interactions. Recent work in our laboratory (19) indicates that the spectra of (+)-*anti*-BPDE-DNA, (-)-*anti*-BPDE-DNA, and *syn*-BPDE-DNA correspond to the binding of the BPDE isomers to the N-2 of guanine and that a given BPDE stereoisomer can assume different binding configurations (20, 21). Thus "DNA host-engineered selectivity" has imparted a degree of resolution to FLNS that was not anticipated at the outset of our studies.

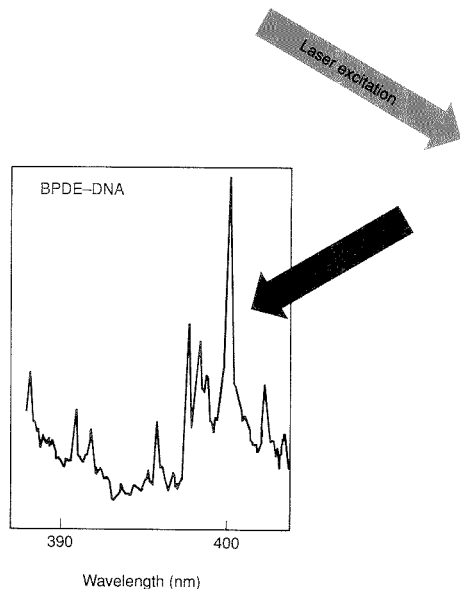


Figure 5. Schematic of the nucleotide adduct within the DNA macromolecule. Selective laser excitation leads to an FLN spectrum that represents a spectral "fingerprint" of the target molecule.

FLNS has also been used to determine five BP-nucleoside adducts synthesized by one-electron oxidation of BP in the presence of guanosine, deoxyguanosine, and deoxyadenosine (13). The results showed that a major depurination adduct from the binding of BP to DNA in rat liver nuclei is 7-(benzo[a]pyren-6-yl)guanine (N7Gua). Only 20 pg of the adduct was required, an amount that can be obtained from one rat, whereas analysis by the common method of collisionally activated decomposition MS would require sacrificing many rats.

FLNS analysis of in vivo DNA adducts

FLNS also can be used for in vivo studies. FLN spectra of (+)-*anti*-BPDE-DNA and *syn*-BPDE-DNA (Figure 7) have been used to identify the major diol epoxide adduct of fish liver DNA from English sole exposed to BP in laboratory-controlled experiments (22, 23). Of particular interest in this study

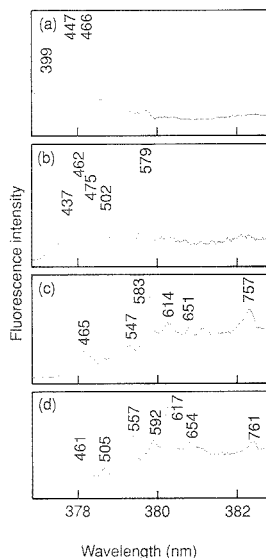


Figure 6. Comparison of the vibrationally excited FLN spectra for three different DNA adducts.

All spectra were obtained in the standard gly/H₂O glass at 4.2 K with an excitation wavelength of 371.6 nm. (a) Mixture of BPT and DNA at a concentration of 10⁻⁵ M, (b) (+)-*anti*-BPDE-DNA with 0.5% bases modified, (c) (-)-*anti*-BPDE-DNA with 1.5% bases modified, and (d) *syn*-BPDE-DNA at a concentration of ~1 adduct in 10⁷ bases. The peaks are labeled with their corresponding excited-state vibrational frequencies (in cm⁻¹).

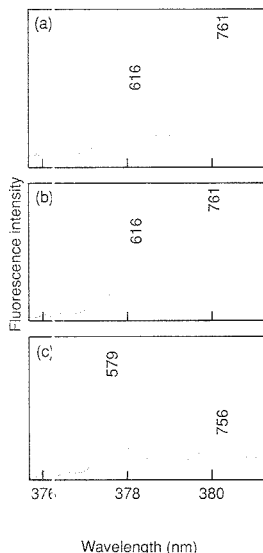


Figure 7. Comparison of the FLN spectrum of fish liver DNA (a) extracted from fish exposed to BP, (b) with standard FLN spectra of *syn*-BPDE-DNA, and (c) (+)-*anti*-BPDE-DNA.

The modification levels are ~1 adduct in 10⁷ bases, ~1 adduct in 10⁷ bases (determined radio-metrically) and ~1 adduct in ~200 bases, respectively.

was whether the expected N-2-deoxyguanosine (N-2-dG) adduct from (+)-*anti*-BPDE is formed. Despite the very low damage level of the DNA (~1 adduct in 10⁷ bases as determined by an independent method), the FLN spectrum exhibits a good signal-to-noise ratio. As expected, a major adduct is derived from BPDE, establishing the importance of the monooxygenation mechanism. However, comparison of the fish DNA spectrum with the FLN spectra of *syn*-BPDE and (+)-*anti*-BPDE-DNA shows that the adduct is not derived from (+)-*anti*-BPDE but from *syn*-BPDE.

Although the major adduct is derived from *syn*-BPDE, weaker contributions from (+)-*anti*- and (-)-*anti*-BPDE-DNA adducts cannot be excluded. Both *anti*- and *syn*-BPDE are strongly mutagenic in bacterial and mammalian cells, but *anti*-BPDE generally shows greater activity than *syn*-BPDE in most tests (24). Thus the high proportion of *syn*-BPDE-DNA adducts in English sole exposed to the high dosage of BP used in these experi-

Make

THE SOURCE
Your Source for STABLE ISOTOPES

Isotec Inc. offers the scientific community one of the world's largest selections of stable isotopes and labelled compounds

18
15
13
CD

- Amino Acids
- Fatty Acids
- Sugars
- Substrates (for breath tests and other metabolic studies)

You Get More From

THE SOURCE

- > 99% chemical purity
- High isotopic enrichment
- Competitive prices
- Fast delivery

Plus . . .

metal stable isotopes, helium-3 and other noble gas isotopes, other enriched stable isotopes, multiply-labelled compounds and custom synthesis

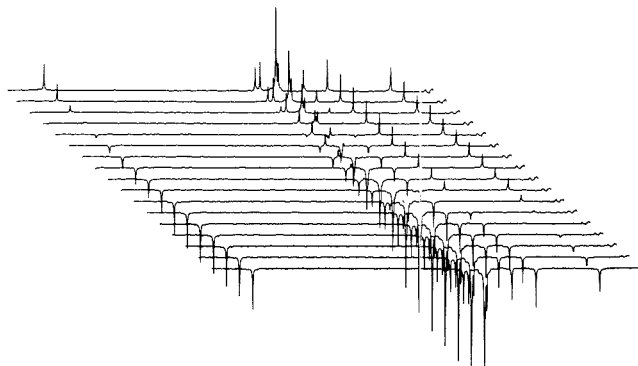
Call or write for your NEW complete price list today!

ISOTEC INC.
A Matheson, USA Company

3858 Benner Road, Miamisburg, OH 45342
(513) 859-1808 (800) 448-9760
Telex: 288278 Fax: (513) 859-4878

CIRCLE 75 ON READER SERVICE CARD

Search spectra online



C13-NMR/IR Now available on STN®

Now there's a new way to identify chemical substances online through their CNMR or IR spectra. Discover the Carbon 13 Nuclear Magnetic Resonance/Infrared file and see how invaluable it can be in your research!

The file and its sources

In C13-NMR/IR you'll find almost 120,000 spectra for 90,000 compounds. Data are drawn from significant journals, spectral catalogs, and unpublished spectra from BASF and other industrial labs.

The workshop Not familiar with searching spectra online? Our workshop shows

you how to

- find spectra by searching a substance name or molecular formula
- predict a C13 spectrum or shift
- find exact or similar structures
- find substances using CAS Registry Numbers

How to get started The C13-NMR/IR file is available only through the STN International network. If you're already an STN user, arrange access to C13-NMR/IR by calling Customer Service at 800-848-6538 or 614-447-3600. If you aren't yet using STN, return the enclosed coupon.

Yes! I'd like more information about C13-NMR/IR on STN International. Please rush me my FREE information package.

Name _____

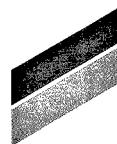
Organization _____

Address _____

Phone _____

Mail to: STN International, c/o Chemical Abstracts Service,
Dept. 38389, P.O. Box 3012, Columbus, OH 43210 U.S.A.

In Europe, contact STN International c/o FIZ Karlsruhe, P.O. Box 2465,
D-7500 Karlsruhe 1, Federal Republic of Germany. Telephone: (+49)
7247/808-555.



STN®
INTERNATIONAL
The Scientific & Technical
Information Network

STN is operated in North America by Chemical Abstracts Service, a division of the American Chemical Society; in Europe, by FIZ Karlsruhe; and in Japan, by JICST, the Japan Information Center of Science and Technology.

ments presents an interesting problem.

Similar results were obtained recently by Varanasi et al. (22) using ³²P post-labeling. They showed that whereas fish exposed to 2–15 mg BP/kg b.w. yielded mainly the *anti*-BPDE–DNA adduct, fish exposed to 100 mg BP/kg b.w. exhibited a dominant contribution from *syn*-BPDE–DNA adducts. Moreover, in rat dermal fibroblasts (16) the relative quantities of (+)-*anti*-BPDE–dG (~7%) have been much smaller than those determined in rabbit dermal fibroblasts (~90%). In rat dermal fibroblasts, *syn*-BPDE–dG represented more than 40% of the adducts, whereas in rabbit cells it accounted for only ~5%. Large quantities of *syn*-BPDE–DNA adducts were also observed in hamster epidermal cells (25). Given that the level of adduct formation and the relative amounts of different adducts appear to depend on the BP dosage level, FLNS should prove useful for a detailed study of this effect.

Future directions

Because it can provide high-resolution analyses of macromolecular adducts at the low concentration levels produced by *in vivo* exposure to genotoxic agents, FLNS should play an important role in future studies of the initial phases of chemical carcinogenesis as well as DNA repair mechanisms.

The versatility of FLNS is underscored by its application to nucleoside adducts both in glasses and sorbed on TLC plates (12). Because it is difficult to identify TLC spots from complex samples, and because the spots can diffuse and are likely to be heterogeneous, interfacing FLNS with the sensitive ³²P-postlabeling procedure (26) for detection of nucleotide adducts is potentially useful. It is important to analyze for both stable macromolecular adducts and depurinated adducts; one cannot assume that the DNA “nick” produced by depurination cannot produce miscoding or error-prone DNA repair.

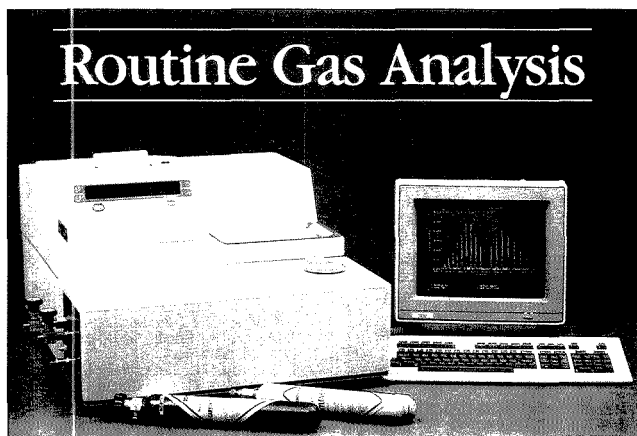
Another future avenue for FLNS is suggested by recent studies of globin–carcinogen adducts and by the apparent correlation of globin adduct levels with DNA adduct levels in target tissues (27). Because globin adducts are not subject to repair, and because greater amounts of globin than DNA are available from blood, FLNS of globin might be the basis for a practical and reliable body burden assessment methodology (28).

Recent 77 K selective laser-excited fluorescence studies of (+) and (–)-*anti*-BPDE–DNA and *syn*-BPDE–DNA have demonstrated that even non-line-narrowed spectra can be used

to distinguish between these adducts and to establish that a given stereoisomer can assume more than one DNA binding site (19). The use of fluorescence quenchers such as acrylamide allows classification of adduct sites as exterior or interior (quasi-intercalated) types. The combination of selectively laser-excited 77 K fluorescence spectroscopy and FLNS with molecular modeling and energy minimization calculations should enhance understand-

ing of the structure of DNA adduct sites as well as structure–DNA repair relationships.

Ames Laboratory is operated for the U.S. Department of Energy by Iowa State University under contract no. W-7405-Eng-82. This work was supported by the Office of Health and Environmental Research, Office of Energy Research. We are indebted to our collaborators A. M. Jeffrey (who sparked our interest in chemical carcinogenesis), U. Varanasi, N. E. Geacintov, E. L. Cavalieri, and E. G. Rogan, without whom the work described herein would not have been possible. The develop-



Routine Gas Analysis

Industrial Process Monitoring/ Ambient Air Monitoring/Quality Control

- Excellent sensitivity: ppb to % levels
- Multicomponent analysis
- Powerful quantitative software
- One-button operation!

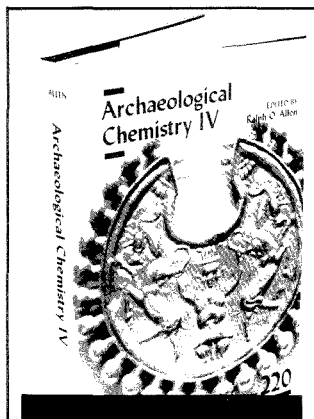
The new 8220 Gas Analyzer from Nicolet: A system versatile enough for wide-ranging applications, yet dedicated in design for easy operation by inexperienced operators. The 8220 is designed specifically for repetitive gas analysis applications where the speed, sensitivity, and specificity of FT-IR are required.

Nicolet

INSTRUMENTS OF DISCOVERY

5225-5 Verona Road / Madison, WI 53711 / (608) 271-3333

CIRCLE 112 ON READER SERVICE CARD



Archaeological Chemistry IV

Our knowledge of the past has been greatly enhanced by archaeological chemistry. Now you can learn more about this fascinating field—the applications and techniques used by chemists, new possibilities in determining age, authenticity, ancient diets, etc., analysis of inorganic and organic materials, and more in this exciting new volume.

Twenty-seven chapters examine the growing contributions that chemists and biochemists have made to the study of prehistoric materials in archaeological samples. Divided into five sections, the topics include:

- lithic and ceramic materials
- metals
- art objects
- organic materials
- fibers

New and existing techniques are provided including instrumental neutron activation analysis, trace element analysis, X-ray diffraction, IR microspectroscopy, carbon dating, radiocesium dating, electron spin resonance, monoclonal antibody formation, scanning electron microscopy, and photomicrography.

Separate chapters discuss the Shroud of Turin, composition of Nile sediments, classification of Mexican majolica ceramics, metals of the Mediterranean Bronze Age, composition of coins of the Roman Republic, the tomb of Neferfari, historical silk fabrics, and more.

Ralph O. Allen, *Editor*, University of Virginia
Developed from a symposium sponsored by the Division of the History of Chemistry of the American Chemical Society

ACS Advances Series No. 220
524 pages (1989) Clothbound
ISBN 0-8412-1449-2 LC 89-7953
US & Canada \$89.95 Export \$107.95

ORDER EXPORT

American Chemical Society
Distribution Office, Dept. 15
1155 Sixteenth St., N.W.
Washington, DC 20036

or CALL TOLL FREE

800-227-5558

(in Washington, D.C. 872-4363) and use your credit card!

ment of FLNS as an analytical tool owes much to previous members of the group: J. C. Brown, M. J. Sanders, M. McGlade, I. Chiang, R. S. Cooper, and D. Zamzow.

References

- (1) Brown, J. C.; Duncanson, J. A., Jr.; Small, G. J. *Anal. Chem.* 1980, 52, 1711-15.
- (2) Renge, I.; Mauring, K.; Sarv, P.; Avarmaa, R. *J. Phys. Chem.* 1986, 90, 8611-16.
- (3) Fünfschilling, J.; Walz, D. *Photochem. Photobiol.* 1983, 38, 389-93.
- (4) Avarmaa, R.; Renge, I.; Mauring, K. *FEBS Lett.* 1984, 167, 186-90.
- (5) Koloczek, H.; Fidy, J.; Vanderkooi, J. R. *J. Chem. Phys.* 1987, 87, 4388-94.
- (6) Jankowiak, R.; Cooper, R. S.; Zamzow, D.; Small, G. J.; Duskocil, G.; Jeffrey, A. M. *Chem. Res. Toxicol.* 1988, 1, 60-68.
- (7) Miller, E. C.; Miller, J. A. *Cancer* 1981, 47, 2327-45.
- (8) *World Health Organization Monograph on the Evaluation of the Carcinogenic Risks of the Chemical to Man: Polynuclear Aromatic Compounds*; International Agency for Research in Cancer, World Health Organization: Lyon, France, 1983; Vol. 32.
- (9) Harvey, R. G.; Geacintov, N. E. *Acc. Chem. Res.* 1988, 21, 66-71.
- (10) Jeffrey, A. M. In *Polycyclic Hydrocarbons and Carcinogenesis*; Harvey, R. G., Ed.; American Chemical Society: Washington, DC, 1985; Chapter 8.
- (11) Cavaliere, E.; Rogan, E. *Environ. Health Perspect.* 1985, 64, 69-84.
- (12) Cooper, R. S.; Jankowiak, R.; Hayes, J. M.; Lu, P.; Small, G. J. *Ancl. Chem.* 1988, 60, 2692-94.
- (13) Zamzow, D.; Jankowiak, R.; Cooper, R. S.; Small, G. J.; Tibbels, S. R.; Cremonosi, P.; Devanesan, P.; Rogin, E. G.; Cavaliere, E. L. *Chem. Res. Toxicol.* 1989, 2, 29-34.
- (14) Sanders, M. J.; Cooper, R. S.; Jankowiak, R.; Small, G. J.; Heisig, V.; Jeffrey, A. M. *Anal. Chem.* 1986, 58, 816-20.
- (15) Slaga, T. J.; Bracken, W. J.; Gleason, G.; Levin, W.; Yagi, H.; Jerina, D. M.; Conney, A. H. *Cancer Res.* 1979, 39, 67-71.
- (16) Alexandrov, K.; Sala, M.; Rejas, M. *Cancer Res.* 1988, 48, 7132-39.
- (17) Moore, C. J.; Pruess-Schwartz, D.; Mauthe, R. J.; Gould, M. N.; Baird, W. M. *Cancer Res.* 1987, 47, 4402-06.
- (18) Zinger, D.; Geacintov, N. E.; Harvey, R. G. *Biophys. Chem.* 1987, 27, 31-38.
- (19) Jankowiak, R.; Lu, P.; Small, G. J.; Geacintov, N. E., submitted for publication in *Chem. Res. Toxicol.*
- (20) Kim, S. K.; Brenner, H. C.; Soh, B. J.; Geacintov, N. E. *Photochem. Photobiol.*, in press.
- (21) Kim, S. K.; Geacintov, N. E.; Brenner, H. C.; Harvey, R. G. *Carcinogenesis*, in press.
- (22) Varanasi, U.; Reichert, W. L.; Le Eberhart, B. T.; Stein, J. E. *Chem. Biol. Interact.*, in press.
- (23) Jankowiak, R.; Lu, P.; Nashimoto, M.; Varanasi, U.; Small, G. J., unpublished work.
- (24) Newbold, R. F.; Brooks, P. *Nature (London)* 1976, 261, 53-55.
- (25) DiGiovanni, J.; Sina, J. F.; Ashurst, S. W.; Singer, J. M.; Diamond, L. *Cancer Res.* 1983, 43, 163-70.
- (26) Randerath, K.; Randerath, E.; Agrawal, H. D.; Gupta, R. C.; Schurdik, M. E.; Reddy, M. V. *Environ. Health Perspect.* 1985, 62, 57-65.
- (27) Wogan, G. N. In *Methods for Detect-*

ing DNA Damaging Agents in Humans: Application in Cancer Epidemiology and Prevention; Bartsch, H.; Hemminki, K., Eds.; IARC Scientific Publications: Lyon, France, 1988; pp. 32-51.

(28) Weston, A.; Willey, J. C.; Manchester, D. K.; Wilson, V. L.; Brooks, B. R.; Choi, J.-S.; Poirier, M. C.; Trivers, G. E.; Newman, M. J.; Mann, D. L.; Harris, C. C. In *Methods for Detecting DNA Damaging Agents in Humans: Application in Cancer Epidemiology and Prevention*; Bartsch, H.; Hemminki, K., Eds.; IARC Scientific Publications: Lyon, France, 1988; pp. 181-89.



Gerald J. Small is professor of chemistry at Iowa State University and senior chemist at Ames Laboratory—USDOE. He received his Ph.D. in physical chemistry from the University of Pennsylvania in 1967. Following a two-year appointment as a research fellow at the Australian National University, he joined the faculty of ISU in 1969. His research interests include molecular electronic spectroscopy, linear and nonlinear laser spectroscopies, energy and electron transfer in photosynthesis, carcinogen metabolism and cellular macromolecular damage, and structural disorder and tunneling in amorphous solids.



Ryszard Jankowiak is an associate scientist at Ames Laboratory—USDOE. He received his Ph.D. in physics from the Technical University in Gdansk (Poland) in 1981 and was a research associate and visiting scientist at the Philipps University in Marburg (West Germany) from 1981 to 1985. His research interests include molecular electronic spectroscopy, laser bioanalytical spectroscopy, chemical carcinogenesis, photosynthesis, and structural disorder and tunneling in amorphous solids at very low temperatures.

NEED AN ARTICLE FROM AN EARLIER ISSUE?

GET IT FROM CAS DOCUMENT DELIVERY SERVICE®

Does your research depend on locating an article published in this journal a few years back? The CAS Document Delivery Service can provide copies of articles from **all ACS journals from initial publication to the present.**

You'll also find CAS DDS an excellent source for documents related to chemistry and allied disciplines drawn from **the more than 10,000 scientific and technical publications received at Chemical Abstracts Service each year.**

Order articles, patents, and reports back to

1975 (1970 for Soviet material). Most orders are on their way within 24 hours. Call for more information. Ask about our FREE 1989 Directory of Publications.

Chemical Abstracts Service®
2540 Olentangy River Road
P.O. Box 3012
Columbus, OH 43210

Phone: (toll-free) 800-848-6538, ext. 3670
or 614-447-3670

Chemical Abstracts Service is a division of the American Chemical Society.

NO ONE UNDERSTANDS PARTICLE SIZING BETTER THAN MALVERN

Nearly twenty years' experience of photon correlation spectroscopy (PCS) and particle sizing has given Malvern an unrivalled understanding of the technology and of the needs of colloid and particle scientists. The AutoSizer IIc and SYSTEM 4700c are designed to meet these needs.

The AutoSizer IIc with its clear and simple operation and Malvern's most advanced software is ideal for routine particle sizing from 3 nanometres to 3 microns.

SYSTEM 4700c is designed for research applications in

PCS or total intensity light scattering including particle sizing, molecular weight determination and particle dynamics studies. Both incorporate Malvern's advanced SERIES 7032 Multi-8 correlators with up to 264 channels and eight separate sample times (SYSTEM 4700c).

We would like to tell you more about the system that's right for you. Please contact us now with details of your current or proposed application.



MALVERN

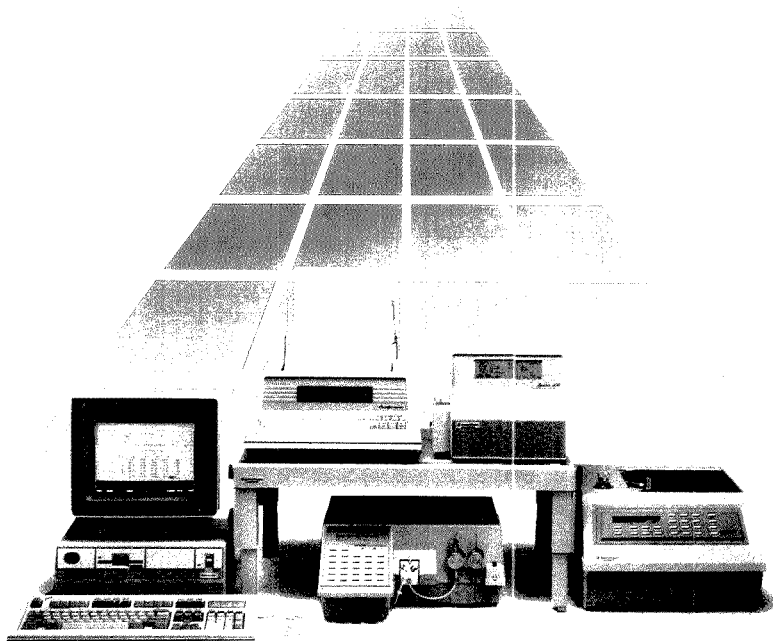
Malvern Instruments, Inc.,
10 Southville Road, Southborough, MA 01772.
Telephone: (508) 430 0200 Telex: 311397 Fax: (508) 460 9692

U.K. Malvern Instruments Ltd., Spring Lane South, Malvern, Worcestershire WR14 1AQ.
Telephone: (0684) 892456 Telex: 339679 MALINS G Fax: (0684) 892789

W. Germany Mitek GmbH, Arzbergerstrasse 10, D-8036 Herrsching.
Telephone: 08152 2046 Telex: 5270249 Fax: 08152 4374

CIRCLE 96 ON READER SERVICE CARD

SPECTRA-PHYSICS LC SYSTEMS 5 YEARS AHEAD!



Guaranteed Performance.

A Spectra-Physics LC System is guaranteed to meet the needs of any laboratory, either research and development or quality control.

Whether you're performing pharmaceutical analysis, peptide mapping or gel permeation chromatography, our LC systems are designed to provide unsurpassed performance.



Reliability.

It's easy to say our instruments and systems are reliable, but we back up our reliability claims with the industry's only 5-year warranty.

Not just a warranty on selected components, but a full 5-year warranty covering the entire LC System.

If your lab is ready now for a high-performance, highly reliable LC system, call Spectra-Physics toll-free (800) 424-7666.

 **Spectra-Physics**

Discover the Quality

CIRCLE 150 FOR SALES REPRESENTATIVE. CIRCLE 151 FOR INFORMATION.

Chromatography, Spectroscopy, Electrochemistry, and Chemometrics

Electroanalytical Chemistry, Vol. 15: A Series of Advances. Allen J. Bard, Ed. xii + 376 pp. Marcel Dekker, 270 Madison Ave., New York, NY 10016. 1989. \$110

Reviewed by Alanah Fitch, Department of Chemistry, Loyola University of Chicago, 6525 N. Sheridan Rd., Chicago, IL 60626

Electroanalytical Chemistry, Vol. 15, contains reviews in three areas of current interest in electrochemistry.

The chapter by H.H.J. Girault and D. J. Schiffrin, "The Electrochemistry of Liquid-Liquid Interfaces," includes a historical section, a section on terms and definitions, and several sections devoted to current research being performed at various types of liquid-liquid interfaces. This area is of importance for the understanding of basic electrochemical processes and as a model for transport across biological membranes. The interrelationships between energy terms derived from different theoretical models and the interrelationships between those terms and measured parameters are not well described for a general electrochemical audience. As a consequence, the discussion of current research is not likely to be well understood by the general electrochemical audience. However, the scope of literature surveyed should allow the interested reader to consult the original material. One area not addressed is the applicability of data obtained at the liquid-liquid interface to the problems of charge transport at the interface between a modified electrode surface and a bulk solution.

The chapter by S. Gottesfeld, "Ellipsometry: Principles and Recent Applications in Electrochemistry," is beautifully written and of exceptional clarity. The author gives enough background information on specular reflection of light from the solid-electrolyte interface to allow the general electrochemical reader to knowledgeably read the synopsis of recent research. Ample and repetitive references to more detailed

sources are given. Following this background, the author devotes a section to helping the reader develop an intuitive feel for the format of the ellipsometric data. Both the power and weaknesses of ellipsometry are evenly addressed, and a lucid discussion of results that have been obtained at submonolayer, monolayer, and thick-film electrodes is included. This review is an excellent introduction to the field as well as a good source of literature references.

The chapter by R. M. Wightman and D. O. Wipf, "Voltammetry at Ultramicroelectrodes," is well written. Introductory material is heavy on the solution of the diffusion equations that are necessary for understanding the unique behavior of ultramicroelectrodes. This detail, of interest to the electrochemist, may discourage a less electrochemically informed reader. Particularly useful are the sections summarizing the applications of ultramicroelectrodes and a final, detailed, step-by-step, experimental section describing the creation of an ultramicroelectrode and the measurement of the associated nanoampere currents. These final two sections together constitute a recipe for starting research in this rapidly growing field.

Chemometrics: A Textbook. D. L. Massart, E.G.M. Vandeginste, S. N. Deming, Y. Michotte, and L. Kaufman. 464 pp. Elsevier Science Publishing, 52 Vanderbilt Ave., New York, NY 10017-3872. 1988. \$92

Reviewed by Gary W. Small, Department of Chemistry, University of Iowa, Iowa City, IA 52242

The increased availability of laboratory computers has motivated many chemists to learn to use computer-based data analysis techniques. The interdisciplinary nature of data analysis has always been a barrier to efficient learning, however. For most chemists, there is simply not enough time to master the language of the statistics or elec-

trical engineering literature for the purpose of learning how to apply a given data analysis procedure. There have been few truly usable sources to which a chemist could turn to learn state-of-the-art techniques in data analysis.

This problem has been addressed in recent years through the realization that, in itself, data analysis is an essential branch of analytical chemistry. The popular umbrella term for this field is "chemometrics," and a growing literature is developing that is dedicated to this discipline. Massart and coauthors have contributed significantly to this literature by writing a textbook that an analytical chemist can use to sample the available techniques in data analysis.

The strength of the book is its point of view. It is written by a group of analytical chemists and is designed to be read by analytical chemists. Written as a tutorial, the first third of the book is organized around familiar analytical concepts (e.g., precision and accuracy, calibration, sensitivity, and limit of detection). The focus of this discussion is the manner in which statistical techniques address these analytical concepts. This section of the work lays the theoretical foundation for the rest of the book. The latter two-thirds of the material focus on more advanced concepts such as signal-processing techniques, experimental design and numerical optimization, and the analysis of multivariate data by pattern recognition and principal components analysis. The final four chapters address the growth in importance of process analytical chemistry by introducing the concepts of operations research, decision making, and process control.

For the most part, the writing is lucid and the order of presentation logical. The mathematical notation is as consistent as possible, given the breadth of material presented. Numerous examples are cited throughout the book. Taken mostly from the analytical chemistry literature, these examples are extremely effective in helping to illustrate the data analysis or data-pro-

cessing techniques described in the text. The book is suitable as a text for a graduate-level course in chemical data analysis. A background in mathematics and statistics commensurate with an undergraduate chemistry degree should be sufficient to allow an interested reader to use the book effectively.

In selecting the specific topics to be discussed in the text, the authors faced an impossible dilemma—breadth of topics covered versus the level of detail provided for each topic. The principal criterion used in the selection of topics appears to have been relevance to common analytical applications. One can quibble about some of the specific choices and about the relative emphasis of some of the topics, but overall the authors are to be commended for producing a book that introduces a varied

“Massart and coauthors have undertaken a difficult task and have produced a solid and useful addition to the chemometrics literature.”

selection of data analysis techniques that can be applied to common chemical problems.

For the most part, the choice of topics reflects those techniques in common use. Two omissions that perhaps should have been included are robust regression methods and Kalman filtering. Notably, however, methods not used often enough—such as those from nonparametric statistics—are described effectively. To their credit, the authors have included a well-chosen selection of references to provide the reader with additional sources for most of the major topics covered. In cases in which a variety of possible techniques are available for a given application, the authors provide some qualitative recommendations. Although the specialist may disagree slightly with some of the recommendations, they reflect the authors' experiences and thus serve a useful tutorial function.

Massart and coauthors have undertaken a difficult task and have produced a solid and useful addition to the chemometrics literature. The book is highly recommended to the analytical chemist seeking an overview of available techniques in data analysis.

Two-Dimensional NMR Methods for Establishing Molecular Connectivity. Gary E. Martin and Andrew S. Zektzer. 508 pp. VCH Publishers, Suite 909, 220 East 23rd St., New York, NY 10010-4606. 1988. \$59

Reviewed by Martha Bruch, University of Texas, Southwestern Medical Center, Department of Pharmacology, 5323 Harry Hines Blvd., Dallas, TX 75235

This well-written book is a comprehensive guide to the maze of two-dimensional (2D) correlated experiments available for establishing molecular connectivity via scalar coupling. The first chapter is a good, thorough introduction to the general concepts and considerations associated with 2D NMR spectroscopy. This introduction is followed by discussions of techniques for establishing proton-proton connectivity (Chapter 2) and ^{13}C - ^1H connectivity (Chapter 3) via homonuclear and heteronuclear scalar coupling. These chapters are followed by descriptions of homonuclear and heteronuclear relayed coherence transfer experiments in Chapter 4. Techniques for obtaining ^{13}C - ^{13}C connectivity via multiple quantum coherence transfer are considered in Chapter 5.

For each of the experiments considered in Chapters 2-5, the pulse sequence is listed explicitly along with the appropriate phase cycling, and this makes each experiment easy to understand and implement. Examples are given for most experiments, and the use of the same compound (e.g., strychnine) as an example for many different experiments facilitates direct comparison between these experiments and aids in overall comprehension of the various techniques. However, more diversity in the choice of examples, which often involve polynuclear aromatic compounds, would be desirable. The final two chapters, which contain application problems as well as solutions to these problems, make this book quite instructive for the novice and set it apart from other books in this field.

Although there are few errors overall, some crucial concepts are given only cursory treatment by the authors and this could confuse the uninitiated reader. For instance, the authors do not devote sufficient space to the important distinction between phase-sensitive and absolute-value spectra, although both types of data are presented. Also, the authors spend little time considering the very real problem of signal loss attributable to spin-spin relaxation during the evolution period, which is particularly problematic for

analysis of macromolecules.

Overall, the content and organization are quite good. The authors should be commended for the thoroughness of their discussion of 2D correlated spectroscopy; every variation reported in the literature is included. However, in the case of ^{13}C - ^1H correlated spectroscopy, less space should have been devoted to the conventional form (heteronucleus detected) of these experiments, and more space devoted to the more sensitive, proton-detected, form of these experiments. Another problem area is the sections on data processing that are included with the description of each experiment. These discussions tend to be incomplete and redundant and should have been included in a more general section on processing of 2D data. By far the biggest disappointment is the absence of a section on the use of the nuclear Overhauser effect (NOE) to establish molecular connectivity since 2D-NOE experiments are typically used in conjunction with 2D correlated experiments to make line assignments. Nevertheless, this book should be quite useful for the organic chemist and is a good guide for any chemist interested in the application of 2D NMR spectroscopy for structural analysis.

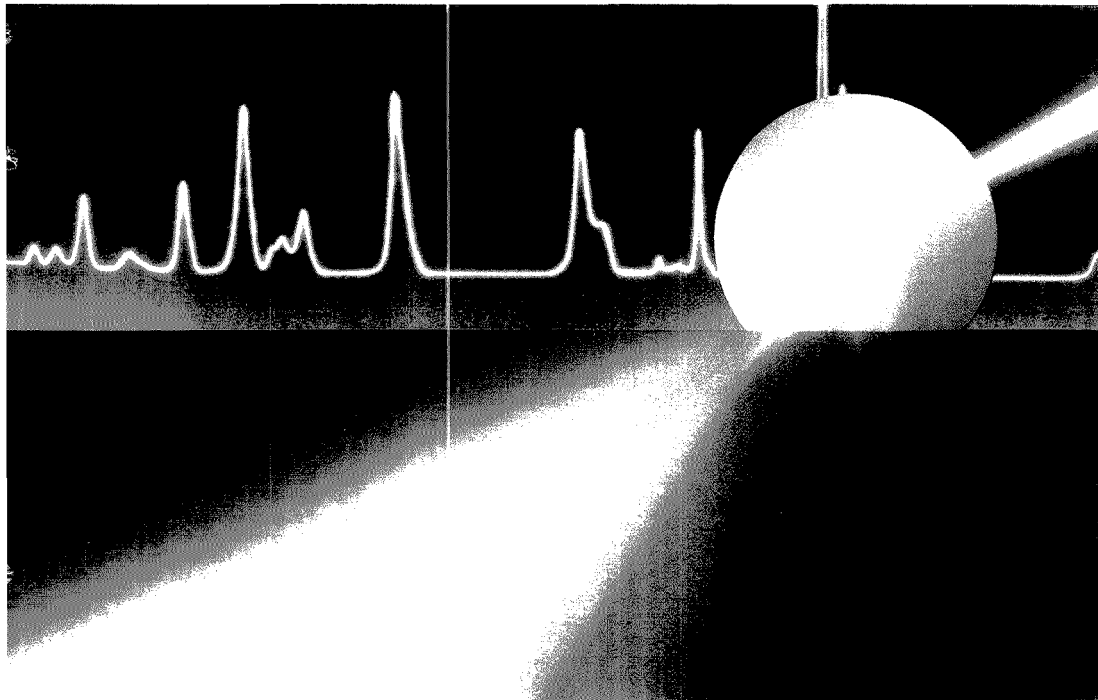
Techniques of Chemistry, Vol. 20: Techniques for the Study of Ion-Molecule Reactions. James M. Farrar and William H. Saunders, Jr., Eds. xiv + 652 pp. John Wiley & Sons, 605 Third Ave., New York, NY 10158. 1988. \$100

Reviewed by Maurice M. Bursley, Department of Chemistry, CB#3290, Venable Hall, The University of North Carolina at Chapel Hill, Chapel Hill, NC 27599-3290

This book, containing 11 chapters, continues a long-standing series. The first several chapters discuss methods for acquiring data on bulk properties, and the remaining chapters review methods for microscopic information. Each chapter is written by a specialist or specialists.

Although many of the topics deal with fundamentals studied on instruments whose general utility has not yet been made apparent to the instrument manufacturers, their potential for analytical use is high. The chapters that deal with techniques that can be performed on commercial instruments (likely to be of interest to a broad audience) are well written and thorough. Specialists will note that the coverage of the book is not universal, but the principal methods are there. This book

UV/VIS at its best – from the world leader. Perkin-Elmer.



Only Perkin-Elmer — the world leader in UV/VIS spectroscopy — gives you price/performance at its best. The Lambda 6 UV/VIS System blends exceptional value, performance, and flexibility into one affordable system.

PERFORMANCE AT ITS BEST

Only the Lambda 6 System delivers proven performance at such an attractive price. Double-beam design, low stray light, and low noise guarantee accurate spectroscopic results for quantitative, multiwavelength, and kinetic analyses.

SOFTWARE AT ITS BEST

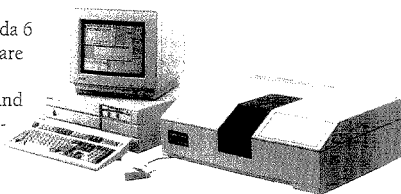
Our new UV Data Manager software is graphically oriented with pull-down menus, windows, an extensive HELP feature, and a mouse pointing device. It puts you in complete command of the instrument, accessories, and data processing routines without being a PC expert.

VERSATILITY AT ITS BEST

With the PC-controlled Lambda 6 System, data handling capabilities are never limited. Data can be quickly exported to third-party software. And with our powerful OBEY macrolanguage, you can write custom programs tailored to your lab needs.

FREE VIDEO OFFER

Send now for your free Lambda 6 System video — UV/VIS at its best. For more information and a free video, call 1-800-762-4000 or write Perkin-Elmer Corp., 761 Main Ave., Norwalk, CT 06859-0012 USA.



PERKIN ELMER

CIRCLE 127 ON READER SERVICE CARD

is a good resource for gaining a solid background in these basic methods. References on the hotter topics include some in 1987, whereas the more introductory chapters do not have much past the early 1980s, but that is not a flaw.

Ion-molecule reactions have a halolved place in analytical MS, and we are now at the 20th anniversary of the publication of the CI technique. Even the broader techniques discussed in the earlier chapters of this book, however, have barely been tapped for their analytical potential. Discussions of the more specific techniques could strike a creative spark in the analytical chemist, for the application of these techniques, in some cases, has not yet begun.

Some of the breadth of thought is mirrored in the rather different styles in which different chapters have been written. The editors have preserved such differences while maintaining evenness, so that the volume is generally uniform. More importantly, it is remarkably clear. It also seems free of distracting typographical errors.

The creative mass spectrometrists ought to have this book on the laboratory shelf. Period. It is that impressive.

Practical HPLC Method Development.

Lloyd R. Snyder, Joseph L. Glajch, and Joseph J. Kirkland. xvi + 260 pp. John Wiley & Sons, 605 Third Ave., New York, NY 10158. 1988. \$45

Reviewed by Joe P. Foley, Department of Chemistry, Louisiana State University, Baton Rouge, LA 70803-1804

This book addresses one of the most time-consuming aspects of an HPLC separation: method development. As the title implies, the authors' primary objective is to provide a practical approach to this subject. Much to their credit, I found their approach not only very practical but also logical, systematic, and efficient.

HPLC method development is obviously a very broad subject and thus is a challenging one to cover in a single book of any size. To meet this challenge, the authors assumed that the reader is reasonably familiar with the basics of HPLC. They also directed most of their attention to the "reversed-phase separations of small molecules" while providing adequate coverage (based on present usage) of the normal phase and ion-pairing separation modes. Brief discussions of ion exchange, size exclusion, and chiral separations are presented in a single chapter. Subjects completely excluded from the present volume are sample pre-

treatment, hydrophobic interaction chromatography, and general separations of biological samples (peptides, proteins, nucleic acids, etc.), although the latter topic is planned for a later edition after a "unified scheme" becomes feasible.

The book that resulted consists of nine chapters, a three-page glossary of symbols and terms, and an eight-page subject index. Chapter 1 provides a good introduction and overview. Chapter 2 discusses the role of the mobile phase and, to a lesser degree, the type of stationary phase and temperature. Chapter 3 describes the role of the column (stationary phase) in more detail and includes a useful listing (Table 3.1) of several commercially available columns ranked according to their suitability for basic compounds. Chapter 4 is devoted to solvent optimization for reversed-phase, ion-pairing, and normal-phase chromatography for "easy, moderate, and hard" samples. Chapter 5 explores the optimization of other variables for each of these methods for especially difficult samples, and it also includes a brief discourse on multidimensional techniques. Chapter 6 provides a thorough discussion of gradient elution in reversed-phase chromatography. Chapter 7 briefly discusses special samples and techniques (ion exchange, size exclusion, chiral separations, and trace analysis by LC). Chapter 8 is included to fulfill a secondary objective of the authors: to introduce the reader to some practical tools based on the use of the computer in HPLC method development. By design, their survey excludes software that is not commercially available or is part of an expensive HPLC system. Chapter 9, arguably the most important section of the entire book, lists in recipe form the method development procedures for isocratic reversed-phase, gradient reversed-phase, isocratic ion-pairing, and isocratic normal-phase separations.

Despite the fact that this book is a first edition, I have only a few minor criticisms and suggestions. First, a minor drawback is that it contains no discussion of gradient elution for ion-pairing and normal-phase systems. Although the authors correctly note that the basic principles are the same as for reversed-phase gradient elution—which they discuss in considerable detail—it would seem appropriate, particularly for the novice, to at least suggest the rate and shape of the gradients to use for the ion-pairing or normal-phase separation modes, because there will probably be a few occasions when these types of separations are necessary. I am also surprised that the au-

thors did not translate into more usable terms what Equations 6.4 and 6.4a imply about the preferred gradient rate in reversed-phase chromatography (i.e., $7\%/min/t_0$ for methanol-water, $7\%/min/t_0$ for acetonitrile-water, and $7\%/min/t_0$ for tetrahydrofuran-water, where t_0 is the retention time of an unretained solute).

Another mild disappointment is the authors' use of the half-height equation ($N = 5.54 (t_R/W_{1/2})^2$) for the estimation of column efficiency (Equation 2.3a). Although arguably one of the more practical equations for estimating plate count, the half-height equation is also one of the least accurate for asymmetric (tailed) peaks (*Anal. Chem.* 1984, 56, 1583 A), with significant errors even in the asymmetry range designated as acceptable by the authors (A_s between 0.9 and 1.3). In my opinion, other practical but more accurate equations such as those in the above citation should be considered by the authors for future editions of this book.

Two other minor changes that I suggest for later editions or printings of this book are as follows: First, the addition of page numbers to each chapter's table of contents would greatly facilitate the search for a subject within a specific chapter. Second, for improved clarity I recommend the addition of "Solvent Optimization" to the title of Chapter 4 and the addition of "Isocratic" prior to "Reversed-Phase" in the title of Table 9.1.

These minor criticisms notwithstanding, I found this to be an excellent book for both the novice and the expert. The scope of the book is appropriate and its objectives are fulfilled admirably. It is clear, concise, and well organized and cross-referenced. A noteworthy feature of this monograph is its one-of-a-kind method development "recipes" in Chapter 9. It also contains several figures and tables that will be helpful to the reader. Personal favorites include Figure 2.14 and Table 2.2 for predicting the strengths of preferred mobile phases in reversed- and normal-phase chromatography (to facilitate quick switches) and two nomographs in Chapter 9 for estimating solvent composition of subsequent isocratic (or gradient) runs based on a single preliminary gradient run. To the authors' credit, none of the book relies on the commercial software (some of their own) described in Chapter 8, although it is occasionally mentioned. Finally, a good proofreading has been done to keep typographical errors to a minimum. As of this writing, the only error I have noticed occurs in the half-height equation for plate count on p. 27. The proportionality constant

should read 5.54 instead of 5.56.

In summary, I highly recommend this book for the institutional library and for the office or laboratory of anyone who uses HPLC.

Gas and Liquid Chromatography in Analytical Chemistry. Roger M. Smith. xiv + 402 pp. John Wiley & Sons, 605 Third Ave., New York, NY 10158. 1988. \$131

Reviewed by I. S. Krull, Northeastern University, Boston, MA 02115

This is a well-written, clear, and concise summary of modern gas and liquid chromatography, with up-to-date references and bibliographies for each chapter. It is an excellent overview of both of these important areas of modern chromatography, and it attempts to introduce undergraduate and first-year graduate students to the current status. It succeeds admirably.

The book is clearly directed toward honors undergraduate (seniors) or first-year graduate students taking introductory courses in analytical separations or chromatography. It is weak on fundamental kinetic separation the-

ory, advanced physical chemistry equations, mechanisms of separations, how separations really occur on the chromatographic time scale, and related modes of understanding chromatography. The book is very practically oriented, and it describes how chromatography has evolved, what it can do today, the basic instrumentation and components available, how these fit together in a chromatographic system, and how samples are prepared and injected.

Approximately 40% of the book deals with GC, another 40% with TLC and HPLC, and the remainder with data handling and automation and future developments in GC, HPLC, SFC, FFF, and other techniques. There are excellent appendices describing the current literature of chromatography, applications of GC and HPLC, practical problems in chromatography, problem solving and instrument troubleshooting, record keeping and data interpretation, and bibliographies.

The book is laid out systematically, leading the student from the basic concepts of chromatography to basic instrumentation for each separate area, then to columns and stationary phases, mobile-phase selection, detectors, sam-

ple identification and quantification, and special techniques. The book is easy to read, even for beginning separations students, undergrad or graduate. It leads the reader from page to page, chapter to chapter, section to section, logically, clearly, and concisely. It was a pleasure to read, useful, and informative, and it contains an above-average number and quality of cited references. There is no author index, but the subject index is more than adequate. The references were up to date, some as recent as 1987 and 1988, and they were the leading references in each subject area. There were review references as well as bibliographies, with titles of books and review or original literature citations included, along with all authors, full journal citation, year, and pages. References were to important books, review papers, and key authors in each area.

Professor Smith is to be congratulated for knowing his literature as well as he shows, and for being able to incorporate so much of it into each chapter of his book. There are illustrative, typical chromatograms, instrumentation diagrams, schematics of instrument arrangements, tables upon tables of stationary phases, packed columns, im-

When Buying TitraLab™ be Sure to Check your Golf Clubs

TitraLab™ Titration Systems ensure you more time away from tedious routine tasks.

TitraLab automatically switches between electrodes and titrant/reagent burettes according to your methods. Time is saved and errors are eliminated.

Live titration curves on the screen make method development faster, and errors during routine operation can be seen immediately.

Time for instrument set-up is kept to a minimum by guided dialogue in plain English, German or French.

Check with your Radiometer product specialist to determine which TitraLab system will suit your needs, and find out about Radiometer's application support.

If you need precision and reliability in titration, be sure to contact your local Radiometer office and experience the convenience of TitraLab yourself.

- when you need to be sure -

RADIOMETER ANALYTICAL A/S
KROGSHOJVEJ 49 · DK-2880 BACSVAERD · DENMARK
CIRCLE 138 ON READER SERVICE CARD

ANALYTICAL CHEMISTRY, VOL. 61, NO. 18, SEPTEMBER 15, 1989 • 1041 A

Improved solid sample analysis for any GC, MS or FTIR

CDS Pyroprobe® Models 1000 and 2000

Pyrolysis: An alternative procedure with these benefits

- ▣ More repeatable for better quantitation
- ▣ Zero sample preparation time
- ▣ Faster, easier and cheaper to use

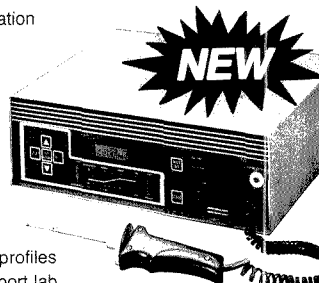
New Features

- ▣ Interchangeable calibrated probe rods
- ▣ Interfaces to GC, MS and FTIR
- ▣ Heating rates from 0.01°C/min. to 20,000°C/sec.
- ▣ Final temperatures to 1400°C
- ▣ Programmable, multistep heating profiles
- ▣ Applications bibliography and support lab
- ▣ Trade-ins accepted

Ask about our complete line of
headspace/purge and trap instruments

For information and
FREE application notes,
call toll free:

800-541-6593



CDS Pyroprobe 1000
for simplified solid sample
preparation



A Product Line of Autoclave Engineers
7000 Limestone Road, Oxford, PA 19363
Fax: 215-932-4158 Telex: 83-5308

CIRCLE 30 ON READER SERVICE CARD

There are 224 reasons why...

**most chemists
in the U.S. belong to the
American Chemical Society.**

The fact is, there are more than 137,000 chemists in this vital, career-enhancing society — *the largest scientific organization in the world!* To learn those reasons, write, use coupon or CALL TOLL FREE 1-800-ACS-5558

American Chemical Society, 1155 Sixteenth St., NW, Washington, DC 20036

Yes!

I would like to know 224 reasons to
join the American Chemical Society.
Please send free brochures to:

Name _____

Address _____

City, State, ZIP _____

BOOKS

mobilized/coated capillary columns, relative retention indices, and similar chromatographic data.

Obviously, more information could have been included; for example, on the subject of GC/MS a separate chapter could have been written. One felt that major subject areas were only being introduced and that the student would have to go to individual references to find out more about areas of importance. This is always the danger in writing a book that attempts to be everything to everybody at the undergraduate level. So much conciseness and condensation occur that major areas are only glossed over, and much of the meat must be omitted or referenced.

If there is any criticism of the book, it is that nobody can possibly cover all areas of chromatography in a single introductory text, even at this outrageous price. Thus, things are described fundamentally—too basically, too concisely—without any real depth or feeling for the matter. One comes away from the book without a real understanding of why things work—not do they work, but why. The underlying mechanisms of separations are never really discussed for any approach. The fundamentals of all forms of chromatography are covered in a single inadequate chapter (20 pages) so concise that most of the basic understanding and equations are condensed to the point where a real understanding must come from outside readings. This is the true fault of the book: It tries to do too much with too few pages. It almost, but not quite, succeeds in some areas, but obviously must fail in others, such as supercritical fluid chromatography, affinity HPLC, ligand-exchange chromatography, and chromatofocusing. It might have been better to write separate, fundamental books for each chromatographic area—one for GC, another for HPLC, one for SFC, etc. To try to cover all areas of chromatography in 400 pages is almost impossible, although the author has done an admirable job.

The book is to be recommended for those being introduced to separations in analytical chemistry, as a first text at the undergraduate level. As such, it will admirably introduce beginning analytical students to chromatography as practiced today, what it can do, what it can't do, and where to proceed next to learn more advanced areas, more equations, more theory, and more mechanistic understanding. It will serve as an excellent introductory text, an overview, or perhaps a review for those away from chromatography for some time, not as a reference text, but a course text.

Chromatographic Enantioseparation: Methods and Applications. Stig G. Allenmark. 224 pp. John Wiley & Sons, 605 Third Ave., New York, NY 10158. 1988. \$65

Reviewed by William H. Pirkle, School of Chemical Sciences, University of Illinois, Urbana, IL 61801

Chromatographic Enantioseparation, refreshingly easy to read, was read initially during a flight from St. Louis to Washington, DC. The book elicited immediate strong approval on several grounds. First, the printing and the abundant figures and drawings are crisp, clear, and pleasing to the eye. Second, Allenmark, one of the early developers of chiral stationary phases for liquid chromatographic separation of enantiomers, writes clearly and his familiarity with the field is evident. The book is a fairly concise yet complete account of this important field. Allenmark manages to give an even-handed treatment of all the topics covered.

The book begins with a short account of stereochemical concepts and nomenclature, progresses to the various techniques used to study enantiomers, and then to a discussion of modern chromatographic methods. With this foundation laid, Allenmark proceeds to a general discussion of the theory of chiral chromatography and then to the meat of the text: chiral gas chromatography and chiral liquid chromatography. Both these topics are well covered, fully referenced, and as up to date as publication schedules allow. The book continues with an extensive section on analytical applications, preparative-scale enantioseparations, and a look to future trends, and concludes with a compilation of synthetic procedures for the preparation of about a dozen chiral phases for liquid chromatography.

The book has been circulated among my research group and has met with unanimous approval. It is judged as being useful, well organized, and easy to read. In the opinion of this reviewer, it is must reading for every graduate student in organic, analytical, and inorganic chemistry, as well as pharmacy and biochemistry. It has a place in most research groups working in these areas and in most pharmaceutical house laboratories. It appears to be more suitable as a reference book than a textbook despite the inclusion of a few exercises at the end of some chapters. It is an excellent place to start for someone new to the field wishing to acquire a good background quickly.

The book is relatively free of errors, although one misstatement does appear in the section dealing with NMR

methods for determining enantiomeric purity. Contrary to statement, enantioselective interaction with the chiral solvent (or chiral solvating agent) is not a prerequisite for peak separation. For example, the methyls of dimethylsulfide become anisochronous in the presence of chiral-solvating agents even though Me_2SO is achiral. It is also noted that in Figure 7.15, the chiral recognition model shown is not the one presented in the literature; two of the interaction sites are interchanged.

Electroanalytical Techniques in Clinical Chemistry and Laboratory Medicine. Joseph Wang. x + 177 pp. VCH Publishers, Suite 909, 220 East 23rd St., New York, NY 10010-4606. 1988. \$59

Reviewed by George Harrington, Department of Chemistry, Temple University, Beury Hall, 13th and Norris St., Philadelphia, PA 19122

This is a small book designed to encourage the use of electroanalytical techniques by the electrochemically uninitiated analyst working in biologi-

cal areas. If such workers take the time to read this book the author may achieve his purpose. Similarly, the electroanalytical chemist who has never gone beyond the polarography of cadmium should find that this book can open new vistas.

The book contains five chapters. The first is on voltammetry and controlled-potential techniques, the second covers ion-selective electrodes, the third is titled "Electrochemical Biosensors," the fourth surveys the use of electrochemical detectors in HPLC and other flowing systems, and the fifth concerns in vivo electrochemistry. The last chapter could be of interest to the experienced electrochemist.

Besides explaining the various techniques, with many applications as illustrations, each chapter has a section on recent developments and a commentary on future prospects. Thus the non-specialist can develop a sense of where electroanalytical chemistry is going in the future and can look forward to the availability of even more useful techniques at a later date.

Theory is kept to a bare minimum in an attempt not to overwhelm the reader, and in most instances the theory

OUR STANDARDS ENDURE THE TEST OF TIME.

Conostan oil-based calibration standards combine the convenience of blended standards and an exceptional stability for the analysis of metals in oil. These metallo-organic sulfonates remain stable in liquid form for more than a year—and individual concentrates have exhibited even longer shelf lives. For a complete list of single and multi-element standards that endure the



test of time, write or call for our free brochure.

 Standards to Burn
CONOSTAN®

Conostan Division
Conoco Specialty Products Inc.
P.O. Box 1267
Panola City, OK 74603
Phone: (405) 767-3078
Fax: (405) 767-3843

CIRCLE 27 ON READER SERVICE CARD

and equations are adequate. The section on differential pulse polarography could have been beefed up a bit since this is the one purely analytical technique most likely to be used. For example, the author mentions two standard additions to quantitate a differential pulse polarogram without saying why two are necessary. A sample calculation would also have been helpful, because most literature articles are not likely to show how this is done but merely give the results.

The book has several strong points. It is well written and easy to read. There are more than 700 literature references cited that describe applications of various techniques. Many of the references are quite recent. The interested reader is likely to find a mention of his or her compound somewhere in the book.

On the other hand, the book has some weak points. The index is extremely sparse. Many compounds cited within the text as examples of applications are not included in the index. Thus a scan through the index to see if any of the techniques could be of use for a particular compound might suggest that the compound is not covered

when in fact it is. The book could have used an index of compound, mentioned. Another shortcoming is that the book tends to make the various techniques seem a little too easy to use. Some discussion of problems and how to recognize them would have been helpful. This is especially true for the chapter on ion-selective electrodes and that on electrochemical detectors for HPLC. We all know that sometimes these devices can be like the little girl in the nursery rhyme; that is, when she is good she is very, very good, but when she is bad she is horrid.

In any event, the author's objective is commendable and his efforts should help fill a void that needs to be filled.

Spectroscopy of Surfaces. R.G.H. Clark and R. E. Hester, Eds. xxi + 488 pp. John Wiley & Sons, 605 Third Ave., New York, NY 10158. 1988. \$293

Reviewed by David M. Hercules, Department of Chemistry, University of Pittsburgh, Pittsburgh, PA 15260

This volume successfully addresses the informed nonexpert in the area of sur-

face spectroscopy. The chapters would make good text material for beginning graduate courses or advanced undergraduate courses at the honors level. The presentations generally give principles and theoretical background (not too much) and representative examples of various spectroscopic techniques and how they can be applied to the study of surfaces. In general, the examples are broadly defined and well chosen. Analytical and physical chemistry graduate students could profit from reading this well-written text. Generally the references cited by the authors are in balance—they are drawn broadly, not just from their own work.

The book consists of eight chapters: three on Raman spectroscopy and one each on SIMS, IETS, EELS, IR reflection absorption, and electron-excited spectroscopies. In my opinion, Chapter 3 seems to be out of place in this volume. Although it is a well-done chapter, it focuses on the use of SERS to study biochemical systems. The remaining chapters focus on the use of spectroscopic techniques to study surface phenomena per se.

The emphasis on electron-excited spectroscopies is not to my liking.

**Reaching Perfection
in MS and SEM.**

*"A man's reach should
exceed his grasp..."
Robert Browning*

Galileo detectors for Mass Spectrometry and Electron Microscopy.

What silicon chips did for computers, Galileo high-performance detectors are doing for GC/MS, MS and SEM analysis.

Whether your projects involve environmental or pharmaceutical analysis, analysis of organic compounds or general spectroscopy applications, a Galileo detector will speed sample identification while providing accurate and precise analysis.

When research projects require frequent sample analysis over a long period of time, you'll want the latest and best technology backing you up. Galileo is the innovator in analytical instrument detectors. If you demand high performance and are concerned about down time, rapid analysis, dynamic range and cost, insist on Galileo scientific detectors. You'll wonder how you ever got along without us.

Write us and ask how to ensure that your instruments have Galileo scientific detectors.

Galileo Electro-Optics Corp.
Scientific Detector Products Group
P.O. Box 550, Dept. AA
Sturbridge, MA 01566
(508) 347-9191

GALILEO
Galileo Electro-Optics Corp.

CIRCLE 60 ON READER SERVICE CARD

Chapter 6 is commendable for including techniques such as ESDIAD, but why discuss EELS as part of Chapter 6 when there is a whole chapter on EELS itself? Auger spectroscopy gets particularly short shrift in this chapter given its wide use, particularly in the semiconductor industry. The most glaring omission is that of a chapter on (or any treatment of) photoelectron spectroscopy (ESCA, XPS). Given that ESCA is the only surface technique (versus effect) yet to merit a Nobel prize, its absence is striking.

I found Chapter 4 on SIMS to be quite good, although this obviously reflects my own prejudice with regard to a research topic. It deals with fundamentals, ion versus neutral beams, inorganics versus organics, and imaging—all of these are treated in balance. This chapter certainly will be required reading for my graduate students. In addition, I read two chapters discussing areas in which I am not an expert and found them to be quite educational: Chapter 1, Raman spectroscopy of thin films; and Chapter 5, inelastic electron tunneling spectroscopy. I found both to be very interesting and informative. I felt that Chapter 1 is particularly good.

I am favorably impressed by the volume as a whole despite its complete slight of ESCA. The price of the volume is \$203 (41.6¢ per page). The quality is very good—for this price, it ought to be. If you have a rich uncle or believe in Santa Claus, your interest in this book would be a good hint to drop.

Books Received

Luminescence Techniques in Solid State Polymer Research. Lev Zlatkevich, Ed. ix + 318 pp. Marcel Dekker, Inc., 270 Madison Ave., New York, NY 10016. 1989. \$125

Topics include general mechanisms, polymer analysis at nearly ambient temperatures, spectroscopy, thermal oxidative stability, and photooxidation. The six contributing authors are from England, Australia, and the United States. References (from the 1970s to the mid-1980s) and an index are included.

Flow Injection Analysis, 2nd ed. Jaromír Růžička and Elo H. Hansen. xx + 498 pp. John Wiley & Sons, 605 Third Ave., New York, NY 10158. 1988. \$75

This is volume 62 from *A Series of Monographs on Analytical Chemistry and Its Applications*. The chapters are entitled Introduction, Principles, Theoretical Aspects of FIA, Techniques, Components of an FIA Apparatus, Ex-

perimental Techniques and FIA Exercises, Review of the Flow Injection Literature, and Flow Injection Analysis Now and in the Future. Also included are a general index, an author index, and references.

Flow Injection Atomic Spectroscopy. José Luis Burguera, Ed. xii + 353 pp. Marcel Dekker, Inc., 270 Madison Ave., New York, NY 10016. 1989. \$125

This is volume 7 in the series *Practical Spectroscopy*. The chapters are titled General Introduction, Theoretical Aspects, Basic Components and Automation, Analytical Methods and Techniques, Separation Techniques, Applications in Agricultural and Environmental Analysis, Applications in Clinical Chemistry, and Current Trends. Most of the references are from the 1980s. Two appendices and author and subject indexes are included.

X-Ray Structure Determination, 2nd ed. George H. Stout and Lyle H. Jensen. xv + 453 pp. John Wiley & Sons, 605 Third Ave., New York, NY 10158. 1989. \$45

Chapter titles include Diffraction of X-Rays, Crystals and Their Properties,

Data Reduction, Theory of Structure Factors and Fourier Syntheses, Heavy Atom Methods, Refinements of Crystal Structure, Ambiguities and Uncertainties, Intensity Data Collection, and Random and Systematic Errors. An appendix and an index are included.

Ion Chromatography Applications. Robert E. Smith. 177 pp. CRC Press, Inc., 2000 Corporate Blvd. N.W., Boca Raton, FL 33431. 1988. \$110

Chapters are titled Basic Principles and Theory, Conventional Methods, Nonconventional Methods, and Applications. References date from the 1970s to the mid-1980s. An index is included.

Laboratory Manual for the Examination of Water, Waste Water and Soil. H. H. Rump and H. Krist. xi + 190 pp. VCH Publishers, Suite 909, 220 E. 23rd St., New York, NY 10010-4606. 1989. \$33

This book covers safety, quality control, analytical methods, sample collection, field and laboratory measurements, and interpretation of results. The book opens flat for laboratory bench-top use. Statistical tables and an index are included.



OUR STANDARD DELIVERY IS ANYTHING BUT STANDARD.

Constan oil-based calibration standards are just a telephone call away. Standard orders are filled the day they are received, and are on the way to you within 24 hours. Orders for custom blends usually take only a

day longer. Constan orders are shipped UPS, air express, or as you designate. For service that's anything but standard, call or write for our free brochure describing the full line of single and multi-element

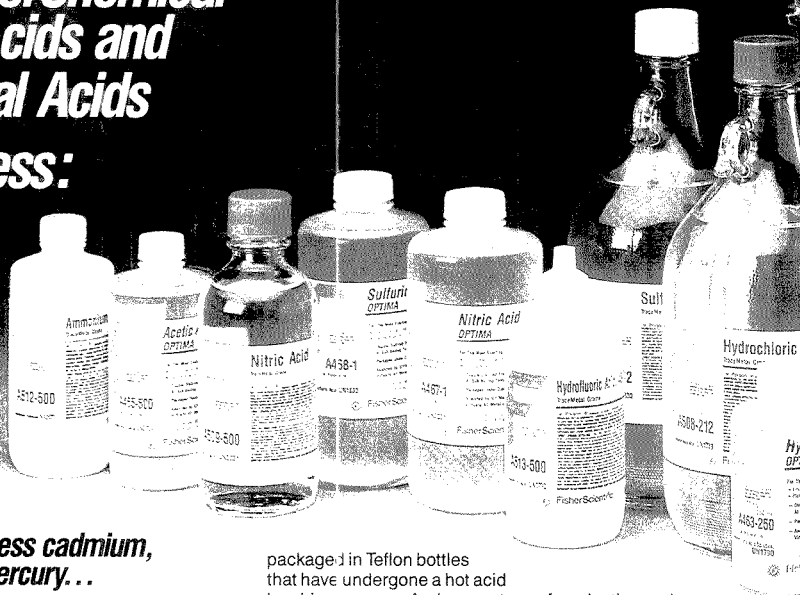
Constan standards for the analysis of metals in oils.



Constan Division
Conoco Specialty Products Inc.
P.O. Box 1267
Panola City, OK
Phone: (405) 767-3078
Fax: (405) 767-5843

CIRCLE 28 ON READER SERVICE CARD

**Expect more
from FisherChemical
Optima™ Acids and
TraceMetal Acids
...and get less:**



**Less aluminum, less cadmium,
less lead, less mercury...**

Move up to Fisher acids

Why settle for "high purity" when you can get the world's highest purity? Choose the acids that offer the most by providing the least: FisherChemical Optima Acids for the lowest metal content and highest purity available anywhere...and FisherChemical TraceMetal Acids, for exceptionally low metal content and incomparable value.

**Fisher Optima Acids—
The first acids good enough to be Optima**

FisherChemical's new Optima Acids offer the lowest metal content of any acids available. Most metals are present in concentrations of less than one part per billion, and many are in the parts per trillion range, as indicated on the certificate of analysis supplied with each bottle. Optima Acids are the obvious choice for environmental testing, plasma analysis, electronic research...any application that demands the utmost purity and precision.

Each step in the creation of Optima Acids ensures the lowest level of metals in the acids you receive. Optima Acids are double-distilled in Teflon* or pure quartz stills at temperatures below the boiling point of the acid, then

packaged in Teflon bottles that have undergone a hot acid leaching process. And every stage of production and packaging takes place in Class 100 clean room environments.

Fisher TraceMetal Grade Acids—exceptional value
FisherChemical's new TraceMetal Acids provide extraordinary purity at a lower cost and are ideal for many applications that require extremely low metal content. TraceMetal Acids are produced with low metal content in mind; the competition's so-called "metal-analyzed acids" are simply lot-selected ACS acids. TraceMetal Acids far surpass the purity of these products...and in fact are as pure as, or even purer than, many competitors' top-of-the-line acids...yet cost considerably less.

Careful sub-boiling distillation...ICP analysis... specially treated containers designed to maintain exacting specifications...and a Certificate of Analysis with each bottle are the keys to TraceMetal Acid purity.

Select Optima or TraceMetal Acetic, Hydrochloric, Hydrofluoric, Nitric, Perchloric, Sulfuric Acids and Ammonium Hydroxide.

*Teflon is a registered trademark of E.I. du Pont de Nemours & Co., Inc.

Expect more from FisherChemical

FisherChemical

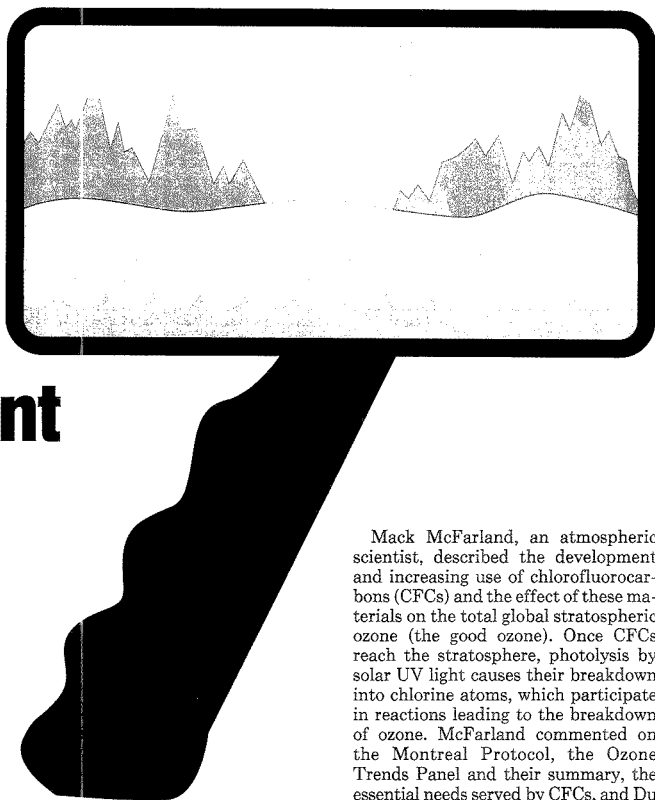


Fisher Scientific

Excellence in Serving Science...Since 1902

CIRCLE 50 ON READER SERVICE CARD

Looking at the Environment



Two recent meetings, the 19th International Symposium on Environmental Analytical Chemistry and the Fifth Annual Waste Testing and Quality Assurance Symposium, sparked the interest of both analytical and environmental scientists. Although the meetings were quite different, they complemented each other well, providing attendees with a good overview of new techniques and equipment useful in environmental analysis.

On May 22-24, 150 scientists from around the world gathered off the coast of Georgia on Jekyll Island to participate in the 19th International Symposium on Environmental Analytical Chemistry sponsored by the U.S. Environmental Protection Agency, the University of Georgia, the International Association of Environmental Analytical Chemistry, and the Divisions of Analytical Chemistry and Environmental Chemistry of the American Chemical Society. The symposium was started in Halifax, Nova Scotia, in 1971, and since 1974 has been held alternately in Europe and the United States to facilitate the international exchange of ideas and experiences. While continuing the traditional emphasis on recent advances in analytical chemistry applicable to environmental studies, the program was expanded this year to include environmental process chemistry, because research in this area is dependent on reliable measurement and speciation of chemicals at concentrations typical of those in the ambient environment. Conversely, an understanding of chemical processes is essential for determining the species

and distribution of both organic and inorganic pollutants.

Invited speakers from government, industry, and university laboratories discussed current developments in the analysis of organic and inorganic pollutants as well as research to define the mechanisms of chemical transformations and to improve measurement of equilibrium and kinetic constants.

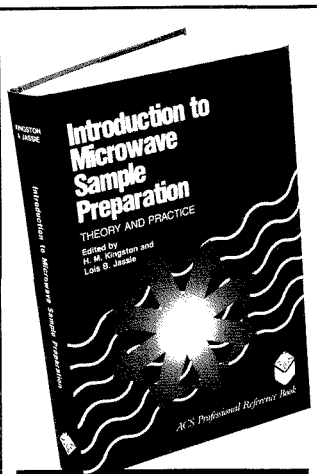
FOCUS

Each day's session began with a plenary presentation addressing a problem of vital interest to environmental analytical and process chemists. The plenary lectures, centering around the theme "Atmospheric Changes: Climate and Health," were given by Mack McFarland of Du Pont, Charles Jackman of NASA, and Lester Grant of the EPA.

Mack McFarland, an atmospheric scientist, described the development and increasing use of chlorofluorocarbons (CFCs) and the effect of these materials on the total global stratospheric ozone (the good ozone). Once CFCs reach the stratosphere, photolysis by solar UV light causes their breakdown into chlorine atoms, which participate in reactions leading to the breakdown of ozone. McFarland commented on the Montreal Protocol, the Ozone Trends Panel and their summary, the essential needs served by CFCs, and Du Pont's role in the development of alternatives to allow a phase out of CFCs.

Charles Jackman, an atmospheric physicist, emphasized the complexity of the interactions leading to depletion of stratospheric ozone. He commented that natural changes in ozone occur, some of which are related to the 11-year changes in the solar cycle. Man-made influences on stratospheric ozone include CFCs, supersonic transport planes, and nuclear tests; and atmospheric computer models have been developed to estimate how ozone levels are affected by both natural and man-made influences. Jackman stressed that the ozone depletion problem will be with us for a long time, and that even if we immediately cut back the use of CFCs by 85-95% it will be decades before we see any real effect because of the long lifetimes of CFCs.

Lester Grant, a neurophysiologist, described the health-related effects of increased UV-B light penetration to the surface of the Earth resulting from stratospheric ozone depletion. Much has appeared about possible damage to



Introduction to Microwave Sample Preparation: Theory and Practice

New microwave techniques are making sample preparation procedures faster, more convenient, and more controlled. This revolutionary new book gives you what you need to know to get started... the history of the technique, the relevant methodological details, the all-important safety precautions, and a number of specific applications.

Eleven chapters describe equipment and techniques that have been found most effective. They offer direct practical applications of the methods to a variety of sample types, including microwave digestion of botanical, biological, and food samples; selenium analysis; Kjeldahl nitrogen determination; remote operation of microwave systems; and more. As a unique feature, this book presents a fundamental thermodynamic equation relating acid (sample) size, final temperature, heat capacity, and transformations of the basic equation predicting time and temperature for digestion.

A truly multi-disciplinary volume, this book can be used in inorganic elemental analysis, sample digestion, food analysis, environmental sample preparation chemistry, and other areas.

H.M. Kingston and L.B. Jassie, *Editors*
 ACS Professional Reference Book
 300 pages (1988) Clothbound
 ISBN 0-8412-1450-6 LC 88-8139
 US & Canada \$49.95 Export \$59.95

ORDER FROM

American Chemical Society
 Distribution Office Dept. 95
 1155 Sixteenth St., N.W.
 Washington, DC 20036

or CALL TOLL FREE

800-227-5558
 (in Washington D.C. 872-4363) and use your credit card

eyes and the increase in skin cancer; however, only a few reports describe a much bigger hazard—suppression of the immune system. One of the most serious health and pollution problems in the world has been created by excess tropospheric ozone (the bad ozone). Caused by the emission of NO_x and volatile organic compounds (VOCs) from such sources as motor vehicles, oil refineries, and dry-cleaning plants, tropospheric ozone causes damage to lung structure (chronic exposure) as well as transient respiratory problems such as decrements in lung function and certain irritative symptoms such as coughing, wheezing, and chest pain (acute exposure). In addition, the damage caused to forests, crops, and the ecosystem as a whole appears to be enormous, commented Grant.

Sixteen other speakers described a variety of environmental studies, including the fate of textile dyes in aquatic ecosystems, photochemical reactivity of polycyclic aromatic compounds adsorbed on "stack ash," identification of spruce needle phenolics found in needles fumigated in a fog chamber, use of glow discharge quadrupole mass spectrometry and ion trap tandem mass spectrometry for the rapid determination of organic compounds in water and soil, the monitoring of ground and well water for trace levels of agrichemicals, the chemical analysis of clouds and fogs, and the development of a mobile miniaturized ion trap mass spectrometer.

Totally unrelated to ozone and other environmental problems were the talks given by Sanford Asher of the University of Pittsburgh on UV resonance Raman spectroscopy, Stanley Bruckenstein of SUNY-Buffalo on the quartz crystal microbalance, Ira Levin of NIH on near-IR FT-Raman spectroscopy, and Cecil Dybowski of the University of Delaware on the study of surfaces by NMR spectroscopy. These speakers were invited by the symposium organizers to describe techniques that are not routinely used in environmental work but that may, in the not-too-distant future, be widely applied in solving environmental problems.

A tribute to Roland Frei was delivered by Ernest Merian of the Swiss Association for Environmental Research and L. B. Rogers of the University of Georgia. Frei, who passed away suddenly late last year, epitomized the spirit of the International Symposia. He originated the meetings in Halifax in 1971 and continued to have a great influence on the content of the meetings. He was a very pragmatic person who always saw the potential of new methods for environmental analysis

and who insisted that the meetings cover both fundamental research and basic techniques.

The 20th annual symposium will be held in Strasbourg, France, in April 1990. Or one can wait until 1991, when the symposium will return to the beautiful semitropical island in Georgia with broad white beaches, nature trails, and historical splendor.

Waste analysis and quality assurance

In late July more than 650 environmental chemists met in Washington, DC, for the week-long Fifth Annual Waste Testing and Quality Assurance Symposium. Sponsored by the Environmental Protection Agency and managed by the American Chemical Society, the symposium included sessions on air and ground water monitoring, biological test methods, enforcement issues, determination of inorganic and organic pollutants, mobility methods, laboratory information management, quality assurance, and sampling and field methods.

The inaugural EnvirACS Exposition, held in conjunction with the meeting, included exhibits by almost 100 companies and featured instruments and other products of particular interest to environmental chemists. When not listening to technical presentations, symposium attendees had the opportunity to visit this first-ever exposition devoted solely to environmental analysis.

The conference began with a workshop, led by John Warren of EPA's Office of Policy, Planning, and Evaluation, on statistical aspects of waste testing and environmental monitoring. The mechanics of statistical tests commonly encountered when analyzing solid waste data were discussed, and the logic of the tests when used correctly and the impact on false-positive and false-negative rates when key assumptions are violated were demonstrated.

Following the workshop, conferees gathered for presentations by several EPA officials. Jonathan Cannon, acting assistant administrator of the Office of Solid Waste and Emergency Response; Walter Kovalick, deputy director of the Office of Emergency and Remedial Response; Devereaux Barnes, director of the Characterization and Assessment Division, Office of Solid Waste; and Susan Bromm, director of the RCRA Enforcement Division, Office of Waste Programs Enforcement, discussed future developments in EPA's hazardous waste programs. Symposium chairperson David Friedman of the Office of Solid Waste presented an overview of the RCRA Testing Methodology and Qual-

ity Assurance Program; and Joan Barnes, also of the Office of Solid Waste, presented an overview of the Superfund Analytical Services Program.

During the remainder of the symposium, researchers from EPA, academia, and industry made presentations aimed at helping practicing environmental analysts solve problems encountered in their work. New sample preparation methods such as microwave digestion and supercritical fluid extraction (SFE) are joining the tried-and-true standard digestion and extraction methods, and new instrumental methods such as ICP/MS, LC/MS, and SFC are being used more frequently to complement the traditional LC, GC, and GC/MS methods.

Microwave digestion and SFE are advantageous for sample preparation in elemental and organic analysis, respectively. According to David Binstock of the Research Triangle Institute (Research Triangle Park, NC), techniques typically used for preparation of samples for trace elemental analysis are time-consuming and often involve the use of acid digestions and thermal decompositions that may lead to analyte losses, incomplete recoveries, or sample contamination. Microwave digestion, however, can result in significantly reduced preparation time without deterioration of either accuracy or precision.

The increased use of supercritical fluids (SFs) for sample extraction is based on a combination of the properties of SFs and the increased availability of both off- and on-line equipment for SFE, said Viorica Lopez-Avila of Acurex Corp. (Mountain View, CA). Because the high-solute diffusivities of SFs compared with conventional solvents provide much higher extraction efficiencies, extraction conditions can be adjusted so that compounds can be separated according to their volatility and polarity. Very little organic solvent is needed for collection of extracted materials, and the SF can be completely separated from the extracted material in the release step by reducing the pressure to ambient pressure. A study of supercritical extraction of EPA priority pollutants from various matrices (i.e., sand, urban dust, coal, coal fly ash, and soil) indicates that SFE has the potential to be a useful technique for the environmental chemist.

Several speakers discussed the use of inductively coupled plasma mass spectrometry (ICP/MS) for the determination of trace elements in water and solid waste. According to Thomas Hinners of the EPA Environmental Monitoring Systems Laboratory (Las

Vegas, NV), ICP/MS offers detection limits below a part per billion for multi-element analysis with the convenience and speed of nebulizer sample introduction. An interlaboratory study comparing the analysis of nearly 36,000 water, fly ash, sediment, industrial sludge, and soil samples by atomic absorption spectroscopy, ICP-atomic emission spectroscopy (ICP-AES), and ICP/MS showed that analytical precision is more variable with ICP/MS than with ICP-AES for several elements, possibly because of the additional dilutions necessary for ICP/MS analysis. Preliminary results indicate that ICP/MS is suitable for determination of many elements, but they do not support using ICP/MS to determine potassium, selenium, silver, sodium, and vanadium in solid waste.

For the determination of organics, LC/MS is becoming more popular because of its ability to separate and quantitate nonvolatile or thermally labile compounds that are not amenable to GC or GC/MS. LC/MS methods using both thermospray and the new particle beam LC/MS technology to characterize nyes, chlorinated herbicides and esters, carbamate pesticides, and other environmentally important compounds were described.

As indicated by the symposium's title, a large part of the meeting was devoted to quality assurance and quality control issues, including the definition and classification of hazardous waste matrices, determination of detection limits, laboratory accreditation and audits, quality control in field sampling, multivariate analysis of QA/QC data, interlaboratory quality assurance, and the use of laboratory automation and laboratory information management systems.

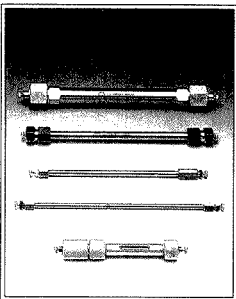
Finally, various field methods and sampling protocols, including several portable instruments for on-site determination of pollutants, were described. For example, Albert Robbat and George Xyrafas of Tufts University described a fieldable GC/MS for identification and quantitation of PCBs; and Marcus Wise, Michael Gurein, and Michelle Buchanan of Oak Ridge National Laboratory described a direct-sampling ion trap mass spectrometer that can be used for the rapid determination of volatile organics in water, soil, and air.

Next year's symposium will again be held in Washington, DC, July 16-20, 1990, and promises to be even better than this year's, with stimulating technical presentations and the second annual Env rACS Exposition.

Sharon Boots
Mary Warner

Chromatography Specialists

HPLC



Packings

- Silicas NUCLEOSIL® and POLYGOSIL®
- Aluminium oxide
- Cellulose, Polyamide

Packed columns

- Guard columns
- Cartridge system
- Preparative columns
- Columns for special applications

Accessories

- Valves and fittings
- Micro syringes
- Vials and accessories and many more

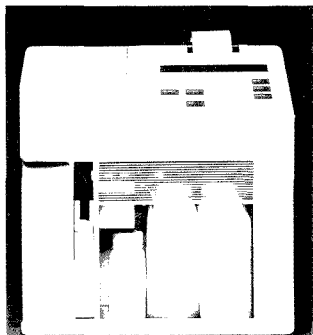
Please ask for further information



MACHEREY-NAGEL GmbH & Co. KG
P.O. Box 101352 - D-5160 Düren - W. Germany
Tel. (02421) 698-0 - Teletax (02421) 66716
Switzerland: MACHEREY-NAGEL AG
P.O. Box 224 - CH-4702 Oensingen
Tel. (062) 762066 - Teletax (062) 762864

CIRCLE 94 ON READER SERVICE CARD

NEW PRODUCTS



Model 2300 STAT glucose and L-lactate analyzer features autocalibration and automatic sample aspiration. Measurement ranges for glucose and lactate are 0–500 and 0–135 mg/dL, respectively. YSI 401

Process analysis. Model 304 on-line chemical oxygen demand analyzer provides real-time monitoring of oxidizable species in water sources, such as industrial and municipal sewage and waste. The system is based on a dichromate reflux/colorimetric method. Ionic 404

UV-vis. Dual-beam UV-vis spectrophotometer, designed for preparative and process HPLC, features flow rates up to 10 L/min and pressures up to 3000 psi. The system includes two 20- μ L prep flow cells and a 10- μ L analytical flow cell. IBF Biotechnics 405

Water purification. Water polisher accepts water pretreated to at least 10 megohms and delivers 18-megohm water directly into a chromatography pump. The unit meets specifications for chloride, sulfate, and sodium and also provides ultra-low organic carbon levels. Dionex 406

Particle size. Microscan measures particle diameters ranging from 300 to 0.1 μ m. Using a scanning method whereby the sample cell remains stationary, the system automatically moves the X-ray beam and detector in increments of 0.0001 in. at seven distinct rates per analysis. Quantachrome 407

Metals. Spectrovac FSQ arc/spark emission spectrometer, designed for use in foundries and other rugged production environments, provides simultaneous multielement analysis of ferrous-based materials such as cast iron, steel, and their alloys, as well as determination of nonferrous metals such as aluminum, copper, zinc, and lead. Baird 408

Fluorescence. Model FL-750A fluorescence spectrophotometer features excitation/emission scanning in seven variable speeds, including synchronous scanning of both monochromators. Interchangeable sampling modes permit use of accessories for HPLC and TLC/gel scanning. McPherson 409

Gradient LC. Peptide-mapping system is capable of routine peptide mapping at the 5–10-pmol level and is compatible with high-speed and narrow-bore peptide columns. Typical precision of retention time is 0.1–0.2% RSD. Perkin-Elmer 410

EPR. ECS106 EPR spectrometer features automated tuning and calibration, signal display in real time, digital phase-sensitive detection, analog/digital conversion with 500 ns per point, and a 32-bit multiprocessor data system. Bruker Instruments 411

Carbamates. Gradient HPLC system with a 400- μ L sample loop determines *N*-methylcarbamates in drinking water and raw source water. The system includes a low-pressure ternary gradient controller and fluorescence detector. Fisher Scientific 412

LC. Beam Boost is a reagentless post-column photochemical reactor that can be placed between the column and any UV, photodiode, or fluorescence detector. A knitted configuration of the Teflon coil around a 254- or 366-nm lamp produces increased detector response of 10–200-fold. Advanced Separation Technologies 413

GC. Thermal desorption unit monitors trace amounts of airborne compounds that are difficult to detect using solvent desorption methods. A chamber that saves up to 90% of the sample is featured. Supelco 414

Software

Mathematics. Fortran scientific subroutine library contains more than 100 pretested mathematical and statistical operations. Subroutines include matrices with real and complex elements, polynomials, interpolation, differential equations, numerical analysis, and statistics. John Wiley & Sons 415

Data analysis. MacSpin 2.0, which runs on all current versions of Macintosh computers, converts raw numerical data into rotating three-dimensional graphics for analysis and presentation. Features include grid surfaces and connecting lines, animation in a fourth dimension, and slicing and masking. D² Software 416

Manufacturers' Literature

Chromatography. Brochure describes series 4500i chromatographs for HPLC and ion chromatography. Detectors, automation options, and post-column delivery systems are discussed. 4 pp. Dionex 418

Thermal analysis. Report discusses three DSC kinetics methods and how they can be used to determine key material properties, including optimum cure temperature and estimated lifetime. 16 pp. Du Pont 419

Student chemistry. Brochure describes unknown chemical samples for student laboratory analysis. Included are qualitative and quantitative unknowns and student reference standards. Thorn Smith Laboratories 421

Electrochemistry. Application note ECD-17 discusses the determination of 1,1-dimethylhydrazine, a decomposition product of daminozide (Alar). Detection limits, detector conditions, and procedures are discussed. EG&G Princeton Applied Research 422

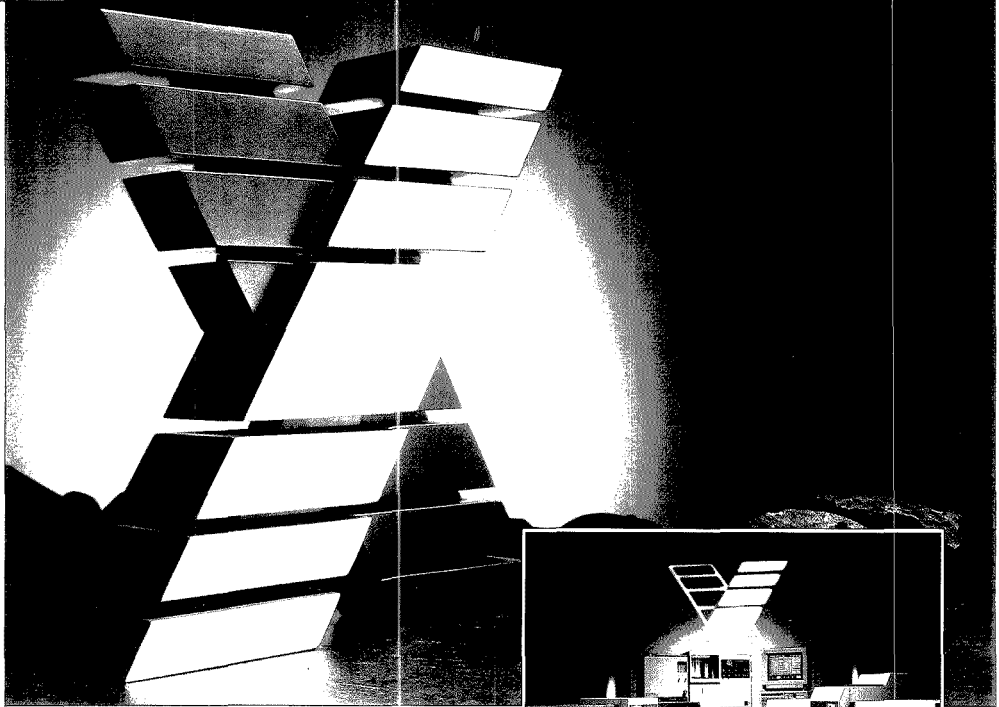
For more information on listed items, circle the appropriate numbers on one of our Readers' Service Cards



PHILIPS

What are the eXtra elements in Philips AA?

Philips Analytical



The Philips AA range is renowned for reliability, performance and innovation. Now we've added a host of eXciting new automation facilities to make these the most complete AA instruments yet.

On-line digital balance, furnace program optimisation, flexible report writing... Find out about the eXtra AA benefits by sending for the special colour brochure. It'll give you a full eXplanation.



PU9100X – low-cost, high performance flame and furnace systems with full Data Station convenience.

PU9200X – flexible, fully-automated systems meeting your exact requirement.

PU9400X – top-of-the-range, automatic, multi-element AA with 'intelligent' operation.

eXceptional AA... with plenty eXtra.



PHILIPS ANALYTICAL - BIGGER IDEAS FOR BETTER ANALYSIS

For more information about the Philips Analytical AAX range contact:

Philips Scientific Analytical Division York Street, Cambridge Great Britain CB1 2PX Tel: 0223 358866 Telex: 817331 Fax: 0223 312764

or telephone direct **Austria:** (0222) 60101 – 1792 **Belgium:** (02) 525 62 75 **Denmark:** (01) 57 22 22 **Finland:** (09) 502 63 56 **France:** (1) 48 42 81 62

Germany: (0561) 501 384 **Italy:** (02) 64 49 12 **Netherlands:** (040) 783 901 **Norway:** (02) 68 02 00 **Sweden:** (08) 782 1591

Switzerland: (01) 498 22 11.

CIRCLE 125 ON READER SERVICE CARD

AA26

Make your ideas heard! Learn how to design and give technical talks to any audience.....

Effective Oral Presentations



A New Audio Course from the American Chemical Society

Special 30-day free examination offer for ACS members!

Did you ever see someone's good ideas get lost in a bad presentation? Make sure your ideas get the attention they deserve! Learn how to present your ideas clearly and convincingly with this new ACS Audio Course.

Effective Oral Presentations shows you just what goes into a successful presentation—and gives you the tools to make your's better. It offers a structured approach to designing and presenting a technical talk to any audience—from organizing your ideas...to preparing visual aids...to developing your personal style and delivery. In just a few short hours you'll gain skills that can help you give your presentations clarity and impact....and make you a stand-out communicator on the job. You'll learn to:

- Decide what to say to an audience—and how to say it
- Prepare visual aids that both communicate your ideas and capture attention
- Overcome stage fright
- Use your personality and appearance to enhance your presentation

Here's what you'll be able to do after taking this course:

- Analyze an audience to determine the organization and content that will work best
- Master the two most critical parts of a talk—the introduction and conclusion
- Project confidence and enthusiasm
- Critique and modify your own speaking voice
- Use visual aids that say just enough—but not too much

Raise your profile on-the-job! Become a convincing communicator when presenting technical material. Learn how with **Effective Oral Presentations**.

Who Should Take This Course

Anyone who presents technical material—whether research seminars, progress reports, sales presentations, etc.—to a management or nontechnical audience can benefit from **Effective Oral Presentations**.

Brief Course Outline

- **Text Preparation:** Selecting, Organizing, and Supporting Your Ideas; The Introduction; The Conclusion
- **Visual Aids:** Using Visual Aids; Types of Visual Aids; Criteria for Using; Transparencies and Slides
- **Personal Preparation, Delivery:** Personal Style; Voice and Diction; Barriers to Communication

The Instructor

W.F. (Fred) Oettle works in industrial relations, training, and recruiting for E.I. du Pont de Nemours & Co.

The Unit

Effective Oral Presentations consists of three cassettes (three hours of taped instruction) and a 50-page manual. It comes in one compact package, so that you can keep it with you to study when you want—at work, at home, or even while traveling.

From concept to delivery, **Effective Oral Presentations** can give your talks snap and polish—and make your ideas heard. To order, use the coupon below or call 1-800-227-5558.

Order Form

Please send me **Effective Oral Presentations** (Catalog No. B3):

	US &			
	Qty.	Canada	Export	Total
Complete Course	_____	\$350	\$420	_____
Additional Manuals	_____	\$18	\$22	_____
		Total order		_____

Payment Options:

1. Payment enclosed (make check payable to American Chemical Society).
2. Purchase order enclosed.

P.O. # _____

3. Charge my MasterCard/VISA
 AMEX Diners Club/Carte Blanche

Account No. _____

Name of cardholder _____

Expires _____

Signature _____

4. Send me my course to examine free for 30 days. I am an ACS member. ACS membership no. (above your name on your C&EN mailing label): _____

Signature _____

Ship to:

Name _____

Address _____

City _____

State, ZIP _____

Phone _____

Please allow 3-4 weeks for delivery. Prices quoted in U.S. dollars. Foreign payment must be in U.S. currency by international money order, UNESCO coupons, or U.S. bank draft.

Mail this order form to American Chemical Society, Distribution Office Dept. 15, P.O. Box 57136, West End Station, Washington, DC 20037.

LC. Sourcebook for Analytical HPLC Columns includes information on packing materials and column geometries for a variety of analyses. 48 pp. Waters Chromatography Division of Millipore 420

Vacuum gauges. Brochure describes hot and cold cathode, capacitance manometer, and Pirani digital vacuum gauges. Photographs show the possible sensor configurations for measuring at different pressure ranges. Leybold Inficon 423

Catalogs

Fluid handling. Catalog features fluid-handling products made of high-purity inert plastics. Included are fittings, tubing, valves, and piping. 112 pp. Fluoroware 425

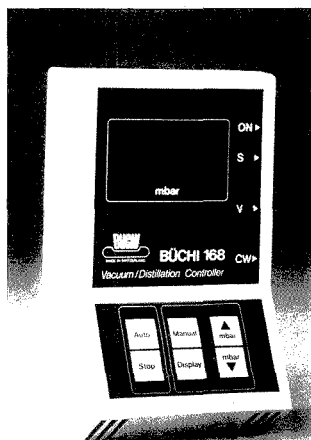
Laboratory products. Catalog includes balances, beakers, centrifuge accessories, chromatography supplies, cryoware, dialysis equipment, electrodes, filters, meters, pipets, and vials. 96 pp. J. & H. Berge 426

Instrumentation. Catalog features test and measurement instruments, including signal sources, digital oscilloscope, and high-speed waveform digitizers. LeCroy 427

FT-IR. Catalog includes microsampling accessories; reflectance accessories; and liquid-, solid-, and gas-sampling accessories. Tips to help users avoid operational and analysis problems are included. 36 pp. Foxboro 428

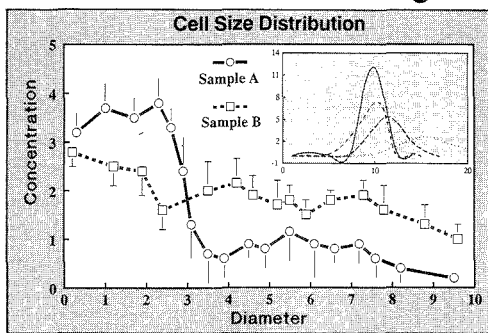
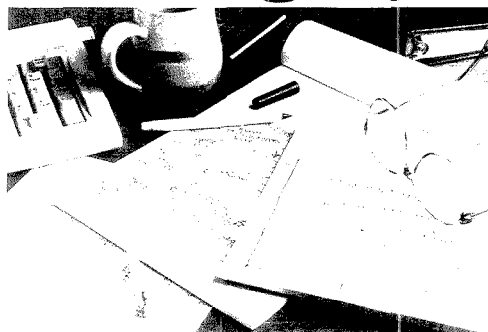
Software. Catalog features PC-based data acquisition and analysis software. Packages for analysis, statistics, graphics, and instrument interfacing and control are described. Comparison charts for all products are included. Asyst Software Technologies 429

Filters. Catalog features inorganic membrane filters, including disposable syringe filters for HPLC sample preparation and disposable membrane filter discs for mobile-phase filtration, gravimetric analysis, and microdialysis. Technical and performance specifications are included. Anotec Separations 430



Büchi Model B-168 vacuum/distillation controller can be used to safely evaporate temperature-sensitive samples and to control foaming. The unit controls vacuums up to 1200 mbar. Brinkmann Instruments 402

The agony. The ecstasy.



We know it takes a lot of work to produce good scientific data. Which is why you owe it to yourself to check out SlideWrite Plus. You see, our powerful presentation graphics software for the IBM PC and compatibles can turn the data you worked so hard to capture into high impact charts, graphs, slides and over-

heads — and do it all *in minutes*. SlideWrite Plus gives you powerful graphing features, full drawing capability, flexible labeling with 16 great fonts, and *extremely* high quality output on printers, plotters, and cameras. And that's just for starters. It's no wonder SlideWrite Plus tied for first place in a recent *PC Week* poll!

Call us for a free demo diskette right now. We'll show you how SlideWrite Plus can help your results *get* results.

Call for your FREE full-featured trial diskette! (408) 749-8620

Advanced Graphics Software
333 West Maude Ave., Sunnyvale, CA 94086

SlideWrite Plus™ We make your data look terrific.

CIRCLE 3 ON READER SERVICE CARD

ANALYTICAL CHEMISTRY, VOL. 61, NO. 18, SEPTEMBER 15, 1989 • 1051 A

What's New in Ion Analysis?

New is the consideration of this field as a whole by METROHM. Only those involved with electrochemical analysis in its entirety can offer the user the optimum method.

What manufacturer except METROHM can offer you:

- Titration
- Polarography
- Ion chromatography
- pH measurement
- Conductance measurement
- Ion selective analysis
- KF water determination
- Photometry with light guide
- Stability measurement of oils and fats
- Electrodes and sensors

Metrohm

Measurement in Chemistry
Worldwide with Metrohm

METROHM Ltd.
CH-9101 HERISAU Switzerland
Phone 071 / 53 11 33
Telefax 071 / 52 11 14
Telex 88 27 12

Brinkmann

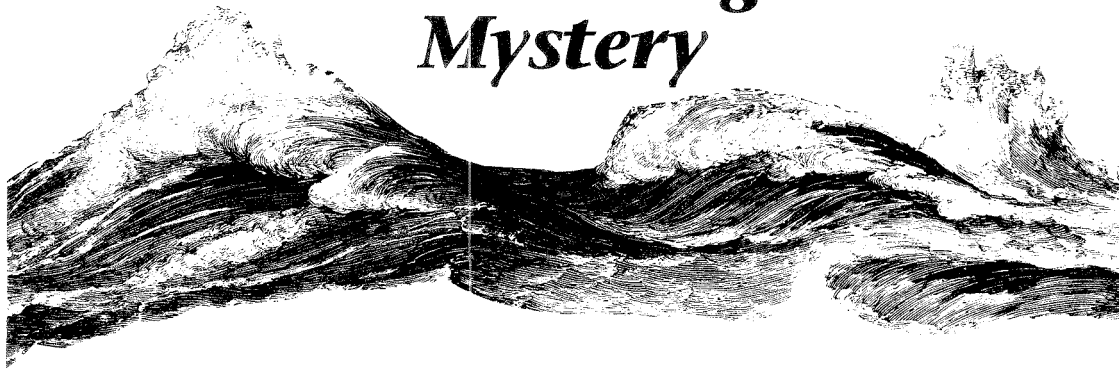
INSTRUMENTS, INC.
Cantiague Rd., Westbury, New York 11590
(516) 334-7500 (800) 645-3050

METROHM — for comprehensive solutions to problems in the entire field of ion analysis through electrochemistry: from the sample preparation via the automated analysis procedure up to the final result — selective and highly sensitive.

**Ion analysis —
quite simply with METROHM**

CIRCLE 98 ON READER SERVICE CARD

The Amnesic Shellfish Poisoning Mystery



**Michael A. Quilliam and
Jeffrey L. C. Wright**

Atlantic Research Laboratory
National Research Council of Canada
1411 Oxford Street, Halifax
Nova Scotia, Canada B3H 3Z1

In late 1987 a mysterious and serious outbreak of food poisoning occurred in Canada. Symptoms of the poisoning included vomiting and diarrhea, followed in some cases by confusion, memory loss, disorientation, and coma. Three elderly patients died, and other victims still suffer from neurological problems. The term amnesic shellfish poisoning has been proposed for this clinical syndrome.

Epidemiologists from Health and Welfare Canada (HWC) attributed the illnesses to restaurant meals of cultured blue mussels (*Mytilus edulis* L.). Using the Association of Official Analytical Chemists' mouse bioassay for "red-tide" paralytic shellfish poison (1, 2), HWC and Department of Fisheries and Oceans (DFO) scientists demonstrated that these mussels did contain toxic material and traced the problem to mussels harvested from a localized area of eastern Prince Edward Island. Intraperitoneal injections of acidic aqueous extracts of suspect mussels into mice caused death with some unusual neurotoxic symptoms very different from those of paralytic shellfish poison and other known toxins.

It was not known whether the toxic agent was a man-made pollutant or a natural toxin. The scientific detective story that unfolded was followed closely by a concerned Canadian public and made front-page newspaper headlines for several weeks. For health, political, and economic reasons, scientists in Canadian government laboratories were eager to solve the mystery quickly.

Initial methodologies

Several laboratories attempted analyses for certain targeted toxic substances such as heavy metals and organophosphorous pesticides. All of these analyses yielded negative results. Experiments also were conducted to compare the analytical "fingerprints"

of extracts of toxic and nontoxic control mussels. Any differences between the chromatograms or spectra of these extracts might be attributable to the toxic agent and allow for its identification. Methods used to generate such fingerprints included TLC, HPLC with a UV-vis diode array detector (DAD), GC/MS, and NMR spectrometry.

Some interesting differences were immediately obvious in the TLC and HPLC-DAD chromatograms of lipid-soluble fractions from digestive glands of toxic and control mussels. However, examination of the UV-vis spectra of the compounds giving rise to these differences revealed absorption bands at >400 nm that were characteristic of phytoplankton pigments. Indeed, the digestive glands of the toxic mussels were found to be engorged with a green plankton.

In retrospect these observations provided hints about differences in mussel diets and strongly suggested a natural toxin, but they gave no information about the nature of the toxin itself. Such an approach might have led eventually to detection and identification of the toxin, but it was soon established that lipid-soluble fractions were not toxic in the mouse bioassay. A more systematic approach was necessary.

On December 12, 1987, a team of scientists was assembled at the Atlantic Research Laboratory (ARL) of the National Research Council in Halifax,



Nova Scotia. This team consisted of all available chemists and marine biologists from ARL as well as some scientists from DFO, including personnel experienced with the mouse bioassay procedure. This team developed a strategy based on bioassay-directed separations and analyses (e.g., 3) that

led to the identification of the toxin on the afternoon of December 13, just 102 h after the start of the concerted investigation.

Bioassay-directed strategy

The general principles of the bioassay-directed approach used are summa-

rized in Figure 1a. Extracts of both toxic and control mussels were taken in parallel through a series of preparative separation steps (Figure 1b). After each fractionation, the mouse bioassay was used quantitatively and qualitatively to determine which fraction(s) contained the toxin (or toxins if a mixture was present). Various chromatographic and spectroscopic techniques were also used to profile toxic fractions and the corresponding fractions from control samples. The objectives were to determine possible differences between toxic and control fractions that might correspond to the toxin(s) and to determine whether a fraction was simple enough to begin structure elucidation. Application of various spectroscopic methods to the purified toxin then provided clues about the structure of the compound, and relevant chemical literature was searched to determine if the toxin was a known compound.

To avoid large statistical fluctuations associated with sampling inhomogeneities, all experiments were conducted using large portions of toxic and control tissue homogenates. Dose control in the bioassay was of crucial importance for effective tracking and for establishing a toxicity balance. The toxic symptoms in mice (which included scratching, trembling, and death by asphyxiation) were quite different from those observed with known shellfish toxins, and it was essential to establish a dose-response curve for the bioassay. The working curve is shown in Figure 2. Note the narrow dynamic range, which implied that effective tracking of toxicity required that each bioassay correspond to material extracted from about 0.6 g of mussel tissue (the midpoint of the dynamic range). To determine the toxicity balance, the weight equivalent of mussel tissue extracted for each bioassay injection had to be known.

The preparative fractionation scheme used and the results of the mouse bioassay at each stage are presented in Figure 1b. A classical natural products extraction procedure using mild aqueous methanol at room temperature was selected for initial work in case the toxin was a labile compound. Later it was found that greater extraction efficiency could be achieved with more rigorous extraction methods. A partitioning between water and dichloromethane followed by XAD-2 column chromatography revealed that the toxin was water soluble. The final stage of the purification process was a dual approach invoking two separate fractionation procedures based on differ-

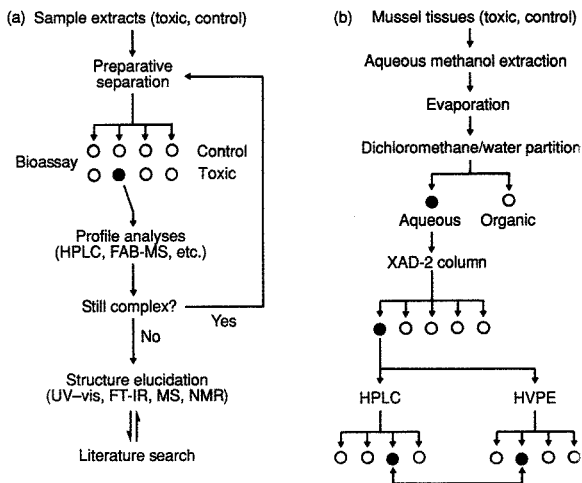


Figure 1. Flow charts illustrating (a) the general principles of the bioassay-directed analysis strategy and (b) the extraction and fractionation procedures used in the toxic mussel investigation.

The filled circles indicate a positive test in a mouse bioassay; open circles indicate a negative test.

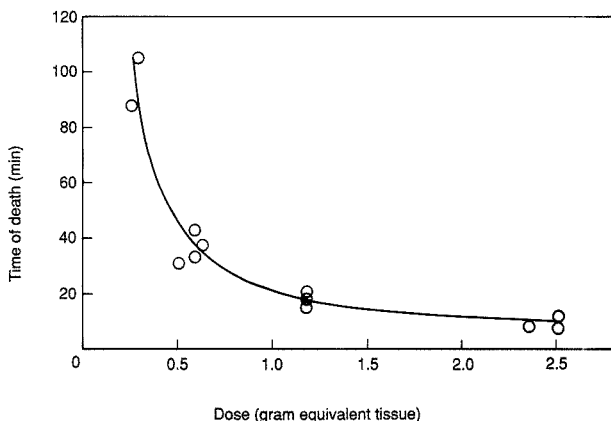
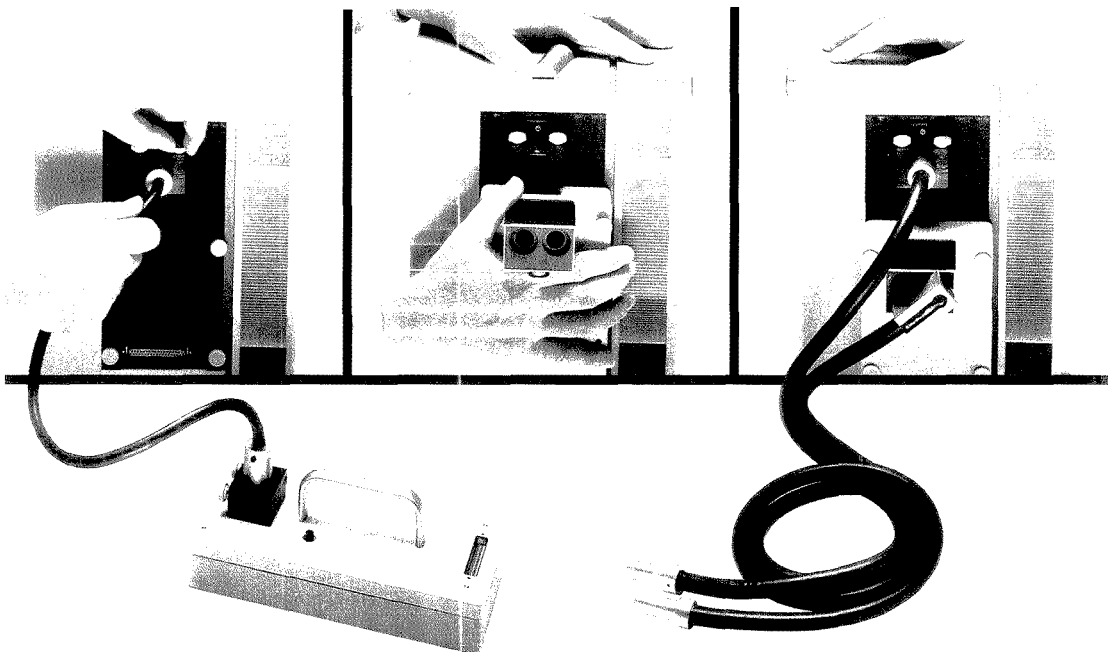
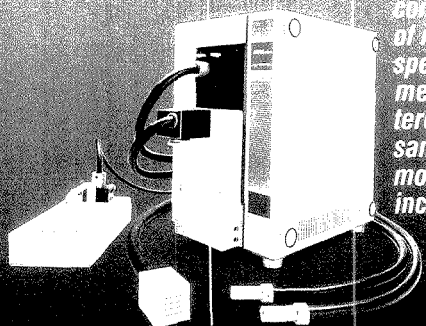


Figure 2. Working dose-response curve relating mouse time of death to the weight of mussel tissue equivalent in the injected dose.



**SWITCH FROM NIR REFLECTANCE TO TRANSMISSION
IN THE TIME IT TAKES TO READ THIS:**



Perstorp Analytical Company's NIRSystems introduces a complete line of modular NIR spectrophotometers with interchangeable sampling modules, including an array of fiber optic probes.

of all instruments are all range-based for in-plant use. Get the full story today on this remarkable advance in state-of-the-art spectroscopy. Call toll-free, 800-343-2036 for full information.

NIRSystems™
A Perstorp Analytical Company

2441 Linden Lane, Silver Spring, MD 20910

CIRCLE 110 ON READER SERVICE CARD

ent physicochemical properties. HPLC exploits differing partition ratios between a polar mobile phase and a non-polar stationary phase, whereas high-voltage paper electrophoresis (HVPE) depends on different electrophoretic mobilities of charged species under a strong electric field. Thus the chances of erroneous identification of the toxin were minimized, especially by cross-checking toxic fractions from HPLC by HVPE and vice versa.

Both HPLC and HVPE also yielded informative profile analyses. A striking example of HPLC-DAD profile analysis comparing fractions of toxic and control mussel extracts is shown in Figure 3. The HPLC conditions were selected on the premise that the unknown toxic substance was a polar, ionizable compound such as a peptide. Chromatograms for absorption at 210 nm \pm 10 nm indicated a peak at about 12 min (just after the tryptophan

peak) for toxic but not for control XAD-2 fractions. Detection at 210 nm \pm 10 nm was used initially to reveal all differences because most compounds absorb at shorter wavelengths. The complete three-dimensional representation of the HPLC-DAD data for the toxic sample at the appropriate time window is shown with the absorption spectrum taken at the peak maximum. The latter spectrum shows an absorption maximum at 242 nm (suggesting a conjugated system such as C=C-C=C). Reconstructed chromatograms for absorption at this wavelength are also shown to accentuate the toxic/control dichotomy. When these same XAD-2 fractions were analyzed using HVPE, a band running just behind glutamic acid but staining yellow rather than red with ninhydrin was observed in the toxic but not in the control extracts.

Furthermore, the HPLC-DAD suspect peak was collected and analyzed

using HVPE, where it gave the same yellow band; the converse cross-check was also successful. Even more important was the finding that these fractions, collected from the two complementary separation techniques operated on a preparative scale, were shown to account for all of the toxicity within the reproducibility of the dose-response curve.

Spectroscopic strategy

While these highly encouraging results were being obtained, complementary profile analyses obtained for all toxic fractions by fast atom bombardment mass spectrometry (FAB-MS) showed that peaks at m/z 312 ($[M + H]^+$) in positive ion mode and at m/z 310 ($[M - H]^-$) in negative ion mode were increasing in prominence as the toxin was progressively purified. No significant corresponding signals arising from a compound of MW 311 were evident in

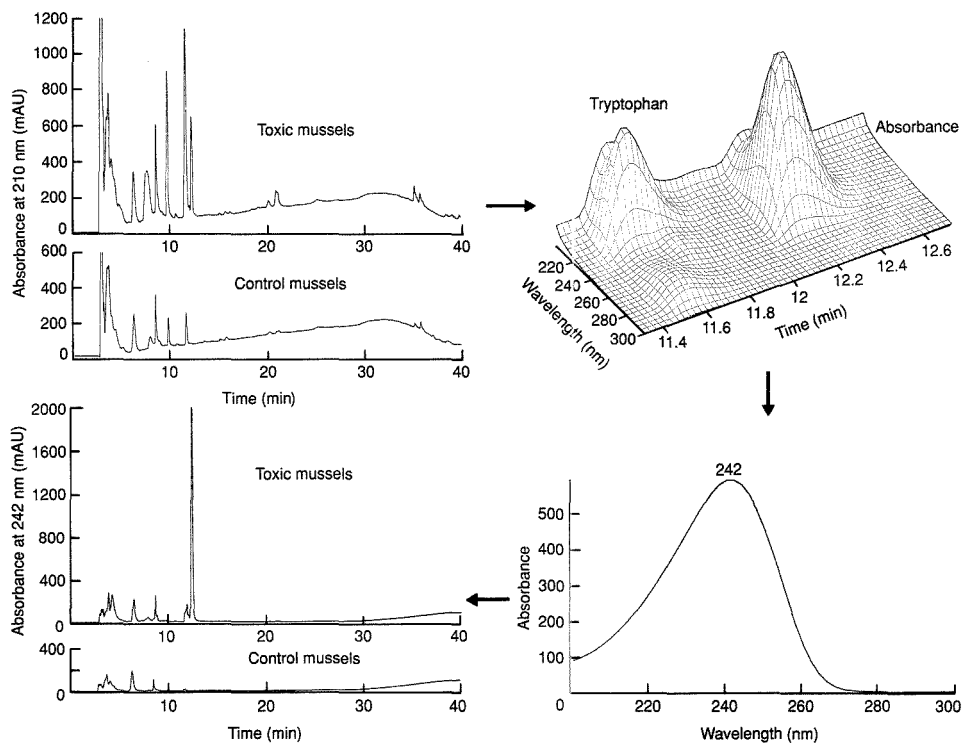
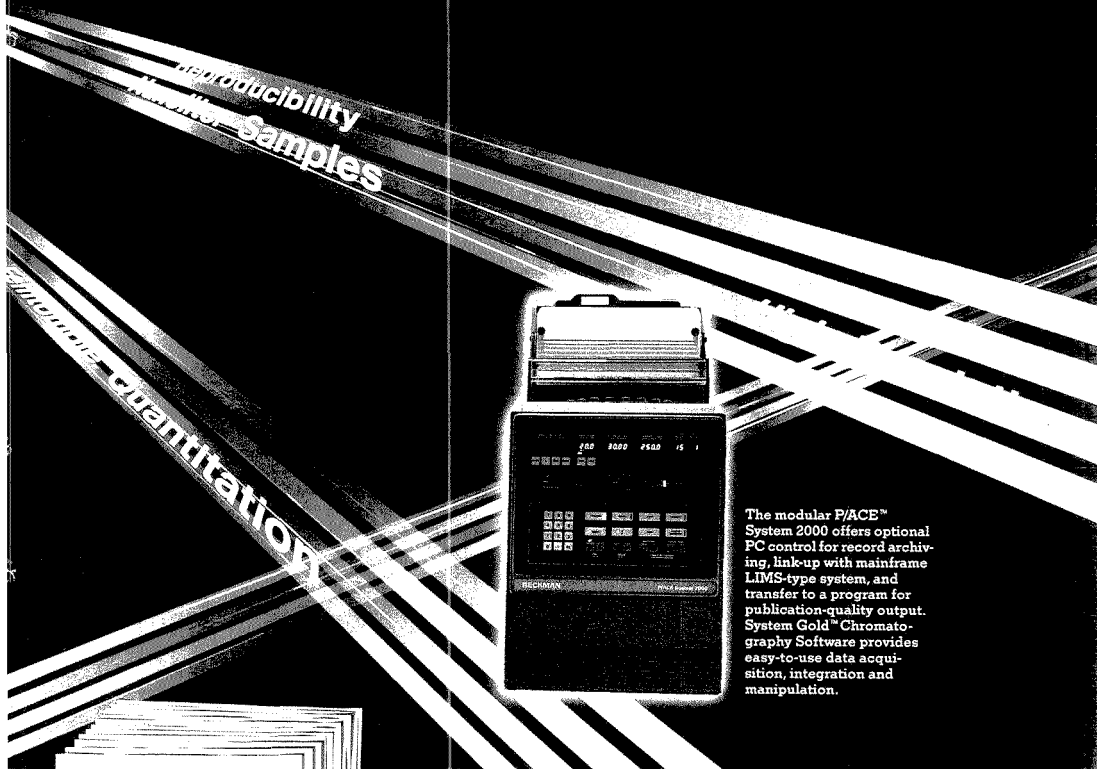


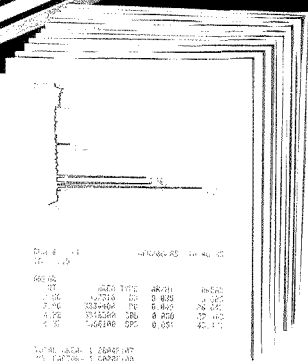
Figure 3. HPLC-DAD profiles of corresponding XAD-2 fractions from toxic and control mussels.

Chromatograms reconstructed from the DAD data at 242 nm show the differences more dramatically. Conditions: 25 cm \times 4.6 mm i.d. Vydac 201TP column with 1.0 mL/min $\text{CH}_3\text{CN}/\text{H}_2\text{O}/\text{CF}_3\text{COOH}$; gradient elution from 5.0:94.9:0.1 to 99.9:0.0:0.1 over 40 min.

Beckman Sets the P/ACE for Automated Electrophoretic Separations...



The modular P/ACE™ System 2000 offers optional PC control for record archiving, link-up with mainframe LIMS-type system, and transfer to a program for publication-quality output. System Geld™ Chromatography Software provides easy-to-use data acquisition, integration and manipulation.



Shows 11 injections in 90 min from a total sample of 5 μ L, accomplished with P/ACE™ Migration time CV less than .25%.

The P/ACE™ System 2000 from Beckman is designed for today and tomorrow. A modular system, P/ACE leads the evolution of capillary electrophoresis.

A removable detector allows multiple future detection options. Interchangeable cartridges let you change capillaries in minutes. Temperature control provides unmatched reproducibility. And sealed vials minimize sample evaporation. All unique to P/ACE. Unique too—the surprisingly affordable price.

Keep P/ACE with the latest in electrophoretic separation techniques! And achieve rapid success separating proteins, peptides, synthetic oligonucleotides, DNA fragments, and more.

Call 800/742-2345, or write to Beckman Instruments, Inc., Spinco Division, Customer Service Department, 1050 Page Mill Rd., Palo Alto, CA 94304. Offices in major cities worldwide.

BECKMAN

A SMITHKLINE BECKMAN COMPANY

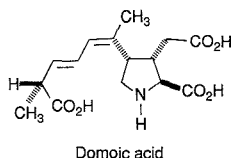
CIRCLE 18 ON READER SERVICE CARD

© 1989 Beckman Instruments, Inc.

any fractions from control mussels. High-resolution MS (peak matching) on an XAD-2 fraction showed the positive ions at m/z 312 to have the composition $C_{15}H_{22}NO_6$. The fragmentation behavior of these ions (tandem MS, Figure 4a), through successive losses of 46 Da ($HCOOH$) and other small neutral species, eventually yielded an intense fragment at m/z 74. This is characteristic of protonated amino acids, as known previously from chemical ionization studies. In the meantime, FT-IR spectra of crude toxic fractions (Figure 4b) suggested the presence of $>NH$, $-COOH$, $-CH=CH-$ (*trans*), and $-CH_3$ groups, and proton NMR spectra (Figure 4c) of concentrated toxic fractions showed signals characteristic of $-CH=CH-CH=C-$, $CH_3-C=C-$, and $CH_3-CH<$ functionalities.

In case the toxin was a known compound, all information produced by the experiments was used as input data for a computerized literature search through the Chemical Abstracts and Registry files maintained by STN International (Columbus, OH). The list of possible compounds was reduced from thousands to one most likely candidate for the toxin—a tricarboxylic amino acid, domoic acid. Known pharmacological properties of this compound (4-7) are consistent with the neurotoxic symptoms caused by the af-

fected mussels, although the compound had not previously been identified as a human intoxicant.



Structure confirmation

At this stage it appeared likely that the toxin was either domoic acid or a closely related compound. Proof of chemical structure was provided by NMR, which required a sizable amount of purified material. Multiple HPLC injections had to be made overnight so that enough toxin could be collected to obtain a good-quality proton NMR spectrum. This also made it possible to acquire an improved FT-IR spectrum. The NMR spectrum was entirely consistent with a previously published spectrum of synthetically produced domoic acid (8) except for some slight variations later shown to reflect pH dependence of the ionic form of the compound. Subsequent work on highly purified mussel toxin has shown that 2D

proton NMR, ^{13}C NMR, melting point, and optical rotation are all consistent with the known properties of domoic acid (8).

Toxicity

Although chromatographic separations of aqueous methanol extracts showed no other detectable toxins, it was still important to establish that domoic acid accounted for all of the toxicity in the original mussel tissue. In the days following, many hours of painstaking work established a toxicity balance. Figure 5 illustrates part of this effort as a dose-response curve for the bioassay, expressed by the amount of domoic acid injected (as determined by a high-speed HPLC assay [9]). The different data points plotted in Figure 5 reflect several toxic mussel samples extracted by different methods.

Domoic acid was first identified in crude extracts of certain seaweed found in Japan (10) and was used there as a folk medicine remedy for intestinal worm infestation. This fact argues against this compound as a toxin. However, when the high levels concentrated in the toxic mussels (up to 900 $\mu g/g$ wet weight) are taken into account, the implication is that as much as 0.2-0.3 g may have been ingested and the difference between therapeutic and toxic doses is easily established.

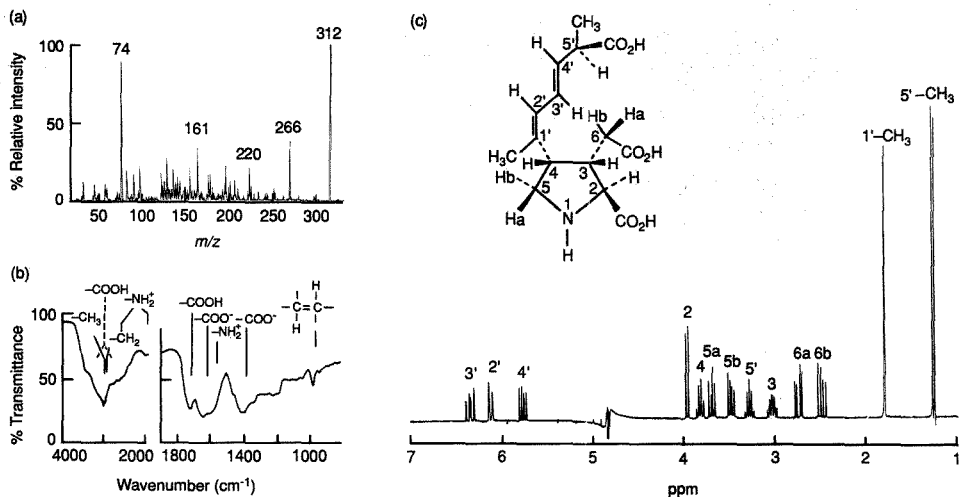


Figure 4. Spectroscopic data for the mussel toxin.

(a) MS/MS fragment ion spectrum of the m/z 312 ion in the positive ion FAB mass spectrum of a toxic XAD-2 fraction, (b) FT-IR spectrum of a thin film of the isolated toxin on CaF_2 window, and (c) 300 MHz proton NMR spectrum of purified toxin dissolved in D_2O .

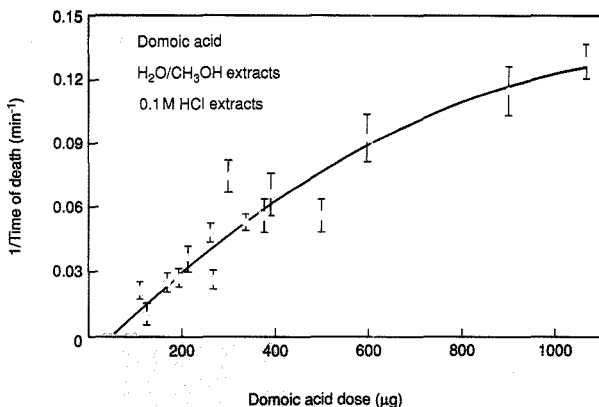
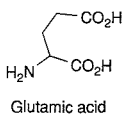


Figure 5. Dose-response curve, plotted as inverse of time of death (TOD) against dose of domoic acid (determined by HPLC analyses), for standard solutions and for different contaminated mussel extracts injected into the mouse.

Each point is the mean of 2-4 replicate measurements of TOD for one solution, and the error bars represent an estimate of the standard deviation. The curve is a second-order polynomial least-squares regression on all data points.

The neurotoxicity of domoic acid results from its effect as a potent glutamate agonist (4-7). Domoic acid can be considered to be a conformationally restricted form of glutamic acid that disrupts normal neurochemical transmission in the brain by binding to certain glutamate receptors of normal cells. This results in continuous stimulation of neurons and the eventual formation of lesions.



Retrospective

A detailed scientific account of the identification of the mussel toxin has been published (11), and a prolonged investigation into the source of the domoic acid was also conducted. The localization of domoic acid in the digestive system of the shellfish clearly pointed to a dietary origin for the toxin. As mentioned earlier, the digestive glands were engorged with plankton, the microscopic examination of which revealed large numbers of an unidentified diatom. Coincidentally, marine biologists patrolling the affected estuary observed a substantial uni-algal bloom of phytoplankton later identified as the

diatom *Nitzschia pungens* forma *multiseries*. This work, which has been described in detail elsewhere (12, 13), also established unequivocally that domoic acid is produced as a secondary metabolite of the diatom.

This is the first report of a shellfish toxin from a marine diatom, and the implications for the shellfish industry are significant. The diatom *N. pungens* is widely distributed in the coastal waters of the Atlantic, Pacific, and Indian oceans, although production of domoic acid in all strains has not yet been demonstrated. It is known, however, that shellfish harvested from other locations on the eastern seaboard contain domoic acid (9).

The cause of the bloom of *N. pungens* cannot be answered with any degree of certainty. One possible explanation is that freshwater runoff from agricultural land caused stratification of the ocean layers and raised the nutrient level in the coastal waters at just the right time in the diatoms' lifecycle. In fact, there was a record-breaking storm with easterly winds on Sept. 7, 1987. It is of interest that a similar, but less dense, bloom of *N. pungens* occurred in the same area in late 1988. In this case, it was found that the rise and fall of cell density of *N. pungens* in the seawater accurately reflected that of domoic acid concentration in water and cultured mussel samples. Nevertheless, a DFO screening program implement-

ed for domoic acid effectively protected the public and the rest of the shellfish industry during this repeat episode. Fortunately, shellfish contaminated with domoic acid clear themselves if kept in clean seawater, so the aquaculturist is not faced with a total loss if toxification of a crop occurs.

In retrospect, the speed with which the toxin was identified is attributable to several factors: its water solubility, which permitted discarding the entire lipid-soluble fraction; the high concentration in the contaminated mussels; the availability of an on-site bioassay that was rapid and reasonably precise; and the fact that the toxin turned out to be a compound that could readily be found in the chemical literature. More important than any of these factors, however, was the dedication and camaraderie of the entire team of scientists, technicians, and support staff who worked with minimal sleep until the mystery was solved.

This article is NRCC publication no. 30557

References

- (1) *Official Methods of Analysis*; Association of Official Analytical Chemists: Arlington, VA, 1984; pp. 18,086-18,092.
- (2) Adams, W. N.; Miescier, J. J. *J. Assoc. Off. Anal. Chem.* 1980, **63**, 1336-43.
- (3) Schuetzle, D.; Lewtas, J. *Anal. Chem.* 1986, **58**, 1060 A-1075 A.
- (4) Zaczek, R.; Coyle, J. T. *Neuropharmacology* 1982, **21**, 15-26.
- (5) Shinozaki, H.; Ishida, M. *Brain Res.* 1976, **109**, 435-39.
- (6) Biscoe, T. J.; Evans, R. H.; Headley, P. M.; Martin, M. R.; Watkins, J. C. *Nature* 1975, **255**, 166-67.
- (7) Takeuchi, H.; Watanabe, K.; Nomoto, K.; Ohfuné, Y.; Takemoto, T. *Eur. J. Pharmacol.* 1984, **102**, 325-32.
- (8) Ohfuné, Y.; Tomita, M. *J. Am. Chem. Soc.* 1982, **104**, 3511-13.
- (9) Quilliam, M. A.; Sim, P. G.; McCulloch, A. W.; McInnes, A. G. *Int. J. Environ. Anal. Chem.* 1989, **36**, 139-54.
- (10) Takemoto, T.; Daigo, K. *Chem. Pharm. Bull.* 1958, **6**, 578-80.
- (11) Wright, J.L.C.; Boyd, R. K.; deFreitas, A.S.W.; Falk, M.; Foxall, R. A.; Jamieson, W. D.; Laycock, M. V.; McCulloch, A. W.; McInnes, A. G.; Odense, P.; Pathak, V. P.; Quilliam, M. A.; Ragan, M. A.; Sim, P. G.; Thibault, P.; Walter, J. A.; Gilgan, M.; Richard, D.J.A.; Dewar, D. *Can. J. Chem.* 1989, **67**, 481-90.
- (12) Subba Rao, D. V.; Quilliam, M. A.; Pocklington, R. *Can. J. Fisheries Aqu. Sci.* 1988, **45**, 2076-79.
- (13) Bates, S. S.; Bird, C. J.; deFreitas, A.S.W.; Foxall, R. A.; Gilgan, M.; Hanic, L. A.; Johnson, G. E.; McCulloch, A. W.; Odense, P.; Pocklington, R.; Quilliam, M. A.; Sim, P. G.; Smith, J. C.; Subba Rao, D. V.; Todd, E.C.D.; Walter, J. A.; Wright, J.L.C. *Can. J. Fisheries Aqu. Sci.* 1989, **46**, 1203-15.

Michael A. Quilliam, an associate research officer with the National Research Council of Canada, received his

Ph.D. in analytical chemistry from the University of Manitoba. After completing postdoctoral work at the Université de Montréal, Quilliam spent nine years as a faculty member in the Chemistry Department of McMaster University before joining ARL in 1987. His research interests include chroma-

tography, spectroscopy, and the application of bioassay-directed analysis to solve problems in environmental toxicology.

Jeffrey L. C. Wright, a senior research officer with the National Research Council of Canada, was the leader of

the mussel toxin team. He received a Ph.D. in bioorganic chemistry from Glasgow University. Wright's research interests include the discovery of bioactive compounds from marine organisms and the application of tandem mass spectrometry to distinguish stereoisomers.



Members of the mussel toxin team. From left to right, front row: P. F. Seto, J.L.C. Wright, P. G. Sim, A.S.W. deFreitas, C. Gillis, C. J. Bird, M. A. Quilliam, M. Falk; second row: M. A. Ragan, P. Odense, A. R. Taylor, A. M. Backman, C. A. Craft, G. K. McCully, P. LeBlanc, V. Pathak, W. D. Jamieson, D.J.A. Richard; third row: D. Robson, J. A. Walter, P. Thibault, M. V. Laycock, D. Tappen, R. K. Boyd, H. Watts, D. O'Neil, C. Vaughan, W. P. Hardstaff, M. Greenwell, A. G. McInnes, M. G. Flack, D. J. Embree, A. W. McCulloch, O. Henderson. Not shown: D. Breuer, D. Dewar, E. W. Dyer, R. A. Foxall, M. Gilgan, N. I. Lewis, M. McInerney-Northcott, J. L. McLachlan.

LABORATORY SERVICE CENTER

Acetylenedicarboxylic Acid, Potassium Salt • Allylisovalerate • Aluminon
4-Aminobenzonitrile • m-Aminophenol • 1-Bromonaphthalene • p-Chloranil
Cinnamaldehyde • Cuprous Bromide • 2,6-Dichloroindophenol, Sodium
Digitonin • Dimethyl Adipate • Dioctyl Sebacate • s-Diphenylcarbazide
Iodine Titration Indicator • Methylene Iodide • 2-Naphthaldehyde
Neocuproine & HCl • Nitroso-R-Salt • Rhodanine • Sodium Butyrate
Sodium Dihydroxyethylglycine • Succinimide • Sulfosalicylic Acid
Syringic Acid • Thionine • 3,4-Toluenedithiol • iso-Valeraldehyde

Write for our Products List of over 3,000 chemicals

Tel: 516-273-0900 • TOLL FREE: 800-645-5566 Telefax: 516-273-0858 • Telex: 497-4275

EASTERN CHEMICAL
A Division of UNITED-GUARDIAN, INC.

P.O. Box 2500
DEPT. AC
SMITHTOWN, N.Y. 11787

Laboratory Service Center (Equipment, Materials, Services, Instruments for Leasing). Maximum space — 4 inches per advertisement. Column width, 2-3/16"; two column width, 4-9/16". Artwork accepted. No combination of directory rates with ROP advertising. Rates based on number of inches used within 12 months from first date of first insertion. Per inch: 1" — \$155; 12" — \$153; 24" — \$150; 36" — \$145; 48" — \$140.

CALL OR WRITE JANE GATENBY

ANALYTICAL CHEMISTRY

500 Post Road East

P.O. Box 231

Westport, CT 06880

203-226-7131/FAX: 203-454-9939

NMR ANALYSIS

MULTINUCLEAR LIQUID or
MULTIFIELD SOLID STATE
SPECTRAL DATA SERVICES, INC.
818 Pioneer
Champaign, IL 61820
(217) 352-7084

HELP WANTED ADS

ROP display at ROP rates. Rate based on number of insertions within contract year. Cannot be combined for frequency.

Unit	1-Ti	6-Ti	12-Ti
1" (25 mm)	\$180	\$160	\$150
	24-Ti	48-Ti	72-Ti
	\$140	\$130	\$125

CALL OR WRITE JANE GATENBY

ANALYTICAL CHEMISTRY

500 Post Road East

P.O. Box 231

Westport, CT 06880

203-226-7131

FAX: 203-454-9939

INDEX TO ADVERTISERS IN THIS ISSUE

CIRCLE INQUIRY NO.	ADVERTISERS	PAGE NO.
3	Advanced Graphics Software, Inc.	1051A
5	*Alltech Chromad	1018A
1	Antek Instruments, Inc.	1017A
18	*Beckman Instruments, Inc.	1057A
20	*Beckman Instruments, Inc. Techmarketing	1012A-1013A
30	*CDS Instruments Altman-Hall Associates	1042A
27, 28	*Conostan Division/Conoco Specialty Products Robert Lamons & Associates	1043A, 1045A
32	Delsi Inc./Nermag Division	1010A
50	*Fisher Scientific Hawbaker Communications, Inc.	1046A
60	*Galileo Electro-Optics Corp. Legasse Associates Advertising Inc.	1044A
65	*Hewlett-Packard Company Brooks Communications	OBC
63	*Hitachi Instruments, Inc.	1020A
80-86	*Instruments SA, Inc./J-Y Division Kathy Wyatt & Associates	1015A
77	*Isco, Inc. Farneaux Associates	1025A
75	*Isotec, Inc. Kenyon Hoag Associates	1029A
88	*Kratos Analytical Carol Marketing Associates, Inc.	1027A
92	*Leybold Vacuum Products, Inc. CD Werbeagentur GmbH	1022A
94	*Macherey-Nagel GmbH & Co. KG MP Design Werbeagentur	1049A
96	*Malvern Instruments, Inc.	1035A
100-107	*Matheson Gas Products Kenyon Hoag Associates	1019A
98	*Metrohm Ltd. Ecknauer & Schoch Werbeagentur ASW	1052A
112	*Nicolet Analytical Instruments	1031A
110	*NIRSystems Barrett Advertising	1055A
127	Perkin-Elmer Corporation Graystone	1039A
125	*Phillips Scientific/Analytical Division Connors Publicity, Ltd.	1050B
129	Precision Scientific Winterkorn Lillis Inc.	IFC

CIRCLE INQUIRY NO.	ADVERTISERS	PAGE NO.
138	Radiometer Analytical A/S	1041A
150, 151	*Spectra-Physics	1036A
156	*Thermo Jarrell Ash Corporation Noort Inc.	1009A

Directory section, see page 1060A.
 * See ad in ACS Laboratory Guide.
 ** Company so marked has advertisement in Foreign Regional edition only.
 Advertising Management for the American Chemical Society Publications

CENTCOM, LTD

President

Thomas N. J. Koerwer

Executive Vice President Senior Vice President

James A. Byrne Benjamin W. Jones

Clay S. Holden, Vice President

Robert L. Voepel, Vice President

Joseph P. Stenza, Production Director

500 Post Road East
 P.O. Box 231
 Westport, Connecticut 06880
 (Area Code 203) 226-7131
 Telex No. 643310
 FAX: 203-454-9939

ADVERTISING SALES MANAGER

Bruce E. Poorman

ADVERTISING PRODUCTION MANAGER

Jane F. Gatenby

SALES REPRESENTATIVES

Philadelphia, PA . . . Patricia O'Donnell, CENTCOM, LTD., GSB Building, Suite 405, 1 Belmont Avenue, Bala Cynwyd, Pa. 19004. Telephone: 215-667-9666, FAX: 215-667-9353

New York, NY . . . John F. Raftery, CENTCOM, LTD., 60 East 42nd St., New York, N.Y. 10165. Telephone: 212-972-9660

Westport, CT . . . Edward M. Black, CENTCOM, LTD., 500 Post Road East, P.O. Box 231, Westport, Ct. 06880. Telephone: 203-226-7131, Telex 643310, FAX: 203-454-9939

Cleveland, OH . . . Bruce E. Poorman, John C. Guyot, CENTCOM, LTD., 325 Front St., Suite 2, Berea, Ohio 44017. Telephone: 216-234-1333, FAX: 216-234-3425

Chicago, IL . . . Michael J. Pak, CENTCOM, LTD., 540 Frontage Rd., Northfield, Ill. 60093. Telephone: 312-441-6383, FAX: 312-441-6382

Houston, TX . . . Michael J. Pak, CENTCOM, LTD. Telephone: 312-441-6383

San Francisco, CA . . . Paul M. Butts, CENTCOM, LTD., Suite 1070, 2672 Bayshore Frontage Road, Mountain View, CA 94043. Telephone: 415-969-4604

Los Angeles, CA . . . Clay S. Holden, CENTCOM, LTD., Newton Pacific Center, 3142 Pacific Coast Highway, Suite 200, Torrance, CA 90505. Telephone: 213-325-1903

Boston, MA . . . Edward M. Black, CENTCOM, LTD. Telephone: 203-226-7131

Atlanta, GA . . . John F. Raftery, CENTCOM, LTD. Telephone: 212-972-9660

Denver, CO . . . Paul M. Butts, CENTCOM, LTD. Telephone: 415-969-4604

United Kingdom
 Reading, England . . . Malcolm Thiele, Technomedia Ltd., Wood Cottage, Shurlock Row, Reading RG10 0QE, Berkshire, England. Telephone: 073-434-3302, Telex #848800, FAX: 073-434-3848.

Lancashire, England . . . Technomedia Ltd., c/o Meconomics Ltd., Meconomics House, 31 Old Street, Ashton Under Lyne, Lancashire, England. Telephone: 061-308-3025

Continental Europe . . . Andre Jamar, International Communications, Inc., Rue Mallat 1, 4800 Verviers, Belgium. Telephone: (087) 22-53-85, FAX: (087) 23-03-29

Tokyo, Japan . . . Sumio Oka, International Media Representatives Ltd., 2-29 Toranomon, 1-Chome Minato-ku Tokyo 105 Japan. Telephone: 502-0656, Telex #22633, FAX: 591-2530

New Titles

from the
American
Chemical
Society

It's the Good Book!

Biotechnology and Materials Science Chemistry for the Future

Biotechnology and materials science—two different fields unified through the science of chemistry. Now you can get a better understanding of these two disciplines and their tremendous impact on technology. This new book presents discussions of exciting advances by outstanding researchers in these pivotal fields. Learn the history behind present-day biotechnology and see where advances are predicted. Look at the progress being made in new recombinant DNA technology and materials produced by high-technology. Written in non-technical language, this 11-chapter book is beautifully illustrated in full color. Scientist and non-scientist alike will find this book both informative and enjoyable.

Mary L. Good, Editor

Jacqueline K. Barton, Associate Editor

135 pages (1988)

Cloth: US & Canada \$24.95 Export \$29.95

ISBN 0-8412-1472-7

Paper: US & Canada \$14.95 Export \$17.95

ISBN 0-8412-1473-5

New edition of the ACS best-seller!

Cancer: The Outlaw Cell Second Edition

Completely revised and updated! This new book consists of articles on the most promising research and clinical treatment from leading scientists in the field. Special emphasis is on the basic concepts for biology and medicine, new developments, and an appraisal of advances in non-surgical modes of therapy used in treatment. Beginning with an overview, this 14-chapter book includes subjects such as the genetic basis of cancer, cancer and the immune response, angiogenesis, and immunotherapy. *Cancer: The Outlaw Cell* is an easy-to-understand book for anyone interested in cancer research and medicine.

Richard E. LaFond, Editor

306 pages. (1988)

Cloth: US & Canada \$29.95 Export \$35.95

ISBN 0-8412-1419-0

Paper: US & Canada \$19.95 Export \$23.95

ISBN 0-8412-1420-4

How to use statistics in research...

Practical Statistics for the Physical Sciences

Learn how to get the information you need from research data with this dynamic new book on statistical procedures. Written in understandable, easy-to-follow steps, this book teaches you the concepts underlying the use of statistics in research. Worked-out examples are provided to illustrate each procedure, and commonly-used formulas, tables, and reference information are also included. No prior knowledge of statistics is necessary to use this practical "how-to" book. *Practical Statistics for the Physical Sciences* is a comprehensive reference—vital to anyone who works with statistical data.

Larry L. Havlicek and Ronald D. Crain

522 pages. Cloth. (1988)

US & Canada \$59.95 Export \$71.95

ISBN 0-8412-1453-0

Implementing a GLP program...

Good Laboratory Practices An Agrochemical Perspective

Requirements for good laboratory practices (GLP) are here to stay! Learn how to implement a GLP program that meets federal standards with this new book. You'll get an overview of good laboratory practices from EPA, academic, and industrial perspectives. You'll become familiar with current practices, probable changes, what needs to be done, why, and how to do it. With 19 chapters, this book will give you a better understanding of GLP standards with regard to compliance, quality assurance, and standard operating procedures. Also included is the text of the proposed FIFRA Generic Good Laboratory Practices Standards. An excellent guide for anyone involved in the implementation of a GLP program.

Willa Y. Garner and Maureen Barge, Editors

ACS Symposium Series 369

168 pages. Cloth. (1988)

US & Canada \$39.95 Export \$47.95

ISBN 0-8412-1480-8

Send your purchase order or payment to **American Chemical Society, Distribution Office Dept. 147, P.O. Box 57136, Washington, DC 20037.** Or call toll-free (800) 227-5558.

EDITOR: GEORGE H. MORRISON

ASSOCIATE EDITORS: Klaus Biemann,
Georges Guiochon, Walter C. Herlihy,
Robert A. Osteryoung, Edward S. Yeung**Editorial Headquarters**1155 Sixteenth St., N.W.
Washington, DC 20036
Phone: 202-872-4570
Telefax: 202-872-6325

Managing Editor: Sharon G. Boots

Associate Editors: Louise Voress,
Mary WarnerAssistant Editors: Grace K. Lee,
Alan R. Newman

Editorial Assistant: Felicia Wach

Director, Operational Support: C. Michael
Philippe

Production Manager: Leroy L. Corcoran

Art Director: Alan Kahan

Designer: Amy Meyer Phifer

Production Editor: Elizabeth E. Wood

Circulation: Claud Robinson

Editorial Assistant, LabGuide: Joanne Mullican

Journals Dept., Columbus, Ohio

Associate Head: Marianne Brogan

Journals Editing Manager: Joseph E. Yurvati

Associate Editor: Rodney L. Temos

Staff Editor: Sharon K. Hatfield

Advisory Board: Bernard J. Bulkin, Michael S.
Epstein, Renaat Gijbels, Peter R. Griffiths,
Thomas L. Isenhour, Nobuhiko Ishibashi,
James W. Jorgenson, Peter C. Jurs, Mary A.
Kaiser, David L. Nelson, Lawrence A. Pachla,
Ralph E. Sturgeon, George S. Wilson, Mary J.
Wirth, Andrew T. Zander, Richard N. Zare
Ex Officio: Sam P. Perone**Instrumentation Advisory Panel:** James B.
Callis, Bruce Chase, R. Graham Cooks, L. J.
Cline Love, Sanford P. Markey, Ronald E. Ma-
jors, Linda B. McGown, Gary W. Small, R. Mark
Wightman

Published by the

AMERICAN CHEMICAL SOCIETY1155 16th Street, N.W.
Washington, DC 20036**Publications Division**

Director: Robert H. Marks

Journals: Charles R. Bertsch

Special Publications: Randall E. Wedin

Manuscript requirements are published in the
January 1, 1989 issue, page 91. Manuscripts
for publication (4 copies) should be submitted
to ANALYTICAL CHEMISTRY at the ACS Washing-
ton address.The American Chemical Society and its editors
assume no responsibility for the statements
and opinions advanced by contributors. Views
expressed in the editorials are those of the
editors and do not necessarily represent the
official position of the American Chemical
Society.

- Anderegg, R. J., 2118
Arnold, D. P., 2109
- Berman, S. S., 2118
Blanche, M. S., 2047
Bowen, J. M., 2047
- Castro, M. E., 2040
Chicz, R. M., 2059
Compton, S. V., 2047
- daCunha, A. R., 2126
David, P. A., 2082
Dobashi, Y., 2121
- Fink, S. W., 2050
Freas, R. B., 2050, 2054
- Ghosh, A., 2118
- Hanson, C. D., 2040
Hara, S., 2121
Heise, H. M., 2009, 2016
- Irgum, K., 2079
- Janatsch, G., 2009, 2016
Jayaweera, P., 2102
- Kalivas, J. H., 2024
Kerley, E. L., 2040
Ketterer, M. E., 2031
Kruse-Jarres, J. D., 2009, 2016
- Magee, L. J., Jr., 2124
Marbach, R., 2009, 2016
Massart, D. L., 2098
McLaren, J. W., 2118
McLean, M. A., 2054
Morita, M., 2116
- Nakamura, K., 2121
Nomura, A., 2076
Novotny, M., 2082
- Olesik, J. W., 2002
Osteryoung, J., 2086, 2092,
2124
- Peachey, R. M., 2109
Pesek, J. J., 2067
Peters, M. J., 2031
Petty, J. D., 2109
- Ramaley, L., 2102
Regnier, F. E., 2059
Reschl, J. J., 2031
Roberts, N., 2024
Russell, D. H., 2040
- Sakaki, K., 2076
Sandoval, J. E., 2067
Shibata, Y., 2116
Siu, K. W. M., 2118
Smith, L. J., 2002
Stout, S. J., 2126
Sturgeon, R. E., 2118
Sutter, J. M., 2024
Sweetman, D. R., 2109
- Tesfalidet, S., 2079
Tsunoda, K.-i., 2076
- Wechter, C., 2092
Wikiel, K., 2086
Williamsen, E. J., 2002
- Yamada, J., 2076
Yokochi, T., 2076
- Zupan, J., 2098

Signal Fluctuations Due to Individual Droplets in Inductively Coupled Plasma Atomic Emission Spectrometry

John W. Olesik,* Lisa J. Smith, and Eric J. Williamsen

Department of Chemistry, Venable and Kenan Laboratories, CB 3290, University of North Carolina, Chapel Hill, North Carolina 27599-3290

Large emission intensity fluctuations are observed from analyte species in inductively coupled plasmas. Relative standard deviations are as large as 71% when emission is viewed with time resolution of 10 μ s. Low in the plasma, peaks in atom emission intensity are accompanied by depressions in ion emission. This behavior appears to be due to local cooling by aerosol droplets. High in the plasma, peaks in atom emission are followed by peaks in ion emission. These emission spikes result from atomization and ionization of analyte from vaporizing particles. Laser light scattering experiments show that droplets or particles exist in a conventional 1.0-kW plasma up to 20 mm above the load coil. Emission signals detected high in the plasma correlate with laser light scattering signals below.

Intensity fluctuations in inductively coupled plasma (ICP) atomic emission spectroscopy limit the precision attainable. In order to improve precision using internal standardization, the analyte and internal standard signals must correlate with one another. Therefore, several studies have focused on characterization of noise (1-7) and correlation (8-11) among different ICP emission signals.

Noise power spectra (noise power versus frequency of the noise) (1, 3-7) have been measured to characterize ICP emission. Four different noise sources have been identified. White noise is due to completely random variations in intensity and therefore has a constant noise power as a function of frequency. White noise is present in all measurement systems. White noise can be minimized by using a narrow detection bandwidth, such as by integrating the signal. One source of white noise results from the counting statistics of discrete photons arriving at the photocathode of a photomultiplier.

Whistle noise occurs at specific frequencies. Noise at 60 Hz and its harmonics is present due to the use of 60-Hz ac power. A second type of whistle noise has been observed on ICP emission with a frequency between 200 and 400 Hz. The corresponding peak in the noise power spectrum is broader than the sharp 60-Hz peak. The noise frequency varies with the applied power and gas flow rates. Plasma rotation (5) and vortex ring formation (7) have been hypothesized as the source of the noise.

Flicker noise (1/f noise) increases in magnitude at lower frequencies. The flicker noise originates from drift in the plasma power, detection system, or sample introduction system. Virtually every component of the analytical system can contribute to drift. For example, changes in the load coil cooling water temperature affect emission intensities (12).

The nebulization process is probably the main source of 1/f noise. Noise power spectra of Ar I emission observed with and without nebulization of water show that the 1/f noise is increased by the sample introduction system. Carbon emission intensity precision was found to be an order of magnitude better when the sample was introduced as a gas than when entering the plasma as an aqueous aerosol containing sugar (13).

Flicker noise cannot be reduced by integration. However, internal standardization can be used to improve analysis precision if the internal standard signal correlates highly (positively or negatively) with the analyte signal. The degree of correlation between emission signals from the ICP has been found to be dependent on the elements and spectral lines observed (8, 11).

The production and transfer of aerosol into the plasma can produce signal instability. Changes in spray chamber pressure can produce large variations in emission signals (10). Rapid pressure fluctuations can be traced to liquid droplets running down the drain hose (10). Electrostatic effects can also produce fluctuations in the emission intensities (13).

In this paper we focus on signal fluctuations that appear to be due to individual aerosol droplets and their vaporization products. We have observed fluctuations that consist of "spikes" or "dips" in emission intensity. Because these fluctuations occur on a fast time scale (10-200 μ s) and they do not appear at fixed time intervals, their presence is not discernible in the noise power spectra.

The presence and species dependence of the emission intensity fluctuations have been observed independently by two different research groups. We observed the fluctuations in intensity versus time data while we were acquiring spatially resolved noise power spectra (15, 16). Our original goal was to use noise-power spectra as a diagnostic of nebulizer performance. Farnsworth et al. (17) observed intensity fluctuations with a spatially dependent magnitude while obtaining intensity versus height data by continuously moving the ICP. Both groups saw that intensity fluctuation patterns for atom emission were different from those from ion emission. Cicerone and Farnsworth (18) have described a method to measure gas flow velocities in the central channel of the ICP by using the signal fluctuations.

Herein we describe four different sets of experiments to characterize the intensity fluctuations and identify their origin. Single-channel measurements were used to obtain representative intensity versus time data. The distribution of intensities (number of occurrences at particular intensity intervals) was obtained from these data. From these data one can assess the normalcy of the distribution. A dual channel detection system was used to investigate the correlation between signals from different spectral lines and locations in the plasma.

Laser light scattering experiments in a 1.0-kW plasma (at heights from 4 to 20 mm above the load coil) detected the presence of droplets or large particles. Emission intensities were measured simultaneously to test for correlation between the presence of scatterers and emission intensity fluctuations. Experiments that use two nebulizer/spray chamber combinations simultaneously were carried out to determine if intensity fluctuations resulted from the presence of individual aerosol droplets or from analyte atoms (ions) generated from them.

EXPERIMENTAL SECTION

Inductively Coupled Plasma. A Plasma-Therm Model HFL-1500G power supply and Model AMNPS-1 impedance

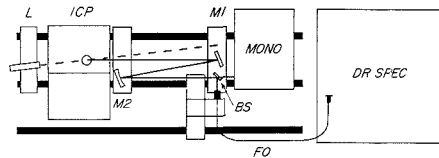


Figure 1. Optical system: L, He-Ne laser; ICP, inductively coupled plasma; M1, plane mirror; M2, spherical mirror, 0.5 m focal length; BS, beamsplitter; FO, fiber optic bundle; MONO, monochromator; DR SPEC, direct reading spectrometer.

matcher were used, operating at 40.68 MHz. Outer and intermediate gas flow rates were controlled by needle valves and monitored with rotameters. Conventional (Fassel, Plasma-Therm type) and low-flow torches (both purchased from Precision Glassblowing of Colorado) were used. Outer argon flow rates were between 16 and 18 L/min for the conventional torch and 8 to 10 L/min for the low-flow torch. Intermediate flow rates of 0.6–0.9 L/min were used.

Sample Introduction System. Concentric, pneumatic nebulizers (Meinhard Model TR-30-A3) were used with Scott-type dual barrel spray chambers (Plasma Therm Model SC-2). In experiments employing a single nebulizer-spray chamber, the central gas flowing through the nebulizer was controlled by a pressure regulator. A calibration of pressure versus mass flow rate using a Brooks Model 5850/5876 controller was performed so that the flow rate could be calculated from the pressure measurement subsequently. In the dual nebulizer-spray chamber experiments the mass flow controller was used to control the argon flow through the second nebulizer. Sample was pumped to the nebulizer at a rate of approximately 1.0 mL/min using a peristaltic pump (Gilson Miniplus 2 or Scientific Industries Model 203). A total central gas flow rate of 1.0 L/min or less was used.

Spectrometers. Two spectrometers were employed for the single-channel and dual-channel measurements. A Jarrell-Ash Atom Comp 750 direct reading spectrometer was used to observe Ca I and Ca II emission from the same location in the plasma. The direct reading spectrometer is a 0.75 M Paschen mount system with a 2400 grooves/mm grating and 50- μ m exit slits. The effective entrance slit width was 105 μ m (the diameter of the fiber optic). In other experiments, a McPherson Model 270 0.35-m monochromator with a 1200 grooves/mm grating blazed at 500 nm was also used.

Detection Electronics. The current signals from two photomultipliers in the spectrometers were fed directly into a pair of Keithley Model 427 current amplifiers. The output rise time was set to 0.01 or 0.03 ms for emission measurements and 0.1 ms for detection of laser scattering experiments. Gains of 10^6 or 10^8 V/A were used. The outputs of the two current amplifiers were connected to a Nicolet Model 3091 digital oscilloscope. The two 4000-point data sets were transferred as ASCII data to an IBM PC via an RS-232 interface operating at 9600 baud. Software to transfer the data and convert it into real numbers (including scale factors) was written in ASYST (MacMillan Software Co.) and IBM Assembly Language. A sampling rate of 5 μ s per point was used.

Optics. The optical system is shown in Figure 1. A 0.5-m focal length spherical mirror (Opco Laboratory, $\lambda/4$ wave, 4 in. diameter, Al with magnesium fluoride overcoat) formed an image of the plasma with a magnification of 0.5. A plane 4 in. diameter mirror (Opco Laboratory, $\lambda/4$ wave, Al with magnesium fluoride overcoat) was also used. A beamsplitter (Melles Griot models 03FNQ007 or 03FNQ015, with transmittance values of 50% and 10%, respectively) was used to direct a portion of the light onto the end of a 1.5-m long fiber optic bundle (General Fiber Optics part no. 24-0.1/6.0-0.25/3.0-1.5). The fiber optic bundle consisted of a 2 \times 24 array of 105 μ m diameter core (125 μ m diameter with cladding), UV transmitting fibers. A 1.5-mm mask was mounted in front of the fiber-optic bundle so that a region of the plasma approximately 3 mm high was viewed simultaneously. The other end of the fiber-optic bundle is arranged in a 1 \times 48 array. The slitlike fiber optic bundle was mounted in place of the entrance slit of the direct reading spectrometer, acting as a 105 μ m \times 6 mm slit.

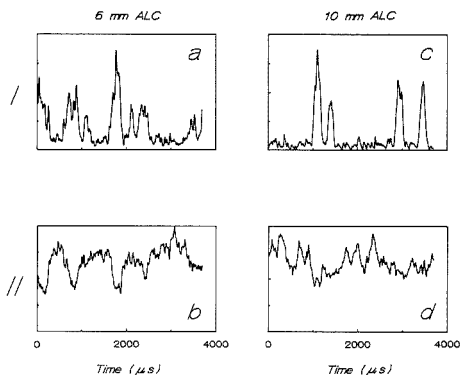


Figure 2. Time-resolved emission at 6 and 10 mm above the load coil: (a) Ca I 422 nm, 6 mm above the load coil; (b) Ca I 393 nm, 6 mm above the load coil; (c) Ca I emission 12 mm above the load coil; (d) Ca II emission 12 mm above the load coil.

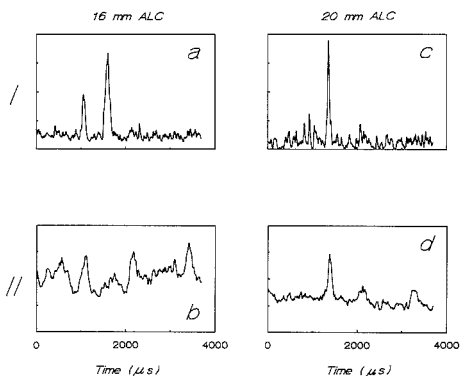


Figure 3. Time-resolved emission at 16 and 20 mm above the load coil: (a) Ca I 422 nm, 16 mm above the load coil; (b) Ca I 393 nm, 16 mm above the load coil; (c) Ca I emission 20 mm above the load coil; (d) Ca II emission 20 mm above the load coil.

The 0.35-m monochromator and collection end of the fiber-optic bundle were placed at the sagittal focus of the mirror.

Selection of Vertical Observation Zone. A computer-controlled linear actuator (Airpax K92211-P1) was used to move a ball slide (Dell Tron) holding the collection end of the fiber-optic bundle. A similar, second linear actuator/ball slide combination was used to position a 1 mm high mask mounted in front of the entrance slit of the 0.35-m monochromator.

Time-Resolved Laser Light Scattering. A 5.0-mW He-Ne laser (Uniphase) was used for time-resolved light scattering measurements. The laser was positioned so that scattered light was collected at a small angle from the laser beam in the forward direction (Figure 1).

Laser Scattering Image Detection. One-dimensional laser light scattering images were obtained by using a nitrogen laser pumped dye laser, image rotating collection optics, monochromator, and gateable photodiode array detector. This instrumental system is described in detail in ref 14.

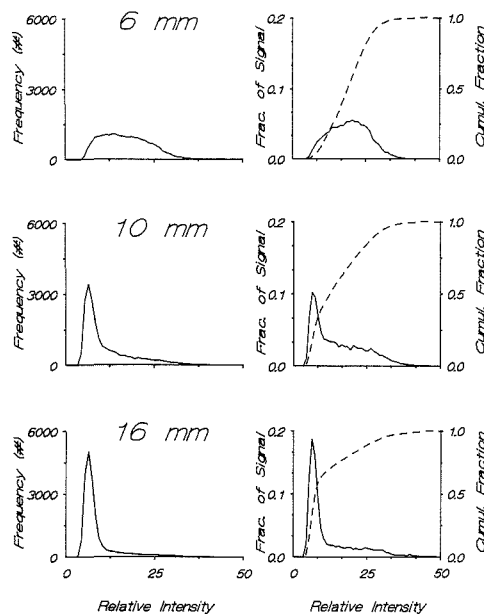
RESULTS AND DISCUSSION

1. Characterization of the Signal Fluctuations. Large fluctuations were observed (Figures 2 and 3) when analyte emission from the ICP was acquired at a rate of 5 μ s per point. Relative standard deviations are listed in Table I for Ca I and Ca II emission as a function of height in the plasma.

The nature and magnitude of the fluctuations are species and viewing height dependent (Figures 2 and 3). Ca I emission

Table I. Variation (Relative Standard Deviation) in Ca I, Ca II Emission Intensities

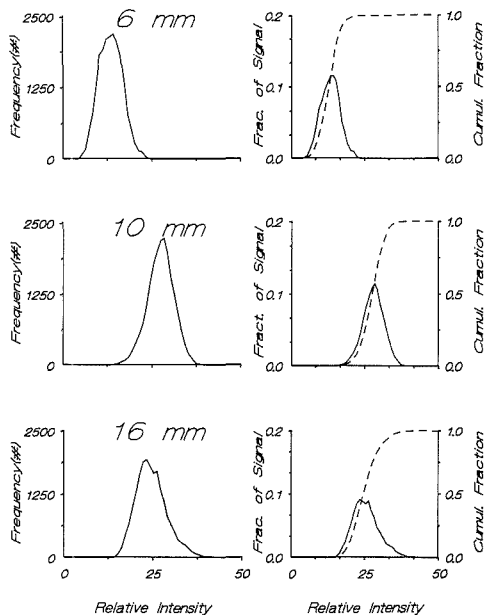
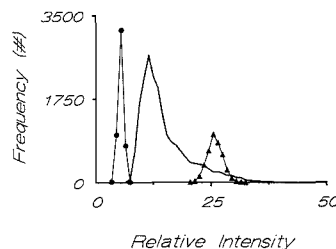
height above load coil, mm	% Ca I	% Ca II
6	41	26
8	67	17
10	71	14
12	68	14
14	57	16
16	51	18
18	45	18
20	26	21

**Figure 4.** Frequency distribution, normalized frequency distribution, and cumulative fraction of integrated signal for Ca I emission at 6, 10, and 16 mm above the load coil. Sample was 100 ppm Ca.

consisted of large spikes on top of a small constant signal (Figure 2a,c; Figure 3a,c). The relatively constant base line is due to both Ca I emission and continuum emission from the plasma. The Ca I emission spikes become less frequent as one looks higher in the plasma. In contrast, Ca II emission has a large dc component at all heights in the plasma (Figure 2b,d; Figure 3b,d). The dc component is due mainly to Ca II emission. The continuum background contributes less than 10% of the dc component signal. Ba and Mg atom and ion intensities behave similarly to Ca atom and ion intensities.

Plots of the intensity frequency distributions for Ca I and Ca II are dramatically different (Figures 4 and 5). At each of the observation heights (6, 10, and 16 mm above the load coil) the data are plotted in three different ways. Each data set, consisting of 20 000 intensity measurements, is plotted as the number of occurrences versus intensity (a-c in Figures 4 and 5). Fifty equal-sized intensity intervals were used.

The observed fluctuations in the emission signals are not due to photon shot noise. At a relative intensity of 15 on the Ca I emission frequency distributions, the theoretical standard deviation of the shot noise is approximately 1.5 relative intensity units.

**Figure 5.** Frequency distribution, normalized frequency distribution, and cumulative fraction of integrated signal for Ca II emission at 6, 10, and 16 mm above the load coil. Sample was 100 ppm Ca.**Figure 6.** Frequency distributions for Ca I emission (—), background emission (●), and chemiluminescent light emission (▲).

We repeated the measurement of Ca I intensities and continuum background with a single 0.35-m monochromator with higher light throughput than the fiber-optic/direct reading spectrometer system. The data are shown in Figure 6. This was done to be sure that the shapes of the frequency distributions shown in Figure 4 were not due to continuum background, shot noise, or the minimum detectable photocurrent.

The continuum intensity data (acquired while distilled water was introduced into the plasma) was narrowly distributed with an average relative intensity of 5.5. The Ca I intensities were widely distributed with a most probable relative intensity of 11.5.

The standard deviation of the theoretical shot noise was calculated to be 0.65 relative intensity unit for an average relative intensity of 25. (This corresponds to a standard deviation 2.6×10^{-7} A for an average signal of 1.0×10^{-5} A.) We experimentally obtained an estimate of the shot noise by using a chemiluminescent light source (American Cyanamid Cyalume Chemical Light). The monochromator was used in zero order. The slits of the monochromator were adjusted to

produce a photomultiplier tube output current of 1×10^{-5} A (a relative intensity of 25). The standard deviation was 6.6×10^{-7} A (1.65 relative intensity units). From these data (Figure 6) it is clear that the observed fluctuations in emission intensities are not due to photon shot noise or changes in the continuum background. Instead the intensity variations are due to fluctuations in the statistics of free atom and ion production.

An occurrence of an intense spike will contribute more to the time-integrated emission intensity than a low-intensity data point. In order to relate the frequency distribution to the integrated intensity value, the frequency distribution was normalized and expressed as the fraction of the signal. The points contained in the solid line in the plots on the right side of Figures 4 and 5 were obtained by multiplying the frequency by the value of the center of the intensity interval and then dividing by the total time-integrated intensity. At 16 mm above the load coil, almost 20% of the time-integrated Ca I intensity (which included background) (Figure 4f) comes from data points with a relative intensity of 7. Less than 2% of the time-integrated intensity originates from data points with a relative intensity of 25.

The dashed lines in the plots on the right side of Figures 4 and 5 show the cumulative fraction of the signal. For example, more than 85% of the time-integrated Ca I intensity comes from data points with intensities less than or equal to 25 at 16 mm above the load coil (Figure 4f). More than 50% of the signal originates from data points with intensities less than or equal to 8.

The intense spikes in the Ca I signal make a major contribution to the time-integrated intensity. At 10 mm and 16 mm above the load coil the intense spikes are infrequent but large enough to contribute significantly to the time-integrated intensity. This is particularly true when one realizes that the continuum background emission intensity is near the most frequent intensity (Figure 4f). As a result, the intensities at 422 nm (Ca I) are not normally distributed about the mean.

The minimum and maximum observed Ca I intensities do not change dramatically at 6, 10, and 16 mm above the load coil. However, the shape of the distribution of intensity values changes, leading to changes in the integrated signal. Different integrated Ca I intensities (e.g. at different heights in the plasma) are therefore mainly a function of the number of intense spikes per unit time rather than the variations in the intensity of individual spikes.

In contrast, the Ca II intensities are more normally distributed about the mean as shown in Figure 5. The entire distribution of intensities moves along the intensity axis while the shape and width of the distribution change little. The observed minimum and maximum intensities are a function of height. At 6 mm above the load coil the distribution is slightly skewed toward low intensities (Figure 5a). This is due to dips in the Ca II emission (Figure 2b). At 16 mm above the load coil a tail on the high-intensity side of the mean becomes more significant. This is due to intense spikes in the ion signal (Figure 3b; also see Figure 3d).

2. Source of the Fluctuations. The emission intensity is proportional to the number of excited-state atoms (ions) in the observation zone. At least three different potential origins of changes in intensity with time must be considered. Emission intensity fluctuations could be due to time-dependent changes in (1) the excitation efficiency, (2) shifts in the atom-ion equilibrium, or (3) vaporization, atomization, and ionization of sample particles following desolvation of individual sample droplets.

Changes in excitation efficiency (excitation temperature) would most likely lead to a concurrent increase or reduction of both atom and ion emission. Only the magnitude of the

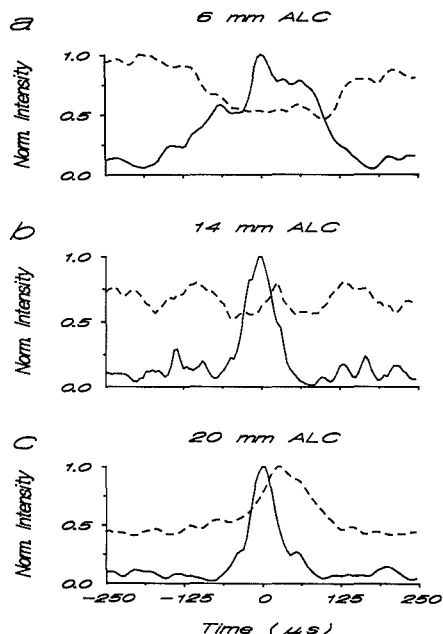


Figure 7. Time-resolved Ca I (—) and Ca II (---) emission: (a) 6 mm above the load coil; (b) 14 mm above the load coil; (c) 20 mm above the load coil.

changes in emission intensity would be dependent on the particular spectral line observed. However, if shifts in the atom-ion equilibrium are dominant, an increase in atom emission would be accompanied by a decrease in the ion emission intensity.

Intensities of "soft" lines (19–22) (atom lines with low excitation potentials, elements with low ionization potentials) of Ca and Ba correlate well with each other as do "hard" (ion) lines of Ca and Ba. However, there is a poor correlation between atom and ion emission when the entire data set for each is compared. Therefore, we focused on the largest spikes in the atom signals. Data were acquired simultaneously for Ca I and Ca II emission at the same location in the plasma by using the optical fiber to transfer light to the direct reading spectrometer. The digital oscilloscope was triggered off of a large spike in the Ca I signal.

a. Correlation between Ca I Emission Spikes and Ca II Emission. Low in the plasma, spikes in the Ca I signal were accompanied by depressions in the Ca II signal (Figure 7a). The data shown in Figure 7a are from a single oscilloscope trace. However, the simultaneous occurrence of Ca I spikes and Ca II dips was consistent. This suggests that a shift in the atom-ion equilibrium had occurred, perhaps due to local cooling of the plasma.

High in the plasma, each large spike in the Ca I signal was followed by a peak in the Ca II intensity (Figure 7c). The time between maxima in the atom and ion signals varied between approximately 30 and 60 μ s. Here, it appears that a pulse of sample is atomized, followed by ionization as it passes by the observation volume. At 14 mm above the load coil no clear correlation was observed between spikes in the Ca I emission and the Ca II emission behavior (Figure 7b).

The data described above are consistent with the presence of individual droplets of sample solution. Low in the plasma, small droplets have been desolvated, vaporized, and atomized.

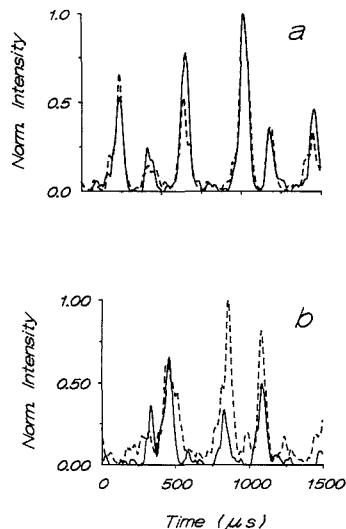


Figure 8. Time-resolved Ca I (---) and Ba I (—) emission at 8 mm above the load coil: (a) Ca and Ba in same solution, introduced into both nebulizers; (b) Ca solution introduced through nebulizer 1, Ba solution introduced through nebulizer 2.

However, some large droplets apparently have not been totally desolvated. In the region of the plasma near the desolvating droplet, the temperature should be lower than the bulk of the plasma due to cooling by the water vaporization and atomization. As a result, one would expect a shift in the equilibrium of atoms and ions toward more atoms and fewer ions. The emission data low in the plasma (Figure 7a) show such a shift.

Higher in the plasma desolvation should be complete (there are fewer incompletely desolvated droplets). The remaining analyte particle then undergoes vaporization. The vaporizing particle will produce a locally high concentration of atoms. The atoms should then be quickly ionized by the plasma. The emission behavior at 20 mm above the load coil (Figure 7c) is consistent with this process.

Myers and Tracy (11) observed a somewhat similar correlation behavior for Sr I and Sr II on a much slower time scale. At 5 mm above the load coil, Sr I and Sr II emission signals were anticorrelated. At 20 mm above the load coil Sr I and Sr II emission signals correlated. The correlation apparently disappears at a location between 10 and 15 mm above the load coil. However, unlike our faster time scale data, Sr I emission at 5 mm above the load coil correlated with Sr II emission at 20 mm above the load coil without lag.

b. Dual Nebulizer Studies. If the above description of the origin of the signal fluctuations is true, the behavior low in the plasma should be independent of the source of droplets. Therefore, we combined the output from two nebulizer/spray chamber systems before sending it into the plasma. A 100 ppm Ca solution was introduced through one of the nebulizers and a 100 ppm Ba solution through the second nebulizer.

If the desolvating droplets cause a cooling of the plasma, leading to an increased number of atoms and decreased number of ions, the behavior should be independent of the nebulizer from which the droplet originates. Therefore, Ba I and Ca I signals should correlate with each other. In contrast, if the signal fluctuations result from vaporization and atomization of desolvated analyte particles, the Ba I and Ca I emission should not correlate. The Ba and Ca atoms originate from different droplets.

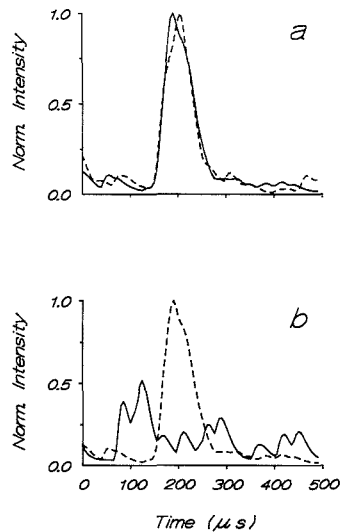


Figure 9. Time-resolved Ca I (---) and Ba I emission (—) at 19 mm above the load coil: (a) Ca and Ba in same solution, introduced into both nebulizers; (b) Ca solution introduced through nebulizer 1, Ba solution introduced through nebulizer 2.

The Ca I and Ba I signals do correlate low in the plasma, as shown in Figure 8. Whether the Ca and Ba are introduced in the same nebulizer, or from different nebulizers, peaks in the Ca I signal are accompanied by peaks in the Ba I signal. The results were similar when the Ca and Ba solutions were switched. Further, depressions in Ca II accompanied peaks in the Ba I signal and depression in the Ba II signal accompanied peaks in the Ca I signal.

As a result, it appears that shifts in the atom-ion equilibrium are responsible for the signal fluctuations observed low in the ICP. This behavior is most likely due to cooling by individual vaporizing droplets of solution.

High in the plasma (16–20 mm above the load coil) Ca I and Ba I signals correlated when introduced through the same nebulizer but did not correlate if separate nebulizers were used (Figure 9). (Approximately 5% to 10% of the time the Ca I and Ba I signals did correlate when Ca and Ba were introduced from separate nebulizers. This could be due to coalescence of two droplets.) Similarly, Ca II and Ba II signals peaked at the same time only if introduced through the same nebulizer, regardless of which nebulizer was used. Ca II and Ba II emission peaked slightly after Ba I signals in time (Figure 10) when Ca and Ba were introduced through the same nebulizer. When Ca and Ba were introduced into separate nebulizers, no correlation between Ca II emission and Ba I emission was observed.

Therefore, the spikes in Ca and Ba atom emission intensities observed high in the plasma appear to originate from vaporization and atomization of individual analyte particles high in the plasma. The atoms are then rapidly ionized.

c. Laser Light Scattering. If there are droplets and particles large enough to survive during their travel in the plasma, they should be detectable by using laser light scattering. We performed laser light scattering with two different systems. Previously, we had observed large scattering signals while attempting to make saturated laser-induced fluorescence measurements in 1.0-kW plasmas.

Two observations became clear. First, scattering could be detected, even in the normal analytical zone of a 1.0-kW

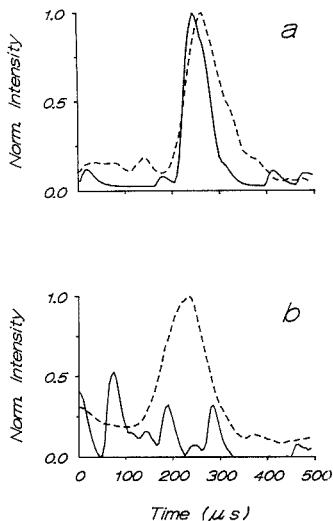


Figure 10. Time-resolved Ca II (---) and Ba I emission (—) at 19 mm above the load coil: (a) Ca and Ba in same solution, introduced into both nebulizers; (b) Ca solution introduced through nebulizer 1, Ba solution introduced through nebulizer 2.

Table II. Laser Light Scattering Intensity as a Function of Height in the Center of a 1.0-kW ICP

height above load coil, mm	rel intens	height above load coil, mm	rel intens
4	113 000	14	700
6	25 200	16	700
8	12 600	18	600
10	15 860	20	800
12	980	22	0

plasma (14). Previously laser scattering has been observed low in an operating ICP (11). As expected, we observed that the scattering intensity decreases with height in the plasma (Table II). The decrease in scattering intensity can be attributed to two factors: fewer droplets or particles to scatter light and smaller droplets as desolvation proceeds. Only large droplets should be able to travel to points high in the plasma without being totally desolvated. The number of spikes in the Ca atom emission intensity per second also decreases with height in the plasma.

Second, the scattering was confined to a narrow zone in the center of the plasma. Normalized Sr I emission and scattering signals are shown in Figure 11a. At 6 mm and 9 mm above the plasma we were able to detect scattering from a single laser pulse. Scatterings due to four separate, individual laser pulses at 6 mm above the load coil are shown in Figure 11b. These data show that large droplets or particles are present in the operating, 1.0-kW plasma. No scattering was detectable when liquid sample was not delivered to the nebulizer.

We then detected time-resolved laser light scattering (using a CW He-Ne laser) and emission signals simultaneously. If vaporizing particles are responsible for the emission spikes high in the plasma, there should be a correlation between laser light scattering signals at a particular height in the plasma and emission spikes above.

The He-Ne laser was directed through the plasma 10.5 mm above the load coil. The scattered light was detected by the 0.35-m monochromator. Ca I emission was observed at locations from 10.5 to 16.5 mm above the load coil by moving

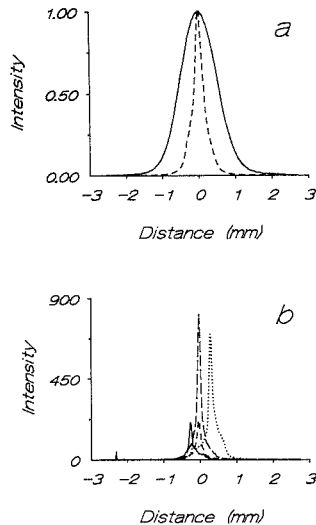


Figure 11. (a) Comparison of laterally resolved Sr I emission (—) and radially resolved laser light scattering profiles (---) at 6 mm above the load coil. (b) Laser light scattering signals detected from single laser pulses.

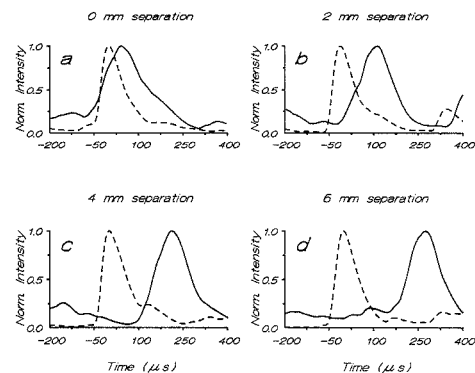


Figure 12. Comparison of time-resolved laser light scattering and Ca I emission signals. Laser light scattering (---) was detected at 10.7 mm above the load coil. Emission signals (—) were detected at (a) 10.7 mm, (b) 12.7 mm, (c) 14.7, and (d) 16.7 mm above the load coil.

the collection end of the fiber optic (transferring light to the direct reading spectrometer). The digital oscilloscope was triggered off the laser scattering signal.

The laser light scattering and Ca I emission signals correlated with each other (Figure 12). Ca I emission spikes were observed at increasing delays as the separation between the laser scattering observation zone and the emission observation zone was increased. Therefore, the emission spikes are related to scatterers, here probably droplets or large analyte particles, detected below.

CONCLUSIONS

Individual droplets lead to large fluctuations in both atom and ion emission signals in the ICP. Desolvating droplets low in the plasma appear to affect the ion-atom equilibrium by causing local cooling of the plasma. Particles vaporized higher in the plasma lead to spikes in the atom emission signal.

Ionization leads to a slightly later peak in the ion emission signal.

The presence of the observed signal fluctuations could have a significant impact in three areas. First, the application of equilibrium models of ICPs may be suspect. For example, ion-to-atom intensity ratios are dramatically affected by the infrequent, but intense, atom emission spikes. Particularly low in the plasma, the ion-to-atom intensity ratio fluctuates widely. Emission intensity is not linearly related to temperature. Therefore, the average temperature determined from a ratio of time-integrated ion-to-atom intensities may not be equal to the actual average temperature of the plasma. Further, the deviation of the ion-to-atom intensity ratio based temperature from the actual average temperature may be species dependent.

Second, time-integrated analyte signals may be significantly affected by the unique behavior of the large droplets. One could envision matrix effects and intensity versus concentration relationships being droplet size dependent.

Third, the droplets may provide invaluable means of studying vaporization, atomization, and ionization processes in a temporally resolved manner in the ICP. The fluctuations may be valuable as a diagnostic for nebulizer operation (such as changes in the droplet size distribution). Experimental results addressing some of these questions will be addressed in a forthcoming paper (23).

ACKNOWLEDGMENT

The UNC Instrument shop (Ken Vickers, Don Tice, Don Brewer, and Harlan Mangum) are acknowledged for design and construction of equipment essential for this research. Lisa Chen is thanked for aiding in the processing of experimental data. Loan of the intensified diode array by Princeton Applied Research Corporation is gratefully acknowledged.

LITERATURE CITED

- (1) Walden, G. L.; Bower, J. N.; Nikdel, S.; Bolton, D. L.; Winefordner, J. D. *Spectrochim. Acta Part B* **1980**, *35B*, 535-546.
- (2) Salin, E. D.; Horlick, G. *Anal. Chem* **1980**, *52*, 1578-1582.
- (3) Duursma, R. P. J.; Smit, H. C.; Maessen, F. J. M. *J. Anal. Chim. Acta* **1981**, *133*, 393-408.
- (4) Benetti, P.; Bonelli, A.; Cambiaghi, M.; Frigieri, P. *Spectrochim. Acta, Part B* **1982**, *37B*, 1047-1053.
- (5) Belchamber, R. M.; Horlick, G. *Spectrochim. Acta, Part B* **1982**, *37B*, 17-27.
- (6) Furuta, N. 1988 Winter Conference on Plasma Spectrochemistry, San Diego, CA, Abstract Th1, Jan 1988.
- (7) Winge, R. K.; Eckels, D. E.; DeKalb, E. L.; Fassel, V. A. *J. Anal. At. Spectrom.* **1988**, *3*, 849-855.
- (8) Greenfield, S. *Developments in Atomic Plasma Spectrochemical Analysis*; Barnes, R. M., Ed.; Heyden: London and Philadelphia, 1981; p 1.
- (9) Belchamber, R. M.; Horlick, G. *Spectrochim. Acta, Part B* **1982**, *37B*, 1037-1046.
- (10) Belchamber, R. M.; Horlick, G. *Spectrochim. Acta, Part B* **1982**, *37B*, 1075-1078.
- (11) Myers, S. A.; Tracy, D. H. *Spectrochim. Acta, Part B* **1983**, *38B*, 1227-1253.
- (12) Kornblum, G. R.; Klok, A.; de Galan, L. *Spectrochim. Acta, Part B* **1984**, *38B*, 1363.
- (13) Myers, S. A.; Tracy, D. H., Federation of Analytical Chemistry and Spectroscopy Societies Meeting, Philadelphia, PA, 1980, Abstract 5; *ICP Inf. Newsl.* **1980**, *6*, 233.
- (14) Olesik, J. W.; Williamsen, E. J. Simultaneous Detection of One-Dimensional Laser-Induced Fluorescence or Laser Light Scattering Images in Plasmas *Appl. Spectrosc.*, in press.
- (15) Williamsen, E. J.; Olesik, J. W. Pittsburgh Conference on Analytical Chemistry and Applied Spectroscopy, Atlantic City, NJ, Paper 918, March 1987.
- (16) Olesik, J. W.; Williamsen, E. J.; Hadnagy, M. J. Winter Conference on Plasma Spectrochemistry, San Diego, CA, paper T20, January 1988.
- (17) Farnsworth, P. B. Federation of Analytical Chemistry and Spectroscopy Societies Meeting, Detroit, MI, paper 569, October 1987.
- (18) Cicerone, M. T.; Farnsworth, P. B. *Spectrochim. Acta, Part B*, in press.
- (19) Boumans, P. W. J. M. *Philips Tech. Rev.* **1974**, *34*, 305.
- (20) Boumans, P. W. J. M. Basic Concepts and Characteristics of ICP-AES. In *Inductively Coupled Plasma Emission Spectroscopy*; John Wiley and Sons: New York, 1987; Part 1.
- (21) Blades, M. W.; Horlick, G. *Spectrochim. Acta, Part B* **1981**, *36B*, 861.
- (22) Olesik, J. W. Consideration of Norm Temperature and Local Thermodynamic Equilibrium Models for Emission and Ionization in Inductively Coupled Plasmas. *Spectrochim. Acta, Part B* **1989**, *44B*, 625.
- (23) Smith, L. J.; Olesik, J. W. Signal Fluctuations in Inductively Coupled Plasma Emission Spectroscopy: Dependence on Chemical Species, Sample Matrix, Nebulizer and Plasma Conditions, unpublished work.

RECEIVED for review January 24, 1989. Accepted May 1, 1989. Support for this research was provided by a Du Pont Science and Engineering Grant, a Du Pont Young Faculty Grant, NIH Biomedical Research Support funds, a UNC University Research Council Grant, and the Department of Chemistry, University of North Carolina at Chapel Hill.

Multivariate Determination of Glucose in Whole Blood by Attenuated Total Reflection Infrared Spectroscopy

H. M. Heise* and Ralf Marbach

Institut für Spektrochemie und angewandte Spektroskopie, Bunsen-Kirchhoff-Strasse 11, D-4600 Dortmund 1, FRG

Günter Janatsch and J. D. Kruse-Jarres

Institut für Klinische Chemie und Laboratoriumsmedizin, Katharinenhospital, Kriegsbergstrasse 60, D-7000 Stuttgart 1, FRG

A spectral analysis of whole EDTA blood was undertaken by using attenuated total reflection and Fourier-transform infrared spectroscopy. The concentration of blood glucose was measured by an enzymatic method using glucose dehydrogenase and ranged between 40 and 290 mg/dL with an average concentration of 90.4 mg/dL. Multivariate calibration with the partial least-squares (PLS) algorithm was performed on spectral data between 1500 and 750 cm^{-1} showing a varying background from different unidentified interfering compounds. Cross validation was carried out for optimizing the PLS model. PRESS^{1/2} was 19.8 mg/dL, which was calculated on the basis of 127 standards, whereas the estimated standard deviation for the calibration fit was computed to be 11.9 mg/dL. Infrared spectroscopy can be used for monitoring glucose levels within the normal physiological range in a complex matrix like whole blood as an alternative to electrochemical sensors.

INTRODUCTION

In clinical chemistry, many of today's substrate determinations are carried out by chemical, enzymatic, or immunological methods. An extensive review article on the measurement of blood glucose is given by Burrin and Price (1) who classify the existing glucose methods into two categories, chemical procedures and enzymatic procedures; some introductory remarks on the latter will be given.

Within the enzymatic determinations, the method using hexokinase/glucose-6-phosphate dehydrogenase is still accepted as the reference method and sets the standards for accuracy and precision (2, 3). The second enzyme considered is glucose oxidase, the use of which has been reported and an example of which is a recent publication employing flow injection analysis (FIA) (4). Because of its convenience and speed, another method with glucose dehydrogenase is widespread; it produces similar results to the first reference method mentioned (5) and is available in kit form. For our blood samples, this method was programmed on an analyzer and produced the wet chemical glucose concentration values. Dry reagent chemistry systems for which photometric measurements can be included to obtain greater sensitivity and a wider analytical range (see ref 1) have become very popular.

Some basic problems in the assessment of biochemical phenomena and reactions cannot be solved by random checks, and constant monitoring techniques are necessary. Electrochemical biosensors (6) can be used for this purpose, but solid-phase chemistry is involved. The sensors often employ the concept of immobilized enzymes on top of an ion-selective electrode, which are able to measure a substrate or a product

of the enzyme either potentiometrically or amperometrically. In spite of the efforts of many interdisciplinary groups, the response of the sensors deteriorates, when used over an extended period of time e.g. for invasive measurements (7-9). As well as the sensors containing an electrode, other types have been proposed, which are reviewed in ref 10 and 11.

A different approach is undertaken with spectroscopic techniques, where no special reagents are necessary. Infrared spectroscopy has been suggested for monitoring glucose concentrations. For aqueous media, infrared measurements usually require a very short cell path length in the range of 10-50 μm ; to cope with the strong water absorption bands, attenuated total reflectance (ATR) has been extensively used with aqueous samples (12). Applications, especially with Fourier-transform IR spectroscopy, can be found for measuring carbohydrates in aqueous solutions (13, 14). Other papers have been concerned with protein adsorptions onto the ATR crystal, which can be important, when measuring whole blood (see first references in ref 15). Kaiser claimed that it would be possible to monitor glucose in whole blood by employing the ATR technique in combination with a CO₂ laser (16), but single wavelength measurements cannot be successful because of the blood matrix complexity. Further studies were recently undertaken with an ATR cylindrical cell using FT-IR spectroscopy for biological fluids including spiked blood serum, where the concentration of the glucose was much greater than normal physiological concentrations. A calibration using the glucose absorption maximum at 1036 cm^{-1} was carried out, and the problem of the glucose calibration as traditionally performed was briefly discussed (17). Our approach, which follows, makes use of multivariate calibration with information from a broad spectral infrared range.

MULTIVARIATE CALIBRATION

The objective of quantitative analysis is the prediction of analyte concentrations in mixtures of unknown composition. With spectroscopic data, all methods are based on Beer's law by which a linear relationship between the measured absorbances and the concentrations is defined. The regression methods may be classified into two categories. The first one, namely the classical approach, makes use of Beer's law as it is normally formulated regressing some standard spectra with known composition against the sample spectrum to be analyzed. So the classical methods comprise the algorithms known as spectral fitting techniques. Within the category of classical methods, the so-called K-matrix approach, using the pure component spectra as standards (regressors), can be found widespread in the literature of applied spectroscopy. Matrices and vectors will be represented by upper and lower case boldface letters, respectively, others are scalars. With matrix calculus the basic equation can be written as

$$\mathbf{a} = \mathbf{Kc} + \mathbf{e} \quad (1)$$

where the columns of \mathbf{K} ($N \times L$ matrix) represent the com-

* Author to whom correspondence should be addressed.

ponent spectra, and the elements of the L -dimensional vector \mathbf{c} are chosen as to fit the measured absorbance spectrum \mathbf{a} represented by N spectral data points; \mathbf{e} is a vector due to measurement errors.

With the assumption that the problem of collinearity among the regressors in the matrix \mathbf{K} , i.e. the similarity between the different component spectra, is not too large, eq 1 may be solved by an ordinary least-squares approach. A serious problem arises with the K-matrix method applied to complex samples, for which some component spectra contributing to the measured absorbance spectrum \mathbf{a} are not taken into consideration. Thus, false modeling leads to systematic errors (bias) in the estimation of the vector \mathbf{c} (18, 19). Bias can also be produced when existing interference effects from molecular interactions are not taken into account. For practical reasons, however, the component spectra are often not available.

This problem can be solved by using mixture spectra of known composition, which may be used to estimate the pure component spectra in a preceding step. Alternatively, the mixture spectra may be used as regressors (columns of \mathbf{K}), and the individual concentrations are computed by simple matrix multiplication after the estimation step ("Q-matrix approach" (15)).

Because of the composition complexity of the blood samples, the K-matrix approach is inappropriate for the quantitative analysis of blood glucose studied in this paper. Instead, the second category of analytical quantitative methods formed by the so-called "inverse modeling" or P-matrix method (18) was used. By this approach, one concentration is fitted by weighting the different absorbance values of the spectrum

$$\mathbf{c} = \mathbf{a}^T \mathbf{p} + \mathbf{e} \quad (2)$$

With eq 2 the role of absorbance and concentration values as dependent and independent variables in Beer's law are exchanged.

The vector \mathbf{p} is determined by regressing several mixture spectra \mathbf{a}_i ($i = 1, \dots, M$) against their concentrations \mathbf{c} of the compound to be calibrated

$$\mathbf{c} = \mathbf{A}^T \mathbf{p} + \mathbf{e} \quad (3)$$

The rows of the $M \times N$ matrix \mathbf{A}^T contain the absorbance values at N wavenumbers. The error vector \mathbf{e} is now defined to arise from uncertainties in the measurement of the reference vector \mathbf{c} , whereas any statistical fluctuation in the spectra comprising \mathbf{A}^T are presumed to be uncorrelated with \mathbf{e} (20). To obtain statistically significant results from eq 3, it is necessary to provide an over-determined equation system, which leads to the constraint of the number of observations M greater than that of the linear independent absorbance values at N wavenumbers, i.e. $M > rg(A)$. With the numerical determination of $rg(A)$, usually the minimum of (M, N) is obtained, since the spectral noise in \mathbf{A}^T is much greater than roundoff errors due to the finite computing accuracy. For equation systems with $N \geq M$, consistent solutions may be obtained.

The supposition for using the P-matrix approach is that the calibration population must span all important influences on the sample spectra from constituents, interaction effects between compounds, and measurement conditions. This is necessary to simulate future samples and to predict their concentration values on this population basis. Samples with a different type of composition and interferences may then be deleted from the population as outliers.

The problem of systematic errors as found in the classical approach due to unknown constituents does not arise with the inverse model. However, we find too many regressors raising the problem of collinearity considerably greater than with the classical approach. With sensitive calibrations, it is quite often the case that many standards in \mathbf{A} are similar,

which could exaggerate the collinearity problem to a degree, where an ordinary least-squares solution of eq 3, even computed with a numerical method of high quality, leads to unacceptable results. By the inverse approach, the elimination of bias has been achieved at the cost of a dramatic increase of variance. A strategy is needed providing reasonable solutions of eq 3, which introduce a small bias, but reduce the variance significantly. This means that we look for the best predictor in the sense of the mean-square error (20).

This strategy is followed by several algorithms, the most prominent being the ridge regression (21), the principle component regression (PCR), and the partial least-squares (PLS) algorithm (22, 23). While the matrix \mathbf{A}^T is factorized in PCR by the singular value decomposition (SVD), with PLS the matrix \mathbf{A}^T is decomposed into a bidiagonal matrix \mathbf{B} and two orthonormal ones (24).

$$\mathbf{A}^T = \mathbf{UBV}^T \quad (4)$$

As with PCR the analyst has to select those factor modes \mathbf{u}_s , \mathbf{v}_i in eq 4 which are supposed to imply prediction ability. These are considered for the inverse regression matrix \mathbf{A}^{TT} only

$$\hat{\mathbf{p}}_s = \mathbf{A}^{TT} \mathbf{c} = \mathbf{V}_s \mathbf{B}_s^{-1} \mathbf{U}_s^T \mathbf{c} \quad (5)$$

where the index s indicates the modes \mathbf{u}_s , \mathbf{v}_i selected for the calibration (symbols marked by a circumflex are estimated variables).

The factorization of eq 4 is not as unique as that given by the SVD. A unique orthogonalization is accomplished by fixing the first column vector \mathbf{v}_1 , after which the decomposition into modes \mathbf{u}_i , \mathbf{v}_i can be iteratively computed (25). The decisive feature of PLS is the definition of the starting vector as

$$\mathbf{v}_1 = \mathbf{Ac} / \|\mathbf{Ac}\| \quad (6)$$

which can be explained as a scaled sample estimate of the covariance vector between the measured spectrum and the concentration. With the starting vector \mathbf{v}_1 properly estimated, the PLS modes of eq 4 can be shown to arise in an order of decreasing predictive power. By this, the problem of selecting the best regression inverse is considerably alleviated (26).

For the application described in this paper, the optimum number of PLS factors was determined from the minimum of the PRESS statistics computed from cross validation (27) using the "leave one out" strategy. The PRESS values (PRESS i.e. prediction error sum of squares) are calculated from

$$\text{PRESS}(R) = \frac{1}{M} \sum_{i=1}^M (c_i - \mathbf{a}_i^T \hat{\mathbf{p}}_{(i),R})^2 \quad (7)$$

where the vector $\hat{\mathbf{p}}_{(i),R}$ is obtained from a PLS inversion (rank R) of eq 3, where the i th standard has been omitted. With the optimum number of PLS factors obtained, the calibration results of the model have to be scrutinized for outliers. Outlier standards arise from systematic errors in the measurement of the infrared spectrum and/or its corresponding glucose reference value; this category includes those standards obtained by correct experimental treatment, but which, for some reason, do not have sufficient resemblance with the average standard.

Since the calibration residuals

$$\mathbf{r} = \mathbf{c} - \mathbf{A}^T \hat{\mathbf{p}} = (\mathbf{I} - \mathbf{A}^T \mathbf{A}^{TT}) \mathbf{c} \quad (8)$$

differ in their variance levels, they have to be put on an equal footing for comparison. This may be done, for example, by using the Studentized residuals $t_i = r_i / [\hat{\sigma}^2 (1 - h_{ii})^{1/2}]$, where the "leverage value" h_{ii} is the i th diagonal element of the matrix $\mathbf{A}^T \mathbf{A}^{TT}$ and $\hat{\sigma}^2$ is the sample variance estimate (28). The

h_{ii} may also be considered as an unscaled sample estimate of the Mahalanobis distance between the i th standard spectrum and the average spectrum of all M standards (29), thus giving an idea of the influence on the regression fit of each spectrum.

Another criterion is needed to decide whether or not these influences have an adverse effect on the fit. We used Cook's distance (28, 29)

$$D_i = \{t_i^2 / r g(A^i)\} \{h_{ii} / (1 - h_{ii})\} \quad (9)$$

by which the change in the regression vector $\hat{\mathbf{p}}$ is rated, when the i th standard is omitted. Cook's distance D_i combines two factors: the first one gives the degree to which a standard can be considered outlier and the second one takes care of the standard influence on the fit. Standards with significant values of D_i or t_i were deleted. Those with significant residuals but insignificant influence on the fit were assumed to suffer from an imprecise reference determination of the concentration.

EXPERIMENTAL SECTION

Random blood samples were taken by venous puncture from patients of the Katharinenhospital Stuttgart using one-way syringes containing EDTA. The sample population is that of a general hospital with no specialized medical departments. The glucose concentration in whole blood decreases steadily because of its metabolism by the intact blood corpuscles present. Therefore, the blood samples were stored at 4 °C significantly reducing the glycolytic action of the cellular blood components. Whenever a sample of whole EDTA blood was injected into the measuring cell to take an IR spectrum, another portion of that specimen was transferred to a hemolyzing reagent containing maleimide (Boehringer Mannheim GmbH, Mannheim, Federal Republic of Germany) by which glycolysis was stopped. Within this solution, the glucose concentration remains constant for several hours, so that the samples could be collected and analyzed by a Hitachi 705 analyzer (Boehringer Mannheim) for glucose by the enzymatic glucose dehydrogenase method (see e.g. ref 5). Reagents were provided from the analyzer trading company.

For analyzer control, lyophilized sera (normal range, M + D Monitrol I; pathological range, M + D Monitrol II) from American Hospital Supply Deutschland GmbH (Bereich Merz+Dade, Munich, Federal Republic of Germany) were used. The glucose concentration is company-certified by several different methods from reference laboratories. For direct comparison, the values from the glucose dehydrogenase method were chosen.

The infrared spectra were recorded with a spectrometer Model 1750 from Perkin-Elmer equipped with a deuterated triglycine sulfate (DTGS) detector. The instrument was purged with nitrogen to reduce atmospheric absorption. In order to achieve a satisfactory signal-to-noise ratio, 20 interferogram scans at a spectral resolution of 8 cm^{-1} were averaged. Apodization was performed with a normal Norton-Beer function, and interpolation resulted in a wavenumber interval of 1 cm^{-1} ; the spectral range stored for further processing was between 3000 and 750 cm^{-1} .

The cell used for the whole blood measurements was a micro CIRCLE accessory from Spectra Tech (internal volume 25 μL) assembled as a flow cell with connection fittings drilled out to give larger inner diameters. The essential part of the cell is its ZnSe crystal (length 38.1 mm, diameter 3.18 mm); both ends are 45° cones. The IR beam is focused by the accessory optics onto the ATR crystal at angles between about 35° and 55°. More technical information on the micro CIRCLE accessory including the number of solution-sensing internal reflections and average incidence angle has recently been published (30). For our CIRCLE cell we determined the effective pathlength at the wavenumber of the glucose absorption maximum (1037 cm^{-1}) to be 13.1 μm by comparing the ATR absorbance of an aqueous glucose solution with that from a transmittance experiment using a cell with CaF_2 windows of 50 μm thickness. The aqueous solution was prepared with anhydrous D-(+)-glucose for biochemical purposes (Merck, Darmstadt, Federal Republic of Germany). The wavenumber-dependent pathlength will vary slightly for the blood samples because of small differences in the refractive indices compared to the aqueous glucose solution.

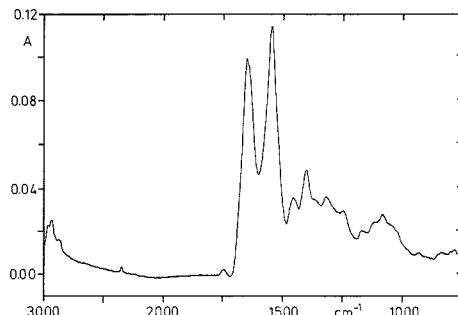


Figure 1. Absorbance spectrum of whole blood with ATR cylindrical cell (ZnSe crystal).

For temperature control a heating/cooling jacket was employed. The cell was maintained at 37 °C for all measurements. It was filled by using a programmable MicroLab P handpippet with a 1-mL gastight syringe (1001 TLL) and a miniature valve HV 4-4 from Hamilton. PTFE tubing with an inner diameter of 0.2 mm was used for connecting the parts. For cell cleaning, with an aqueous solution of 5% Extran from Merck, and rinsing, a HPLC-pump Model 590 (Waters Millipore, Eschborn/Ts., Federal Republic of Germany) was employed. The spectral background was recorded with an aqueous solution of 0.9% NaCl, which was also used for rinsing the cell. With the recording of the background completed, 0.8 mL of the sample was injected. The total volume from the syringe to the outlet of the cell is 200 μL . The spectrometer was started 30 s after filling the cell. The measurement time for the 20 scans was 75 s. Rinsing and cleaning again followed this step.

From 30 to 40 samples can be measured before polishing of the ATR crystal is necessary. The adsorption of protein is manifested by an increased pressure built-up during cell cleaning and filling. After polishing, which was carried out using CeO_2 powder, a readjustment of the optics is necessary and the cell transmittance is slightly reduced to that of the "undamaged" crystal.

The PLS method was programmed on an IBM compatible Commodore PC-20 in Turbo-Pascal. The spectra from the Perkin-Elmer spectrometer were transformed into JCAMP-DX-format (31), which is a standard accepted by the spectrometer manufacturers for universal data exchange. With the Perkin-Elmer JCAMP-DX procedure the absorbance values had been reduced to four decimal digits. The resultant ASCII files are used for data input in the PLS calibration.

To include a constant regression term, a column of ones was appended to the regression matrix before PLS decomposition. The bidiagonalization stops when the length of a PLS vector is less than the smallest number existing in the JCAMP-DX-files (0.0001), which is a conservative criterion leading to a much higher rank than is needed for choosing the optimum model. At the same time, the residual sum of squares is watched to detect a consistent solution of the regression equation. In such a case the PLS factorization is stopped, because the obtained results lack statistical significance.

RESULTS AND DISCUSSION

The absorbance spectra of 150 blood samples were calculated directly by using the single beam spectra without matching the water absorptions. An example of the resulting spectra is given in Figure 1. Below 3000 cm^{-1} , the absorption bands from aliphatic C-H stretching and overtone C-H bending vibrations can be seen, but further information is negligible down to 750 cm^{-1} . Therefore, the following considerations are only concerned with the lower spectral range from that limit down to 750 cm^{-1} . The overcompensation of the water absorption in the blood absorbance spectrum by using the background recorded with the 0.9% NaCl solution is especially evident for the 1650- cm^{-1} protein absorption band

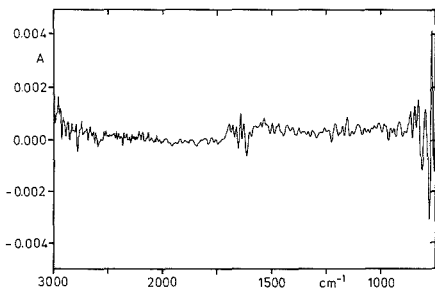


Figure 2. Noise level for the ATR spectra of whole blood in absorbance units.

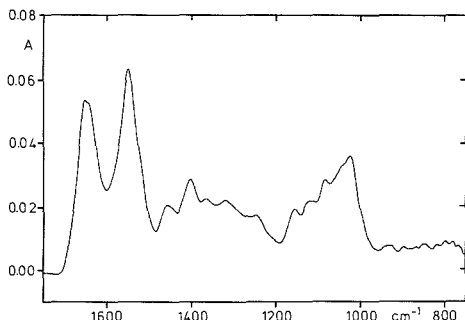


Figure 3. ATR spectrum of whole blood containing plasma expander.

of amide I, which should be more intense than the amide II band at 1540 cm^{-1} . The multivariate calibration is not affected as long as the negative contribution of the water absorption is reproducibly constant.

The noise level in our spectra can be estimated from two background measurements with the 0.9% NaCl solution under the same spectrometer and cell conditions. In Figure 2 the noise level at the end of our experimental program is shown. The surface of the ZnSe crystal deteriorated during the measurements, reducing the transmittance slightly. So the noise level for most of the spectra was even lower than the one shown in Figure 2.

Some spectra were deleted from the population because of spectrometer drift at the beginning of a measurement series. There were some blood samples from two patients who had received an infusion of plasma expander containing polyhydroxyethyl starch (Pfrimmer, Erlangen, Federal Republic of Germany) which is evident in the range above 1000 cm^{-1} (see Figure 3). These extreme standards are outside the normal or even pathological range of the population, and they are based on a medical operation, the information of which can be provided to the clinical laboratory. Other cases were obvious where the sampling was incorrect; e.g. one patient had received a glucose infusion so that a concentration of greater than 1000 mg/dL resulted in the blood sample taken.

Figure 4 gives an impression of the difficulties in the glucose determination by infrared spectrometry. Different aqueous glucose solutions were measured with the same ATR cell. From these, an absorbance spectrum of the pure glucose in the aqueous medium could be calculated. The glucose absorbance features for a concentration of 145 mg/dL are compared with an absorbance spectrum of whole EDTA blood, for which the same concentration could be determined by our glucose dehydrogenase reference method. It is quite interesting to see how weak the glucose absorption bands are in comparison to the blood spectrum.

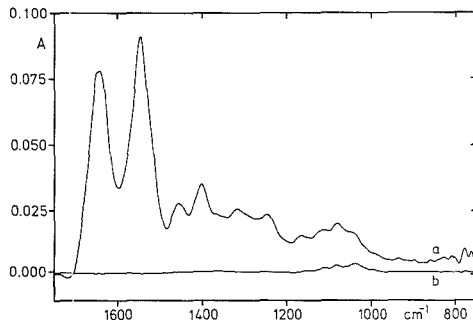


Figure 4. Comparison of the ATR spectrum of whole blood (a) containing a glucose concentration of 145 mg/dL with the glucose signal (b) from an aqueous solution of the same concentration.

To obtain statistically interpretable results with the inverse model, it is necessary that the number of standards exceeds the number of independent spectral data points. Since the spectral resolution was 8 cm^{-1} , it is meaningless to use a smaller data interval; otherwise variables in the matrix A^T would exist, for which only linear combinations, or to use spectroscopic language, interpolated absorbance values of already existing variables are created. With 135 standards left over for the calibration, there was the need to reduce the range of the original spectral fingerprint region ($1750\text{--}750\text{ cm}^{-1}$). This was done considering two pieces of information: on the one hand, the ATR infrared absorbance spectrum of an aqueous glucose solution and, on the other, the property correlation spectrum (PCS) (32). The latter can be defined by exchanging regressor and regressand in the inverse model. After mean-centering the spectra and concentration values (or property values), the least-square solution \hat{s}_0 of the linear equation system

$$A^T_{mc} = c_{mc} s^T_0 + E \quad (10)$$

can be considered for a calculation of the property correlation spectrum \hat{s}

$$\begin{aligned} \hat{s} &= c_{av} \hat{s}_0 \\ &= c_{av} A^T_{mc} c_{mc} / \{c^T_{mc} c_{mc}\} \end{aligned} \quad (11)$$

When the data A, c for the PLS calibration are mean-centered, the PLS-starting vector v_1 (see eq 6) is identical with the vector \hat{s} , apart from a scaling factor.

The property correlation shows that part of a spectrum which is related to the average property, and it is a scaled sample estimate of the covariance vector $\text{cov}[a, c]$. To improve the prediction model one tries to evaluate those spectral regions containing the most information and to avoid interferences from signals of other compounds. The problem that frequently appears is that the concentration of some other components can be correlated to the substance looked for. This can lead to a calibration where the functional dependence e.g. of the glucose concentration is not genuinely related to the spectral contribution of this compound.

By use of the Perkin-Elmer software the property correlation spectrum of glucose was obtained from the 135 standards, which had been left over for the regression after preliminary checking. An inspection shows that there is a negative glucose correlation to the blood protein and water (absorption band at 1640 cm^{-1}) (see Figure 5). Since we were interested in the rapidly changing blood glucose, which is unlikely to be correlated to the total protein concentration with a much smaller variation in time and which produces the major features in the PCS spectrum, the spectral range considered for the regression was limited to that from 750 to 1500 cm^{-1} . Simultaneously, the spectral range with the critical

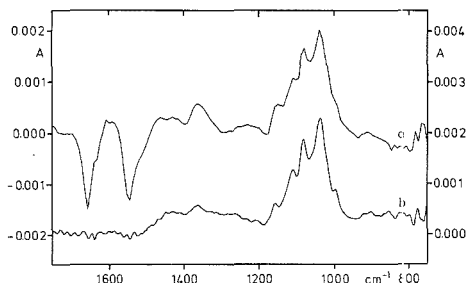


Figure 5. Comparison of the property correlation spectrum of glucose in whole blood (a; left ordinate axis) with the glucose absorbance spectrum from an aqueous solution (b; right ordinate axis); concentration is 90 mg/dL which is the average value for glucose in the studied population.

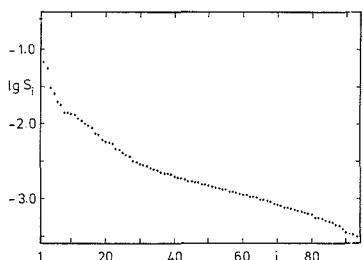


Figure 6. Decadic logarithm of the singular values of matrix **A** consisting of 135 mean-centered spectra within the range of 1500–750 cm^{-1} (data interval 8 cm^{-1} , 94 data points).

water absorption band is excluded. For the considered interval the property correlation spectrum bears a unique resemblance to the aqueous glucose absorbance spectrum which is plotted with a wavenumber spacing of 1 cm^{-1} . The lower data point density of 8 cm^{-1} for the PCS is especially derogatory to the glucose absorption bands, but the result of the comparison is that the calibration is based on a true glucose signal.

An interesting point is the influence of hematocrit to the spectral absorption features. In a further investigation (33), we studied several substrates in heparinized human blood plasma. The average spectrum of that population showed a striking conformity with the average of the whole blood spectra, apart from the fact that the protein absorption bands for plasma are slightly less intense due to the smaller protein content and, secondly, that the increase in glucose concentration is manifested in the plasma spectrum around the glucose absorption maxima with more intense spectral bands. A further discussion can be found in ref 33. Neither in the physiological nor in the pathological range did we find any dependence of the glucose determination on hematocrit.

To obtain an impression of the rank of the matrix **A** including the 135 standards, a singular value decomposition (SVD) was calculated (data interval 8 cm^{-1}). The mean-centered spectra were considered so that the first and greatest eigen (or singular) value for which the corresponding eigenvector looks like the spectral average is not given. In Figure 6 the logarithm of the singular values is shown. This presentation has the advantage that the absolute values can be read off. The smaller singular values do not approach a constant level which could be explained by measurement noise and rounding errors during computation, respectively. Although we find a high collinearity in the IR blood spectra, the calibration matrix \mathbf{A}^T is treated as a matrix with full column rank by the PLS algorithm. Also for the whole wavenumber

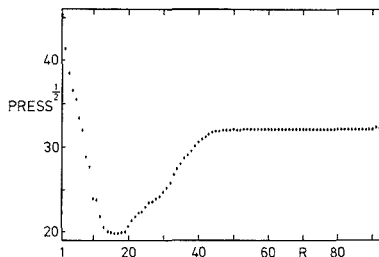


Figure 7. $\text{PRESS}^{1/2}$ statistics in mg/dL for the different PLS models.

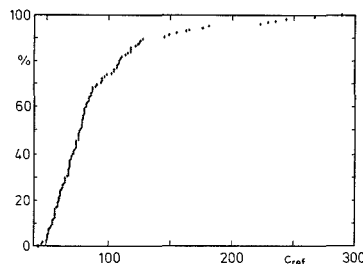


Figure 8. Distribution function of the glucose concentration values of whole blood samples studied by an Hitachi analyzer with glucose dehydrogenase; the concentration values are given in mg/dL.

range from 1750 to 750 cm^{-1} with 126 variables the same statement can be given.

For further data handling the matrix \mathbf{A}^T was transformed into bidiagonal form, and for all PLS models with increasing rank the $\text{PRESS}^{1/2}$ statistics were calculated. In Figure 7 the $\text{PRESS}^{1/2}$ results for optimizing the PLS model are shown. The optimum rank obtained was $R_0 = 16$, but due to the function flatness up to this value, a smaller PLS rank is tolerable without a significant change in the prediction potential. The striking feature of the $\text{PRESS}^{1/2}$ statistics is the plateau above, approximately, rank of 40. Modes of higher rank are prediction irrelevant. Only the modes up to this limit alter the $\text{PRESS}^{1/2}$ statistics and contain relevant information, although those above the optimum rank cause more increase in variance than a decrease in bias concerning the predictions with calibration models of different rank.

By use of the optimum model the results and the statistics for outlier detection were calculated and a stepwise deletion of standards was carried out which influenced the regression considerably. There were eight standards deleted as outliers on the basis of the population of 135 standards.

The distribution function for the 127 remaining standards is given in Figure 8 where the abscissa values represent the concentration values obtained by the enzymatic reference method. There are no special features in this population from a general hospital. About 80% of the samples were in the physiological norm range of 50–120 mg/dL. For the higher concentrations the distribution function is influenced by pathological cases causing a considerable asymmetry around the average value of 90.4 mg/dL.

The coefficient of determination for the calibration as defined with (28)

$$R^2 = 1 - \frac{\sum_{i=1}^M (c_i - \hat{c}_i)^2}{\sum_{i=1}^M (c_i - c_{av})^2} \quad (12)$$

was $R^2 = 0.94$. The estimated standard deviation was 11.9 mg/dL; with this value a coefficient of variation of 13.1% resulted. In Figure 9 the independent predictions of the

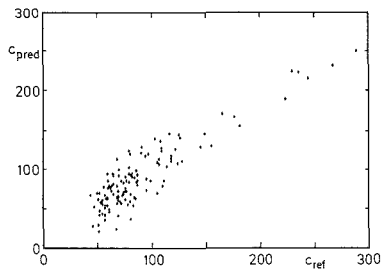


Figure 9. Predictions of glucose concentrations for 127 standards, rank of the PLS model $R_0 = 16$ (concentration values in mg/dL).

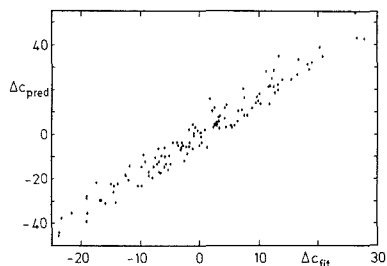


Figure 10. Plot of the prediction errors versus the concentration residuals of the fit (concentration differences in mg/dL).

selected model are shown. The ordinate values are obtained for one spectrum with a model consisting of the remaining $M - 1$ standards ($M = 127$); the abscissa values are the results from the enzymatic reference determinations. In addition to the $\text{PRESS}^{1/2}$ value, the prediction quality of the calibration model was assessed by an "a posteriori" linear least-squares regression of the independent predictions versus the reference values ($c_{\text{pred}} = b_0 + b_1 c_{\text{ref}}$) yielding $b_0 = 13.3$ mg/dL, $b_1 = 0.853$, and $R^2 = 0.81$. These values are given only for an estimate of the deviations from the ideal result, i.e. the identity function.

The large differences in the results from the calibration fit and the independent predictions are illustrated in Figure 10, where the prediction errors are plotted versus the calibration residuals obtained. A straight line fit of these data pairs yielded values of $b_0 = -0.01$ mg/dL, $b_1 = 1.74$, and $R^2 = 0.95$. The slope can be used as an estimate for the average increase (nearly a factor of 2) of the prediction errors compared to the calibration residuals.

The assessment of the analytical quality of the reference method is important for this study. For operational checks of the Hitachi analyzer, by which the reference values for the glucose concentrations had been determined, several daily measurements were carried out using certified reference sera, so that accuracy (bias) and precision (standard deviation) could be estimated for monthly measurements. For the estimate of the bias the certified concentrations were assumed to be the true values. Some typical results are given in Table I. The number of determinations during 1 month is sufficient to evaluate the accuracy and precision of the enzymatic glucose determinations. It can be noticed that the bias seems to be dependent on time and concentration whereas the standard deviations differ less. The variation in bias influences the calibration model producing a greater variance for the predicted concentrations. The average reliability considering both bias and standard deviation is estimated to be in the order of about ± 4 mg/dL; this single value is obtained from four reference sera providing only information on small concen-

Table I. Accuracy and Precision of the Hitachi Reference Glucose Determinations in Whole Blood; Concentration Values in mg/dL

	1/88	2/88	3/88	4/88	5/88	6/88
Monitrol I						
certified value	71.0	71.0	71.0	76.0	76.0	76.0
no. of measmts	35	46	38	47	52	49
bias	-1.9	-4.3	-3.9	0.3	2.5	2.2
σ_y	2.4	1.7	2.0	1.9	1.8	2.0
Monitrol II						
certified value	241.0	241.0	241.0	245.0	245.0	245.0
no. of measmts	47	44	32	44	54	44
bias	-3.8	-5.7	-4.9	-1.0	1.2	0.9
σ_y	3.7	4.3	3.2	4.9	3.7	3.4

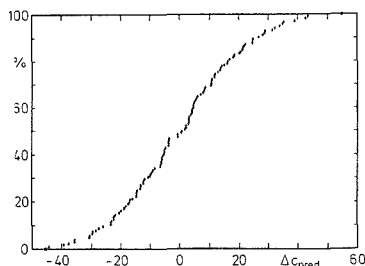


Figure 11. Distribution function for the prediction errors for 127 standards with the PLS model of rank $R_0 = 16$ (concentration units in mg/dL).

tration intervals in the normal and pathological range. Unfortunately, the glucose concentration in the sera could not be determined by the IR-method, since these standards—due to a different matrix—do not belong to the population of whole blood samples, so that a direct comparison of the analytical performance for the two methods is impossible. Whole blood reference standards are not available, one reason being that the glucose concentration is not stable. The quality of the PLS calibration must be judged by the value of $\text{PRESS}^{1/2} = 19.8$ mg/dL, which is an estimate of the reliability of the IR predictions within the blood glucose concentration range of the considered population. For this, the variation of composition leading to different possible interferences, is much greater than that of the reference sera which had been used to obtain accuracy and precision of the reference method. As a final remark, we find the standard deviation obtained in the PLS calibration fit to be no measure for the prediction quality of the sensitive calibration model.

In Figure 11 the error distribution function of the independently predicted concentrations is shown which resembles a Gaussian distribution. This statement is underlined by the fact that within the $\text{PRESS}^{1/2}$ value of ± 19.8 mg/dL, about 68% of the samples are contained. With the distribution given, one can conclude that about 95% (Gaussian 2σ) of the blood samples can be predicted with an uncertainty in the glucose determination of less than ± 40 mg/dL.

Another point that deserves a critical discussion is the adsorption of protein onto the ATR crystal. We studied the time dependence of this process. After a background measurement the ATR cell was filled with a plasma for which a spectrum was recorded after different time intervals, so that the adsorption kinetics could be monitored. Figure 12 shows the time dependent difference spectra with the reference as the first spectrum taken after filling the cell. Since the starting time for the spectrometer was constant after filling the cell, the influence of the protein adsorption on spectrum variation is only small. Irreversible protein adsorption onto the ATR

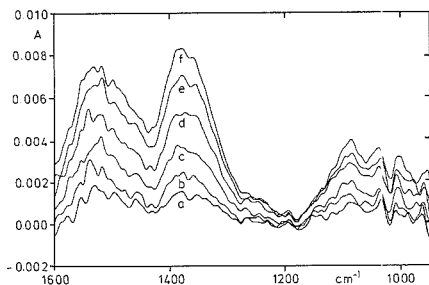


Figure 12. Adsorption kinetics of protein onto ZnSe; difference ATR absorbance spectrum of plasma after (a) 75 s, (b) 150 s, (c) 5 min, (d) 10 min, (e) 20 min, and (f) 30 min; the reference spectrum was taken after filling the cell.

crystal could be compensated for by considering a new background spectrum every time a blood sample was measured. Further studies on the systematic errors induced by irreversible adsorption are necessary.

This is a first feasibility study of the glucose determination by IR-spectrometry, so that further checks on other existing interferences and, for example, on run-to-run precision have to be carried out. Improvements can be expected by obtaining a higher precision for the glucose reference concentration values using for instance multiple determinations. The calibration part can presumably also be improved by giving higher weight to the spectral regions with strong glucose absorptions/correlations. Another important point concerns the available signal/noise ratio which was achieved with a DTGS detector. Doubling the measurement time could be tolerated, improving the S/N by $2^{1/2}$, but the use of a liquid-nitrogen-cooled mercury cadmium telluride (MCT) detector is recommended, especially as the noise above 750 cm^{-1} is comparatively large. Another point is the uncertainty in repositioning the CIRCLE-cell after a crystal polishing. This type of imprecision has recently been studied (34) and has to be considered more carefully, especially, when the detection limits are approached.

CONCLUSION

It may be concluded that infrared spectroscopy will play a more important role in clinical chemistry. So far only the study of urinary calculi is carried out by infrared transmittance measurements using KBr pellets. Recently a quantitative study with principal component regression was published (35). With the analysis of biological fluids like blood, plasma, or serum another field can be opened. There are other blood substrates that are of similar concentrations and show quite different spectral absorption features. Simultaneously to this investigation of whole blood, an analysis of plasma was carried out studying whole protein, urea, cholesterol, and other components, the results of which are reported in a second paper (33). For glucose in whole blood the precision of an IR spectrometric method utilizing the attenuated total reflectance technique has been studied by using a PLS calibration with the inverse model based on a general hospital population. An important aspect is, that no other reagents are necessary, apart from aqueous solutions for cell cleaning and rinsing; the latter

(0.9% NaCl in H_2O) is also used for background measurements. Additionally, nearly continuous monitoring of glucose seems possible. However, further improvements have to be achieved before this method can be employed in the clinical laboratory for routine work.

ACKNOWLEDGMENT

Special thanks are due to Mrs. M. Hillig and Mr. U. Gless for technical assistance.

LITERATURE CITED

- (1) Burrin, J. M.; Price, C. P. *Ann. Clin. Biochem.* **1985**, *22*, 327-342.
- (2) Neese, J. W.; Duncan, P.; Bayse, D.; Robinson, M.; Cooper, T.; Stewart, Ch. Development and Evaluation of a Hexokinase-Glucose-6-phosphate Dehydrogenase Procedure for Use as a National Glucose Reference Method. *HEW Publ.* **1976**, *CDC 77-8330*.
- (3) Haeckel, R. *Fresenius' Z. Anal. Chem.* **1986**, *324*, 207-208.
- (4) Toci, J. *Analyst* **1988**, *113*, 475-478.
- (5) Lambrecht, J. *GIT Labor-Medizin* **1983**, *6*, 38-43.
- (6) Frew, J. E.; Hill, H. A. O. *Anal. Chem.* **1987**, *59*, 933A-944A.
- (7) Hirst, A. D.; Stevens, J. E. *Ann. Clin. Biochem.* **1985**, *22*, 460-488.
- (8) Mullen, W. H.; Churchouse, S. J.; Keedy, F. H.; Vadgama, P. M. *Anal. Proc.* **1986**, *23*, 145-146.
- (9) Churchouse, S. J.; Mullen, W. H.; Keedy, F. H.; Battersby, C. M.; Vadgama, P. M. *Anal. Proc.* **1986**, *23*, 146-148.
- (10) Owen, V. M. *Ann. Clin. Biochem.* **1985**, *22*, 559-564.
- (11) Kruse-Jarres, J. D. *J. Clin. Chem. Clin. Biochem.* **1988**, *26*, 201-208.
- (12) Bartick, E. G.; Messerschmidt, R. G. *Am. Lab.* **1984**, *16*, 56-61.
- (13) Back, D. M.; Michalska, D. F.; Polavarapu, P. L. *Appl. Spectrosc.* **1984**, *38*, 173-180.
- (14) Hopkinson, J. H.; Mouston, C.; Reynolds, N.; Newberry, J. E. *Analyst* **1987**, *112*, 501-505.
- (15) Nyden, M. R.; Forney, G. P.; Chittur, K. *Appl. Spectrosc.* **1988**, *42*, 588-594.
- (16) Kaiser, N. Methods for Determining the Contents of Metabolic Products in the Blood; U.S. Patent No. 4,169,676 Oct. 1979; *IEEE Trans. Biomed. Eng.* **1979**, *26*, 597.
- (17) Bauer, B.; Floyd, T. A. *Anal. Chim. Acta* **1987**, *197*, 295-301.
- (18) Brown, C. W. *Spectroscopy* **1986**, *1*, 32-37.
- (19) Wonnacott, T. J.; Wonnacott, R. J. *Regression: A Second Course in Statistics*; Wiley: New York, 1981, p 501.
- (20) Bibby, J.; Toutenburg, H. *Prediction and Improved Estimation in Linear Models*; Wiley: New York, and Akademie-Verlag: Berlin, 1977.
- (21) Marquardt, D. W. *Technometrics* **1970**, *12*, 591-612.
- (22) Wold, S.; Ruhe, A.; Wold, A.; Dunn, W. J. *SIAM J. Sci. Stat. Comput.* **1984**, *5*, 735-743.
- (23) Haaland, D. M.; Thomas, E. V. *Anal. Chem.* **1988**, *60*, 1193-1202.
- (24) Manne, R. *Chem. Int. Lab. Sys.* **1987**, *2*, 187-197.
- (25) Golub, G.; Kahane, W. J. *SIAM Numer. Anal. Ser. B* **1965**, 205-223.
- (26) Naes, T.; Martens, H. *Commun. Statist. Simula. Computa.* **1985**, *14*, 545-576.
- (27) Geladi, P.; Kowalski, B. R. *Anal. Chim. Acta* **1986**, *185*, 19-32.
- (28) Gunst, R. F.; Mason, R. L. *Regression Analysis and Its Application*; Marcel Dekker: New York, 1980.
- (29) Fox, J. *Linear statistical models and related methods*; John Wiley: New York, 1984.
- (30) Sperline, R. P.; Muralidharan, S.; Freiser, H. *Appl. Spectrosc.* **1986**, *40*, 1019-1022.
- (31) McDonald, R. S.; Wilks, P. A., Jr. *Appl. Spectrosc.* **1988**, *42*, 151.
- (32) Honigs, D. E.; Hietje, G. M.; Hirschfeld, T. *Appl. Spectrosc.* **1984**, *38*, 317-322.
- (33) Janatsch, G.; Kruse-Jarres, J. D.; Marbach, R.; Heise, H. M.; *Anal. Chem.*, following paper in this issue.
- (34) Braue, E. H.; Pannella, M. G. *Appl. Spectrosc.* **1987**, *41*, 1213-1216.
- (35) Hesse, A.; Sanders, G.; Döring, R.; Oelichmann, J. *Fresenius' Z. Anal. Chem.* **1988**, *330*, 372-373.

RECEIVED for review December 20, 1988. Accepted June 16, 1989. The work in the Katharinenhospital was supported by the municipal authorities of Stuttgart including the purchase of experimental equipment. Further funds were given by the Breuninger Foundation and the State Savings Bank (Landesgirobank) Stuttgart. The financial support of the Ministerium für Wissenschaft und Forschung des Landes Nordrhein-Westfalen and the Bundesministerium für Forschung und Technologie for the ISAS institute is acknowledged.

Multivariate Calibration for Assays in Clinical Chemistry Using Attenuated Total Reflection Infrared Spectra of Human Blood Plasma

Günter Janatsch and J. D. Kruse-Jarres

Institut für Klinische Chemie und Laboratoriumsmedizin, Katharinenhospital, Kriegsbergstrasse 60, D-7000 Stuttgart 1, FRG

Ralf Marbach and H. M. Heise*

Institut für Spektrochemie und angewandte Spektroskopie, Bunsen-Küchhoff-Strasse 11, D-4600 Dortmund 1, FRG

A spectral analysis of human blood plasma was undertaken by use of a Fourier-transform infrared spectrometer with a circular attenuated total reflection cell. The concentrations of total protein, glucose, triglycerides, total cholesterol, urea, and uric acid were measured by chemical or enzymatic methods. For these constituents the partial least-squares (PLS) algorithm was used for a multivariate calibration including the infrared fingerprint region of the plasma spectra. Best results were achieved for total protein with an average prediction error (PRESS^{1/2} based on cross validation) of 2.1 g/L; other PRESS^{1/2} results were for glucose 22 mg/dL, triglycerides 33 mg/dL, cholesterol 31 mg/dL, urea 4.4 mg/dL, and uric acid 1.6 mg/dL.

INTRODUCTION

In clinical chemistry, the analysis of blood constituents is important for diagnostic and therapy purposes. The blood substrates are the most frequently determined compounds analyzed in this field (1). The concentration values provide diagnostics for recognizing risk parameters. A few examples will be given. The monitoring of the glucose level is important with, for example, diabetes mellitus. In the study of fat metabolism total cholesterol and triglycerides are monitored. Organ-specific parameters are provided by the concentration values of whole bilirubin for liver and of creatinine and urea for kidney malfunction diagnosis.

For an accurate determination of blood substrate concentrations in the clinical laboratory, one usually provides blood plasma. By centrifugation, the cellular components containing erythrocytes (red cells), leucocytes (white cells), and blood platelets are removed to exclude perturbations of the chemical analysis or to ensure that the metabolism of the corpuscles does not falsify the concentration values. The latter point is particularly important for glucose testing. The concentration of this constituent begins to decrease immediately after sampling because of the glycolytic action of erythrocytes and leucocytes. However, even with plasma samples stored for a long time at -20 °C, a decrease in glucose concentration has been observed (2).

There are relatively large differences in the concentration scale of the various substrates. For instance, the reference range for total protein is given with 60-80 g/L, and for glucose 50-120 mg/dL; upper limits of 7.0 mg/dL are reported for uric acid (dependent on sex), and values of about 1.5 mg/dL for creatinine and total bilirubin in nonpathological conditions. Some analytical methods for certain substrate determinations

can be quite specific and independent of matrix effects, especially when enzymes are involved and their reaction products are used in the quantitative analysis. For the constituents mentioned, a photometric measurement step usually concludes the analytical procedures. The consumption of reagents can be quite a costly factor, which is another point of concern in a clinical laboratory.

A different approach for the analysis of blood substrates can be undertaken by using spectroscopic techniques. Since the advent of Fourier-transform spectrometers, infrared spectroscopy has been widely adopted in quantitative analytical chemistry (3). Fourier-transform infrared (FT-IR) spectroscopy is being resorted to more and more frequently for special applications in biochemistry, because of the high signal-to-noise ratio provided by this technique even when aqueous phase systems are studied. For instance, a review on biomembranes (4) exemplifies this situation. Another application of FT-IR in this field is the study of blood protein adsorption including the kinetics of these reactions (see e.g. ref 5-8). Additionally, single constituents have been studied in biological fluids; the potential of FT-IR for the analysis of glucose has been reported (9), and further, an application of quantitative spectroscopy to the determination of the principal lipids found in blood serum has been given (10). An analysis of human plasma protein mixtures in aqueous solution can also be cited (11). A quantitative study of cholesterol in serum obtained by using near-IR reflectance spectrometry has recently been published (12).

In clinical chemistry, the qualitative analysis of urinary calculi has been established; as an extension, a quantitative study for this subject by principal component regression (PCR) was presented (13). We have undertaken a partial least-squares (PLS) analysis of glucose in whole blood with FT-IR spectroscopy using a circular attenuated total reflection (ATR) cell (14). It can be shown, that the quantitative potential for other constituents, which is intrinsic to the infrared spectrum of blood or plasma, promises a decrease of the work load in clinical chemistry, as a simultaneous analysis of many substrates can be carried out. A further advantage is that no consumption of any specific reagents is necessary. The results of a PLS analysis of human heparinized plasma for several substrates will be reported.

MULTIVARIATE CALIBRATION

Univariate calibration, as traditionally performed by choosing single wavelength information of a spectrum, has its limitations in complicated multicomponent systems. There are a great number of papers concerned with multivariate calibration using a broad spectral range. The classical calibration starts with the Lambert-Beer law and models the sample spectrum with several standard spectra, derived from

* Author to whom correspondence should be sent.

the pure compounds or mixtures of known concentrations. However, systematic errors are caused by unknown components contributing significantly to the infrared spectrum. Furthermore, interactions between constituents of the sample may modify the spectra compared to standard conditions where these interactions are lacking, also inducing an error.

To avoid these problems, the inverse model has been proposed, and several approaches were reported to solve the ill-conditioned multiple linear regression systems arising here. For a broader discussion of the involved problem of biased linear estimators, see ref 15 and 16, where ridge regression can be considered to give one class. Different approaches are provided with a principal component regression (PCR), e.g. ref 17, and partial least squares (PLS) (18), for which a recent application may serve as an example (19). In order to get these prediction models to work efficiently and reliably, one must ascertain that the calibration samples span the range with all possible interfering compounds or other systematic error types to avoid extreme extrapolations. The actual concentrations of the interferents are not necessary for this model.

Our multivariate calibration is based on the partial least-squares algorithm applied to each component, one after another. This is known in the literature under the nomenclature PLS1. Recently, Manne (20) has shown that this is equivalent to a transformation of the linear regression matrix to a bi-diagonal form. Our method optimization was carried out by cross-validation (21, 22) choosing the prediction error: sum of squares (PRESS) minimum. To provide the test standards used to assess the prediction ability of a model, each standard was omitted once from the calibration and predicted by the regression result using the remaining data. By this method, as many independent predictions as standards are available (see also ref 14).

In this study a multicomponent analysis for heparinized human blood plasma will be reported. In the preceding paper (14), the concentration value of only one constituent, glucose, was measured by an analytical reference method for whole blood specimens. In principal, a different algorithm (PLS2) (20) was designed for the case with several compound variables to be fitted, e.g. to the measured spectroscopic data. As Manne pointed out, the use of PLS1 for each dependent compound variable may well be worthwhile, because of its speed and efficiency; furthermore, it is only the PLS1 algorithm that has the all-decisive property to span the (sample) covariance vector between spectrum and component concentration with a minimum number of PLS eigenvectors, thus providing the PLS eigenvectors in an order of decreasing predictive power. The use of PLS1 is also justified in the light that the outlier detection can produce quite different candidates for the removal of standards which had been analyzed for the plasma constituents considered by different analytical methods.

EXPERIMENTAL SECTION

Blood specimens were provided from patients of the Katharinenhospital Stuttgart. The standards were sampled over a period of 2 months. The population is that of a general hospital with no special prominent medical features. There was no patient discrimination of the grounds of sex or age. About 90% of the concentration values for the different considered substrates were within the reference ranges given in ref 1. After centrifugation of the cellular components, the heparinized plasma samples were analyzed for, among other parameters, several blood substrates on an automated SMAC analyzer from Technicon Corp. (Tarrytown, NY). The following substrates were studied: total protein, glucose, triglycerides, total cholesterol, urea, and uric acid.

A photometric determination was used in the final analysis step for all methods programmed on the analyzer, with flow cells of 10 or 12 mm path length measuring at wavelengths between 340 and 570 nm. More experimental details are given in the following references. For total protein the Technicon SMAC method is based on a study of Skeggs and Hochstrasser (23) where a biuret

reagent was used. In the analyzer, a method for the determination of the glucose concentration was implemented (24) which uses an immobilized enzyme combination of hexokinase and glucose-6-phosphate dehydrogenase as catalyst. For the determination of triglycerides, the enzymatic method using lipase in the first reaction step follows the procedure of Bucolo and David (25). The analysis of the cholesterol concentrations was performed by making use of cholesterol esterase and cholesterol oxidase (26), whereas the SMAC method for urea is a modification of the carbamido-diacetyl reaction (27). Diacetyl monoxime is used which is hydrolyzed to give diacetyl which reacts with urea. For the determination of uric acid, the analyzer-bound uricase (urate oxidase) method was considered, being developed by Yeh and co-workers (28). For the SMAC analyzer the original reagents were all from Technicon Corp. (Bad Vilbel, Federal Republic of Germany).

Different lyophilized sera were used for SMAC-analyzer control. Monitor I and Monitor II were supplied from American Hospital Supply Deutschland (Bereich Merz + Dade, Munich, FRG), and Seroquant was obtained from Behringwerke (Marburg, FRG). The first two sera concentrations were company-certified and had been determined by using several reference methods. The results of these methods were chosen which were equivalent to the programmed ones on the SMAC analyzer. For Seroquant, analyses were carried out in our laboratory with comparison to a certified reference serum obtaining concentration values which were assumed to possess similar qualities as the company-certified values.

Plasma spectra were recorded by using a Perkin-Elmer spectrometer with a DTGS detector. The measuring cell was a CIRCLE cell, with ZnSe crystal, thermostated at 37 °C. Twenty interferograms with resolution 8 cm^{-1} and weak Norton Beer apodization were averaged for signal/noise ratio improvement. More details on the apparatus have been reported in the preceding paper (14). After completion of a new background spectrum—for this the ATR cell was filled with 0.9% aqueous NaCl solution—each of the plasma spectra were recorded. The measurement time for one sample including the background recording was about 4 min. The absorbance spectra were transformed into JCAMP-DX format (29), so that they could be handled by the PLS software running on a Commodore PC-20 (IBM compatible). The property correlation spectra (for more details, see also ref 30) and average spectra were calculated with software provided by Perkin-Elmer.

For comparison of the property correlation data, reference spectra of pure compounds were recorded with a Perkin-Elmer 1800 or Bruker IFS 113 V spectrometer. The following substances were purchased from different suppliers: D-(+)-glucose monohydrate, urea, and uric acid for biochemical purposes (Merck, Darmstadt, FRG) and albumin from bovine serum (Sigma Chemie, Deisenhofen, FRG), cholesterol (Schuchardt, Hohenbrunn, FRG), and egg lecithin (Fluka, Neu-Ulm, FRG).

RESULTS AND DISCUSSION

The study using the plasma infrared spectra to determine several substrate concentrations was aimed to show the feasibility of employing inverse calibration in clinical chemistry. With this in mind, our target population is defined which is supposed to be represented by the plasma samples considered. As well as the measurement of the reference concentration values, high-quality infrared spectra were also necessary for the calibration. A typical absorbance spectrum of heparinized human plasma measured with the CIRCLE microcell is shown in Figure 1 including the related noise level. This reveals that the energy limitation due to absorptions of the ZnSe crystal and water for the lowest wavenumber region above 750 cm^{-1} leads to a restriction for its quantitative usage.

In Figure 2 the plasma average spectrum of the population considered for the calibration is compared to the average of whole blood samples which had been calculated in the calibration study of glucose (14). Nearly perfect conformity can be observed for both spectra. The lower concentration of protein for plasma is expected, as the removal of the cellular components changes the overall protein content. It is conspicuous that the spectra are not influenced by the haematocrit of the whole blood fluid. Another apparent feature from

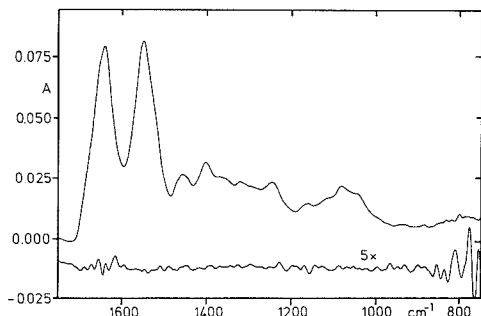


Figure 1. Absorbance infrared spectrum of heparinized human plasma measured with an ATR cylindrical cell (ZnSe crystal); in the lower trace the associated noise level is shown.

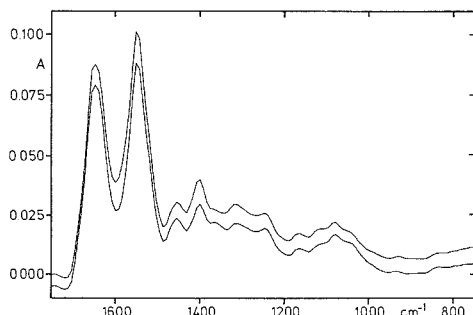


Figure 2. Average infrared spectrum of whole blood from a population of 135 standards (upper trace); average spectrum of heparinized human plasma from a population of 75 standards (lower trace). All spectra were recorded with the same ATR cylindrical cell; for clarity the plasma spectrum is offset by -0.005 absorbance unit.

the comparison in Figure 2 is, that the glucose level in plasma is higher than that in blood. The reason is, that the water

content of the erythrocytes, about 73%, is less than that of the blood plasma, about 93%. The glucose molecules are freely diffusible between plasma and erythrocytes, but due to the greater water concentration in plasma, the average glucose level is about 13% higher than that in whole blood specimens.

Looking at the property correlation spectrum (PCS) of total protein, one can say that most of the plasma absorption features, with the exception of the region from 1000 to 1200 cm^{-1} , can be related to the protein spectrum. In Figure 3A a comparison of the protein PCS is presented with an absorbance spectrum of albumin measured by the normal KBr pellet method. The absorbance scale is valid only for the PCS spectrum (lower trace), whereas the scale for all reference substrate spectra shown is arbitrary. The similarity of the protein spectra is striking apart from the strongest absorption bands (amide I 1650 cm^{-1} and II 1540 cm^{-1}). The broad half-width for these bands in the PCS spectrum can be explained by the solid-phase state, whereas the different intensity ratio for both bands in the PCS is related to the fact that no scaled absorbance subtraction had been performed for the ATR spectra to match the water absorptions. The greater water concentration of the 0.9% NaCl solution used for the background measurements, as compared to the plasma, leads to a considerable reduction of the amide I absorption band intensity because of an overcompensation for the very strong 1640- cm^{-1} water vibration band.

The number of standards used for the calibrations were 78 or less due to outlier exclusion. To obtain statistically significant results, it was necessary to limit the number of independent wavenumbers (spectral data points) to a smaller value, so that only a part of the fingerprint region from 1750 to 750 cm^{-1} was selected by inspection of the property correlation and KBr pellet spectrum.

Another reason for the selection of certain wavenumber intervals is to minimize indirect calibrations based on correlations between plasma component concentrations, which can be manifested in the spectral space by the property correlation spectrum. An indirect calibration can be avoided—even for perfectly correlated substrates—by using a wavenumber range

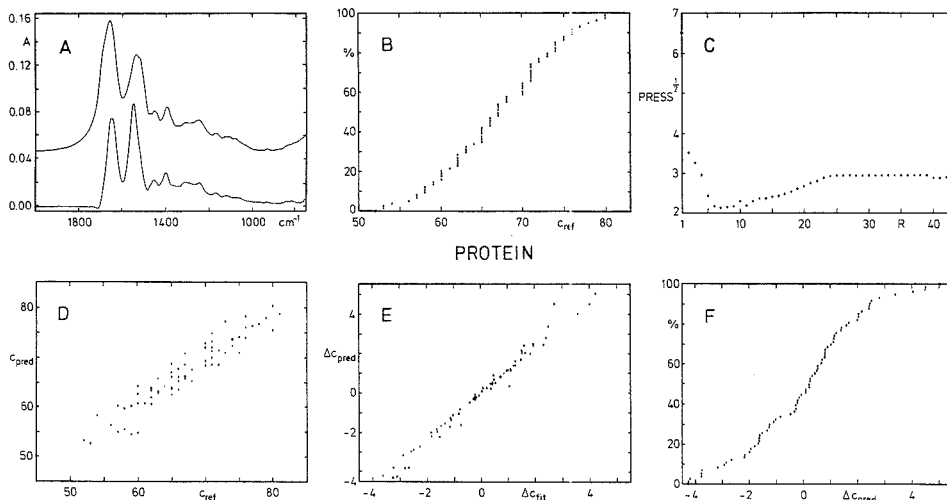


Figure 3. Calibration results for total protein in human heparinized plasma; concentration units are given in g/L: (A) infrared spectrum of albumin measured with the KBr pellet technique (upper trace), property correlation spectrum of total protein (see text) (lower trace); (B) distribution curve for the standard concentrations measured by the reference method; (C) $\text{PRESS}^{1/2}$ statistics for calibration models of different rank; (D) predicted concentration values versus measured reference values ($c_{\text{pred}} = 5.1 + 0.924c_{\text{ref}}$; $R^2 = 0.91$); (E) plot of prediction errors versus PLS calibration residuals ($\Delta c_{\text{pred}} = 1.22\Delta c_{\text{ref}}$; $R^2 = 0.98$); (F) distribution function for the prediction errors.

Table I. Correlation Matrix for the Substrate Concentrations of the Studied Patient Population

	protein	glucose	triglycerides	cholesterol	urea	uric acid
protein	1.00	0.05	0.14	0.44	-0.12	0.24
glucose	0.05	1.00	-0.40	-0.21	0.36	0.21
triglycerides	0.14	0.40	1.00	0.26	0.25	0.28
cholesterol	0.44	-0.21	0.26	1.00	-0.30	0.15
urea	-0.12	0.36	0.25	-0.30	1.00	0.54
uric acid	0.24	0.21	0.28	0.15	0.54	1.00

with only negligible spectral overlap to other component spectra. The use of compound correlations is in principle an advantageous feature of the inverse modeling approach, provided the samples are representative enough for the larger population of future specimens, for which the substrate concentrations have to be determined. However, a problem may arise from different physiological substrate kinetics existing in pathological cases with more extreme concentrations, so the approach using certain wavenumber intervals can claim to be a more generally applicable.

In addition to the PCS, we studied the compound interdependence by evaluating the correlation matrix between the different substrate concentrations, which is given in Table I. The highest correlations exist for urea and uric acid with a coefficient of 0.54, whereas the other values were lower. These results indicate that the influence leading to indirect calibrations is limited, especially in view of the additional selection of the spectral data. With the algebraic and statistical advantages of the PLS1 algorithm mentioned, this justifies its application.

The results for the different calibrations are summarized in Table II for the plasma substrates determined. For a better illustration of the individual calibrations performed, Figures 3 to 8 are shown. In part A of these figures, the spectral information is given for the compound studied; for glucose the absorption spectrum from an aqueous solution recorded with the CIRCLE cell is shown, whereas for the other sub-

strates KBr pellet spectra are reproduced, with the exception of lecithin, which was measured as a film. In part B of the figures, the distribution function for the standard concentrations is plotted; with part C, the PRESS^{1/2} results are shown by which the optimum prediction model with PLS rank R_0 is selected. Part D gives the independent predictions from the infrared ATR spectra versus the reference values.

These data were fitted by least squares to a straight line ($c_{\text{pred}} = b_0 + b_1 c_{\text{ref}}$). The results of the fit b_0 , b_1 , and R^2 provide, in addition to the PRESS^{1/2} value, a measure of the prediction quality of the optimum PLS model chosen. R^2 given above is the determination coefficient of the fit (31). With these data the deviation from the ideal result, the identity function, is clarified. The scatter in the corresponding calibration plot is smaller by a factor, which can be estimated from the slope of the plot (E), where the prediction errors are plotted versus the concentration residuals obtained with the optimal partial least-squares fit. Finally in part F, the distribution function of the prediction errors is shown, demonstrating graphically the variance produced by the prediction model.

For operational checks of the SMAC analyzer, several measurements were performed daily by using the reference sera. From the control charts the data for a period of 3 months was collected; on this basis bias and standard deviation could be estimated for the substrates of interest. The bias is the difference between the measured mean and the certified value. In Table III the results for judging the reliability of the programmed methods considering precision and accuracy are summarized.

There should be some individual comments made for each plasma substrate calibrated. The spectral range used for the whole protein calibration covers the main absorption bands. There is more spectral information down from 1350 cm⁻¹, which could possibly be considered with a fit enclosing more standards. The calibration samples span the concentration range from 50 to 90 g/L; it would be desirable to produce the reference values with one digit after the decimal point for improvement. The independently predicted concentrations versus the reference values are shown in Figure 3D.

Table II. Results^a of the PLS Calibration Using ATR Infrared Spectra of Heparinized Human Blood Plasma

compound	range/ $\Delta\bar{\nu}$ (cm ⁻¹)	M	M/N	R_0	R^2	Y_{av}	σ	PRESS ^{1/2}
protein	1700-1350/8	75	1.67	7	0.94	66.9	1.8	2.1
glucose	1180-950/8	78	2.60	7	0.73	118.8	17.7	22.0
triglycerides	1500-1400/8 1275-1000/8	74	1.51	8	0.83	154.6	26.9	32.6
cholesterol	1430-1150/8	78	2.10	7	0.71	172.7	27.5	30.6
urea	1700-1400/8 1200-1000/8	76	1.46	9	0.98	30.7	3.1	4.4
uric acid	1700-1400/8 1200-1150/8	76	1.65	4	0.54	5.1	1.6	1.6

^a For total protein the results are in g/L, other concentrations are in mg/dL; M is the number of standards considered, N the number of spectral data points. R^2 is the determination coefficient for the calibration fit, R_0 the optimum PLS rank chosen; Y_{av} is the average concentration for the sample population; σ estimated standard deviation of the PLS calibration fit; PRESS, i.e. mean square prediction error (see text).

Table III. Reliability of the Different Substrate Reference Methods Using Measurements with Certified Sera during a Period of Three Months^a

compound	Monitrol I				Seroquant				Monitrol II			
	certified value	n	bias	σ_y	certified value	n	bias	σ_y	certified value	n	bias	σ_y
protein	63	70	1.3	1.1	58	59	0.3	1.5	45	69	2.2	1.0
glucose	74	66	0.8	3.0	107	63	0.9	3.9	241	66	6.9	7.8
triglycerides	77	57	1.1	5.6	110	47	2.6	7.0	189	58	-12.2	12.6
cholesterol	181	58	-8.8	7.4	121	49	2.1	6.8	123	59	-5.6	10.9
urea	14.0	67	1.2	0.7	22.0	62	0.1	0.9	54.0	70	-1.1	1.4
uric acid	54.0	66	-4.5	2.1	72.0	56	-0.7	2.3	86.6	71	0.4	1.9

^a n is the number of analyses; concentration units for total protein are in g/L, for uric acid in mg/L, others in mg/dL.

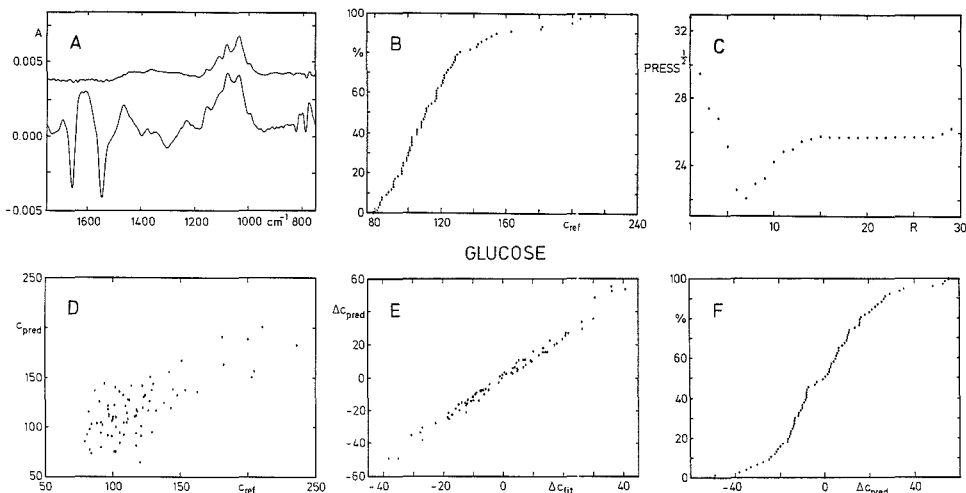


Figure 4. Calibration results for glucose in human heparinized plasma; concentration units are given in mg/dL: (A) infrared spectrum of glucose measured in aqueous solution with a concentration of 119 mg/dL (upper trace), property correlation spectrum of glucose (lower trace); (B, C, and F) see caption of Figure 3; (D) predicted concentration values versus measured reference values ($c_{\text{pred}} = 42.6 + 0.640c_{\text{ref}}$; $R^2 = 0.56$); (E) plot of prediction errors versus PLS calibration residuals ($\Delta c_{\text{pred}} = 0.1 + 1.29\Delta c_{\text{fit}}$; $R^2 = 0.98$).

In Figure 3E, the prediction errors versus the calibration residuals are shown; the slope of a least-squares fitted straight line provides the average increase of the prediction errors compared to the residuals of the PLS regression. From Figure 3F, it is evident that for 95% of the samples the total protein content can be predicted with an uncertainty of less than ± 4.2 g/L. When compared with the reliability of the programmed reference method (see Table III), the conclusion can be drawn that the uncertainty inherent in the PLS infrared prediction model is about the same as that achieved with the reference procedure.

For glucose a rather asymmetric distribution function for the sample concentration values is found (see Figure 4B). The normal range of about 80–150 mg/dL contains about 90% of the specimens. The residual values represent pathological cases. A comparison can be made to the calibration results for whole blood spectra (14). For the latter, a larger number of standards, 127, was available, so that a broader spectral range (1500–750 cm^{-1}) could be chosen. For that spectrum population, a convincing similarity of the glucose property correlation spectrum to the aqueous phase absorption signal has been shown. For plasma, there are differences, possibly because of the smaller number of standards; however, the major absorption bands of the glucose above 1000 cm^{-1} show up (see Figure 4A). The exclusion of the range from 1750 to 1500 cm^{-1} can be justified on grounds of the negative correlation of the protein bands to glucose. It can be argued that the rapidly changing glucose level should be independent from the slowly varying protein concentration (see also ref 14). The range of the H_2O absorption band (1640 cm^{-1}), which is rather sensitive to compensation, is also excluded. Because of the smaller population of standards available for the plasma study, the spectral range considered was from 1180 to 950 cm^{-1} .

The optimum rank for the calibration models is at $R_0 = 7$, much smaller than for the determination of glucose in whole blood ($R_0 = 16$), which is due to the narrow spectral interval chosen, although the value for $\text{PRESS}^{1/2} = 22$ mg/dL is of similar magnitude as found for the whole blood result with a value of 20 mg/dL. The lower relative prediction error for plasma glucose is due to the greater average value as discussed earlier. With this similarity in the results, a plausible con-

clusion may be drawn that a further improvement can be expected by using a much greater number of standards representing the possible population of samples in a better way. The prediction errors for the results, achieved with the present best plasma PLS model, are about 5 times as large as the uncertainty determined for the reference method using the certified samples.

For the triglycerides the signals that can be related to this compound category are even smaller than those obtained for glucose (see Figure 5A). The second spectrum in Figure 5A was measured with lecithin which was chosen as a representative for that class of substrates. The standard concentrations range from 50 to about 300 mg/dL with a small asymmetry in the distribution function to be noticed. There is a double minimum in the $\text{PRESS}^{1/2}$ statistics, the first of which occurs at a rank of $R_0 = 8$ which is also the absolute minimum. Relevant information is only contained in up to a rank of about $R = 25$, which is evident from the "plateau" in the $\text{PRESS}^{1/2}$ statistics. This value is greater than that obtained for the compounds already discussed, and this can be explained by the broader wavenumber range considered for the calibration. The scatter in the calibration fit calculated for that model is about a factor of 1.27 smaller than shown for the independent prediction values versus reference concentrations (see Figure 5D). The average prediction error is about 4 times worse than the uncertainty inherent in the reference method used for the triglyceride determination. The rather poor reference result for Monitor II (see Table III) can be explained by larger systematic deviations occurring during a full month.

The concentration range for total cholesterol tackled with this calibration was from 70 to 300 mg/dL. There is a flaw in the sample distribution at 160 mg/dL, and about 70% of the samples are between 150 and 220 mg/dL (see Figure 6B). A positive correlation to the protein amide I and II bands can be noticed, and the other apparent feature is the negative correlation of the glucose absorption to the cholesterol concentration. The spectral range considered for the calibration was chosen from 1430 to 1150 cm^{-1} . The sharp minimum of the $\text{PRESS}^{1/2}$ statistics occurred for $R_0 = 7$; relevant information for prediction models is contained up to a rank of R

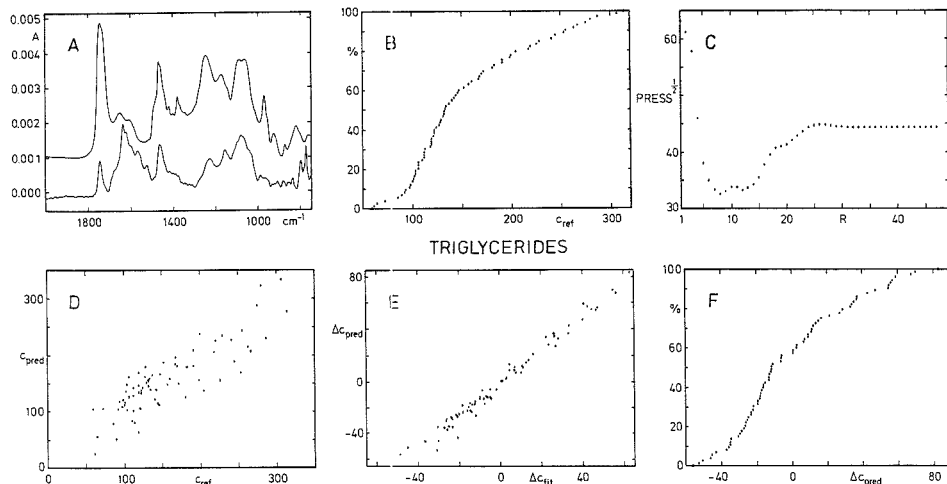


Figure 5. Calibration results for triglycerides in human heparinized plasma; concentration units are given in mg/dL: (A) infrared spectrum of lecithin measured as film on a KBr pellet (upper trace), property correlation spectrum of triglycerides (lower trace); (B, C, and F) see caption of Figure 3; (D) predicted concentration values versus measured reference values ($c_{\text{pred}} = 33.4 + 0.790c_{\text{ref}}$; $R^2 = 0.73$); (E) plot of prediction errors versus PLS calibration residuals ($\Delta c_{\text{pred}} = -1.0 + 1.27\Delta c_{\text{fit}}$; $R^2 = 0.98$).

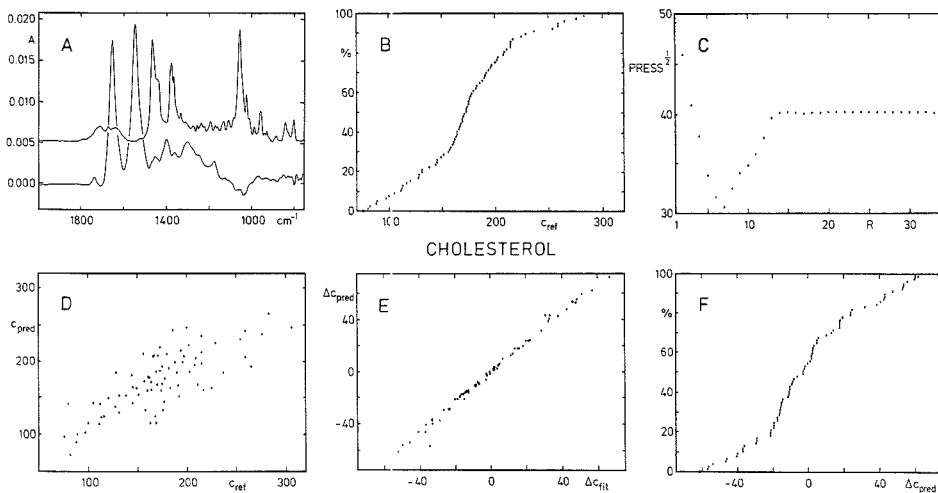


Figure 6. Calibration results for total cholesterol in human heparinized plasma; concentration units are given in mg/dL: (A) infrared spectrum of cholesterol measured with the KBr pellet technique (upper trace), property correlation spectrum of total cholesterol (lower trace); (B, C, and F) see caption of Figure 3; (D) predicted concentration values versus measured reference values ($c_{\text{pred}} = 59.1 + 0.660c_{\text{ref}}$; $R^2 = 0.61$); (E) plot of prediction errors versus PLS calibration residuals ($\Delta c_{\text{pred}} = -0.4 + 1.16\Delta c_{\text{fit}}$; $R^2 = 0.99$).

= 13 (see Figure 6C). The prediction results for total cholesterol are plotted in Figure 6D, where the actual data scattering for the calibration fit is reduced by a factor of 1.16, which is obtained from the slope result of a straight line fit of the prediction errors versus the calibration residuals. When assessing precision and accuracy for the determination of this compound by its reference method, one finds that the IR method is about a factor of 3 worse, which is surprising in view of the small absorption features considered.

A favorable case is given for the urea analysis in plasma, where a convincing calibration can be performed due to the unique infrared absorption spectrum. The PCS of urea (see Figure 7a, lower spectrum) is slightly perturbed by influences

from protein. Nine PLS factors are needed to produce reasonable prediction results. The $\text{PRESS}^{1/2}$ function (Figure 7C) for ranks greater than for the minimum possesses the smallest slope for all curves found for the substrates studied. The distribution function of the sample concentrations is asymmetric and comparable to that of glucose. The concentration range for urea extends from 5 to 125 mg/dL. The scatter in the uncritical calibration fit is again reduced by a factor of 1.47 compared to Figure 7D. The uncertainty of the prediction results is about a factor of 3 worse than that of the reference method chosen.

At the beginning of this study, it was decided not to try a calibration for those substrates with a rather low concentration

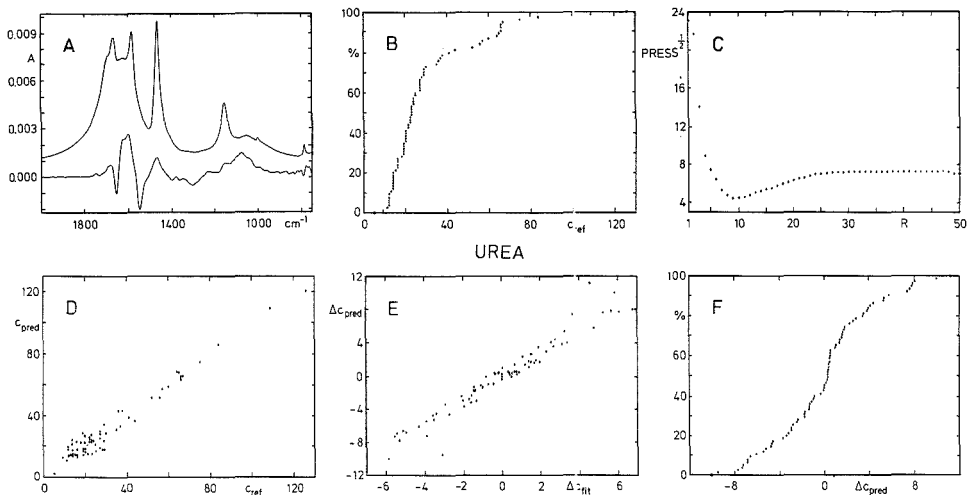


Figure 7. Calibration results for urea in human heparinized plasma; concentration units are given in mg/dL: (A) infrared spectrum of urea measured with the KBr pellet technique (upper trace); property correlation spectrum (lower trace); (B, C, and F) see caption of Figure 3; (D) predicted concentration values versus measured reference values ($c_{\text{pred}} = 1.1 + 0.966c_{\text{ref}}$; $R^2 = 0.96$); (E) plot of prediction errors versus PLS calibration residuals ($\Delta c_{\text{pred}} = 1.47\Delta c_{\text{fit}}$; $R^2 = 0.94$).

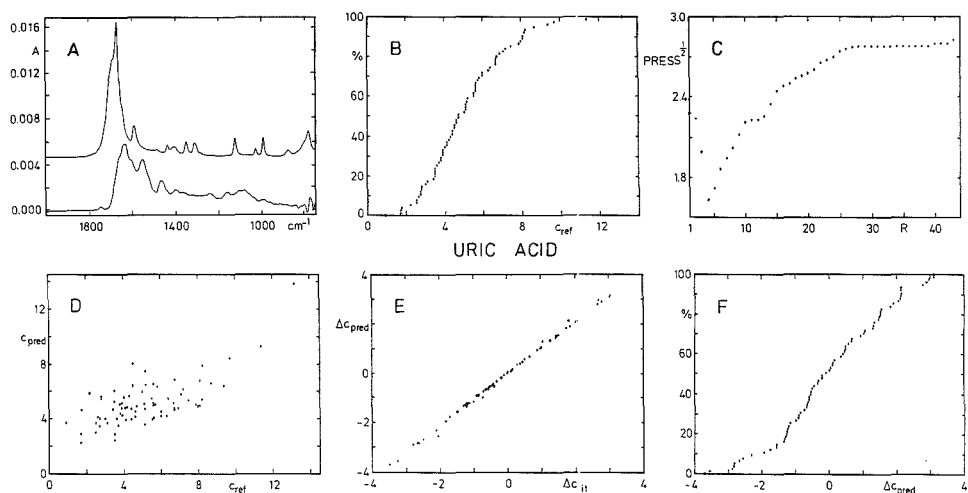


Figure 8. Calibration results for uric acid in human heparinized plasma, concentration units are given in mg/dL: (A) infrared spectrum of uric acid measured with the KBr pellet technique (upper trace); property correlation spectrum (lower trace); (B, C, and F) see caption of Figure 3; (D) predicted concentration values versus measured reference values ($c_{\text{pred}} = 2.5 + 0.51c_{\text{ref}}$; $R^2 = 0.48$); (E) plot of prediction errors versus PLS calibration residuals ($\Delta c_{\text{pred}} = 1.1\Delta c_{\text{fit}}$; $R^2 = 0.998$).

such as found for uric acid. Utilizing the infrared ATR plasma spectra, we were surprised by the PLS results we obtained later. When looking at the spectrum of uric acid, one notices the very intensive pseudo carbonyl absorption band at about 1680 cm^{-1} —there is a tautomeric equilibrium for uric acid (see Figure 8A); this leads to a rather favorable condition for the determination of this compound by infrared spectroscopy. However, due to the low concentrations of this substrate, which range from 1 to 13 mg/dL (about 80% of the sample population is between 3 and 8 mg/dL), the poor precision in the calibration is expected. For a plot of the calibration results, the scatter is reduced by a factor of 1.1 compared to that obtained for the independent predictions (Figure 8D).

The relative prediction error is 30% based on an average concentration of 5.1 mg/dL in the population studied. The reliability of the uric acid reference determination is high, due to the enzymatic uricase method used. For Monitrol I, a negative systematic error of about 8% of the certified value occurred for the determinations, but accuracy and precision for the other two sera are convincingly better (see Table III). The infrared PLS model evaluated in this study can predict concentration values for uric acid with an uncertainty of $\pm 3.2\text{ mg/dL}$ (95% confidence limit; see also Figure 8F).

We also calculated calibrations for creatinine and bilirubin, for which relative prediction errors of about 50% based on $\text{PRESS}^{1/2}$ and the average concentration of the population

resulted. We decided not to include these results, because the quality of the spectra has certainly to be improved to achieve a better performance of the IR method with the rather low concentrations of about 1 mg/dL to be considered.

The performance comparison between the reference methods and the PLS infrared methods disfavors the latter. It must be remembered that the mean square prediction error (PRESS) of the infrared methods is calculated, taking into account the entire concentration range of the distributions, whereas standard deviation and bias for the reference methods are provided only for fixed concentration values. There is a much greater variation including possible interferences in the population studied by infrared spectrometry. A direct comparison of the infrared and the reference methods using the serum standards is not possible, since these do not belong to the population of studied plasma samples, so that the results of the inverse calibrations are not applicable for predicting serum substrate concentrations. The "a posteriori" straight line fits of the predicted versus reference concentrations by least squares always give a positive ordinate intercept and a slope smaller than 1.0 providing an impression of the concentration-dependent bias of the prediction models chosen. Evidently, high concentrations are underestimated and low ones overestimated. The better the quality of the prediction model is, the less affected is the average prediction error $PRESS^{1/2}$ by bias.

Improvements for the substrate determination by infrared spectroscopy have been discussed in ref 14 at greater length, so only the main points shall be stressed. It is possible to measure the ATR spectrum with a better signal-to-noise ratio making use of photon detectors (commonly used are liquid-N₂-cooled HgCdTe semiconductors) instead of the pyroelectric thermal DTGS detector. A cut down of the measurement time is also possible (20 scans in 75 s for our spectrometer configuration). Apart from better infrared spectra, the other factor considered for improvement is the number of standards used; the uncertainty for the predictions can be reduced by considering a larger sample population. In addition, a systematic investigation is necessary to study the influence of the spectral range to be chosen for the calibration. A weighted partial least-squares analysis with more emphasis on the spectral regions with strong absorption features of the components studied could further improve the calibration results. There is certainly room for improvement when considering the statistical algorithm.

Systematic deviations by protein adsorptions onto the ATR crystal have been studied by measuring the kinetics of this reaction (14). It can be concluded, that these influences on the plasma spectrum can be reduced to a negligible level by an accurate timing of the measurements. However, further studies are needed for an estimate of these perturbation effects on the different concentration results.

CONCLUSION

With this extensive study of heparinized human plasma by infrared spectroscopy and chemical or enzymatic reference methods, it can be shown that, with the implementation of a numerically stable and efficient algorithm, prediction models can be constructed which make use of infrared spectra. A fast, multicomponent analysis without any consumption of special expensive reagents is possible with the small sample volume required. The experimental equipment can be modified without difficulties, so that only 200 μ L of blood or plasma is necessary for the analysis. The advantage of the circular ATR microcell for these measurements must be emphasized. The final conclusion of this investigation is that Fourier

transform infrared spectroscopy may play a more important role for analytical applications in clinical chemistry. However, for propagating this method for broad clinical use, it is necessary to achieve further improvements.

ACKNOWLEDGMENT

Special thanks are due to Mrs. M. Hillig and Mr. U. Gless for technical assistance.

Registry No. Cholesterol, 57-88-5; urea, 57-13-6; uric acid, 69-93-2.

LITERATURE CITED

- (1) Stamm, D.; Wisser, H. "Blutanalytik." In *Analytiker-Taschenbuch*; Bock, R., Fresenius, W., Günzler, H., Huber, W., Tölg, G., Eds.; Springer-Verlag: Berlin, 1983; Vol. 3, 87-119.
- (2) Giampietro, O.; Navelesi, R.; et al. *Clin. Chem.* **1980**, *26*, 1710-1712.
- (3) Griffiths, P. R.; de Haseth, J. A. *Fourier Transform Infrared Spectrometry*; J. Wiley & Sons: New York, 1986.
- (4) Casal, H. L.; Mantsch, H. H. *Biochim. Biophys. Acta* **1984**, *779*, 381-401.
- (5) Chittur, K. K.; Fink, D. J.; Leininger, R. I.; Hutson, T. B. *J. Colloid Interface Sci.* **1986**, *111*, 419.
- (6) Chittur, K. K.; Fink, D. J.; Hutson, T. B.; Gendreau, R. M.; Jakobsen, R. J.; Leininger, R. I. In *Proteins at Interfaces*; Horbett, T., Brash, J. L., Eds.; American Chemical Society: Washington, D.C. 1987; ACS Symposium Series 343, pp 362-377.
- (7) Gendreau, R. M.; Winters, S.; Leininger, R. I.; Fink, D. J.; Hassler, C. R.; Jakobsen, R. *J. Appl. Spectrosc.* **1981**, *35*, 353.
- (8) Winters, S.; Gendreau, R. M.; Leininger, R. I.; Jakobsen, R. *J. Appl. Spectrosc.* **1982**, *36*, 404.
- (9) Bauer, B.; Floyd, T. A. *Anal. Chim. Acta* **1987**, *197*, 295-301.
- (10) McClure, G. L.; Roush, P. B.; Williams, J. F.; Lehmann, C. A. Application of Computerized Quantitative Spectroscopy to the Determination of the Principal Lipids Found in Blood Serum. In *Computerized Quantitative Infrared Analysis*; McClure, G. L., Ed.; American Society for Testing and Materials: Philadelphia, PA, 1987; ASTM STP 934, p 131.
- (11) Nyden, M. R.; Forney, G. P.; Chittur, K. *J. Appl. Spectrosc.* **1988**, *42*, 588-594.
- (12) Peuchant, E.; Salles, C.; Jensen, R. *Anal. Chem.* **1987**, *59*, 1816-1819.
- (13) Hesse, G.; Sanders, G.; Döring, R.; Oelichmann, J. *Fresenius' Z. Anal. Chem.* **1988**, *330*, 372-373.
- (14) Hesse, H. M.; Marbach, R.; Janatsch, G.; Kruse-Jarres, J. D. *Anal. Chem.*, preceding paper in this issue.
- (15) Trenkler, G. *Biased Estimators in the Linear Regression Model*; Hain: Königstein/Ts., 1981.
- (16) Marquardt, D. W. *Technometrics* **1970**, *12*, 591-612.
- (17) Fredericks, P. M.; Lee, J. B.; Osborn, P. R.; Swinkels, D. A. *J. Appl. Spectrosc.* **1985**, *39*, 311-316.
- (18) Naes, T.; Martens, H. *Commun. Statist. Sim. Comput.* **1985**, *14*, 545-576.
- (19) Martens, H.; Karstang, T.; Naes, T. *J. Chemom.* **1987**, *1*, 201-219.
- (20) Manne, R. *Chem. Int. Lab. Sys.* **1987**, *2*, 187-197.
- (21) Stone, M. *J. R. Statist. Soc.* **1974**, *B36*, 111-135.
- (22) Osten, D. W. *J. Chemom.* **1988**, *2*, 39-48.
- (23) Skeggs, L. T., Jr.; Hochstrasser, H. *Clin. Chem.* **1964**, *10*, 918-936.
- (24) Léon, L. P.; Chu, D. K.; Stasiv, R. O.; Snyder, L. R. New More Specific Methods for the SMA 12/60 Multichannel Biochemical Analyzer. In *Advances in Automated Analysis Technicon International Congress 1976*; Mediad Inc.: Tarrytown, NY, 1977; Vol. 1, pp 152-156.
- (25) Bucolo, G.; David, H. *Clin. Chem.* **1973**, *19*, 475-482.
- (26) Lie, R. F.; Schmitz, J. M.; Pierre, K. J.; Gochman, N. *Clin. Chem.* **1976**, *22*, 1627.
- (27) Marsh, W. H.; Fingerhut, N. B.; Miller, H. *Clin. Chem.* **1965**, *11*, 624-627.
- (28) Yeh, C. K.; Krower, J. S.; Bauer, R. S. *Clin. Chem.* **1983**, *29*, 1285.
- (29) McDonald, R. S.; Wilks, P. A., Jr. *J. Appl. Spectrosc.* **1988**, *42*, 151.
- (30) Honigs, D. E.; Hietfle, G. M.; Hirschfeld, T. *J. Appl. Spectrosc.* **1984**, *38*, 317-322.
- (31) Gunst, R. F.; Mason, R. L. *Regression Analysis and Its Application*; Marcel Dekker: New York, 1980.

RECEIVED for review December 20, 1988. Accepted June 16, 1989. The work at the Katharinenhospital was supported by the municipal authorities of Stuttgart, including the purchase of experimental equipment. Further funds were granted by the Breuninger Foundation and by the State Savings Bank (Landesgirobank) Stuttgart. Financial support from the Ministerium für Wissenschaft und Forschung des Landes Nordrhein-Westfalen and the Bundesministerium für Forschung und Technologie for the ISAS institute is acknowledged.

Global Optimization by Simulated Annealing with Wavelength Selection for Ultraviolet–Visible Spectrophotometry

John H. Kalivas,* Nancy Roberts, and Jon M. Sutter

Department of Chemistry, Idaho State University, Pocatello, Idaho 83209

The problem of process optimization is routinely encountered by chemists. One favored technique for determination of a best or optimal set of operating conditions for a given system has been the simplex algorithm. The major defect of simplex lies in its inability to guarantee that the global optimum of a system has been located. This assurance is gained only by the convergence of repetitive trials with widely spaced starting points to the same global optimum. The generalized simulated annealing (GSA) method is promoted as a global optimum location technique, due to the ability of the algorithm to walk out of local optima and converge upon the global optimum. Mathematical models with multiple optima are used to compare the convergence of simplex with GSA, and successful global optimum location by GSA is demonstrated. GSA locates the global optimum regardless of the starting position. GSA is also demonstrated as a viable route for wavelength selection.

INTRODUCTION

The need for optimization of a chemical process is a common occurrence for most chemists. Historical optimization techniques include one-at-a-time optimization, the use of factorial designs, the steepest ascent methods, and the modified simplex algorithm (1). Unfortunately, each of these methods has drawbacks that limit their applications. One-at-a-time optimization is essentially useless for systems in which there is any interdependence of the variables, and the use of a factorial design is ill-suited to optimization location until the optimum is known to lie within the boundaries of the design. The method of steepest ascent/descent requires using derivatives (or gradients) of the function, which is generally unknown. Perhaps the most often used technique is the simplex algorithm. In the absence of a priori information about the system under investigation, simplex is easily implemented. Calculations associated with simplex are relatively simple, and computer software for implementation of the algorithm abounds. The major drawback of simplex is that although an optimum for the system will be located, there is no guarantee the optimum located is the global optimum. Because of this, it is often necessary to run repeated trials of simplex using widely spaced starting points. The convergence of successive trails to the same optimum is the criterion used for assurance of global optimum location. Recently, a method similar to simplex, termed optplex, was introduced (2). Unlike simplex, optplex makes use of both the worst and best responses in order to locate an optimum. A characterization of the response surface is required and the optimum located is still not definite.

The generalized simulated annealing algorithm (GSA), as described by Bohachevsky et al. (3), is a function optimization algorithm which converges to the global optimum. Simulated annealing was first introduced by Kirkpatrick et al. (4) and Cerny (5), for use with combinatorial optimization processes. The name was derived from the similarity of the optimization to modeling the physical process involved in annealing solids. Simulated annealing has also been referred to as Monte Carlo

annealing and statistical cooling. A popular example for the use of the algorithm on discrete data sets is the optimization of the so-called traveling salesman problem (6).

This paper will present a background for simulated annealing, concentrating on the generalization described by Bohachevsky et al. (3), and application of the algorithm to continuous functions. Additionally, GSA will be applied to wavelength selection for UV–vis spectrophotometry.

Wavelength selection was chosen because of the numerous investigations in performing automatic selections (7–24). The proposed methods require complex computations and many do not assure selection of the global optimum wavelength set. Sasaki et al. developed a procedure based on the branch and bound method which significantly reduced the number of computations (8). Using least squares for quantitative analysis, Sasaki et al. obtained the smallest variance when repetitive measurements at select wavelengths were used compared to using complete spectral scans for a fixed time. Bialkowski recently provided mathematical evidence for their observations with spectral scanning instruments (25). Similar results have been acquired (9, 10). Several other investigations using least squares have shown improvements in results are possible if wavelength ranges which highlight spectral features are used (11–13). In particular, if a spectrum consists of areas that contain no information (essentially base line), then the nonspecific wavelengths measuring those areas should be avoided. Including the nonspecific sensors in calculations could degrade concentration predictions. Using recursive least squares, Thijssen et al. demonstrated that significantly improved concentration predictions can be obtained when optimal wavelengths are used (14).

Besides reasons already mentioned, least-squares results improve with select wavelengths because collinearity or spectra overlap is reduced. Biased regression methods exist which are not severely effected by collinearity. Thus, complete spectra can be used, avoiding the determination of proper wavelength sets. Two of the most common techniques used in spectral chemical analysis are principle component regressor (PCR) and partial least squares (PLS) (26, 27). Even though wavelength searches are not necessary, the proper number of factors to include in an analysis must be established, which represents a computational search as well. Furthermore, Otto and George have recently used PLS in conjunction with different empirically chosen spectral ranges (15). Better prediction errors were acquired by using a range containing 13 of the possible 30 wavelengths. The improved results were not attributed to improved selectivity but to higher precision in the near-IR range compared to the UV range where most of the remaining wavelengths resided. Their results suggest that PLS and possibly PCR could benefit from wavelength selection.

The purpose of this paper is not to advocate using selected wavelengths but to demonstrate the potential use of GSA and offer a viable route to choosing proper wavelengths.

SIMULATED ANNEALING

The physical process of annealing involves heating a solid material or materials in a heat bath to a melting temperature at which all particles of the solid are randomly arranged. The

liquid phase is then slowly cooled by gradually reducing the temperature of the bath. During this gradual cooling, the particles reach equilibrium at each temperature T , tending to arrange themselves in low-energy ground states. This thermal equilibrium is characterized by the probability of being in a state with energy E , $P\{E = E\}$ which is given by the Boltzmann distribution

$$P\{E = E\} = \frac{1}{Z(T)} \exp\left(\frac{-E}{kT}\right) \quad (1)$$

where k is the Boltzmann constant, $Z(T)$ is a normalization factor known as the partition function, and the exponential is referred to as the Boltzmann factor. With decreasing temperature, the Boltzmann distribution tends toward the states with the lowest energy, and as the temperature approaches zero, only those states with a minimum energy have a nonzero probability of occurrence.

The thermal equilibrium process was modeled by Metropolis et al. (28) with a Monte Carlo method in which sequential states of a substance were generated by using an iterative process. Chiefly, with a given current positioning of particles composing the substance, a new positioning is chosen by applying a small perturbation to the system resulting in relocation of randomly chosen particles. The difference in the energy of the two states ΔE is computed, and if the difference is negative (meaning the perturbed state is at a lower energy than the original state), then the process continues using the perturbed state as the new current positioning. If, however, $\Delta E > 0$, then the probability of accepting the perturbed state is given by the *Metropolis criterion*

$$P = \exp\left(\frac{-\Delta E}{kT}\right) \quad (2)$$

With this criterion, the substance will eventually evolve into a state of thermal equilibrium.

The simulated annealing algorithm solves optimization problems by applying Metropolis' criterion to a series of configurations for the system being optimized. A defined cost function C for the optimization problem assumes the role of energy in the algorithm, while a control parameter c takes the place of the temperature T and the Boltzmann constant k . With an initial configuration s for the system, configuration t in the neighborhood of s is chosen (corresponding to the perturbation in the Metropolis algorithm). The probability of t being the next accepted configuration is 1 if, for minimization, the difference between the cost functions for configurations t and s is less than or equal to zero, i.e., $\Delta C(ts) = C(t) - C(s) \leq 0$. If $\Delta C(ts) > 0$, then the probability P for acceptance of configuration t is given by

$$P = \exp\left(\frac{-\Delta C(ts)}{c}\right) \quad (3)$$

This criterion permits a nonzero probability of moving to a configuration with a cost function higher than the current configuration. The acceptance criterion for such a detrimental configuration is based upon drawing a random number p from a uniform distribution on the interval $[0, 1]$ and comparing the result with P from eq 3. If the resulting random number is smaller than or equal to P , then the detrimental configuration is accepted, otherwise a new configuration in the neighborhood of s is computed and the evaluation of the cost function is repeated. This probability criterion allows the algorithm to move out of local minima, through a biased random walk. The iterative process is continued until the probability distribution of the configurations for the system approaches the Boltzmann distribution, eq 1, which with the redefinition of terms appears as

$$P\{\text{configuration} = i\} = \frac{1}{Q(c)} \exp\left(\frac{C(i)}{c}\right) \quad (4)$$

where $Q(c)$ is a normalization constant dependent on the control parameter c , the equivalent of the partition function mentioned earlier. Implementation of simulating annealing requires an initial value of the control parameter c . Kirkpatrick et al. (4) have suggested that the initial value be experimentally determined such that approximately 20% of the random configurations are rejected. When the configuration approaches the Boltzmann distribution for a particular value of c , the control parameter is then lowered and the iterative process continues. The algorithm terminates at some small value of c for which few, if any, configurations are accepted. These repetitive iterative runs are often referred to as cooling cycles in reference to the lowering of temperature for the Boltzmann probability and have also been discussed in terms of Markov chains (6).

Simulated annealing was generalized (GSA) by Bohachevsky et al. for use with continuous functions, with the modification of the cost function C being defined on a n -dimensional continuous variable space represented as $C(\mathbf{x}) = C(x_1, x_2, \dots, x_n)$ where $x_i \in \mathbb{R}$, $i = 1, 2, \dots, n$. The optimization then consists of finding $\mathbf{x} \in \mathbb{R}^n$ such that $C(\mathbf{x})$ is optimized (for the present discussion assume a minimization). A step size Δr was introduced along with a normalized n -dimensional vector \mathbf{v} corresponding to random perturbations of the elements of the current evaluation site \mathbf{x} . This vector of random perturbations is formed by obtaining n random numbers u_1, u_2, \dots, u_n from $N(0, 1)$, then computing \mathbf{v} : $v_i = u_i / (u_1^2 + u_2^2 + \dots + u_n^2)^{1/2}$, $i = 1, 2, \dots, n$. The random step vector \mathbf{v} is then multiplied by the step size Δr and added to \mathbf{x} to give the new evaluation site \mathbf{y} . More importantly, the probability function P for acceptance of a detrimental step was modified so that the probability tends toward zero as the random walk approaches the global minimum. This was achieved by inclusion of the difference between the current function minimum at \mathbf{x} and the projected function minimum at the optimal \mathbf{x}_0 . The acceptance criterion for a detrimental step is then

$$P = \exp\left(\frac{-\beta \Delta C(\mathbf{y}\mathbf{x})}{C(\mathbf{x}) - C(\mathbf{x}_0)}\right) \quad (5)$$

where $\beta = 1/c$. Detrimental steps occur when $(\Delta C(\mathbf{y}\mathbf{x}) > 0)$ and the probability of acceptance, P , is compared to a random number p from a uniform distribution on $[0, 1]$. The detrimental step \mathbf{y} is accepted when $p \leq P$. If the function optimum \mathbf{x}_0 is assumed to be zero, then the acceptance criterion reduces to

$$P = \exp\left(\frac{-\beta \Delta C(\mathbf{y}\mathbf{x})}{C(\mathbf{x})}\right) \quad (6)$$

When $C(\mathbf{x}_0)$ is unknown, a conservative estimate of the optimum should be used. If the estimated value for $C(\mathbf{x}_0)$ is high, $C(\mathbf{x}) - C(\mathbf{x}_0)$ will eventually become negative. At that point, a new estimation of the anticipated global minimum may be used. For function maximization, detrimental steps occur when $\Delta C(\mathbf{y}\mathbf{x})$ is negative and the denominator in eq 5 is changed to $C(\mathbf{x}_0) - C(\mathbf{x})$. Vanderbilt and Louie have also applied simulated annealing to continuous functions (29).

GSA also requires an empirical choice of the controlling parameter (in this case β). With the generalization of the probability function such that $P \rightarrow 0$ as the global optimum is approached, the need for successive trials (cooling cycles) is eliminated, thus β remains constant throughout the optimization process. The choice of β is subjective and depends upon both the function or system being optimized and the step size Δr chosen. Different choices of Δr produce different $\Delta C(\mathbf{y}\mathbf{x})$. Thus, if Δr is changed, a resulting change in β will

Table I. Functions Evaluated

name	function	boundaries	optimization
GSA1	$1x^2 + 2y^2 - 0.3 \cos(3\pi x) - 0.4 \cos(4\pi y) + 0.7$	$-1 \leq x, y \leq 1$	minimization
SIN2	$1 + \sin^2(x) + \sin^2(y) - 0.1 \exp(-x^2 - y^2)$	$-10 \leq x, y \leq 10$	minimization
3DPOLY	$9 - 8x - 6y - 4z + 2x^2 + 2y^2 + z^2 + 2xy + 2xz$	$0 \leq x, y \leq 3.0$ $0 \leq z \leq 1.5$ $x + y + 2z \leq 3.0$	minimization
YIELD	$20 + 0.8T + 0.8C + 0.022TC - 0.015T^2 - 0.015C^2 + \text{error}$	$0 \leq T, C \leq 200$	maximization
error: N[0, 1]			

be necessary to maintain optimum performance of the algorithm. The criterion suggested by Bohachevsky for determination of β is that 50%–90% of the detrimental steps should be accepted. This corresponds to the inequality $0.5 < P < 0.9$. An experimental determination of this average value of P can be made on a set number of initial steps as an indication of the algorithm's performance, and β may be changed to allow P to fall within the limits, if necessary. A poor choice of β will result in either the acceptance of too few or too many detrimental steps, resulting in failure of the algorithm in a local minimum, or wandering of the algorithm away from the global minimum. Given a fixed step size, increasing the value of β will increase the number of rejected detrimental steps, causing the algorithm to wander less (but possibly locking it onto a local optimum), while decreasing β will result in less rejected detrimental steps, increasing the wandering of the algorithm.

The step size chosen should be large enough to allow the algorithm to move out of a local minimum in two three steps. A balance between sensitivity and mobility of the algorithm must be achieved. Because the algorithm is a random walk, the value of Δr should be large enough to allow adequate exploration of the response surface. Due to the fixed step size, GSA cannot shrink to converge upon the exact location of the global optimum, as can simplex. A possible solution is to perform simplex or a factorial design in the region of the optimum defined by GSA to determine its exact location. A variable step size simulated annealing was addressed by Vanderbilt and Louie (29) but was not approached in this work.

EXPERIMENTAL SECTION

The generalized simulated annealing algorithm, written in FORTRAN, was tested on the four mathematical functions listed in Table I, three of which contain multiple optima. The results of the optimization with GSA were compared to those achieved by using the modified simplex method. The optimum was considered located by GSA when at least 25 steps were taken without acceptance. For simplex, steps were taken until it became apparent that simplex was circling the optimum. Gaussian noise with 1% RSD was added to all simulated and real spectra.

All computations were carried out on an HP Vectra, using Numerical Algorithms Group (NAG) mathematical and graphics libraries (The Numerical Algorithms Group, Inc., Downers Grove, IL). Simplex calculations were performed using SIMPLEX-V software (Statistical Programs, Houston, TX). The GSA program is available from the authors.

RESULTS AND DISCUSSION

Mathematical Functions. Figure 1 shows the three-dimensional plot of the GSA1 function listed in Table I. This function was tested by Bohachevsky et al. for the performance of the GSA algorithm and has a global minimum equal to zero at x and y coordinates (0, 0). For this function, $C(x_0) = 0$ was used in eq 5. By use of values established previously (3), $\Delta r = 0.15$, $\beta = 3.5$, and starting at (1.0, 1.0), convergence to the global optimum was achieved (Figure 2). Note that the

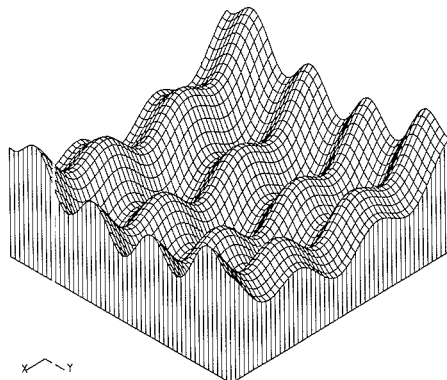


Figure 1. Three-dimensional plot of the GSA1 function.

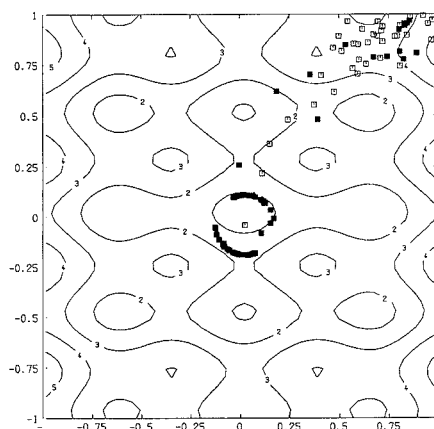


Figure 2. Contour plot of the GSA1 function showing the convergence of GSA to the global optimum with $\beta = 3.5$ and $\Delta r = 0.15$. □, represents accepted steps; ■, represents rejected steps. Contour levels are as follows: 1 = 0.30, 2 = 0.89, 3 = 1.50, 4 = 2.1 and 2.7.

optimum defined by GSA is not exactly 0 due to the inability of the algorithm to shrink the step size when in the neighborhood of the optimum. Two GSA optimizations were performed by using the same starting locations. Table II reveals that because of the random nature of GSA, different paths to the global optimum are taken. Additionally, GSA was able to locate the optimum regardless of the initial coordinates. Simplex varied in its success, dependent upon the starting point. The third simplex was started in a local optimum (0, -0.93) and failed to converge to the global optimum, as noted in Table II. The successful trials for the simplex algorithm may have occurred in part due to the overall slope of the function toward the global optimum, allowing simplex to travel over local optima while expanding toward the global optimum. Table II lists the number of steps taken by both algorithms, as well as at which step the optimum was located (i.e., an optimum located on the 56th of 150 steps is listed as having 56/150 steps). Table II shows the range of P values is indeed $0.5 < P < 0.9$ and this range corresponds to rejection of approximately 20% of the random configurations.

The second function listed in Table I, referred to as the SIN2 function, presented the greatest challenge to both algorithms. The function has several local optima (minima) with function values = 1.0, while the global optimum located at

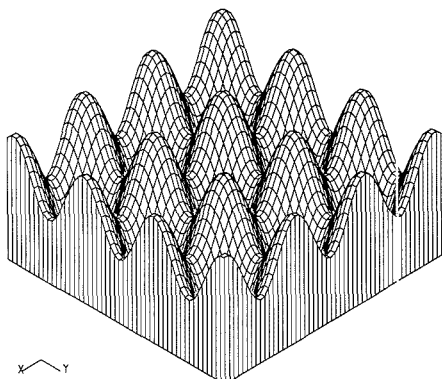
Table II. Simplex and GSA Searches of the GSA1 Function (Global Optimum Location = (0, 0) and Optimal Response = 0)

Simplex Results ^a					
optimum coordinate		optimum response	optimum/total no. of steps		
0.62	0.93 ^b	2.28	29/32		
0.00	0.00 ^c	0.00	39/44		
-0.01	-0.93 ^d	1876	18/22		

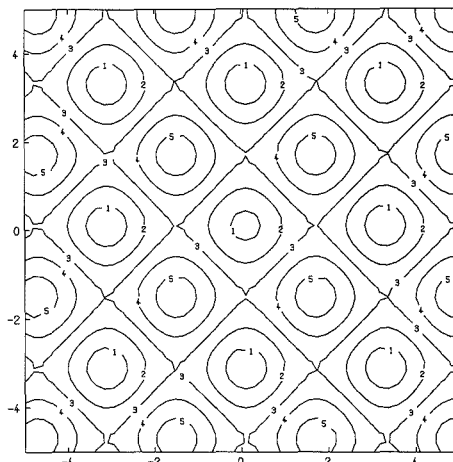
GSA Results^{a,e}

P range ^f	% rejected ^f	optimum coordinate		optimum response	optimum/total no. of steps
0.2-0.8	59	0.058	0.033 ^b	0.08	79/150
0.7-0.9	18	0.025	-0.042 ^c	-0.07	56/150
0.7-0.9	19	0.078	-0.003 ^c	0.08	83/150
0.1-0.6	76	0.070	0.028 ^d	0.09	487/520

^aStep size = 0.15. ^bInitial coordinate = (0.85, 0.85). ^cInitial coordinate = (1.00, 1.00). ^dInitial coordinate = (0.00, -0.83). ^e β = 3.5. ^fFirst 100 steps.

**Figure 3. Three-dimensional plot of the SIN2 function.**

the origin has a function value = 0.9. Figures 3 and 4 show the three-dimensional and contour plots for the function, respectively. Simplex converged to the global optimum only once in seven trials, with the successful trial the result of starting simplex in a valley leading directly to the global optimum. All other trials resulted in convergence upon one of the local optima, as listed in Table III. The GSA algorithm converged to the global optimum in 4 of the 11 trials listed. Since the global optimum was very close in value to the local optima, GSA also tended to become stranded in the local optima. Because of this, the assumption that the global optimum $C(x_0)$ was zero (rather than 0.9) was used for all GSA trials. This somewhat improved the performance of the algorithm as the probability values P did not converge as rapidly when local optima were approached. However, taking this approach eliminated the ability of GSA to halt on the global optimum. It became necessary to track the minimum function value obtained and to then postanalyze the data to determine the location of the optimum. In this case, the stopping criteria were that no further improvement of the cost function evaluation was noted in 50 steps. Once again, GSA does not converge upon the exact location of the global optimum due to the inability of the algorithm to shrink Δr . The source of the SIN2 function was an optimization article by Price (30),

**Figure 4. Contour plot of the SIN2 function. Contour level 1 = 1.20, 2 = 1.60, 3 = 2.00, 4 = 2.40, and 5 = 2.80.****Table III. Simplex and GSA Searches of the SIN2 Function (Global Optimum Location = (0, 0) and Optimal Response = 0.9)**

Simplex Results						
initial coordinate		step size	optimum coordinate		optimum response	optimum/total no. of steps
5.0	5.0	0.10	6.28	6.28	1.00	48/54
-5.0	5.0	0.10	-6.28	6.28	1.00	31/52
0.0	1.4	0.10	0.00	0.00	0.90	43/46
0.0	-3.1	0.10	0.00	-3.14	1.00	14/14
5.0	5.0	0.25	6.28	6.28	1.00	51/61
5.0	5.0	2.00	3.14	3.14	1.00	37/43
5.0	5.0	4.00	0.73	-9.38	1.44	49/49

GSA Results ^a						
β	P average ^b	% rejected ^b	optimum coordinate		optimum response	optimum/total no. of steps
7.0 ^c	0.75	10	6.28	6.27	1.000	452/500
10.0 ^c	0.68	7	6.30	6.30	1.001	248/300
20.0 ^c	0.50	22	3.16	3.14	1.000	174/300
0.5 ^d	0.80	6	-0.01	-0.28	0.951	17/100
0.8 ^d	0.65	9	0.29	-0.22	1.000	74/200
1.2 ^d	0.50	15	0.19	0.11	0.955	312/400
1.5 ^d	0.50	31	0.12	-0.03	0.917	234/300
3.5 ^d	0.30	72	3.19	-3.20	1.006	200/300
1.0 ^e	0.70	16	-6.30	-6.30	1.000	74/200
1.5 ^e	0.65	40	-0.11	0.02	0.913	63/150
2.0 ^e	0.75	24	3.64	-3.14	1.000	114/200

^aInitial coordinate = (5.0, 5.0). ^bFirst 100 steps. ^cStep size = 0.10. ^dStep size = 2.0. ^eStep size = 4.0.

in which the proposed controlled random search procedure identified the global optimum after 700 search steps.

Performance of the GSA algorithm versus simplex on the 3DPOLY function, a polynomial in three variables, is listed in Table IV. The 3DPOLY function was one investigated by Price in which 4000 steps were required for location of the optimum (30). The optimum for the system lies on the boundary constraint of $x + y + 2z \leq 3.0$. Simplex failed in one trial at a step size of 0.2 and was successful on two trials

Table IV. Simplex and GSA Searches of the 3DPOLY Function (Global Optimum Location = (1.33, 0.77, 0.44) and Optimal Response = 0.1111)

Simplex Results ^a							
step size	optimum coordinate			optimum response	optimum/total no. of steps		
0.10	1.32	0.78	0.45	0.1112	78/100		
0.10	1.36	0.80	0.42	0.1140	105/132		
0.20	1.08	0.86	0.53	0.1753	73/90		
GSA Results ^a							
β	P range ^b	% rejected ^b	optimum coordinate		optimum response	optimum/total no. of steps	
2.5 ^c	0.5-0.9	4	1.33	0.95	0.32	0.2066	200/230
5.0 ^c	0.6-0.9	14	1.34	0.78	0.43	0.1141	379/410
7.0 ^c	0.6-0.8	28	1.31	0.74	0.47	0.1171	211/250
1.5 ^d	0.3-0.9	13	1.31	0.77	0.45	0.1119	140/200
2.5 ^d	0.3-0.5	26	1.34	0.97	0.34	0.1603	125/200
7.0 ^d	0.3-0.5	14	1.31	0.82	0.43	0.1197	196/250

^aInitial coordinate = (0.0, 0.0, 0.0). ^bFirst 100 steps. ^cStep size = 0.10. ^dStep size = 0.20.

at a step size of 0.1. GSA successfully converged most often to the optimum when β was chosen such that the percentage of rejected steps (in the first 100) was in the neighborhood of 20%, rather than the criteria of $0.5 < P < 0.9$. The best performance of the algorithm (location of the optimum in the smallest number of steps) occurred when the P values were at an average value of 0.6 in the first 100 steps. For example, with $\Delta r = 0.2$ and $\beta = 1.5$, a minimum of 0.1119 was identified on the 140th of a total of 200 steps. The GSA algorithm converged at both $\Delta r = 0.1$ and $\Delta r = 0.2$, with the 0.2 step size converging in less than half the number of steps than the 0.1 step size trial required. Again, assumption of a minimum at 0.0 necessitated tracking the function values for later analysis of the location of the global optimum.

The performance of GSA on the last function, the YIELD model, emphasized the need for accurate determination of the controlling factor β . The function, whose contour plot is shown in Figure 5, was obtained from a discussion of various optimization techniques by Bayne and Rubin (31). The YIELD model represents a chemical synthesis where concentration, C, and temperature, T, are optimized to maximize the yield. Their data regarding optimization of the function are listed in Table V. The optimum identified by the authors was 100 mg/g; however, the addition of the random error component allowed values greater than 100 mg/g in the GSA iterations. For GSA, the global optimum was assumed to be 101 mg/g. The step size used for GSA was set to 5.0, which corresponded to the initial step size used by Bayne and Rubin for the steepest ascent, simplex, and modified simplex algorithms. At $\beta = 1.5$ and $\Delta r = 5.0$, the GSA algorithm rejected only 2 of the first 100 steps. With a corresponding average P equal to 0.89, the algorithm was unable to locate the global optimum and wandered on the response surface as shown in Figure 5. However, with $\beta = 10.5$ and $\Delta r = 5.0$, the average P was 0.50, and 24 of the first 100 trials were rejected. Figure 6 illustrates the path of GSA under these conditions. This added discrimination allowed GSA to identify an improved maximum yield of 100.52, in comparison to the 99.38 yield identified by the modified simplex algorithm. When the random error component is removed, the GSA maximum is 99.89, compared to 99.13 for the simplex optimization.

Wavelength Selection. Locating the ideal set of wavelengths requires a figure of merit to base decisions on. The

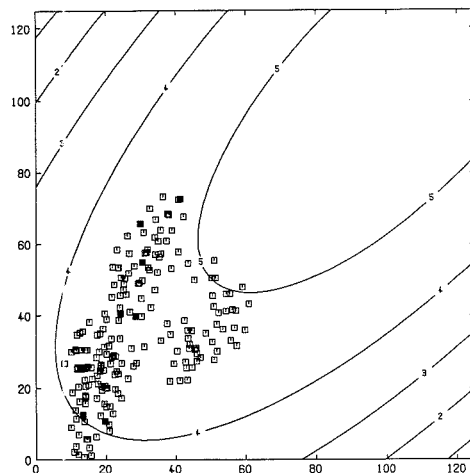


Figure 5. Contour plot of the YIELD function showing failure of GSA in locating the optimum with incorrect parameters of $\beta = 1.5$ and $\Delta r = 5.0$: □ represents accepted steps, ■ represents rejected steps. Contour level 1 = -86, 2 = -45, 3 = 3.5, 4 = 38, and 5 = 79.

Table V. Searches of the YIELD Function (Global Optimum Location = (T = 100.0, C = 100.0) and Optimal Response = 100.0)

method	optimum coordinate		yield, mg/g	no. of steps		
	T	C				
steepest ascent	75.0	76.4	95.79	33		
1 factor at a time	55.0	40.0	74.14	28		
simple simplex	77.5	77.2	97.70	56		
modified simplex	93.37	101.30	99.38	20		
GSA Results ^a						
β	P average ^b	% rejected ^b	optimum coordinate		yield, mg/g	optimum/total no. of steps
1.5	0.89	2	50.95	55.43	82.09	111/150
3.5	0.75	17	99.70	98.96	100.59	197/226
5.0	0.75	14	97.10	94.71	100.21	228/250
7.0	0.75	22	104.37	103.18	100.24	199/250
9.0	0.55	21	94.25	100.76	100.18	235/250
10.0	0.50	21	77.99	100.66	100.52	174/200
10.5	0.50	24	100.65	97.84	100.52	148/200
11.5	0.47	43	96.87	98.25	100.57	147/200

^aInitial coordinate = (20.0, 20.0); step size = 5.0. ^bFirst 100 steps.

various criteria proposed in the literature have chiefly dealt with minimizing accuracies and precisions for concentration estimates. This investigation minimized a criterion which averages the selectivity and sensitivity information, termed accuracy, for all components. Past studies have shown this figure of merit to perform satisfactory (12). We are not stressing the importance of the decision-making criterion but rather our emphasis is on, given a figure of merit, how can one determine the proper number and location of wavelengths.

How continuous the response surface is for wavelength selection depends on the degree of spectral digitization. Because our spectra were digitized at integer intervals, wavelength arrays in the GSA program were declared as integers. This introduced the possibility of acquiring duplicate

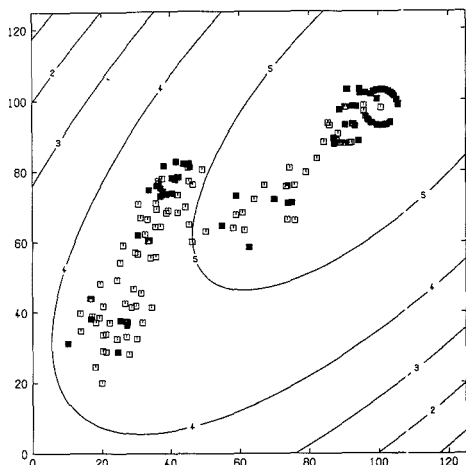


Figure 6. Contour plot of the YIELD function showing the convergence of GSA to the global optimum with correct parameters of $\beta = 10.5$ and $\Delta r = 5.0$: \square represents accepted steps, \blacksquare represents rejected steps. Contour levels are the same as those given in Figure 5.

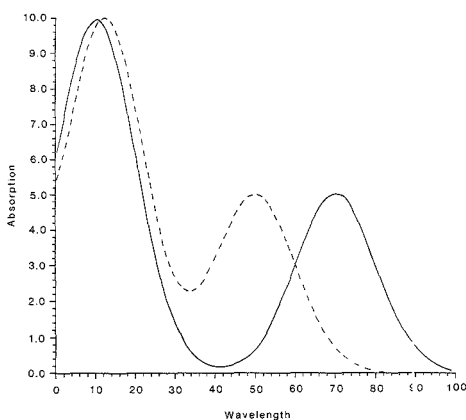


Figure 7. Two-component simulated Gaussian curves with amplitudes of 10 and 5 units, and half-bandwidths of 10 units. Peaks occur at 10, 12, 50, and 70 wavelength units, respectively.

wavelengths in an array due to truncation of random r numbers from $N(0, 1)$. Duplicate wavelengths were interpreted as a desire on the part of GSA to cluster wavelengths in a spectral area. Duplicate wavelengths in new wavelength sets of size n can be avoided by selecting n random wavelengths from the population of p digitized wavelengths. However, the controlled stepping ability would be lost resulting in possible large variations of the criterion. Determination of proper β values would then be more difficult.

The initial phase of testing GSA involved simulated absorption spectra using Gaussian curves. Figure 7 shows two simulated pure component spectra which were investigated with simplex and GSA. Chemical analysis of a sample containing these components would require a minimum of two wavelengths. The three-dimensional response surface for all possible two-wavelength combinations is illustrated in Figure 8 while a contour plot is presented in Figure 9. The z axis contains accuracy values which have been inverted for

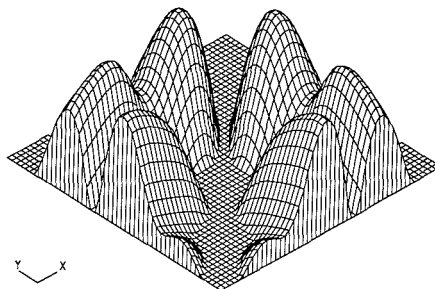


Figure 8. Three-dimensional graph of the response surface corresponding to Figure 7 for two wavelength combinations. Accuracy values have been inverted for graphical enhancement.

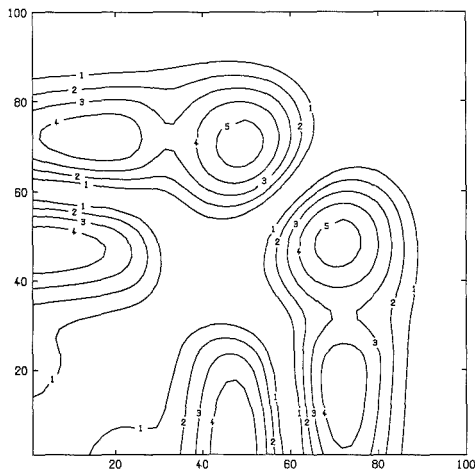


Figure 9. Contour plot for Figure 8. For graphical enhancement, accuracy values have been inverted such that contour level 1 = 69, 2 = 110, 3 = 150, 4 = 190, and 5 = 220.

Table VI. Comparison of GSA and Simplex for Wavelength Selection

study ^a	initial wave-lengths	optimal wave-lengths	optimum accuracy (10^{-3})	optimum/total no. of steps
GSA ^b	20, 80	50, 73	4.026	82/150
simplex	20, 80	50, 72	4.052	26/40
GSA ^b	1, 2	50, 72	4.021	141/200
simplex	1, 2	10, 47	4.620	30/50

^aStep size = 5.0. ^b $\beta = 0.15$.

graphical enhancement. Both Figures 8 and 9 reveal several local optima and one global optimum at wavelength combination (49, 71). The global combination is not (50, 70). This is attributed to the accuracy criterion demanding simultaneous maximization of sensitivity and selectivity. Table VI contains the results of GSA and simplex for the listed situations. For the GSA cases, the expected minimum for accuracy in eq 5 was set to zero because the minimum value was not known and zero is the most ideal accuracy value. Adjustments to β were performed until six to nine of the first ten detrimental steps were accepted. Table VI reveals that GSA was impartial to the starting set of wavelengths while simplex was dependent on the initial set. When the optimization routines were started

Table VII. Optimization of the Number and Location of Wavelengths for RNA constituents

step size	β	optimal wavelengths, nm	optimum accuracy (10^{-3})	optimum/total no. of steps
5.0	0.27	222, 238, 274, 286	6.177	65/100
5.0	0.20	220, 226, 252, 270, 284	5.380	82/125
3.0	0.17	220, 222, 256, 274, 276, 286	4.438	15/100
3.0	0.14	220, 222, 256, 274, 276, 286, 290	4.054	18/100
3.0	0.10	220, 220, 248, 262, 272, 276, 280, 288	3.830	172/200
3.0	0.06	220, 222, 248, 262, 272, 276, 278, 280, 290	3.632	3/100
3.0	0.05	220, 222, 246, 256, 270, 272, 276, 280, 286, 290	3.439	4/100
3.0	0.04	220, 222, 246, 256, 270, 272, 276, 280, 286, 288, 290	3.342	1/100

* Initial wavelengths (nm) = 228, 238, 248, and 258, thereafter, wavelength 290 nm was added to each final set for the next optimization.

at wavelength combination (1, 2), GSA was able to move beyond the local minima wavelength combinations in the vicinities of (10, 12), (10, 50), and (12, 70).

In another study, simulated Gaussian curves were generated such that all absorption occurred within the first 30 wavelength units out of 100. GSA and simplex were both started at the upper end where only base line was present, wavelength combination (90, 91). Simplex could not progress to the absorption region. GSA was capable of migrating to the absorption region and locate the global optimum. Other similar studies were performed where the number of components and severity of spectral overlap varied. Evidently, when spectral overlap existed, the accuracy criterion constantly favored those wavelengths that were located on the sides of absorption bands. Wavelengths at peak maxima were always designated for orthogonal simulated spectra. Additionally, from these investigations, β values between 0.1 and 0.5 emerged as appropriate values. Depending on the specific spectral situation, fine tuning of β is necessary to achieve the proper percentage of accepted detrimental steps.

GSA was applied to a previously studied four-component system containing RNA constituents adenylic, cytidylic, and guanylic, and uridylic acids (10, 14, 24). Spectra for these compounds were recorded from 220 to 290 nm and digitized at 2-nm intervals (24). The minimum expected accuracy was set to zero. When four wavelengths out of the possible 36 were requested, GSA converged to wavelengths 222, 238, 274, and 286 nm from initial wavelengths 228, 238, 248, and 258 nm. The first row in Table VII shows the results. After this optimization, a fifth wavelength was added to the optimal four wavelengths and GSA was performed again. This procedure of increasing the number of wavelengths and locating their positions was repeated until differences in accuracy values were approximately the same. At this point, an ideal number of wavelengths as well as their location were assumed to be reached. This occurred with 10 wavelengths and Table VII shows the progression. Notice that as the accuracies decrease, so does β . Wavelengths are added to an already existing optimal set thereby reducing $\Delta C(yx)$ and requiring a smaller β for proper acceptance of detrimental steps. These results are similar to those of Thijssen et al. The slight differences are possibly due to the noise content of the spectra. Mark recently demonstrated the ability of computer wavelength selection procedures to obtain different wavelengths under similar circumstances (22). The noise content of spectra was recognized as the source of discrepancy. Bershtein also studied this system and decided six wavelengths measured six times

was best (10). A list of selected wavelengths was not available for comparison with those selected by GSA.

CONCLUSIONS

GSA is a new versatile method for optimization problems. In particular, when a system is known to contain several optima, GSA is not handicapped in determining the location of the global optimum. Additionally, GSA locates the optimum regardless of the initial coordinates. Areas that could greatly benefit by using GSA include operation research, liquid chromatography, and design of calibration samples for quantitative analysis.

The principle restriction of GSA is the necessity of determining proper values of β and Δr . Proper β values were determined most often when Kirkpatrick's suggestion was used. Specifically, choose β such that 20% of the steps are rejected. By use of suitable parameters, GSA is capable of global optimum location. This study has shown that GSA can be safely terminated after 25 nonaccepted steps are taken. This study has shown that GSA is effective in locating the global optimum more frequently than simplex, often in situations where simplex converges to a local optimum. However, when simplex locates the global optimum, it does so in a significantly reduced number of steps. Much of this may be attributed to the ability of the simplex algorithm to expand and contract step sizes along the path to the optimum. Our laboratory is currently investigating alterations to simulated annealing to enhance the search procedure and reduce the number of steps required for optimum location.

LITERATURE CITED

- Messart, D. L.; Vandeginste, B. G. M.; Deming, S. N.; Michotte, Y.; Kaufman, L. *Chemometrics: a textbook*; Elsevier: Amsterdam, 1986; Chapter 18.
- Smith, S. B., Jr.; Sainz, M. S.; Schleicher, R. G. *Spectrochim. Acta, Part B* **1987**, *42B*, 323.
- Bchachevsky, Inor O.; Johnson, Mark E.; Stein, Myron L. *Technometrics* **1986**, *28*, 209.
- Kirkpatrick, S.; Gelatt, C. D., Jr.; Vecchi, M. P. *IBM Res. Rep.* **1982**, *RC 9355*.
- Cerny, V. *J. Opt. Theory Appl.* **1985**, *45*, 41.
- van Laarhoven, P. J. M.; Aarts, E. H. L. *Simulated Annealing: Theory and Applications*; D. Reidel Publishing: Dordrecht, 1988.
- Chu, A. H.; Lopatin, W. *Clin. Chem.* **1986**, *32*, 1666.
- Sesaki, K.; Kawata, S.; Minami, S. *Appl.* **1986**, *40*, 185.
- Frans, S. D.; Harris, J. M. *Anal. Chem.* **1985**, *57*, 2680.
- Bershtein, I. Y. *Z. Anal. Chem.* **1988**, *332*, 227.
- Rossi, D. T.; Pardue, H. L. *Anal. Chim. Acta* **1985**, *175*, 153.
- Juul, L.; Kallvas, J. H. *Anal. Chim. Acta* **1988**, *207*, 125.
- Li-Shi, Y.; Levine, P. *Anal. Chem.* **1989**, *61*, 677.
- Trijssen, P. C.; Vogels, L. J. P.; Smit, H. C.; Kateman, G. *Z. Anal. Chem.* **1985**, *320*, 531.
- Otto, M.; George, T. *Anal. Chim. Acta* **1987**, *200*, 379.
- Warren, F. V., Jr.; Bidlingmeyer, B. A.; Delaney, M. F. *Anal. Chem.* **1987**, *59*, 1890.
- Warren, F. V., Jr.; Bidlingmeyer, B. A.; Delaney, M. F. *Anal. Chem.* **1987**, *59*, 1897.
- Etel, S.; Glasser, E.; Abdulla, S.; Steffens, U.; Walter, V. *Z. Anal. Chem.* **1982**, *313*, 24.
- Lieber, A.; Kowalski, B. R. *J. Chemom.* **1988**, *2*, 67.
- Wirsz, D. F.; Blades, M. W. *J. Anal. At. Spectrosc.* **1988**, *3*, 363.
- Hunings, D. E.; Hietje, G. M.; Hirschfeld, T. *Appl. Spectrosc.* **1984**, *38*, 844.
- Mark, H. *Appl. Spectrosc.* **1988**, *42*, 1427.
- Dynshaw, S. M.; Brown, C. W.; Caputo, B.; Modell, M. D. *Anal. Chem.* **1988**, *60*, 1873.
- Zschelle, F. P., Jr.; Murray, H. C.; Baker, G. A.; Peddicord, R. G. *Anal. Chem.* **1982**, *34*, 1776.
- Blalkowski, S. E. *Appl. Spectrosc.* **1988**, *42*, 807.
- Buebe, K.; Kowalski, B. R. *Anal. Chem.* **1987**, *59*, 1007A.
- Gamperline, P. J. *J. Chemom.*, in press.
- Matropolis, N.; Rosenbluth, A.; Rosenbluth, M.; Teller, A.; Teller, E. *J. Chem. Phys.* **1953**, *21*, 1087.
- Vanderbilt, D.; Louie, S. G. *J. Comput. Phys.* **1984**, *36*, 259.
- Pice, W. L. *Computer J.* **1977**, *20*, 367.
- Bayne, C.; Rubin, I. *Practical Experimental Designs and Optimization Methods for Chemists*; VCH: Deerfield Beach, FL, 1986.

RECEIVED for review May 1, 1989. Accepted June 20, 1989. This research was supported in part by Grant 622 from the Faculty Research Committee, Idaho State University, Pocatello, ID, and in part by a grant from Research Corporation.

Multivariate Calibration in Inductively Coupled Plasma Mass Spectrometry

Michael E. Ketterer* and John J. Reschl

United States Environmental Protection Agency, National Enforcement Investigations Center, Box 25227, Building 53, Denver Federal Center, Denver, Colorado 80225

Michael J. Peters

ICF Technology, Inc., 165 South Union Boulevard, Suite 802, Lakewood, Colorado 80228

To date, the existence of isobaric molecular ion interferences resulting from the formation of species such as MO^+ and MCl^+ has been considered to be a significant shortcoming of inductively coupled plasma mass spectrometry (ICP/MS). In the present study, this problem has been circumvented through the use of two multivariate calibration methods, namely multiple linear regression (MLR) and principal components regression (PCR). The methods function by utilizing information from multiple, partially selective sensors and have been applied to the $^{90}Mo^{16}O^+ / ^{90}Cd^+$ and $^{90}Zr^{16}O^+ / ^{90}Mo^{16}O^+$, $^{90}Ru^{16}O^+ / ^{90}Cd^+$, $^{90}In^+$, $^{90}Sn^+$ systems. For the former system, it was possible to determine low levels of Cd in the presence of Mo, by using either MLR or PCR; traditional univariate determinations of Cd at single isotopes were unsatisfactory. Both PCR and MLR were satisfactory for determining Cd in the presence of Zr, Mo, Ru, In, and Sn; moreover, no major advantages of PCR over MLR were observed. The ICP/MS application of MLR and PCR, as well as that of other multivariate calibration approaches not considered herein, merits further study.

INTRODUCTION

Inductively coupled plasma mass spectrometry (ICP/MS) is rapidly becoming an established method of trace multielement analysis (1-10). This technique offers detection limits in the range of 0.01-0.1 $\mu g/L$ for many elements, the capability of performing on the order of 10 elemental determinations/min, and the unique ability to provide isotopic information about the sample. Based on these characteristics, ICP/MS's performance in many applications compares favorably to that of flame and electrothermal atomic absorption spectroscopy as well as to that of inductively coupled plasma atomic emission spectroscopy (ICP/AES).

The existence of isobaric molecular ion interferences resulting from the formation of species such as MO^+ and MCl^+ has been considered to be a significant shortcoming of ICP/MS (11-19). These interferences result in a systematic error source that must be circumvented in order to obtain meaningful analytical results. To date, various researchers have approached this problem by employing plasma operating conditions that result in a lower yield of molecular species (20) and by utilizing aerosol processing devices (21) that dissolve the aqueous aerosol being introduced into the plasma. A method of actually calculating the degree of formation of the interferant MO^+ , and subtracting its signal from that of M^+ , the analyte, has been proposed (22). This method employs thorium as an internal standard for oxide formation; the ThO^+/Th^+ ratio is measured in the sample and is used to calculate the anticipated MO^+ signal on the basis of previously established correlations. None of these strategies are entirely

satisfactory and/or successful in all cases.

In recent years, the use of multivariate calibration methods such as multiple linear regression (MLR), the generalized standard addition method (GSAM), partial least-squares regression (PLSR), and principal components regression (PCR) has become widespread in analytical chemistry (23-36). These techniques have been applied to a variety of methods such as Fourier transform infrared spectroscopy, ICP/AES, anodic stripping voltammetry, and near-infrared reflectance spectroscopy. All multivariate calibration approaches have the common feature of utilizing information from multiple, partially selective sensors in order to determine analyte(s) in the presence of interferant(s). The aforementioned multivariate calibration techniques differ principally in the methodology used to manipulate the data obtained and calculate the unknown concentrations.

To date, multivariate calibration has not been applied to the previously described interference problems in ICP/MS. It will be shown that these interference problems can be successfully corrected by using two multivariate external calibration techniques, namely MLR and PCR. As representative examples of this interference problem, the determination of low levels of Cd in the presence of a Mo matrix and the determination of low levels of Cd, In, and Sn in the presence of high levels of Zr, Mo, and Ru have been investigated. The latter system also presents some isobaric element-element interferences for Cd, In, and Sn in the m/z 112-116 range; either MLR or PCR offers the possibility of deconvoluting these spectra in the absence or presence of molecular species such as ZrO^+ , MoO^+ , and RuO^+ . A critical comparison of univariate calibration, MLR, and PCR will be presented.

EXPERIMENTAL SECTION

Materials. Deionized, distilled water, prepared in-house, was used as the solvent for all solutions. Baker Instra-Analyzed nitric acid (70 wt % aqueous solution) and hydrochloric acid (30 wt % aqueous) were used as received; 1% (v/v) of each was added as a preservative to standard and sample solutions. Stock solutions of 5000 mg/L Zr, Mo, and Ru were prepared by dissolving $(NH_4)_2MoO_4$, $ZrOCl_2 \cdot 6H_2O$, and $(NH_4)_2RuCl_6$ (Spex Industries) in water; 1000 mg/L Cd, In, Sn, and Rh stock solutions (Spex) were used as received.

Calibration. For the Mo-Cd system, standards and unknown solutions, containing mixtures of Mo (0-50 mg/L) and Cd (0-0.1 mg/L), were prepared with 0.1 mg/L Rh added as an internal standard. The experimental designs for the calibration standards' and unknown samples' concentrations are shown in Table I; the calibration standards' design is essentially a two-factor, three-level full factorial design with replications as indicated in Table I. In Table II, experimental designs are shown for the standards and samples used to investigate the Zr-Mo-Ru-Cd-In-Sn system; the interferants' and analytes' concentrations were varied in the ranges 0-50 and 0-0.1 mg/L, respectively. Three-level, six-factor partial factorial designs were used for this system. For both

Table I. Experimental Design for Calibration Standards and Unknown Samples for the Mo-Cd System

standard(s)	Mo, mg/L	Cd, mg/L	sample(s)	Mo, mg/L	Cd, mg/L
1, 2, 3	0.000	0.000	A, B, C	0.000	0.0100
4	0.000	0.0500	D, E, F	0.000	0.0900
5, 6, 7	0.000	0.100	G, H, I	5.00	0.0100
8	25.0	0.000	J, K, L	5.00	0.0900
9, 10, 11	25.0	0.0500	M	12.5	0.0500
12	25.0	0.100	N	25.0	0.0250
13, 14, 15	50.0	0.000	O	25.0	0.0750
16	50.0	0.0500	P	37.5	0.0500
17, 18, 19	50.0	0.100	Q, R, S T, U, V	45.0 45.0	0.0100 0.0900

systems, the sample concentrations were selected to adequately assess the calibrations' performances over a variety of analyte-interferent concentration conditions. In all studies, the standards were run in random order; following completion of the standardization, the samples were examined in a random order; this approach is referred to as a "stratified-random" strategy.

Inductively Coupled Plasma Mass Spectrometry. A Sciex Elan Model 250 ICP mass spectrometer, equipped with mass flow meters (Precision Flow Devices) for all gas streams and a peristaltic sample delivery pump (Rainin Instrument Co.), was used in these studies. A Neslab RBC-3 refrigerated circulating bath was used to maintain the nebulizer spray chamber at a temperature of 10 °C. A Meinhard type TR-C concentric glass nebulizer was used in all studies. Instrumental operating conditions were as shown in Table III. No attempt was made to reduce the formation of MoO⁺ by using reduced nebulizer Ar flow rates; this flow was instead adjusted to yield the highest intensities of analytes such as ¹¹²Cd⁺, ¹¹⁵In⁺, and ¹²⁰Sn⁺. MO⁺/M⁺ values were as shown in Table III. Ion optics parameters were adjusted to yield satisfactory signal to noise behavior; these settings were as shown in Table III. No adjustment of any of these parameters was made during analytical operation of the instrument; lengthy modification of these settings between analytical operations was generally unnecessary.

For the Mo-Cd system, ion intensities were measured for the *m/z* values 103, 106, 108, 110-114, and 116 by using the mass spectrometer software parameters listed in Table III; the signals obtained at *m/z* 106, 108, 110-114, and 116 were normalized to the *m/z* 103 (¹⁰³Rh⁺) signal. This internal standardization was intended to minimize the effects of changes in nebulizer efficiency as well as changes in the transmission of analyte ions through the sampling interface and ion focusing optics. The *m/z* values 103, 106, 108, and 110-124 were scanned in the study of the Zr-Mo-

Ru-Cd In-Sn system; once again, ¹⁰³Rh⁺ was used as an internal standard.

Computations. To perform conventional, univariate calibration of the Mo-Cd system, results for those standards containing no Mo were modeled by using simple linear regression. This calibration was performed for signals at the individual Cd isotopes listed in Table IV. These linear models were used to predict the Cd concentrations in the unknown sample solutions. Also shown in Table IV are some univariate calibration processes studied for the Zr-Mo-Ru-Cd-In-Sn system; for the In at *m/z* 115 and the Sn at *m/z* 122 models, all of the standards, including those containing the other analytes and potential interferents, were included in the model.

Several multiple linear regression calibrations were performed for both systems; the analyte and sensor combinations discussed in this paper are shown in Table IV. Analyte concentrations were treated as independent variables, and normalized ion intensities were treated as dependent variables. Modeling was done in a stepwise fashion, starting with the model expected for each sensor based on the isotopic abundances of the analytes and interferents; insignificant terms were deleted (e.g. Ru at *m/z* 114) and unanticipated terms were included (e.g. Zr at *m/z* 111; Mo at *m/z* 124).

The principal components regression (PCR) procedure for calibration and unknown determination consisted of several steps, as outlined in Figure 1. The reader is referred to the literature (32, 33) for detailed descriptions of the process and examples of its application to similar problems. All computations for MLR and PCR as well as univariate calibration were performed with a commercially available statistics software package (Statgraphics, STSC, Inc.).

RESULTS AND DISCUSSION

Standards Correlation Matrices. The matrix of correlation coefficients obtained for the Mo-Cd standards' data set is shown in Table V. An examination of this matrix indicates that the Cd isotopes appear to be divided into three groups: one consisting of *m/z* 110, 111, 112, 113, 114, and 116, and two distinct individual signals, *m/z* 106 and 108. These categories are consistent with the abundances of the Cd isotopes and the Mo isotopes whose oxygen adducts produce the interferent species. The existence of many significant correlations in the data set indicates that dimension reduction processes such as principal components analysis are applicable.

Table VI depicts the correlation matrix obtained from the standards data set for the Zr-Mo-Ru-Cd-In-Sn system. In general, interpretation of this matrix is less obvious than that from the Mo-Cd system; the larger number of covariances alone complicates the abstraction of meaningful information.

Table II. Experimental Designs for the Calibration Standards and Test Samples for the Zr-Mo-Ru-Cd-In-Sn System

std(s)	Zr ^a	Mo	Ru	Cd	In	Sn	sample(s)	Zr	Mo	Ru	Cd	In	Sn
1a, 1b, 1c	0.000	0.000	0.000	0.000	0.000	0.000	A1, A2, A3	0.000	0.000	0.000	0.0100	0.0100	0.0100
2	0.000	25.0	25.0	0.0500	0.0500	0.0500	B	20.0	20.0	20.0	0.0500	0.0500	0.0500
3a, 3b	0.000	50.0	50.0	0.100	0.100	0.100	C1, C2	40.0	40.0	40.0	0.0900	0.0900	0.0900
4	25.0	0.000	50.0	0.000	0.0500	0.0500	D	0.000	0.000	40.0	0.0500	0.0500	0.0900
5a, 5b	25.0	25.0	0.000	0.0500	0.100	0.100	E	20.0	20.0	0.000	0.0900	0.0900	0.0100
6	25.0	50.0	25.0	0.100	0.000	0.000	F1, F2	40.0	40.0	20.0	0.0100	0.0100	0.0500
7a, 7b	50.0	0.000	25.0	0.0500	0.000	0.100	G	0.000	20.0	40.0	0.0100	0.0900	0.0500
8	50.0	25.0	25.0	0.100	0.0500	0.000	H	20.0	40.0	0.000	0.0500	0.0100	0.0900
9	50.0	50.0	0.000	0.000	0.100	0.0500	I1, I2	40.0	0.000	20.0	0.0900	0.0500	0.0100
10a, 10b, 10c	0.000	0.000	25.0	0.100	0.100	0.0500	J	0.000	40.0	0.000	0.0900	0.0500	0.0500
11	0.000	25.0	50.0	0.000	0.000	0.100	K1, K2, K3	20.0	0.000	20.0	0.0100	0.0900	0.0900
12	0.000	50.0	0.000	0.0500	0.0500	0.000	L	40.0	20.0	40.0	0.0500	0.0100	0.0100
13	25.0	0.000	50.0	0.0500	0.100	0.000	M	0.000	20.0	20.0	0.0900	0.0100	0.0900
14a, 14b	25.0	25.0	0.000	0.100	0.000	0.0500	N1, N2	20.0	40.0	40.0	0.0100	0.0500	0.0100
15	25.0	50.0	25.0	0.000	0.0500	0.100	O	40.0	0.000	0.000	0.0500	0.0900	0.0500
16	50.0	0.000	0.000	0.100	0.0500	0.100	P1, P2	0.000	40.0	20.0	0.0500	0.0900	0.0100
17	50.0	25.0	25.0	0.000	0.100	0.000	Q	20.0	0.000	40.0	0.0900	0.0100	0.0500
18	50.0	50.0	50.0	0.0500	0.000	0.0500	R	40.0	20.0	0.000	0.0100	0.0500	0.0900
19a, 19b	50.0	50.0	50.0	0.100	0.100	0.100	S1, S2, S3	40.0	40.0	40.0	0.0100	0.0100	0.0100
20a, 20b, 20c	50.0	50.0	50.0	0.000	0.000	0.000							

^a Zr and all other elemental concentrations are in milligrams per liter.

Table III. Operational Parameters for ICP/MS

forward rf power = 1250 W; reflected power = 5 W
 plasma Ar flow = 14.9 std L/min
 auxiliary Ar flow = 1.37 std L/min
 nebulizer Ar flow = 1.10 std L/min
 sample uptake rate = 2.0 mL/min
 sampling depth = 25 mm^a
 mass spectrometer pressure = 1.8×10^{-5} Torr
 electron multiplier voltage = 3930 V
 deflector voltage = 4030 V
 B lens setting = 30; E₁ lens setting = 42
 P lens setting = 17; S₂ lens setting = 20
⁹⁶Mo¹⁸O⁺/⁹⁶Mo⁺ = 0.000913 ± 0.000075 ($n = 2$)^b
⁹⁰Zr¹⁶O⁺/⁹⁰Zr⁺ = 0.00774 ± 0.00053 ($n = 5$)^c
⁹⁷Mo¹⁸O⁺/⁹⁷Mo⁺ = 0.00136 ± 0.00014 ($n = 5$)^c
¹⁰²Ru¹⁶O⁺/¹⁰²Ru⁺ = 0.000421 ± 0.000038 ($n = 5$)^c
 measmt mode = multichannel; measmt time = 10 s
 dwell time = 0.050 s; cycle time = 0.100 s
 measmts/peak^d = 1; repeats/integration = 1

^aThis refers to the distance from the top of the load coil to the tip of the sampling orifice. ^bThis ratio applies to the Mo-Cd system and was measured at the beginning and at the end of the entire experiment; the stated uncertainty reflects the range of the two values. ^cThese ratios apply to the Zr-Mo-Ru-Cd-Ir-Sn system and were measured at the beginning and end of the entire experiment and at evenly spaced intervals; the stated uncertainty reflects one sample standard deviation. ^dThis indicates that a single measurement at the nominal mass value was made for each m/z scanned.

Worth noting are the following: First, there appears to be a Zr-related block (masses 106, 108, 110), a disperse Mo- and Cd-related block (masses 111-114, 116), and an Sn-related block (masses 117-120, 122, 124). The m/z 113 and 115 sensors are apparently associated with In, although their mutual correlation coefficient (0.6817) is diminished due to the influence of other signals such as ¹¹³Cd⁺ and ⁹⁷Mo¹⁶O⁺ at m/z 113. The masses 117-120 and 122 are apparently Sn-associated, with little influence from other signals. The m/z 124 sensor, which might be expected to be strictly associated with ¹²⁴Sn⁺, shows a lower correlation with the Sn group sensors; there is apparently an influence at m/z 124 from some other species; further investigation revealed that a Mo-containing species influencing m/z 124 was responsible for the lack of fit to the m/z 122-124 correlation. A scatter plot of the Sn concentration vs the normalized m/z 124 signal is shown in Figure 2; clear delineations exist for standards containing 0, 25, and 50 mg/L Mo.

There do not appear to be any obvious features in the matrix of Table VI that are related to Ru; the RuO⁺ signals are weak due to the low values of ¹⁰²Ru¹⁶O⁺/¹⁰²Ru⁺ observed (see

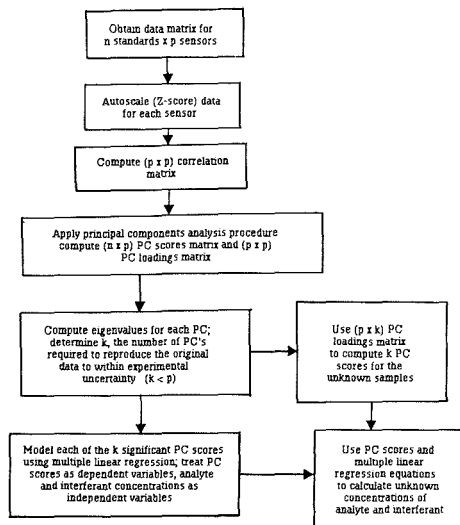


Figure 1. Flow chart description of the steps involved in the principal components regression (PCR) process.

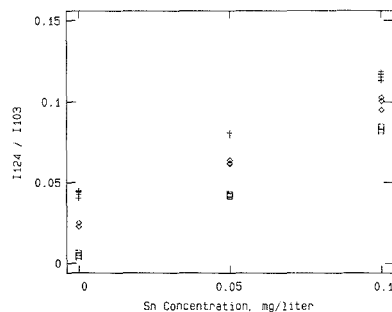
Figure 2. Calibration plots for the determination of Sn at m/z 124, showing the influence of Mo: squares, 0 mg/L Mo; diamonds, 25 mg/L Mo; plus signs, 50 mg/L Mo.

Table III). The influence of RuO⁺ at masses 112, 114-118, and 120 does exist; however, for m/z 114, it is negligibly small, and for the remaining sensors, it represents a minor contri-

Table IV. Univariate, Multiple Linear Regression, and Principal Components Regression Calibration Schemes

system	analyte(s)	sensor(s)	method	correlation ^a	results
Mo-Cd	Cd	106	univariate ^b	0.9982	Table VII
Mo-Cd	Cd	111	univariate ^b	0.9998	Table VII
Mo-Cd	Mo, Cd	106, 108, 111	MLR	0.9974, 0.9976, 0.9966	Table VIII
Mo-Cd	Mo, Cd	106, 108, 111	MLR, amended ^c	0.9976, 0.9985, 0.9990	Table VIII
Mo-Cd	Mo, Cd	all ^d	PCR	0.9986, 0.9958	Table IX
Mo-Cd	Mo, Cd	all ^d	PCR, amended ^c	0.9993, 0.9976	Table IX
Zr-Mo-Ru-Cd-In-Sn	Cd	111	univariate ^e	0.9988	Table X
Zr-Mo-Ru-Cd-In-Sn	In	115	univariate ^e	0.9994	Table X
Zr-Mo-Ru-Cd-In-Sn	Sn	122	univariate ^f	0.9986	Table X
Zr-Mo-Ru-Cd-In-Sn	Zr, Mo, Ru, Cd, In, Sn	106, 108, 110, 113, 115, 116, 120	MLR	0.9988, 0.9988, 0.9988, 0.9966, 0.9994, 0.9994, 0.9994	Table XI
Zr-Mo-Ru-Cd-In-Sn	Zr, Mo, Ru, Cd, In, Sn	all ^g	PCR	0.9994, 0.9990, 0.9996, 0.9996, 0.9912, 0.9956	Table XII

^aCorrelations (r -squared) are shown in the order corresponding to that of the sensors. ^bStandards containing no Mo were included in the models. ^cA time-dependent term was incorporated into these models to compensate for slight changes in MoO⁺/Mo⁺. ^dAll sensors mentioned in the text were included in the model. ^eThe model was constructed from standards 1a-c and 10a-c (see Table II). ^fAll standards were included in the model.

Table V. Matrix of Correlation Coefficients^a Obtained for the Mo-Cd System Standard Solutions

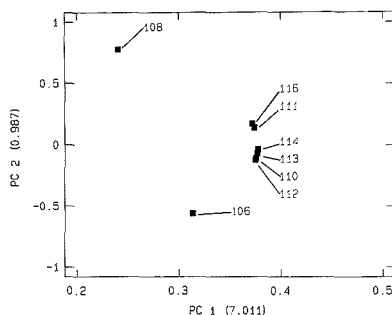
106	1.000																		
108	0.099	1.000																	
110	0.884	0.550	1.000																
111	0.744	0.738	0.970	1.000															
112	0.892	0.536	0.999	0.965	1.000														
113	0.865	0.583	0.999	0.978	0.998	1.000													
114	0.850	0.607	0.997	0.984	0.996	0.999	1.000												
116	0.721	0.760	0.960	0.999	0.956	0.971	0.978	1.000											
<i>m/z</i>	106	108	110	111	112	113	114	116											

^a Correlation coefficients having an absolute value of greater than 0.359 are significant at the 99% confidence level, as determined by the formula $t_{Cl,df} = r(1 - r^2)^{-1/2}(n - 2)^{1/2}$, where Cl = confidence level = 0.99 (two-sided); n = number of measurements = 19; df = degrees of freedom = $19 - 2 = 17$; and $t = 2.898$.

tribution to the total variance. Thus, the influence of RuO⁺ is confounded amongst the Mo/Cd- and Sn-related blocks. Despite the obscurity of the Ru-related information in the standards data set, it will be shown that the Ru concentrations can be predicted in the test samples by using MLR or PCR (vide infra).

Univariate and Multiple Linear Regression Calibration. Table IV lists the univariate, MLR, and PCR calibration schemes used for both the Mo-Cd and the Zr-Mo-Ru-Cd-In-Sn systems. Each calibration model was evaluated by examining the correlation coefficients and residuals plots for the individual equations; correlation coefficients of 0.995 or greater (i.e. r -squared of 0.99 or greater) were considered acceptable; the residuals plots were inspected for any systematic lack of fit; none was detected for any of the regressions performed. The Mo-Cd system was found to be well-described by MLR using m/z 106, 108, and 114; addition of other sensors (m/z 110, 111-113, 116) to the model brought about little change in the predicted sample values. The Zr-Mo-Ru-Cd-In-Sn system could be modeled as a whole, using seven sensors (m/z 106, 108, 110, 113, 115, 118, and 120). Alternatively, though, it could be treated as several smaller systems. Clearly, a very large number of potentially useful MLR modeling systems exist in addition to those listed in Table IV.

Principal Components Analysis. A principal components analysis of the signals for the Mo-Cd standards at m/z 106, 108, 110, 111, 112, 113, 114, and 116 yielded two significant principal components, having eigenvalues of 7.011 and 0.987, respectively. Collectively, these two principal components accounted for 99.97% of the original variance of the data; the original data set could be closely replicated from the data scores and original variable loadings of these two principal

**Figure 3.** Principal components loadings plot for the Mo-Cd system standards; data set, showing the position of each sensor in the new PC axes; eigenvalues are shown in parentheses.

components. Therefore, it was not necessary to consider any of the six additional principal components in order to adequately model the system.

Figure 3 illustrates the loadings of the original signals upon the first two principal components of the Mo-Cd system; this plot effectively depicts and clarifies the information present in the correlation matrix of Table V and the suggested groupings of the sensors. This plot is also useful as a guideline for constructing MLR calibration schemes; it suggests that a good MLR model should consist of m/z 106, 108, and one of the remaining sensors. It is also seen that high similarity between the m/z 110-114, 116 group exists, and that models consisting of sensors from only this group are less desirable; this type of model leads to a matrix of regression parameters having a determinant of close to zero, which may lead to a numerically unstable inverted matrix of regression parameters, and inaccurate and imprecise predictions. These considerations are discussed in detail by Beebe and Kowalski (37).

The loadings plot for the first two principal components of the Zr-Mo-Ru-Cd-In-Sn system is shown in Figure 4. These two principal components had eigenvalues of 8.285 and 3.154 for the first and second components, respectively; together, these two components account for 76.26% of the variance of the entire standards data set. The first six principal components accounted for 99.99% of the system's variance; the remaining nine components were neglected. Loadings plots for component pairs other than the first vs the second were examined as well; these plots contain successively less information. The plot shown in Figure 4 is the best two-dimensional representation of the standards' responses

Table VI. Matrix of Correlation Coefficients^a Obtained for the Zr-Mo-Ru-Cd-In-Sn System Standard Solutions

106	1.000																		
108	0.999	1.000																	
110	0.994	0.995	1.000																
111	0.349	0.368	0.445	1.000															
112	0.620	0.631	0.701	0.938	1.000														
113	0.006	0.020	0.104	0.861	0.732	1.000													
114	0.025	0.042	0.132	0.938	0.798	0.930	1.000												
115	-0.116	-0.112	-0.079	0.293	0.217	0.682	0.369	1.000											
116	0.091	0.103	0.160	0.622	0.584	0.666	0.660	0.408	1.000										
117	0.096	0.102	0.136	0.362	0.379	0.425	0.388	0.348	0.942	1.000									
118	0.080	0.086	0.121	0.353	0.368	0.424	0.386	0.349	0.945	0.997	1.000								
119	0.059	0.063	0.099	0.338	0.352	0.419	0.381	0.344	0.941	0.982	0.993	1.000							
120	0.070	0.075	0.110	0.343	0.358	0.420	0.381	0.347	0.943	0.990	0.998	0.999	1.000						
122	0.077	0.081	0.116	0.340	0.359	0.414	0.376	0.341	0.940	0.983	0.994	0.999	0.999	1.000					
124	0.205	0.226	0.248	0.513	0.485	0.476	0.465	0.322	0.918	0.906	0.906	0.894	0.901	0.897	1.000				
<i>m/z</i>	106	108	110	111	112	113	114	115	116	117	118	119	120	122	124				

^a Correlation coefficients having an absolute value of greater than 0.206 are significant at the 99% confidence level as determined by the formula $t_{Cl,df} = r(1 - r^2)^{-1/2}(n - 2)^{1/2}$, where Cl = 0.99, two-sided confidence level; n = number of measurements = 31; df = degrees of freedom = $31 - 2 = 29$; and $t = 2.756$.

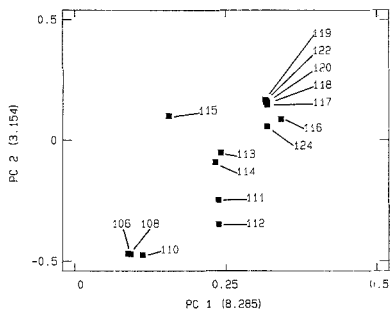


Figure 4. Principal components loadings plot for the Zr-Mo-Ru-Cd-In-Sn system standards data set; eigenvalues are shown in parentheses.

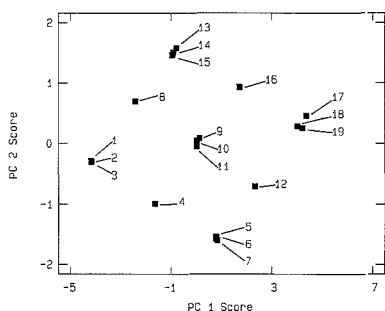


Figure 5. Principal components scores plot for the Mo-Cd system standards data set, showing the position of the standards in the new PC axes.

at the 15 sensors used; however, it should be borne in mind that it is a projection of the data matrix into two dimensions, and additional features exist that are seen only in additional loadings plots (e.g. PC1 vs PC3, PC2 vs PC3, etc.). Some features noted in Figure 4 are the similarities of m/z 106, 108, and 110 (Zr-related); the uniqueness of m/z 115 (In); the Sn group of m/z 117, 118, 119, 120, and 122; and the separation of m/z 124 from the Sn group and its partial association with the disperse Mo-Cd group (m/z 111, 112, 113, 114, 116).

In Figure 5, the principal components scores plot for the Mo-Cd system standards is shown; this plot shows the positions of the standards in the new principal components axes. It is evident that this plot closely resembles the original design of the experiment, although the PC axes are positioned at an angle relative to those in the original design. The three-point clusters in the corners and center of the scores plot represent triplicate standards as indicated in Table I. The within-cluster distances provide a rough indication of the experimental uncertainty associated with the various regions of the plot.

When the information from the correlation matrix and the PC loadings and scores plots is combined, it is evident that two "latent variables", namely the Cd and Mo concentrations, exist for the Mo and Cd system, as would be expected. Similar considerations apply to the Zr-Mo-Ru-Cd-In-Sn system; six latent variables exist; each PC score is a linear combination of signals derived from the six individual analytes.

The scores plot shown in Figure 6, for the Zr-Mo-Ru-Cd-In-Sn system, is much more complex than that of Figure 5; however, a rationale should exist for the location of each point. Some specific features are that the Zr concentrations are high in standards found in the bottom of the plot, and the high Sn standards are located in the upper right-hand

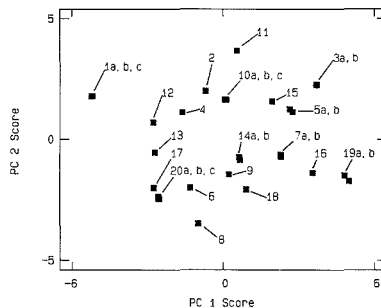


Figure 6. Principal components scores plot for the Zr-Mo-Ru-Cd-In-Sn system standards data set.

Table VII. Results for the Determination of Cd in the Mo-Cd System Using Univariate Calibration at m/z 106 and 111

sample(s)	bias at 106, ^a %	precisn at 106, ^b %	bias at 111, %	precisn at 111, %
A, B, C	+4	6	+1	2
D, E, F	-1.1	2.0	0	1.6
G, H, I	+4	7	+88	4.7
J, K, L	+0.7	1.4	+8.9	0.2
M	+3.8	N/A ^c	+44	N/A
N	+20	N/A	+180	N/A
O	-3.5	N/A	+56	N/A
P	+1.6	N/A	+130	N/A
Q, R, S	+14	11	+870	2.2
T, U, V	-0.1	1.7	+81	1.6

^aRelative bias (of the mean, if applicable); true values for Mo and Cd shown in Table I. ^bRelative standard deviation. ^cNot applicable; no replicates performed.

corner. The plot of Figure 6 is most readily examined by using Figure 4 as a template to assist in interpretation. As a practical note, extensive interpretation of these plots is not generally necessary in order to implement a calibration scheme; however, a wealth of information can be recovered by this practice.

Multiple Linear Regression Modeling of Principal Component Scores. For both systems, the standards data scores for all significant principal components (PC1, PC2 for Mo-Cd; PC1-PC6 for Zr-Mo-Ru-Cd-In-Sn) were modeled by using multiple linear regression as depicted in Figure 1. Correlations where r -squared was at least 0.99 were obtained in all cases. An analysis of variance (ANOVA) of the residuals, as described by Deming and Morgan (38), was performed for both Mo-Cd PCR equations; this analysis indicated that there was no significant lack of fit for either PC model; thus, both sets of PC scores are described within the experimental uncertainty of the data. The level of experimental uncertainty observed in this study was considered to be acceptable for this type of analytical method and application.

Sample Results. For Mo-Cd system samples containing Mo, univariate Cd determinations at individual m/z 's were found to be grossly unsuccessful, with the exception of those performed at $^{106}\text{Cd}^+$. Results at m/z 106 and 111 are shown in Table VII; it is noted that this $^{106}\text{Cd}^+$ isotope is the only Cd isotope that is not obscured by a MoO^+ species. This isotope, however, is not always practical for quantitation due to its low abundance (1.2%); the precision and accuracy of the results reflect this low abundance. Furthermore, it is conceivable that a sample matrix would produce significant levels of species such as $^{90}\text{Zr}^{16}\text{O}^+$, which would produce the same type of interference; univariate calibration would then

Table VIII. Results for the Determination of Mo and Cd in the Mo-Cd System Using Multiple Linear Regression at m/z 106, 108, and 111

sample(s) ^a	Mo found	Mo bias, ^b %	Mo precis, ^c %	Cd found	Cd bias, %	Cd precis, %
A. Model Containing No Explicit Time Dependency						
A, B, C	ND ^d	NA ^e	NA	0.0099	-1	1
D, E, F	ND	NA	NA	0.0890	-1.1	0.9
G, H, I	4.9	-2	8	0.0101	+1	2
J, K, L	4.5	-10	4	0.0889	-1.2	0.9
M	12.0	-4.0	NA	0.0499	-0.2	NA
N	24.2	-3.2	NA	0.0235	-6.0	NA
O	23.1	-7.6	NA	0.0737	-1.7	NA
P	34.8	-7.2	NA	0.0497	-0.6	NA
Q, R, S	43.3	-3.8	1.3	0.0097	-3	8
T, U, V	41.2	-8.4	0.7	0.088	-2	2
B. Model: $i_{m/z} = k_1[\text{Cd, mg/L}] + k_2[(\text{MoO}^+/\text{Mo})_{\text{initial}} - bt][\text{Mo, mg/L}]$						
A, B, C	ND ^f	NA	NA	0.0102	+2	3
D, E, F	ND	NA	NA	0.090	0	2
G, H, I	5.3	+6	7	0.0103	+3	2
J, K, L	4.8	-4	5	0.0892	-0.9	0.3
M	12.5	0	NA	0.0504	+0.8	NA
N	26.2	+4.8	NA	0.0256	+2.4	NA
O	24.2	-3.2	NA	0.0750	0	NA
P	37.7	+0.5	NA	0.0508	+1.6	NA
Q, R, S	46.0	+2.2	1.2	0.009	-7	15
T, U, V	44.2	-1.8	0.8	0.088	-2	2

^aTrue Mo and Cd concentrations are shown in Table I. ^bBiases are expressed in relative percent deviation between the mean (if applicable) and the true value. ^cPrecision is expressed in relative standard deviation. ^dNot detected; upper-bound estimate of the detection limit (see text) is 4 mg/L. ^eNot applicable. ^fNot detected; upper-bound LOD estimate is 4 mg/L Mo.

Table IX. Results for the Determination of Mo and Cd in the Mo-Cd System Using Principal Components Regression

sample(s) ^a	Mo found	Mo bias, ^b %	Mo precis, ^c %	Cd found	Cd bias, %	Cd precis, %
A. Model Containing No Explicit Time Dependency						
A, B, C	ND ^d	NA ^e	NA	0.0101	+1	2
D, E, F	ND	NA	NA	0.0895	-0.6	0.6
G, H, I	4.8	-4	8	0.0101	+1	3
J, K, L	4.3	-14	4	0.0898	-0.2	0.3
M	11.8	-5.6	NA	0.0509	+1.8	NA
N	23.2	-7.2	NA	0.0265	+6.0	NA
O	23.6	-5.6	NA	0.0736	-1.9	NA
P	34.8	-7.2	NA	0.0510	+2.0	NA
Q, R, S	43.0	-4.4	1.7	0.0106	+6	8
T, U, V	40.9	-9.1	2.2	0.0891	-1.0	0.4
B. Model: $(\text{PC SCORE})_n = k_1[\text{Cd, mg/L}] + k_2[(\text{MoO}^+/\text{Mo})_{\text{initial}} - bt][\text{Mo, mg/L}]$						
A, B, C	ND ^f	NA	NA	0.0101	+1	2
D, E, F	ND	NA	NA	0.0895	-0.6	0.5
G, H, I	5.3	+6	8	0.0101	+1	3
J, K, L	4.5	-10	4	0.0898	-0.2	0.3
M	12.3	-1.6	NA	0.0509	+1.8	NA
N	25.2	+0.8	NA	0.0265	+6.0	NA
O	24.7	-1.2	NA	0.0736	-1.9	NA
P	37.8	+0.8	NA	0.0504	+2.0	NA
Q, R, S	45.7	+1.6	0.6	0.0106	+6	9
T, U, V	44.3	-1.6	2.5	0.0891	-1.0	0.4

^aTrue Mo and Cd concentrations are shown in Table I. ^bBiases are expressed in relative percent deviation between the mean (if applicable) and the true value. ^cPrecision is expressed in relative standard deviation. ^dNot detected; upper-bound estimate of the detection limit (see text) is 4 mg/L. ^eNot applicable. ^fNot detected; upper-bound LOD estimate is 4 mg/L Mo.

fail at m/z 106; this situation is encountered in the Zr-Mo-Ru-Cd-In-Sn example.

The m/z 111 Cd results of Table VII, which reflect the presence of a systematic positive bias due to uncorrected MoO^+ , are typical of univariate Cd results for this system determined at the other Cd isotopes. Results at other isotopes can be rationalized based on the relative abundances of the ^{107}Cd and ^{106}Mo isotopes. It is also expected that the results at Cd isotopes other than ^{106}Cd are dependent upon the particular instrumental operating conditions used; these results might be somewhat improved or degraded by adjustment of parameters such as plasma power, sampling depth, and nebulizer Ar flow rate. However, these strategies cannot completely eliminate the formation of MoO^+ , and the signal

to noise ratio at all of the Cd isotopes tends to diminish as one attempts to produce a lower MoO^+/Mo .

In contrast, the results for Cd determined for the Mo-Cd system samples by using the MLR and PCR approaches are wholly acceptable over the entire Mo-Cd range investigated (refer to Tables VIII and IX, respectively.) No obvious differences exist between the MLR and PCR results; in the case of this relatively simple system, MLR would be preferred on the basis of its being more straightforward. The results of Tables VIII and IX suggest that one could successfully determine 5 mg/kg Cd in a matrix containing up to 25 000 mg/kg Mo, such as might be present in a ferrous alloy. Indications of the methods' precisions are also given in Tables VIII and IX; it is seen, as expected, that MLR and PCR are least precise

Table X. Results for the Determination of Cd, In, and Sn in the Zr-Mo-Ru-Sn-In-Sn System Using Univariate Calibration at m/z 111, 115, and 122, Respectively

sample(s)	% Cd bias, % precis ^a	% In bias, % precis	% Sr bias, % precis
A1, A2, A3	+2, 3	-3, 1	-6, 1
B	+61, NA ^b	-0.6, NA	-1.0, NA
C1, C2	+67, 2.2 ^c	-1.0, 1.9	-0.3, 1.8
D	+74, NA	-0.4, NA	-3.3, NA
E	+36, NA	+0.7, NA	+4, NA
F1, F2	+650, 1.6	+2, 2	+5.0, 0.9
G	+180, NA	-1.8, NA	-5.4, NA
H	+100, NA	0, NA	+3.1, NA
II, I2	+30, 1.0	-2, 5	+9, 3
J	+49, NA	+4.8, NA	+0.4, NA
K1, K2, K3	+130, 1.4	+2.3, 0.7	+2.2, 1.3
L	+95, NA	+1, NA	+7, NA
M	+21, NA	+2, NA	+0.2, NA
N1, N2	+480, 4.3	-4, 6	-1, 9
O	+45, NA	-2.7, NA	-1.2, NA
P1, P2	+70, 0.6	-0.2, 0.2	-8, 4
Q	+12, NA	+5, NA	-0.2, NA
R	+440, NA	+1.5, NA	+4.2, NA
S1, S2, S3	+620, 2.4	+6, 2	+10, 2

^aRelative bias (of mean if applicable) and relative precision (if applicable). All Cd, In, and Sn concentrations are shown in Table II. ^bNot applicable; no replicates performed. ^cPrecision is given by relative standard deviation for $n = 3$ and relative percent difference for $n = 2$.

under adverse conditions, such as for samples Q, R, and S.

Tables VIII and IX illustrate that Mo can be determined as well by using the PCR approach, although determination directly at ⁹⁹Mo⁺ in a diluted sample, or with an alternative method such as ICP/AES, might be preferred. Systematic negative biases appear to exist for the Mo determinations presented in Tables VIII and IX; these biases were thought to be derived from small changes in the MoO⁺/Mo⁺ value (and hence the model parameters) with time. A linear drift correction was performed, by modeling the standards' signals or PC scores as shown below:

$$D = k_1[\text{Cd, mg/L}] + k_2[(\text{MoO}^+/\text{Mo}^+)_{\text{initial}} - bt][\text{Mo, mg/L}] \quad (1)$$

where D is the dependent variable (either a principal component score or an internal-standard-normalized intensity); b is a constant that was determined from two measurements of MoO⁺/Mo⁺ (before and after the entire experiment), and t is the time in minutes. Significant improvements were seen in the accuracy of Mo concentrations determined by using these amended models; amended results for the Mo-Cd MLR and PCR systems are shown in Tables VIII and IXB, respectively. This amended approach may be impractical for routine use; a more versatile solution might be to incorporate Lichte's method (22) of using a MO⁺/M⁺ internal standard such as Th in the multivariate calibration modeling scheme.

In Table X, some Zr-Mo-Ru-Cd-In-Sn system results are shown for the univariate determinations of Cd at m/z 111, In at m/z 115, and Sn at m/z 122. The Cd results are strongly positively biased (with the exception of samples A1-A3, which contained no Zr or Mo) and are demonstrative of the shortcomings of univariate calibration in this type of interference situation. On the other hand, it is seen that univariate calibration is successful for the determination of In (at 115) and Sn (at 122) despite the presence of the other matrix components. Therefore, it is most practical to determine them by using this simple approach.

The Zr-Mo-Ru-Cd-In-Sn system may be treated as a single calibration problem using MLR; this has been performed for a calibration system that utilizes m/z 106, 108, 110,

Table XI. Results for the Determination of All Species in the Zr-Mo-Ru-Cd-In-Sn System Using Multiple Linear Regression at m/z 106, 108, 110, 113, 115, 118, and 120

sample(s) ^a	% Zr bias, % precis	% Mo bias, % precis	% Ru bias, % precis
A1, A2, A3	ND, ^b NA, ^c NA	ND, NA, NA	ND, NA, NA
B	-4.0, NA	-10, NA	+5, NA
C1, C2	-2.8, 1.6 ^d	-20, 13	+8, 17
D	ND, NA, NA	ND, NA, NA	-5, NA
E	-3.0, NA	+10, NA	ND, NA, NA
F1, F2	0, 5	-10, 11	0, 7
G	ND, NA, NA	-10, NA	-3, NA
H	-0.5, NA	-5, NA	ND, NA, NA
II, I2	+0.8, 0.4	ND, NA, NA	-5, 6
J	ND, NA, NA	0, NA	ND, NA, NA
K1, K2, K3	-4.5, 1.0	ND, NA, NA	+5, 21
L	+0.5, NA	-10, NA	-8, NA
M	ND, NA, NA	0, NA	+10, NA
N1, N2	-10, 8	-5, 2	+5, 13
O	-7.8, NA	ND, NA, NA	ND, NA, NA
P1, P2	ND, NA, NA	-13, 6	+10, 1
Q	-1.5, NA	ND, NA, NA	+5, NA
R	-0.5, NA	+10, NA	ND, NA, NA
S1, S2, S3	-0.5, 2.0	-20, 6	-5, 5

sample(s)	% Cd bias, % precis	% In bias, % precis	% Sn bias, % precis
A1, A2, A3	-2, 3	-6, 2	-10, 0.9
B	-0.2, NA	-0.8, NA	-0.8, NA
C1, C2	+4.1, 1.7	-0.9, 2.1	-1.0, 0.6
D	-4.8, NA	-0.4, NA	-1.7, NA
E	-0.3, NA	+0.7, NA	-10, NA
F1, F2	+80, 20	0, 2	+3.0, 0.2
G	0, NA	-1.4, NA	+1.2, NA
H	+7.0, NA	-10, NA	+2.4, NA
II, I2	+7, 7	-2, 5	-0.3, 0.3
J	+2.3, NA	+3.8, NA	+1.0, NA
K1, K2, K3	+20, 10	+1.9, 0.8	+2.1, 0.4
L	+7.6, NA	+6, NA	+8.0, NA
M	-1.7, NA	-2, NA	+0.3, NA
N1, N2	0, 44	-2, 6	+10, 16
O	-0.6, NA	-3.0, NA	-4.2, NA
P1, P2	0, 2.0	+0.1, 0.2	0, 4
Q	-1.8, NA	+7, NA	+1.4, NA
R	+40, NA	-4.0, NA	+2.3, NA
S1, S2, S3	+40, 20	+11, 2	+11, 3

^aTrue value are shown in Table II. ^bNot detected; upper-bound estimates (see text) of LOD's are 2, 20, and 20 mg/L for Zr, Mo, and Ru, respectively. True LOD's are likely to be at least an order of magnitude lower. ^cNot applicable; no replicates performed. ^dPrecision is given by relative standard deviation for $n = 3$ and relative percent difference for $n = 2$.

113, 115, 118, and 120. The results from this system are shown in Table XI. The system as a whole performs quite well with the exception of the determination of 0.0100 mg/L Cd in samples containing Zr (samples F1 and F2, K1-K3, N1 and N2, R, S1-S3). The successful determination of Ru indicates that multivariate calibration can be used even where a species produces a signal that is weak compared to those derived from interferants; in this example, 50 mg/L Ru yielded approximately 1900 ions/s at m/z 118 (¹⁰²Ru-¹⁶O⁺) while 0.100 mg/L Sn yielded approximately 15000 ions/s at ¹¹⁸Sn⁺. No particular advantage over univariate calibration is seen for using MLR in the determination of In or Sn.

The results of Table XII illustrate the determination of all analytes using all 15 sensors via the PCR method. Some improvement in precision and accuracy over MLR is seen for the Mo results, presumably due to the incorporation of additional information into the calibration model. Still, however, the determination of 0.0100 mg/L Cd in the presence of Zr is problematic, although both MLR and PCR produce acceptable Cd results at higher Cd levels. The results of Tables

Table XII. Results for the Determination of All Species in the Zr-Mo-Ru-Cd-In-Sn System Using Principal Components Regression at All Sensors

sample(s) ^a	% Zr bias, % precisn	% Mo bias, % precisn	% Ru bias, % precisn
A1, A2, A3	ND, ^b NA, ^c NA	ND, NA, NA	ND, NA, NA
B	-4.5, NA	0, NA	0, NA
C1, C2	-2.8, 1.8 ^d	+3, 17	+8, 14
D	ND, NA, NA	NA, NA	0, NA
E	-3.0, NA	0, NA	ND, NA, NA
F1, F2	0, 4	+3, 4	0, 24
G	ND, NA, NA	+15, NA	+18, NA
H	-3.5, NA	+5, NA	ND, NA, NA
I1, I2	+1.8, 0.9	ND, NA, NA	-7.5, 2.2
J	ND, NA, NA	+8, NA	ND, NA, NA
K1, K2, K3	-5.0, 1.4	ND, NA, NA	-10, 15
L	+1.3, NA	-10, NA	-5, NA
M	ND, NA, NA	+10, NA	+5, NA
N1, N2	-5, 8	+13, 14	+5, 11
O	-8.3, NA	ND, NA, NA	ND, NA, NA
P1, P2	ND, NA, NA	0, 5	+8.0, 4.3
Q	-0.5, NA	ND, NA, NA	-8, NA
R	-1.5, NA	-5, NA	ND, NA, NA
S1, S2, S3	0, 2.2	-5, 5	-2.5, 1.5

sample(s)	% Cd bias, % precisn	% In bias, % precisn	% Sn bias, % precisn
A1, A2, A3	+8, 3	-5, 4	-6, 1
B	-1.2, NA	-0.4, NA	-0.4, NA
C1, C2	-3, 3	-1, 2	-1.0, 0.4
D	+0.4, NA	+0.2, NA	-1.3, NA
E	+1.4, NA	+1.1, NA	-7.5, NA
F1, F2	-12, 9	-4, 1	+3.4, 0.7
G	-18, NA	-1.3, NA	+0.6, NA
H	-2.2, NA	-13, NA	+2.7, NA
I1, I2	+3.4, 0.8	0, 4	-0.3, 0.3
J	+2.2, NA	+4.2, NA	+2.0, NA
K1, K2, K3	-10, 16	+1.4, 1.4	+2.7, 0.7
L	+4.2, NA	+8.0, NA	+2.0, NA
M	-0.6, NA	+1.4, NA	+1.3, NA
N1, N2	-50, 110	-2, 5	+16, 9
O	-4.2, NA	-3.7, NA	-4.4, NA
P1, P2	-4, 3	0, 0.2	+8, 2
Q	-0.3, NA	+16, NA	+1.6, NA
R	-21, NA	-5.5, NA	+2.0, NA
S1, S2, S3	-20, 20	+10, 5	+8, 2

^aTrue values are shown in Table II. ^bNot detected; upper-bound estimates (see text) of LOD's are 2, 20, and 30 mg/L for Zr, Mo, and Ru, respectively. True LOD's are likely to be at least an order of magnitude lower. ^cNot applicable; no replicates performed. ^dPrecision is given by relative standard deviation for $n = 3$ and relative percent difference for $n = 2$.

XI and XII are demonstrative of the limitations of multivariate calibration as applied to this problem and this particular data set. However, the analyst might be able to improve the system's performance by attempting to reduce the formation of ZrO^+ ; for example, decreasing the nebulizer Ar flow rate from 1.10 to 0.90 L/min would be likely to reduce the ZrO^+/Zr^+ value to a level where determination of 0.0100 mg/L Cd in the presence of high levels of Zr becomes feasible.

Estimated Detection Limits. Detection limits (LOD's) were estimated by using information derived from the samples data set according to the equation shown below:

$$LOD = tS \quad (2)$$

where S is the standard deviation of the analyte concentration in a low-concentration standard, and t is the appropriate t statistic (the 99.5% confidence level was used; probability of α error is 0.005). In most cases three measurements were available, so $t_{0.995,2df}$ has a value of 9.925. This method of estimating upper bounds of detection limits is that suggested by Currie (39) for application in multicomponent analysis

situations. These estimates represent upper bounds on the true detection limits (for the same statistical criteria) for two reasons: (a) The value of t is larger than the corresponding value of the z statistic for the 99.5% confidence level, which would be used if the true population standard deviation was known, or at least 30 measurements were available; (b) the standard deviation of a low-concentration standard is likely to be larger than the standard deviation of a blank (39). Thus, these upper bounds on the detection limits should overestimate the true detection limits by an order of magnitude or even more. This is evident in cases such as samples Q, R, and S in Table IX, where an upper bound of the Cd detection limit is 0.009 mg/L, and a relative standard deviation of 8% is observed for three measurements of these 0.0100 mg/L Cd samples. The numbers of significant figures used in Tables VII–XI are based upon precision results of duplicate and triplicate determinations rather than the lowest concentration digit of the estimated detection limit.

Different detection limits could be estimated for the various calibration systems, and in different interferent concentration situations; for example, in the Mo–Cd system, the standard deviation of the Cd concentrations in samples Q, R, and S leads to an estimated detection limit for Cd in a 45 mg/L Mo matrix; similarly, samples A, B, and C produce an estimated detection limit for Cd in the absence of Mo. Some resulting estimated detection limits for the calibration systems and interference conditions examined are shown in Table XIII. In general, the following trends were observed: (a) The estimated detection limits for a given species and interferent condition were very similar for both the MLR and PCR methods; (b) the presence of an interferent matrix appeared to have a degenerative influence upon the estimated detection limit (e.g., Cd in the absence and presence of Mo and Zr); and (c) estimated detection limits for species such as In and Sn, which were not significantly affected by the isobaric interferences, do not appear to be sensitive to matrices such as Zr, Mo, and Ru. Note that for three samples, differences of less than a factor of 4.35 are not significant at the 95% confidence level, as determined by an F -test for comparing sample variances. Table XIII also shows some estimated univariate calibration detection limits for Cd in the presence of interferents. These estimated detection limits appear to be worse than those in the absence of interferent; however, discussion of any sort regarding detection limits under these severe, uncorrected interference situations is really a moot point, as no positive identification of the signal's source can be made. Thus, when one performs univariate calibration of Cd in the presence of high levels of Zr and/or Mo, there is insufficient information available at any single sensor to assign the signal to a particular source (such as being due to 20 mg/L Zr as opposed to 0.05 mg/L Cd). The large advantage of multivariate calibration (both MLR and PCR) in these situations is that correct signal assignment can be made.

No physical differences in the instrumental conditions account for the differences in the estimated detection limits shown in Table XIII; these differences are strictly a consequence of different calibration methods. The calibration method should be viewed as an integral part of the analytical method, rather than some black box attached to the beginning (or end) of the experimental process (40).

CONCLUSION

In summary, it has been demonstrated that two multivariate calibration methods, namely MLR and PCR, are useful in correcting for molecular ion interferences in ICP/MS. Furthermore, element–element isobaric interference situations (e.g., Cd and In at m/z 113) are resolvable without the use of commonly employed “elemental equations” (22). These multivariate calibration procedures, which operate by utilizing

Table XIII. Estimated Detection Limits for Various Analytes, Calibration Methods, and Interferant Conditions

analyte	calibration method	interferant conditions, mg/L	estimated LOD, ^a mg/L	samples ^b	table
Cd	univariate, <i>m/z</i> 106	0 Mo	0.006	A, B, C	VII
Cd	univariate, <i>m/z</i> 106	45 Mo	0.01	Q, R, S	VII
Cd	univariate, <i>m/z</i> 111	0 Mo	0.002	A, B, C	VII
Cd	univariate, <i>m/z</i> 111	45 Mo	0.02	Q, R, S	VII
Cd	MLR, <i>m/z</i> 106, 108, 114	0 Mo	0.0007	A, B, C	VIIIA
Cd	MLR, <i>m/z</i> 106, 108, 114	45 Mo	0.008	Q, R, S	VIIIA
Mo	MLR, <i>m/z</i> 106, 108, 114	0.01 Cd	4	G, H, I	VIIIA
Mo	MLR, <i>m/z</i> 106, 108, 114	0.09 Cd	2	J, K, L	VIIIA
Cd	MLR, time dependency ^c	0 Mo	0.003	A, B, C	VIIIB
Cd	MLR, time dependency	45 Mo	0.01	Q, R, S	VIIIB
Mo	MLR, time dependency	0.01 Cd	4	G, H, I	VIIIB
Mo	MLR, time dependency	0.09 Cd	3	J, K, L	VIIIB
Cd	PCR, all <i>m/z</i> 's	0 Mo	0.002	A, B, C	IXA
Cd	PCR, all <i>m/z</i> 's	45 Mo	0.009	Q, R, S	IXA
Mo	PCR, all <i>m/z</i> 's	0.01 Cd	4	G, H, I	IXA
Mo	PCR, all <i>m/z</i> 's	0.09 Cd	2	J, K, L	IXA
Cd	PCR, time dependency	0 Mo	0.002	A, B, C	IXB
Cd	PCR, time dependency	45 Mo	0.009	Q, R, S	IXB
Mo	PCR, time dependency	0.01 Cd	4	G, H, I	IXB
Mo	PCR, time dependency	0.09 Cd	2	J, K, L	IXB
Cd	univariate, <i>m/z</i> 111	0 Zr, Mo, Ru	0.001	A1, A2, A3	X
Cd	univariate, <i>m/z</i> 111	40 Zr, Mo, Ru	0.007	S1, S2, S3	X
In	univariate, <i>m/z</i> 115	0 Zr, Mo, Ru	0.001	A1, A2, A3	X
In	univariate, <i>m/z</i> 115	40 Zr, Mo, Ru	0.002	S1, S2, S3	X
Sn	univariate, <i>m/z</i> 122	0 Zr, Mo, Ru	0.002	A1, A2, A3	X
Sn	univariate, <i>m/z</i> 122	40 Zr, Mo, Ru	0.002	S1, S2, S3	X
Zr	MLR, seven sensors ^d	0 Mo 20 Ru, 0.01 Cd, 0.09 In, Sn	2	K1, K2, K3	XI
Mo	MLR, seven sensors	40 Zr, Ru, 0.01 Cd, In, Sn	20	S1, S2, S3	XI
Ru	MLR, seven sensors	20 Zr 0 Mo, 0.01 Cd, 0.09 In, Sn	20	K1, K2, K3	XI
Cd	MLR, seven sensors	0 Zr, Mo, Ru, 0.01 In, Sn	0.003	A1, A2, A3	XI
Cd	MLR, seven sensors	40 Zr, Mo, Ru, 0.01 In, Sn	0.03	S1, S2, S3	XI
In	MLR, seven sensors	0 Zr, Mo, Ru, 0.01 Cd, Sn	0.002	A1, A2, A3	XI
In	MLR, seven sensors	40 Zr, Mo, Ru, 0.01 Cd, Sn	0.002	S1, S2, S3	XI
Sn	MLR, seven sensors	0 Zr, Mo, U, 0.01 Cd, In	0.0008	A1, A2, A3	XI
Sn	MLR, seven sensors	40 Zr, Mo, Ru, 0.01 Cd, In	0.003	A1, A2, A3	XI
Zr	PCR, 15 sensors ^e	0 Mo 20 Ru, 0.01 Cd, 0.09 In, Sn	3	K1, K2, K3	XII
Mo	PCR, 15 sensors	40 Zr, Ru, 0.01 Cd, In, Sn	20	S1, S2, S3	XII
Ru	PCR, 15 sensors	20 Zr 0 Mo, 0.01 Cd, 0.09 In, Sn	30	K1, K2, K3	XII
Cd	PCR, 15 sensors	0 Zr, Mo, Ru, 0.01 In, Sn	0.003	A1, A2, A3	XII
Cd	PCR, 15 sensors	40 Zr, Mo, Ru, 0.01 In, Sn	0.02	S1, S2, S3	XII
In	PCR, 15 sensors	0 Zr, Mo, Ru, 0.01 Cd, Sn	0.004	A1, A2, A3	XII
In	PCR, 15 sensors	40 Zr, Mo, Ru, 0.01 Cd, Sn	0.005	S1, S2, S3	XII
Sn	PCR, 15 sensors	0 Zr, Mo, Ru, 0.01 Cd, In	0.0009	A1, A2, A3	XII
Sn	PCR, 15 sensors	40 Zr, Mo, Ru, 0.01 Cd, Sn	0.002	S1, S2, S3	XII

^a All detection limits are upper-bound estimates based on limited data ($n = 3$) and probably overestimate the true detection limits by a factor of 10 or greater (see text). ^b Sample group that was used to calculate this estimated LOD (see Tables I and II). ^c A time-dependent model was used (see eq 1) with the same sensor combination. ^d The following sensors were used: *m/z* 106, 108, 110, 113, 115, 118, and 120. ^e All 15 sensors were used (see text).

information from more than one partially selective sensor, appear to be promising solutions to what has been considered to be a potential pitfall in using ICP/MS.

It has been found, for the particular cases studied (Mo-Cd and Zr-Mo-Ru-Cd-In-Sn), that MLR and PCR produce essentially equivalent results; thus, MLR might be preferred as it is often simpler to apply to smaller problems. Indeed, MLR may well be the method of choice for applying multivariate calibration to most isobaric interference situations in ICP/MS. MLR should, however, be used with caution, especially for more complicated interference situations, and in cases where nearly collinear columns in the data set exist, as discussed by Beebe and Kowalski (37). In these cases, PCR may be preferred, as no collinearities exist among the columns of the principal components scores matrix (they are orthogonal), and PCR always produces a model that utilizes all of the pertinent information in the calibration data matrix. With MLR, a large amount of effort may be required to adequately model larger problems (e.g. 10-15 independent analytes and 30-40 sensors); iterative (stepwise) modeling may be lengthy in order to include all anticipated and unanticipated contributions to the variance of each sensor. Nevertheless, MLR

is expected to be very useful for most isobaric interference situations in ICP/MS. Perhaps a useful approach would be to use principal components loadings and scores plots from the standards data matrix as a basis for constructing proper MLR models.

It should also be noted that any form of multivariate calibration is unnecessary if the problem can be adequately dealt with by using univariate calibration, such as was encountered for ¹¹⁵In and ¹²²Sn in this study. The need for multivariate calibration in real samples should be judged on a case-by-case basis; for example, univariate calibration is probably adequate for the determination of Cd in most drinking water samples, while the determination of Cd in soils or geological materials may encounter the ZrO⁺ and MoO⁺ interferences demonstrated in this study.

In practice, these calibration approaches are not difficult to implement, particularly with automated sample preparation and introduction and a proper data management system. Multivariate calibration schemes do tend to require a large number of standards, which is disadvantageous in terms of analysis time. For problems consisting of more than two or three variables, proper partial factorial calibration designs are

essential. Indeed, experimental design in multivariate calibration is an extensive subject in itself (41, 42).

Multivariate calibration approaches other than MLR and PCR might be preferred under certain circumstances; for example, GSAM would be useful in situations where the MO^+/M^+ values are matrix-dependent, or if a high dissolved solids content produced large differences in analyte sensitivity between sample and standard solutions. GSAM may also be practical where only a few samples are involved, as no external calibration is performed. The partial least-squares method (PLS) has been successfully applied to underdetermined systems (31), i.e. those systems where fewer sensors than analytes exist. PLS may be useful in some situations such as the determination of As and Se in soil digestates, where a complex variety of oxygen-, chlorine-, potassium-, and argon-containing molecular species may cause problems.

LITERATURE CITED

- (1) Gray, A. L. *Analyst* **1975**, *100*, 289-299.
- (2) Houk, R. S.; Fassel, V. A.; Flesch, G. D.; Svec, H. J.; Gray, A. L.; Taylor, C. E. *Anal. Chem.* **1980**, *52*, 2283-2289.
- (3) Date, A. R.; Gray, A. L. *Analyst* **1981**, *106*, 1255-1267.
- (4) Date, A. R.; Gray, A. L. *Analyst* **1983**, *108*, 159-165.
- (5) Date, A. R.; Gray, A. L. *Int. J. Mass Spectrom. Ion Phys.* **1983**, *46*, 7-10.
- (6) Date, A. R.; Gray, A. L. *Spectrochim. Acta* **1983**, *38B*, 29-37.
- (7) Gray, A. L.; Date, A. R. *Analyst* **1983**, *108*, 1033-1050.
- (8) Gray, A. L.; Date, A. R. *Int. J. Mass Spectrom. Ion Phys.* **1983**, *48*, 357-360.
- (9) Date, A. R.; Gray, A. L. *Spectrochim. Acta* **1985**, *40B*, 115-122.
- (10) Olivares, J. A.; Houk, R. S. *Anal. Chem.* **1985**, *57*, 2674-2679.
- (11) Houk, R. S.; Svec, H. J.; Fassel, V. A. *Appl. Spectrosc.* **1981**, *35*, 330-334.
- (12) Douglas, D. J.; Quan, E. S. K.; Smith, R. G. *Spectrochim. Acta* **1983**, *38B*, 39-48.
- (13) Doherty, W.; Vander Voet, A. *Can. J. Spectrosc.* **1985**, *30*, 135-141.
- (14) Douglas, D. J.; Houk, R. S. *Prog. Anal. At. Spectrom.* **1985**, *8*, 1-18.
- (15) Gray, A. L. *J. Anal. At. Spectrom.* **1986**, *1*, 247-249.
- (16) McLeod, C. W.; Date, A. R.; Cheung, Y. Y. *Spectrochim. Acta* **1986**, *41B*, 169-174.
- (17) Vaughn, M. A.; Horlick, G. *Appl. Spectrosc.* **1986**, *40*, 434-445.
- (18) Date, A. R.; Cheung, Y. Y.; Stuart, M. E. *Spectrochim. Acta* **1987**, *42B*, 3-20.
- (19) Gray, A. L.; Williams, J. G. *J. Anal. At. Spectrom.* **1987**, *2*, 81, 82.
- (20) Horlick, G.; Tan, S. H.; Vaughn, M. A.; Rose, C. A. *Spectrochim. Acta* **1985**, *40B*, 1555-1572.
- (21) Hutton, R. C.; Eaton, A. N. *J. Anal. At. Spectrom.* **1987**, *2*, 595-598.
- (22) Licht, F. E.; Meier, A. L.; Crock, J. G. *Anal. Chem.* **1987**, *59*, 1150-1157.
- (23) Saxberg, B. E. H.; Kowalski, B. R. *Anal. Chem.* **1979**, *51*, 1031-1038.
- (24) Jochum, C.; Jochum, P.; Kowalski, B. R. *Anal. Chem.* **1981**, *53*, 85-92.
- (25) Kalivas, J. H.; Kowalski, B. R. *Anal. Chem.* **1981**, *53*, 2207-2212.
- (26) Kalivas, J. H.; Kowalski, B. R. *Anal. Chem.* **1982**, *54*, 560-565.
- (27) Gerlach, R. W.; Kowalski, B. R. *Anal. Chim. Acta* **1982**, *134*, 119-127.
- (28) Kalivas, J. H. *Anal. Chem.* **1983**, *55*, 565-567.
- (29) Lindtner, W.; Persson, J. A.; Wold, S. *Anal. Chem.* **1983**, *55*, 643-648.
- (30) Ststrom, M.; Wold, S.; Lindberg, W.; Persson, J.; Martens, H. *Anal. Chim. Acta* **1983**, *150*, 61-70.
- (31) Frank, I. E.; Kalivas, J. H.; Kowalski, B. R. *Anal. Chem.* **1983**, *55*, 180C-1804.
- (32) Mancel, J. *Am. Stat.* **1982**, *36*, 15-24.
- (33) Cowie, I. A.; McNicol, J. W. *Appl. Spectrosc.* **1985**, *39*, 257-266.
- (34) Fredricks, P. M.; Lee, J. B.; Osborn, P. R.; Swinkels, D. A. *J. Appl. Spectrosc.* **1985**, *39*, 303-310.
- (35) Gemertine, P. J.; Boyette, S. E.; Tyndall, K. *Appl. Spectrosc.* **1987**, *41*, 454-459.
- (36) Donhue, S. M.; Brown, C. W.; Caputo, B.; Modell, M. D.; *Anal. Chem.* **1988**, *60*, 1873-1878.
- (37) Beete, K. R.; Kowalski, B. R. *Anal. Chem.* **1987**, *59*, 1007A-1017A.
- (38) Deming, S. N.; Morgan, S. L. *Experimental Design: A Chemometric Approach*; Elsevier: Amsterdam, 1987; Chapter 9.
- (39) Curris, L. A. *ACS Symp. Ser.* **1988**, No. 361, 1-62.
- (40) Delaney, M. F. *Anal. Chem.* **1984**, *56*, 261R-277R.
- (41) Mark, H. *Anal. Chem.* **1986**, *58*, 2814-2819.
- (42) Cahr, F.; Compton, S. *Appl. Spectrosc.* **1988**, *42*, 856-872.

RECEIVED for review January 27, 1989. Accepted June 20, 1989. This work was supported by the U.S. Environmental Protection Agency. Mention of specific suppliers and products is for information purposes only and does not constitute official endorsement.

Ion Detection by Fourier Transform Ion Cyclotron Resonance: The Effect of Initial Radial Velocity on the Coherent Ion Packet

Curtiss D. Hanson, Eric L. Kerley, Mauro E. Castro, and David H. Russell*

Department of Chemistry, Texas A&M University, College Station, Texas 77843

Ion detection by Fourier transform ion cyclotron resonance (FT-ICR) is accomplished by observing a coherent ion packet produced from an initially random ensemble of ions. The coherent packet is formed by excitation with a resonant oscillating electric field. Ions that are out of phase with the applied radio frequency (rf) electric field experience a continuous misalignment of the electric field vector. The misalignment creates a net force of the electric field perpendicular to ion motion. The perpendicular component of the rf electric field creates a frequency shift resulting in phase synchronization of the ion ensemble. The phase coherence of the ion packet affects both the sensitivity and the resolution of FT-ICR.

INTRODUCTION

Over the past decade, there has been rapid development in Fourier transform ion cyclotron resonance (FT-ICR). As

noted in several reviews (1-10), the growth in FT-ICR can be attributed to the performance characteristics of the instrument (i.e., the ability to perform high-resolution mass measurements, the extended mass range ($m/z > 10,000$) (11, 12), and the ability to perform high-resolution mass measurements at high mass). FT-ICR had its foundation in the concept of the ion trap. The ability to store ions for long periods of time (milliseconds to seconds), provides a high degree of flexibility in terms of ion manipulation and detection. For example, ion storage permits both high sensitivity and versatility required to perform tandem mass spectrometry (MS) experiments (e.g., photodissociation (13) and collision induced dissociation (CID) (14, 15)).

Ion cyclotron resonance was developed during the mid 1960s (16), based on work performed a decade before (17-19), primarily for studying ion-molecule reactions. During this period the major emphasis was placed on the development of mass analysis techniques. The principal method of sample ionization was electron impact which produces ions having near thermal kinetic energies. Thus, the mass analysis

techniques that evolved during this period were designed and developed for ions for low translational energies.

Recent advancements in "soft" ionization methods which are suitable for nonvolatile, thermally labile, and polar compounds (viz., fast atom bombardment (FAB) (20), secondary ion mass spectrometry (SIMS) (21), and laser desorption (22)) have greatly expanded the scope of mass spectrometry. Although these ionization methods have been adapted for use with FT-ICR (23, 24) and are capable of producing intact molecular ions, the kinetic energies (>thermal) imparted to the sample ions can have adverse effects on the instrument performance. In order to realize the theoretical potential of FT-ICR, the effect of initial ion kinetic energy on ion trapping and detection must be evaluated. Further, developments in FT-ICR must be based on a thorough understanding of the dynamics of the ion trap. Specifically, the effect of the crossed electric and magnetic fields on ion trajectories in the ICR cell, as well as the impact of ion motion and ion energy on detection, requires further investigation. Although there has been much success in FT-ICR since its introduction by Comisarow and Marshall (25), the theoretical performance (26, 27) has only been realized for a relatively narrow range of operating conditions (e.g., ions produced by electron impact with low translational energies). Extending the operating mass range of FT-ICR to include high molecular weight biomolecules (>2500 amu) revealed fundamental problems with mass analysis by FT-ICR, viz., the inability to perform high-resolution mass measurement at high mass (12, 28, 29). Although impressive mass resolution has been recorded for small peptides which can be efficiently ionized (and therefore produce a large number of intact molecular ions) the short duration of the time-domain transient signal for peptide ions above 2000 daltons seriously limits high-resolution mass measurements. Recently Wilkins and co-workers reported high-resolution data for high mass ions formed by laser desorption. These results differ from other analysis methods in that the ions studied are nonpolar organic polymers, and laser desorption produces a high abundance of ions and neutrals. The high yield for ions and neutrals can result in both ion/ion and ion/neutral relaxation processes (30, 31), which potentially quench radial and axial ion motion and improve both ion trapping (sensitivity) and mass resolution.

Ion detection by FT-ICR is accomplished by observing the image current produced by a coherent ion packet. Therefore, the performance characteristics associated with the technique arise from the ability to produce synchronous ion motion from an ensemble of ions having random initial velocities and ICR orbital phase angles (32, 33). A coherent packet of ions is defined by an ensemble of ions which can be presented by a rotating monopole. To meet this requirement the ion ensemble must be spatially well-defined. Spatial definition is a combination of radial distribution (i.e., energy distribution) and radial dispersion (i.e., phase relationship). Signal intensity and resolution are dependent upon the spatial distribution of the ensemble and the length of time the packet is observed. Loss of signal or resolution in FT-ICR is, therefore, attributed to the loss of coherent ion motion (34).

In this paper we examine several factors that influence the production of a coherent ion packet. The effect of random initial phases on the final translational energy distribution (i.e., radial distribution) was recognized early in the development of ICR (35-37), but because of the low magnetic fields used (ca. 0.7-0.9 T) and thermal ion kinetic energies (e.g., kinetic energies of ions produced by electron impact) the effect of the phase angle on the production of a coherent ion packet was negligible. Clearly such considerations are different today; the high mass FT-ICR instruments use high magnetic fields (3-7 T) and external ion sources which impart significant

translational energies to the ions. Under these conditions the effect of the ions phase angle is no longer insignificant and cannot be neglected.

The effects of ion motion and phase angle are difficult to study in a simple cubic ICR cell. Although the two-section ion cell was initially developed to deal with the FT-ICR requirements of ion detection at high vacuum (38), the work presented in this paper illustrates the flexibility of this cell to address problems of ion motion and the dynamics of ion detection. This paper examines the nonideal effects on ion motion resulting from (i) significant radial translational energy (>thermal), (ii) initially random phase angles, and (iii) the process that leads to phase synchronous motion of an initially random ion population. Experimental results from two-section ion cell studies and theoretical ion trajectories determined by numerical computer solution of the equation of ion motion are used to examine the effects of initial radial velocity on the ability to create coherent ion motion.

EXPERIMENTAL SECTION

All experiments were performed on a prototype Nicolet Analytical Instruments FTMS-1000 spectrometer equipped with a 3-T superconducting magnet. The vacuum system has been modified to accommodate a two-section cell (39, 40). The two-section cell consists of two cubic cells ($3.81 \times 3.81 \times 0.81$ cm) mounted collinearly along the central axis of the magnetic field. The two cells share a common trap plate that also serves as a conductance limit for the differential pumping system. The aperture in the conductance limit has a radius of 2 mm. The vacuum in both sections of the differentially pumped system is maintained by oil diffusion pumps. Background pressures for both sections of the vacuum system were 1×10^{-8} Torr or less. Gaseous reagents are admitted to the vacuum system by variable leak valves (Varian Series 951) and maintained at 2×10^{-7} Torr. Ionization was performed by electron impact (50-eV electrons, 200 nA). Detection of the ions in either the source or the analyzer region of the cell was performed by electronically switching the rf excite pulses between the cell regions.

RESULTS AND DISCUSSION

The motion of a charged particle in a magnetic field (B) is constrained to a circular orbit of angular frequency (ω) in a plane perpendicular to the magnetic field lines. The Lorentz force ($qv_{xy}B$) acting on the ion is directly proportional to the ion's velocity perpendicular to the magnetic field, v_{xy} (i.e., the component of the velocity vector in the X - Y plane). The radius of the cyclotron orbit is obtained by equating the Lorentz force to the centrifugal force. Because the frequency of the cyclotron motion is inversely proportional to mass (m), the mass-to-charge value (m/z) of an ion can be determined by measuring the frequency of the cyclotron motion in a static magnetic field.

Having introduced the rudiments of ion motion in the FT-ICR experiment, it is necessary to consider the problems arising in ion trapping and ion detection in experiments involving (i) the ideal case where ions with thermal kinetic energies are trapped in the center of the ion cell (e.g., electron impact ionization) and (ii) the case where ions with significant translational energies are stored in the ion cell (e.g., ions formed by FAB, SIMS, or laser desorption mass spectrometry (LDMS) within the cell or injected from external ion sources).

In a typical electron impact ionization FT-ICR experiment, ions are formed over a period of several milliseconds (many cyclotron orbits) from neutrals having random motions. Ion formation therefore results in an initial ensemble of ions which is phase incoherent. The initial translational energy of the ion population corresponds to the thermal kinetic energy distribution of the neutrals prior to ionization. Because the ions are formed from the neutral molecules have random velocity vectors with respect to the direction of the magnetic field, the original theoretical development of FT-ICR was

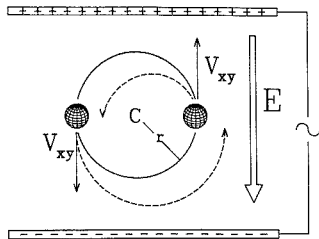


Figure 1. Trajectories for two ions having the same angular frequency but different phase being accelerated by a resonant rf electric field. An ion which is in phase and resonant with the applied rf electric field is accelerated to a larger cyclotron radius. Conversely, an ion which is out of phase is decelerated to lower translational energies and therefore a smaller cyclotron radius.

based on an initial ion population having subthermal energies.

The mechanism for creation of a coherent packet of ions is acceleration by a resonant oscillating electric field (i.e., rf irradiation). Ions of a given m/z ratio are continuously accelerated by rf electric potential gradients which are in phase with the ion's motion. Ions that have an initial random phase relationship with respect to the oscillating electric field must be forced into phase coherence prior to a net acceleration (41). Therefore, an ion must be both (i) resonant with and (ii) in phase with the applied rf field to acquire translational energy.

The excitation rf field can be described as a sum of two phase-related counterrotating electric fields (35).

$$\mathbf{E}(t)_{\text{sum}} = \mathbf{E} \sin(\omega t) = \mathbf{E}^+(t) + \mathbf{E}^-(t) \quad (1)$$

where

$$\mathbf{E}^+(t) = (1/2) \mathbf{E}(\sin \omega t i + \cos \omega t j) \quad (2)$$

$$\mathbf{E}^-(t) = (1/2) \mathbf{E}(\sin \omega t i - \cos \omega t j) \quad (3)$$

The sum of the components results in an electric field which has magnitude and direction. The frequency of the resultant oscillating electric field (ω_{rf}) is determined by the period between the maximum electric field vectors. Only that part of $\mathbf{E}(t)_{\text{sum}}$ which rotates in phase with the ion's velocity vector is effective in accelerating the ions. That is, $\mathbf{E}^+(t)$ corresponds to the inphase accelerating contribution and an ion rotating in phase with $\mathbf{E}^+(t)$ is accelerated to a larger cyclotron radius.

The effect of excitation on ions which are out of phase is illustrated in Figure 1. An ion which has a velocity vector that is in phase with respect to the electric field (A) is accelerated resulting in an increase in the cyclotron radius. Conversely, ion motion (B) that is out of phase with respect to the electric field results in deceleration and a smaller radius of the cyclotron orbit (40, 42-44).

The effect of phase angle on ion excitation can be observed in a two-section cell by utilizing the conductance limit orifice as an ion skimmer (39, 40). The experimental procedure is illustrated in Figure 2. Following the ionization pulse, all ions are accelerated by using frequency swept excitation until the radius of the ion's cyclotron orbit is larger than the radius of the aperture of the conductance limit. Following the initial excitation (S1), a delay is introduced to allow the phase of a second rf excitation (S2) to vary with respect to the phase of the ion packet. Thus, the phase relationship between S1 and S2 is a function of the delay. If S2 is initiated following a delay corresponding to $(N/2)\tau$ ($N = 2, 4, 6, \dots$ and τ is the period of the cyclotron orbit) the second excitation will be in phase with the ion motion (see Figure 2A), whereas a delay corresponding to $(N/2)\tau$ ($N = 1, 3, 5, \dots$) shifts the phase of the second excite pulse by 180° and the ions are decelerated (Figure 2B) resulting in a reduction of the radius of the ion's

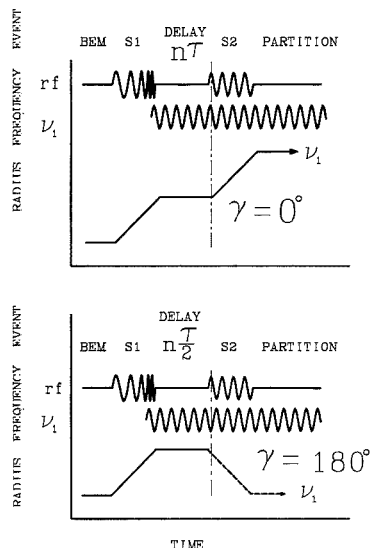


Figure 2. Phase angle of an ion's motion with respect to the applied rf excitation determined by a delay between two distinct excite pulses. A delay corresponding to an integral number of cyclotron periods (τ) results in a second excitation which is in phase with the ion motion. Conversely, a delay corresponding to an integral number of $\tau/2$ produces an out-of-phase excitation resulting in a decrease of the cyclotron radius.

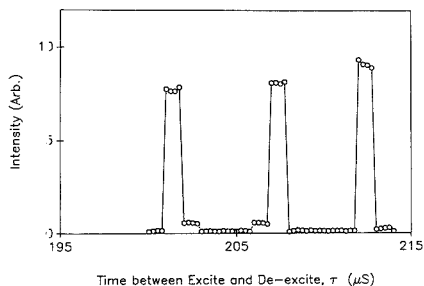


Figure 3. Effect of phase angle on excitation observed by monitoring partitioning efficiency of I_2^{++} as a function of a phase delay between two excite pulses. The maxima in the plot correspond to delays which correspond to out-of-phase deceleration of the ion ensemble to radii that can be partitioned from the source to analyzer region.

cyclotron orbit. Only ions which are de-excited by out-of-phase excitation can be partitioned into the analyzer region, and the ion intensity observed in the analyzer region is a measure of the partitioning efficiency (40).

To illustrate the dependence of excitation on the phase angle, I_2^{++} was formed in the source region, partitioned, and detected in the analyzer region. Prior to partitioning from the source to analyzer regions, the ions are accelerated ($120 \text{ V/m}, 25 \mu\text{s}$) to sufficiently large cyclotron radii such that ion partitioning cannot occur. The radii of these ions are then further modulated by a second excitation ($120 \text{ V/m}, 250 \mu\text{s}$). The phase of the second excitation is determined by a variable time delay between the two excite pulses. Contained in Figure 3 is a plot of signal intensity (m/z 254 in the analyzer region) versus the period between the first and second excite pulses. The maxima correspond to I_2 being de-excited to smaller radii by an out-of-phase second excitation. Because the relative

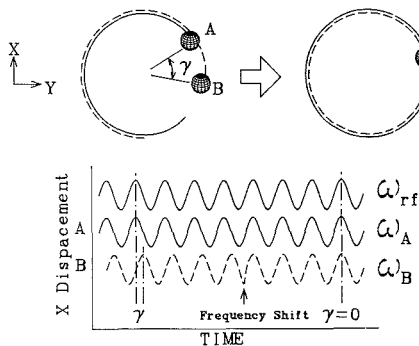


Figure 4. Two ions (I and II) having the same frequency but different phases ($\gamma = 0$) can only be driven into phase coherence ($\gamma = 0$) by shifting the frequency of the out-of-phase ion.

phases of the ion motion and second excitation pulse are shifted by 180° once every period, the period between the maxima is ca. $5.5 \mu\text{s}$ (the period of the cyclotron orbit of m/z 254). The narrow peak width observed in the phase-specific partitioning of iodine demonstrates the significance of the relative phase of ion motion with respect to the applied excitation. It is apparent that excitation and de-excitation are strongly phase dependent because molecular iodine is *only* partitioned during discrete time intervals (i.e., narrow phase distribution). It should be noted that the phase-specific scheme of separating ions requires ion packets of small radial and angular distribution with respect to the FT-ICR cell. That is, ions must be formed with low kinetic energies in the X-Y plane (e.g. electron impact ionization) such that they can be "driven" into phase coherence. Only ion packets having well-defined phase coherence give rise to phase-specific excitation/de-excitation of the entire ion ensemble. It should be noted that sample pressures were maintained at 2×10^{-7} Torr or lower in order to minimize adverse effects caused by ion-neutral collisions (45).

Owing to the strong dependence of ion acceleration on phase angle, it is necessary to "drive" ions having initially random phase angles into synchronous alignment with the rf electric field prior to a net gain of translational energy (41). Phase advancement is the mechanism whereby ions having initially random phases are advanced into synchronous motion with the applied resonant rf field. Illustrated in Figure 4 are the frequencies generated by the motion of two ions relative to a resonant rf electric field. In the figure, ion I is initially inphase with the applied rf field and ion II is initially shifted by a phase angle γ . In order for the relative phase of ion II to be "driven" into phase with ion I and the applied rf electric field, the period of the cyclotron orbit (and therefore frequency) of ion II must be changed. An essential feature of ICR is that the cyclotron frequency is related to the mass-to-charge ratio of the ion and the magnetic field strength and *independent* of the translational energy of the ion. Acceleration of an ion in a magnetic field results in a larger cyclotron radius and *not* in a change in frequency.

The frequency shift required to move an out-of-phase ion into synchronous alignment with the applied electric field is illustrated by evaluating the forces affecting ion motion. As shown in Figure 5, the orbit of an ion (I) which is in continuous alignment with a resonant rf electric field ($\omega_{rf} = \omega_c$) is described by the Lorentz force (F_L) balanced by the centrifugal force (F_C). Because the force applied by the electric field (F_E) is perpendicular to both F_L and F_C , the effect of F_E on the angular frequency of ion I is zero and the angular frequency

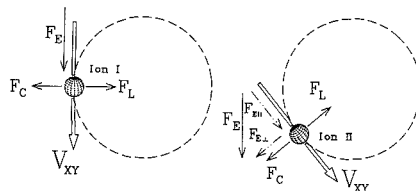


Figure 5. Angular frequency of an ion determined by balancing the radially outward forces with the radially inward forces. Thus, the frequency of an ion which is out of phase with respect to an applied rf electric field is different than an ion which is inphase (ω_c) due to a perpendicular component of the applied electric field ($F_{E\perp}$). Such differences in the frequencies allows the out-of-phase ion to phase advance.

(ω_I) is obtained by equating the Lorentz and centrifugal forces (see eq 4).

$$(mv^2)/r = qvB \quad (4)$$

and

$$\omega_I = v/r = qB/m = \omega_c$$

Conversely, an ion that is out of phase with E_{rf} is affected by both parallel and perpendicular components of the electric field. Therefore, the orbit of the out-of-phase ion II is obtained by equating the total outward radial force ($F_C + F_{E\perp}$, where $F_{E\perp} = qE_{\perp} = qE \sin \gamma$ in Figure 5) with F_L . Thus

$$(mv^2)/r + qE_{\perp} = qvB \quad (5)$$

and

$$\omega_{II} = \frac{v}{r} = \frac{qvB - qE_{\perp}}{mv} < \omega_c \quad (6)$$

If ion II is accelerated by an rf electric field having a frequency equal to the *natural* cyclotron frequency of ion II ($\omega_{rf} = \omega_c = qB/m$), the ion motion and the rf electric field will have different frequencies. Because ω_{II} is a discrete frequency compared to ω_{rf} , the relative phase angle (between ω_{II} and ω_{rf}) changes. It can be seen from eq 6 that $\omega_{rf} > \omega_{II}$, allowing the phase of the applied rf electric field to align with the phase of ion II (initially leading the rf electric field by γ in Figure 5). Conversely, if ion II has a phase angle equivalent to $-\gamma$ (i.e., $\gamma = 181^\circ - 359^\circ$), ω_{II} would be increased by $+qE_{\perp}$, allowing the ion to advance into phase with the applied rf electric field. As the relative phase angle (γ) approaches zero, ω_{II} approaches ω_{rf} due to the alignment of the electric field with the ion motion. When $E_{\perp} = 0$, there is no component of the electric field radially outward and $\omega_{II} = \omega_{rf}$. Thus, ion II remains both resonant and inphase with the applied rf electric field following phase advancement.

In the case where $F_{E\perp}$ is initially negligible with respect to F_L (i.e., $qvB \gg qE_{\perp}$), the frequency shift of ion II caused by the misalignment of the electric field is also small; thus $\omega_{II} \approx \omega_c$. Under these initial conditions the time required for phase advancement (τ_{phase}) of ion II is increased due to the relative force of the magnetic field. Rapid phase synchronization occurs under conditions where the perpendicular component of the applied electric field is significant with respect to the force of the magnetic field. Because the force of the magnetic field is velocity dependent, the relative force on an ion by qvB and qE_{\perp} is also velocity dependent. Therefore, phase advancement occurs more quickly for low-velocity ions.

As shown in Figure 1, an ion that is 180° out of phase will have no perpendicular component of the applied rf electric field. Because the frequency of the out-of-phase ion is the same as the natural cyclotron motion of the ion (i.e., the frequency of the applied rf electric field), phase advancement

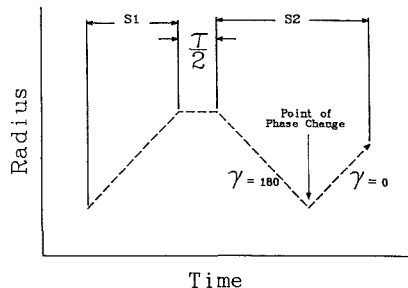


Figure 6. Plot of ion radius versus time. An ion that is decelerated by a second excitation pulse undergoes phase advancement. Following phase synchronization, the ion gains translational energy due to the resonant excitation resulting in a larger cyclotron radius.

does not occur and the ion remains out of phase. A continuous misalignment of the rf electric field with respect to an ion's velocity vector results in deceleration and not phase synchronization. Such an ion is decelerated to a velocity where the force of the electric field is strong with respect to the magnetic field. Under these conditions the ion undergoes phase advancement and moves synchronously with the electric field (46).

The radial velocity of an ion undergoing phase advancement can be determined experimentally in a two-section cell. The sequence used to investigate the radial velocity of an ion during phase advancement is illustrated in Figure 6. Following the ionization pulse, ions of a given m/z value are accelerated to larger cyclotron radii by an rf pulse. The ions are decelerated by a second rf excitation pulse following a delay corresponding to a 180° phase shift. The radius of the out-of-phase ions is reduced until the ions are decelerated to a velocity at which the electric field is no longer negligible. At this interface the ions are "driven" into phase. Following phase synchronization, the ion's radial velocity (radius) increases due to inphase rf excitation.

The radial velocity of I_2^{++} at the point of phase advancement is determined by observing the signal intensity of ions partitioned from source to analyzer regions as a function of the length of the de-excite pulse (see Figure 7). Only ions that are decelerated to radii smaller than the dimensions of the conductance limit are partitioned and observed in the analyzer region. Conversely, ions that are decelerated below the velocity for phase advancement become inphase with ω_{rf} and subsequently gain radial velocity. Ions that gain energy following phase advancement are accelerated to radii sufficiently large to prohibit partitioning. Therefore, the maximum signal intensity of I_2^{++} observed in the analyzer region corresponds to the minimum energy (i.e., smallest radius). Because the minimum energy during the deceleration process corresponds to the radial velocity of the ion undergoing phase advancement, the maximum intensity can be related to the velocity at which phase advancement occurs.

The maximum in the plot contained in Figure 7 occurred after ca. $225 \mu\text{s}$ of rf excitation. Because the initial excitation was $250 \mu\text{s}$ in length, the difference between the two excitation times can be related to the energy of I_2^{++} undergoing phase advancement. I_2^{++} gained ca. 30 eV of energy during the first excitation pulse. Because the energy which was removed by the second excitation corresponds to ca. 25 eV , the energy at which phase advancement occurs is ca. 5 eV .

Phase advancement occurs as $F_{E\perp}$ increases with respect to F_L ; therefore, the length of the de-excitation period is a function of the difference in the initial angular velocity of an ion (v_θ/r) to the angular velocity at which the ion phase advances. Further, ions which are stored in the ion cell with

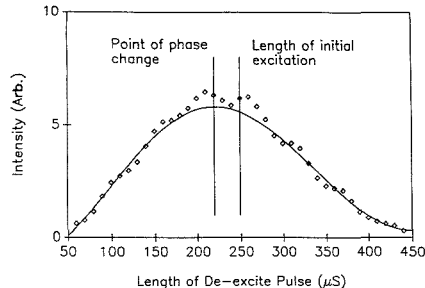


Figure 7. Plot of intensity of I_2^{++} following partitioning as a function of the de-excitation period (S2) subsequent to a $250\text{-}\mu\text{s}$ inphase acceleration. The translational energy of the ion undergoing phase advancement is determined by the difference between the initial energy of the ion and the energy required to reduce its velocity to the point of phase synchronization.

greater than thermal translational energies must interact with the rf excitation for a period of many cyclotron orbits prior to advancing into synchronous motion. Maximum acceleration occurs when the ion's velocity vector is synchronous with the applied excitation. It is important to note that the total excitation time (τ_{total}) of the ion ensemble is limited by the time that an inphase ion can be accelerated prior to ejection from the ICR cell. Because τ_{total} is constant for all ions regardless of phase, different times required for phase advancement (τ_{phase}) result in differences in the net period of excitation of the individual ions of the ensemble

$$\tau_{\text{net}} = \tau_{\text{total}} - \tau_{\text{phase}}$$

The effect of initial radial velocity on the final dimensions of the ion packet has been simulated by trajectory calculations (41). Ion location is determined by calculating the resultant vectors of the electric and magnetic fields. This procedure is used to study the effects of individual factors (i.e., initial kinetic energy) on ion motion. The effects of initial angular velocity on phase synchronization are illustrated by observing the effect of rf excitation for an ion that is initially inphase ($\gamma = 0$) compared to that of an ion that is initially out of phase ($\gamma = 180^\circ$). Figure 8A contains a temporal plot of the calculated trajectories for two ions (m/z 500) having thermal kinetic energies and a relative phase angle of 180° . The trajectories result from acceleration of the ions with a resonant, single frequency rf field (900 v/m). Because the initial radial velocity is low, $F_L \approx F_{E\perp}$, phase advancement and phase synchronization occur quickly and the ions are excited as a coherent packet. Conversely, ions which have initial radial velocities corresponding to 3 eV of kinetic energies follow markedly different trajectories (see Figure 8B). Because $F_L > F_{E\perp}$, the ion which is out of phase experiences a continuous misalignment with the electric field resulting in a different trajectory compared to that of an ion which is initially inphase. The simulations show that instantaneous phase synchronization prior to a net gain of translational energy results in better spatial definition of the ion ensemble following excitation. The spatial distribution of the ion packet following excitation is defined by the relative differences in the temporal locations of the ions comprising the ion ensemble. For example, the ions having well-defined (i.e., coherent) dimensions have negligible differences in their temporal positions relative to the average radius of the ensemble.

Ions which are produced by electron impact have initial velocities which correspond to the translational energies of the neutrals prior to ionization. Owing to the low initial radial velocity of the ions produced, phase advancement of out-of-phase ions occurs quickly and the final radial distribution is

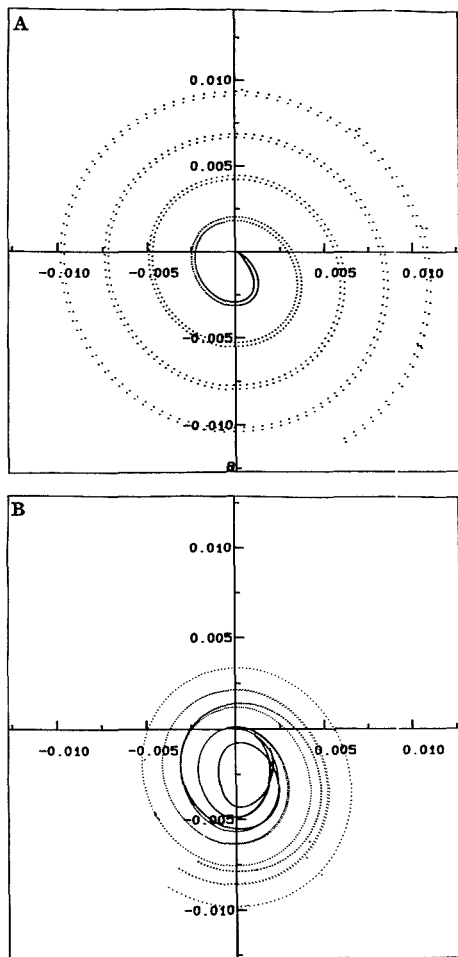


Figure 8. Temporal plots of ion location determined by numerical solution of the equations of ion motion for (A) ions having initially thermal translational energies (0.05 eV) and (B) ions having significant (3 eV) initial radial translational energies. The effect of initial radial velocity on packet coherence following excitation is illustrated by comparing the different trajectories for two ions which are phase shifted by 180° .

small with respect to the radius after excitation. The initial dimensions of the ion population produced by electron impact correspond to the dimensions of the electron beam in the X - Y plane and in the Z direction by the location of the electrostatic trap plates. Diffusion of the ions into the X - Y plane is a function of the ion density and the magnetic field strength. In the absence of space charge effects the diffusion of the ion population into the X - Y plane is also negligible. Because the initial spatial distribution is small and the ion's radial velocity is low, the distribution of cyclotron orbit centers is also small. Conversely, ions which are injected into the ion cell from an external source are given sufficient translational energies to move the ions from the source to analyzer regions. The initial dimensions of the ion population created by ion injection correspond to the focusing characteristics of the ion optics. Optics that have substantial focusing characteristics in the

X - Y plane or produce fringing fields cause redirection of ion velocity into the X - Y plane (47). Therefore, injected ions acquire translational energies of several orders of magnitudes greater than the translational energies of ions which rapidly undergo phase synchronization. The time required for deceleration of ions by out-of-phase excitation produces a significant final radial distribution following excitation of the ensemble of ions.

CONCLUSIONS

As illustrated in the preceding section, rapid phase synchronization of ions is achieved in excitation fields where $F_{E\perp} > F_L$. The high power required to generate an electric field of this magnitude is difficult to use because of the poorly defined excitation field lines which result from cubic ICR cells. It has been shown that ion evaporation along the Z axis occurs as a result of excitation fields which have components of the electric field vectors in the Z direction (48, 49). During high-power excitation, significant electric field gradients are produced along the Z axis which lead to loss of sensitivity (50, 51).

Although phase advancement of ions can occur quickly (i.e., within the period of a single orbit) in excitation fields where $F_{E\perp} > F_L$, phase synchronization occurs over many cyclotron periods in weaker excitation fields. Therefore, phase synchronization can be achieved by long irradiation times during which ions have sufficient time to interact with the rf field. Phase synchronization caused by long irradiation times selectively discriminates against high mass ions. Because the dimensions of the cyclotron radius are dependent on both angular velocity in the X - Y plane and the mass of the ion, high mass ions absorb less energy before being ejected from the ion cell. Thus, the impact of phase synchronization of the ion packet increases with m/z ratio.

The initial distribution of cyclotron orbit centers is a function of radial velocity and m/z ratio. Because the radius of the cyclotron orbit is directly dependent on both the angular velocity in the X - Y plane and the m/z ratio of the ion, high mass ions injected from an external ion source result in a poorly defined distribution of orbit centers. As a result of the initial spatial distribution, significant initial radial velocities, and the inability to phase advance, it becomes increasingly difficult to produce a coherent packet of high mass ions.

Ion detection by FT-ICR is dependent on the production and detection of a well-defined ion ensemble. The inability to produce a spatially defined cyclotron ion packet results in the loss of the expected performance characteristics. For example, the detected image current is directly dependent on the number of ions in the packet and the distance that the packet is from the detection plate. An energy distribution caused by initially high radial velocities and random phases reduces the interaction of the low-energy ions with the receive plates of the ICR cell. Thus, an ion packet which has poor spatial definition suffers loss of sensitivity. In the case of low abundance biomolecules, further signal loss due to other mechanisms for ion evaporation can lead to rapid loss of the time-domain transient signal (i.e., loss of resolution).

ACKNOWLEDGMENT

We wish to thank Dr. R. Kenefick and S. Cornford for many helpful discussions.

LITERATURE CITED

- Gross, M. L.; Rempel, D. L. *Science* **1984**, *226*, 261.
- Wilkins, C. L.; Gross, M. L. *Anal. Chem.* **1981**, *53*, 1661A.
- Russell, D. H. *Mass Spectrom. Rev.* **1986**, *5*, 167-189.
- Wanczek, K. P. *Int. J. Mass Spectrom. Ion Processes*, in press.
- Marshall, A. G. *Acc. Chem. Res.* **1985**, *18*, 316-322.
- Laude, D. A.; Johman, C. L.; Brown, R. S.; Wiel, D. A.; Wilkins, C. L. *Mass Spectrom. Rev.* **1986**, *5*, 107-166.
- Buchanan, M. V.; Cornisarow, M. B. In *Fourier Transform Mass Spectrometry: Evolution, Innovation, and Applications*; ACS Symp. Series

- 359; Buchanan, M. V., Ed.; American Chemical Society: Washington, DC, 1987; pp 1-20.
- (8) Nibbering, N. M. M. *Adv. Phys. Org.* **1988**, *24*, 1.
- (9) Freiser, B. S. In *Techniques for the Study of Ion-Molecule Reactions*; Farrar, J. M., Saunders, W., Eds.; Wiley: New York, 1988.
- (10) Hanson, C. D.; Kerley, E. L.; Russell, D. H. In *Treatise on Analytical Chemistry*, 2nd ed.; Wiley: New York, 1988; Vol. 11, Chapter 2.
- (11) Hunt, D. F.; Shabanowitz, J.; Yates, J. R.; Russell, D. H.; Castro, M. E. *Proc. Natl. Acad. Sci. U.S.A.* **1987**, *84*, 620.
- (12) Ijames, C. F.; Wilkins, C. L. *J. Am. Chem. Soc.* **1988**, *110*, 2687.
- (13) Dunbar, R. C. *Molecular Ions: Spectroscopy, Structure and Chemistry*; North Holland: Amsterdam, 1983; p 231.
- (14) Carlin, T. J.; Freiser, B. S. *Anal. Chem.* **1983**, *55*, 571.
- (15) Bricker, D. L.; Adams, T. A.; Russell, D. H. *Anal. Chem.* **1983**, *55*, 2417.
- (16) Anders, L. R.; Beauchamp, J. L.; Dunbar, R. C.; Baldeschwieler, J. D. *J. Chem. Phys.* **1966**, *45*, 1062.
- (17) Sommer, H.; Thomas, H. A.; Hipple, J. A. *Phys. Rev.* **1951**, *82*, 697; **1949**, *76*, 1877; **1950**, *78*, 806; **1950**, *80*, 487.
- (18) Sommer, H.; Thomas, H. A.; Hipple, J. A. *Phys. Rev.* **1949**, *76*, 1877.
- (19) Sommer, H.; Thomas, H. A.; Hipple, J. A. *Phys. Rev.* **1950**, *80*, 487.
- (20) Barber, M.; Bordoli, R. S.; Elliot, G. J.; Sedgwick, R. D.; Tyler, A. N. *Anal. Chem.* **1982**, *54*, 645A.
- (21) Benninghoven, A.; Jaspers, D.; Sichteremann. *Appl. Phys.* **1976**, *11*, 35.
- (22) Posthumus, M. A.; Kistemaker, P. G.; Meuzelaar, H. L. C.; TenNoever de Brauw, M. C. *Anal. Chem.* **1978**, *50*, 985.
- (23) McCrery, D. A.; Ledford, E. B.; Gross, M. L. *Anal. Chem.* **1982**, *54*, 1437.
- (24) Castro, M. E.; Russell, D. H. *Anal. Chem.* **1984**, *56*, 578.
- (25) Comisarow, M. B.; Marshall, A. G. *Chem. Phys. Lett.* **1974**, *25*, 282.
- (26) Marshall, A. G.; Comisarow, M. B.; Parisod, G. *J. Chem. Phys.* **1979**, *71*, 4434-4444.
- (27) Wilkins, C. L.; Gross, M. L. *Anal. Chem.* **1981**, *53*, 1661A.
- (28) Hanson, C. D.; Castro, M. E.; Russell, D. H.; Shabanowitz, J. In *Fourier Transform Mass Spectrometry: Evolution, Innovation, and Applications*; Buchanan, M. V., Ed.; ACS Symposium Series 359; American Chemical Society: Washington, DC, 1987; pp. 100-115.
- (29) Grese, R. P.; Rempel, D. L.; Gross, M. L. In *Fourier Transform Mass Spectrometry: Evolution, Innovation, and Applications*; Buchanan, M. V., Ed.; ACS Symposium Series 359, American Chemical Society: Washington, DC, 1987; pp 34-59.
- (30) Ledford, E. B.; Rempel, D. L.; Gross, M. L. *Anal. Chem.* **1984**, *56*, 2744-2748.
- (31) Rempel, D. L.; Huang, S. K.; Gross, M. L. *Int. J. Mass Spectrom. Ion Processes* **1986**, *70*, 163-184.
- (32) Comisarow, M. B.; Marshall, A. G. *J. Chem. Phys.* **1976**, *64*, 110.
- (33) Marshall, A. G. *Anal. Chem.* **1979**, *51*, 1710.
- (34) McIver, R. T.; Ledford, E. B.; Hunter, R. L. *J. Chem. Phys.* **1980**, *72*, 2555.
- (35) Buttrill, S. E. *J. Chem. Phys.* **1969**, *50*, 5690.
- (36) Besuchamp, J. L. *J. Chem. Phys.* **1967**, *46*, 1231.
- (37) Marshall, A. G. *J. Chem. Phys.* **1971**, *55*, 1343-1354.
- (38) Ghaderi, S.; Littlejohn, D. In *Proceedings of the 33rd Annual Conference on Mass Spectrometry and Allied Topics, San Diego*; American Society for Mass Spectrometry, 1984; p 727.
- (39) Kerley, E. L.; Russell, D. H. *Anal. Chem.* **1989**, *61*, 53-57.
- (40) Hanson, C. D.; Kerley, E. L.; Russell, D. H. *Anal. Chem.* **1989**, *61*, 83-85.
- (41) Baykut, G.; Watson, C. H.; Eyley, J. R. In *Proceedings of the 36th Annual Conference on Mass Spectrometry and Allied Topics, Denver*; American Society for Mass Spectrometry, 1987; pp 387-388.
- (42) Marshall, A. G.; Wang, T. L.; Ricca, T. L. *Chem. Phys. Lett.* **1984**, *107*, 233.
- (43) Pflander, P.; Bodenhausen, G.; Rapin, J.; Houriet, R.; Gaumann, T. *Chem. Phys. Lett.* **1987**, *139*, 195.
- (44) Hanson, C. D.; Kerley, E. L.; Castro, M. E.; Russell, D. H. In *Proceedings of the 37th Annual Conference on Mass Spectrometry and Allied Topics, San Francisco*; American Society for Mass Spectrometry, 1988; p 612.
- (45) Kerley, E. L.; Hanson, C. D.; Russell, D. H., unpublished results at Texas A&M University, 1989.
- (46) McIver, R. T.; Hunter, R. L.; Baykut, G. *Anal. Chem.* **1989**, *61*, 489.
- (47) Kerley, E. L.; Hanson, C. D.; Castro, M. E.; Russell, D. H., manuscript in preparation, to be submitted to *Anal. Chem.*
- (48) Huang, S. K.; Rempel, D. L.; Gross, M. L. *Int. J. Mass Spectrom. Ion Processes* **1986**, *72*, 15.
- (49) Kotel, P. M.; Allemann, M.; Kellerhals, H.; Wanczek, K. P. *Int. J. Mass Spectrom. Ion Processes* **1985**, *65*, 97.
- (50) van der Hart, W. J.; van de Guchte, W. J. *Int. J. Mass Spectrom. Ion Processes* **1988**, *82*, 17.
- (51) Shibanowitz, J., personal communication.

RECEIVED for review December 2, 1988. Accepted May 30, 1989. This work was supported by the National Institutes of Health-General Medical Sciences (GM-33780) and the National Science Foundation (CHE-8418457). Some of the equipment was purchased from funds provided by the TAMU Center for Energy and Mineral Resources. We gratefully acknowledge the Texas Agricultural Experiment Station for providing a portion of the funds for purchase of the Nicolet FTMS 1000 mass spectrometer.

Comparison of Sample Preparation Methods for the Fourier Transform Infrared Analysis of an Organo-Clay Mineral Sorption Mechanism

John M. Bowen,* Senja V. Compton,¹ and M. Sterling Blanche

Western Research Institute, P.O. Box 3395, University Station, Laramie, Wyoming 82070

Several methods of sample preparation and Fourier transform infrared (FT-IR) analysis techniques for the observation of a sorption interaction between a clay mineral and an organophosphate were compared to determine if spectral changes induced by these methods would change the interpretation of the sorption interaction. The methods of sample preparation included the traditional free-standing (unsupported) thin clay films, supported thin clay films, and KBr disks. The FT-IR analysis techniques examined were photoacoustic spectroscopy (PAS) and diffuse reflectance spectroscopy (DRIFT). The organo-mineral interaction used as a model for this study was between dimethyl methylphosphonate and calcium saturated montmorillonite. The results showed that none of the methods affected the interpretation of the sorption interaction. It was found that the spectra obtained by using the KBr disk method, the method most likely to affect the interaction, did not change with time. Thus, interpretation of the sorption mechanism due to the loss of interlamellar water or the exchange of the clay interlamellar cation with K^+ from the KBr matrix did not change as a function of preparation method or detection method.

INTRODUCTION

The transport of organic contaminants through porous media, and the computer modeling of that transport, are of great importance for the prediction of groundwater quality at present (1). Germane to this is the characterization of interactions between mineral surfaces and organic compounds that are implicated as environmental contaminants (2-4). Through the use of Fourier transform infrared (FT-IR) spectroscopy, the mechanism of an organo-mineral sorption interaction can be determined by an analysis of the direction and magnitude of band shifts and intensity variations when the spectrum of the organic compound is compared against that of the organo-mineral complex (5-7).

The methods traditionally used in the analysis of organo-mineral interactions have included KBr disks and unsupported clay films. The use of KBr disks has been discouraged, especially when the mineral is a swelling clay such as montmorillonite, to avoid possible artifacts caused by the supporting material, which could change the interpretation of the interaction (8-11). Interactions between a support material and a sample affect the positions or intensities of the vibrational bands in the infrared spectrum of the organo-mineral complex. Thus, the method of choice for the infrared analysis of organo-mineral interactions has been the use of a thin unsupported film of the mineral cast from a smooth surface, treated with the organic compound, and suspended in the IR beam. This ensured that no unwanted interactions would take

place between the organo-mineral complex and the support material (8, 12, 13). However, thickness reproducibility is difficult to attain with the unsupported film method, causing problems with spectral replication and signal to noise levels. If the films are thick enough to be self-supporting, the result can often be total absorption of the IR energy below about 1100 cm^{-1} . In addition, any instrumental nonlinearity on the absorbance scale results in a poor comparison of band ratios observed for thick and thin films. It is of interest, therefore, to determine the effects of various sample preparation techniques on a particular organo-mineral interaction.

For this study, four sampling methods were compared against the recommended thin unsupported clay film methodology. These included thin clay films supported on a ZnSe plate, KBr disks, and two newer methods of detection that utilize little or no sample preparation, photoacoustic spectroscopy (PAS) and diffuse reflectance spectroscopy (DRIFT). The organo-clay complex used in this study is the interaction between dimethyl methylphosphonate (DMMP) and calcium saturated montmorillonite (SAZ-1). Spectral quality, ease of sample preparation, and changes in the interpretation caused by sample preparation effects are discussed in this study.

EXPERIMENTAL SECTION

Two infrared spectrometers were used in this study. The thin-film and KBr studies were performed on a Nicolet MX-1 FT-IR equipped with a room-temperature deuterated triglycine sulfate (DTGS) detector. The thin-film and KBr disk data were collected at 1-cm^{-1} resolution at 160 scans. A Digilab FTS-65 spectrometer equipped with a room-temperature DTGS detector was used for the photoacoustic (PAS) and diffuse reflectance (DRIFT) studies. The Bio-Rad PAS accessory consisted of a sample cube, microphone, and associated electronics, was equipped with a KBr (potassium bromide) window, and was fitted with a 9-mm-deep sample cup. Carbon lamp black powder (Fisher Scientific Co., Fair Lawn, NJ) was used as the background reflectance material. The spectra were recorded at 2-cm^{-1} resolution with a measurement time of 8 min. The Spectra-Tech (Stamford, CT) diffuse reflectance accessory was used for the DRIFT studies. Diamond powder (Spectra-Tech) was used as the background reference material as well as the sample diluent to minimize any effects of cation exchange or hydration, which could possibly arise from the use of alkali halide diluent. The spectra were recorded at 1-cm^{-1} resolution, with a measurement time of 15 min. Details of the experimental procedures for PAS and DRIFT are discussed elsewhere (14). Although the spectra showed differences between instruments, as different methods of detection and detectors were involved, the spectra derived from each instrument were internally consistent.

Montmorillonite clay (SAZ-1) was obtained from the Clay Minerals Society Repository, University of Missouri, Department of Geology. The SAZ-1 montmorillonite was saturated with Ca^{2+} or K^+ . The clay was suspended in a 1 M $CaCl_2$ or KCl solution for a day. After saturation, the sample was washed repeatedly with deionized water, and dried at room temperature.

The dimethyl methylphosphonate was acquired from Alfa Chemicals (Danvers, MA). After FT-IR validation of its spectrum for positive identification (15), the DMMP was used without further purification.

* Author to whom correspondence should be addressed.

¹ Bio-Rad, Digilab Division, 237 Putnam Ave., Cambridge, MA 02139.

Reference DMMP spectra were acquired by each of the methods for comparison among the techniques. A KBr reference blank was prepared by dispersing the neat compound into powdered KBr pressed at 8 tons for 1 min to produce a KBr disk with interspersed DMMP. FT-IR analysis showed that the DMMP absorption bands correspond to those frequencies reported for neat smears of DMMP (15, 16). The DRIFT measurement was done by intimately mixing the DMMP in diamond powder, while the PAS measurement is of the DMMP in the PAS sample cell. In the case of the PAS spectrum of the DMMP, the P=O band appeared to be 4 cm^{-1} lower than the same band from the KBr method. This effect may be due to the fact that PAS is also observing the vapor-phase DMMP in the PAS sample chamber in addition to the neat liquid form (17).

In all cases, the organo-clay complex was made by vapor deposition of the DMMP at 40 °C. The samples were separated and analyzed in triplicate by each method. The KBr disks were made from an approximate weight of 0.1 g of a mixture prepared as a 100:1 ratio of infrared grade KBr to organo-clay complex. The disks were examined immediately upon manufacture. Time study samples were stored under desiccation and were reexamined at intervals of 1, 3, 4, 6, and 10 days.

Unsupported thin clay films were made by deposition of the clay slurry onto a sheet of polystyrene. After air-drying at room temperature, the thin films were removed by bending the coated sheet across a sharp edge. Supported clay films were manufactured by depositing a clay-water slurry on a ZnSe plate and allowing the clay slurry to air-dry at room temperature. These procedures were followed by vapor deposition of DMMP.

Spectra of the Ca^{2+} and K^+ saturated montmorillonite and the organo-clay complexes were collected in triplicate by using each of the five techniques mentioned previously. KBr disk spectra of these materials and the corresponding organo-clay complexes were obtained in order to compare the effect of the cation exchange of K^+ for Ca^{2+} on the spectra.

RESULTS AND DISCUSSION

The model interaction, which is described in detail elsewhere (7, 12) has been determined with some certainty to proceed through $d-\pi$ backbonding between the P=O moiety of DMMP and the interlamellar cation of the montmorillonite clay. This apparent mechanism is deduced from the observation of shifts in the vibrational bands of the DMMP molecule from their position in the FT-IR spectrum of the pure compound. Although all of the band shifts were considered to determine the interaction mechanism, for the purpose of this comparison, only the P=O band shift is considered. This band undergoes the largest shift, approximately 32 cm^{-1} to lower frequencies for the Ca^{2+} saturated SAZ-1 and 22 cm^{-1} for the K^+ saturated clay, and is slightly dependent upon detection technique. In order for a sample preparation effect to change the interpretation of the organo-clay sorption mechanism, this band shift would have to undergo a change in magnitude or direction. Possible sample preparation effects that might cause changes in the shift of the organo-mineral complex bands include exchange of K^+ ions from the KBr for the interlamellar cations in the clay mineral. If a significant amount of cation exchange were to take place, the P=O band shift would be expected to decrease to about 22 cm^{-1} , the shift observed for K^+ saturated SAZ-1 montmorillonite. A similar decrease in band shift could be expected if the interaction were to proceed through a hydration sphere. Another change that could affect the interpretation would include a change in the amount of the interlamellar water, inclusive of the cationic hydration sphere. This could be observed by a change in the magnitude of the OH stretch region around 3600 cm^{-1} , as well as in the magnitude of the P=O shift.

After the organo-mineral complexes were prepared, the position of the P=O band was determined. The band shifts were calculated from the P=O band position of the organo-clay complex compared against that of the DMMP found from the same instrumental technique, as described above.

Table I. P=O Band Positions and Shifts for Each of the Five Sample Preparation Techniques or Detection Methods

method	P=O position, ^a cm^{-1}		shift, cm^{-1}
	DMMP	DMMP-clay complex	
KBr disk	1245 ^a	1213	32
unsupported thin film	1245 ^a	1211	34
supported thin film	1245 ^a	1212	33
FT-IR/PAS	1241 ^b	1210	31
	1245 ^a		35
FT-IR/DRIFT	1243 ^c	1211	32
KBr disk of K^+ -SAZ-DMMP	1245 ^a	1223	22

^a Location of P=O band of DMMP smeared on KBr disk.

^b Location of P=O band obtained with PAS cell. As this results in a vapor spectrum, this is also compared against neat DMMP.

^c Location of P=O band obtained with DRIFT cell. ^d FT-IR/PAS wavenumber assignments were 2- cm^{-1} resolution; all others were 1- cm^{-1} resolution. Wavenumbers listed refer to the highest datum point.

The positions and related shifts of the P=O band for each technique have been listed in Table I. It is apparent from these results that the magnitude of the shift of the P=O band in the Ca^{2+} -clay-DMMP complex is in all cases $32.4 \pm 3 \text{ cm}^{-1}$ compared with a shift of 22 cm^{-1} for the K^+ -clay-DMMP complex. The high value was obtained from the unsupported thin clay film and diffuse reflectance methods while the low value was obtained by PAS, measured from the PAS position of neat DMMP. However, it is well-known that PAS tends to enhance the spectra of gases and otherwise weak bands. The PAS spectrum of neat DMMP is mainly due to the vapor phase of the sample in the PAS cell rather than the condensed phase (2, 17). Therefore, the P=O band shift given in Table I has also been compared against the position of neat DMMP smeared on a KBr disk, as it would be inappropriate to compare the complexed DMMP band position with that of vapor-phase DMMP. It is apparent from the wavenumber shifts that all of the sample preparation techniques provide equivalent data, enabling the identical interpretation to be made from each of the techniques.

Of the sample preparation techniques studied, the KBr disk technique offers the greatest potential to affect the shift of the P=O band through the reaction with the KBr supporting material, due to the intimate contact between the sample and the support. Therefore, the organo-clay complex prepared as the KBr disk was subjected to a time study where the sample was sampled periodically over a 10-day period. It can be seen in Figure 1 that the location of the P=O band did not change during the period of the study. A gradual loss of water in the sample, with time, was seen to take place through the observation of the decrease in the intensity of the O-H stretching region around 3300 cm^{-1} , indicating a slow loss of water associated with the clay mineral by the KBr or desiccant. Whatever the cause of the reaction, it is quite slow compared to the time required to obtain a spectrum. Thus, spectra obtained quickly are unlikely to be affected by dehydration effects. Presumably, most investigators would be able to obtain a spectrum of the sample before this effect became significant.

Figure 2 shows representative spectra obtained from the unsupported thin clay film, the clay film supported on a ZnSe window, and the KBr disk technique. The unsupported clay film shown was the thinnest that could be made self-supporting, but was still thick enough to almost completely absorb the IR energy below about 1100 cm^{-1} . Due to this effect, the P=O band is nearly saturated, making the determination of the peak position difficult. The spectrum of the supported film is thin enough that saturation of the in-plane Si-O stretch

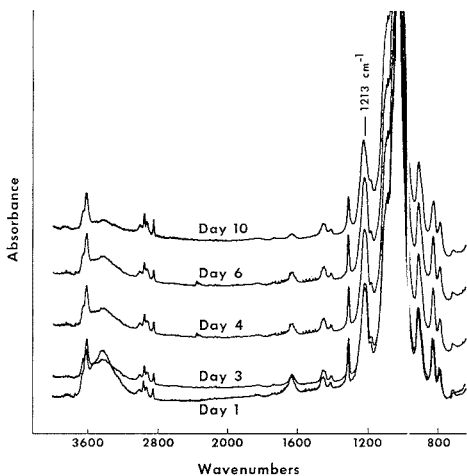


Figure 1. FT-IR spectra of DMMP-Ca montmorillonite in a KBr disk taken with time.

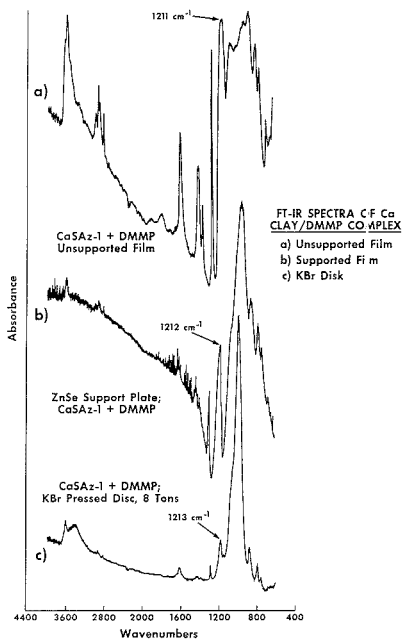


Figure 2. FT-IR spectra of DMMP-Ca montmorillonite complex obtained by differing methods: a, unsupported film; b, thin film supported on a ZnSe disk; c, in a KBr disk.

at $\sim 1100\text{ cm}^{-1}$ is not significant. However, even after desiccation, the spectrum around 1650 cm^{-1} is obscured by the rotational spectrum of water vapor, indicative of free water desorbing from the surfaces of the clay mineral. As sufficient time was allowed for nitrogen to purge the sample compartment, the water vapor in the spectrum is assumed not to come from the atmosphere. The OH stretch region is also obscured by these vapor bands and exhibits very low intensity when compared to the KBr disk spectrum. Both of the thin clay

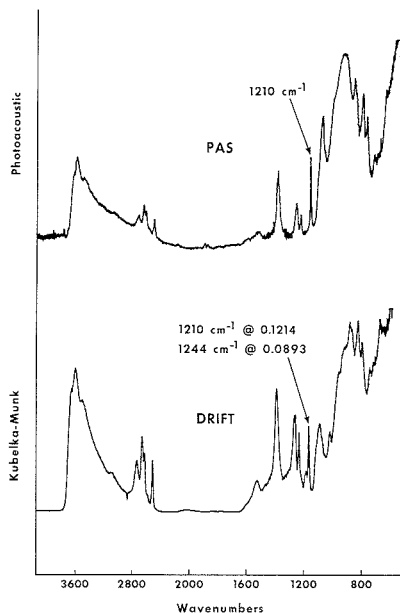


Figure 3. FT-IR spectra of the DMMP-Ca montmorillonite complex obtained by PAS and diffuse reflectance (DRIFT).

film samples required overnight drying, while the KBr disk sample was run immediately upon preparation. Of these three traditional techniques, the KBr disk method provided the most reproducible spectra due to the ability to precisely control the amount of the organo-clay complex in the sample examined.

Figure 3 illustrates spectra of the DMMP-clay complex obtained by PAS and diffuse reflectance. These techniques require little sample preparation and provide reproducible spectra. Further, it has been shown that PAS will provide equivalent information for this sorption mechanism (12). These spectra are similar to those produced by the methods described above but differ in the mechanism of energy detected. As photoacoustic spectroscopy is much more sensitive to gases than the other methods (14), the fine structure of water vapor, outgassed into the PAS cell during the data collection period, is observed in the OH stretch region at around 3300 cm^{-1} and the HOH bending regions around 1635 cm^{-1} . Although these spectra were not spectrally subtracted from spectra of the pure mineral phase for this study, this practice can be used to enhance the spectrum of the organo-mineral complex. Rockley and Rockley (12), using this method, reported that PAS spectra underwent spectral subtraction more reliably than spectra from the KBr disk method.

The diffuse reflectance spectra were also valuable in determining surface interactions not detected in the other methods. They showed that although the major portion of the P=O band was shifted to about 1210 cm^{-1} , a small P=O band exists at around 1244 cm^{-1} possibly due to the presence of uncomplexed DMMP on the surface of the clay mineral.

CONCLUSIONS

The interpretation of a particular sorption interaction mechanism between an organophosphonate and montmorillonite, a swelling clay mineral, is independent of the sample preparation technique or instrumental detection method used to obtain a spectrum. Within the detection ability of FT-IR,

the use of KBr as a supporting substrate did not influence the interpretation of this sorption interaction over a period of 10 days.

Of the five techniques, the most satisfactory in terms of spectral quality and ease of use were the PAS and diffuse reflectance methods. As with the thin-film techniques, these methods absolutely ensure that no sample/substrate interactions can take place. Interactions severe enough to change the interpretation of the sorption mechanism appear to be unlikely with even the KBr disk method if the samples are analyzed in a timely fashion. These techniques also provide information concerning the surface of the samples, such as the presence of unadsorbed organic compound as evidenced by diffuse reflectance.

LITERATURE CITED

- (1) Hounslow, A. W. In *Proceedings of the First International Conference on Ground-Water Quality Research*; Ward, C. H., Ed.; John Wiley and Sons: New York, 1984.
- (2) Hermosin, M. C.; Perez Rodriguez, J. L. *Clays Clay Miner.* **1981**, *29*, 143-152.
- (3) Garwood, G. A.; Condrate, R. A. *Clays Clay Miner.* **1978**, *26*, 273-278.

- (4) Farmer, V. C. *Soil Sci.* **1971**, *112*, 62-68.
- (5) Fueti, P.; Ristori, G. G.; Cecconi, S.; Franci, M. *Clays Clay Miner.* **1983**, *31*, 312-314.
- (6) Isaacson, P. J.; Sawhney, B. L. *Clay Miner.* **1982**, *18*, 253-256.
- (7) Bowen, J. M.; Powers, C. R.; Ratcliffe, A. E.; Rockley, M. G.; Hounslow, A. W. *Environ. Sci. Technol.* **1988**, *22*, 1178-1181.
- (8) White, J. L. *Soil Sci.* **1971**, *112*, 22-31.
- (9) Salzman, S.; Yariv, S. *Soil Sci. Soc. Am. Proc.* **1975**, *39*, 474-479.
- (10) Farmer, V. C. *Spectrochim. Acta* **1957**, *8*, 374-389.
- (11) Shuval, S.; Yariv, S. *Clays Clay Miner.* **1979**, *27*, 19-28.
- (12) Rockley, M. G.; Rockley, N. L. *Appl. Spectrosc.* **1987**, *106*, 471-475.
- (13) Theng, B. J. K. *The Chemistry of Clay Organic Reactions*; John Wiley and Sons: New York, 1974.
- (14) Griffiths, P.; de Haseth, J. *Fourier Transform Infrared Spectroscopy*; John Wiley and Sons: New York, 1986.
- (15) Van der Veken, B. J.; Herman, M. A. *Phosphorus Sulfur* **1981**, *10*, 357-362.
- (16) Pouchart, C. F. *The Aldrich Library of FT-IR Spectra*, ed. I; Aldrich Chemical Co.: Milwaukee, WI, 1985.
- (17) Davis, D. M.; Hoffland, L. D. *SPIE 1985 Fourier Comput. Infrared Spectrosc.* **1985**, *553*, 146, 147.

RECEIVED for review February 21, 1989. Accepted June 20, 1989. The authors express appreciation to the U.S. Department of Energy for funding this work under Cooperative Agreement DE-FC21-86MC11076.

Enhanced Analysis of Poly(ethylene glycols) and Peptides Using Thermospray Mass Spectrometry

Saul W. Fink and Royal B. Freas*

Department of Chemistry, University of Houston, Houston, Texas 77204-5641

The effects of a needle-tip repeller electrode on thermospray mass spectra of poly(ethylene glycols) and peptide samples have been studied. A significant increase in ion current was observed for increased repeller potentials in the low-mass region (m/z 300 to m/z 1100) and the high-mass region (m/z 1100 to m/z 1900). The change in ion current is due to a change in ion extraction efficiency because of increased ion diffusion rates. The amount of peptide sample needed for direct injection studies was decreased 1 to 2 orders of magnitude by using an ion source with both a needle-tip repeller electrode and a restricted vaporizer probe tip.

INTRODUCTION

Liquid chromatography/mass spectrometry (LC/MS) facilitates analyses of polar, nonvolatile, and thermally labile compounds. The thermospray technique has proven to be a useful and practical methodology as an LC/MS interface (1-4). Thermospray is an ionization technique as well as an interface for LC/MS (5-7). Ions can be generated with and without supplemental ionization (5). Thermospray ionization (without supplemental ionization) is a "soft" ionization process. That is, the mass spectra exhibit abundant molecular ions and little or no fragmentation. Therefore, molecular weight information of a sample can be obtained, although structural information is often unavailable.

Thermospray and other soft ionization techniques have expedited the use of mass spectrometry to analyze biomolecules (8). Rapid peptide sequencing with sensitive detection using thermospray mass spectrometry has been reported using on-line column enzymatic hydrolysis by immobilized car-

boxypeptidase Y (9). Hemoglobin variants have been identified in peptide mapping studies by using thermospray mass spectrometry (10). Other studies of peptides and proteins using thermospray have been conducted (11).

The thermospray ion source has been modified recently to increase the versatility and sensitivity of the technique. These modifications include a smaller desolvation chamber, an auxiliary tip heater, and a repeller electrode inside the ion source block (12). Several repeller electrode geometries have been designed and studied (12-18). A blunt-tip repeller electrode has been used to induce fragmentation of several compounds (12-15). A needle-tip repeller electrode has been shown to improve high mass sensitivity (greater than m/z 1100) (16-18).

We have constructed a needle-tip repeller electrode to study the effect it has on the thermospray mass spectra of poly(ethylene glycol) (m/z 300 to m/z 1900) and peptide and protein samples. In addition, a smaller orifice for the vaporizer probe tip has been used to increase sensitivity. The smaller orifice produces smaller droplets, which increases ion abundances by increasing ion evaporation (12, 16-18). By use of the needle-tip repeller electrode and a smaller vaporizer probe tip orifice, the detection limits for the peptide samples studied on our instrument have been lowered. We discuss the results of these improvements in this paper.

EXPERIMENTAL SECTION

A thermospray ion source (Vestec Thermospray LC-MS Model 721A) was used to interface a liquid chromatographic gradient system (Scientific Systems, Inc., Model 230) to a quadrupole mass spectrometer (Hewlett-Packard Model 5988A). The poly(ethylene glycol) (PEG) samples were introduced into the mass spectrometer

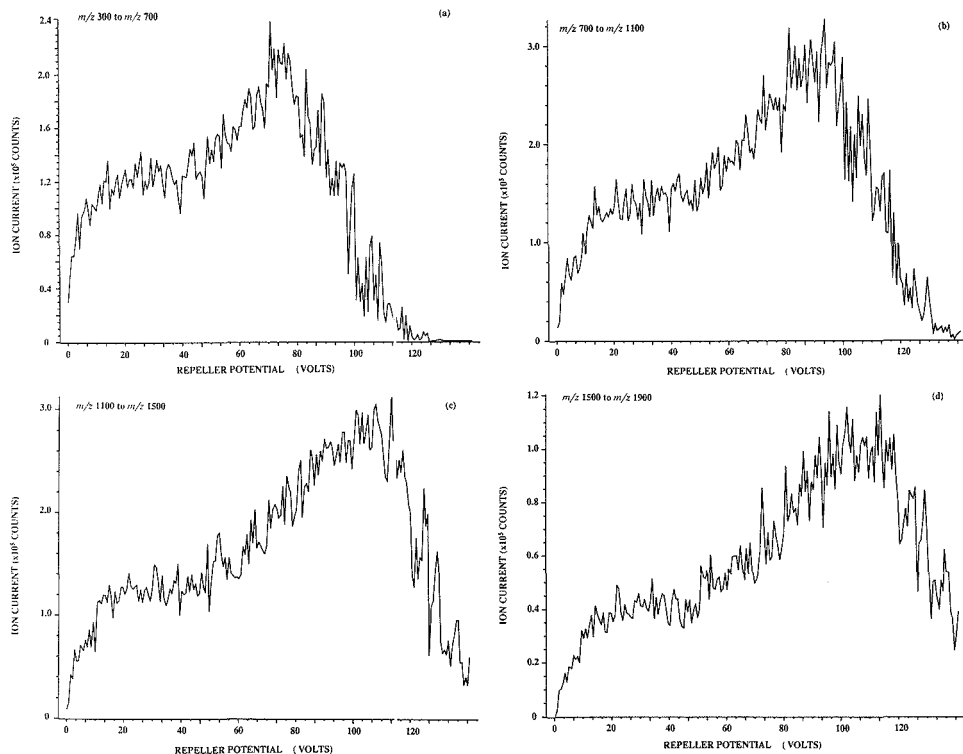


Figure 1. (a) A plot of repeller potential versus ion current showing the effect of increasing repeller potentials for positive ions of PEG from m/z 300 to m/z 700. (b) A plot of repeller potential versus ion current showing the effect of increasing repeller potentials for positive ions of PEG from m/z 700 to m/z 1100. (c) A plot of repeller potential versus ion current showing the effect of increasing repeller potentials for positive ions of PEG from m/z 1100 to m/z 1500. (d) A plot of repeller potential versus ion current showing the effect of increasing repeller potentials for positive ions of PEG from m/z 1500 to m/z 1900.

by direct flow. The peptide and protein samples were introduced with an injection system (Rheodyne Model 7125) fitted with a 20- μ L loop.

The ion source and vaporizer temperatures for these studies were optimized to give maximum response for each sample. The auxiliary tip heater was adjusted so a temperature of 330–325 °C was maintained. The temperatures for the PEG studies were inlet temperature $T_1 = 95$ –96 °C, vaporizer exit temperature $T_2 = 255$ –265 °C, downstream vapor temperature = 285–300 °C, and block temperature = 355–360 °C. The temperature for the peptide and protein samples were inlet temperature $T_1 = 82$ –85 °C, vaporizer exit temperature $T_2 = 230$ –250 °C, downstream vapor temperature = 270–285 °C, and block temperature = 365–380 °C.

The mobile phase used was 0.1 M ammonium acetate dissolved in deionized water and filtered with a 0.45- μ m filter. The flow rate was 1.0 mL/min. The PEG solution was prepared by mixing equimolar amounts (1×10^{-4} M) of four samples of PEG, which had average molecular weights of 300, 600, 1000, and 1450. Solutions of bradykinin and angiotensin I with concentrations ranging from 1×10^{-4} to 1×10^{-6} M were prepared with the mobile phase. The reagents were obtained commercially and they were used without further purification or filtration.

The needle-tip repeller electrode consisted of a threaded rod machined to a fine point (0.1 mm diameter) and placed opposite the ion exit aperture in the ion source block. The tip of the repeller electrode was located 2 mm from the ion exit aperture. This distance was optimal for signal response on our instrument (19). The vaporizer probe was modified as described elsewhere (23) to include a tip with a fused silica capillary tube (10 μ m i.d.) for the PEG studies and a stainless steel capillary tube (100 μ m i.d.) for the peptide studies. A fused silica capillary tube was not

easily aligned with the probe axis and it was not easily cleaved to present an aperture face perpendicular to the spray axis. Both of these defects can deform and deflect the vaporized spray away from the ion sampling region. The alignment and perpendicular cleavage are more easily made for a stainless steel capillary tube. Using a stainless steel capillary tube has resulted in better signal-to-noise ratios and greater reproducibility than when using the fused silica capillary tube, presumably due to a better defined and centered thermospray jet.

RESULTS AND DISCUSSION

Needle-Tip Repeller Studies. The effects of applying potentials to the needle-tip repeller electrode are displayed in the positive ion chromatograms of PEG shown in Figure 1. We observed about an order of magnitude increase in low-mass (m/z 300 to m/z 1100) ion current as well as for high-mass (m/z 1100 to m/z 1900) ion current. A similar increase in low- and high-mass ion current was seen for negative ions, as shown in Figure 2. Robbins and Crow had previously reported that a needle-type of repeller electrode improves high mass sensitivity for PEG samples, but they did not report any effect for ions less than m/z 1000 (16). Figure 3 shows a plot of the repeller potential that gave the maximum ion current at intervals of every 100 mass units. The repeller voltage was stepped every 10 V. Within error limits, the plot shows the same linear correlation for both negative and positive ions.

One possibility for increased low-mass ion current with increasing needle-tip repeller potentials may be due to increased fragmentation of high-mass ions. A blunt-tip repeller electrode has been used to induce fragmentation of several compounds (15, 16). However, the blunt-tip repeller has not been reported to

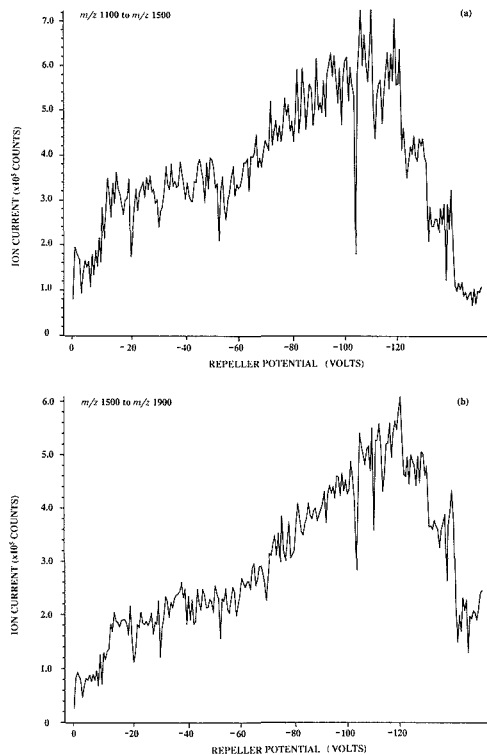


Figure 2. (a) A plot of repeller potential versus ion current showing the effect of increasing repeller potentials for negative ions of PEG from m/z 1100 to m/z 1500. (b) A plot of repeller potential versus ion current showing the effect of increasing repeller potentials for negative ions of PEG from m/z 1500 to m/z 1900.

Repeller Potential at Maximum Ion Response

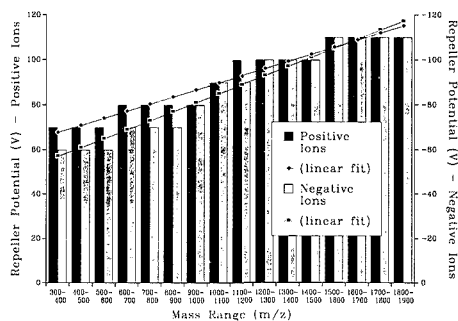


Figure 3. Plot of the repeller potentials (± 10 V) that give the maximum ion current for mass range intervals of 100 mass units. The results for positive and negative ions are nearly identical within error limits and linearly increase with mass.

increase sensitivity. Figure 4 is a mass spectrum of PEG from m/z 300 to m/z 700 at a repeller potential of 70 V. The most abundant ions correspond to ammoniated and protonated molecules. No significant differences other than absolute ion abundances were observed between this spectrum and a mass spectrum obtained at a repeller potential of 0 V. No fragmentation was observed. Thus, the increase in ion current can be attributed

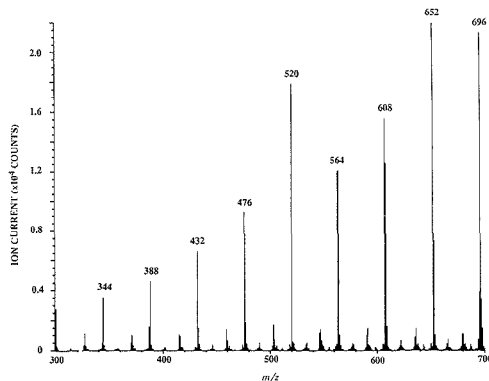


Figure 4. Positive-ion mass spectrum of PEG from m/z 300 to m/z 700 at a constant repeller potential of 70 V. The major ions correspond to $[M + \text{NH}_4]^+$ adducts. No significant fragmentation was observed, and the spectrum is qualitatively similar to that taken at a repeller potential of 0 V.

to an increase in abundance of molecular species and it is not due to fragmentation.

The ion current was observed to reach a maximum and then to decrease more rapidly than it increased. The maximum responses for the low-mass ions occur at lower repeller potentials (70–90 V) than for the high-mass ions (greater than 90 V). This suggests that the operative mechanism for ion-current enhancement is proportional to the mass of the ion. There are several plausible explanations for the enhanced ion current. One possible explanation is increased ion extraction efficiency from the ion source due to increased ion diffusion (discussed below). Another possible explanation is an increased abundance of ions because of field-assisted ion evaporation from the droplets. A third possibility is field ionization of neutral species. This latter is probably not an important effect because the field generated by the needle-tip repeller potential at 100 V is roughly 10^8 V/m, about 2 to 3 orders of magnitude less than that required for field ionization (20).

If ion diffusion is the operative effect, then there should be a mass dependence for the change in ion current. The equations that correlate ion diffusion (or mobility) through a plasma establish that heavier ions diffuse more slowly than lighter ions (21). We observed a similar corresponding change in ion current when increasing the repeller potentials. That is, the ion current due to low-mass ions increased at lower repeller potentials than did the high-mass ions. This suggests that the change in ion current is due to an increase in ion diffusion rates.

The ion current decreased more rapidly past the maximum, then it increased (Figures 1 and 2). This suggests that the ions are not extracted efficiently from the ion source at higher repeller potentials. One cause for this is that the ions may be deflected away from the ion exit aperture due to the increased (repeller) field. As stated above, the low-mass ion current increased at lower repeller potentials while the high-mass ion current increased at higher potentials. Therefore, the low-mass ions would be deflected away at lower repeller potentials than high-mass ions. Observation of this further suggests the change in ion current is due to an increase in the ion diffusion rates.

The increase in ion currents may also be due to an increase in the ion evaporation process. We suggest two possible explanations for an increase in ion evaporation. One possibility is due to the production of smaller droplets by the new vaporizer probe tip (16, 17). For smaller droplets, a greater charge-to-surface-area ratio for the droplets is maintained, thereby facilitating ion expulsion from the droplet. Another possibility is field-assisted ion evaporation, where the electrostatic repeller field induces expulsion of the ions from the droplets formed during the thermospray process (22). The increase in ion evaporation, which can lead to an increase in ion currents, can be a combination of both possibilities. However, it is unclear exactly how field-assisted ion

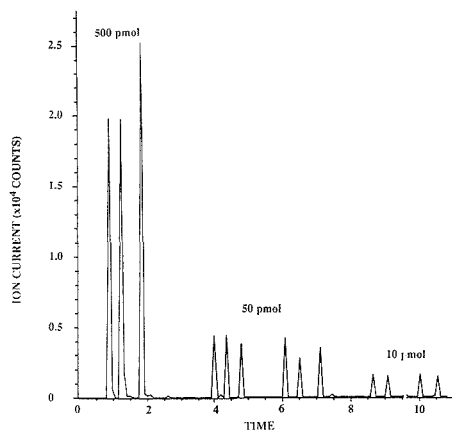


Figure 5. Total ion chromatogram of directly injected samples containing 500, 50, and 10 pmol of bradykinin.

evaporation should show a mass dependence. If the repeller effect were due solely to increased ion evaporation, the ion current would reach a plateau at a certain repeller potential. A decrease in ion current (as was observed) would not be expected. Thus, we believe that the PEG data represent increased ion extraction efficiency due to increased ion diffusion, principally because of the observed decrease in ion current. That is, a major effect of the repeller is to increase ion mobility through the thermospray ion plasma. In fact, the data in Figure 3 also suggest that it is increased ion mobility that is responsible for the change in ion current. The optimum repeller potential depended solely upon the mass and not the charge of the ion, affecting both positive and negative ions similarly. This indicates that the repeller potential only affects ion mobility and not the ionization process, which can be different for positive and negative ions. Experiments for other compounds also indicate that increased ion diffusion is a predominant effect (23). In addition, preliminary experiments indicate that changing the distance of the repeller tip from the ion exit aperture changes the absolute value of the optimum repeller potential, but not the value of the maximum ion current (19). That is, larger potentials are required at larger distances to optimize extraction of the ions via electrostatic repulsion.

Peptide Studies. Thermospray LC/MS can be a powerful tool for peptide sequencing and peptide mapping studies. Previous models of the thermospray ion source (without a needle-tip repeller and a restricted probe tip) required from 0.2 to 10 nmol of peptides for detection. The amount of peptide sample needed for previous on-line column thermospray studies was typically on the order of 1–10 nmol (9, 10). The amount of sample required to produce spectra by direct injection (without an on-line column) was typically 200–500 pmol or more (9, 10).

The needle-tip repeller electrode has been used to determine sensitivity for some synthetic peptides. We have detected peptide samples on the order of picomoles. Figure 5 shows the total ion chromatogram for the several injections of 500, 50, and 10 pmol of bradykinin. Figure 6 shows the mass spectrum obtained for 10 pmol of bradykinin (molecular weight 1060). Similar sensitivities have been obtained for another peptide angiotensin I (molecular weight 1296). The spectra were obtained by scanning the mass spectrometer over the range of m/z 600 to m/z 1400. Figure 6 shows a signal-to-noise ratio of about 5:1 for the molecular ion $[M - H]^-$ of bradykinin. The response in the ion chromatogram (Figure 5) for the 10-, 50-, and 500-pmol samples is due almost entirely to the molecular ion $[M - H]^-$. The other signals shown in the spectrum were not reproducible; they are probably due to neutral noise owing to the high pressures in the thermospray ion source and the line-on-sight location of the detector conversion dynode from the ion exit aperture. Other soft ionization methods (i.e. continuous-flow fast-atom bombardment and ion spray) have detected these and other similar synthetic peptides

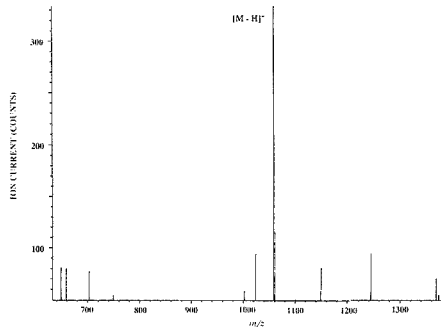


Figure 6. Negative-ion mass spectrum of 10 pmol of bradykinin showing the $[M - H]^-$ ion.

on the order of picomoles as well (24, 25). Our results are comparable to these other techniques, and they represent an enhancement of 1 to 2 orders of magnitude in sensitivity when compared to a thermospray ion source without a repeller and a restricted probe tip (9, 10, 26).

The optimum signal response was found at a repeller potential of 60–70 V, comparable to the results obtained for the PEG sample. It is necessary to scan a large mass range when conducting peptide mapping and peptide sequencing studies. A repeller range of 60–70 V provides an optimum response over the entire mass range of the instrument (m/z 2000). Therefore, we now conduct our peptide studies with a repeller at a potential of about 70 V.

CONCLUSIONS

Peptide mapping studies using on-line column enzymatic digests (9, 10) require more material (typically 5–10 nmol) than when samples are analyzed by direct injection. This is due to column losses and peak broadening as well as the fact that the peptides are being cleaved into from 10 to 100 smaller peptide sequences. Increased ion current obtained by using the needle-tip repeller and restricted vaporizer probe tip will facilitate protein sequencing and protein mapping studies by requiring less sample. Our studies presented here suggest that subnanomole sample sizes are now feasible.

An increase in sensitivity for peptides of 1 to 2 orders of magnitude was observed when results were compared to a thermospray ion source without a restricted vaporizer tip or repeller electrode. Both a repeller and the restricted tip together are needed to produce a symbiotic overall increase in sensitivity. Alone, each modification does provide an increase in sensitivity, but the overall increase was greater when the modifications were used together.

The PEG studies indicate that an enhancement of about an order of magnitude in ion response can be obtained from the repeller electrode (when using a restricted vaporizer tip). The effect of the needle-tip repeller appears solely to be more efficient ion sampling. No fragmentation was observed when using the needle tip repeller as has been seen for the blunt tip repeller. The remaining order of magnitude comes from using a restricted probe tip. This latter could arise from more efficient vaporization due to more uniform and smaller droplet sizes and more efficient ion evaporation (22). More uniform and smaller droplet sizes would permit a more uniform and more efficient repeller field for enhancing ion extraction. This explains why using a needle-tip repeller in conjunction with a restricted vaporizer is more effective for enhancing sensitivity using thermospray.

ACKNOWLEDGMENT

The authors thank Dr. Marvin L. Vestal (Vestec Corp.), Dr. Donald A. Flory, and Dr. Douglas F. Dyckes (UH) for their many helpful discussions about thermospray LC/MS as well

as peptide and protein chemistry.

LITERATURE CITED

- Schellenberg, K. H.; Linder, M.; Groeppelin, A.; Erni, F. *J. Chromatogr.* **1987**, *394*, 239-251.
- Taylor G. W.; Watson, T. *J. Chromatogr.* **1987**, *394*, 135-146.
- Mellon, F. A.; Chapman, J. R.; Pratt, J. A. E. *J. Chromatogr.* **1987**, *394*, 209-222.
- Artigas, F.; Gelpi, E. *J. Chromatogr.* **1987**, *394*, 123-134.
- Blakely, C. R.; Carmody, J. J.; Vestal, M. L. *J. Chromatogr.* **1978**, *158*, 261-276.
- Blakely, C. R.; Carmody, J. J.; Vestal, M. L. *J. Am. Chem. Soc.* **1980**, *102*, 5931-5933.
- Vestal, M. L. *Science* **1984**, *26*, 275-281.
- Burlingame, A. L.; Ballie, T. A.; Derrick, P. *J. Anal. Chem.* **1986**, *58*, 185-211.
- Stachowiak, K.; Wilder, C.; Vestal, M. L.; Dyckes, D. F. *J. Am. Chem. Soc.* **1988**, *110*, 1758-1765.
- Stachowiak, K.; Dyckes, D. F. *Peptide Res.*, in press.
- Rudewicz, P. *J. Biomed. Environ. Mass Spectrom.* **1988**, *15*(8), 461-3.
- Coutant, J. E.; Ackerman, B. L.; Vestal, M. L. Presented at the 35th Annual Conference on Mass Spectrometry and Allied Topics, Denver, CO, 1987.
- Zakett, D.; Kallos, G. J.; Savickas, P. J. Presented at the 34th Annual Conference on Mass Spectrometry and Allied Topics, Cincinnati, OH, 1986.
- McFadden, W. F.; Garteiz, D. A. *J. Chromatogr.* **1987**, *394*, 101-108.
- Fink, S. W.; Freas, R. B. Presented at the 36th Annual Conference on Mass Spectrometry and Allied Topics, San Francisco, CA, 1988.
- Robbins, R. H.; Crow, F. W. *Rapid Commun. Mass Spectrom.* **1988**, *2*, 30-34.
- Robbins, R. H.; Crow, F. W. Presented at the 34th Annual Conference on Mass Spectrometry and Allied Topics, Cincinnati, OH, 1986.
- McLean, M. A.; Flory, D. A.; Vestal, M. L.; Freas, R. B. Presented at the 36th Annual Conference on Mass Spectrometry and Allied Topics, San Francisco, CA, 1988.
- Finck, S. W.; McLean, M. A.; Freas, R. B., unpublished results.
- Wong, S. S.; Geissmann, U.; Karas, M.; Rollgen, F. W. *Int. J. Mass Spectrom. and Ion Phys.* **1984**, *56B*, 139.
- Mason, E. A. In *Plasma Chromatography*, Carr T. W., Ed.; Plenum: New York, 1984; pp 43-93.
- Kaita, V. Ph. D. Dissertation, University of Houston, 1987.
- McLean, M. A.; Freas, R. B. *Anal. Chem.*, following paper in this issue.
- Brins, A. P.; Covey, T. R.; Henion, J. D. *Anal. Chem.* **1987**, *59*, 2642-2646.
- Caprilli, R. M.; DaGue, B.; Fan, T.; Moore, W. T. *Biochem. Biophys. Res. Commun.* **1987**, *148*, 291-299.
- Vestal, M. L., Vestec Corp., personal communication.

RECEIVED for review October 14, 1988. Revised manuscript received March 10, 1989. Accepted June 21, 1989. Our work has been supported by the Environmental Protection Agency and the National Institutes of Health (Grant GM-32772). The thermospray ion source that was modified for these studies was provided by Vestec Corp.

Enhanced Analysis of Sulfonated Azo Dyes Using Liquid Chromatography/Thermospray Mass Spectrometry

Matthew A. McLean¹ and Royal B. Freas*

Department of Chemistry, University of Houston, Houston, Texas 77204-5641

Modifications to a thermospray vaporizer probe and ion source have been made that enhance ion evaporation resulting in increased sample ion current. These modifications include restricting the thermospray vaporizer exit orifice and the addition of a needle-tip repeller electrode to the thermospray ion source. The interaction and effect of probe-tip size, repeller voltage, and flow rate on sulfonated azo dye detection are reported. An increase in signal response for sulfonated azo dyes was observed. An efficient chromatographic separation procedure for sulfonated azo dyes, which is compatible with thermospray mass spectrometric detection, is also presented. Five disulfonated azo dyes were separated and detected by using selected ion monitoring. Mass spectra of disulfonated dyes show a number of molecular ions and adduct ions that provide unequivocal molecular weight information.

INTRODUCTION

Thermospray (1, 2) has proven to be useful for the on-line coupling of liquid chromatography (LC) with mass spectrometry (MS) (3). The utility of thermospray MS as an analytical tool has been demonstrated by its increasing usage in the fields of environmental analysis and biomedical research (4, 5).

Thermospray allows the entire mass flow of a conventional liquid chromatograph (0.5-2 mL/min) to enter the mass spectrometer. This is accomplished by additional vacuum

pumpup of the ion source and the controlled partial vaporization of the effluent as it traverses a conductively heated capillary tube. The vaporization process causes a supersonic jet of vapor to form, which contains particles and liquid droplets. Heat is supplied to the ion source to compensate for cooling of the expanding jet and to allow for the continued vaporization of the solvent.

The most commonly used mode of ionization is thermospray ionization (TI). No supplemental source of electrons is needed in this mode. Instead, a volatile buffer is added to the mobile phase. The volatile buffer acts as a source of charge on the droplets that emerge from the heated thermospray vaporizer. The partial vaporization of the solvent causes charge to concentrate in the unevaporated solvent droplets. Coulombic repulsive forces become greater than cohesive forces and the droplets break apart (Rayleigh instability). Evaporation of solvent molecules from these smaller droplets continues due to heat transferred from the walls of the source block. A high electric field is created on the droplets as the volumes of the droplets decrease. Ion evaporation starts to occur when the field strength on the droplets exceeds about 10^9 V/m (6). At this point, ions are ejected directly from the condensed phase into the gas phase. Hence, intact molecular ions of nonvolatile and thermally labile compounds can be obtained.

Although ion evaporation predominates for compounds that are multiply charged in solution, other compounds have been shown to undergo ionization by gas-phase ion/molecule reactions in the thermospray ion source (7-10). Dual-beam thermospray experiments have shown that a number of compounds are ionized via chemical ionization (CI) (7). In this case, neutral molecules are evaporated from thermospray droplets and are ionized via collisions with solvent and buffer ions in the gas phase. Compounds that undergo ionization

* Author to whom correspondence should be addressed.

¹ Present address: Exxon Research and Engineering, Annandale, NJ 08801.

via a CI-type mechanism will show a direct correlation between analyte volatility and thermospray sensitivity. For many compounds this appears to be the case and good sensitivity is achieved with compounds having some volatility. Compounds that exhibit poor sensitivity with thermospray, such as sulfonated azo dyes, are compounds that are extremely nonvolatile and exist as preformed ions. Our goal is to develop thermospray methods to enhance the ionization process and analysis of these latter species and thus expand the utility of thermospray to extremely nonvolatile and intractable compounds.

To evaluate ion evaporation in thermospray, a model system must be developed that can directly relate the enhancement of this process to mass spectrometric response. We have chosen sulfonated azo dyes as model compounds to study ion evaporation for both theoretical and practical reasons. It is important to choose a class of compounds that are ionized in solution, so that the chemical ionization process makes little contribution to the measured mass spectrometric response. Sulfonated azo dyes will be ionized in solution at virtually all pH levels encountered in reverse-phase chromatography because they have low pK_a values. This ensures that these species will evaporate as ions and not as neutral molecules. The inherent lack of sensitivity that sulfonated azo dyes show to thermospray ionization is a direct consequence of their lack of volatility and ionized character. Only ionization techniques that produce ions directly from the condensed phase have the ability to analyze this class of compounds. With the exception of electrospray/atmospheric pressure ionization (11, 12), reproducible mass spectral analyses have not been readily obtained. This makes sulfonated azo dyes challenging test compounds that are not easily analyzed by thermospray or other mass spectrometric methods. Sulfonated azo dyes were also chosen for practical reasons as well. There is a definite need for an LC/MS procedure to be developed that will identify sulfonated azo dyes in the environment. This need has arisen because of the dumping of toxic dye wastes into the environment (13) and the proposed listing of many dyes in the Appendix VIII and IX Hazardous Constituent Lists (14). The Environmental Protection Agency is particularly concerned about the release of azo dyes into the environment due to the toxicity of aromatic amines that are synthetic precursors and degradation products of azo dyes (15). A regulatory program for the dye industry has been implemented that requires mass spectrometric procedures to be developed for the qualitative analysis of azo dyes in industrial wastes, groundwater, and surface water. For these reasons, we have been actively involved in developing a thermospray LC/MS procedure to routinely analyze sulfonated azo dyes in aqueous media.

EXPERIMENTAL SECTION

All experiments were performed on a quadrupole mass spectrometer (Hewlett-Packard, Model 5988), coupled to a gradient high-performance liquid chromatography (HPLC) system (Scientific Services Model 230) using a modified thermospray LC/MS interface (Vestec Thermospray LC-MS Model 721A). A Hewlett-Packard Model 9133 work station was used to control the mass spectrometric parameters and for all data collection.

Vaporizer Modifications. Modifications to the thermospray vaporizer and ion source were necessary to enhance ion evaporation and signal ion current in thermospray. These modifications include restriction of the thermospray vaporizer exit orifice and the addition of a needle-tip repeller to the thermospray ion source. Schematic representations of these modifications are shown in Figure 1.

Restriction of the thermospray vaporizer exit orifice was accomplished by cutting off the tip of a commercially available thermospray vaporizer insert. A Valco $1/4$ -in. nut was welded to the outer portion of the insert and machined down to the same diameter as the insert casting. Capillary tubing was fed through

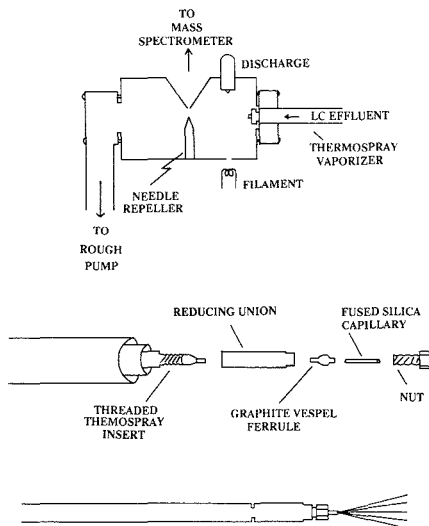


Figure 1. Schematic of modifications made to the thermospray ion source and vaporizer probe.

the nut and secured with a standard Valco ferrule. A Valco $1/16$ - to $1/32$ -in. zero-dead-volume reducing union was used to hold the fused silica capillary in place with the appropriate size graphite or Vespel ferrule and a $1/32$ -in. nut. The zero-dead-volume union was machined down to $1/4$ -in. in diameter so it could be inserted into the thermospray ion source.

Ion Source Modifications. The thermospray ion source was modified by machining away a step restriction in the ion volume and replacing the standard blunt repeller with a needle-tip repeller constructed from a threaded rod (Figure 1). The repeller was electrically isolated from the ion source block using ceramic insulators and it was held by two locknuts threaded onto each end of the rod. The threaded rod (1.5 mm diameter) was machined to a point (0.1 mm diameter) and positioned coaxially with the ion extraction cone at a distance of approximately 1 mm from the ion exit aperture. This distance was found to optimize performance. Increasing the distance had an effect of increasing the repeller potential needed for maximum ion current response. Decreasing the distance resulted in a decrease of the maximum ion current.

Data Acquisition. Data showing the effect of repeller voltage and flow rate on ion intensity were obtained by using selected ion monitoring of $[M - Na]^+$ and $[M - 2Na]^2+$ ions and are shown in Figure 2. An aqueous solution of 10^{-5} M Direct Red 81 dye was continuously pumped into the mass spectrometer. The repeller voltage was ramped from zero through a voltage corresponding to maximum ion current for each flow rate and tip size. The averaged ion intensity was recorded at each repeller setting. The repeller voltage was increased until the ion current was zero or drastically reduced from the maximum value.

Negative-ion mass spectra (Figures 3-7) were obtained by injecting 200 μ L of 10^{-4} M aqueous dye solution directly into the mass spectrometer with a Rheodyne Model 7010 injector. The mass spectrometer was scanned from m/z 300 to m/z 1000 in about 2 s. The flow rate was 1.2 mL/min and the thermospray vaporizer-tip orifice size was 100 μ m.

Liquid Chromatography. Chromatographic separation of selected disulfonated azo dyes was performed by using reverse-phase ion-pair chromatography. A 3-min linear gradient of 100% 0.01 M aqueous ammonium acetate to 100% 35/65 acetonitrile/water was performed with a 1-min initial hold. The $[M - 2Na + H]^+$ ion was monitored for each dye. The HPLC water was obtained by filtration of house-distilled water through a Milli-Q water purification system (Waters-Millipore). Acetonitrile was HPLC grade (Mallinckrodt) and the ammonium acetate

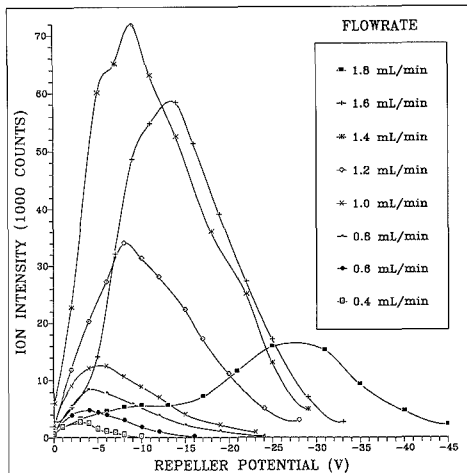


Figure 2. Plot of ion abundance versus repeller potential for Direct Red 81 dye at several different flow rates.

buffer was reagent grade (Fisher Scientific). The dyes used were commercial dye preparations supplied by EPA-EMSL (Las Vegas, NV) and NCTR (Jefferson, AR). The HPLC column was a reverse-phase 4.6 × 100 mm Spherisorb ODS II column with 3- μ m particle size packing (Custom LC).

Thermospray Parameters. Thermospray parameters were adjusted to give maximum ion current for an aqueous solution of dye being pumped into the mass spectrometer. The optimum temperatures with a tip size of 100 μ m and flow rate of 1.2 mL/min were as follows: control, 60–70 °C; tip, 215–225 °C; block, 305–310 °C; tip heater, 330–350 °C.

RESULTS AND DISCUSSION

Thermospray Vaporizer. The design of the thermospray vaporizer is of critical importance in optimizing thermospray ionization. The nature of the aerosol generated in thermospray is determined by the physical characteristics of the probe and the amount of heat supplied to the LC solvent. Optimum response is achieved when near complete vaporization occurs at the tip of the thermospray vaporizer. When the probe temperature is too low, thermospray ionization is weak. Droplet sizes under these conditions are large and the charge-per-unit area on the surface of the droplets does not reach the value needed for ion evaporation. The spray emerging from the thermospray vaporizer at elevated temperatures is a superheated dry vapor. This vapor contains few droplets from which thermospray ionization can occur and thermospray ionization is lost. Therefore, the fraction of solvent vaporized is of critical importance because it has a direct effect on droplet size and on the field strength of the emerging droplets. The physical dimensions of the probe exit orifice also has an effect on droplet size and size distribution of the aerosol. Decreasing the size of the thermospray vaporizer orifice has the effect of decreasing the average droplet size of the spray entering the ion source. The initial field strength on the droplets is thus increased and a subsequent increase in ion evaporation occurs. In theory, the smaller the thermospray vaporizer exit orifice can be made, the better sensitivity one should obtain. Practical limitations such as probe plugging and back-pressure limits on LC pumps put constraints on the lower size limit of the probe orifice. The method of restricting the probe exit presented here has the advantage of reproducibly decreasing the probe exit to a known value using inexpensive and commercially available materials. A major limitation of using fused silica capillary

tubing is the poor reproducibility of spray trajectories due to the uneven edge created when the tubing is cut. This problem may be overcome by using laser-drilled apertures (16) or capillary needle tubing as the probe orifice.

Ion Source. The needle-tip repeller enhances response for sulfonated azo dyes by influencing ion-extraction yields (focusing and increasing ion mobility) and possibly by affecting ion-evaporation rates directly. It has been suggested that needle tip repellers can enhance ion evaporation from thermospray droplets due to the high electric field created within the ion source (17). This high field can induce unsymmetric charging of the droplets. Large localized field strengths on the droplets can result and form microscopic protuberances like those used to explain field desorption mass spectrometry. An enhancement of the ionization process would be expected to result under these circumstances. In our studies, repeller effects were observed that indicate ion-extraction efficiency is being enhanced. However, due to the high pressures within the thermospray ion source, the effect the repeller has on gas-phase ion trajectories, and hence ion-extraction efficiency, is not well-defined. Studies of poly(ethylene glycols) and peptides show enhancements of molecular ion abundances that appears to be related to increased ion extraction efficiency (18).

Observed Results. Figure 2 shows graphs of ion intensity for Direct Red 81 versus repeller potential at various flow rates. With a repeller potential of zero, no appreciable ion signal is observed. As the repeller voltage is increased, the signal goes through a maximum. The signal is lost as the repeller voltage is continually increased. This loss indicates that the repeller has an electrostatic effect on the ions being sampled from the ion source. An alternate explanation for the increased ion signal may be the deceleration of thermospray droplets in the vicinity of the ion sampling cone (16). This would increase the number of ions evaporated in the vicinity of the sampling region and would be responsible for an increase in signal. Ion mobility experiments show that droplet velocities can be influenced with field strengths created by repellers in thermospray ion sources (19).

The optimum repeller voltage for a given tip size depends on flow rate. As the flow rate is increased, the repeller voltage corresponding to maximum ion intensity also increases. Due to higher pressures in the ion source, a higher repeller voltage is needed to influence droplet trajectories. This general trend is shown in Figure 2 for the 100- μ m tip size. Similar data were obtained for the 50- μ m tip.

Optimum flow rate also changes with tip size. As the orifice size is decreased, so does the flow corresponding to optimum results. The best result for the 50- and 100- μ m tips were obtained at a flow rates of 0.8 and 1.4 mL/min, respectively. This suggests there may be an optimum droplet size and size distribution for ion evaporation to occur that depends on flow rate and exit orifice size.

Other criteria that affect ion intensity for sulfonated dyes, such as ion extraction contribution due to pressure effects and neutralization reactions occurring within the ion source, also depend on flow rate. At lower flow rates, the pressure dependence on ion sampling is smaller so that ion intensity is less. At higher flows, the decrease in signal can be caused by neutralization reactions occurring between dye anions and solvent molecules due to the higher frequency of collisions.

We have found it necessary to have both the restricted probe exit and the needle-tip repeller to obtain mass spectra of the sulfonated dyes. Full-scan mass spectral data for various disulfonated azo dyes are shown in Figures 3–7. Characteristic ions at $[M - Na]^-$ and $[M - 2Na]^{2-}$ are observed for these compounds in water. As a small amount of ammonium acetate is added, other pseudomolecular ions such as $[M - 2Na + H]^-$

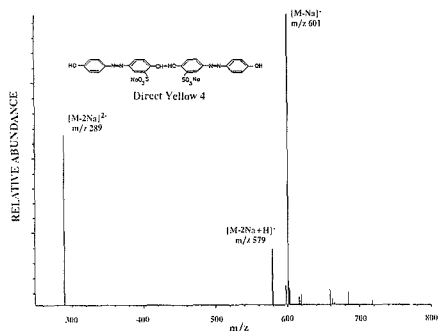


Figure 3. Thermospray mass spectrum of Direct Yellow 4 azo dye showing the $[M - Na]^+$, $[M - 2Na]^2+$, and $[M - 2Na + H]^-$ ions at m/z 601, 289, and 579.

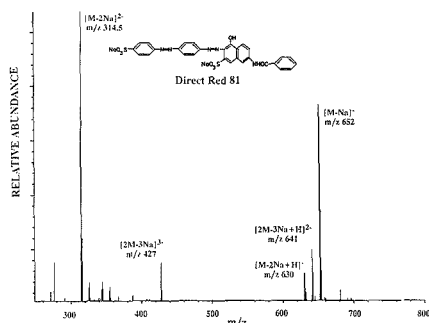


Figure 4. Thermospray mass spectrum of Direct Red 81 azo dye showing the $[M - Na]^+$, $[M - 2Na]^2+$, $[M - 2Na + H]^-$, $[2M - 3Na]^3+$, and $[2M - 3Na + H]^2+$ ions at m/z 652, 314.5, 630, 427, and 644.

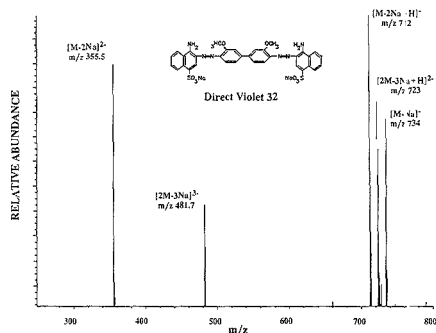


Figure 5. Thermospray mass spectrum of Direct Violet 32 azo dye showing the $[M - Na]^+$, $[M - 2Na]^2+$, $[M - 2Na + H]^-$, $[2M - 3Na]^3+$, and $[2M - 3Na + H]^2+$ ions at m/z 734, 355.5, 712, 481.7, and 723.

and $[2M - 3Na + H]^2+$ appear. The addition of these ions in the mass spectrum gives unambiguous molecular weight information for the sulfonated dye sample. In most cases, molecular weight information is adequate to identify the sulfonated azo dye in question. Confirmation of such an assignment can be achieved by MS/MS or by matching the LC retention time to that of a standard.

HPLC Separation. A number of problems were encountered in developing a suitable LC/MS procedure for sulfonated azo dyes. Foremost was developing an LC procedure that would separate sulfonated azo dyes while still being

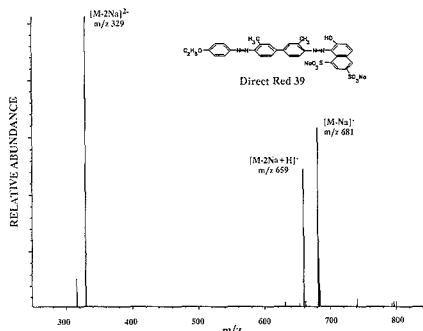


Figure 6. Thermospray mass spectrum of Direct Red 39 azo dye showing the $[M - Na]^+$, $[M - 2Na]^2+$, and $[M - 2Na + H]^-$ ions at m/z 681, 329, and 659.

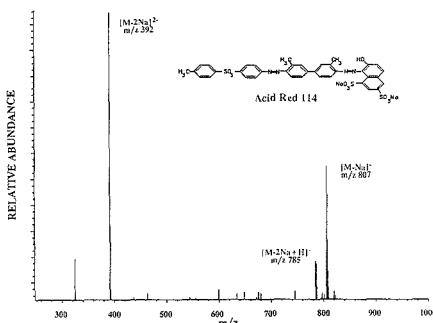


Figure 7. Thermospray mass spectrum of Acid Red 114 azo dye showing the $[M - Na]^+$, $[M - 2Na]^2+$, and $[M - 2Na + H]^-$ ions at m/z 807, 392, and 785.

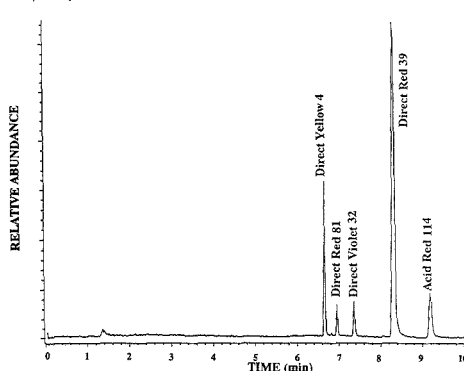


Figure 8. Reconstructed ion chromatogram for five sulfonated azo dyes.

compatible with thermospray MS detection. Previous results indicated that ammonium acetate concentrations higher than 0.01 M were detrimental to sulfonated azo dye detection due to neutralization reactions occurring in the ion source (20). As a result, a reverse-phase LC procedure using a low concentration of ammonium acetate as an ion-pairing agent was developed. Figure 8 shows the reconstructed ion chromatogram for a mixture of five disulfonated azo dyes. The separation was achieved by using a linear gradient dilution of 0.01 M aqueous ammonium acetate to a 35:65 mixture of aceto-

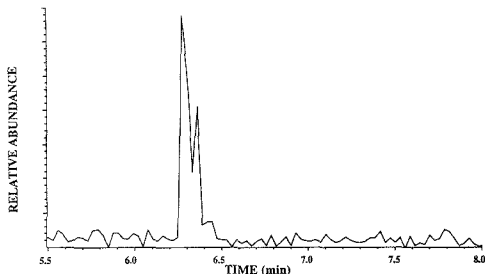


Figure 9. Reconstructed ion chromatogram for 10 ng of Direct Yellow 4 injected on-column.

nitrile/water. The dyes were detected by using selected ion monitoring of the $[M - 2Na + H]^-$ ion for each dye. All dyes were present in levels of about 500 ng assuming 50% purity of the commercial dye preparations used to make up the sample. Other ions such as the $[M - 2Na]^{2-}$ and $[M - Na]^-$ were also present and could be used for molecular weight confirmation. On-column detection limits for these dyes obtained by using selected ion monitoring were in the range of 5–20 ng with a signal-to-noise ratio of 10 (Figure 9).

CONCLUSIONS

Modifications to a thermospray vaporizer and ion source enhance the ion-evaporation process that occurs in thermospray. Sulfonated azo dyes were used as model compounds to determine the effect of these modifications on the ion evaporation process. Restriction of the thermospray vaporizer decreases the droplet size of the spray entering the mass spectrometer ion source. The decreased droplet size increases the charge-per-unit area on the thermospray droplets and a subsequent increase in ion evaporation results. A needle repeller in the thermospray ion source enhances sulfonated azo dye detection. Results indicate that the repeller has a direct effect on ion-extraction efficiency. Both restriction of the vaporizer exit aperture and the needle-tip repeller are needed to obtain mass spectra of sulfonated azo dyes. The mass spectra obtained gave pseudomolecular ions, which can be used to obtain the molecular weight of an unknown dye species. The identity of a dye can be confirmed by using the reported separation procedure and selected ion monitoring.

Future work in our laboratory will focus on increasing thermospray response for sulfonated azo dyes. Laser-drilled apertures and capillary needle tubing will be used to restrict the thermospray vaporizer exit orifice in order to achieve more

reproducible spray trajectories. An electrically assisted thermospray device and an on-axis thermospray ion source are now being investigated. Promising results for sulfonated dye detection have been obtained with electrospray ionization (11, 12) and perhaps thermospray can be improved by electrically charging the droplets during the vaporization process. On-axis ion sources are designed to act as concentration devices for nonvolatile species that are at higher concentration at the center of the spray. The use of an on-axis ion source should therefore, take advantage of the nonvolatile nature of the sulfonated azo dyes and increase sensitivity for these and other nonvolatile compounds.

ACKNOWLEDGMENT

We thank Dr. Marvin L. Vestal and Dr. Donald A. Flory for providing invaluable assistance and helpful discussions.

LITERATURE CITED

- (1) Blakley, C. R.; Carmody, J. J.; Vestal, M. L. *Anal. Chem.* **1980**, *52*, 1636–1641.
- (2) Blakley, C. R.; Carmody, J. J.; Vestal, M. L. *J. Am. Chem. Soc.* **1980**, *102*, 5931–5933.
- (3) Gurtiez, D. A.; Vestal, M. L. *LC* **1985**, *3*, 334–346.
- (4) Bullar, T. A.; Budde, W. L. *Anal. Chem.* **1988**, *60*, 2076–2083.
- (5) Taylor, G. W.; Watson, D. J. *Chromatogr.* **1987**, *394*, 135–146.
- (6) Thomson, B. A.; Iribarne, J. V. *J. Phys. Chem.* **1979**, *71*, 4451–4463.
- (7) Buitfering, L.; Schmelzeisen-Redeker, G.; Rollgen, F. W. *J. Chromatogr.* **1987**, *394*, 109–116.
- (8) Smith, R. W.; Parker, C. E.; Johnson, D. M.; Burse, M. M. *J. Chromatogr.* **1987**, *394*, 261–270.
- (9) Alexander, A. J.; Kebarle, P. *Anal. Chem.* **1986**, *58*, 471–478.
- (10) Bursey, M. M.; Parker, C. E.; Smith, R. W.; Gaskell, S. J. *Anal. Chem.* **1985**, *57*, 2597–2599.
- (11) Covey, T.; Lee, E.; Henion, J. Presented at 36th Annual Conference on Mass Spectrometry and Allied Topics, San Francisco, CA, 1988.
- (12) Covey, T.; Bruins, A. P.; Henion, J. *Org. Mass Spectrom.* **1988**, *23*, 178–186.
- (13) Nelson, C. R.; Hites, R. A. *Environ. Sci. Technol.* **1980**, *14*, 1147–1149.
- (14) *Fed. Regist.* **1986**, 40-CFR, Parts 261 and 271 (proposed).
- (15) Parris, G. E. *Residue Rev.* **1980**, *76*, 1–30.
- (16) Vestal, C. H.; Wilkes, J. G.; Fergusson, G. J.; Vestal, M. L. Presented at the 36th Annual Conference on Mass Spectrometry and Allied Topics, San Francisco, CA, 1988.
- (17) Robbins, R. H.; Crow, F. W. *Rapid Commun. Mass Spectrom.* **1988**, *2*, 33–34.
- (18) Fink, S. W.; Freas, R. B. *Anal. Chem.*, preceding paper in this issue.
- (19) Katta, V. Ph.D. Dissertation, University of Houston, 1987.
- (20) Flory, D. A.; McLean, M. A.; Vestal, M. L.; Betowski, L. D. *Rapid Commun. Mass Spectrom.* **1987**, *1*, 48–50.

RECEIVED for review October 14, 1988. Revised manuscript received March 10, 1989. Accepted June 21, 1989. The Environmental Protection Agency and Vestec Corporation are acknowledged for financial support of this work. The mass spectrometer was purchased with funds from the National Institutes of General Medical Sciences.

Single Amino Acid Contributions to Protein Retention in Cation-Exchange Chromatography: Resolution of Genetically Engineered Subtilisin Variants

Roman M. Chicz¹ and Fred E. Regnier*

Department of Biochemistry, Purdue University, West Lafayette, Indiana 47907

Genetically engineered proteins were used to determine the amino acid contributions of surface residues to subtilisin retention in cation-exchange chromatography. Crystallographic data were used to correlate the observed chromatographic behavior with enzymatic structure. Retention times of variants in gradient elution varied by as much as 33% compared to the wild type. The role of both charged and uncharged residues was investigated in isocratic separations and found to significantly influence protein retention in this electrostatically dominant separation method. This study demonstrates the ability of ion-exchange chromatography to discriminate between protein variants differing by a single residue in 275 amino acids.

INTRODUCTION

Through site-directed mutagenesis, it is possible to change any amino acid in a protein (1, 2). This makes it possible to focus structure-function investigations on amino acid contributions at specific positions in the three-dimensional structure and to design proteins for applications with properties superior to those found in the wild type. Some areas of interest already under investigation include catalytic properties, substrate specificity, allosteric regulation, antigenicity, increased pH stability, thermostability, and chemical stability (3-5). Site-directed mutagenesis is also useful to study the mechanism of chromatographic retention. These variant protein structures serve as mimics of variants formed during protein biosynthesis and purification in biotechnology. Variant proteins that result from errors in translation, posttranslational modification, or site-specific mutation are difficult to separate from the wild type or target variants by molecular weight discriminating methods such as size exclusion chromatography and sodium dodecyl sulfate electrophoresis (6). Because protein assembly in genetically engineered systems produced errors at a higher rate than in natural systems (7), analytical methods must be developed to detect and separate these protein impurities.

Substitutions of internal amino acids have been shown to destabilize protein stability which then increased intracellular degradation of these expression products (8). Therefore, these types of errors are normally removed prior to product purification. In biologically active proteins, the majority of structural variations occur on the protein surface. This is important for two reasons. It limits gross changes in protein tertiary or quaternary structure and maximizes the possibility that surface-mediated separation procedures will be able to discriminate between the major and minor protein products. However, the limits in resolving power of modern separation techniques relative to changes at single sites in protein

three-dimensional structure remain to be determined.

It is well established that only a fraction of the total amino acids in a protein determine chromatographic behavior in a specific separation mode (9). For this reason, it is probable that no single separation method can recognize all the possible structural variants and impurities in genetically engineered protein preparations. However, the greatest discrimination will be achieved by those separation methods that probe the broadest area of the protein surface. For example, the protein/column contact in bioaffinity chromatography may be as small as a few hundred square angstroms. In contrast, the contact area in nonbioaffinity separations such as ion-exchange, reversed-phase, and hydrophobic-interaction chromatography may range from one face to the whole external surface of a polypeptide (9). The dominant factors regulating contact surface area are steric limitations incurred by the three-dimensional structure of the protein and amino acid distribution within the molecule. The impact of three-dimensional structure on chromatographic behavior has been shown in ion-exchange (10), reversed-phase (11), and hydrophobic-interaction chromatography (12).

The stoichiometric displacement model (SDM) (13) of chromatographic retention has been applied to the study of structural changes with respect to protein retention in both ion-exchange (14) and reversed-phase (15) chromatography. The model attempts to quantitate the average number of interactions between a protein and the stationary phase of the column through a parameter referred to as the *Z* number. A second parameter in this model, the *I* value, describes the affinity of the solute for the stationary phase along with any nonspecific interactions involved with solute retention. With this model, it has been possible to correlate changes in primary structure with protein retention.

This study investigates how single amino acid substitutions at chosen positions in genetically engineered subtilisin affect protein retention in cation-exchange chromatography. Variants with substitutions at multiple sites on the protein surface were used to determine whether subtilisin has a "footprint" region in cation-exchange chromatography. Position 166 was chosen as the site for detailed studies on microenvironmental contributions to subtilisin retention after preliminary experiments indicated this location to be chromatographically significant. The amino acid substitutions at this position were used to quantitate the impact of single charged, hydrophobic, or neutral hydrophilic groups on the chromatographic behavior of a protein. The objective was to determine the discriminatory power of cation-exchange chromatography in the separation of subtilisin single amino acid variants. Quantitation of variant protein/column electrostatic interactions was achieved by isocratic elution and subsequent application of the SDM.

EXPERIMENTAL SECTION

Proteins and Reagents. *Bacillus amyloliquefaciens* subtilisin wild type and site-directed variants were a generous gift of Genencor, Inc. (South San Francisco, CA). These proteins were

¹ Present address: Department of Biochemistry and Molecular Biology, Harvard University, 7 Divinity Ave., Cambridge, MA 02138.

used without further purification. All reagents were of AR grade or comparable quality.

To prevent autolysis, proteins were stored in 50% aqueous propylene glycol/5 mM CaCl₂/10 mM TES (pH 7.6) at -12 °C. Protein concentrations were approximately 10 mg/mL.

Equipment. Protein retention measurements were made with a Varian 5000 chromatographic system, equipped with a UV-100 detector (Walnut Creek, CA) and a Valco Model C6U injector with a 15- μ L sample loop (Houston, TX). A 10- μ m particle size Mono-S strong cation-exchange column, 5.0 \times 0.5 cm i.d. (Pharmacia, Uppsala, Sweden) of 0.13–0.18 mmol/mL ion-exchange capacity was used in all experiments. Protein absorbance was monitored at 280 nm, and eluent conductance was monitored with an Anspec AN400 ion chromatograph (Ann Arbor, MI). Data were collected on a Kipp & Zonen BD41 dual-channel chart recorder (Delft, Holland).

Mobile Phase. Mobile-phase buffers were chosen so that the buffer pK_a was within one pH unit of the desired eluent pH: sodium acetate (Mallinckrodt, Paris, KY) (pH 5.0 and 5.5); 2-(*N*-morpholino)ethanesulfonic acid (MES) (Calbiochem-Behring, LaJolla, CA) (pH 6.0); *N*-tris(hydroxymethyl)methyl-2-aminoethanesulfonic acid (TES) (Sigma, St. Louis, MO) (pH 7.0). Buffer A was prepared to have an ionic strength of 0.01 M. Buffer B was a mixture of buffer A and either 0.10 M or 0.15 M NaCl, depending on the protein being studied.

All aqueous solutions were prepared with deionized water and were adjusted to the desired pH at room temperature with either HCl or NaOH. All solutions were prepared fresh daily, filtered through a Rainin Nylon-66 (0.45- μ m) filter (Woburn, MA), and deaerated prior to use.

Chromatography. Retention maps were determined by using gradient elution at a flow rate of 1 mL/min. The term "retention map" refers here to a plot of chromatographic retention on a gradient eluted cation-exchange column versus mobile phase pH. Either 20-min or 30-min linear gradients were used depending on the final ionic strength needed to elute the variant being studied. In all cases, the gradient slope was maintained constant. All sample injections were performed in triplicate by using either a 15- μ L or 100- μ L sample loop. Gradient elution was also performed to separate the position 166 variants. Enzymatic activity of collected fractions was determined from a modified progress-curve analysis (16). Detection of autolytic peptide contaminants was verified by using a HP-1040A high-speed diode array spectrophotometric detector operated with a HP-85 personal computer (Hewlett-Packard, Postfach, Federal Republic of Germany) scanning at two wavelengths, 276 and 286 nm. The ratio of the peaks at these two wavelengths provides information regarding the enzymatic activity by monitoring the three tryptophan residues located on the surface of the protein. Autolysis of subtilisin cleaves the enzyme after residue 40, thus removing the catalytically essential Asp 32 and changing the structural integrity of the tryptophan residues. An increase in the ratio between these two wavelengths corresponds to an inactive autolyzed subtilisin fragment (17).

Isocratic analyses were carried out at values ranging from *k'* values of 1 to 15. Ionic strength was determined with a conductivity monitor. Initial values of ionic strength for isocratic elution were obtained from gradient elution. Between 15 and 20 salt concentrations were chosen from each analysis. All sample injections were performed in duplicate with injection volumes varying, depending on the variant, between 4 and 70 μ L (volume was constant for any one analysis). The solvent perturbation peak observed by both the UV and conductance detectors, was taken as the retention time for unretained protein (*t*₀).

Calculations. Calculations and statistical analyses were done as previously reported (18). Computer analysis of isocratic retention parameters was performed to choose the appropriate *Z* numbers and *I* values for correlation to the gradient elution studies. The distances between the 34 charged amino acids and position 166 were calculated by using the *x*, *y* and *z* coordinates for specific charged side chain atoms and the α -carbon of position 166 as reported by Alden (19).

RESULTS

Enzymatic Properties. Because of the commercial significance of subtilisin in laundry detergents (20), a series of

Table I. Subtilisin Residue Substitutions

variant	amino acid/position in wild type	substitution
FQK	Multiple Substitutions	
	Met-50	Phe
	Glu-156	Gln
FQK F:275	Gly-166	Lys
	Met-50	Phe
	Glu-156	Gln
	Gly-166	Lys
QK	Gln-275	Arg
	Glu-156	Gln
QD	Gly-166	Lys
	Glu-156	Gln
SD	Gly-166	Asp
	Glu-156	Ser
D166 E166 S166 N166 C166 M166 H166 K166 R166 P166 V166 Y166	Single Substitutions	
	Gly-166	Asp
	Gly-166	Glu
	Gly-166	Ser
	Gly-166	Asn
	Gly-166	Cys
	Gly-166	Met
	Gly-166	His
	Gly-166	Lys
	Gly-166	Arg
	Gly-166	Pro
	Gly-166	Val
	Gly-166	Tyr

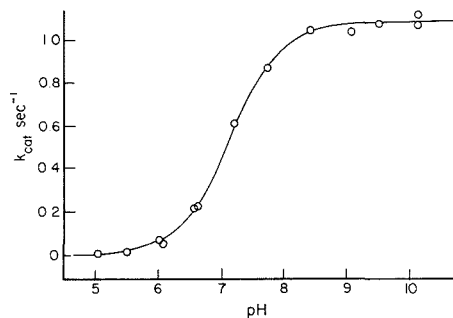


Figure 1. pH dependence of k_{cat} for subtilisin toward *p*-nitrophenyl butyrate. Subtilisin KM pH dependence was shown to be relatively constant throughout this range. Adapted from ref 30.

genetically engineered variants of the enzyme were available. These variants have been studied for their substrate specificity, kinetics, and their stability against oxidizing agents (21). Variants with surface residue alterations were chosen for the type and location of amino acid substitution (Table I). Only substitutions that have been determined to be solvent accessible by X-ray crystallography (22) were chosen.

The function of subtilisin as an endopeptidase unfortunately allows this enzyme to act as a substrate for itself. Hence, autolysis is a problem that has to be circumvented in order to study native subtilisin. Although enzyme inhibitors may be used to prevent autolysis, the most effective inhibitor, i.e. phenylmethanesulfonyl fluoride, diisopropyl fluorophosphate, halomethyl ketones, or boronic acid, derivatize the active site serine or histidine (13–16) and change the chromatographic behavior of the enzyme. Noncovalently bound proteinaceous inhibitors also change the surface characteristics of the enzyme by forming a complex with subtilisin (27–29). To prevent or suppress autolysis without inhibitors requires alteration of the enzyme's kinetics. Previous work has shown that an acidic

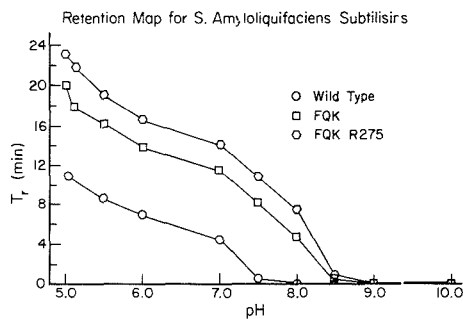


Figure 2. Retention map for wild-type subtilisin and the FQK and FQK R275 variants. Retention time is plotted against pH using a 30-min linear gradient from 0 to 0.15 M NaCl.

environment reduces subtilisin enzymatic activity (Figure 1). Inhibition of subtilisin under acidic conditions is due to protonation of the active site histidine (31).

Retention Map. Retention in cation-exchange chromatography depends on the mobile-phase pH with respect to the isoelectric point (pI) of the protein. Below the pI, retention generally increases on a cation-exchange column as the surrounding environment becomes more acidic and the protein surface becomes more positively charged. Gradient-elution retention versus mobile-phase pH was plotted to determine the optimum conditions for variant resolution. Figure 2 confirms that the retention of subtilisin increases with a decrease in pH. Peak shape was symmetrical from pH 5.0 to 7.0, but began to broaden slightly above pH 7.0. This corresponds to the increased enzymatic activity found in the pH profile curve. At pH 8.0, secondary peaks attributed to autolysis products began to appear, while the main protein peak became smaller. Retention decreased to zero above pH 8.0 for wild type and pH 8.5 for the variants. Eluted subtilisin retained over 90% enzymatic activity in standard assays. Irreversible adsorption was observed when attempting to elute subtilisin at pH values below 5.0. This most likely occurred as a result of protein denaturation. Below pH 5.0, internal histidine protonation disrupts tertiary structure (32). Denatured subtilisin was removed from the column by using the manufacturer's recommended column cleaning procedure.

Protein retention differed between the wild type and multiple substitution variants. At every pH studied, wild-type subtilisin eluted first, followed by the FQK and FQK R275 variants. The family of curves represent the substituted amino acid contributions to retention at different mobile-phase pH. This reflects the charge difference between the proteins with FQK having a +2 and FQK R275 having a +3 surface charge relative to the wild type. The curve shape is similar for each subtilisin variant with only the absolute retention time changing, suggesting that no gross conformational changes occur in the tertiary structure of the multiple substituted variants. The Met-to-Phe substitution at position 50 is neutral and would not be expected to play a direct role in an ion-exchange separation. However, substitutions at positions 156, 166, and 275 seem to influence subtilisin retention behavior (Figure 2). Positions 156 and 166 both lie in proximity to each other within the substrate binding cleft, while residue 275 is the carboxy terminus and lies 31 and 36 Å away from the other two positions, respectively (19).

These results also verified subtilisin surface charge symmetry previously determined by X-ray crystallography. Earlier work on the pH effects in protein retention (13) demonstrated that symmetrically charged proteins are not retained beyond their pI in ion-exchange chromatography.

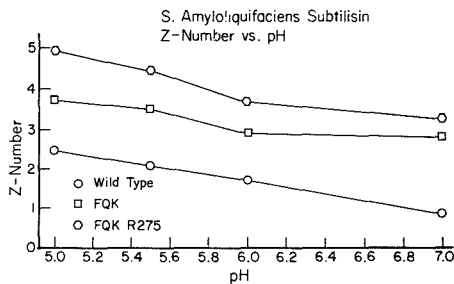


Figure 3. Plot of Z number versus pH for wild-type subtilisin and FQK and FQK R275 variants. Experimental conditions are the same as those described in the retention map of Figure 2.

Table II. Multiple Substitution Variant Z Number and I Value Analysis at pH 5.0

variant	Z number	I value
wild type	2.60 ± 0.06	6.69 × 10 ⁻⁴
FQK	3.71 ± 0.05	3.82 × 10 ⁻⁴
FQK R275	4.80 ± 0.05	4.35 × 10 ⁻⁵
QK	3.73 ± 0.05	5.64 × 10 ⁻⁴
QD	3.36 ± 0.03	1.21 × 10 ⁻⁴
SD	2.54 ± 0.05	7.77 × 10 ⁻⁴

Subtilisin was shown not to be retained beyond its pI in this study, thus providing dynamic experimental evidence confirming the static crystallographic structural data on surface charge symmetry. To quantitate the contribution of these amino acid substitutions to retention, Z number analyses were done.

Multiple Substitution Variants. SDM Analysis. Isocratic analyses were performed to determine Z numbers of the wild type and the variants under various pH conditions. The Z number for subtilisin corresponds to the average number of protein surface charges interacting with the column. As the mobile-phase pH in isocratic analyses approached the pI, the protein surface became less positive while both the retention and the Z number decreased (Figure 3) in the wild type, FQK, and FQK R275 variants. Comparison of the Z numbers between the FQK and FQK R275 variants shows that the addition of a positive charge increased the Z number by approximately 1 at pH 5.0. Removal of the negative charge at position 156 combined with the addition of a positive charge at position 166 changed the Z number by approximately 1.25 when compared to the wild-type subtilisin.

Analysis of Figure 1-3 clearly points to pH 5.0 as the optimal mobile-phase pH. The chromatographic behavior of subtilisin is satisfactory and minimization of autolysis without the use of inhibitors can be accomplished at this pH. Although there is a large reduction in enzymatic activity at pH 5.0, the three-dimensional structure undergoes little, if any, change. Further chromatographic studies were performed at pH 5.0.

Three variants with double mutations at position 156 and 166 were utilized to determine (1) the contribution of the position 50 substitution to chromatographic behavior and (2) the position 156 and 166 contributions. Table II summarizes the Z number determinations for the double mutation variants and the FQK variants. The Z number for the FQK and the QK variants was found to be the same, suggesting no change in the number of electrostatic interactions. Hence, position 50 does not have a direct electrostatic effect on subtilisin cation-exchange chromatographic behavior.

The double mutation variants at position 156 and 166 showed altered electrostatic behavior. In the SD and QD variants, an aspartate was substituted at position 166. The

Table III. Position 166 Variant Retention Times: pH 5.0; 30-min Linear Gradient 0 to 0.15 M NaCl

variant	retention time, min	variant	retention time, min
D166	7.10	H166	10.00
E166	7.55	R166	11.90
wild type	8.30	K166	12.05
N166	8.45	P166	18.15
C166	8.65	V166	18.30
S166	8.70	Y166	18.40
M166	8.75		

QD variant had a Z number less than the QK, but still greater than the wild-type protein. This implies that the glutamine substitution at position 156 also effects the number of electrostatic interactions between the protein surface and the column, hence altering retention. Perhaps this dual substitution compensates for itself, and for this reason the Z numbers for both the SD and the wild type are the same.

The previous retention map was completed by using a 30-min linear gradient elution of single solute injections. Although these proteins differed from the wild type by only three and four amino acids, respectively, the substitutions occurred at multiple locations, which complicates any explanation of the retention process. The most desired probe would be one in which one position can be manipulated with a choice of amino acid substitutions. Position 166 was chosen as the location for the study of amino acid contribution to protein retention after review of the initial experimental results and consultation with the scientific staff at Genencor. Including the wild-type subtilisin, 12 genetically engineered proteins with site-specific substitutions at this position were used.

Position 166 Variants. Position 166 substitutions were chosen to acquire an understanding of the direct and indirect contributions amino acids make to protein retention. Histidine, arginine, and lysine were selected to determine how much of a direct effect positively charged residues have on a cation-exchange column. All three substituted amino acids were fully ionized at pH 5.0; however the side chains differ sterically, which could influence the electrostatic interaction. The aspartate and glutamate residues were picked to see whether or not a negative charge would decrease retention, possibly as a result of electrostatic repulsion. Finally, various neutral substitutions were chosen to examine how polar and nonpolar amino acids effect the solvent in the substrate binding cleft and the dependence of protein retention on solvent association.

Gradient Elution. Amino acid contributions to retention at position 166 were initially investigated by the separation of the variant proteins using gradient elution. The first variants examined were the H166, K166, and R166 variants. From the initial work with the FQK variants, it was assumed that position 166 would allow direct interaction between the positively charged residues and the sorbent surface. Table III lists the retention times for all the position 166 variants. All three positive charge substitution variants showed an increase of retention over the wild-type subtilisin. The K166 and R166 variants coeluted and were both retained over 12% longer than the wild type while the H166 variant retention differed from the wild-type subtilisin by 5.7%.

Figure 4 demonstrates the resolving power of cation-exchange chromatography with the separation of two subtilisin variants from the wild type. Both the D166 and E166 variants eluted before the wild-type subtilisin. This was expected since both variants have a -1 net charge difference compared to the wild type and the substituted residues should be repelled from the negatively charged sorbent surface when located at position 166. What was not predicted was the resolution

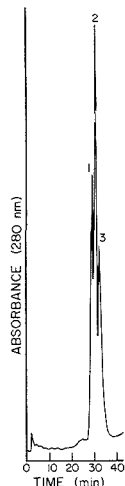


Figure 4. Separation of negatively charged position 166 substitution variants from the wild type. Chromatography performed at pH 5.0, using a 30-min linear gradient from 0 to 0.15 M NaCl at a flow rate of 0.5 mL/min. Numbered peaks correspond to (1) D166 variant, (2) E166 variant, and (3) wild-type subtilisin.

between the D166 and E166 variants. This is rather remarkable considering that these two variants differ by only one methylene group in a protein of 27 500 molecular weight. Obviously, more than just an electrostatic effect contributes to retention at this position. Hence, nonpolar and polar uncharged substitutions were next made to investigate the nonelectrostatic contributions to chromatographic behavior at this location.

Position 166 is located in the substrate binding cleft of subtilisin where sufficient solvent accessibility in the region allows water molecules to reside (33). The wild-type subtilisin contains glycine at this position, which allows for a minimum in steric hindrance. To check the possible effect of solvent displacement, five amino acid substitutions were chosen at this location. The C166, N166, M166, and S166 variants all coeluted with wild-type subtilisin. Comparison of the hydrophobic character of amino acid residues in globular proteins reveals that the hydrophobicity index for serine, asparagine, and glycine is virtually the same (34). Normally, methionine is considered to behave as a hydrophobic amino acid; however, it has been shown to behave as though it contains a polar group (35). Although all four variants elute almost with the wild-type enzyme, there is a slight discrimination. From Table III, it can be seen that the variants are all retained somewhat longer than the wild type. No resolution was detected when all five proteins were coinjected nor could any combination of variants be separated. It appears that polar noncharged residues do not significantly perturb the local environment, therefore no separation was observed.

Nonpolar amino acid replacements were next used to investigate the role of solvent perturbation in the environment of position 166 on protein/sorbent adsorption. The P166, V166, and Y166 variants were obtained and found to have similar retention times, all of which were substantially different from the wild type and the other position 166 variants studied. It was thought that these substitutions could effect protein retention by changing the hydration layer; however, it was not expected that these variants would be retained longer than the positively charged replacements. Because the net charge does not change, the retention effect must be due

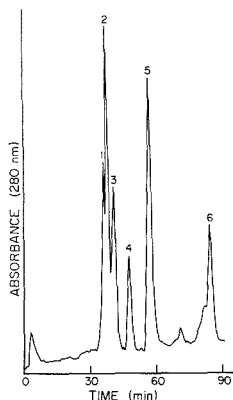


Figure 5. Resolution of six single position subtilisin variants: (1) D166; (2) E166; (3) wild type; (4) H166; (5) K166; (6) P166. Chromatography was performed at pH 5.0, using an 140-min linear gradient from 0 to 0.15 M NaCl at a flow rate of 0.5 mL/min.

Table IV. Position 166 Variant *Z* Number and *I* Value Summary at pH 5.0

variant	<i>Z</i> number	<i>I</i> value
D166	2.85 ± 0.02	1.12 × 10 ⁻⁴
E166	3.00 ± 0.03	8.44 × 10 ⁻⁴
wild type	2.60 ± 0.06	6.69 × 10 ⁻⁴
N166	2.63 ± 0.03	7.54 × 10 ⁻⁴
S166	2.85 ± 0.03	2.39 × 10 ⁻⁴
M166	2.81 ± 0.02	2.82 × 10 ⁻⁴
H166	3.13 ± 0.01	1.86 × 10 ⁻⁴
K166	3.12 ± 0.06	2.46 × 10 ⁻⁴
R166	3.15 ± 0.03	2.46 × 10 ⁻⁴
P166	3.77 ± 0.04	4.10 × 10 ⁻⁴
V166	3.65 ± 0.04	5.59 × 10 ⁻⁴
Y166	3.73 ± 0.03	4.06 × 10 ⁻⁴

to either a change in the contact region between the protein surface and the sorbent, a change in the binding affinity, or both.

The changes in retention time among the position 166 variants imply multiple mechanisms of interaction depending on the type of residue substitution. The prominent role of a single amino acid in protein chromatographic behavior is seen in the separation of six different subtilisin variants (Figure 5). Here, it is evident that minute changes on the protein surface have a notable effect on subtilisin cation-exchange retention. However, the type of contribution, be it direct electrostatic interaction or indirect influence of the local environment, cannot be determined experimentally from the gradient elution studies.

SDM Analysis. In an attempt to further explain amino acid contribution to protein chromatographic behavior, isocratic analyses were performed to quantitate the *Z* numbers and *I* values for the position 166 variants. Variants grouped together as a consequence of their elution order in gradient elution have similar *Z* numbers and *I* values (Table IV). The resolution between variants is also reflected in these parameters with either the *Z* number of the *Z* values differing between separated species. As expected, positive charge substituted variants all have a larger *Z* number than the wild-type subtilisin. A significant increase in *Z* number was also observed for negative charge substituted variants and nonpolar variants with the polar uncharged variants all having *Z* numbers similar to the wild type. The increased *Z* numbers were unexpected since none of these substituted residues should directly in-

teract with the negatively charged sorbent surface. In the case of the D166 and E166 variants, the *I* value is between 6 and 8 times less than the wild type value, compensating for the observed increase in *Z* number. This explains why these variants elute before the wild type. The nonpolar residue replacements coeluted and were retained 33% longer than wild-type subtilisin. These variants have the largest *Z* numbers of all the position 166 subtilisins and were also retained the longest in the gradient elution experiments. An explanation for the increased *Z* numbers for these variants will be presented in the discussion section. Regardless of the retention mechanism, the isocratic data confirm the trend of increasing *Z* numbers corresponding to longer retention times for gradient eluted subtilisin.

DISCUSSION

Multiple Substitution Variants. Determination of amino acid influence on chromatographic behavior with genetically engineered proteins is a complicated matter due to the potential indirect effects residue substitution can have on other locations in the protein. Comparison between the FQK and FQK R275 variants shows a difference in *Z* number of approximately 1 throughout the pH range studied. Lysine substitution at the carboxy-terminus of the FQK R275 variant increased the *Z* number by 1 due to direct interaction between the substituted residue and the column. The difference in *Z* number between the wild type and FQK was approximately 1.25 even though the net charge difference between the two proteins is +2. The addition of the lysine at position 166 could allow for direct electrostatic interaction between the protein and the sorbent, hence increasing the *Z* number by 1, but not 1.25. It is concluded that removal of the negative charge at position 156 contributes slightly to the increase in *Z* number.

Comparison of the QK, K166, QD, and D166 variants shows that glutamine substituted at position 156 increases the *Z* number by approximately 0.5 unit and that the glutamine contribution was greater than serine. Thus, the type of neutral amino acid as well as the location has an impact on chromatographic behavior. It must be acknowledged, however, that the double substitution may incorporate a cooperative effect and the exact contributions of the single amino acids may not be additive. The *Z* number trend determined at pH 5.0 for the double substitution variants, the positively charged position 166 variants, and the wild type enzyme parallel the results found in a kinetic study on these same variants that examined the binding of a negatively charged P_i substrate (36). That paper concluded the presence of a charged residue at position 166 significantly lowered the effect of the charge at 156. It was also found that the average change in substrate preference was greater for a charged substrate at position 166 compared to position 156. In a different study, position 156 was investigated for its role in electrostatic effects on the active site histidine (37) and it was reported that substitution of a serine at this location lowered the pK_a of His 64 by up to 0.4 unit. Furthermore, it was reported that substitution of a charged amino acid may result in changes in the structure and orientation of water around the protein. Such reorientation of solvent and the surrounding counterions could affect the pK_a of the active site by structural changes in addition to direct electrostatic interactions. Hence, position 156 influences the function of subtilisin in multiple ways. Replacement of glutamate at this position significantly alters not only the chromatographic behavior of subtilisin but also the substrate binding and kinetic catalysis.

Position 166 Variants. Correlation of the early isocratic analyses with the previously mentioned kinetic substrate data suggested that position 166 leads to direct electrostatic interactions with the cation-exchange sorbent. Separation of the position 166 variants from the wild-type subtilisin was

possible when the substitution involved either a charged or a relatively hydrophobic residue. Changes in retention were expected for charge substitutions, but the large differences associated with the hydrophobic residue replacements were a surprise.

Positively Charged Replacements. The positively charged position 166 variants were retained longer than the wild type in the gradient separation due to increased electrostatic interaction with the sorbent stationary phase. Isocratic analyses of these variants acknowledged greater direct electrostatic contact with an increase in Z number for all three variants compared to the wild type. Separation of the H166 from R166 and K166 variants occurred as a result of different binding affinities for these amino acids at this position. The I value difference supports this explanation. Although the Z number for H166 was similar to the other two positively charged variants indicating a parallel increase in direct electrostatic interaction with the column, the I value was found to be less by one-third, explaining the elution order in the gradient separation. The lower affinity for the histidine residue may be due to the less extended conformation of the side chain compared to the lysine and arginine residues. Both R166 and K166 coeluted in gradient elution and had similar Z numbers and I values at pH 5.0. Arginine substitution for lysine in FQK backbone subtilisins was shown to alter both the Z number and the I value at pH 6.0 and above (18). These variants were separated from each other above pH 7.0 in a 30-min linear gradient. Perhaps at pH 5.0, the differences between the arginine and lysine side chains are not reflected in the chromatographic behavior of subtilisin while at more alkaline mobile-phase conditions the subtle differences between these two amino acids could be discriminated.

Negatively Charged Replacements. With the addition of a negative charge at position 166 the net charge of the molecule decreased by one. Yet, the Z numbers for both the D166 and E166 variants were found to be greater than the wild type. The elution order in the gradient separation (D166, E166, and wild type) may be explained by the sharp decrease in I value between the wild type and the negatively charged variants (6- to 8-fold). Structural data determined by X-ray crystallography shows a hydrogen-bond complex between Glu 156 and Asp 166, with a less ordered complex between Glu 156 and Glu 166 (38). This alters the negative charge associated with the ionized carboxyl of these two variants and may shift the chromatographic contact region resulting in an increased Z number compared to the wild type. The affinity for the interactions is nevertheless effected by the partial negative charge; hence both variants elute before the wild-type subtilisin. A previous report on a glutamate-to-aspartate substitution in a different protein found that the extra distance incurred by the glutamate side chain lengthened the distance between the existing hydrogen bond at this position such that the pair was reduced to a weak electrostatic interaction (39). Nevertheless, the structural difference between the two variants is large enough to be detected chromatographically. A comparison was not made between these variants and the kinetic substrate analysis because no data are available on negatively charged substrate binding to these variants. In any event, the ability to separate these two variants, which only differ by one methylene group in a molecule of 27 500 molecular weight, is a tribute to the resolving power of ion-exchange chromatography.

Neutral Nonpolar Replacements. The uncharged amino acid contributions to retention are the most difficult to account for because there should not be any direct electrostatic interaction from these residues. Knowledge pertaining to protein structure is essential for a plausible explanation regarding potential indirect effects of residue substitution. Such

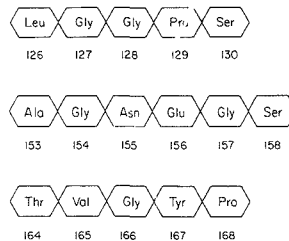


Figure 6. Primary sequence of subtilisin segments lining the S_1 binding site.

information is available for position 166 in subtilisin. An integral part of this location in the molecule is the surrounding microenvironment. The primary sequence around position 166 including residues 126–130, 153–158, and 164–168, which form the S_1 substrate binding subsite, is listed in Figure 6. Although the majority of the residues in this area are hydrophilic, the amino acids immediately adjacent to and the segments located across from position 166 (residues 123–130) are relatively hydrophobic. Substitution of a hydrophobic residue at this location could alter the water orientation within the substrate binding cleft by removing the only hydrophilic residue in this part of the cleft. The two types of water molecules associated with proteins can be distinguished as periphery water, which provides the hydration shell, and internal water, which fills cavities in the protein and diminishes local charge-charge interactions (40). The binding cleft was recently reported as containing eight of the approximately 400 localized solvent molecules in close contact with protein atoms and thus considered as molecules of the first hydration layer (41). Furthermore, these solvent molecules were determined to be highly cross-connected and hydrogen bonded to polar groups of subtilisin. Cross-connected water structures refer to the highly conserved hydrogen bonding networks involving internal water molecules and the corresponding protein. This network includes the bridging between the internal water molecules/protein surface and water molecules considered to be part of the first hydration layer (42). Of the eight solvent molecules located in the S_1 subsite, four are within contact range of position 166 (S473, S478, S752, and S756). Substitution of a hydrophobic residue for a hydrophilic one at a location adjacent to a water molecule changes the energetics of the water (43). Reorientation of highly cross connected water molecules within the substrate binding cleft could lead to alteration in the hydration layer of subtilisin. An unrelated study using genetically engineered proteins reported that mutational changes could leave an enzyme structure totally unaffected but could alter the structure of the solvent shell around the enzyme (44). A recent examination into the increased thermostability of an engineered subtilisin revealed that a single amino acid substitution at position 218 repositioned a water molecule, presumably to optimize hydrogen bonding with the position 218 side chain (45). These examples support the possibility that the displacement of highly structured water may have occurred with the hydrophobic amino acid substitution of subtilisin at position 166, subsequently modifying the retention process.

The retention of P166, V166, and Y166 was found to be greater than any other position 166 variant. Addition of a hydrophobic residue to an already hydrophobic environment could alter the water structure by entropically driven rearrangement of the fixed solvent molecules (internal water molecules considered to be an integral part of the protein structure). Crystallographic data for these particular variants are not available; however, the X-ray structure of the position 166 isoleucine substituted variant shows the rearrangement

Table V. Charged Amino Acid Side Chain Distance from Position 166 α -Carbon

atom	residue	coordinates			distance, Å
		x	y	z	
CA*	Gly-166	17.90	38.70	23.70	
NZ	Lys-170	18.60	45.30	23.10	6.66
CD	Glu-156	14.60	35.80	18.00	7.20
CD	Glu-195	21.80	46.10	23.10	8.39
CG	Asp-197	29.50	41.80	23.50	17.01
CE1	His-64	20.20	25.00	23.00	13.91
CZ	Arg-186	22.60	39.00	10.40	14.11
NZ	Lys-136	22.70	46.40	34.70	14.26
CZ	Arg-247	31.40	41.30	27.90	14.38
CG	Asp-140	25.10	43.20	36.80	15.61
CG	Asp-32	20.90	23.60	26.90	15.72
CG	Asp-259	28.30	47.40	10.90	18.65
NZ	Lys-265	35.40	46.70	19.60	16.67
CE1	Lys-226	31.20	25.40	17.30	15.87
CE1	His-67	24.80	20.80	18.00	20.01
CD	Glu-112	22.50	33.30	43.20	20.75
NZ	Lys-141	22.80	37.60	44.80	21.69
CG	Asp-181	29.10	30.30	6.40	25.26
CG	Asp-60	19.40	16.50	26.90	25.48
CG	Asp-98	10.70	17.00	27.80	25.23
NZ	Lys-94	16.40	17.10	33.00	25.57
CG	Asp-120	37.00	28.60	37.30	25.53
CD	Glu-54	12.60	15.90	33.90	25.53
CG	Asp-61	13.80	13.90	28.90	25.67
NZ	Lys-256	40.90	46.70	12.70	26.72
NZ	Lys-12	42.80	31.40	15.40	27.43
CE1	His-17	40.70	21.60	21.60	28.58
CG	Asp-96	23.10	10.00	28.30	28.53
NZ	Lys-27	35.80	22.30	40.80	28.70
NZ	Lys-213	18.70	8.80	18.90	30.30
CE1	His-39	28.10	10.00	22.50	30.48
CE1	His-238	48.30	33.70	28.40	31.17
CG	Asp-41	32.90	10.80	22.00	31.72
NZ	Lys-237	50.50	30.20	25.10	33.72
NZ	Lys-43	35.30	10.40	35.80	35.36

*Target atom.

of a highly ordered S_1 subsite water molecule by 0.6 Å (38). The substitution of proline, valine, and tyrosine at position 166 may have altered the cross-connected water structure of the adjacent solvent molecule in a similar manner, subsequently shifting the protein hydration layer and altering the chromatographic contact behavior of subtilisin.

Russell and Fersht have reported that neutral substitutions for negatively charged amino acids influenced the pK_a of nearby residues, within a radius of about 15 Å, regardless of the medium between the two locations (46). The conclusions reached were that electrostatic forces reign over a long range and their influence could extend through portions of protein as well as through solvent channels within the molecule. Distances between all charged residues and position 166 were determined to consider if any shifts in pK_a could account for the apparent shift in hydration found with the nonpolar substitution variant results. The results are described in Table V. Of the 34 charged amino acids in subtilisin, eight are within 15 Å of position 166. At pH 5.0, seven of these eight should be completely ionized, hence little or no influence on the side chain pK_a would be expected for these residues. The remaining residue within 15 Å of position 166 is the active site histidine, which, as explained earlier, is already protonated at pH 5.0. Therefore, the longer retention time and subsequent increase in Z number for the P166, V166, and Y166 variants were not caused by electrostatic adjustment in the side chain pK_a of any neighboring amino acids. Although electrostatic forces may conduct through different dielectric media, influencing nearby side chains, water molecules must be adjacent to the location of the action for hydrogen bonding to

occur. Perturbation of protein hydration by neutral amino acid substitution most likely occurred as a result of direct steric repulsion of water from the substituted residue and not by any indirect electrostatic influence.

A change in the solvent cage around the protein could determine surface residue accessibility with the sorbent stationary phase by perturbing the energetics of protein solvation and hence the equilibrium constant for protein/column binding. Slight repositioning of water molecules by as little as 0.6 Å has been shown to adversely affect substrate binding enough to destabilize the transition-state intermediate and decrease the k_{cat} for the enzymatic reaction (47). Variant retention and consequent increase in Z number most likely resulted from altered protein/column association due to the change in subtilisin hydration caused by the nonpolar substitution. All three variants had similar Z numbers and I values suggesting that the contributions of proline, valine, and tyrosine to subtilisin retention were analogous. The hydrophobicity indices for these three residues are listed consecutively and away from that of glycine, implying that they have similar hydrophobic behavior (48). Hence, any reorientation of the protein hydration layer due to alteration of the cross-connected cleft water was similar for each substituted amino acid and little or no discrimination in retention should be expected between these variants. In a previous study, significant indirect influence of amino acid contribution to retention in which a substituted charged histidine residue effected the hydrophobic-interaction chromatography (HIC) of avian lysozyme natural occurring variants was reported (12). That study also concluded not only that the hydrophobic residues, involved in the dominant mode of interaction, contribute to HIC protein retention but that the indirect contributions of hydrophilic residues are important. Therefore, residue substitutions which indirectly alter the chromatographic contact area microenvironment may have significant ramifications in cation-exchange protein retention.

Neutral Polar Replacements. The solvent displacement hypothesis was further tested by using polar uncharged residues. Since the hydrophobicity index for the polar replacements and glycine is similar, substitution of Gly 166 with the polar amino acids should not displace the solvent structure in the S_1 binding cleft, although it may slightly alter the water orientation due to steric constraints. Gradient elution of the polar substituted position 166 variants demonstrated no difference in retention compared to the wild-type subtilisin. No major change in protein/column association occurred. The polar residues did not directly alter the interaction with the cation-exchange sorbent. The Z numbers and I values were observed to vary slightly depending on the variant; however, these two retention parameters compensated for each other allowing the variants to coelute with the wild type. Absolute retention times varied enough for possible resolution between wild type and M166; however, no separation between these two proteins was achieved. Thus, although small discrepancies occurred in the isocratic analyses and absolute retention times of S166, N166, and M166 compared to the wild type, the overall retention of these variants as well as C166 was found to be similar to the wild type.

CONCLUSION

On the basis of the separation of subtilisin single amino acid substitution variants in multiple chromatographic modes (49, 50), no single separation techniques can resolve all the possible similar structure impurities associated with genetically engineered protein production. The limiting factor is surface recognition, which is dependent on the mechanism by which a particular separation technique discriminates between different species. Cation-exchange chromatography is a surface-mediated method that discriminates between proteins

on the basis of accessible positive charge, namely ionized histidine, lysine, and arginine. This approach probes a broad area of the protein surface and is a good general procedure for resolving similar structure impurities associated with purification applications in biotechnology.

Cation-exchange chromatography was shown to separate six single substitution variants of subtilisin not only on the basis of charge but also by nonpolar residue contributions. From this study, it may be concluded that both neutral and charged amino acids located in the microenvironment of the contact region can effect protein chromatographic behavior. This separation method does have limitations, as was shown in the coelution of certain subtilisin variants, such as not being able to discriminate between variants which do not alter the microenvironment of the chromatographic contact area. However, the resolution of two variants differing by only a methylene group in a 27 500 dalton protein demonstrates the resolving power of cation-exchange chromatography.

This study also demonstrates how important the contribution of single amino acids are to the retention of globular proteins. It can be concluded that amino acid contribution to protein retention includes both the indirect influence of residues within the microenvironment of the chromatographic contact surface area as well as the direct interactions between the protein surface residues and the column stationary phase. Indirect effects include both electrostatic manipulation of neighboring residue pK_a values as well as steric perturbation of hydrogen bonded water molecules. The role of protein associated water in separation processes requires further investigation. Cation-exchange chromatography has been established as an effective analytical technique for the separation of genetically engineered proteins. Future considerations in protein design may include insertion of specific surface residues to aid in the purification of biotechnology products.

ACKNOWLEDGMENT

Wild-type subtilisin as well as the engineered variants were the gracious gift of Genencor, Inc. Helpful discussions with the Genencor scientific staff regarding subtilisin structure and function were appreciated. We thank Rick Bott, Dave Estell, and Scott Power for exchanging results prior to publication.

LITERATURE CITED

- Hutchinson, C. A., III; Phillips, S.; Edgell, M. H.; Gillism, S.; Jahnke, P.; Smith, M. J. *Biol. Chem.* **1978**, *253*, 6551-6560.
- Smith, M. *Annu. Rev. Genet.* **1985**, *19*, 423-462.
- Leatherbarrow, R. J.; Fersht, A. R. *Protein Eng.* **1986**, *1*, 7-16.
- Wetzel, R. *Protein Eng.* **1986**, *1*, 3-6.
- Knowles, J. R. *Science* **1987**, *236*, 1252-1258.
- Muraki, M.; Morikawa, M.; Jigami, Y.; Tanaka, H. *Protein Eng.* **1988**, *2*, 49-54.
- Dixon, J., Purdue University, 1988, personal communication.
- Pakula, A. A.; Young, V. B.; Sauer, R. T. *Proc. Natl. Acad. Sci. U. S. A.* **1986**, *83*, 8629-8633.
- Regnier, F. E. *Science* **1987**, *238*, 319-323.
- Drager, R. R.; Regnier, F. E. *J. Chromatogr.* **1987**, *406*, 237-246.
- Gang, X.; Regnier, F. E. *J. Chromatogr.* **1985**, *332*, 147-168.
- Fausnaugh, J.; Regnier, F. E. *J. Chromatogr.* **1986**, *359*, 131-146.
- Kopaciewicz, W.; Rounds, M. A.; Fausnaugh, J.; Regnier, F. E. *J. Chromatogr.* **1983**, *266*, 9-21.
- Drager, R. R.; Regnier, F. E. *J. Chromatogr.* **1986**, *359*, 147-155.
- Gang, X.; Regnier, F. E. *J. Chromatogr.* **1984**, *296*, 15-30.
- Estell, D. A.; Graycar, T. P.; Wells, J. A. *J. Biol. Chem.* **1985**, *260*, 6513-6521.
- Estell, D. A.; Genencor, Inc., 1988, unpublished results.
- Chicz, R. M.; Regnier, F. E. *J. Chromatogr.* **1988**, *443*, 193-203.
- Alden, R. A.; Birtoft, J. J.; Kraut, J.; Robertus, J. D.; Wright, C. S. *Biochem. Biophys. Res. Commun.* **1971**, *45*, 337-344.
- Durham, D. R. *J. Appl. Bacter.* **1987**, *63*, 381-386.
- Wels, J. A.; Powers, D. B.; Bott, R. R.; Katz, B. A.; Ultsch, M. H.; Kosiakoff, A. A.; Power, S. D.; Adams, R. M.; Heyneker, H. H.; Cunningham, B. C.; Miller, J. V.; Graycar, T. P.; Estell, D. A. *Protein Engineering*; Alan R. Liss, Inc.: 1987; Chapter 25.
- Bott, R.; Ultsch, M.; Wells, J.; Powers, D.; Burdick, D.; Struble, M.; Burnier, J.; Estell, D.; Miller, J.; Graycar, T.; Adams, R.; Power, S. *Am. Chem. Soc. Symp. Ser.* **1987**, *334*, 140-147.
- Neet, K. E.; Koshland, D. E., Jr. *Proc. Natl. Acad. Sci. U.S.A.* **1966**, *56*, 1606-1611.
- Matsubara, H.; Nishimura, S. *J. Biochem.* **1958**, *45*, 503-510.
- Robertus, J. D.; Alden, R. A.; Birtoft, J. J.; Kraut, J.; Powers, J. C.; Wilcox, P. E. *Biochemistry* **1972**, *11*, 2439-2449.
- Mathews, D. A.; Alden, R. A.; Birtoft, J. J.; Freer, S. T.; Kraut, J. *J. Biol. Chem.* **1975**, *250*, 7120-7126.
- McHalen, C. A.; Svendsen, I.; Jonassen, I.; James, M. N. G. *Proc. Natl. Acad. Sci. U.S.A.* **1985**, *82*, 7242-7246.
- Hirano, S.; Akagawa, H.; Mitsui, Y.; Itakura, Y. *J. Mol. Biol.* **1984**, *178*, 389-413.
- Bode, W.; Papamokos, E.; Musil, D.; Seemueller, U.; Fritz, H. *EMBO J.* **1986**, *5*, 813-818.
- Philipp, M.; Bender, M. L. *Mol. Cell. Biochem.* **1983**, *51*, 5-32.
- Ottensen, M.; Svendsen, I. *Methods Enzymol.* **1970**, *19*, 199-215.
- Glaser, A. N. *J. Biol. Chem.* **1967**, *242*, 433-436.
- Estull, D. A.; Grayar, T. P.; Miller, J. V.; Powers, D. B.; Burnier, J. P.; Ng, P. G.; Wells, J. A. *Science* **1986**, *233*, 659-663.
- Manavalan, P.; Ponnuswamy, P. K. *Nature* **1978**, *275*, 673-674.
- Rose, G. D.; Geselowitz, A. R.; Lesser, G. J.; Lee, R. H.; Zehfus, M. H. *Science* **1985**, *229*, 834-838.
- Wels, J. A.; Powers, D. B.; Bott, R. R.; Graycar, T. P.; Estell, D. A. *Proc. Natl. Acad. Sci. U.S.A.* **1987**, *84*, 1219-1223.
- Russell, A. J.; Thomas, P. G.; Fersht, A. R. *J. Mol. Biol.* **1987**, *193*, 803-813.
- Bot, R. R.; Power, S. D.; Genencor, Inc., 1987, unpublished results.
- Daar, I. O.; Artymiuk, P. J.; Phillips, D. C.; Maquat, L. E. *Proc. Natl. Acad. Sci. U.S.A.* **1986**, *83*, 7903-7907.
- Saenger, W. *Annu. Rev. Biophys. Chem.* **1987**, *16*, 93-114.
- Bode, W.; Papamokos, E.; Musil, D. *Eur. J. Biochem.* **1987**, *166*, 673-692.
- Baler, E. N.; Hubbard, R. E. *Prog. Biophys. Mol. Biol.* **1984**, *44*, 97-179.
- Fersht, A. R.; Shi, J.-P.; Knill-Jones, J.; Lowe, D. M.; Wilkinson, A. J.; Blow, D. M.; Brick, P.; Carter, P.; Waye, M. M. Y.; Winter, G. *Nature* **1985**, *314*, 235-238.
- Fersht, A. R.; Wilkinson, A. J.; Carter, P.; Winter, G. *Biochemistry* **1985**, *24*, 5858-5861.
- Bryan, P. N.; Rollence, M. L.; Pantoliano, M. W.; Wood, J.; Finzel, B. C.; Gilliland, G. L.; Howard, A. J.; Poulos, T. L. *Proteins: Struct., Funct., Genet.* **1986**, *1*, 326-334.
- Russell, A. J.; Fersht, A. R. *Nature* **1987**, *328*, 496-500.
- Bott, R.; Ultsch, M.; Kosiakoff, A.; Graycar, T.; Katz, B.; Power, S. J. *Biol. Chem.* **1988**, *263*, 7895-7906.
- Yungster, L. M.; Cramer, R. D., III. *Mol. Pharmacol.* **1981**, *20*, 603-608.
- Chicz, R. M.; Regnier, F. E. *Anal. Chem.* **1989**, *62*, 1742-1749.
- Chicz, R. M.; Regnier, F. E. *J. Chromatogr.*, in press.

RECEIVED for review April 10, 1989. Accepted June 21, 1989. This work was supported by NIH Grant Number 25431. This is paper No. 11947 of the Purdue University Agricultural Experiment Station.

Synthesis and Characterization of a Hydride-Modified Porous Silica Material as an Intermediate in the Preparation of Chemically Bonded Chromatographic Stationary Phases

Junior E. Sandoval* and Joseph J. Pesek

Department of Chemistry, San Jose State University, San Jose, California 95192

A novel synthetic approach to produce chemically bonded silica-based chromatographic stationary phases is presented and discussed. The procedure involves the preparation of a silica intermediate containing stable silicon hydride (silane) surface species followed by the catalytic addition of these to organic compounds bearing a terminal vinyl group. This paper deals with the preparation of the hydride intermediate via chlorination of silica followed by reduction with lithium tetrahydridoaluminate. Several spectroscopic and thermoanalytical techniques were used to obtain information regarding the structural characteristics of the surface-reduced silica material. It was found that the surface SiH species formed were hydrolytically stable at low pH and thermally stable in the presence of oxygen at temperatures up to about 450 °C. Postreaction treatment of the hydride-derivatized solid with aqueous hydrochloric acid was also found to be essential to remove aluminum byproducts from the silica surface while presumably increasing the extent of silane formation.

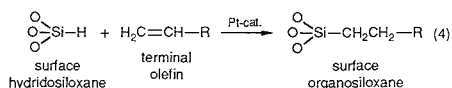
INTRODUCTION

Because of their high versatility and superior selectivity, chemically modified silicas have been used as supports in a wide variety of chromatographic applications. Numerous synthetic procedures have been developed to attach organic moieties (R) onto the silica surface. Reaction of fully hydroxylated silica with triorganochlorosilanes (silanization) to give organosiloxane-type linkages has been the most commonly used approach (1, 2). A vast majority of commercially available bonded phases belong to this category, *n*-octyl- and *n*-octadecyldimethylsilyls being the preferred modifying groups. In another approach, direct Si-R linkages have been formed by sequentially reacting silica with thionyl chloride (SOCl₂) and a proper Grignard (3, 4) or organolithium reagent (5, 6). Based upon steric considerations as well as relative bond strengths in silicon chemistry (7-9), the latter method should provide not only a closer attachment and a denser coverage of organic functionalities onto the silica surface but also a more hydrolytically stable bonded phase than that obtained by the corresponding organosiloxane-type structure. Silanization, however, is by far more popular presumably because of the commercial availability of a variety of silanizing reagents and the relative ease with which the reaction is carried out. It thus seems clear that to replace the currently available silanization technology for making bonded phases, any new approach has to demonstrate greater simplicity of the synthetic procedure, superior coverage of the silica surface, and/or higher hydrolytical stability of the attached groups.

The overall synthetic scheme for silica silanization generally involves several steps, as shown in Figure 1. A prebonding reaction is carried out to prepare the silanizing reagent, usually via catalytic addition of a SiH group to a terminal olefin (hydrosilation). The primary silica derivatization reaction involves the nucleophilic attack of surface silanols at the central silicon atom of the silanizing reagent. Additional silanization of the modified support (end-capping), this time

with trimethylchlorosilane or hexamethyldisilazane, is usually carried out to somewhat reduce the surface concentration of unreacted silanols left by the primary bonding reaction.

A cursory look at the reaction scheme of Figure 1 reveals that by using the prebonding reaction 1, an alternate Si-C bond can be formed directly between the silica surface and the organic group



Since the two bulky methyl groups will no longer be present, this alternate scheme should result in a closer packing of the anchored organic groups as well as a more stable bonded phase. Naturally, the new synthetic strategy would require that (i) silicon hydride (silane) species were already present on the solid support and (ii) the heterogeneous hydrosilation reaction proceeded with a good yield. The latter prerequisite appears to be of immediate importance since without a good yield of the adduct, attempting to synthesize surface SiH species would be pointless. A cursory literature survey in which special attention was paid to the addition of hydrosiloxane (O₂SiH) groups to terminal olefins revealed several important points about what can be expected from olefinic addition with this class of silanes.

The addition of silicon hydrides to alkenes has been recognized as one of the most important laboratory methods to form Si-C bonds. The reaction's minimal interference with other reactive functionalities (e.g.: CO₂R, CN, NH₂, etc.) has permitted the attachment of silicon to organic molecules which otherwise cannot be introduced by regular organometallic procedures (7). Hydrosilation is generally carried out in the presence of a transition-metal catalyst. A variety of inorganic and organic platinum complexes have functioned as very effective catalysts for the addition reaction, chloroplatinic acid in a 2-propanol solution (also known as "Speiers" catalyst) being the most commonly used form. Only as little as 10⁻⁶ mol of platinum/mol of silicon hydride is normally required for an effective hydrosilation (7, 8). The addition is rapid and can be done at room temperature or under reflux to ensure a high yield. The mechanism of the reaction in homogeneous phase has been thoroughly studied and is thought to involve a hexacoordinated platinum intermediate formed by the addition of the Si-H group to the olefin-catalyst complex. Details can be found elsewhere (7, 10).

Indirect evidence for the feasibility of the addition of surface silicon hydride groups to terminal olefins can be obtained from the works by Chalk and Harrod (10) and Musolf and Speier (11). In their reports, organosiloxanes of the type (RO)₂SiH and (R₃SiO)₂SiH (R = CH₃-, C₂H₅-) have been shown to give the adducts at yields above 90%. More recently, and perhaps more relevant, Laub and co-workers (12) have successfully used hydrosilation to attach a variety of mesomorphic (liquid crystal) molecules bearing a terminal vinyl group to the backbone of poly(methylhydrosiloxane) (-[OCH₂SiH]_n-) materials. The mesomorphic nature of the polymeric adduct

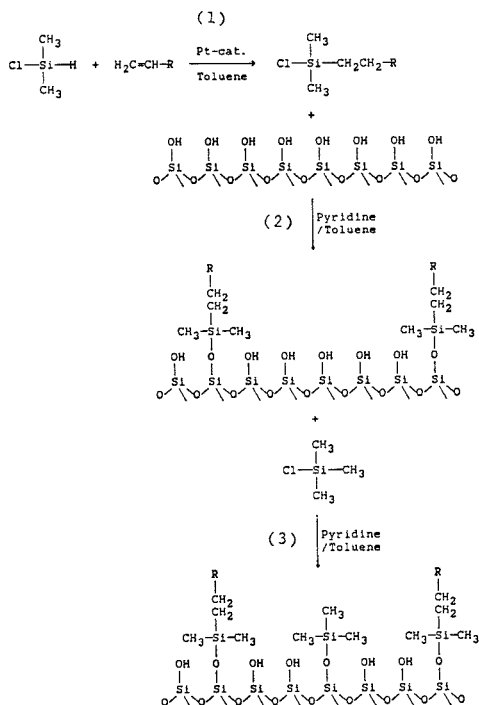


Figure 1. Typical reaction scheme for the silanization of silicas: (1) prebonding reaction (preparation of the silanizing reagent); (2) primary bonding reaction; (3) "end-capping".

when produced in significant yield was probably responsible for its remarkably high selectivity as a stationary phase for the gas chromatographic separations of polycyclic aromatic hydrocarbons. It might therefore be concluded at this point that hydrosilation of terminal olefins onto the surface of a silica-containing SiH species seems to have great potential as an alternate approach for the preparation of chemically bonded chromatographic phases.

With the establishment of the feasibility of the heterogeneous hydrosilation, it is possible to focus on the production of an intermediate silica support bearing silicon hydride as its primary surface species. Two major approaches can be envisioned: (i) chemical derivatization of fully hydroxylated porous silicas and (ii) direct preparation of a porous poly(hydridosiloxane) ($\text{HSiO}_{1.5}$)_n gel. The commercial availability of a variety of silicas with well-characterized geometries along with the relatively simple chemistry involved in its hydride derivatization (see below) make the former approach the first choice. However, it should also be pointed out that procedures similar to those for preparing regular silica have been explored for the preparation of poly(hydridosiloxane) materials. For instance, a xerogel of this kind has been synthesized via hydrolytic polymerization of triethoxysilane (13). The product has been extensively characterized (13-18) and may provide a convenient starting support material for surface hydrosilation of terminal olefins.

Reduction with an inorganic hydride can be conveniently applied to producing SiH groups on the silica surface after converting the SiOH to SiCl groups. Because of its extensive silanol conversion and simplicity, reaction with SOCl_2 in toluene as a solvent is a very common method for chlorinating silica (9). The product has been usually prepared as an in-

termediate for further silica derivatization, for instance, by reaction with organometals to produce Si-alkyl or Si-aryl surface groups. Similarly with other surface modifiers, complete silanol conversion is limited by steric hindrance due to the slightly larger cross-sectional area of a chloride group compared to that of the original hydroxyl (about 0.24 and 0.21 nm^2 , respectively) (9). Because of the good yields (typically >90%) obtained, lithium tetrahydroaluminate dissolved in an ether solvent is by far the preferred reducing reagent for the preparation of hydroorganosilanes (8). Diethyl ether is usually employed as the solvent but tetrahydrofuran (THF), dioxan, and ethylene glycol dimethyl ether have also been used. Other reducing agents include sodium hydride in a hexamethylphosphoric triamide (HMPT) solution, calcium hydride in the presence of alkylaluminum hydride, and trimethylamine hydrochloride in the presence of magnesium in a HMPT medium (8). The reaction involves the nucleophilic attack of highly polarized hydride species on the silicon atom, via a pentacoordinated intermediate (8, 19). The facile nature of the leaving group, a halide, along with the high strength of the nucleophile, hydride, explain the commonly found high reactivity and elevated yield of the reaction. Similar behavior can therefore be expected from the analogous heterogeneous reduction of chlorinated silica.

Reduction of silica can also be carried out by chemisorption of hydrogen from a pyrolytically activated support, in a fashion similar to that reported by Morterra and Low (20, 21). Formation of surface silane groups was observed when nonporous methoxylated silica (Aerosil) was pyrolyzed under vacuum at about 750 °C (20). Subsequent hydrogen-treatment of the 830 °C pyrolysis product led to the extensive formation of Si-H species, as evidenced by IR spectroscopy (21). Although a quantitative evaluation of the extent of surface reduction was not attempted, IR data also showed that a significant amount of silanol groups were also present in the hydrogenated silica. Yet, this material was found to be strongly hydrophobic and to exhibit good stability on the presence of oxygen and water vapor at temperatures up to 350 and 400 °C, respectively. Not surprisingly, these observations are consistent with those from poly(hydridosiloxane) xerogels (17).

It should be pointed out that this behavior contrasts with that of simple organohydrosilanes ($\text{R}_n\text{-SiH}_{3-n}$, $n = 1-3$, R = alkyl) which are sensitive to hydrolytic cleavage, particularly in alkaline media (22, 23). The observed stability of silicon hydride species in silica, however, should not be entirely surprising especially if one considers the similarly high chemical and thermal stability of polymeric siloxanes. In siloxane chemistry (7, 8) it has been widely accepted that the stability of these compounds is largely due to the decreased Si-H bond polarization which results from the multiple ($p \rightarrow d$), backbonding between the oxygen free electron pair and the empty d orbital of the silicon atom. An obvious consequence of the high stability is that it makes surface-reduced silica a very convenient synthesis intermediate which can be handled under fairly regular laboratory conditions. In contrast, highly reactive intermediates such as chlorinated silica in a Grignard synthesis will always require carefully controlled conditions to avoid their degradation into undesirable products.

The general purpose of this work was to investigate the feasibility of bonding organic moieties to silica supports via the heterogeneous hydrosilation of terminal olefins with surface silicon hydride species. The overall synthetic procedure involves two major steps: (1) Preparation of a chemically and thermally stable silica intermediate in which the original surface silanol groups are replaced by silicon hydride species; and (2), attachment of organic functionalities containing a

terminal vinyl group via addition with the surface hydrides. In this paper we report the results obtained from the preparation of such an intermediate, accomplished by chlorination of silica followed by reduction of the silicon chloric groups to their corresponding hydrides. Diffuse reflectance infrared Fourier transform (DRIFT) spectrometry, ^{29}Si cross-polarization magic angle spinning nuclear magnetic resonance (^{29}Si -CP-MAS-NMR), and electron spectrometry for chemical analysis (ESCA) were used to obtain information about the chemical nature of the reduced silica surface. Thermoanalytical techniques such as thermogravimetric analysis (TGA) and differential scanning calorimetry (DSC) were also used to further characterize the new hydride-derivatized material.

EXPERIMENTAL SECTION

Materials. Toluene and diethyl ether (EM Industries, Inc.) were dried by allowing them to stand with calcium hydride (Sigma Chemical Co.) for several days, refluxing, and then distilling from the hydride immediately before use (24). A 0.2 M lithium tetrahydroaluminate (Sigma Chemical Co.) ether solution was prepared and used as the reducing reagent. Thionyl chloride (Gold Label, Aldrich Chemical Co.) was used as received. IR-quality potassium bromide (Harshaw/Filtrol Partnership) powder was used for the FT-IR spectra. Partisil-40 (Whatman, Inc., Clifton, NJ) with a 40- μm mean particle size, 85- \AA mean pore size, and 350 m^2/g surface area (manufacturer's typical data) was used as the silica material.

Spectrometry. DRIFT spectra were taken in the 4000–450- cm^{-1} region with a Perkin-Elmer Model 1800 FT-IR spectrometer equipped with a deuterated triglycine sulfate (DTGS) detector. A Spectra-Tech DRIFT accessory equipped with a 13-mm diameter, 2-mm depth sample cup was used. KBr was ground in an agate mortar and dried in an oven at 120 $^{\circ}\text{C}$ for at least 24 h. After cooling down, the KBr matrix was mixed with an equal amount (by weight) of silica material and finally kept overnight in a vacuum desiccator at room temperature. Samples were filled into the DRIFT accessory's cup with gentle tapping until a small sample mound was formed. A very smooth sample surface was then obtained by pressing down a microscope slide onto the cup while moving it in a circular motion. Before a spectrum was obtained the height of the sample cup was adjusted by using the alignment routine provided with the standard Perkin-Elmer software. This resulted in a reproducible positioning of the sample surface at the optimum height so that a maximum signal throughput was consistently obtained. Spectra were collected at a nominal resolution of 2 cm^{-1} with a weak Norton-Beer apodization. Two hundred sample scans were ratioed against pure KBr as reference. Wavenumbers corresponding to maximum absorption were assigned by utilizing a "peak" routine provided with the instrument's standard software. Band intensities (absorbance units) for triplicate DRIFT spectra of samples prepared in this manner had a relative standard deviation equal to or better than 7%. Spectra shown were normalized to 100% transmittance. ^{29}Si -CP-MAS-NMR spectra were obtained at Catalytica Corp. (Mountain View, CA) on a Bruker MSF-400 NMR spectrometer at 79.5 MHz. The cross-polarization time used in all experiments was 5 ms with an MAS rate of 5 kHz. The recycle time was 10 s and typically 2000 scans were required to obtain a good signal to noise ratio. External TMS was used as a chemical shift reference.

ESCA measurements were done at Surface Science Laboratories (Mountain View, CA) with a Surface Science Laboratories Model SSX-01 spectrometer equipped with an Al K α X-ray excitation source. Spectra were obtained at an energy resolution of about 1 eV from a 600 \times 1000 μm sample spot. Typically, the X-ray beam penetrated the top \sim 100 \AA of selected silica samples.

TGA measurements were carried out at Lockheed Missile & Space Company, Inc. (Sunnyvale, CA), with a Perkin-Elmer Model TGS-2 analyzer equipped with uncovered alumina crucibles. Typically 30 mg of selected silica samples were loaded in the analyzer, heated to 110 $^{\circ}\text{C}$ at a rate of 10 $^{\circ}\text{C}/\text{min}$. and held at this temperature until deflection of the weight signal was no longer detected. The temperature was then raised at the same rate up to 1000 $^{\circ}\text{C}$ and again held at this value until no further weight loss could be detected.

DSC experiments were performed with a Perkin-Elmer Model DSC-7 instrument. Uncovered platinum pans loaded with about 10-mg silica samples were subjected to the same heating cycle described above for TGA measurements, with the final temperature being 700 $^{\circ}\text{C}$. Both DSC and TGA experiments were performed under oxidizing (air) as well as inert (N_2) atmospheres.

Silica Derivatization. All reactions were carried out under a dry N_2 atmosphere in glassware that had been previously dried at 120 $^{\circ}\text{C}$ overnight. The LiAlH_4 ether solution was prepared in a N_2 -flushed glovebag. Transfer of liquids was carried out either with a glass syringe (<20 mL) or by means of a stainless steel cannula and N_2 pressure, via silicone rubber septa (25). Prior to reaction, the silica was dried under vacuum at 120 $^{\circ}\text{C}$ overnight and then cooled in a vacuum desiccator.

Chlorination of Silica. A 5.00-g portion (approximately 14 mmol of silanol, assuming 4.6 groups/ nm^2) of dried silica was suspended in 60 mL of freshly distilled, dry toluene, and 10.2 mL of thionyl chloride (about a 10-fold molar ratio excess with respect to silanol content) was added. The mixture was magnetically agitated and the chlorination was allowed to proceed under reflux for at least 48 h, after which the excess SOCl_2 was distilled off. Removal of any remaining SOCl_2 was carried out by washing the dark purple product at least 8 times with 30-mL portions of dry toluene while magnetically stirring for 15 min. After each washing, and once the solid had settled, the solvent was carefully aspirated off to waste by means of a vacuum applied to a glass pipet. Finally, the chlorinated silica was washed with one 30-mL portion of dry diethyl ether, remaining in a final fresh ether aliquot.

Reduction of Chlorinated Silica. A 70-mL portion of 0.2 M LiAlH_4 ether solution (about a 4-fold molar ratio, hydride:original silanol) was added slowly to the chlorinated silica/ether suspension. An immediate reaction was evidenced by a color change from dark purple to white. The reaction was allowed to proceed for 2 h under a gentle reflux. A dry-ice condenser was found to be appropriate to safely condense relatively volatile intermediate reduction byproducts, namely $\text{AlH}_n\text{Cl}_{3-n}$ ($n = 1$ to 3). The excess of LiAlH_4 was carefully aspirated off and destroyed by adding dry ethyl acetate (about 10 mL) followed by 2-propanol dropwise with stirring until hydrogen evolution ceased (26). This also confirmed that an excess of the reducing reagent was present at the end of the reduction reaction. The product was next washed as described above with eight 30-mL portions of dry ether to remove any remaining aluminum hydride and/or chloride species in solution. The "reduced silica" was then dried overnight in a vacuum oven at 120 $^{\circ}\text{C}$.

Hydrolytic Stability Tests. A suspension consisting of 10 mL of test solution (0.01 M NaOH, water, or 0.1 M HCl) per gram of selected reduced silica is magnetically agitated at room temperature for 60 min (or as otherwise specified). The solid is then filtered through a glass fritted funnel, washed with several portions of deionized water, then ether, and finally dried under vacuum at 120 $^{\circ}\text{C}$ overnight.

RESULTS AND DISCUSSION

DRIFT Data. The Si-H group is readily identified by a strong stretching band in the range 2300–2100 cm^{-1} , along with a relatively weak bending band between 760 and 910 cm^{-1} (27), the former being located in a region where the absorption due to the silica matrix is minimal. When chlorinated silica was reduced with an excess of LiAlH_4 , a broad peak was produced at about 2280–2200 cm^{-1} . The shape of the peak suggested a multiplet whose resolution could be enhanced by applying a spectral deconvolution routine (Perkin-Elmer's standard software), as shown in Figure 2. The position of the composite band is consistent with that of SiH species in which the silicon atom is bonded to several electronegative atoms (20, 21, 27, 28). Although the multiplet may be attributed to more than one possible SiH species (namely $\equiv\text{SiH}$ and $\equiv\text{Si}(\text{OH})\text{H}$ which originated from single and geminal silanols respectively), the formation of surface AlH (alane) species, which is also feasible under the reaction conditions, may also explain at least partially the low-frequency component of the broad absorption. Due to the excess of reducing reagent, the presence of unreacted silanols, and the virtual absence of shielding effect

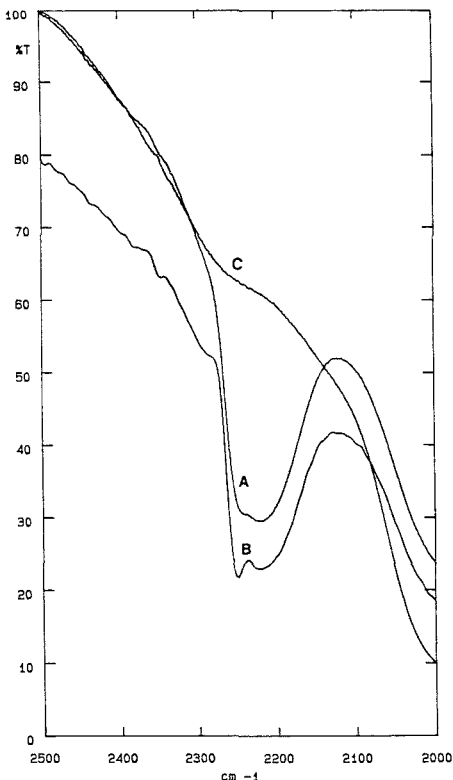
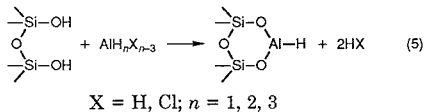


Figure 2. Partial DRIFT spectrum of reduced silica: (A) chlorinated silica reacted with excess LiAlH_4 ; (B) curve A after spectral deconvolution, a doublet at 2250 and 2222 cm^{-1} is strongly suggested; (C) unreacted (fully hydroxylated) silica. Curve B has been displaced downward for better illustration.

from hydrogen atoms as the reduction of chlorinated silica progresses, the silanols become increasingly accessible to attack by the reducing reagent, leading to the formation of surface alane species



This situation is contrary to that of most (if not all) silica derivatizations, in which the original surface species become progressively inaccessible to the modifier's attack. Indirect as well as direct evidence support our hypothesis that surface alane species are formed during the late stages of reduction: (i) Reactions similar to that described above have been shown to occur between fully hydroxylated silica and other Lewis acids such as aluminum trichloride and hydroborane (9, 29); (ii) the stretching mode of Al-H species is known to occur at somewhat lower wavenumbers (about 1700–1900 cm^{-1} , depending on substitution and extent of solvation) as compared to that of SiH groups (30, 31); and (iii) slow but unequivocal gas evolution ($\text{X} = \text{H}$ in reaction 5) was observed after the reacting mixture was allowed to settle for several minutes and the reaction flask was gently tapped (in fact, gas evolution was more readily observed by using a much larger excess of reducing reagent). To confirm our hypothesis of aluminum

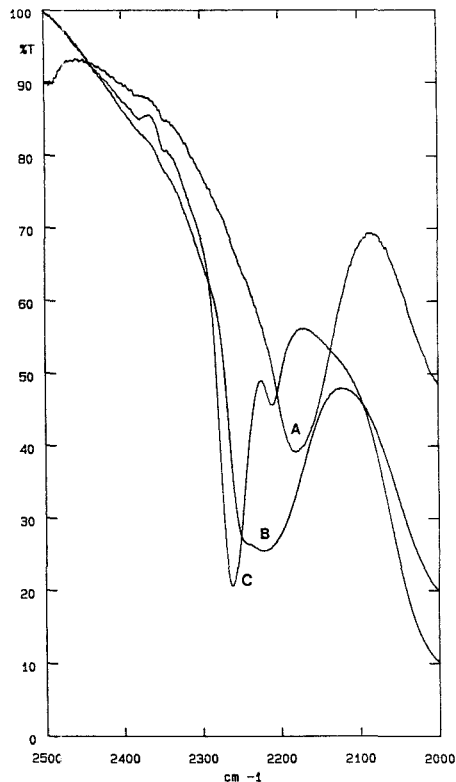


Figure 3. Partial DRIFT spectra of hydride-derivatized silicas: (A) fully hydroxylated silica reacted with LiAlH_4 ; (B) chlorinated silica reacted with excess LiAlH_4 ; (C) chlorinated silica reacted with substoichiometric amount of LiAlH_4 .

chemisorption, a small amount of unreacted (i.e., fully hydroxylated) silica was treated with ethereal LiAlH_4 . A relatively broad and asymmetrical peak at 2181 cm^{-1} , very likely due to surface alane species formed through reaction 5, was obtained. As in the case with silanes, one can expect substitution on the central atom with oxygen-containing groups to cause Al-H stretching frequency shift toward higher values as compared to those for unsubstituted alanes. As clearly shown in Figure 3, surface alane species (curve A) formed as a byproduct during the reduction step are a major contributor to the broad DRIFT absorption observed in reduced silica (curve B). On the other hand, when chlorinated silica was reacted with a *substoichiometric* amount of LiAlH_4 (roughly 1 mequiv of hydride per 3 of original silanol) a major peak at 2262 cm^{-1} along with a small shoulder at 2211 cm^{-1} were produced, as also shown in Figure 3 (curve C). Under these conditions reduction should occur preferentially at the SiCl sites, and therefore the high-frequency component of the original broad peak (curve B) can be reasonably attributed to strongly absorbing $\equiv\text{SiH}$ species. On the other hand, without further experimental evidence, it would be highly speculative to simply assign the 2211- cm^{-1} shoulder to $\equiv\text{Si}(\text{OH})\text{H}$ species.

It is a well-known fact that silica-alumina surfaces are easy to form because of the structural similarities between the two oxides (29, 32). Potential difficulties associated with the presence of chemisorbed aluminum in reduced silica are 2-fold.

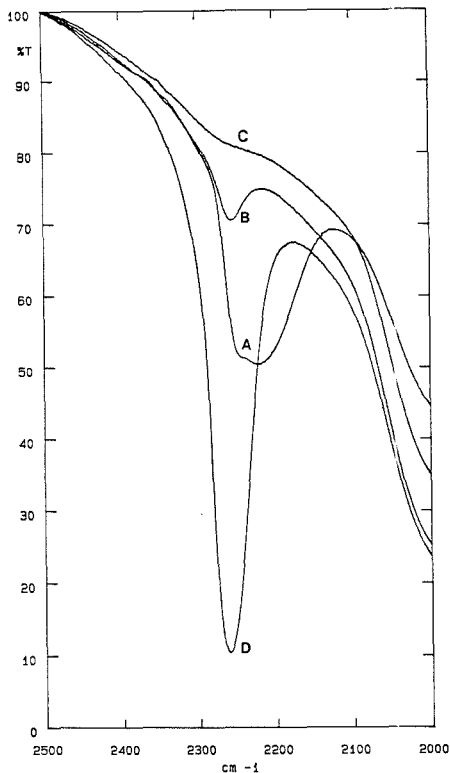


Figure 4. Partial DRIFT spectra showing the effect of hydrolysis on reduced silica: (A) chlorinated silica reacted with excess LiAlH_4 ; (B) product A treated with 0.01 M NaOH for about 2 h; (C) same as B with overnight treatment; (D) product A treated with 0.1 M HCl for about 1 h.

First, alumina-like sites on the silica surface will make the latter more complex, and therefore increasingly difficult to predict and perhaps to derivatize. This appears to be due to the intrinsically more complicated nature of alumina surfaces: multiple aluminol types as well as Lewis-acidity and oxidative capabilities of the alumina sites (29). Second, but perhaps more important, if not removed, surface alane species will reduce a platinum(II) catalyst to the inactive platinum-black form when the reduced silica is used in the subsequent bonding reaction 4 (7, 10, 14). To investigate the hydrolytic stability of silane as well as alane surface species, small portions of reduced silica (chlorinated solid reacted with excess LiAlH_4) were treated with 0.01 M NaOH, deionized water, and 0.1 M HCl. As evidenced from slow gas evolution and confirmed by DRIFT spectra (see Figure 4) treatment with aqueous alkali ($\text{pOH} \sim 2$) resulted in the complete elimination of both alane as well as silane species (curve C) while water ($\text{pOH} \sim 7$) does so at a much slower rate. Acidic ($\text{pOH} \sim 13$) treatment on the other hand resulted in the complete elimination of the low-frequency alane component of the originally broad band and, interestingly, a significant increase in the intensity of the 2260 cm^{-1} Si-H band (curve D). These observations can be readily interpreted in terms of the well-known hydrolytical cleavage of alanes and silanes which results in the formation of silanol and aluminol species, respectively, along with H_2 evolution (8, 13, 30). On the other hand, the observed enhancement of the Si-H band intensity

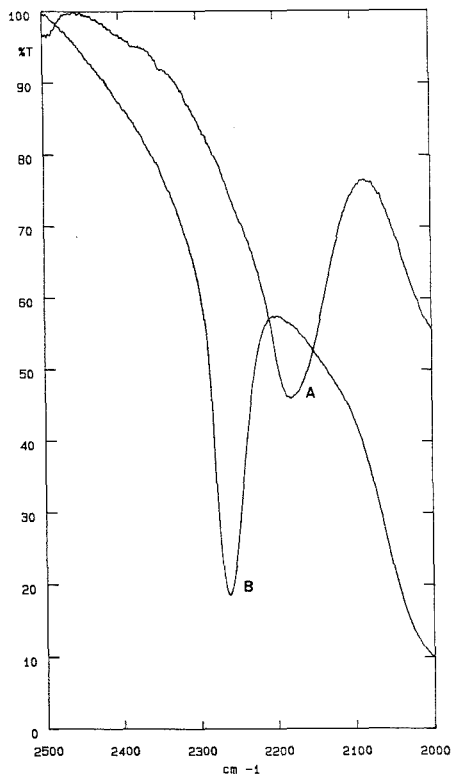


Figure 5. Partial DRIFT spectra showing the effect of hydrolysis on surface alanes: (A) fully hydroxylated silica reacted with LiAlH_4 ; (B) product A treated with 0.1 M HCl.

may be attributed to the effect of either or both of two factors: (i) the hydrolytic removal of IR-active $=\text{Al}-\text{H}$ species from the silica matrix which may cause an increase of the effective penetration of IR radiation and thus a more intense SiH absorption; and (ii) the formation of additional surface SiH species at the expense of adjacent alanes. While the effect of an absorbing matrix on DRIFT intensity has been documented in a previous work by Brimmer and Griffiths (33), there is a need at this point to further elucidate the role of alane species on the enhanced SiH absorption. Two related hydrolysis experiments were thus carried out in which the following silica derivatives were treated with 0.1 M HCl solution: (i) the product of the reaction between fully hydroxylated silica and ethereal LiAlH_4 (containing AlH but no SiH groups); and (ii) the product of the reaction between chlorinated silica and a *substoichiometric* amount of LiAlH_4 (containing SiH groups but virtually no AlH groups). The results are illustrated in Figures 5 and 6, respectively. The former clearly shows the formation of a band at the SiH frequency along with concomitant collapse of the AlH absorption, indicating that silane groups may be formed at the expense of alane species. The fact that product (ii) shows a virtually unchanged SiH band upon acid treatment (Figure 6) is also consistent with this reasoning (i.e., in the absence of AlH species, no additional SiH groups are formed). Figure 7 further illustrates the effect of low-pH hydrolysis on reduced silica: the enhancement of the Si-H stretching band upon acid treatment is also accompanied by reappearance of the free-

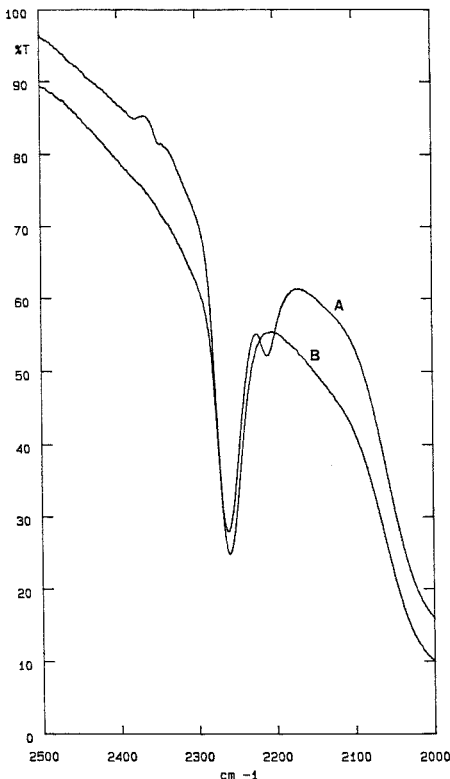


Figure 6. Partial DRIFT spectra showing the effect of hydrolysis on partially reduced silica: (A) chlorinated silica reacted with substoichiometric amount of LiAlH_4 ; (B) product A treated with 0.1 M HCl for about 1 h.

silanol stretching peak at 3739 cm^{-1} . These observations could be accounted for on the basis of a nucleophilic substitution reaction between a surface hydride (alane) species and a protonated siloxane bridge, followed by the hydrolytic removal of the aluminum species, according to the reaction scheme depicted in Figure 8. Protonation of the strained siloxane bridge (a) is postulated here as a means to facilitate its cleavage and thus promote the nucleophilic attack of the neighboring hydride. Additionally, solvation (hydration) of the chemisorbed alane group (b) is likely to occur under these conditions.

Another interesting point is that the Si-H stretching mode became one of the most prominent bands in the infrared spectral region under consideration, with an intensity which is comparable to those for silanol and water bands (Figure 7, curve B). Finally, it should be mentioned that a weak absorption band at 885 cm^{-1} characteristic of the Si-H bending vibration (17) was also present in the DRIFT spectra of reduced silica. This is depicted in Figure 9 along with the corresponding curve for native silica. Of course, because of the multiple interferences in this region, mainly from Si-O vibrations, the stretching mode is much more useful for characterization purposes.

^{29}Si -CP-MAS-NMR Data. Another potential method for studying the changes in silica surfaces is ^{29}Si -CP-MAS-NMR (34). In order to further substantiate the possible presence of an alane species, several types of modified surfaces were compared. When fully hydroxylated silicas were treated with

LiAlH_4 , a peak near -83 ppm appeared. In general, thorough acid washing could be used to remove this peak. These data support the DRIFT spectra which shows the formation of an additional surface species when silica is reacted with LiAlH_4 or when chlorinated silica is reacted with an excess of LiAlH_4 . This species is then removed upon acid treatment.

ESCA Data. The ESCA technique can produce valuable information about many chemisorbed species present on the reduced silica surface, with the exception of hydrogen. Figure 10 shows partial ESCA spectra of unreacted silica (curve A), along with the reduced material before (curve B) and after (curve C) treatment with aqueous hydrochloric acid. Five consecutive 10-min washings with the acid (10 mL of 0.5 M solution per gram of solid) were carried out to thoroughly eliminate unwanted species present on the surface. Clearly, this procedure efficiently removes chemisorbed aluminum (characterized by two peaks with binding energies of 75 and 116 eV) from the untreated material down to the background levels of unreacted silica. Curve B also shows the presence of chemisorbed chloride (binding energies of 195 and 266 eV), probably in the form of $=\text{Al}-\text{Cl}$ produced via a process similar to that of reaction 5.

Curiously enough, traces of chemisorbed carbon (binding energy 281 eV) are also significantly removed through acid treatment. This is also observable in Figure 7 in the form of very weak C-H stretching peaks in the $2900\text{--}3000\text{ cm}^{-1}$ region. Carbon chemisorption can be explained in terms of a secondary reaction (solvolysis) taking place during the reduction of chlorinated silica in ethereal medium (7)



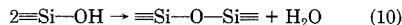
Subsequent removal of the carbonaceous species during acid treatment is consistent with the well-known hydrolytic instability of the Si-O-C linkage (8, 9).

As mentioned before, complete elimination of surface alanes from reduced silica is necessary in order to minimize the deactivation (via reduction) of a Pt(II) catalyst during the surface hydrosilation of terminal olefins. Treatment of the reduced material with aqueous acid must therefore be incorporated as a mandatory step in the synthesis of the silica intermediate.

Thermal Data. The behavior of poly(hydridosiloxanes) and related materials (7, 21) in the presence of oxygen at temperatures above 350°C has been associated with the oxidative degradation of silane species into silanol groups



Since it is an exothermic process which involves a mass increase, oxygen chemisorption on reduced silica can be analyzed by both TGA and DSC. Figure 11 shows that a weight increase in air (curve A) occurs, starting and peaking at about 440 and 530°C , respectively. Clearly, this weight gain peak was superimposed on a loss weight process which started at about 230°C , as indicated by the heating of a similar sample under inert N_2 atmosphere (curve B). This weight loss is due to the well-known silanol condensation process



Due to the opposite effects on sample weight from the simultaneous reactions 9 and 10, the TGA data did not provide a satisfactory measure of the extent of surface reduction. Assuming that the oxidation peak height truly represented the weight gain due to reaction 9, attempts to measure the surface concentration of SiH species only accounted for about 10% of the silanol content in the starting (unreacted) silica material. While this apparently low result might suggest a poor efficiency of the chlorination/reduction reaction sequence, the relatively rapid decline of the TGA oxidation peak indicates the strong possibility that once formed the new

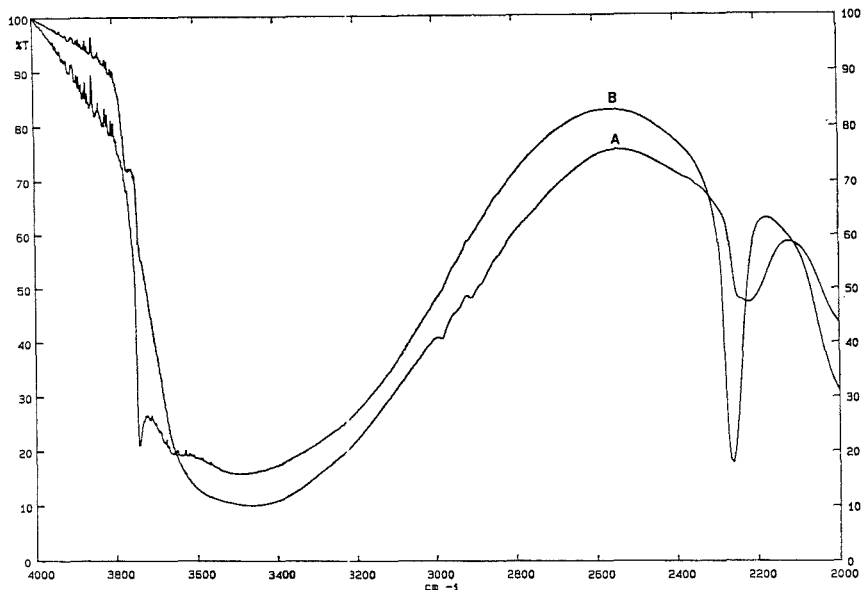


Figure 7. Partial (high-frequency range) DRIFT spectra of reduced silica before (A) and after (B) treatment with aqueous HCl.

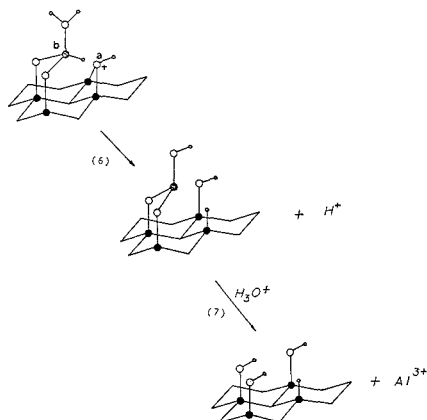


Figure 8. Reaction scheme for the acid treatment of reduced silica: (6) siloxane-bridge cleavage, (7) hydrolytic removal of chemisorbed aluminum; (filled circle) silicon, (open circle) oxygen, (dashed circle) aluminum, (small open circle) hydrogen.

silanols undergo rapid condensation, precluding a full development of the TGA peak.

Figure 12 illustrates typical DSC curves for reduced silica under inert (A) and oxidizing (B) atmospheres, respectively. Clearly, an exothermic peak at about 485 °C is a further confirmation of the occurrence of reaction 9. Subjecting the same oxidized sample to a second heating cycle showed no traces of an exothermic peak, indicating that a complete silane degradation had taken place during the first run. Unfortunately, the unavailability of appropriate standards precluded the use of DSC data for quantitative purposes.

Extent of Surface Reduction. As mentioned in the previous section, serious experimental complications prohibited the utilization of thermoanalytical data to determine the

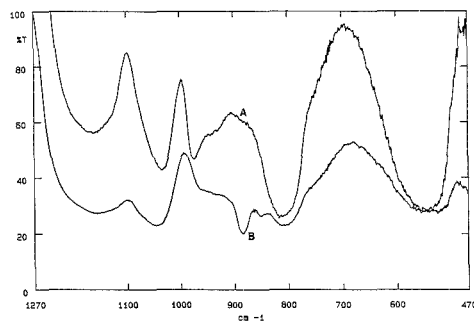


Figure 9. Partial DRIFT spectra of unreacted (A) and acid-treated reduced (B) silicas showing the absence and presence respectively of the SiH bending band. Curve A has been displaced upward for better illustration.

extent at which reduction of the silica surface has taken place. DRIFT information was used in a similarly qualitative fashion to monitor the SiH surface coverage by means of the characteristic (and strong) silane stretching band at 2260 cm^{-1} . Although this band was located in an interference-free IR region (Figure 7), its use for quantitative purposes was not possible because of experimental difficulties associated with lack of appropriate standards, a relatively low reproducibility in the preparation of the DRIFT sample surface, and a presumably poor linear dynamic range (12, 33), all leading to unreliable calibration.

In an alternate approach to determine silane surface coverage, the reducing ability of SiH species, in particular the reduction of certain metal cations such as Pd(II), Pt(II), Ag(I), and Hg(II), among others, was evaluated. It has been claimed (14) that reduction of the forementioned ions by poly(hydrosiloxane) xerogels occurred even in strongly acidic solutions and resulted in a metalized xerogel which no longer exhibited a hydrophobic behavior. When reduced silica was

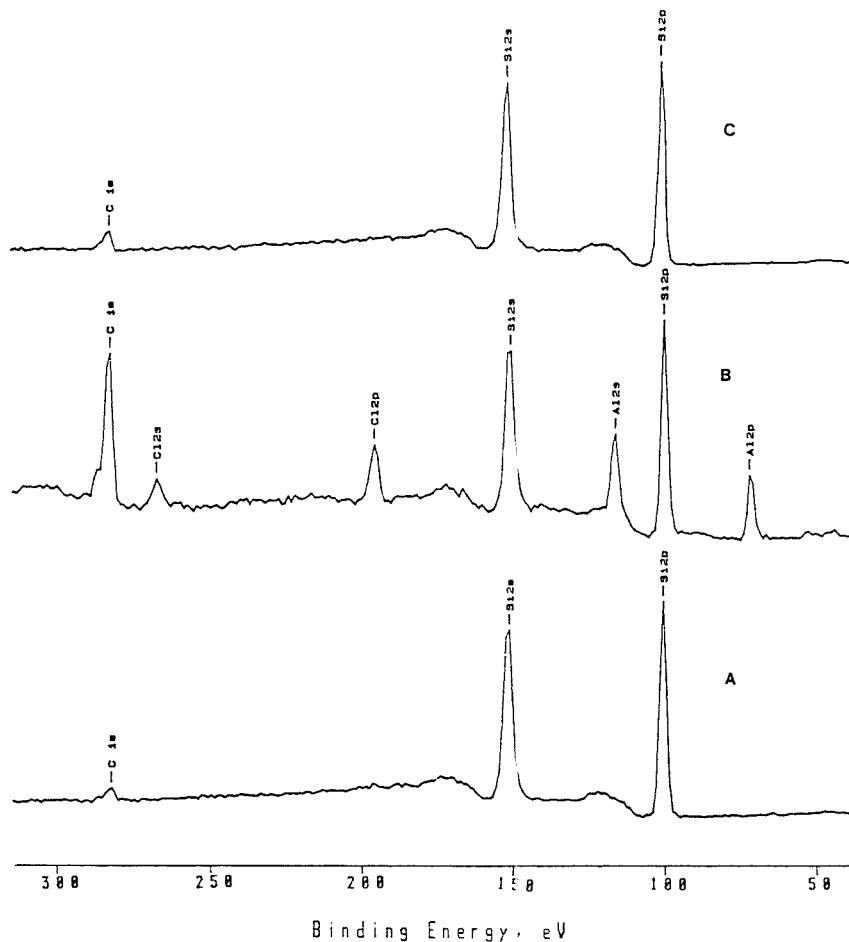


Figure 10. Partial ESCA spectra of silicas: (A) unreacted silica; (B) reduced silica (chlorinated A reacted with excess LiAlH_4) before HCl treatment; (C) product B after acid treatment.

treated overnight with an excess of 10 mM PdCl_2 solution in a 0.5 M HCl matrix, deep darkening of the solid support was readily observed. At the same time, extensive clearing of the supernatant liquid occurred along with a decrease in the concentration of the metal in solution (as confirmed by plasma emission spectrometry). However, testing the darkened solid by DRIFT showed that, even after a 48-h treatment period, the reduction did not proceed with complete consumption of silane as evidenced by the remaining of a strong SiH stretching peak. This is probably a result of the accumulative deposition of finely dispersed metallic particles which eventually clogged the pores and physically blocked further interaction of internal SiH species with metallic ions from the bulk liquid. No further attempts were made at this point to estimate the extent of surface SiH concentration.

CONCLUSIONS

The main goal of this part of the investigation was to produce a silica intermediate bearing surface silicon hydride species. This material was successfully produced by a chlorination/reduction procedure that sequentially converts the surface silanols into silicon chloride and then silicon hydride

groups. Final treatment of the reduced silica product with aqueous hydrochloric acid appeared to be an important synthetic step not only for an efficient removal of undesirable surface silane byproducts (as evidenced by ESCA data) but also as a means to further increase the formation of silane groups (as indicated by DRIFT evidence). Similarly with related materials from the literature (e.g. poly(hydrosiloxane) xerogels and certain H_2 -treated pyrolyzed silicas) the surface silane species were hydrolytically stable at low pH and thermally stable at temperatures up to 420 °C. Thermoanalytical information indicated that the surface silane species undergo complete oxidation when heated under an oxygen-containing atmosphere at temperatures above 470 °C.

We are presently developing methods for the surface hydrosilation of terminal olefins on the hydride-modified silica. While some parts of this subsequent work require carefully designed synthetic procedures and extensive spectroscopic characterization, preliminary experiments indicate that surface bonding does actually take place. This is evidenced, for instance, in the case of simple 1-olefins by the appearance of intense C-H stretching IR bands in the $3000\text{--}2800\text{-cm}^{-1}$ region concomitant with a considerable decline of the Si-H stretching

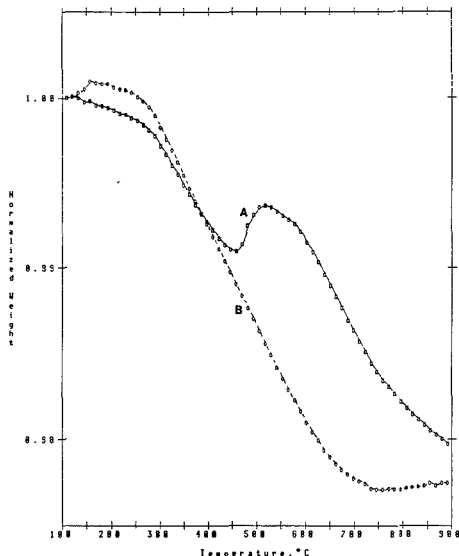


Figure 11. TGA curves of acid-treated reduced silica, in air (A) and N_2 (B).

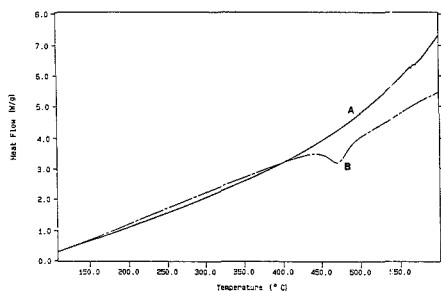


Figure 12. DSC curves of acid-treated reduced silica, in N_2 (A) and air (B).

band at 2260 cm^{-1} . Optimization of the extent of surface coverage as well as the application of this reaction to the attachment of a variety of vinyl-terminated organic moieties are currently under way. Additional research will also be undertaken in the evaluation of other substrates such as poly(hydridosiloxane) xerogels as alternate intermediates in the heterogeneous hydrosilation of terminal olefins.

ACKNOWLEDGMENT

The authors are indebted to Mr. R. D. Cormia from Surface

Science Laboratories for providing the ESCA spectra, Dr. A. Cooper from Lockheed Missiles & Space Company, Inc., for the TGA data, and Dr. C. Schramm from Catalytica Corp. for the ^{29}Si -CP-MAS-NMR data. The supply of the silica material by Dr. C. H. Lochmüller from Duke University is also gratefully acknowledged. The assistance of Dr. G. Gutnikov from California State Polytechnic University in the translation of various Russian papers is also appreciated.

LITERATURE CITED

- (1) Van Den Driest, P. J.; Ritchie, H. J.; Rose, S. *LC-GC, Mag. Liq. Gas Chromatogr.* **1988**, *6*, 124-132.
- (2) Unger, K. K.; Anspach, B. *TrAC, Trends Anal. Chem.* **1987**, *6*, 121-125.
- (3) Locke, D. C.; Schmermund, J. T.; Banner, B. *Anal. Chem.* **1972**, *44*, 90-92.
- (4) Pesek, J. J.; Swedberg, S. A. *J. Chromatogr.* **1986**, *361*, 83-92.
- (5) Saunders, D. H.; Barford, P. M.; Olszewski, L. T.; Rothbart, H. L. *Anal. Chem.* **1974**, *46*, 834-838.
- (6) Unger, K.; Thomas, W.; Adrian, P. *Kolloid-Z. Z. Polym.* **1973**, *251*, 45-52.
- (7) *Organometallic Compounds of the Group IV Elements. The Bond to Carbon*; MacDiarmid, A. G., Ed.; Marcel Dekker: New York, 1968; Vol. 1, Part 1.
- (8) Pawlenko, S. *Organosilicon Chemistry*; Walter de Gruyter & Co.: Berlin, New York, 1986.
- (9) Unger, K. K. *Porous Silica - Its Properties and Use as Support in Column Liquid Chromatography* (Journal of Chromatography Library, Vol. 16); Elsevier Scientific Publishing Co.: New York, 1979.
- (10) Chalk, A. J.; Harrod, J. F. *J. Am. Chem. Soc.* **1965**, *87*, 16-21.
- (11) Musolf, M. C.; Speier, J. L. *J. Org. Chem.* **1964**, *29*, 2519-2524.
- (12) Apfel, M. A.; Finkelmann, H.; Janini, G. M.; Laub, R. J.; Luehrmann, B. H.; Price, A.; Roberts, W. L.; Shaw, T. J.; Smith, C. A. *Anal. Chem.* **1985**, *57*, 651-658.
- (13) Slinyakova, I. B.; Budkevich, G. B.; Neimark, I. E. *Kolloidn. Zh.* **1965**, *27*, 759-764.
- (14) Budkevich, G. B.; Slinyakova, I. B.; Neimark, I. E. *Kolloidn. Zh.* **1966**, *28*, 21-26.
- (15) Slinyakova, I. B.; Korol, A. N. *Ukr. Khim. Zh.* **1967**, *33*, 373-376.
- (16) Budkevich, G. B.; Slinyakova, I. B.; Neimark, I. E. *Kolloidn. Zh.* **1970**, *32*, 17-23.
- (17) Budkevich, G. B.; Slinyakova, I. B.; Neimark, I. E.; Zhaigalio, Y. V. *Ukr. Khim. Zh.* **1971**, *37*, 429-433.
- (18) Kurennaya, L. I.; Slinyakova, I. B. *Kolloidn. Zh.* **1975**, *37*, 178-181.
- (19) Corriu, R. J. P.; Guerin, C. J. *Organomet. Chem.* **1980**, *198*, 231-320.
- (20) Morterra, C.; Low, M. J. D. *J. Phys. Chem.* **1969**, *73*, 321-326.
- (21) Morterra, C.; Low, M. J. D. *J. Phys. Chem.* **1969**, *73*, 327-333.
- (22) West, R. J. *Am. Chem. Soc.* **1954**, *76*, 6015-6017.
- (23) Baines, J. E.; Eaborn, C. J. *Am. Chem. Soc.* **1955**, *77*, 4023-4024.
- (24) Perrin, D. D.; Armarego, W. L. F.; Perrin, D. R. *Purification of Laboratory Chemicals*, 2nd ed.; Pergamon Press: New York, 1980.
- (25) Shriver, D. *The Manipulation of Air-Sensitive Compounds*; McGraw-Hill: New York, 1969.
- (26) West, R. J. *Am. Chem. Soc.* **1954**, *76*, 6012.
- (27) Smith, A. L.; Angelotti, N. C. *Spectrochim. Acta* **1959**, *15*, 412-420.
- (28) *Analysis of Silicones*; Smith, A. L., Ed.; John Wiley & Sons: New York, 1974.
- (29) Hair, M. L. *Infrared Spectroscopy in Surface Chemistry*; Marcel Dekker: New York, 1967.
- (30) Mackay, K. M. *Hydrogen Compounds of the Metallic Elements*; E.&F.N. Spon Ltd.: London, 1966.
- (31) Ehrlich, R.; Young, A. R.; Lichstein, B. M.; Perry, D. D. *Inorg. Chem.* **1963**, *2*, 650-652.
- (32) Iler, R. K. *The Chemistry of Silica - Solubility, Polymerization, Colloid and Surface Properties, and Biochemistry*; John Wiley & Sons: New York, 1979.
- (33) Brimmer, P. J.; Griffiths, P. R. *Anal. Chem.* **1986**, *58*, 2179-2184.
- (34) Kohler, J.; Chase, D. B.; Farlee, R. D.; Vega, A. J.; Kirkland, J. J. *J. Chromatogr.* **1986**, *352*, 275-305.

RECEIVED for review March 10, 1989. Accepted June 15, 1989.

Supercritical Fluid Chromatographic Determination of Fatty Acids and Their Esters on an ODS-Silica Gel Column

Akira Nomura,* Joseph Yamada, Kin-ichi Tsunoda, Keiji Sakaki, and Toshihiro Yokochi

National Chemical Laboratory for Industry, Tsukuba, Ibaraki 305, Japan

Free fatty acids and their esters were determined by supercritical fluid chromatography (SFC) on an inert packed column using supercritical carbon dioxide as a mobile phase without addition of any modifier. The column used was ODS-silica gel having a pore diameter of 300 Å and end-capped as enough as possible to decrease residual silanol groups on the silica surface. The retention behavior of free fatty acids and their esters was investigated in terms of the density of a mobile phase, and they were separated according to a reversed-phase mode like in liquid chromatography. Lipids extracted from fungus and their esterified products were separated by the SFC using a pressure programming mode and a constant pressure mode, respectively, and the chromatograms obtained with both FID and UV detector were compared.

Supercritical fluid chromatography (SFC) continues to attract considerable attention after several years of rapid growth. A wide variety of its applications have been investigated in analytical, as well as in industrial sectors (1). The analysis of fatty acids and their esters has been of great interest in the field of food, chemical, and pharmaceutical industries. Fatty acids and their esters have been usually determined by either gas chromatography (GC) or high-performance liquid chromatography (HPLC). However, nonvolatility of longer-chain acids and thermally labile property of unsaturated acids make analysis by GC much more difficult. Poorer detection limits have been the drawback in the HPLC analysis because UV absorption and fluorescence detection are impossible for saturated compounds (2).

Free fatty acids were analyzed by capillary SFC using supercritical CO₂ as a mobile phase, and the effects of temperature and stationary-phase polarity on efficiency and chromatographic peak shape were investigated (3, 4). Direct coupling of supercritical fluid extraction (SFE) and capillary SFC was applied to the separation of free acids (5). The separation of mixed mono-, di-, and triglycerides by capillary SFC was performed by using a carbon dioxide mobile phase without thermal degradation (6). The capillary SFC is a preferred method for high-resolution separation of thermally labile compounds, and a flame ionization detector (FID) gives the same high sensitivity in capillary SFC as is found in capillary GC. The capillary SFC, however, has some drawbacks in, such as, very small amounts of sample introduction and lack of capability for scale up to preparative separation. The separation and detection of free fatty acids in simple mixtures by SFC/Fourier transform infrared detection were carried out on packed columns using supercritical CO₂ and Freon 23 as a mobile phase (7). Packed column SFC directly coupled with a mass spectrometer was applied to triglycerides (8). Free fatty acids were separated on an ODS-silica column using a modifier control column containing formic acid installed before an injector and were detected by FID (9). Esterified fatty acids from lipids in fungi and neutral lipids containing γ -linolenic acid were separated on a ODS-silica column, and their retention behaviors were compared with those in HPLC (10, 11).

We have investigated the chromatographic behavior of ODS-silica gels for SFC having various pore structures by pressure programming SFC (12). We have also reported the preparation of inert silica-based packings and their properties for SFC (13).

This paper describes the determination of free fatty acids and their esters on an inert ODS-silica gel column using carbon dioxide as a mobile phase without a modifier.

EXPERIMENTAL SECTION

Apparatus. The SFC system used was the same as described elsewhere (12) except that a FID was connected by splitting a mobile phase between the separation column and the UV detector. FID of either Shimadzu Model GC-7A or Shimadzu Model GC-R1A was used for this purpose. The flow rate of a mobile phase was controlled by changing the size of a restrictor made of fused silica capillary tube. The restrictor made of the capillary tube of 50 μ m i.d. \times 200 mm was usually used unless otherwise specified. The flow rate of CO₂ introduced to the FID was controlled by the restrictor made of the capillary tube of 25 μ m i.d. \times 200 mm having a small orifice at the end. Column temperature was held at 45 °C throughout the experiment.

Materials. Kaseisorb ODS-300-5 for SFC (4.6 mm i.d. \times 250 mm; particle size, 5 μ m; specific surface area, 100 m²/g; pore diameter, 300 Å; carbon content, 6.0%) from Tokyo Kasei Co., Ltd., Japan, was used as a test column for SFC, which was based on Kaseisorb LC ODS-300-5 for HPLC, and was end-capped as completely as possible. Kaseisorb LC ODS-100-5 (4.6 mm i.d. \times 250 mm; particle size, 5 μ m; pore diameter, 100 Å) and Kaseisorb LC ODS-300-5 (4.6 mm i.d. \times 250 mm; 5 μ m; 300 Å), both from Tokyo Kasei were used to compare the column properties for SFC. Free saturated fatty acids (C₆-C₂₆; 6:0-26:0), free unsaturated fatty acids (18:1, 18:2, 18:3, 20:4), methyl palmitate (16:0-Me), methyl stearate (18:0-Me), methyl oleate (18:1-Me), methyl linolate (18:2-Me), and methyl linolenate (18:3-Me) were all obtained from Tokyo Kasei. Methyl γ -linolenate was obtained from Wako Pure Chemicals. All these standard samples were dissolved in chloroform from Kanto Chemical. The retention time of chloroform was used as *t*₀ to calculate the capacity factor *k'*. Lipids produced in *Mortierella ramanniana* var. *angulispora* cultured in our laboratory were extracted from the fungus with hexane and were conventionally esterified to fatty acid methyl esters. The lipids and the methyl esters were dissolved in chloroform to be applied to SFC determination. Other reagents were of reagent grade and used without purification.

RESULTS AND DISCUSSION

In packed column SFC, silica-based packings such as ODS-silica gel are packed into a conventional HPLC column or microcolumn. When carbon dioxide is used as a mobile phase without a modifier, the residual silanol groups of silica gel base after surface modification interact with polar compounds and cause serious problems, such as irreversible or nonspecific adsorption leading to peak tailing or considerable delay of sample elution. Thus, we have proposed the utilization of silica gel having larger pore diameter (pore size, 1000 Å) and sufficient end-capping of residual silanol groups after primary surface modification in order to prepare inert packings for SFC (13). Although the silica base with larger pore diameter has less silanol groups and less micropores in the pore structure, which makes the end-capping much easier, it is still necessary to develop the inert packings for SFC having smaller

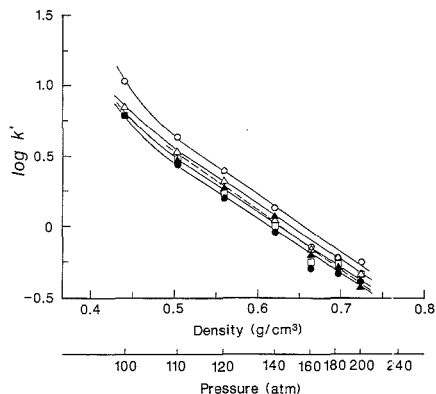


Figure 1. Retention behavior of free fatty acids including essential fatty acids: (O) 18:0; (Δ) 18:1; (\square) 18:2; (\bullet) 18:3; (\blacktriangle) 20:4.

pore size and possessing larger capacity for sample loading when applying to analytical and, particularly, preparative scale SFC separation. Kaseisorb LC ODS-300-5 has a relatively larger pore diameter of 300 Å and usually is used for the separation of proteins in HPLC. This column was further end-capped for the SFC application (Kaseisorb ODS-300-5 for SFC) and was applied to the determination of free fatty acids and their esters using carbon dioxide as a mobile phase without the addition of a modifier.

The retention behavior of essential fatty acids (linoleic, γ -linolenic, and arachidonic acid) as well as stearic and oleic acid according to the density of the mobile phase was investigated on the ODS column for SFC (Kaseisorb ODS-300-5 for SFC) as shown in Figure 1. The separation mode of these fatty acids seems to be reversed phase in terms in LC, that is unsaturated fatty acids having more double bonds eluted faster than those having less double bonds, but that of arachidonic acid was different from others presumably because of its specific molecular structure. A linear relationship between the density of CO_2 and the $\log k'$ value of samples was obtained above the density of 0.5 g/cm^3 (110 atm).

The mixture of standard free saturated fatty acids from 8:0 to 24:0 was applied to the three types of ODS-silica columns, that is Kaseisorb LC ODS-100-5 (A), LC ODS-300-5 (B), and ODS-300-5 for SFC (C), by linear pressure programming mode from 100 to 300 atm, from 100 to 240 atm, and from 100 to 160 atm, respectively, for 20 min, and the chromatograms are shown in Figure 2. Chromatogram A provided almost no peak separation because of large amounts of silanol groups remaining in the smaller pore structure (100 Å), and chromatogram B obtained by the wider pore (300 Å) ODS column gave better separation profiles than A, but the peaks showed unsatisfactory tailing patterns. In the case of chromatogram C obtained by the test column for SFC, the peak shape of the individual fatty acid was much more improved than that of B, but was not sharp enough to provide base-line separation presumably because free carboxyl groups in the molecules interact with the silanol groups still remaining on the surface of the silica base. However, it may probably be the first time that these free fatty acids could be separated to a considerable extent on a packed column using carbon dioxide as a mobile phase without a modifier.

The retention behaviors of free fatty acid and fatty acid methyl esters on the column for SFC were compared to demonstrate the interaction between free carboxyl group and residual silanol group as shown in Figure 3. In reverse-phase LC, stearic acid (18:0) should be retained on a column weakly

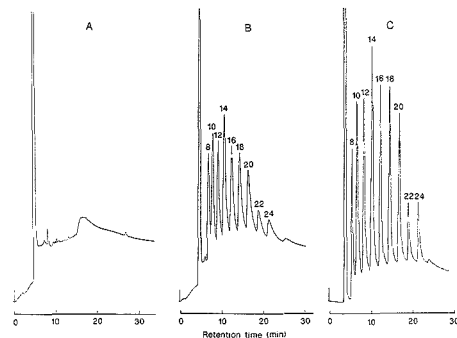


Figure 2. Chromatogram of standard free fatty acid mixture: A, Kaseisorb LC ODS-100-5; B, Kaseisorb LC ODS-300-5; C, Kaseisorb ODS-300-5 for SFC. Number upon the peak shows the carbon number.

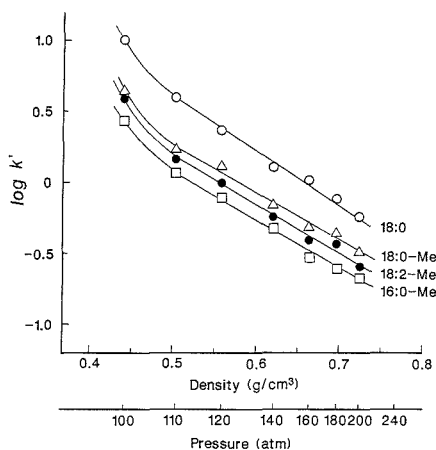


Figure 3. Retention behavior of free fatty acid and fatty acid methyl esters.

and be eluted faster than its methyl ester (18:0-Me) according to less carbon atoms, but the result shows that the stearic acid retained on the column longer than its methyl ester by the interaction between the polar carboxyl group and the residual silanol group. The retention behavior of the methyl esters was reversed phase like in free fatty acids as shown in Figure 1, that is, methyl linolate and methyl palmitate eluted faster than methyl stearate according to the number of double bond and the carbon number, respectively.

The column efficiency, expressed as HETP, was measured by using stearic acid and methyl stearate as samples, and the results are shown in Figure 4. The efficiency measured by methyl stearate was high and comparable to that in HPLC. On the contrary, the efficiency measured by stearic acid was very low, especially in the low density region, because the free carboxyl group interacts with the residual silanol group, which makes the peak wider. The efficiency increases to some extent as the density increases, presumably because the solubility of CO_2 increases and the interaction between the carboxyl group and the silanol group decreases.

To show the applicability of this system to real analytical problems, the present packed type SFC was applied to the separation of lipids extracted from *Mortierella ramanniana* with hexane and their esterified products. Figure 5 shows the

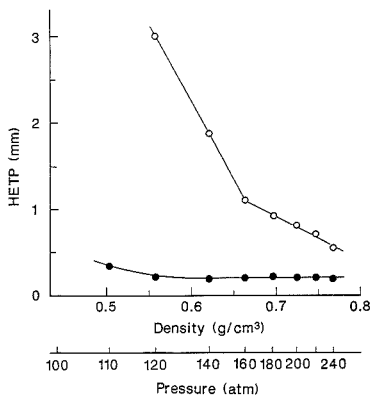


Figure 4. HETP vs density of CO₂ mobile phase: (O) stearic acid; (●) methyl stearate.

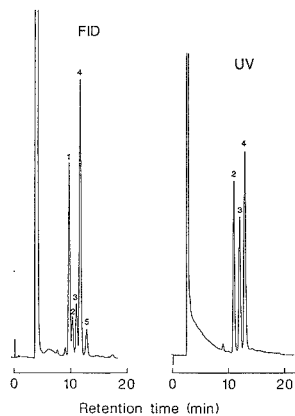


Figure 5. Chromatograms of fatty acid methyl esters from lipids produced by fungus using FID and UV detection: (1) 16:0-Me, (2) γ -18:3-Me, (3) 18:2-Me, (4) 18:1-Me, (5) 18:0-Me; pressure of CO₂, 100 atm; UV detector, 190 nm.

chromatograms of the esterified fatty acid methyl esters detected by FID and UV detector. The amount of the individual methyl ester is approximately proportional to its peak area detected by FID. It is assumed from the result that there are larger amounts of methyl palmitate [1 in Figure 5] and methyl oleate [4] and smaller amounts of methyl γ -linolenate [2], methyl linolate [3], and methyl stearate [5]. On the other hand, the peaks of saturated esters such as methyl palmitate and methyl stearate, which have no double bond, disappeared from the chromatogram obtained with UV detector (at 190 nm, in Figure 5). Moreover, although the content of methyl γ -linolenate was found to be small according to FID detection, its peak was emphasized in the UV detection because of the

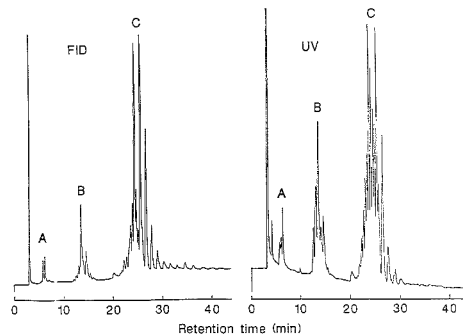


Figure 6. Chromatograms of lipids produced by fungus using FID and UV detection: pressure programming, from 150 to 250 atm for 30 min (hold at 150 atm for 5 min); UV detector, 190 nm.

three double bonds in the molecule. Thus, the use of both UV detector and FID at the same time can provide structural information of analytes. The chromatograms of the lipids extracted from *Mortierella ramanniana* using FID and UV as a detector are shown in Figure 6. Linear pressure programming mode from 150 to 250 atm for 30 min (hold at 150 atm for 5 min) was used for both FID and UV detection. Many peaks were found on both chromatograms and they were grouped into three groups, namely A, B, and C. The profiles of the two chromatograms are similar to each other except that the individual peak response differed according to the sensitivity of FID and UV. Although each peak of these groups was not identified yet, the major peaks in group B and C are considered to consist of diglycerides and triglycerides, respectively. Further study on identifying these peak components should be performed in the future.

LITERATURE CITED

- (1) *Supercritical Fluid Chromatography*; Smith, R. M., Ed.; The Royal Society of Chemistry: London, 1988.
- (2) Stolyhwo, A.; Colin, H.; Guiochon, G. *Anal. Chem.* **1985**, *57*, 1342-1354.
- (3) Markides, K. E.; Fields, S. M.; Lee, M. L. *J. Chromatogr. Sci.* **1986**, *24*, 254-257.
- (4) Doehl, J.; Färbrot, A.; Greibrokk, T.; Iversen, B. *J. Chromatogr.* **1987**, *329*, 175-184.
- (5) Gruer, W.; Bosset, J. O.; Pattner, E. *J. Chromatogr.* **1987**, *388*, 355-349.
- (6) White, C. M.; Houck, R. K. *HRC CC, J. High Resolut. Chromatogr. Chromatogr. Commun.* **1985**, *8*, 293-296.
- (7) Helligeth, J. W.; Jordan, J. W.; Taylor, L. T.; Khorassani, M. A. *J. Chromatogr. Sci.* **1986**, *24*, 183-188.
- (8) Matsumoto, K.; Tsuge, S.; Hirata, Y. *Anal. Sci.* **1986**, *2*, 3-7.
- (9) Hirata, Y. *SFC Applications (1988 Workshop on Supercritical Fluid Chromatography)*; Compiled by K. E. Markides and M. L. Lee; Brigham Young University Press: Salt Lake City, UT, 1988; p 110.
- (10) Sakaki, K.; Sako, T.; Yokochi, T.; Sugeta, T.; Nakazawa, N.; Sato, M.; Suzuki, O.; Hakuta, T. *J. Jpn. Oil Chem. Soc.* **1987**, *36*, 943-946.
- (11) Sakaki, K.; Sako, T.; Yokochi, T.; Suzuki, O.; Hakuta, T. *J. Jpn. Oil Chem. Soc.* **1988**, *37*, 54-56.
- (12) Nomura, A.; Yamada, J.; Tsunoda, K. *J. Chromatogr.* **1988**, *448*, 87-93.
- (13) Nomura, A.; Yamada, J.; Tsunoda, K.; Fukushima, K.; Nobuhara, K. *Anal. Sci.* **1989**, *5*, 335-338.

RECEIVED for review May 19, 1989. Accepted June 15, 1989.

Polymer-Bound Tetrahydroborate for Arsinic Generation in a Flow Injection System

Solomon Tesfalidet and Knut Irgum*

Department of Analytical Chemistry, University of Umeå, S-901 87 Umeå, Sweden

Generation of arsine for subsequent atomic spectrometric determination was carried out in a flow system using a column packed with a macroporous strong anion-exchange resin (Amberlyst A-26) in the tetrahydroborate form as a polymer-supported reducing agent. The analysis cycle comprised regeneration, washing, and injection of acidified sample, and could be repeated every 4 min, resulting in a detection limit for trivalent arsenic of 60 pg in a 40- μ L sample, with a linear working range up to 4 ng. Nickel, cobalt, copper, or iron ions caused less than 10% signal degradation when present in the sample at concentrations between 2500 and 5000 mg/L when L-cystine was added to the hydrochloric acid as masking agent. The column could be used for at least 3 months without performance degradation.

INTRODUCTION

A number of elements belonging to the metalloids and some metals located near these in the periodic system can be separated from their sample matrices by volatilization as hydrides. The reaction is based on reduction of the element of interest by a suitable reducing agent and has been exploited analytically for more than a century (1). Adaptation of the technique to analyte isolation for sample introduction in atomic absorption spectrometry was first demonstrated by Holak (2), who used zinc in hydrochloric acid as the reducing agent. Other hydride ion precursors that have found use in generating hydrides are, e.g., $TiCl_3$ (3) and $SnCl_2$ (4). The hydroborates, which were initially developed as versatile reduction agents in organic synthesis (5), were first introduced for hydride generation by Schmidt and Royer (6), who demonstrated that sodium tetrahydroborate was far more powerful than the reducing agents used earlier. Tetrahydroborate rapidly gained acceptance and has been the reagent of choice for hydride generation ever since its introduction. The less reactive trihydrocyanoborate has lately been proposed as a candidate for that position (7), but the toxicity and high price of that reagent will preclude a more widespread use.

However, several transition-metal ions interfere severely with the hydride generation of several analytes (3). It is generally believed that the cause of this interference is adsorption of the analyte hydrides onto metal colloids that are formed by reduction, if transition-metal salts are present in the matrix (9). Some of the methods proposed to alleviate these interferences in the determination of arsenic include optimizing the hydrochloric acid and tetrahydroborate concentrations (10), the use of masking agents (11-14), and application of a flow injection system instead of the usually employed batch mode or continuous flow systems (15-17). The last method offers, as an additional benefit, better detection limits (18) compared with other reaction schemes.

The use of ion-exchange resins charged with ionic reagents has received considerable attention as insoluble reagents for synthetic purposes (19) and for the purification of reagents and solvents (20). The number of reported applications of polymeric reagent carriers in analysis has been rather limited, in spite of the tremendous potential of this technique in analytical chemical reactions.

Cook et al. (20) have investigated the solvolytic stability and reactivity of tetrahydroborate ions bound to strong base anion-exchange resins and envisioned several application areas for this reagent. Among the suggested uses was batch-mode arsine generation. The polymer-bound tetrahydroborate reagent offered several advantages over sodium tetrahydroborate solutions, such as convenience of use, stability, and minimal introduction of ionic species or organic byproducts to the treated bulk medium. No follow-up reports have realized the beauty of this immobilized reagent. This may have been due to the fact that the procedure was presented as part of a study that dealt with organic synthetic uses of the polymer-bound reagent and to the coupling with diethyldithiocarbamate spectrophotometry, which gave the method a low overall sensitivity. The method did not, therefore, receive the attention it deserved.

In the present work we reinstate polymer-bound tetrahydroborate as a reduction reagent in arsine generation. By integrating a column packed with a macroreticular tetrahydroborate form of strong anion-exchange resin in a flow injection system, we have been able to combine the best features of both techniques—fast and sensitive analysis of small sample volumes with minimal metal ion interference.

EXPERIMENTAL SECTION

Apparatus. The flow injection system incorporated, in the direction of flow, a four-channel peristaltic pump (Gilson Minipuls 3), an Omnifit (Oxford, U.K.) six-port all-poly(tetrafluoroethylene) (PTFE) injection valve with loops of various sizes, a borosilicate glass column (6 mm i.d. \times 100 mm) packed with Amberlyst A-26, and a 100 cm long, 0.5 mm i.d. knitted PTFE tube. The knitted tube functioned as a pressure damper for leveling the flow fluctuations caused by the abrupt hydrogen gas evolution that takes place when the acidic sample is injected. Flow times were manually controlled. The gas-liquid separator was a 30 cm long, 10 mm i.d. slanted borosilicate glass tube, into which the liquid-gas mixture exiting from the flow injection system was directed. The lower part of the separator tube was bent at a 45° angle, and the vertical portion terminated in a water seal. The hydrogen flame gas for the atomizer flowed through the separator tube counter to the liquid flow. See Figure 1 for a sketch of the setup.

Amberlyst A-26 (20-50 mesh, practical grade, chloride form; Serva, Heidelberg, FRG) was washed repeatedly with water, methanol, and again with water. Conversion to the hydroxide and reconversion to the chloride form were carried out in the usual manner, whereafter the resin was packed in the column and converted to the tetrahydroborate(III) form by using a solution of 4% sodium tetrahydroborate(III) in 0.2 M NaOH, followed by thorough washing with water.

A Perkin-Elmer Model 372 atomic absorption spectrophotometer (AAS) was used for monitoring arsenic at the 193.7-nm line. An arsenic electrodeless discharge lamp operated at 8 W was used as light source. The spectral bandwidth of the AAS instrument was set to 2 nm, and the deuterium background corrector was used. The atomizer was an (oxygen-hydrogen) flame in tube type, built by Dedina (21). The oxygen and hydrogen gas flow rates were 15 mL/min and 2 L/min, respectively.

Reagents and Solutions. All chemicals used were of reagent grade. Water was purified by using Milli-Q (Millipore, Bedford, MA) equipment. Stock solutions 1.000 g/L in As(III) or As(V) were prepared by dissolving the appropriate amount of ultrapure As_2O_3 and As_2O_5 (Ventron-Alfa, Karlsruhe, FRG), respectively, in 20 mL of 1 M NaOH and diluting to 1 L with 2 M HCl. A 4%

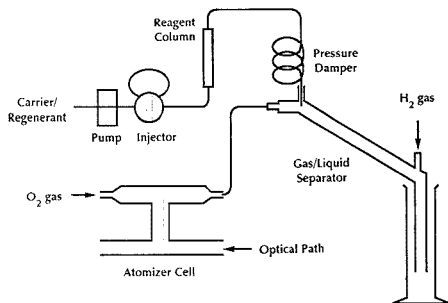


Figure 1. Schematic drawing of experimental setup.

(w/v) solution of NaBH_4 was prepared by dissolving the appropriate amount of sodium tetrahydroborate(III) (Merck, Darmstadt, FRG) in 0.2 M NaOH. L-Cystine (Hopkins & Williams, Chadwell Heath, U.K.) was, in some of the interferent study experiments, added to the hydrochloric acid as masking agent to give a final concentration of 3% (w/v) in the sample. As(III) solutions containing the potential interferents Cu(II), Fe(III), Co(II), and Ni(II) were prepared by adding the appropriate amounts of chloride salts to a test sample containing 50 ng/mL As(III) in 4 M HCl.

Recommended Procedure. A typical analysis was carried out by pumping 4% tetrahydroborate solution through the column for a period of 60 s and washing for the same period of time with the carrier, which was deionized water. Forty microliters of the sample, to which concentrated hydrochloric acid had been added to give a concentration of 4 M, was then injected into the carrier flow. The cycle could be repeated 90 s after injection. The time required between two consecutive injections was thus less than 4 min. For samples suspected of containing high concentrations of interfering metal ions, masking agent can be added as described in the Reagents and Solutions section.

System Optimization. Optimum hydrochloric acid concentration, regeneration time, sample volume, hydrogen and oxygen gas flows, carrier flow rate, and sample volume described in the recommended procedure were found by varying the appropriate parameter, using peak height as quality criterion. Parameters apart from the one under investigation were maintained at the levels set out in the recommended procedure, if not otherwise noted.

Interference Studies. Maximum allowed concentrations for the potential interferent metal ions nickel, copper, cobalt, and iron were evaluated under conditions described in the recommended procedure, using samples with the metal ions added in the manner described above. The responses for tri- and penta-valent arsenic were compared by substituting As(V) for As(III) in a sample run through the recommended procedure.

Linearity and Detection Limit. Triplicate samples with As(III) concentrations ranging from 1.5 to 200 ng/mL were analyzed according to the recommended procedure. The reported detection limit is based on a signal that is 3 times the peak-peak base-line noise.

RESULTS AND DISCUSSION

Tolerance toward transition-metal interferences and simplicity of use have been the objectives of this work. To accomplish this, we decided to use a flow system with polymer-bound tetrahydroborate as reduction reagent. A strong anion-exchange resin can easily be regenerated with tetrahydroborate ions and serves as an ideal reagent administration technique in flow systems. The following equation, where P represents the bulk polymer of the reagent carrier, is a simplified representation of the reactions assumed to take place during the reduction of trivalent arsenic under the prevailing conditions:

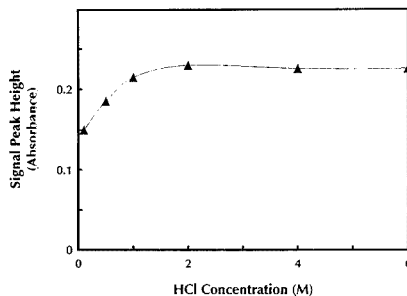
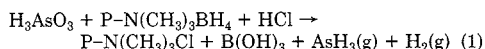


Figure 2. Influence of hydrochloric acid concentration on the signal from trivalent arsenic.

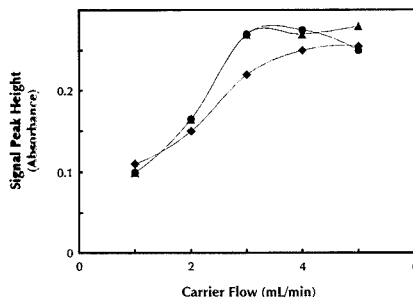


Figure 3. Signal peak height as function of carrier flow rate at three different hydrochloric acid concentration levels: (▲) 2 M HCl; (●) 4 M HCl; (◆) 6 M HCl.

This gross reaction proceeds via hydrogen radicals or hydride transfer and is accompanied by hydrolytic side reactions. Neither reaction mechanisms nor ancillary reactions are investigated in this paper.

Reagent Optimization. Recent investigations in hydride generation chemistry carried out by a number of workers (9, 10, 17, 22) have been our guidelines in optimizing this system. These studies have, among other findings, shown that optimum conditions for minimization of the interference from transition-metal ions are low concentration of tetrahydroborate ion and a relatively high hydrochloric acid concentration. It would therefore be natural to vary these parameters in our efforts to optimize the current system. Hydrochloric acid was included in the optimization procedure, but varying the tetrahydroborate concentration on a polymer-bound reagent can only be accomplished by adding an "inert" anion to the tetrahydroborate regeneration solution to compete with the sites on the anion exchanger in the regeneration step. We have not attempted this, as this would result in longer regeneration times and would require a larger column volume.

Figure 2 shows the dependence of the signal on hydrochloric acid concentration. Maximum peak height was reached at approximately 2 M HCl, whereafter the signal started to decline marginally. We have recommended a hydrochloric acid concentration of 4 M in the sample, as higher HCl concentrations will lead to a decrease in the interference from transition metals (10).

Carrier Flow. The influence of the carrier flow on the signal peak height at three different hydrochloric acid concentrations is depicted in Figure 3. High flows yielded sharper and higher peaks, as the hydride generation reaction is fast and the detector is mass flow sensitive.

Column Regeneration. The regeneration step comprised pumping of the tetrahydroborate anion exchanger rejuvenant

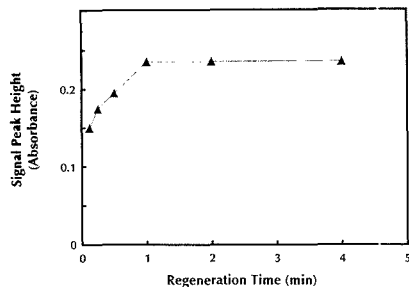


Figure 4. Influence of reagent column regeneration time on signal peak height.

plus a washing stage with the carrier. Washing is necessary to remove excess tetrahydroborate in order to ensure that the reaction will take place only in a heterogeneous fashion on the polymer surface when the acidic sample is introduced. Generation efficiency is shown as a function of regeneration time in Figure 4. A level where further regeneration did not result in better reduction efficiency was reached after 30 s with a pumping rate of 3 mL/min. Washing for the same period of time was sufficient.

Column Dimensions and Particle Size. A 50 mm long, 3 mm i.d. column was tested in addition to the 100 mm long, 6 mm i.d. type recommended. The reagent capacity of the smaller column was sufficient, but the peaks were less symmetric and more noisy. The back-pressure was also rather high for peristaltic pumping due to the smaller frits. Smaller particles (a 40–60 mesh fraction sieved out from the practical grade material) caused the same back-pressure problem as the smaller column, and the 20–50 mesh resin was used as received.

Column Lifetime. The polymeric reagent column could be used for several months without significant degradation in performance. If used with samples relatively high in transition-metal ions, the polymer tended to darken after a while, presumably due to accumulation of colloid metal precipitated by tetrahydroborate reduction. Slight discoloration did not affect the arsenic signal, but the polymer could be reconditioned by treatment with an acidic solution of the amino acid L-cystine, which was recently reported to be a powerful masking agent (14). Pumping a 3% solution of this reagent in 4 M hydrochloric acid through the column restored the original color and activity of the polymer in a few minutes.

Interference Studies. The maximum permissible concentrations of some transition-metal ions causing less than 10% signal degradation when compared to the signal from interferent-free sample solutions are shown in Table I. The acceptable levels ranged from 200 to 500 $\mu\text{g/mL}$ without masking agent added. When L-cystine was added to the samples to a final concentration of 3%, the acceptable transition-metal concentrations were increased by a factor of approximately 10. This is better than methods employing batch generation (9, 10) or conventional continuous flow methods (17, 22), but not as good as the chloride generation method previously reported by us (23).

Metal ions are believed to interfere with hydride generation after being reduced to the elemental state (22) or following conversion to metal borides (7). Since the rate at which metal ions are reduced is slow in comparison with the rate of arsine generation (17), a technique such as flow injection, which shortens the sample/reagent interaction period, will suppress the magnitude of the interferences.

The improved tolerance toward transition-metal interference may also be due to a low concentration of free tetra-

Table I. Maximum Permissible Concentrations (in $\mu\text{g/L}$) for Some Transition-Metal Ions, Causing Less Than 10% Signal Change in a Sample Containing 50 $\mu\text{g/L}$ As(III), As Compared to a Sample without Interferent Added

interferent	acid composition	
	4 M HCl	4 M HCl + 3% L-cystine
Ni	200	2500
Cu	400	5000
Co	500	4000
Fe	600	5000

hydroborate at the site of reaction. When the acidic sample enters the reagent column, protons will participate in the hydrolysis of tetrahydroborate ions bound to the polymer. This results, according to currently accepted assumptions (24), in the formation of hydrogen radicals that reduce the arsenic present in the solution. As long as the tetrahydroborate ion is bound to the polymer, coordination to the ion-exchange group can cause steric hindrance that prevents arsenic from forming complexes with tetrahydroborate, which is proposed as one possible cause of the transition-metal interference (7). Research needed to clarify these mechanisms is, however, beyond the scope of this work.

Sample Loop Size. Significant tailing was observed when a sample loop of 130- μL volume was used. Decreasing the loop volume to 40 μL allowed an increase in sample throughput at the cost of a 35% decrease in signal peak height. The ubiquitous incommensurability between sensitivity and analysis time is thus present also in this technique, with the times set out in the recommended procedure being a reasonable compromise.

Arsenic Species Selectivity. The signal from As(V) amounted to 70% of the signal from the same amount of As(III) under the recommended conditions. This is in the same range as reported for batch methods (25). It is thus not possible to speciate discriminately between tri- and penta-valent inorganic arsenic with the method as described at present.

Detection Limit and Linear Working Range. We achieved a detection limit of 1.5 $\mu\text{g/L}$ for a 40- μL sample. This compares well, on a concentration basis, with batch generation methods. Since batch methods typically use much larger sample volumes, the detection limit in absolute amount of arsenic is better in the proposed method. The calibration curve was linear from the detection limit up to 100 $\mu\text{g/L}$. RSDs for four replicate analyses of solutions containing 6.25 and 50 $\mu\text{g/L}$ As(III) were 3.1 and 1.5%, respectively.

To sum up, hydride generation with subsequent atomic spectrometric detection can be carried out in the ng/mL range on microliter samples with polymer-bound tetrahydroborate used as a reducing agent in a flow injection system. Such a system possesses a potential for minimizing interferences to a level that will enable analyses of samples containing percent amounts of transition-metal ions. Extension of the technique to other hydride-forming elements is in progress.

ACKNOWLEDGMENT

The authors appreciate the help of Michael Sharp in reviewing the manuscript linguistically.

LITERATURE CITED

- Gutzeit, M. *Pharm. Z.* **1879**, *24*, 263.
- Holak, W. *Anal. Chem.* **1969**, *41*, 1712.
- Pollock, E. N.; West, S. J. *At. Absorpt. News.* **1973**, *12*, 6.
- Maruta, T.; Sudoh, G. *Anal. Chim. Acta* **1975**, *77*, 37.
- Brown, H. C.; Schlesinger, H. I.; Burg, A. B. *J. Am. Chem. Soc.* **1959**, *81*, 673.
- Schmidt, F. J.; Royer, J. L. *Anal. Lett.* **1973**, *6*, 17.
- Brown, R. M., Jr.; Fry, R. C.; Moyers, J. L.; Northway, S. J.; Denton, M. B.; Wilson, G. S. *Anal. Chem.* **1981**, *53*, 1560.
- Smith, A. E. *Analyst* **1975**, *100*, 300.

- (9) Welz, B.; Melcher, M. *Analyst* **1984**, *109*, 569.
 (10) Welz, B.; Schubert-Jacobs, M. J. *Anal. At. Spectrosc.* **1986**, *1*, 23.
 (11) Belcher, R.; Bogdanski, S. L.; Henden, E.; Townshend, A. *Analyst* **1975**, *100*, 522.
 (12) Aggett, J.; Aspell, A. C. *Analyst* **1976**, *101*, 341.
 (13) Giumont, J.; Pichett, M.; Rhéume, N. *At. Absorpt. Newsl.* **1977**, *16*, 53.
 (14) Boampong, C.; Brindle, I. D.; Le, X.; Pidwerbesky, L.; Ceccarelli, P. C. *M. Anal. Chem.* **1988**, *60*, 1185.
 (15) Åström, O. *Anal. Chem.* **1982**, *54*, 190.
 (16) Pacey, G. E.; Straka, M. R.; Gord, J. R. *Anal. Chem.* **1986**, *58*, 502.
 (17) Yamamoto, M.; Yasuda, M.; Yamamoto, Y. *Anal. Chem.* **1985**, *57*, 1382.
 (18) Yamamoto, M.; Takada, K.; Kumamaru, T. *Anal. Chem.* **1987**, *59*, 2446.
 (19) Brown, H. C.; Krishnamurthy, S. *Tetrahedron* **1979**, *35*, 567.
 (20) Cook, M. M.; Demko, P. R.; Wagner, S. E.; Mikulski, R. A.; Clements, J. G. *Adv. Chem. Ser.* **1980**, *167*, 195.
 (21) Dedina, J. *Fresenius' Z. Anal. Chem.* **1986**, *323*, 771.
 (22) Yamamoto, M.; Yamamoto, Y.; Yamashige, T. *Analyst* **1984**, *109*, 1461.
 (23) Testalidet, S.; Irgum, K. *Anal. Chem.* **1988**, *60*, 2031.
 (24) Bye, R. *Talanta* **1986**, *33*, 705.
 (25) Welz, B.; Melcher, M. *Analyst* **1984**, *109*, 573.

RECEIVED for review October 18, 1988. Revised manuscript received February 14, 1989. Accepted May 24, 1989. This work was supported by The Swedish Natural Science Research Council through Grant E-EG 8724-103.

Characterization of the Nitrogen and Phosphorus Thermionic Detector Response in Capillary Supercritical Fluid Chromatography

P. A. David and M. Novotny*

Department of Chemistry, Indiana University, Bloomington, Indiana 47405

Selective response of the thermionic detector in the nitrogen and phosphorus modes was characterized with respect to (1) detector gas flow rates, (2) thermionic source composition, and (3) supercritical mobile-phase composition. The most critical detector parameters were the hydrogen detector gas flow rate and the position of the thermionic source with respect to the flame jet. The optimum thermionic source consisted of approximately 73% SiO₂ and 12% each of Rb₂O and Na₂O. Additionally the selective thermionic response could be obtained with silicate sources containing sodium exclusively. However, source background current stability and lifetime were much poorer than those with mixed alkali silicate sources. The detector sensitivity and selectivity were similar with either CO₂ or N₂O mobile phases. Additionally, up to 10 mol % of an organic modifier was added to the supercritical mobile phase without causing large increases in the detector background response. The separation of model nitrogen- and phosphorus-containing compounds was used to demonstrate the feasibility of modified mobile phase pressure programming in conjunction with selective thermionic detection.

INTRODUCTION

The nitrogen- and phosphorus-sensitive thermionic detector, also known as the alkali flame ionization detector (AFID), was first described by Karmen and Giuffrida in 1964 for use in gas chromatography (1). This type of thermionic detector consisted of an alkali-impregnated wire grid, porous ceramic, or compressed salt tip source (2) in contact with a hydrogen flame. The flame in the AFID serves to volatilize the alkali-metal salt which in turn undergoes electron-transfer reactions with heteroatom-containing species (N, P, etc.) in the flame. The popularity of the AFID has diminished due to poor alkali source stability and lifetime. Additionally, the magnitude and quality of the selective response were strongly dependent on each specific AFID design (3).

In 1974, Kolb and Bischoff introduced a design improvement for the selective thermionic detector (4). The Kolb-Bischoff detector employed a rubidium-silicate bead fused

on a platinum wire. This thermionic source modification enhanced the response reproducibility and the source lifetime. The thermionic detector could be operated in either a nitrogen-phosphorus or a phosphorus-only selective mode (5).

In the nitrogen-phosphorus selective mode (NP-mode), the source was present in a dilute hydrogen environment insufficient to maintain a flame. The thermionic source was held at a negative potential and heated externally via a constant current source. Additionally, the flame jet was held at a negative voltage and the collector electrode was grounded.

In the phosphorus-only mode (P-mode), hydrogen flow rate was increased to sustain a flame which also served to heat the thermionic source. Once again, the source was held at a negative potential and the flame jet and collector electrode were grounded.

Fjeldsted et al. (6) initially evaluated the Hewlett-Packard thermionic detector for capillary supercritical fluid chromatography (SFC) with promising results with both CO₂ and N₂O as the supercritical mobile phase. In this detector design, positive ions are collected rather than negative ions, as in the Kolb-Bischoff design (NP-mode) (3). West and Lee (7) have also evaluated a Patterson-type thermionic detector for capillary SFC. This detector consists of a cesium-impregnated ceramic source (8, 9). The alkali-ceramic source can be modified to provide selectivity for electronegative species, such as the nitro group (TID-1-N₂). The Patterson detector performed favorably under SFC density programming conditions in this mode of operation. Additionally, this detection mode permitted the use of a CO₂ mobile phase modified with methanol at a volumetric concentration of 1%. However, mobile-phase modification at this concentration resulted in no differences in selectivity or resolution with respect to a pure CO₂ mobile phase for the separation reported. West and Lee also evaluated the Patterson detector in the TID-2-H₂/air mode. This detector type is analogous to the nitrogen-phosphorus selective Kolb-Bischoff detector. Under SFC mobile-phase density programming conditions, the TID-2-H₂/air mode exhibited significant decreases in background current (i.e. poorer sensitivities) as the mobile-phase density increased.

We have recently reported the use of a selective thermionic detector similar to the Kolb-Bischoff detector in both the nitrogen-phosphorus and phosphorus-only selective detection

Table I. Mobile-Phase Composition Study: Critical Values and Experimental Conditions

	T_c , °C	P_c , atm	T_r^a , °C	P_r , atm
N ₂ O	36.5	71.4	118	135.7
CO ₂	30.9	72.8	100	138.3
N ₂ O/MeOH (NP-mode)	61.3	83.8	198	159.2
CO ₂ /MeOH (NP-mode)	59.3	89.1	192	169.3
N ₂ O/MeOH (P-mode)	51.6	80.6	167	153.1
CO ₂ /MeOH (P-mode)	48.1	83.0	156	159.2
CO ₂ /IPA (Figure 1)	69.6	92.5	110	80–200

^a Experiments performed at: $T_r = 3.24$, $P_r = 1.9$.

modes for capillary SFC (10, 11). We have observed stable detector background currents and low picogram sensitivities with mobile-phase pressure programming for both modes of selective detection. In an attempt to understand these encouraging observations, a thorough characterization of the thermionic response in SFC has been carried out in this work. Three main studies were performed to monitor the thermionic response in both selective modes with respect to (1) detector geometry and gas flow rates, (2) thermionic source composition, and (3) mobile-phase composition.

This report summarizes the results of our studies. Important detector parameters necessary for response optimization will be highlighted and insights into possible mechanisms for the selective thermionic response will be discussed. It will also be demonstrated that the selective nature of this thermionic detector has allowed the use of high concentrations of mobile-phase modifiers in CO₂ or N₂O.

EXPERIMENTAL SECTION

The supercritical fluid chromatograph was a laboratory-built instrument as described previously (11, 12). Mobile-phase delivery and pressure control were accomplished with a Brownlee Labs Micropump with software version G (Applied Biosystems, Santa Clara, CA). The mobile phases employed were SFC grade nitrous oxide or carbon dioxide (Scott Specialty Gases, Plumsteadville, PA). The mobile-phase cylinders were charged with 1500 psi of helium headspace pressure to facilitate rapid filling of the pump without externally cooling the pump heads. Methanol and 2-propanol (Spectrophotometric Grade, Mallinckrodt, Inc., Paris, KY) were filtered through a 0.45- μ m PTFE filter prior to use as mobile-phase modifiers. To prepare the mixed mobile phase, the B syringe of the Brownlee Micropump was first filled with an appropriate modifier. When the B syringe was full, the A syringe was then filled with pure CO₂ or N₂O. Mixing was accomplished by dispensing each mobile phase component into an in-line mixing tee provided in the micropump. The volumetric ratio of components was set by controlling the relative pumping rate in each syringe. The mixing of fluids with greatly different compressibilities required equilibration times of 2–3 h to establish a stable detector background current, thus ensuring a homogeneous mobile-phase mixture.

The approximate mole fraction of each mobile-phase component was calculated by using the densities of the two fluids entering the room-temperature mixing tee and the volume of the mixer. The density of the pure supercritical fluid was calculated by the Lee–Kesler equation (13). The critical temperature of the binary mixtures was calculated via the method of Chueh and Prausnitz (14) and the mixture critical pressure by the approach of Kreglewski and Kay (14). All experiments were performed at a reduced temperature (T_r) of 3.24 and a reduced pressure (P_r) of 1.9. The experimental mobile-phase critical values are listed in Table I. The mixed mobile phases used in the NP mode contained 10 mol % methanol and 6 mol % methanol in the P mode.

Injection was accomplished via an electrically actuated high-pressure valve with an internal sample loop volume of 0.06 μ L (Valco Instruments, Houston, TX). Split injection was used for all analysis with a split ratio of 5:1. The capillary column used was 50 μ m i.d. and 10 m in length. The fused silica surface was deactivated prior to coating through treatment with poly(meth-

Table II. Bead Composition

bead	% SiO ₂	% Rb ₂ O	% Cs ₂ O	% Na ₂ O	% B ₂ O ₃
A	73.3	12.2		12.6	1.8
B	73.8		12.2	11.9	2.1
C	85.6			12.3	2.0
D	83.8	12.2			4.0
E	85.5		12.3		2.2

Table III. Optimum Detector Operating Parameters

	NP-mode	P-mode
H ₂ flow rate, mL/min	1.5–2.0	30–32
air flow rate, mL/min	150–275	250–400
bead position, mm above jet	1.5–2.5	1–1.5
restrictor position, cm below jet	0.5–1.0	0.5–1.0
bead heating current, A	3.0–3.2	
sensitivity, pg/s	1–2	0.1–0.2
selectivity, decades	3.0	2.0

thylhydrosiloxane) (85 cSt) (Petrarch Systems, Bristol, MA) (15). The column was statically coated at 65 °C with a 40 mg/mL solution of SE-33 in Freon 11 to produce a 0.50- μ m film (16). The stationary phase was cross-linked 3 times with *azo-tert*-butane (Alfa Products, Danvers, MA) (17).

Pressure restriction required for operation of a flame-based detector was accomplished by forming an integral restrictor directly at the end of the coated column (18). The detector was a Perkin-Elmer Sigma 3 nitrogen–phosphorus detector (NPD) modified as was previously described (12). Polarization voltage, bead heating current, and signal amplification were provided by a Perkin-Elmer stand-alone NPD electrometer (Model 330-0543, Perkin-Elmer, Norwalk, CT). The thermionic sources were prepared according to the procedure of Lubkowitz et al. (19). The beads contained various mixtures of silicon(IV) oxide (Gold Label, Aldrich Chemical Co., Milwaukee, WI), rubidium or cesium nitrate (Puratronic Grade, Alfa Products, Danvers, MA), and sodium carbonate and boric acid (Reagent Grade, MCB Manufacturing Chemists, Inc., Cincinnati, OH). Beads were prepared by heating the appropriate mixture of these chemicals in a fused silica crucible (Fisher Scientific, Cincinnati, OH) with a propane/oxygen flame. The bead materials formed a molten flux consisting of the corresponding oxides of the original compounds. The composition of the various thermionic sources used can be found in Table II.

All detector gas flow rates were regulated with high-quality rotameters (Aalborg Instruments and Controls, Inc., Monsey, NY) with the exception of the hydrogen flow in the NP detector mode which was regulated via a mass-flow controller (Brooks Instrument Division, Emerson Electric Co., Hatfield, PA). The distance between the thermionic source and the flame jet tip was set with a spacer fabricated from copper wire to establish the appropriate source/jet gap. The copper wire spacer was removed prior to detector operation.

The test solutes used in the bead composition and mobile-phase composition studies were quinoline (NP-mode) and trimethylphosphate (P-mode) (Aldrich Chemical Co., Milwaukee, WI). All nitrogen-containing test solutes were obtained from Aldrich Chemical (Milwaukee, WI) and the phosphorus-containing pesticide standards were supplied by Alltech Associates (Deerfield, IL).

RESULTS AND DISCUSSION

The optimum detector operating conditions are summarized in Table III for both selective detection modes. In the NP-mode, the most crucial parameter to optimize was the hydrogen flow rate. An H₂ flow rate of 1.5–2 mL/min provided optimal detector sensitivity with negligible base-line noise and drift. The use of a mass-flow controller allowed the flow to be precisely maintained. In short-term experiments where better than low pg of N/s sensitivities are required, the H₂ flow rate can be increased up to 3 mL/min. This results in better sensitivities at the expense of bead lifetime. Also, at this H₂ flow, a 5–10% base-line shift (detector background

current shift) occurred during a mobile-phase pressure program at 10 atm/min from 75 to 350 atm.

Other detector parameters of importance were the bead heating current and bead position. The heating current must be maintained at a level corresponding to 10–20 pA of background current in the detector. Bead temperatures which produce this level of background current provide optimal signal/noise characteristics in conjunction with low milliliter-per-minute H₂ flow rates. Additionally, as the thermionic source ages, the heating current must be increased to maintain the appropriate background current. The bead position was maintained at least 1.5 mm above the flame jet to avoid bead cooling as a result of the increased supercritical mobile-phase flow rate during a mobile-phase density program. The thermionic source background current decreases as a result of this cooling. A chromatogram with a negative-sloping base line is diagnostic of a bead position too close to the flame jet. External heating of the thermionic source allows a constant response to be maintained at bead positions 1.5–2.5 mm above the jet.

In the P-mode, the hydrogen flow rate and the bead position were again critical parameters for detector optimization. The maintenance of a flame in the detector requires H₂ flow rates of 30–32 mL/min. Again, higher flows (up to 40 mL/min) resulted in increased signal, but problems occurred due to shorter bead lifetimes and decreased selectivity for phosphorus over carbon. Since the flame also provides for bead heating, the bead position was closer (1–1.5 mm) to the flame jet. In the P-mode, bead position too close to the flame jet resulted in a chromatogram with a positive-sloping base line. This is due to changes in the flame geometry as a result of the increased mobile-phase flow rate during a density program from 75 to 350 atm. We hypothesize that the increased mobile-phase flow acts to elongate the flame which results in the bead residing in a hotter region of the flame. This is manifested in an increasing detector background current during a density program.

If the optimum detector conditions are maintained, a thermionic bead in either selective mode can be used with a minimal decrease in sensitivity for approximately 2 months. It should be noted that the P-mode exhibited approximately an order of magnitude sensitivity over the NP-mode. However, due to the presence of a flame in the P-mode, selectivity was poorer compared to the NP-mode. Additionally, these detectivities and selectivities are approximated 10 times poorer than those obtained under GC conditions.

Table IV summarizes the results of our study of the thermionic detector response for various bead compositions. The values reported are the average of the data obtained with three beads at each composition. In both selective modes, the beads containing 12% of both Rb₂O and Na₂O exhibited the optimum response (bead A). Recently, van de Weijer et al. (20), have reported that the response of the Kolb-Bischoff detector in the NP-mode to organonitrogen compounds can be obtained by using silicate sources containing sodium as the only alkali species. Our results tend to support their findings (bead C). However, we have observed that bead equilibration (burn-in) times are much longer with the sodium-only beads (36 vs 12 h), and detectivities are poorer compared to our mixed rubidium/sodium beads. Additionally, the sodium-only beads (bead C) do not maintain optimum sensitivity for more than 2 weeks.

Additionally, van de Weijer et al. have proposed that the mechanism of thermionic response is that of a gas-phase ionization of sodium atoms (20). In an attempt to verify this mechanism for SFC, silicate sources containing rubidium or cesium-only were fabricated (beads D and E). The substantially poorer sensitivities obtained with these beads tend to

Table IV

A. N-Thermionic Detector Response vs Bead Composition ^a			
bead	sensitivity, pg of N/s	background current, pA	selectivity, decades
A	1.5	15	2.5
B	2.0	15	2.5
C	6.0	12 ^b	1.5
D	27	15	2.2
E	21	15	2.4
B. P-Thermionic Detector Response vs Bead Composition ^c			
bead	sensitivity, pg of P/s	background current, pA	selectivity, decades
A	0.55	5	1.7
B	0.50	6	0.9
C	1.5	1	1.3
D	25.0	4	1.0
E	50.0	2	0.0

^a Mobile phase: N₂O. *T_r* = 3.24. *P_r* = 1.9. ^b This bead required 24–36 h to equilibrate. All other beads stabilized in 12 h. ^c Mobile phase: N₂O. *T_r* = 3.24. *P_r* = 1.9.

Table V

A. N-Thermionic Detector Response vs Mobile-Phase Composition			
	sensitivity, pg of N/s	background current, pA	selectivity, decades
N ₂ O	1.3	10	2.2
CO ₂	1.5	7	2.4
N ₂ O/MeOH	1.4	30	2.5
CO ₂ /MeOH	1.0	15	2.7
B. P-Thermionic Detector Response vs Mobile-Phase Composition			
	sensitivity, pg of P/s	background current, pA	selectivity, decades
N ₂ O	0.55	30	1.7
CO ₂	0.58	40	1.5
N ₂ O/MeOH	0.61	30	1.4
CO ₂ /MeOH	0.66	30	1.3

reinforce the mechanism of sodium exchange into the reactive plasma (NP-mode) or flame (P-mode) region where sodium is ionized by radicals with large electron affinities (i.e. CN, PO, PO₂), although selective response can be obtained with beads.

Table V summarizes the results of studies of the thermionic response with respect to mobile-phase composition. The NP-mode of the thermionic detector exhibited negligible change in response with respect to the pure mobile phases (CO₂, N₂O). The detector also maintained good sensitivity using 10 mol % methanol-modified mobile phases with relatively minor increases in the detector background current. To demonstrate the feasibility of using a modified supercritical fluid mobile phase in conjunction with thermionic detection, separation of a model mixture of nitrogen-containing polycyclic aromatic hydrocarbons was performed. Modification of the CO₂ or N₂O mobile phases with 10 mol % methanol did not result in significant changes in resolution or solute retention. Yonker and Smith (21) and Fields et al. (22) have reported significant changes in solute retention by using supercritical carbon dioxide mobile phases modified with 2-propanol in capillary SFC with UV detection. Addition of 10 mol % 2-propanol to supercritical CO₂ resulted in significant decreases of retention for acridine, aminonaphthalene, and am-

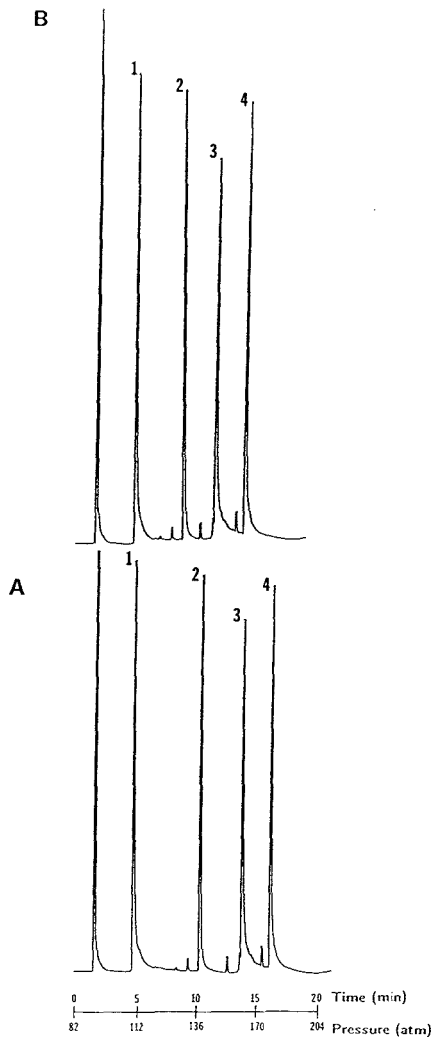


Figure 1. Separation of model nitrogen-containing compounds in the NP-mode: (A) mobile phase 100% CO_2 , (B) mobile phase CO_2 with 10 mol % 2-propanol; peak designation (1) quinoline, (2) acridine; (3) 1-aminonaphthalene, (4) 1-aminopyrene; temperature, 110 °C; detector range, 8×10^{-12} A.

inopyrene, while the capacity factor for quinoline remained unchanged (Figure 1). It is also significant to note that the detector base line remains stable during the pressure program at a detector range of 8×10^{-12} A.

Sensitivity, background current, and selectivity in the P-mode of the thermionic detector were similar for CO_2 , N_2O , and a 6 mol % methanol modification of CO_2 and N_2O . At mobile-phase loadings of greater than 6 mol % methanol, the background current increased dramatically to low nanampere levels and continued to increase during mobile-phase pressure programs. These changing background levels make pressure programming unrealistic. However, a nitrous oxide/6 mol % methanol mobile phase did result in significant retention changes for a model mixture of phosphorothioate pesticides

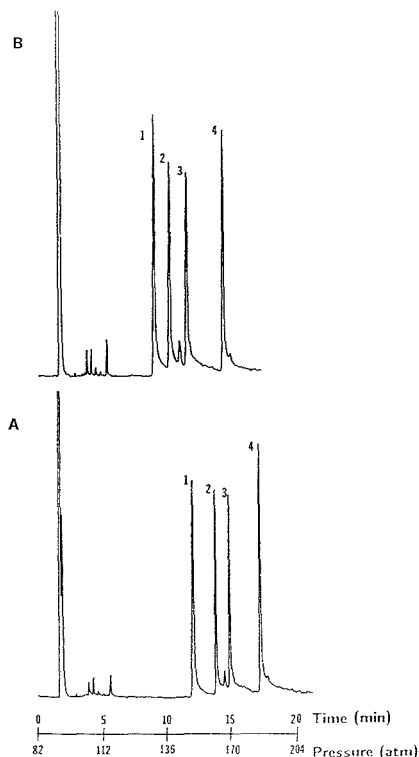


Figure 2. Separation of model phosphorus-containing compounds in the P-mode: (A) mobile phase 100% N_2O , (B) mobile phase N_2O with 6 mol % methanol; Peak designation (1) *O,O*-diethyl *S*-[(ethylthio)methyl] phosphorodithioate (Phorate), (2) *O,O*-diethyl *S*-2-[(ethylthio)ethyl]phosphorodithioate (Di-Syston), (3) diethyl [(dimethoxyphosphinothioyl)thio]butanedioate (Malathion), (4) *O,O,O',O'*-tetraethyl *S,S'*-methylene phosphorodithioate (Ethion), temperature, 110 °C; detector range, 8×10^{-12} A.

(Figure 2). Since this sample exhibited limited solubility in CO_2 or modified CO_2 mobile phases, N_2O mobile phases were used exclusively. It should be noted that N_2O is an oxidant, which may be potentially hazardous when mixed with organic modifiers at high pressures.

Crucial thermionic detector parameters have been identified through a careful characterization of the thermionic response. In both the NP and P selective modes, the hydrogen flow rate and bead position are the most important parameters for response optimization. Thermionic sources containing 12% each of Rb_2O and Na_2O exhibited the optimum sensitivities and lifetimes. Poor sensitivities of thermionic sources containing rubidium or cesium only tend to reinforce the gas-phase ionization mechanism of thermionic response proposed recently by van de Weijer et al. (20). The thermionic detector exhibits sufficient selectivity to permit the use of supercritical mobile phases containing up to 10 mol % of an organic modifier. The thermionic detector could also be extremely useful in SFC with microbore packed columns. These columns provide mobile-phase flow rates compatible with flame-based detectors. Mobile-phase modifications at the 1–2 mol % levels are routinely used with microbore columns to dynamically deactivate active sites on the packing material and permit the analysis of polar compounds. Unfortunately, the use of organic modifiers complicates the use of other flame-based detectors,

except for modifiers which have a negligible response in the flame (i.e. formic acid, formamide, or water). Consequently, the UV or mass spectrometric detectors are used in SFC with modified mobile phases. However, the use of the thermionic detector in microbore SFC could potentially allow highly sensitive detection as well as the use of a wide range of organic modifiers with the exception of those containing nitrogen or phosphorus. Additionally, the decreased solute capacity factors resulting from the use of modified supercritical mobile phases can be important to SFC in terms of decreasing time of analysis for certain compounds.

LITERATURE CITED

- (1) Karmen, A.; Giuffrida, L. *Nature* **1964**, *210*, 1204-1205.
- (2) Lakota, S.; Aue, W. A. *J. Chromatogr.* **1969**, *44*, 472-480.
- (3) Dressler, M. *Selective Gas Chromatographic Detectors*; Elsevier Science Publishers: Amsterdam, 1986.
- (4) Kolb, B.; Bischoff, J. *J. Chromatogr. Sci.* **1974**, *12*, 625-629.
- (5) Kolb, B.; Aver, M.; Pospisil, P. *J. Chromatogr. Sci.* **1977**, *15*, 53-63.
- (6) Fjeldsted, J. C.; Kong, R. C.; Lee, M. L. *J. Chromatogr.* **1983**, *279*, 449-455.
- (7) West, W. R.; Lee, M. L. *HRC CC, J. High Resolut. Chromatogr. Chromatogr. Commun.* **1986**, *9*, 161-167.
- (8) Patterson, P. L.; Gatten, R. A.; Ontiveros, C. J. *Chromatogr. Sci.* **1982**, *20*, 97-102.
- (9) Patterson, P. L. *J. Chromatogr. Sci.* **1986**, *24*, 41-52.
- (10) David, P. A.; Novotny, M. J. *Chromatogr.* **1988**, *452*, 623-629.
- (11) David, P. A.; Novotny, M. J. *Chromatogr.* **1989**, *461*, 111-120.
- (12) Novotny, M.; David, P. *HRC CC, J. High Resolut. Chromatogr. Chromatogr. Commun.* **1986**, *9*, 647-651.
- (13) Lee, B. I.; Kesler, M. G. *AIChE J.* **1975**, *21*, 510-527.
- (14) Reid, R. C.; Prausnitz, J. M.; Poling, B. E. *The Properties of Gases and Liquids*, 4th ed.; McGraw-Hill: New York, 1987; Chapter 5.
- (15) Woolley, C. L.; Kong, R. C.; Richter, B. E.; Lee, M. L. *HRC CC, J. High Resolut. Chromatogr. Chromatogr. Commun.* **1984**, *7*, 329.
- (16) Woolley, C. L.; Tarbet, B. J.; Markides, K. E.; Bradshaw, J. S.; Lee, M. L.; Bartle, K. D. *HRC CC, J. High Resolut. Chromatogr. Chromatogr. Commun.* **1988**, *11*, 113-118.
- (17) Wright, B. W.; Peaden, P. A.; Lee, M. L.; Stark, T. J. *J. Chromatogr.* **1962**, *248*, 17-24.
- (18) Guthrie, E. J.; Schwartz, H. E. *J. Chromatogr. Sci.* **1986**, *24*, 236-241.
- (19) Lutkowitz, J. A.; Semonian, B. P.; Galobardes, J.; Rogers, L. B. *Anal. Chem.* **1978**, *50*, 672-676.
- (20) van de Weijer, P.; Zwerwer, B. H.; Lynch, R. J. *Anal. Chem.* **1988**, *60*, 1360-1367.
- (21) Yonker, C. R.; Smith, R. D. *Anal. Chem.* **1987**, *59*, 727-731.
- (22) Fieds, S. M.; Markides, K. E.; Lee, M. L. *J. Chromatogr.* **1987**, *406*, 221-235.

RECEIVED for review January 9, 1989. Accepted June 27, 1989. This work was supported by Grant CHE 8605935 from the National Science Foundation and a grant-in-aid from Dow Chemical Co.

Square Wave Voltammetry at a Mercury Film Electrode: Experimental Results

Kazimierz Wikiel¹ and Janet Osteryoung*

Department of Chemistry, State University of New York at Buffalo, Buffalo, New York 14214

Experimental results for direct and anodic stripping square wave voltammetry at a silver-based mercury film electrode (SBMFE) are presented for $-2 < \log(I(f/D)^{1/2}) < 1$, where l is film thickness, f frequency, and D diffusion coefficient. Theoretical predictions are firmly confirmed by the experimental results for Pb(II)/Pb(Hg) for the magnitude, shape, and position on the potential scale of the voltammograms. The usefulness of the SBMFE under square wave conditions is established even at high frequency. However, some deviation for square wave experiments at silver-based microelectrodes is observed at high frequency.

The mercury film electrode (MFE) is presently a well-recognized tool for electroanalytical practice. Anodic stripping voltammetry at the MFE by means of pulse techniques is applied frequently in trace analysis (1). Although the theoretical calculations for direct (2) as well as anodic stripping (3, 4) square wave voltammetry have been published, only a few experimental results following these theoretical treatments have been reported. Some results obtained at the glassy-carbon-based MFE (5) and iridium-based MFE (6-8) deviate from theoretical predictions. Markedly smaller than expected reverse current has been observed for both direct and anodic stripping square wave voltammograms when high square wave frequency has been applied. In some cases, however, ideal behavior was observed.

The mercury-plated glassy carbon electrode exhibits behavior predicted for a film electrode quantitatively over a wide range of conditions for linear scan stripping. Mercury on glassy carbon substrates exists as a collection of individual droplets dispersed across the surface. The connection between the droplets and carbon is sufficiently weak that for deposition at a rotating disk electrode even at modest rotation rates (e.g., 2000 rpm) mercury droplets slide across the carbon surface and on to the surrounding insulator (5). Thus differences between experimental results and those of a film model should not be surprising. On iridium substrates coherent films of mercury are formed (6-9). However in both direct and stripping square wave voltammetry at such electrodes anomalies occur at higher square wave frequencies (6, 8).

In this report we present some experimental results obtained at mercury film electrodes under square wave conditions over a wide range of mercury film thickness and square wave frequency using a silver-based mercury film electrode. It has been reported (10, 11) that this type of MFE follows theoretical predictions for the Pb(II)/Pb(Hg) system under cyclic and anodic stripping linear scan conditions. Considering the above discussion, it can be seen that the objective was twofold. One goal was to confirm experimentally the theoretical predictions based on the thin layer model for SWV (2, 3). A related but quite different goal was to demonstrate that the simple model of a film electrode has a practical experimental realization which permits the general extension of square wave voltammetry to mercury film electrodes.

EXPERIMENTAL SECTION

All chemicals used in this study (Pb(NO₃)₂, NaNO₃, CH₃COOH, CH₃COONa, EDTA, HClO₄, Hg₂(ClO₄)₂, NaOH) were analytical

¹ Present address: Institute of Precision Mechanics, Duchnicka 3, 00-967 Warsaw, Poland.

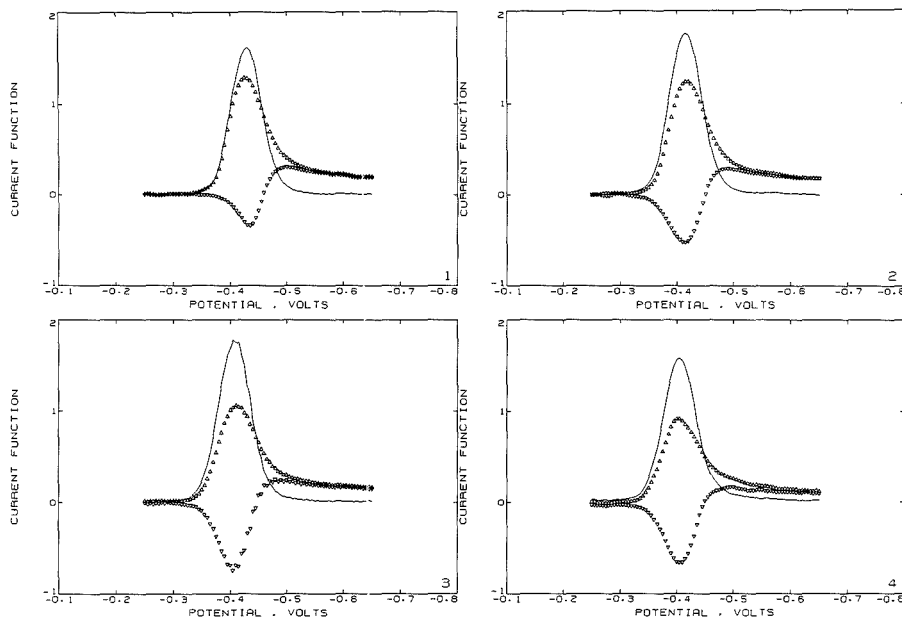


Figure 1. Net (—), forward (Δ), and reverse (∇) current function of DS WV for 2×10^{-4} M Pb(II) in 1 M NaNO₃. SBMFE: $A = 4.4$ mm²; $l = 4.2$ μ m. $\Delta E_s = 5$ mV; $E_{sw} = 25$ mV; $f =$ (1) 6, (2) 30, (3) 120, and (4) 600 Hz.

grade and used as received. An EG&G PARC 273 potentiostat interfaced to a PDP 8/e computer system was employed for voltammetry. A PAR 173 potentiostat equipped with a PAR 179 coulometer was employed for deposition and stripping of mercury. A three-electrode conventional jacketed cell was used with temperature maintained at 25 ± 0.2 °C. An SCE was used as the reference electrode and a platinum wire as the counter electrode. Solutions were deaerated by sparging with high-purity argon.

Silver-based mercury film electrodes (SBMFE) were prepared according to the procedure presented by Stojek and Kublik (10). The electrode was a cylinder formed by sealing 3–4 mm of 0.5 mm diameter silver wire into soft-glass tubing. Final electro-deposition of mercury was preceded by the formation on the silver surface of solid silver amalgam. This was formed by depositing a thick layer, approximately 10 μ m, of mercury directly onto the silver electrode and then storing in deionized water for about 24 h. After that the excess of liquid mercury was stripped electrochemically. In all experiments this solid silver amalgam was in fact the substrate for the mercury film. The quantity $nAC_0^*D_0^{1/2}$ was determined for the SBMFE electrochemically by comparison of linear scan results for cathodic reduction of Pb(II) at the static mercury drop electrode (SMDE PARC 303A, medium size drop, $A = 0.017$ cm²) with results obtained at the SBMFE under exactly the same conditions. The geometric area of the silver substrate was used to calculate the thickness of mercury films from the deposition charge.

Mercury was deposited electrochemically from a solution of 0.05 M Hg(II) in 0.1 M HClO₄. The charge passing during the deposition was monitored coulometrically. The thickness of the mercury film was determined from the charge passed during the oxidation of mercury ($n = 2$) from the substrate in a solution of 0.05 M EDTA in acetate buffer, pH = 4.8. The film thickness is less than 1% of the diameter of the wire. Under microscopic examination it is uniform.

The concentration of lead in the mercury phase, necessary to calculate the current function in anodic stripping experiments, was determined from the charge of the oxidation of lead under linear scan conditions.

As suggested by Stojek and Kublik (10), in order to refresh the surface of mercury, the SBMFE was negatively polarized at ap-

proximately -6 V in 2 M NaOH for approximately 2 s before each set of experiments. This treatment is accompanied by copious evolution of hydrogen and results in a perfectly adherent and reflecting film. The proper preparation of the SBMFE was verified experimentally by comparison of results obtained under linear scan conditions with theoretical predictions presented by De Vries and van Dalen (11) and Donten et al. (12). The agreement was very good. For the time scales employed here cylindrical diffusion should be unimportant.

A silver-based mercury microelectrode was prepared by sealing a silver wire 25 μ m in diameter into a 2- μ L micropipet. After fine polishing with 0.05- μ m alumina suspension, the silver microdisk electrode was dipped into bulk mercury. Microscopic examination of the resulting electrode showed that a hemisphere of mercury with a diameter of approximately 25 μ m had been attached to the silver substrate.

RESULTS AND DISCUSSION

Direct Square Wave Voltammetry (DS WV). According to the theoretical predictions the shape and position of square wave voltammograms obtained for the system $M^{n+}/M(\text{Hg})$ at a MFE depends on the value of mercury film thickness and square wave frequency as combined in the dimensionless parameter Λ which is defined as

$$\Lambda = l(f/D_R)^{1/2} \quad (1)$$

where l is the mercury film thickness, f is the square wave frequency, and D_R is the diffusion coefficient of the species in the mercury phase.

Figure 1 presents typical DS WV voltammograms for the system Pb(II)/Pb(Hg) obtained at an SBMFE with the same mercury film thickness and various frequencies. The values of $\log \Lambda$ given in the figure captions were calculated by using the value $D(\text{Hg}) = 1.25 \times 10^{-5}$ cm²/s (13). The current is displayed as a dimensionless current function defined as

$$\psi(t) = i(t)\pi^{1/2}/nFAD_0^{1/2}l^{1/2}C_0^* \quad (2)$$

where $\psi(t)$ is the dimensionless current function at the time

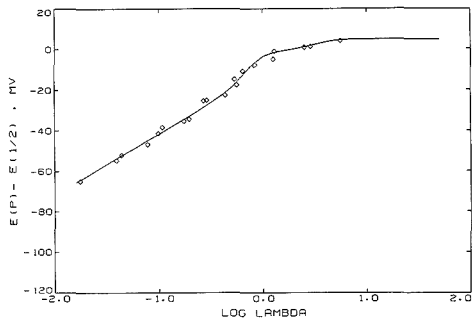


Figure 2. Net DSWV peak position as a function of $\log \Lambda$. Other conditions are given in Figure 1. Solid line denotes theoretical results.

t , $i(t)$ is the current at the same time, n is number of electrons involved in the electrode reaction, F is Faraday's constant, A is the surface area of the MFE, D_0 is the diffusion coefficient of M^{n+} ions in solution, f is square wave frequency, and C_0^* is the bulk concentration of M^{n+} ions. The factor $nAC_0^*D_0^{1/2}$ required to obtain the dimensionless current, $\psi(t)$, from the experimental current, $i(t)$, was determined as described in the Experimental Section.

The curves presented in Figure 1 are very well shaped in terms of net peak as well as both forward and reverse peaks, without any anomalies even for square wave frequency as high as 600 Hz. (It should be emphasized that in the case of glassy carbon and iridium-based electrodes properly shaped square wave voltammograms cannot be obtained reliably at such high frequencies (5–8)). As predicted by theoretical calculations (2) the net current voltammograms retain their symmetrical shape, whereas the individual forward and reverse peaks change shape significantly with changes in dimensionless parameter Λ .

As under linear scan conditions, the position of these voltammograms shifts toward more negative potential as the value of Λ is decreased. Quantitative results for the net peak position obtained at the SBMFE over a wide range of Λ parameter (mercury film thickness 0.25–8 μm ; frequencies 6–600 Hz) are presented in Figure 2. The solid line represents calculated results for two-electron reversible charge transfer at the MFE. The agreement between experimental and theoretical results is very good over the entire range of Λ values. It has been shown (2) that for the thin layer region ($\Lambda < 0.1$) the peak position can be described by

$$n(E_p - E_{1/2}) = -34.1 + 59.2 \log \Lambda, \text{ mV} \quad (3)$$

where E_p is the potential of the net peak and $E_{1/2}$ is the reversible half-wave potential. The least-squares linear regression of $E_p - E_{1/2}$ on $\log \Lambda$ for the range of $\log \Lambda$ from -1.76 to -0.71 yields the experimental value of 29.8 mV/log Λ unit with correlation coefficient of 0.992. This value agrees very well with the theoretically predicted value of 29.6 mV/log Λ unit for a two-electron reversible process.

Figure 1 also shows that the dimensionless peak current depends on the value of the dimensionless parameter Λ . The dimensionless net peak current is larger for Λ values around 1 (Figure 1, curves 2 and 3) and voltammograms obtained with either smaller (curve 1) or larger (curve 4) values of Λ have smaller dimensionless net peak currents. Figure 3 presents some quantitative results for the net, forward, and reverse peak currents as a function of $\log \Lambda$. Generally, the shapes of all of these plots agree reasonably well with the theoretical calculations represented by solid lines. The net and reverse peak current functions are peak shaped with the maximum and minimum, respectively, occurring around the value of \log

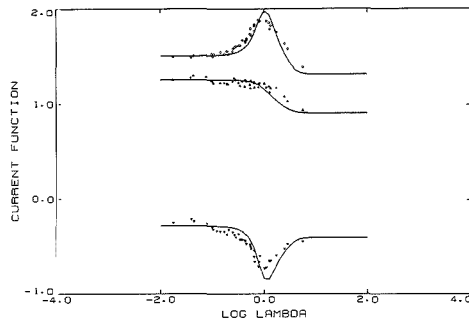


Figure 3. Net (\diamond), forward (Δ), and reverse (∇) DSWV peak current function versus $\log \Lambda$. Conditions are given in Figure 1. Solid lines denote theoretical results.

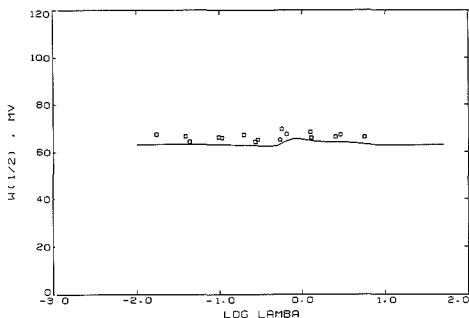


Figure 4. Half-width of the DSWV net peak as a function of $\log \Lambda$. Conditions are given in Figure 1. Solid line denotes theoretical results.

$\Lambda = 0$. Also experimental plots for forward peak current function agree quite well with theoretical predictions. Some spread of experimental points around theoretical lines is caused by inaccuracy in determination of mercury film thickness.

It was calculated theoretically (2) that the net peak half-width is not affected by changes in Λ , remaining relatively constant ($nW_{1/2} = 126 \pm 2$ mV) except around $\log \Lambda = 0$ ($nW_{1/2} = 130$ mV). The values of 120–130 mV obtained experimentally as shown in Figure 4 are in good agreement with theoretical predictions.

Square Wave Anodic Stripping Voltammetry (SWASV). As in the case of DSWV experiments the shape and position of anodic stripping square wave voltammograms are affected by changes in the value of the dimensionless parameter Λ . Figures 5 and 6 show two sets of anodic stripping experiments for the system Pb(II)/Pb(Hg). Curves presented in Figure 5 were obtained at the SBMFE with the same thickness and various frequencies whereas Figure 6 presents results for constant frequency and various thicknesses. As above for DSWV experiments the net peak retains its symmetrical shape whereas both forward and reverse peaks are affected markedly as the value of Λ is changed. Notice that the relative positions of the forward and reverse peaks change with changing value of Λ . For low values of Λ ($\log \Lambda < 0$) the forward peak (oxidation peak) occurs at a potential more negative than the reverse one (Figure 5, curve 1, and Figure 6, curves 1–3). For large values of Λ ($\log \Lambda > 0.5$) the forward peak is at a more positive potential than the reverse one (Figure 5, curve 4) and the shape of voltammograms obtained for such values of Λ resembles the shape of the square wave voltammograms for the reversible couple with unrestricted diffusion control.

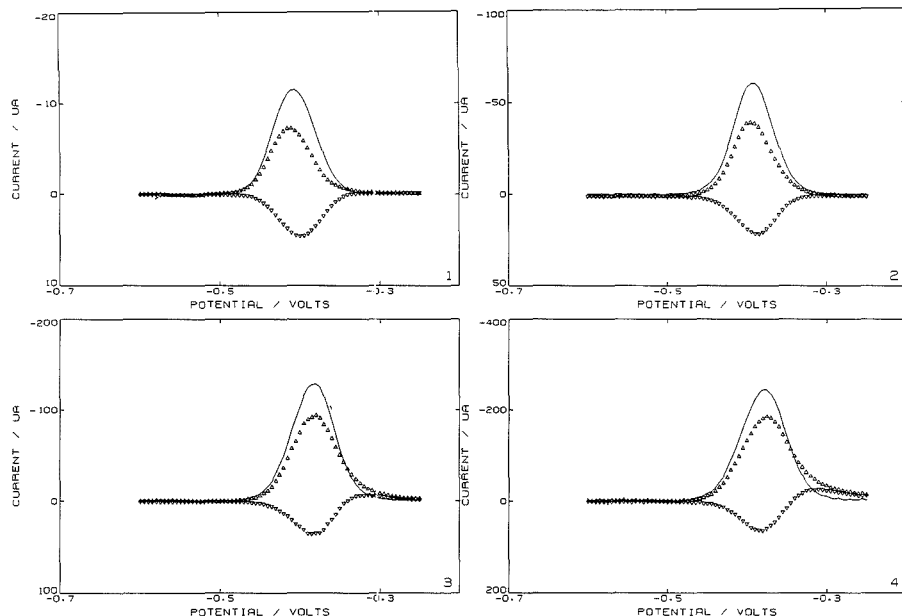


Figure 5. Net (—), forward (Δ), and reverse (∇) current of anodic stripping square wave voltammograms 5×10^{-7} M Pb(II) in 0.1 M NaNO₃. SBME: $A = 6.5 \text{ mm}^2$, $l = 7.2 \text{ }\mu\text{m}$. $\Delta E_s = 5 \text{ mV}$; $E_{sw} = 25 \text{ mV}$; $f =$ (1) 6, (2) 30, (3) 200, and (4) 600 Hz. ($\Lambda =$ (1) 0.50, (2) 1.12, (3) 2.88, (4) 4.99). 60 s (stirring) + 15 s (quiescent) deposition at -0.7 V .

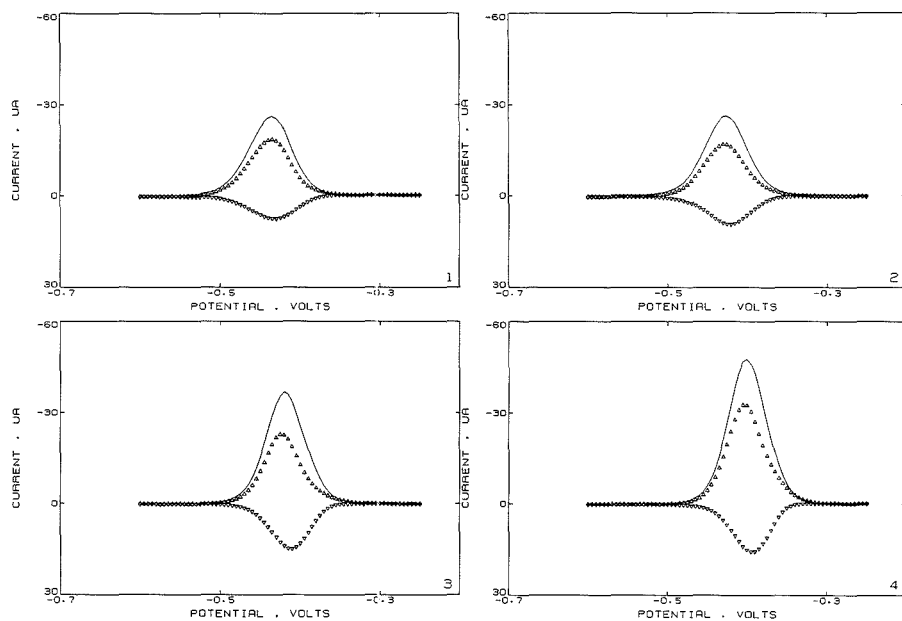


Figure 6. Net (—), forward (Δ), and reverse (∇) current of anodic stripping square wave voltammograms. Conditions as in Figure 5 except $f = 30 \text{ Hz}$ ($\Lambda =$ (1) 0.043, (2) 0.070, (3) 0.17, and (4) 0.76).

In the case of SWASV the dimensionless current function is defined by

$$\psi(t) = i(t)\pi^{1/2}nFA D_R^{1/2} \rho^{1/2} C_R^* \quad (4)$$

where C_R^* is the concentration of metal deposited in the mercury film and other symbols have the same meaning as for eq 1 and 2. It has been shown also (3) that for the thin layer region ($\log \Lambda < -1$) the net peak current function is

strictly proportional to the value of Λ

$$\Delta\psi_p = 0.528\Lambda \quad (5)$$

Figure 7 shows quantitative results for the thin layer region. The plot of the net peak current function versus Λ is a straight line with a slope of $0.525/\Lambda$ unit (correlation coefficient 0.995) which may be compared with the theoretical value of 0.528; i.e., the agreement for this region is excellent. These results are significant from the analytical point of view, since the total current does not depend on mercury film thickness in this region. Replacing the Λ value in eq 5 by its definition (eq 1) and bearing in mind the definition of $\psi(t)$ (eq 4), one can obtain

$$\Delta i_p = (2.874 \times 10^4) n A C_R^* l f \quad (6)$$

Since q_R , the total charge of deposition, is defined as

$$q_R = n F A C_R^* l \quad (7)$$

the final expression for net peak current is

$$\Delta i_p = 0.298 q_R f \quad (8)$$

This means that the anodic stripping net peak current depends straightforwardly on the total amount of metal deposited in the mercury layer, provided that $\log \Lambda$ is smaller than -1 . Thus for the same conditions of metal deposition (the same deposition time and potential, constant mass transport conditions) the peak current depends straightforwardly on the bulk concentration in solution.

The results for peak current function over the entire range of $\log \Lambda$ under investigation are presented in Figure 8. Together with results for the net peak, experimental results for both forward and reverse peak current function are presented. Solid lines represent the theoretically calculated results for the same case. Generally the shape of all three plots agrees with the theoretical shape. There is some deviation of experimental points from the theoretical prediction. However, bearing in mind that the determination of C_R^* , the value of which is necessary to calculate the peak current function in this case, introduces some additional degree of inaccuracy, it seems that the agreement between the experiment and theory is quite good.

Figure 9 shows the experimental results for anodic stripping net peak position as a function of the dimensionless parameter Λ . Again, the solid line represents the results of calculation. Theoretically (3) this dependence was described as follows:

$$n(E_p - E_{1/2}) = -46.7 + 59.2 \log \Lambda, \text{ mV} \quad (9)$$

provided that Λ is smaller than 0.1. Again, the slope of the plot of $(E_p - E_{1/2})$ vs $\log \Lambda$ for a two-electron reversible system should be $29.6 \text{ mV}/\log \Lambda$ unit. The value obtained experimentally by least-squares linear fit (range of $\log \Lambda$ from -1.71 to -0.47 , correlation coefficient 0.986) for the slope, $28 \text{ mV}/\log \Lambda$ unit, is very close to the theoretically predicted value.

The solid line presented in Figure 10 represents theoretical calculations for net peak half-width as a function of $\log \Lambda$. This line was obtained on the basis of results reported by Kounaves et al. (3). The dashed line shows exactly the same dependence but calculated according to Penczek and Stojek (4). Points represent experimental results for the net peak half-width obtained for SWASV. It follows from Figure 10 that the distribution of experimental points is not very much worse than the difference in the results of two different approaches to the calculation, and the experimental value of $W_{1/2}$ is in the range 50–60 mV for the entire range of $\log \Lambda$. Note that the waveform of ref 4 is not exactly the same as that of ref 3. The dashed curve of Figure 10 is the result of ref 4

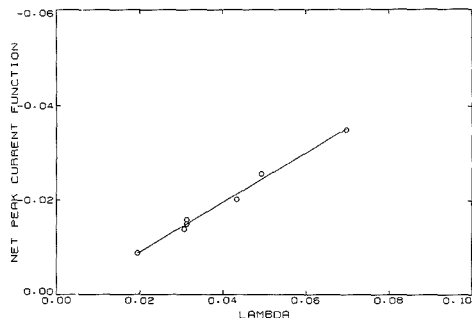


Figure 7. SWASV net peak current function versus dimensionless parameter Λ . Solution and conditions as in Figure 5. Solid line denotes the best linear fit.

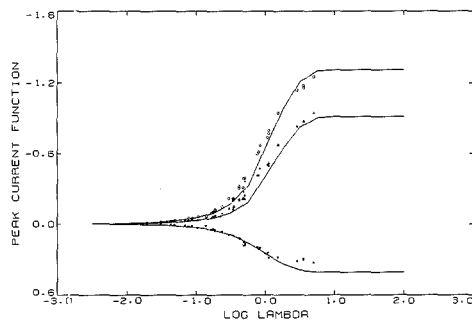


Figure 8. Net (O), forward (Δ), and reverse (∇) SWASV peak current function versus $\log \Lambda$. Solution and conditions are given in Figure 5. Solid lines: denote theoretical results.

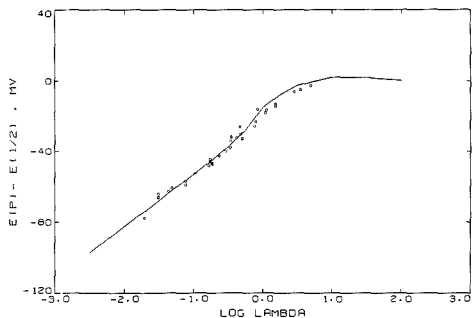


Figure 9. Net SWASV peak position as a function of $\log \Lambda$. Solution and conditions are given in Figure 5. Solid line denotes theoretical results.

modified to take this into account.

Experimental results presented above show that the Pb(II)/Pb(Hg) system behaves as predicted theoretically at the silver-based mercury film electrode under direct and anodic stripping square wave conditions. The excellent behavior of the SEMFE under linear scan conditions has also been reported (10, 12). The present work confirms the usefulness of this type of mercury film electrode also under square wave conditions over a wide range of frequencies.

Results presented above do not contradict the reports of anomalies resulting from application of SWV to other types of mercury film electrodes (5–8). They rather emphasize the

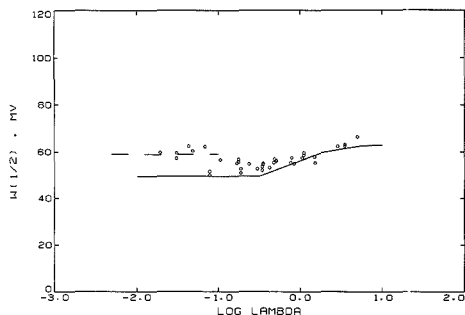


Figure 10. Half-width of the SWASV net peak as a function of $\log \lambda$. Solution and conditions are given in Figure 5. Theoretical results: solid line according to (3); dashed line according to (4).

differences in properties of these electrodes. Although no difference has been observed under linear scan conditions (9, 10, 12, 14), differences are observed under square wave conditions which, because of large amplitude potential pulses, is more demanding.

The SBMFE has two unique characteristics. First, the solid substrate is a well-defined solid amalgam, which provides a chemically favorable environment for adhesion of mercury. Second, a procedure exists whereby the mercury film can be restored to its initial condition after each experiment. It should be emphasized that the performance of the SBMFE deteriorates quickly with use, and the polarization in 2 M NaOH is essential to maintain theoretical response over a working day. A hanging mercury drop also deteriorates in performance rapidly; its reliability is ensured only by using a fresh drop for each experiment. Thus it is perhaps not surprising that the iridium-based MFE displays anomalies at

high frequencies, as there is no procedure for cleaning it. (The procedure for the SBMFE, when applied to an iridium-based MFE, blows the mercury off of the surface.)

There is substantial convenience in carrying out anodic stripping voltammetry at a microelectrode, because the deposition step can be carried out efficiently by diffusion in quiet solution. Figure 11 presents results obtained at the silver-based mercury microelectrode described in the experimental section for 10 mM Pb(II) solution under direct square wave and staircase conditions. For staircase conditions curves obtained both at low and high frequencies are reasonably well shaped. The voltammetric deposition of Pb(II) at low frequency (Figure 11-3) has the characteristic S-shape which is observed when the diffusion layer is comparable in thickness to the small dimension of the electrode. The pronounced enhancement of the anodic current at low frequency is due to accumulation of Pb in the film. At higher frequencies (Figure 11-4) the dimensionless size of the electrode is greater ($(r/D)^2 \approx 7$) and thus the response resembles more closely that expected for unrestricted planar diffusion.

The square wave voltammogram at low frequency (Figure 11-1) displays nearly steady state forward current but a reverse peak because the product is concentrated in the film. Note that the forward limiting current is the same as in the staircase mode (Figure 11-3). The reverse peak is much less pronounced than the staircase reverse peak because the elapsed time at the peak, and hence the extent of electrolysis, is less ($t = (E_i - E)/f\Delta E$ for square wave, $t = (E_i - 2E_f + E)/f\Delta E$ for staircase). On the other hand, the square wave voltammogram obtained at 300 Hz displays no reverse current. This anomaly in the reverse current is consistent with the results of Wechter and Osteryoung (6) for the iridium-based MFE and definitely is not connected with the choice of silver as the substrate for mercury. Thus it may be that the anomalies observed at the iridium-based MFE, which is quite small (the iridium substrate is an embedded disk 127 μm in diameter), have more

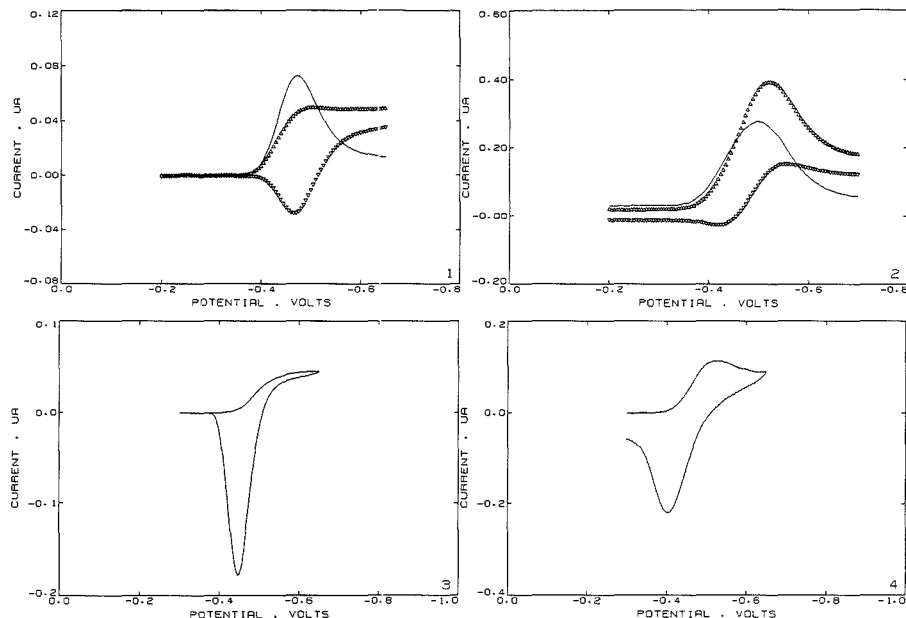


Figure 11. Direct square wave (1, 2) and staircase (3, 4) voltammograms obtained for 10 mM Pb(II) in 1 M NaNO₃ at the silver-based mercury microelectrode ($r = 12.5 \mu\text{m}$). ΔE_s (mV) = (1, 2) 5 and (3, 4) 1.41. f (Hz) (1) 3, (3) 6, and (2, 4) 300. $E_{sw} = 25$ mV.

to do with electrode size than with the nature of the substrate.

The conclusions, then, are that the SBMFE, when macroscopic, behaves ideally when used for square wave voltammetry in either the direct or stripping modes, and that the experimental results agree with the theory for these cases over wide ranges of variation of both frequency and film thickness.

ACKNOWLEDGMENT

We thank C. Wechter and M. Seralathan for their valuable comments and helpful discussion.

LITERATURE CITED

- (1) Osteryoung, Janet G.; Schreiner, M. M. *CRC Crit. Rev. Anal. Chem.* **1988**, *19*, Suppl. 1, S1-S19.
- (2) Kounaves, S. P.; O'Dea, J. J.; Chandresekhar, P.; Osteryoung, J. *Anal. Chem.* **1986**, *58*, 3199.
- (3) Kounaves, S. P.; O'Dea, J. J.; Chandresekhar, P.; Osteryoung, J. *Anal. Chem.* **1987**, *59*, 386.

- (4) Penczek, M.; Stojek, Z. *J. Electroanal. Chem.* **1986**, *213*, 177.
- (5) Schreiner, M. Ph.D. Dissertation, SUNYAB, 1987.
- (6) Wechter, C.; Osteryoung, J. *Anal. Chem.*, following paper in this issue.
- (7) Golas, J.; Galus, Z.; Osteryoung, J. G. *Anal. Chem.* **1987**, *59*, 389.
- (8) Kounaves, S.; Osteryoung, J. Pittsburgh Conference, Atlantic City, NJ, March 1987, Abstr 179.
- (9) Kounaves, S. P.; Buffle, J. *J. Electroanal. Chem.* **1988**, *239*, 113.
- (10) Stojek, Z.; Kublik, Z. *J. Electroanal. Chem.* **1975**, *60*, 349.
- (11) De Vries, W. T.; van Dalen, E. J. *Electroanal. Chem.* **1967**, *14*, 315.
- (12) Donten, M.; Stojek, Z.; Kublik, Z. *J. Electroanal. Chem.* **1984**, *163*, 11.
- (13) Galus, Z. *CRC Crit. Rev. Anal. Chem.* **1975**, 370.
- (14) Stojek, Z.; Stepnik, B.; Kublik, Z. *J. Electroanal. Chem.* **1976**, *74*, 277.

RECEIVED for review March 8, 1989. Accepted June 14, 1989. This work was supported in part by the National Science Foundation under Grant No. CHE8521200.

Square Wave and Linear Scan Anodic Stripping Voltammetry at Iridium-Based Mercury Film Electrodes

Carolyn Wechter and Janet Osteryoung*

Department of Chemistry, State University of New York at Buffalo, Buffalo, New York 14214

The voltammetric response of an iridium-based mercury film electrode is described. Linear scan and square wave voltammetry are used in the direct and anodic stripping modes for the determination of lead. Mercury film electrodes of this geometry (radius 63.5 μm , thickness 1-100 μm) evidence mixed diffusion regimes in solution and within the mercury layer. Experimental results are compared with existing theoretical models.

Mercury film electrodes (MFE) have long been employed for the determination of metals using anodic stripping voltammetry (ASV). They are prepared by depositing a thin layer of mercury (0.001-10 μm) onto a solid substrate (Pt, Ag, Au, carbon). The MFE retains the advantages of the mercury drop, for example the favorable overpotential for hydrogen, yet avoids the hazardous and problematic use of bulk mercury. In addition species soluble in mercury typically display restricted diffusion within the mercury layer. Resolution is increased therefore with respect to the mercury drop, as voltammetric peaks become more narrow. Excellent reproducibility and sensitivity are also achieved, and MFEs are easily adapted to fit a variety of cell geometries, including placement in flow systems.

A variety of potential waveforms have been used with anodic stripping voltammetry. Linear scan ASV (LSASV) at the MFE has a well-developed theory and ample experimental results in the literature. The voltammetric stripping peaks are characterized by peak current (or ψ , the dimensionless peak current), peak position (or $n(E_p - E_{1/2})$, the normalized peak position), and peak half-width (or $nW_{1/2}$, the normalized peak half-width). Pulse voltammetric techniques have also been combined with ASV. These methods are noted for their discrimination against charging currents. Differential pulse, in particular, has often been used for routine analytical investigations. Square wave voltammetry (SWV) appears to be

a favorable technique due to its fast scan capabilities, peak-shaped response, and increased sensitivity compared with differential pulse voltammetry (1). The recent introduction of commercial instruments that perform SWV should increase its use with ASV.

The main purpose of this work is to test the useful range of practical application of the iridium-based mercury film electrode both with respect to the parameters of the electrode itself and those of the voltammetric techniques employed, staircase and square wave voltammetry. Despite the complexity of the resulting diffusional problem as described below, the work is restricted to electrodes employing a 127- μm -diameter substrate, because this small size facilitates the plating process and is readily available.

Iridium-Based Mercury Film Electrodes. Some materials commonly used as substrates present problems with dissolution of the base metal (Pt, Ag, Au) in mercury, or nonwetting of the substrate (carbon) by mercury. Kounaves and Buffle (2) have investigated the properties that make a material suitable for use as a substrate for mercury deposition and concluded that iridium is best because it is wetted by but is not soluble in mercury. They have deposited mercury on an embedded circular iridium electrode of radius 2 mm and determined that no intermetallic Ir/Hg species are formed (3). For films less than 1 μm thick, experimental results confirmed theoretical predictions for LSASV (4). However, for thicker films, whereas the current-scan rate behavior agreed with theory for thin films, the experimental values of peak potential and half-width corresponded to those of a thicker film probably because mercury forms a spherical segment, rather than a flat film.

Golas et al. (5, 6) reported the use of iridium-based mercury film electrodes (IrMFE) for chronoamperometry and linear scan voltammetry. Cohesive films of mercury were achieved, the most stable corresponding to a hemisphere. These electrodes were prepared from 127 μm (0.025 in.) diameter iridium wire, the smallest size commercially available. The use of this

smaller iridium substrate facilitates the electrodeposition of mercury and thus makes it possible to use a much simplified plating procedure. Nonplanar diffusion within solution was observed for slow scan rates and long pulse times. For chronoamperometric experiments with ferrocene at this IRMFE, nearly steady-state currents were achieved within 5 s.

Linear Scan Anodic Stripping Voltammetry. Several years ago, de Vries and van Dalen (7) solved the integral equations for LSASV at the MFE. For small diffusional distances (thin films) compared to the time scale of the experiment ($l^2nf\nu/D_R \rightarrow 0$) the following equations apply:

$$i_p = (1.157 \times 10^6) n^2 A C_R l \nu \quad (1)$$

$$n(E_p - E_{1/2}) = -1.43 + 29.58 \log(l^2 f \nu / D_T) \quad (2)$$

$$n W_{1/2} = 75.53 \quad (3)$$

where the peak current is i_p , film thickness l , and scan rate ν , R refers to the analyte within the mercury film, and the other symbols have their usual electrochemical significance.

Penczek and Stojek (8) derived analogous equations for a micro-MFE (MMFE), i.e., for $r^2nf\nu/D_R \rightarrow 0$, where r is the electrode radius. The peak current differed from that of de Vries and van Dalen only in the numerical constant; however the peak position shifted -36.6 mV, and $nW_{1/2}$ decreased to 59.6 mV. Ciszowska and Stojek (9) compared this theoretical work with experiments performed at a multi-MMFE, composed of 65 carbon fiber disks sealed in epoxy. For LSASV of lead, peak potentials were more negative than those expected from theory, and $nW_{1/2}$ was slightly larger.

Cyclic voltammetry at the MFE was investigated by Donten and Kublik (10, 11). For the case of analyte initially present in the mercury phase, at thin films the peak current is proportional to the film thickness (l) and the scan rate (ν). For the case of analyte initially in solution, the current is independent of film thickness, but depends on $\nu^{1/2}$, as for semi-infinite diffusion.

Square Wave ASV. Wojciechowski et al. (12) employed square wave anodic stripping voltammetry (SWASV) at a mercury drop to avoid the deaeration of the solution and shorten the experimental time scale. The theoretical problem of SWASV at the MFE was treated by Kounaves et al. (12) using the step function method and by Penczek and Stojek (13) using the finite element method. Kounaves et al. present results for the dependence of the dimensionless peak current (ψ), $nW_{1/2}$, and $n(E_p - E_{1/2})$ on $\log \Lambda$ ($\Lambda = l^2 \nu / D_T$)^{1/2}, for values of $n\Delta E_s = 10$ mV and $n\Delta E_{sw} = 50$ mV. Penczek and Stojek present results for the more general case of a series of dimensionless step heights and pulse amplitudes; however the square wave waveform has been redefined to allow comparisons with differential pulse voltammetry. In that work, ΔE_1 is equivalent to $(2\Delta E_{sw} + \Delta E_s)$ of Kounaves et al., and the base potential is that of the immediately preceding step. For thin films, the values of i_p calculated by the two methods agree well, as do the values of $n(E_p - E_{1/2})$, after correcting for different base potentials of the waveforms. It is more difficult to compare the peak half-widths for the thin film case because of the differences in description of the waveform. Wikiel and Osteryoung (14), using a silver-based mercury film electrode, investigated experimentally SWASV of lead, confirming Kounaves' theoretical values of ψ and $n(E_p - E_{1/2})$. However, the experimental values of $nW_{1/2}$ were nearer to 60 mV within the thin film region, compared with the theoretical value of 49.5 mV.

EXPERIMENTAL SECTION

Reagents. Buffer solutions were prepared from sodium carbonate (J. T. Baker Chemical Co.) and acetic acid (Baker) to form a supporting electrolyte solution 1.0 M in sodium acetate and 1.0

M in acetic acid (pH 4.7). Sodium acetate (Suprapur, MCB) and acetic acid were used to prepare 0.1 M solutions. Distilled, deionized water (Milli-Q, Millipore) was employed for all solutions. All other chemicals were used as received.

Instrumentation. A Princeton Applied Research Corp. (EG&G PAR, Princeton, NJ) Model 273 potentiostat/galvanostat was interfaced with a Digital Equipment Corp. PDP 8/e laboratory minicomputer for data acquisition. Staircase voltammograms equivalent to linear scan voltammograms were obtained by measurements at 1/4 and 2/4 of the step for the direct and stripping cases, respectively (15). The waveforms used have been described previously (16). Electrochemical data were obtained with a traditional three-electrode cell, using iridium (working), platinum (counter), and saturated sodium chloride calomel (reference) electrodes. An acetate buffer salt bridge, refilled daily, was utilized to isolate the reference electrode, and all potentials are referenced to this SSCE. The mercury deposition process was viewed in situ with a Leitz Diavert inverted microscope. A PAR Model 173/179 potentiostat/digital coulometer was employed for potential control during the deposition and stripping of the mercury film and also for charge measurements during these processes. A PAR 303 SMDE (medium drop) was used for comparison of the IRMFE with a mercury drop and for determination of the reversible half-wave potential.

Iridium-Based Mercury Electrode. The 127 μm diameter iridium disk electrode was prepared as described previously (5). The surface was polished with a rotating wheel (muffin fan, Rotron Manufacturing Co.) covered with 600- μm carboron paper disks, then 9- μm diamond paste, and finally 1- μm diamond paste on Texmet paper (Buehler, Ltd.). The electrode was then placed in a cell with an optically transparent bottom set upon the microscope stage to allow viewing of the electrode surface from below. Mercury deposition was achieved in 30 mM mercurous perchlorate at -0.40 V vs SSCE. Monitoring the deposition charge allowed calculation of the amount of mercury deposited. The resulting thickness reported is that of a spherical segment, not a flat layer of mercury (4). That is, the "thickness" is the height of the spherical segment with the iridium substrate as base and volume calculated from the stripping charge for mercury dissolution. Deposition efficiencies were calculated for each electrode from the deposition and stripping charges for several films, and ranged from 82% to 99%.

The film formation process followed that indicated by Golas et al. (5). Mercury film electrodes were stable for an entire day, with no change in the mercury thickness. Electrodes stored for 1 week in aerated deionized water retained up to 70% of their mercury. Cohesive films completely covering the iridium surface were observed for charges greater than those corresponding to film thicknesses of 15 μm . Thinner films were achieved by repetitively switching to open circuit during the plating process. Films 5 μm or thinner were deposited by using the method of Kounaves and Buffle (2). A 300-mV symmetrical square wave was superimposed upon a -0.50 mV base potential to deposit the required amount of mercury from the mercurous perchlorate solution. The electrode was then transferred to a deoxygenated cell containing 0.1 M perchloric acid, and potentials between -0.1 V and -0.9 V were applied until the mercury had completely covered the iridium surface. However, this method is labor intensive and frequently unsuccessful, so few films were plated in this manner.

RESULTS AND DISCUSSION

The diffusional model for these small IRMFEs is rather complex. With film thicknesses ranging from 6 to 100 μm , there is a mixed regime of finite and semiinfinite diffusion within the film. Since the shape of the mercury layer is that of a spherical segment, and not a film of uniform thickness, questions arise concerning the uniformity of diffusional patterns within the mercury. The small size of the iridium disk (radius 63.5 μm) also introduces effects of nonplanar diffusion within solution. Individually, some of these complications have been included in existing mathematical models, and several theoretical solutions exist for different cases. However, these theoretical descriptions and existing models do not describe this system. In general, theories have been derived for limiting cases of finite vs semiinfinite, and planar

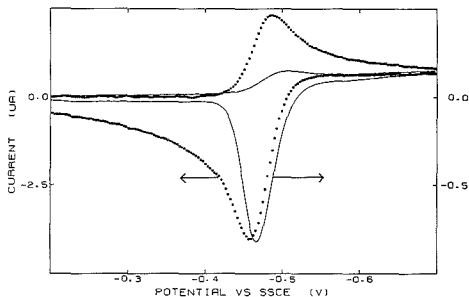


Figure 1. Direct staircase voltammograms at SMDE (●) and IrMFE (—): 0.25 mM Pb(II) in 0.1 M acetate, pH 7, drop area 0.017 cm², film thickness 37.3 µm, frequency 10 Hz, $\Delta E_s = 3$ mV, current sampled at 1/4 of period (equivalent to linear scan at 30 mV/s (15)).

vs nonplanar diffusion. It is the combination of these factors that applies to IrMFEs with radius 63.5 µm and film thickness 6 to 100 µm.

Consider for example a perfect hemisphere on a 60-µm radius substrate. From the point of view of both diffusion in the film and in the solution, an appropriate dimensionless parameter is $\Lambda = r/(Dt)^{1/2}$, where r is the radius and t a characteristic experimental time. For reasonable values (9×10^{-6} cm²/s = D , $t = 0.017$ s), $\Lambda \sim 1$. Thus the film is neither thick ($\Lambda \geq 10$) nor thin ($\Lambda \leq 0.1$) and the external diffusion is neither planar ($\Lambda \geq 10$) nor approaching steady state ($\Lambda \lesssim 0.1$). Comparisons between existing theories and the present experiments are intended to check semiquantitatively on the reasonableness of the behavior, understanding that the models being used do not apply exactly.

Staircase (Linear Scan) Voltammetry. Direct staircase voltammograms for lead for the IrMFE and a mercury drop are illustrated in Figure 1. Lead was chosen as a model system

because of its reversible behavior at mercury electrodes



Nonplanar effects are observed in the cathodic branch for the IrMFE. The anodic peak is much narrower at the film electrode due to depletion of the lead in the mercury layer. Diffusion within the mercury drop broadens the stripping peak at the SMDE and therefore decreases the resolution when compared to thin film electrodes. As expected, the anodic peak potential for the film electrode is more negative than that for the mercury drop. The current density for the IrMFE anodic peak was 19 times greater than that for the drop in unstirred solution.

Similar results are realized for SCASV. For the case of staircase or linear scan ASV at a large thin film electrode, the peak current should be directly proportional to the scan rate, $\nu = \Delta E_s/\tau$. At a large thick film (SILD) the current should depend upon $\nu^{1/2}$. Table I lists values of $\partial \log i/\partial \log \nu$ for a variety of film thicknesses and indicates that the electrode as typically used behaves as if in the intermediate region between fully finite and infinite diffusion within the mercury layer. The peak width for this two-electron system should be 37.8 mV for a thin film and 101.5 mV for a thick film. At 300 mV/s the peak widths (Table I) again follow the trend from thin film to thick film behavior. The peak potential also shifts toward more positive values as the film thickness increases, due to Nernstian considerations. Thus the contribution of finite diffusion decreases as the thickness of the film increases.

Square-Wave Voltammetry. For low frequencies of direct SWV, the contribution of nonplanar diffusion of Pb(II) in solution to the mercury surface becomes significant. This was also observed for ASV. In nonstirred solutions, the stripping current varies linearly with the deposition time for $t_{\text{dep}} > 10$ s. For direct voltammetry, refer to Figure 2-1, for which the value of $\Lambda (=r/(Dt)^{1/2})$ is 4.58. Increasing the frequency

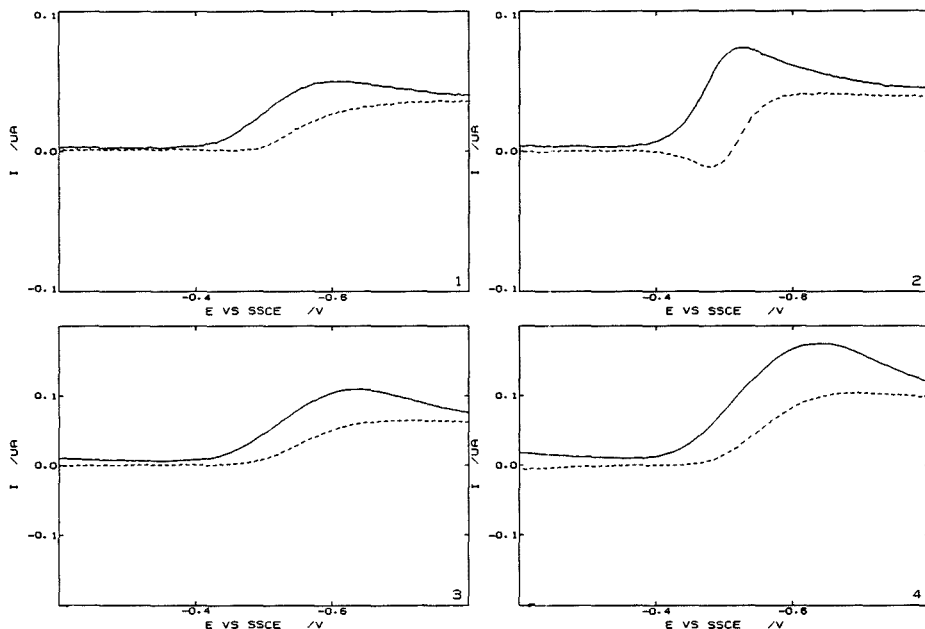


Figure 2. Direct square wave voltammograms for 0.457 µM Pb(II) in 0.1 M acetate buffer (pH 4.7), 30-µm mercury film: $\Delta E_s = 5$ mV, $\Delta E_{\text{sw}} = 25$ mV. Frequencies for curves 1–4 were 5, 10, 30, and 60 Hz, respectively. Key: (—) forward currents, (---) reverse currents.

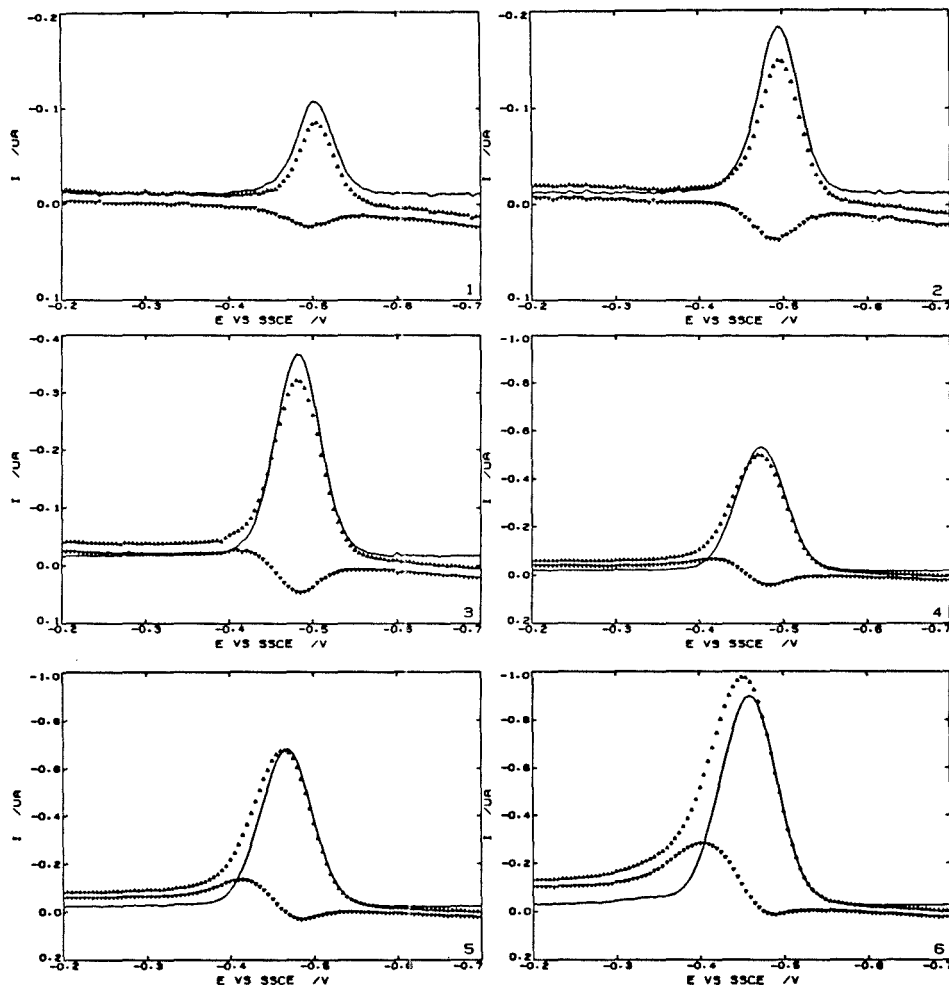


Figure 3. Stripping square wave voltammograms for 50 μM Pb(II) in 1 M acetate buffer, pH 4.7, 13.53- μm film, $\Delta E_s = 5$ mV, $\Delta E_{sw} = 25$ mV, 20-s deposition. Frequencies for curves 1-6 were 5, 10, 30, 60, 100, and 200 Hz, respectively. Key: (\blacktriangle) forward, (\blacktriangledown) reverse, and (—) difference currents.

Table I. Staircase Stripping Voltammetry at the IrMFE^a

l , μM	$\partial \log i / \partial \log \nu^b$	$W_{1/2}^b$, mV	E_p^b (V vs SSCE)
thin	1.0 ^c	37.8 ^c	—
4.4	0.846	55.4	-0.460
9.0	0.734	55.1	-0.459
32.0	0.656	65.2	-0.457
73.9	0.583	79.7	-0.456
thick	0.500 ^d	101.5 ^d	—

^a Deposition at -0.7 V vs SSCE for 20 s, 50 μM Pb(II), unstirred solution. Current sampled at 1/4 of step width, which gives the linear scan current at the equivalent scan rate. ^b $\Delta E_s = 3$ mV, $\tau = 10$ ms. ^c Reference 7. ^d Reference 8. ^e $\nu = \Delta E_s / \tau$.

(Figure 2-2, 10 Hz) reduces this contribution ($\Lambda = 6.5$) and the response is more peak shaped. As the frequency is further increased (Figure 2-3 and 2-4) the forward peak broadens and shifts to more negative potentials, and no reverse current is

observed. Similar behavior of the reverse current was reported by Schreiner (17). This abnormality of the reverse currents causes deviation from linearity for plots of i vs f . At the GCMFE, this behavior was attributed to the geometry of the mercury layer (small droplets of various sizes distributed across the GC surface). However, on the present iridium substrates a cohesive layer of mercury is observed.

Surprisingly, it is also the reverse currents of stripping voltammograms that deviate from expectations (Figure 3). At low frequencies, the reverse (redeposition) current is cathodic in direction. However, as the frequency is increased, the reverse current changes direction and becomes anodic, i.e., the peak lies in the same direction as the forward current. Note that this causes the difference current to decrease with increasing frequency. Thus for both direct and stripping square wave experiments, the reverse currents are observed to follow unusual trends. It is difficult to explain these observations, since the reverse currents correspond to different

processes in the two experiments: redeposition of lead into mercury for the stripping case, and stripping of the lead from the amalgam for the direct voltammetry. It must be emphasized that these patterns were observed for several iridium electrodes, many mercury films of a variety of thicknesses, and several supporting electrolytes. Similar results were also obtained for SWASV at a glassy carbon-based MFE in a conventional cell and also in the wall jet configuration (1). Stirring the solution during the stripping step had no effect. Attempting to renew the mercury surface by adding 10 μM $\text{Hg}(\text{I})$ to the lead solution did improve the response somewhat, but normal reverse currents were never observed for high frequencies. There was no evidence for motion of the film synchronous with the potential excitation as observed stroboscopically on the microscope stage.

The process of cathodizing the film at -6 V in 1 M NaOH to form a sodium amalgam, and then rinsing the electrode with acidic solution, is a commonly used cleaning procedure for mercury film electrodes. For the IrMFE, the formation and oxidation of this amalgam were so vigorous that all traces of mercury were removed from the iridium surface.

Because the reverse currents, and thus the net current, did not exhibit predicted behaviors, the forward currents were used for semiquantitative comparisons with the theoretical response for square wave anodic stripping voltammetry at a MFE (13, 18). The model for these theories assumes a large, flat, uniform mercury film, not the spherical segment used here.

Following the terminology of Kounaves et al., the dimensionless current is given by

$$\begin{aligned}\psi &= i(\pi\tau_{\text{sw}})^{1/2}/nFAD_{\text{R}}^{1/2}C_{\text{R}}^* \\ &= i(\pi\tau_{\text{sw}})^{1/2}V/AD_{\text{R}}^{1/2}q_{\text{R}}\end{aligned}\quad (4)$$

where τ_{sw} is the square wave period and q_{R} is the charge associated with amalgam formation. The thin film model assumes a uniform film of thickness l which is infinite in extent. For that model $V/A = l$ and q_{R} can be calculated readily knowing the mass transport conditions during the deposition step. In the present case we assume that the mercury forms a spherical segment with one base of radius r and height h . The area of the lateral surface is $A = \pi(r^2 + h^2)$ and the volume of the segment is $V = \pi h(3r^2 + h^2)/6$. We approximate the diffusion-limited current for formation of the amalgam by

$$i = (nFAD_{\text{O}}C/r)(2/(\pi\tau)^{1/2} + 1), \tau \leq 1 \quad (5)$$

$$i = knFD_{\text{O}}Cr(1 + k/\pi^{3/2}\tau^{1/2}), \tau \geq 1 \quad (6)$$

where $\tau = 4D_{\text{O}}\tau/r^2$ and k is an empirical value (19) which depends on h/r . Equations 5 and 6 are correct for a hemisphere and correct in first order for a disk. Thus they should provide a reasonable approximation for a spherical segment.

Integration of the current equations and substitution into eq 4 yield a formula for computing the dimensionless current from the experimental quantities

$$\begin{aligned}\psi &= 2i(\pi\tau_{\text{sw}})^{1/2}h(3r^2 + h^2)/\{3r(r^2 + h^2)D_{\text{R}}^{1/2}nFC_{\text{O}}^* \times \\ &\quad [\pi(r^2 + h^2)(1 + 4/\pi^{1/2}) + k(4D_{\text{O}}\tau - r^2)(1 + 2k/\pi^{3/2})]\}\end{aligned}\quad (7)$$

Theoretical and experimental values for ψ , $n(E_{\text{p}} - E_{1/2})$, and $nW_{1/2}$ are presented versus $\log \Lambda$ in Figure 4. The values for the theoretical curves shown in Figure 4 were obtained from voltammograms calculated from the theory of Kounaves (13). Experimental values were obtained from three different film thicknesses, 9, 14, and 44 μm , where l is taken to be h as described in the Experimental Section. Values of ψ were also calculated by using values of q_{R} obtained by integrating linear scan voltammograms. These values were in general somewhat

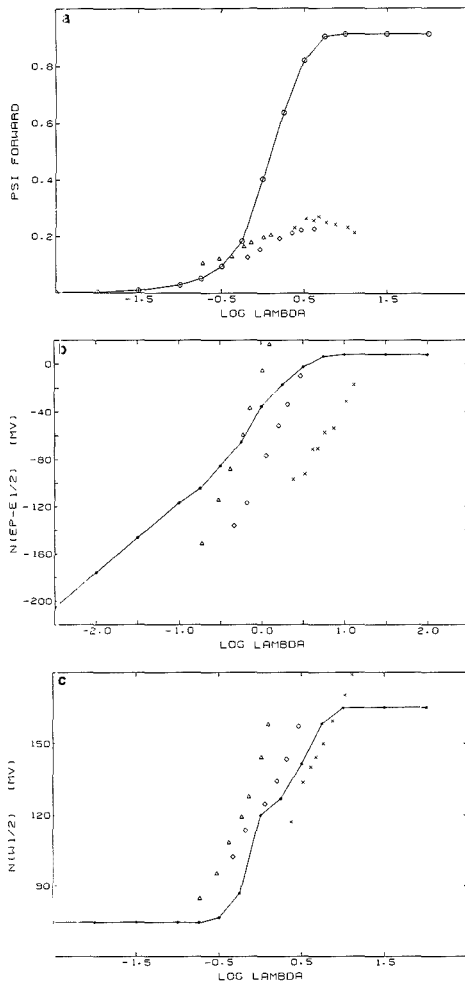


Figure 4. Forward dimensionless current function (a), dimensionless peak position (b), and peak half-width (c) as functions of $\log \Lambda$: (O, ●) theory of Kounaves, experimental results for film thickness (Δ) 9, (\diamond) 14, and (\times) 44 μm ; $n\Delta E_{\text{s}} = 10\text{ mV}$, $nE_{\text{sw}} = 50\text{ mV}$, 20-s deposition.

larger and displayed an anomalous dependence on film thickness. The approach based on eq 7 is internally consistent and yields the same values of ψ for the same value of $\Lambda = h/(D\tau_{\text{sw}})^{1/2}$, independent of h .

Most experiments were performed with a step height of 5 mV and a pulse amplitude of 25 mV (the optimum values for a two-electron, reversible system); however the effect of changing the pulse amplitude was studied also. For a pulse amplitude of 0 mV the experiment is the same as a staircase experiment, with current measurements at the middle and end of the step. As the pulse amplitude is increased, the reverse pulse starts to force the reverse reaction (in this case deposition of the lead back into the film) to occur. At values of $n\Delta E_{\text{sw}}$ greater than 50 mV the pulses broaden the peak by stepping close to $E_{1/2}$ at much less extreme values of the base staircase, without much increase in the peak current, which is limited by diffusion. The optimum pulse amplitude is

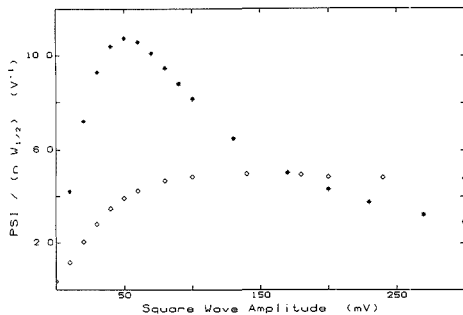


Figure 5. Resolution of the square wave stripping peak (magnitude/half-width) as a function of pulse amplitude: (*) theory of Kounaves, (◇) experimental values for 80 μM Pb(II), 10 Hz, 60- μm film thickness, $\Lambda = 5.55$.

chosen to be that which maximizes the quantity $\psi/nW'_{1/2}$. The theoretical and experimental responses are shown in Figure 5. For calculated voltammograms with a pulse amplitude greater than 100 mV, the peak starts to resemble a mesa, but the experimental curves still retain their peak shape at all values of $n\Delta E_{\text{sw}}$, and a constant value of $\psi/nW'_{1/2}$ is observed.

Analytically, these electrodes exhibit good behavior. Linear calibration curves were obtained for concentrations down to 15 nM for a 3-min deposition in stirred solution, $l = 37 \mu\text{m}$. The sensitivity obtained as the slope of the curve $i_p = a + bC$ was 110.2 nA/ μM , yielding a detection limit ($3\sigma/b$) of 9 nM under these conditions. These experiments were performed in a general purpose laboratory. Ambient levels of lead prevented work at much lower concentrations.

In Situ Deposition. Complete coverage of the iridium surface was not achieved for mercury thicknesses less than 1 μm . Much thinner mercury deposits consisting of droplets were formed by using in situ deposition. A square wave stripping voltammogram is shown in Figure 6. The mercury and lead were codeposited onto the bare iridium electrode at -0.7 V for 120 s. The equivalent thickness of a film, calculated by integrating linear scan stripping peaks, was 43 \AA ($\Lambda = 0.0039$) under these conditions. The advantage of the iridium electrode for in situ deposition is that the mercury layer may be completely removed by electrochemical stripping, and physical methods (removing the electrode from the cell and wiping the surface with a tissue (20)) are not necessary. The square wave forward peak is very narrow (96 mV), in accord with the thin film predictions. The value of ψ is approximately 0.0004. Referring to Figure 4a, this is reasonable. However, the peak shift $n(E_p - E_{1/2}) = -0.135 \text{ V}$ is less negative than that extrapolated from Figure 4b. This may be due to saturation of the mercury film, as expected from the high Pb(II)/Hg(I) ratio and the solubility of lead in mercury (1% (w/w)). This might also broaden the reverse peak. Mercury plated in this manner appears to be acting as a thin film; in the case of linear scan voltammetry, the current is directly proportional to the scan rate (slope = 2.2 ($\mu\text{A}/\text{V}$)/s, in reasonable agreement with the calculated theoretical value, 1.8 ($\mu\text{A}/\text{V}$)/s).

Conclusions. The electrodes described produce a mercury surface that is very stable and suitable for the determination

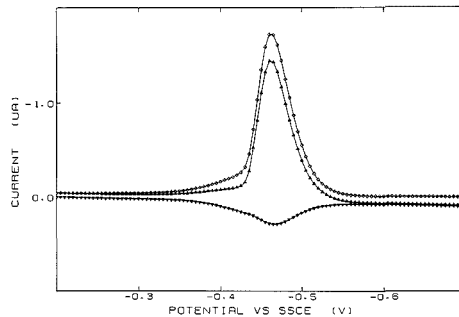


Figure 6. Square wave stripping voltammogram for in situ deposition: 20 μM Hg(I), 5 μM Pb(II), 120-s deposition at -0.7 V in stirred solution. Square wave parameters were as follows: $f = 10 \text{ Hz}$, $\Delta E_s = 5 \text{ mV}$, $E_{\text{sw}} = 25 \text{ mV}$, $l = 43 \text{ \AA}$. Key: (Δ) forward, (∇) reverse, and (\diamond) difference currents.

of amalgam-forming metals. For linear scan voltammetry, the electrodes behave as expected: diffusion in solution is a mixture of nonplanar and semiinfinite planar diffusion, depending on the time scale of the experiment. Within the mercury layer, both finite and infinite diffusion are important. The results for low-frequency square wave voltammetry indicate that these electrodes are analytically useful. Existing theories for thin film voltammetry do not adequately describe the model for this system, and only qualitative agreement is expected. In situ deposition provides a method for producing very thin mercury layers that behave as thin films.

ACKNOWLEDGMENT

Helpful discussions with Mary M. Schreiner, John J. O'Dea, Kazimierz Wikiel, and Samuel Kounaves are gratefully acknowledged.

LITERATURE CITED

- Wechter, C.; Sleszynski, N.; O'Dea, J.; Osteryoung, J. *Anal. Chim. Acta* **1985**, *175*, 45.
- Kounaves, S. P.; Buffle, J. J. *Electroanal. Chem.* **1987**, *216*, 53.
- Kounaves, S. P.; Buffle, J. J. *Electrochem. Soc.* **1986**, *133*, 2495.
- Kounaves, S. P.; Buffle, J. J. *Electroanal. Chem.* **1988**, *239*, 113.
- Golas, J.; Galus, Z.; Osteryoung, J. *Anal. Chem.* **1987**, *59*, 389.
- Golas, Z.; Golas, J.; Osteryoung, J. *Electrochim. Acta* **1987**, *32*, 669.
- de Vries, W. T.; van Dalen, E. J. *Electroanal. Chem.* **1967**, *14*, 315.
- Penczek, M.; Stojek, Z. J. *Electroanal. Chem.* **1985**, *191*, 91.
- Ciszkowska, M.; Stojek, Z. J. *Electroanal. Chem.* **1985**, *191*, 101.
- Donten, M.; Kublik, Z. J. *Electroanal. Chem.* **1985**, *195*, 251.
- Donten, M.; Stojek, Z.; Kublik, Z. J. *Electroanal. Chem.* **1984**, *163*, 11.
- Wojciechowski, M.; Go, W.; Osteryoung, J. *Anal. Chem.* **1985**, *57*, 155.
- Kounaves, S. P.; O'Dea, J. J.; Chandrasekhar, P.; Osteryoung, J. *Anal. Chem.* **1987**, *59*, 386.
- Wikiel, K.; Osteryoung, J. *Anal. Chem.*, preceding paper in this issue.
- Bilewicz, R.; Wikiel, K.; Osteryoung, R. A.; Osteryoung, J. *Anal. Chem.* **1989**, *61*, 965.
- Osteryoung, J.; Osteryoung, R. *Anal. Chem.* **1985**, *57*, 101A.
- Schreiner, M. M. Ph.D. Thesis, University at Buffalo, State University of New York, August 1987.
- Penczek, M.; Stojek, Z. J. *Electroanal. Chem.* **1986**, *213*, 177.
- Stojek, Z.; Osteryoung, J. *Anal. Chem.* **1989**, *61*, 1305.
- Florence, T. M. J. *Electroanal. Chem.* **1970**, *27*, 273.

RECEIVED for review March 14, 1989. Accepted June 14, 1989. This work was supported in part by Grant Number CHE8521200 from the National Science Foundation.

Application of the Three-Distance Clustering Method in Analytical Chemistry

Jure Zupan*¹ and Desire L. Massart

Farmaceutisch Instituut, Vrije Universiteit Brussel, Larbeeklaan 103, Brussels, Belgium

First, the three-distance method (3-DM) was evaluated by comparing produced clusters with clusters obtained by a usual clustering technique (unweighted pair group method), and then the 3-DM was employed for classification of 572 oils (described by eight variables) into nine categories. The training set of 300 oils exhibited 100% recognition ability, and for the rest of the 272 oils in the testing set the classification (prediction) into nine categories (known in advance) was over 90% in all cases. It was concluded that, besides giving results completely comparable with those of the usual clustering methods, the 3-DM is far superior to them where the time factor is concerned. For the classification of 272 objects, 168 s (0.618 s/search) was needed, compared to 10 times more (6.0 s/search) for finding the best match by comparing test compounds with each compound in the reference set (KNN method, with $K = 1$ and $K = 3$).

INTRODUCTION

In previous publications (1-5) it was shown that the three-distance clustering method (3-DM) can be used for the interpretation of chemical structures based on their infrared and ¹³C NMR spectra. In this study we try to show that the method can be applied also to other types of data of interest to analytical chemists. When one is classifying objects (wines, oils, drugs, coals, archaeological pottery, or glasses, etc.) into a number of known or unknown categories, the objects studied are analyzed and described in a multivariate space, each variable being a measurable quantity, usually a concentration of a certain component. In contrast with spectra, which are often represented as a few hundred digitized points (intensities measured at standard wavelengths), the above-mentioned samples are represented by far less variables, usually not more than 20. Additionally, the correlation between the two neighboring intensity points in a spectrum is strong, indicating that the order of variables is important, while in the analysis of components the order of variables is completely irrelevant.

Classification of objects that are interesting from the analytical point of view is usually made by hierarchical clustering on comparatively small amounts of data. However, modern instruments that are able to analyze hundreds of samples per day and are connected to mainframe or laboratory computers now allow the formation of large collections of data, keeping the records accessible not only for inspection, but as well for large-scale statistical and other handling.

Therefore, we were interested in how the 3-DM, which can generate hierarchical order of an unlimited number of multivariate objects, will perform if objects are described with a comparably small number of variables. Such cases are typical in classification of data obtained by chemical analysis (samples of wines, oils, pharmaceutical products, etc.).

We wanted to investigate how this method would perform for classification purposes, both supervised and unsupervised, in multivariate data analysis as applied in analytical chemistry.

Two aspects are investigated: quality of the classification and computation time.

The objects of our study were taken from a set of 572 Italian oils, originating from nine different regions (North and South Apulia, East and West Liguria, Inner and Coastal Sardinia, Umbria, Sicily, and Calabria), each sample described by its content of eight fatty acids. This set has been studied already by other data analysis methods (6-10), so that the results obtained by the 3-DM can be evaluated and compared. Each variable value was scaled to the percentage of the interval span for this variable, and throughout the study all eight variables were taken into account with equal weights.

One of the main problems, both in supervised pattern recognition and clustering, is the difficulty of accommodation of new knowledge. In supervised pattern recognition the classification rule is developed on the basis of a training set. The addition of new objects of known classification and perhaps also new classes in later stages requires that the classification rule be recomputed, starting at the beginning. The exception is the K -nearest neighbor method (KNN), but this leads to the computational problem described later. In clustering too, a new addition requires completely new computation of the classification. Moreover, nearly all supervised and clustering methods do not really allow one to work with more than a few hundred objects. In spectroscopic application, it has been shown that 3-DM permits one to work with many more samples and permits updating of the classification with only partial or local computations in the existing classification scheme.

SHORT DESCRIPTION OF THE 3-DM

Because the 3-DM has been described in many other publications (1-5), only a short description concerned mainly with the differences with the usual hierarchical clustering methods will be given.

The 3-DM is basically an update of a hierarchical clustering. Let us suppose that such a hierarchical clustering has already been obtained and that a small part of it is shown in Figure 1. V_i is a node in the tree, and in a way that will be explained later, it has been decided provisionally that a new object A, which must be classified, belongs to the group of objects O_1-O_7 of which V_i is the parent. Once this decision has been made, one must further decide whether A belongs rather to the objects O_1-O_3 (parent V_1) or O_4-O_7 (parent V_2) or, after all, not similar enough to one of those two groups.

The name of the method points to the fact that the choice of the p th the new object A must take at each node depends on three distances, namely $d_1 = d(A, V_1)$, $d_2 = d(A, V_2)$, and $d_3 = d(V_1, V_2)$.

Each node in the tree represents the objects (oils) that can be accessed from it. The representation of the group V_i is a mean of all variable values from the objects in the i th group:

$$V_i = 1/n_i (\sum_{j=1}^{n_i} x_{j1}, \sum_{j=1}^{n_i} x_{j2}, \dots, \sum_{j=1}^{n_i} x_{j8}) \quad (1)$$

where n_i is a number of objects in the i th group. V_1 therefore represents O_1, O_2, O_3 and is the centroid of those three objects. If d_1 is smallest, then it is concluded that A belongs to V_1 and A moves from V_i to V_1 . If d_2 is smallest, then A moves from

¹ On leave from Boris Kidric Institute of Chemistry, Hajdrihova 19, 61115 Ljubljana, Yugoslavia.

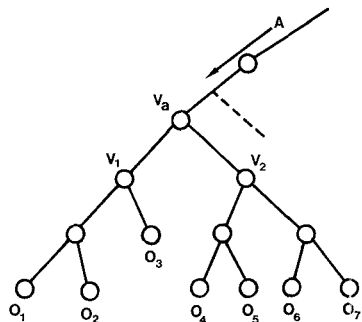


Figure 1. Generation of the clustering hierarchy using the 3-DM. Each node represents all objects accessible through it (V_a , for example, represents objects O_1 – O_7). The new object A traverses the tree and at each node makes a decision based on three distances. If $d_3 = d(V_a, V_2)$ is the smallest distance, a new branch buds between V_a and its ancestor.

V_a to V_2 . If, however, d_3 is the smallest of the three distances, than A is really an outlier compared to V_a , and therefore, a new branch buds between V_a and the ancestor of V_1 (broken line in Figure 1).

One observes that new objects are added to the tree at the root and forced either to traverse it to one of the leaves, or stop in the middle and bud a new branch between two existing nodes. After the objects are updated into the tree, all of them can be tested again to see if they find their present position. If not, they are relocated to a new position. The testing and relocation is repeated until all objects in the tree have fixed, accessible positions.

Building the original tree is carried out in the same way. One starts with two objects as a cluster and then updates this small tree with a third object, etc.

Contrary to the usual clustering methods (11, 12), the 3-DM does not need a similarity matrix between the objects. In fact it is not even necessary to know in advance all objects to be clustered or how many are going to enter the clustering pro-

cedure. The use of a similarity matrix prevents the methods that depend on it from clustering really large sets of objects: There are serious space and time problems with clustering even a thousand objects. As it turns out, for the 3-DM, which requires no similarity matrix, this is no problem at all.

There is of course a price to be paid for these advantages, which is reflected in the fact that there is no guarantee that each object will be clustered with the *very* closest one and that the obtained clusters depend on the sequence in which the objects are updated in the tree. The mentioned dependency of the hierarchy on the sequence order of clustering concerns mainly the relative position of different clusters in the tree and only to a very small extent the membership of clusters.

RESULTS AND DISCUSSION

Evaluation of the 3-DM. First, we wanted to evaluate the method as a clustering procedure (i.e. nonsupervised). For this purpose we randomly selected five objects from each of the nine groups, i.e. a total of 45 objects, and generated a hierarchy of clusters with the 3-DM (3) and one of the more usual clustering methods, namely the unweighted group average method (3, 11, 12). The unweighted group average method was selected because it resembles the treatment of cluster representations made by the 3-DM most closely: Both methods use as the criterion for linking the clusters together the distance between the centroids of the groups.

The hierarchies of clusters were obtained once with Euclidean and once with the Manhattan or city block distance (13). Since the results obtained by both distance measures were almost identical and because of its computational time efficiency, we used for the further study exclusively the Manhattan distance. The resulting hierarchies obtained by both clustering methods are shown in Figure 2.

Both methods clearly separate Inner and Coastal Sardinian, West Ligurian, North Apulian, Umbrian, and East Ligurian oils from the rest, and both methods mix Calabrian and Sicilian oils in one cluster. The few slight differences occur in treating a few South Apulian, East Ligurian, and Sicilian oils. The 3-DM appears to cluster the East Ligurian oils better than the unweighted group average method. On the other hand, the 3-DM mixed one South Apulian oil with the group of

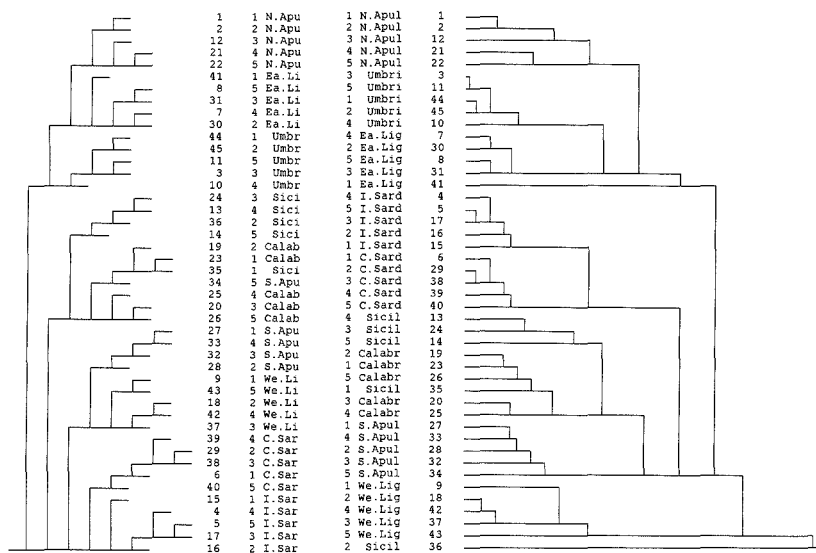


Figure 2. Hierarchies of 45 oils from nine different Italian regions, obtained by the 3-DM (left) and unweighted group average method (right).

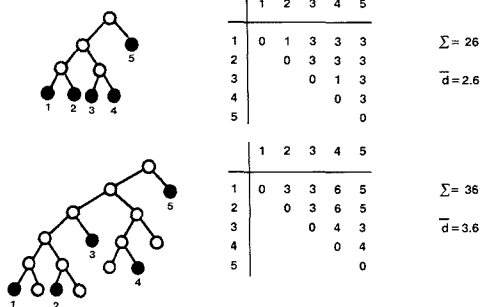


Figure 3. Graph-theoretical distance between the nodes in the tree. The distance between two nodes (not necessarily leaves as is the case in our study) is a number of nodes on the shortest path between both end nodes. For each group of five objects a distance matrix (as shown on the right) was formed and the average distance calculated.

Calabrian and Sicilian oils, while South Apulian oils were clustered separately when the standard clustering method was used.

In order to compare both clustering results in a more quantitative way, a graph-theoretical distance measure was employed. The graph-theoretical distance between two nodes in a graph was taken as the number of nodes between these two along the *shortest* possible path between them. For all five objects in each class C_i , a 5×5 distance matrix D_i was generated and the mean graph-theoretical distance d_i calculated. This tells how close together in the tree the objects of this class are placed. Of course, the smaller the d_i , the better the clustering. It has to be stressed that the mean graph-theoretical distance of a given class C_i depends only on the position of class members in the tree, but does not reflect the actual positions of class members (objects) in the variable space.

As can be seen from Figure 3, the smallest possible average distance in a five-member binary tree d_{\min} is equal to 2.6 nodes. The maximal distance depends on the size of the entire tree. In a 45-object tree the maximal average distance can be almost 10 times larger than the minimal one. Table I gives the average distances for clusters of all nine classes obtained by both methods. The averages of the d_i values are (within error) approximately equal.

Table I. Mean Graph-Theoretical Distance, d_i , between Members of Nine Classes As Obtained by the 3-DM and Unweighted Group Average Clustering Methods

no.	oils class	d_i	
		3-DM	group av
1	North Apulian	2.8	2.8
2	South Apulian	4.6	2.6
3	East Ligurian	2.6	3.4
4	West Ligurian	2.6	2.6
5	Inner Sardinian	2.6	2.6
6	Coastal Sardinian	2.6	2.6
7	Sicilian	4.2	5.0
8	Umbrian	2.6	2.6
9	Calabrian	3.8	3.2
	average	3.1 ± 0.7	3.0 ± 0.4

As a conclusion of this first evaluation of the 3-DM, it can be said that the clusters produced by it are well comparable to clusters produced by the methods using a full $n \times n$ distance matrix.

Encouraged by the obtained results, we used the 3-DM for the generation of a clustering of 300 oils. The obtained hierarchy is schematically shown in Figure 4. After the inspection of positions of all objects in the tree, 14 groups were found to be of interest for our discussion and were marked with capital letters A–N.

South Apulian (SA) oils form the large cluster A containing 75 of all 86 South Apulian oils in the study with only three oils of different origin (from Sicily). Other big clusters are M (Inner Sardinia) and N (Coastal Sardinia). These clusters are completely pure, and they contain all objects of the two classes. Other pure clusters are D, F, G, and L, containing 16 Calabrian, eight Sicilian, 11 Calabrian, and 12 East Ligurian oils, respectively.

In the 3-DM approach the outliers can be identified as small separate clusters branching away from the main path at a given node with a large distance d_1 or d_2 (for additional information see ref 13–15). This property enables the method to handle the appearance of samples from entirely new classes. The new objects form a "nucleus" of a future cluster, which can grow later when objects belonging to the new class are added to the collection. This particular property of 3-DM clustering enables it to develop a new cluster even away from the existing root, i.e., to recognize a completely new type of object (13, 14). In the context of the present work the term "outliers" is used for the oils of given origin that are not

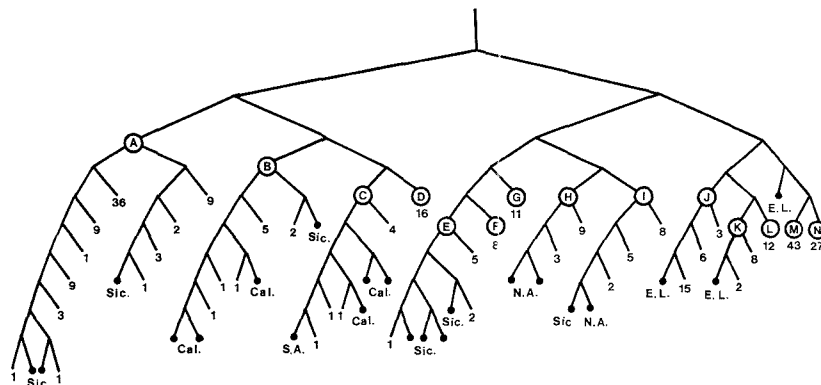


Figure 4. Hierarchy of 300 oils. Capital letters mark the nodes representing major clusters. Numbers at the branch ends indicate how many objects of the same class are deeper in the tree in the direction of the branch. The small full circles mark the objects in the cluster that do not belong to the class. The set contains South (clusters A and B) and North (cluster E) Apulian, East (clusters I and L) and West (cluster J) Ligurian, Inner (cluster M) and Coastal (cluster N) Sardinian, Sicilian (clusters C and F), Umbrian (clusters H and K), and Calabrian (clusters D and G) oils.

classified in groups to which they belong or for a "nucleus" of a new group.

In other groups, the majority of objects from one class are mixed with a few outliers from other classes. An example is cluster C where the outliers from Calabria, South Apulia, and Sicily are joined. From the prediction point of view, such groups are very important because they pinpoint those samples that are rather ill defined, possibly wrong experimentally, or faulty in some other way.

Evaluation in Supervised Recognition. It has to be said again that all 300 objects, if put into the tree at the root again, will travel exactly to their positions, thus "recognizing" themselves in the tree. An important aspect in this recognition scheme is that the recognition is made by only 9 comparisons on the average (the actual number for the individual recognition is in the range from 4 to 15) because the average path in this particular tree is 9.3 nodes long.

The 3-DM hierarchy has therefore 100% recognition ability. The next question is whether it can be used for prediction of properties (16) with correspondingly good prediction ability.

To investigate the prediction ability and the "robustness" of the method, five 300-object trees were generated for this study (one of them is shown in figure 4). Three hierarchies were produced from different sets of objects while two further hierarchies were obtained only by changing the sequence of updating the objects used in one of the previous three trees. The generated hierarchies were used to predict the class for 272 oils *not* used in the generation of each particular tree. All hierarchies have exhibited very similar prediction abilities (from 90.0 to 93.0%) with 27, 25, 21, 20, and 19 wrong predictions.

To be able to compare the quality of the resulting classification, the KNN method for $K = 1$ and $K = 3$ (16) was also compared with one of the generated trees. The KNN method is the only supervised method that permits easy updating of the training set. Therefore, other supervised methods such as linear discriminant analysis were not used.

It is interesting to note that among 272 samples tested with three methods (1NN, 3NN, and 3-DM) 247 were correctly classified by all three methods; therefore the misinterpretation occurs only on a small set of 25 objects (9.1%). The results of predictions of all three methods for all 25 problematic samples are given in Table II.

The prediction results shown at the bottom of Table II can be evaluated from two aspects: as a total prediction regardless of the objects (percentage of correct or wrong answers) or as a comparison of predictions between different methods (wrong prediction of an object with all methods means equal quality for all methods). All three methods have comparably good total prediction abilities: 94.1, 94.8, and 92.6% with very little difference between the 1NN and 3NN methods.

The cause of "errors" could roughly be divided into two categories. The first one is due to the overlap or very close positions of two or more classes, while the second one represents the samples that are "outliers"; i.e. they are placed far out from the rest of the group they belong to.

These findings are in agreement with the actual positions of oil samples in two- and three-dimensional reduced spaces obtained by the principal component analysis (PCA) in the previous studies of these data (7-10).

Among 20 "errors" produced in the 3-DM hierarchy, six objects were classified as the same wrong (although the closest) compound as in the case of the 1NN method, six were linked to the next closest compound which was still in the wrong class (and were predicted incorrectly with the KNN method as well), and eight samples were completely misclassified.

Some of the wrong answers and, in particular, those six that were classified wrongly with *all three* methods are outliers

Table II. Comparison of Prediction Abilities Obtained by Three Methods (KNN for $K = 1$ and $K = 3$ and 3-DM)^a

no.	query sample	methods			all wrong
		1NN	3NN	3-DM	
1	SA061	SI22 -	2:1 +	SA042 +	
2	SA081	SA128 +	3:0 +	CA02 -	
3	SA174	SI20 -	1:2 -	SA59 +	
4	SA175	SI22 -	0:3 -	SI23 -	*
5	SA176	SI17 -	0:3 -	SI20 -	*
6	SA181	SA130 +	3:0 +	IS33 -	
7	NA03	NA01 +	3:0 +	SI09 -	
8	NA06	SI30 -	1:2 -	SI14 -	*
9	NA07	SI09 -	2:1 +	SI09 -	
10	NA16	SA149 -	1:2 -	CA22 -	*
11	NA18	CA21 -	0:3 -	CA21 -	*
12	EL32	EL37 +	3:0 +	WL06 -	
13	EL31	WL38 -	0:3 -	WL38 -	*
14	WL43	WL37 +	3:0 +	EL36 -	
15	WL50	EL49 -	2:1 +	EL49 -	
16	CS24	IS50 -	1:2 -	IS50 -	*
17	SI02	SI20 +	2:1 +	SA200 -	
18	SI03	SI19 +	1:2 -	SI19 +	
19	SI12	CA05 -	1:2 -	CA44 -	*
20	SI35	CA22 -	0:3 -	CA22 -	*
21	SI36	SI28 +	2:1 +	CA27 -	*
22	CA34	SA135 -	0:3 -	SI29 -	*
23	CA35	NA01 -	0:3 -	CA50 +	
24	CA36	SA156 -	1:2 -	CA02 +	
25	CA53	CA49 +	2:1 +	SI13 -	
wrong among 272 samples, %		16 (5.9)	14 (5.2)	20 (7.3)	
conflicting, %		6 (2.2)	4 (1.5)	10 (3.7)	

^aSamples are marked according to their origin (SA, NA, EL, WL, CS, CA, and SI for South and North Apulia, East and West Liguria, Coastal Sardinia, Calabria, and Sicily, respectively). At 1NN and 3-DM the samples to which the query was linked are given, while in the case of 3NN the results produced by the three nearest neighbors are given (for example, 2:1 means that two closest neighbors were in the correct and one in the incorrect class, thus producing the correct decision marked with +. The objects where all three methods gave wrong predictions are marked with an asterisk.

to their classes and cannot be considered as real errors. Such "erroneous" decisions are based on the actual values of variables and are, from the methodological point of view, actually correct decisions. If only the samples with conflicting predictions (last line in Table II) were taken into account, the prediction abilities would be even higher (97.8, 98.5, and 96.3%, respectively). Regardless of which figures are taken into account, the difference in prediction abilities is small and supports the initial hypothesis that the 3-DM gives results comparable to those of the KNN method, which further means that 3-DM can substitute for the KNN, especially when larger sets are studied.

The 3-DM has, however, a large advantage in computational time compared to KNN. The advantage is more apparent as the data sets grow larger (15). For the KNN method to be comparable with the 3-DM, we put both methods to the same footing assuming the distance matrix is not available (this happens if the collection is large). In order to find the best match with the KNN method, the entire set of data has to be scanned, which means that a sequential search through all data is necessary and that the average access time is equal to $N/2$, N being the number of objects in the collection. For the 3-DM, however, the dependence of the average access time t_a can be expressed as a function of the number of objects in the hierarchy:

$$t_a = 3 \log_2 N \quad (2)$$

Indeed, there are $\log_2 N$ nodes on the average path. The factor 3 in eq 2 is derived from the fact that at each node three items have to be retrieved, compared, and/or changed: the node and both its descendants. Expression 2 is valid for completely balanced trees. Due to the nature of objects clustered, the

hierarchy is never perfectly balanced; hence, instead of $\log_2 N$ the average path length has to be taken into account.

Even in this hierarchy of a very modest size (300 items), the search time was about 10 times (the average number of nodes on the path was 9.3) shorter than for the INN method. The actual figures on an IBM PS 80 system were 0.618 and 6.03 s/search, respectively. With hierarchies linking for instance 10 000 data, which could be the number of experiments kept in the memory of future high-capacity instruments, the saving factor would already be about 300.

CONCLUSION

The 3-DM is shown to perform as well as a classical clustering technique and as well as the KNN supervised pattern recognition method. Therefore it has classification abilities similar to those of the other two methods. Moreover, the method has large computational advantages. In comparison to classical clustering, it is not necessary to start a classification run ab initio whenever new objects are submitted. This property enables analytical laboratories to perform large-scale analysis on comparable samples that vary according to the origin of raw material (such as technical chemicals, oils, wines, and jams), or technological differences or different producers (such as drugs, ceramics, glasses, archeological samples, and medical tests for a type of disease).

We hope that the usefulness of the 3-DM for (a) hierarchical clustering of large data sets described by few variables and (b) prediction of classes in supervised application was convincingly shown. The method has a potential for implementation in the next generation of "intelligent" instruments that should be able to learn from the experiments performed by themselves as well.

The 3-DM has one disadvantage in supervised pattern recognition; it is not able to model class, such as SIMCA or UNEQ can.

We believe that handling large amounts of multivariate data is one of the future trends for any quality control work and that the method, which can deal with an almost unlimited amount of such data, is very important in this respect. By formation of a hierarchy of all data, which grows *linearly* with their increase, the classification of a new object is possible in a number of comparisons proportional to $\log_2 N$, N being the number of data in the hierarchy. Logarithmic dependency on the number of objects offers the fastest possible context dependent retrieval known.

LITERATURE CITED

- (1) Zupan, Jure *Anal. Chim. Acta* **1980**, *122*, 337-346.
- (2) Deane, Michael F. *Anal. Chem.* **1981**, *53*, 2356-2358.
- (3) Zupan, Jure *Clustering of Large Data Sets*; Research Studies Press (Wiley): Chichester, U.K., 1982.
- (4) Zupan, Jure *Anal. Chim. Acta* **1982**, *39*, 143-153.
- (5) Novic, Marjana; Zupan, Jure *Anal. Chim. Acta* **1985**, *177*, 23-33.
- (6) Foinea, Massimo; Armanino, C. *Ann. Chim. (Rome)* **1982**, *72*, 127-144.
- (7) Foinea, Massimo; Tiscornia, E. *Ann. Chim. (Rome)* **1982**, *72*, 143-155.
- (8) Derde, Marie-Paule; Massart, Luc D. *Fresenius' Z. Anal. Chem.* **1932**, *373*, 484-495.
- (9) Derde, Marie-Paule; Massart, Luc D. *Anal. Chim. Acta* **1986**, *191*, 1-16.
- (10) Derde, Marie-Paule; Massart, Luc D. *Anal. Chim. Acta* **1986**, *184*, 33-51.
- (11) Messart, Luc D.; Kaufman, Leonard *The Interpretation of Analytical Chemical Data by the Use of Cluster Analysis*; Wiley: New York, 1933.
- (12) Everitt, Brian *Cluster Analysis*; Heineman: London, 1975.
- (13) Zupan, Jure; Munk, Morton E. *Anal. Chem.* **1985**, *57*, 1609-1616.
- (14) Zupan, Jure; Munk, Morton E. *Anal. Chem.* **1986**, *58*, 3219-3225.
- (15) Zupan, Jure In *Proceedings of the International Conference on General Systems Research—Hierarchy as a Special Topic*; New York, 1984; Vol. 2, pp 633-640.
- (16) Messart, Luc D.; Vandeginste, B. G. M.; Deming, S. M.; Michotte, Yvette; Kaufman, Leonard *Chemometrics: a Textbook*; Elsevier: Amsterdam, 1988; Chapter 23, p 395.

RECEIVED for review November 28, 1988. Revised manuscript received May 11, 1989. Accepted June 15, 1989.

Automated Segmented Flow Electrochemical Analyzer

Palitha Jayaweera and Louis Ramaley*

Trace Analysis Research Centre, Department of Chemistry, Dalhousie University, Halifax, Nova Scotia, Canada B3H 4J3

Segmented flow analysis has been combined with pulse voltammetric detection to provide an instrument that can perform multicomponent determinations in the reductive mode at a rate of 100 samples per hour. The instrument features a simple flow system, complete computer control, an in-line deoxygenator, stopped flow analysis, and signal averaging for reduced noise. For metals such as Cd(II) and Pb(II) the detection limits are less than 5×10^{-8} M, the linear range is over 10^4 , and the precision is 0.5% for samples of 5 mL. The carry-over from one sample to the next is 0.7% at a sampling time of 35 s.

Conventional voltammetric analysis applied to static solutions usually involves manual transfer of solutions and lengthy deaeration periods, reducing sample throughput. The use of

a flow system removes these difficulties to a great extent. The selectivity and sensitivity of voltammetric detectors make them good candidates for automated wet chemical analysis. Although amperometry is the most widely used electrochemical technique in flow analyzers, potential scanning methods are becoming more popular. Applications of voltammetry in flowing systems have been recently reviewed (1). A rapid scan voltammetric detector for flowing solutions was first reported by Wang et al. for use in the analysis of discrete samples, flowing streams, and chromatographic effluents (2). Scanning voltammetric detection coupled to high-performance liquid chromatography (HPLC) provides an additional dimension of resolution along the potential axis which helps to resolve some chromatographically overlapped components (3-8). In flow injection analysis (FIA), which usually does not employ a separation step, the extra resolution of voltammetry aids selectivity, and peak potential data provide qualitative in-

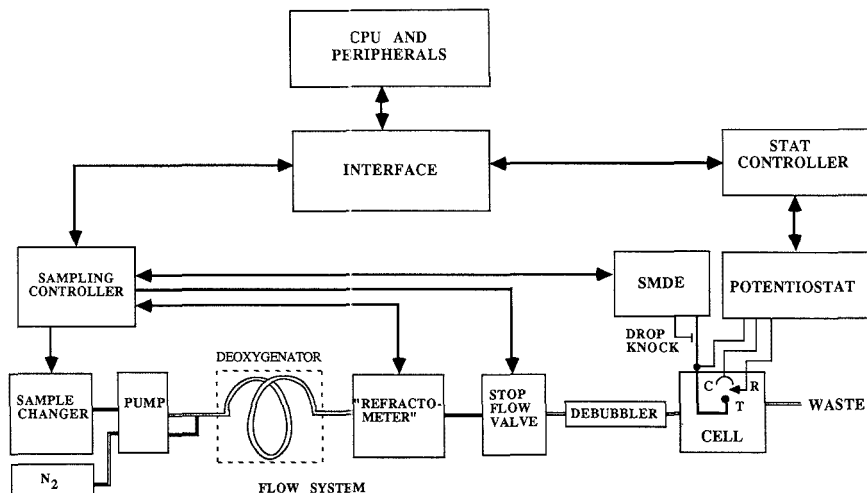


Figure 1. System block diagram.

formation for component identification (9-16).

Since the sample concentration does not normally reach a plateau in FIA, but has the form of a peak, the potential sweep time must be small compared to the half-width of the concentration profile to obtain undistorted voltammograms and the most accurate quantification. To alleviate this problem, larger sample volumes (100-1000 μL) and/or slower flow rates (25-1000 $\mu\text{L}/\text{min}$) have been used with scanning voltammetric detection in FIA (11-16). Unfortunately these lead to low sample throughput (15-20 samples/h).

Segmented flow analysis (SFA), in contrast, uses relatively large sample volumes and produces plateau-like response signals. This makes such analyzers more easily adaptable to scanning voltammetric detection. Furthermore, segmentation of the flow stream can be done with nitrogen instead of air. This helps to deoxygenate the samples since the oxygen in solution, which can interfere in the reductive mode, can diffuse into the nitrogen bubbles which segment the flow stream. The application of square wave polarography in an SFA system has been reported with a 22 sample/h throughput (2). This rather low rate was in part due to the use of a cumbersome deaeration procedure and a dropping mercury electrode (DME) with a long drop life which required synchronization of the drop, the sampling time, and the dwell time.

Yarnitzky (17) has developed an automatic voltammetric electrode, which, although it does not work on the basis of either FIA or SFA, speeds up sampling. Deoxygenation was accomplished by nebulization and sample transfer by a rather complex system of pumps and valves. Results presented demonstrated a sampling rate of 50 per hour (five samples in 6 min). The same system was later used for automated analysis of cephalothin (18) where 12 samples were analyzed in a period of 30 min. This work has provided the basis for the PARC Model 309 voltammetric electrode.

We have developed a simple segmented flow, multisample analyzer which employs rapid scan voltammetric detection at a static mercury drop electrode (SMDE) for use in the reductive mode. The instrument can presently be programmed to perform three rapid scan techniques: square wave voltammetry (constant pulse amplitude), staircase voltammetry, and pulse voltammetry (constant base line, variable pulse amplitude), all with scan reversal capability. The system, which employs inexpensive components but is com-

pletely computer controlled, can analyze more than 100 samples/h. Digital methods of data acquisition and storage, terminal graphics display of voltammograms, signal averaging for improved signal-to-noise ratio, and software control of all experimental parameters are the main features available in this system.

EXPERIMENTAL SECTION

Overall System. A block diagram of the complete instrument is shown in Figure 1. Computer control is provided by a Hewlett-Packard 21MX-M computer (Hewlett-Packard, Inc., Cupertino, CA) with a lab-built interface similar to one previously described (19). Samples are pumped consecutively from the sample changer into the flow stream by a peristaltic pump (Model 375, Sage Instruments, Division of Orion Research, Inc., Cambridge, MA). The sample stream is segmented with nitrogen at the outlet of the pump and any residual oxygen interference can be removed either by passing the sample stream through a deoxygenator or by adding a chemical such as sodium sulfite to the flow stream. The "refractometer" detects the arrival of samples at the electrochemical cell. Just prior to entering the cell samples are debubbled with a tubular debubbler. Voltammetric detection is performed at the computer controlled SMDE. Flow is stopped during the potential scan to minimize the interference of flow noise.

The performance of the electrochemical section of the instrument has been discussed in detail in previous publications (20-22). The potentiostat controller (20) provides waveform and timing information to the potentiostat. The voltage resolution of the waveform is 1 mV. Pulse periods may vary from 50 μs to 65 ms and measurement periods from 25 μs to 65 ms, each with 1- μs resolution. Once programmed, the potentiostat controller functions independently of the computer except for start and stop commands. One of the three electrochemical techniques mentioned above and all of its waveform parameters including the position and length of the current integration window along the pulse can be selected under software control.

The sampling controller oversees the change of samples in the sample tray, the arrival of samples at the cell, and the operation of the SMDE and the flow control valve. It also reports the status of instrument sections under its control to the computer when necessary. Except for the peristaltic pump, all sections of the instrument are under computer control. In addition, these sections contain sufficient hardware to function independently after receiving initial programming commands from the computer. Hence the computer is relieved of most real time control of various functions and is available for other operations.

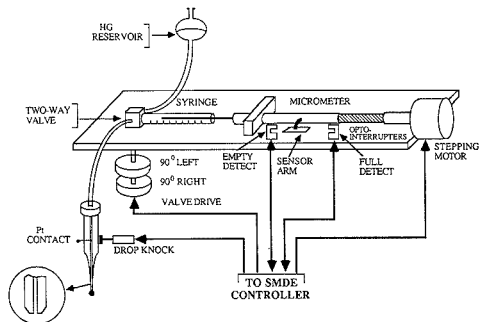


Figure 2. Static mercury drop electrode.

SMDE and Sampling Controller. The lab-built, syringe-driven SMDE is shown in Figure 2. It consists of a stepping motor (SLO-SYN MO61-FD-301, Superior Electric Co., Bristol, CT), a 5 cm micrometer head (Mitutoyo 151-271, 16 threads/cm, MTI Corp., Mississauga, ON, Canada), and a two-way valve (H86728, Hamilton Co., Reno, NV). The stepping motor turns the micrometer which in turn drives the syringe piston (Hamilton 1710, 100 μ L). The two-way valve, which controls the direction of mercury flow, is driven by two rotary solenoids (90° left and 90° right, A-35241-033 and H-2640, Ledex, Inc., Dayton, OH). The opto-interrupters (H13B1, General Electric Co., Syracuse, NY) are used to report the status of the syringe (empty or full) to the controller. The electrode itself is a small bore (1 mm i.d.) glass tube (8 cm \times 6 mm o.d.) the end of which was drawn to a fine tip, 0.08 mm i.d. This tip was cut to a flat, scratch-free surface and bevelled by grinding (see inset in Figure 2). Such a tip helps the drop knocker dislodge the mercury drop more easily. Electrical contact was made about 4 cm above the tip through the glass tube wall. The mercury reservoir, two-way valve, and electrode are connected with poly(tetrafluoroethylene) (PTFE) tubing (1 mm

i.d.). The total volume of mercury in the syringe, electrode, and connecting tubing is about 500 μ L. The drop knocker is a tubular solenoid (747610-034, Redarr, Ltd., Wollesley, ON, Canada) fixed with a plastic hammer which strikes the electrode capillary. By control of the motor, the solenoids, and the two-way valve, drops can be grown and knocked off, and the syringe can be refilled.

A simplified diagram of the SMDE control circuit is shown in Figure 3. A 555 timer, set to 1.0 kHz, provides the base frequency for the circuit. This is divided by 16, in multiples of two, using a binary counter. One of the outputs of this counter is selected by a digital multiplexer (74LS151) as the clock to an up/down counter (74LS193). The clock signal is gated-on or -off depending on the outputs of the drop size counter and opto-interrupters. The outputs of the up/down counter are decoded such that they provide an eight-step sequence (400 steps/revolution) for the stepping motor (23). A modified translator board (SLO-SYN TMS101), originally designed to provide a four-step sequence (200 steps/revolution), is used to translate the logic signals to motor pulses. The modification allows direct access of the external logic signals, which are already coded for the eight-step sequence, to the power transistors which drive the motor. In a manual mode (not shown in Figure 3), control of the motor speed and direction, the two-way valve, and the drop knocker is accessible to the operator through front panel switches, allowing testing for proper operation before starting an experiment.

When a mercury drop is needed, the computer outputs a word to the controller which contains drop size (number of steps) and growing speed (stepping speed) information. The strobe associated with this word loads data into the 12-bit drop size counter and enables the logic. This counter counts down as the motor steps to grow the mercury drop. When the terminal count (zero) is reached, the clock is gated-off to both the drop size counter and the 74LS193 up/down counter, stopping the stepping motor. This also closes the sample flow valve, a simple device consisting of an aluminum wedge fitted to a tubular solenoid (747610-034, Redarr). When this solenoid is energized, the wedge squeezes the flow tubing tightly. Since the flow stream is segmented and the valve is closed only for a short time, usually less than 3 s, the pressure build-up in the system is not large. The mercury drop

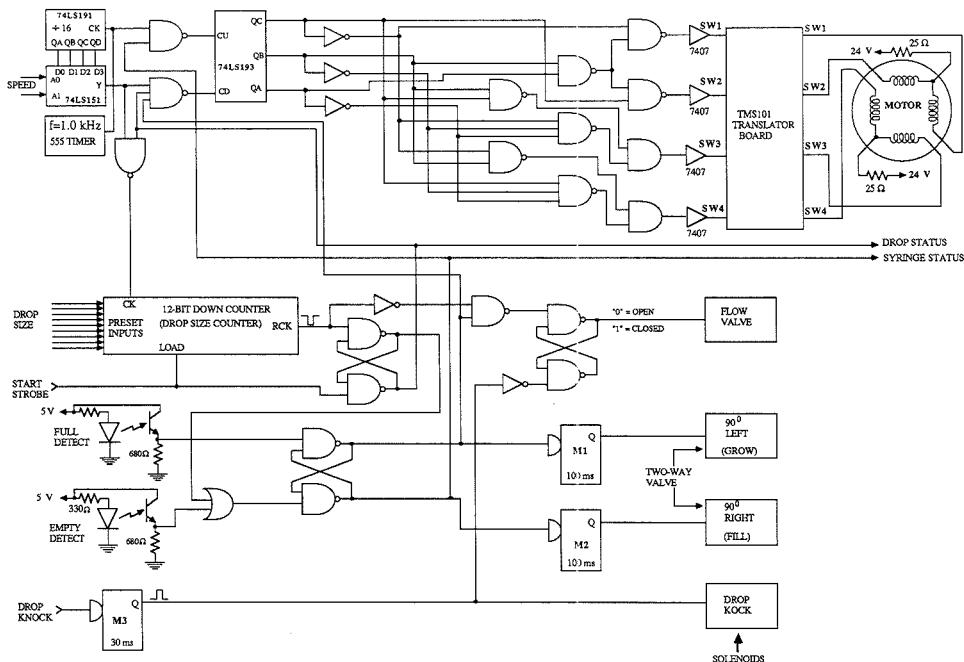


Figure 3. Simplified diagram of the SMDE controller.

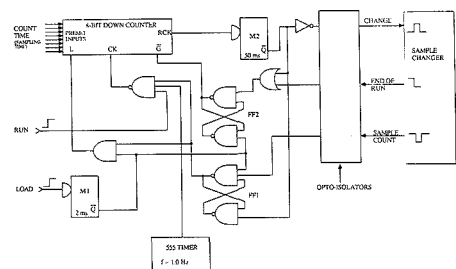


Figure 4. Diagram of the sample changing interface.

is dislodged by issuing a command to the controller which energizes the drop knocker solenoid and opens the sample flow control valve. The ability to vary the drop growth rate was incorporated in the SMDE for use in other experiments and is not necessary for the analyzer described here. All experiments reported below used the fastest growth rate, about 0.2 s/drop. A fixed drop growth rate would result in a simplification of the SMDE controller circuit.

When the appropriate opto-interrupter senses that the syringe is empty, the controller overrides any computer settings and refills the syringe by reversing the direction of the two-way valve and the counting mode of the 74LS193 counter. In this case, the 555 timer signal is directly routed to the up/down counter, running the stepping motor at maximum speed. The other opto-interrupter stops the process when the syringe is full. If the syringe becomes empty during an experiment, the control program aborts the experiment. However, the SMDE is capable of growing more than 200 drops of 0.9 mm diameter with one filling. The sample changer holds a maximum of 50 samples. Thus, four drops can be averaged for each sample in the tray without refilling the syringe.

Two lines report the status of the SMDE controller. The syringe status line is "high" (+5 V) when the syringe is being refilled and the drop status line is high during drop growth. After issuing the drop-grow command, the computer checks syringe and drop status to determine the availability of a stable drop before starting the potential sweep.

Sample Changer and Clock Circuit. Controlling the sample flow involves the change of samples at the sample changer according to programmed time intervals and detecting the arrival of samples at the electrochemical cell. The operation of the sample flow valve is automatically controlled along with the SMDE as described above.

A "Lazy-Susan" type commercial sample changer (Model SP450, Pye Unicam, Ltd., Cambridge, UK) is used to load samples. The SP450 was somewhat modified in order to interface to the computer. Timing in the SP450 is done by a program motor, cams, microswitches, and relays. The noise transmitted from these devices to the digital control circuits was the main problem in interfacing and was overcome by capacitive decoupling of all switches and relays and optically isolating the SP450.

Three signal lines from the SP450 are interfaced to the computer via the circuit shown in Figure 4. A positive pulse of 50 ms on the CHANGE line causes the sampling arm to raise, a new sample to rotate into place, and the arm to lower, taking between 2 and 3 s. When this is accomplished, a negative pulse is output from the sample changer on the SAMPLE COUNT line. When the last sample is in place, the END OF RUN line goes low. Before a run, the computer loads a number corresponding to the number of seconds (1 to 255) of sampling time per sample into the 8-bit down counter (74LS191) by triggering monostable 1 (M1) with a high signal on LOAD. The pulse from M1 also sets FF1 and resets FF2, placing the circuit in the "ready" mode. The run starts when the 1.0-Hz clock from the 555 timer is enabled by a high signal on RUN. The circuit operates automatically from this point on. When the value in the counter reaches zero, a pulse from M2 resets FF1, disabling and reloading the counter and causing a change of sample. When the next sample is in place, the SAMPLE COUNT signal sets FF1 and restarts the timing cycle. When the

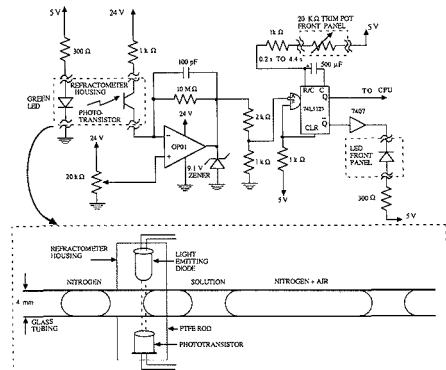


Figure 5. Diagram of the "refractometer".

last sample is in place and its timing period has finished, the pulse from M2 resets FF1 and sets FF2, ending the run.

If the computer detects an error, it disables the clock by setting RUN low (0 V) to prevent further sampling and aborts the experiment. Although the clock circuit provides sampling times down to 1 s, the minimum is set to 10 s by software.

Flow System. The flow stream is segmented uniformly by pumping nitrogen and solution at the same rate through a Y-shaped glass connector. The deoxygenator, if used, comes next in the flow system. It is a 3 m long microporous PTFE tube of 3 mm internal diameter (Gore Tex, The Anspec Co., Inc., Ann Arbor, MI) wound on a glass frame and placed in a 1.5-L sealed bottle. The porous PTFE is connected directly to the ordinary PTFE tubing used in the flow system. This latter is led into the deoxygenator vessel through glass tubes in the vessel cap. Heat shrinkable tubing is used to seal the PTFE tubing to the glass cap. The vessel is completely filled with a 0.2 M Na_2SO_3 solution (pH 10). The first few nitrogen segments leak through the microporous tubing and build up pressure in the bottle. When the pressure is balanced, the flow stream passes through the tubing without any further loss of nitrogen. The pressure balance in the deoxygenator is established during the time that the flow system is being flushed before an experiment. Oxygen in the flow stream diffuses through the porous PTFE tubing and is consumed by oxidation of the sulfite.

The arrival of samples at the cell is detected by a simple optical device, referred to as a "refractometer", mounted on the flow line close to the cell. A green light emitting diode (LED) and a phototransistor are mounted at opposite ends of a 5 cm long PTFE tube (12 mm o.d.) as shown in Figure 5. A 2.5 cm long (4 mm o.d.) glass tube, through which the analyte flows, is passed through the PTFE housing and placed across the optical path.

When the phototransistor and the LED are positioned properly, the phototransistor is sensitive to changes in the refractive index of the flow stream. The current through the phototransistor changes in a square wave fashion as the air and solution segments pass. This signal is amplified and used to drive a retriggerable monostable (SN74LS123), the pulse width of which can be varied between 0.2 s and 4.4 s by a 20-k Ω potentiometer on the front panel of the sampling controller. The Q output of the monostable is sampled by the computer and the Q output is used to drive an LED on the front panel, providing a visual display of the status of the monostable.

Segments within a sample are about 1 cm long. When the autosampler uptake arm changes from one sample to another, air is pumped into the stream. This air bubble combining with nitrogen bubbles forms a 4 to 5 cm long segment between two samples. Once the desired flow rate and the proper segmentation are obtained, the pulse width of the monostable is set such that the monostable is continuously triggered (Q is high) by the short nitrogen segments, and the trigger pattern is broken (Q goes low) by the longer air segments, signaling the arrival of each new sample at the refractometer. Some tolerance must be allowed for small variations in segment size and flow rate. Proper operation is easily

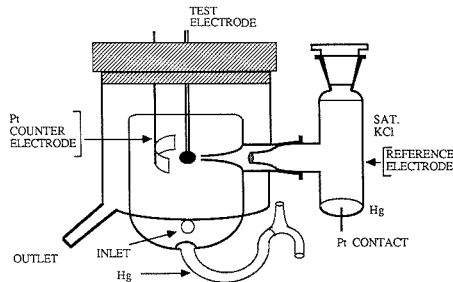


Figure 6. Electrochemical flow cell.

accomplished with the aid of the LED indicator on the front panel while the flow system is being flushed prior to an experiment.

The flow stream is debubbled just before entering the electrochemical cell by a tubular debubbler, a 7 cm long microporous PTFE tube (Gore Tex) of 3 mm internal diameter. The end of this tube is connected to the cell through a 1 cm piece of silicone tubing (0.8 mm i.d.) The constriction due to the small diameter tubing develops enough positive pressure in the porous PTFE tubing to force the gas bubbles through its wall. Similar applications of microporous PTFE have been previously reported (24, 25).

The electrochemical cell, constructed from borosilicate glass, is shown in Figure 6. A small pool of mercury in a "U" tube at the bottom acts as a seal for the solution and it also allows excess mercury to overflow. The solution overflows the inner cell into the outer jacket to which the outlet is connected. The platinum counter electrode, a thin cylindrical foil, sits along the wall of the inner cell above the reference electrode. The cell has a side arm with a ground glass joint for accepting a reference electrode. The side arm extends into the cell as a fine tip so that the SMDE can be placed very close to the tip, minimizing the uncompensated cell resistance. A PTFE cell cap is fitted to the outer jacket of the cell. The effective volume of the cell is about 200 μ L.

The tubing in the autosampler uptake arm is 1.0 mm diameter PTFE fitted with a PTFE needle which dips into sample vials. In the peristaltic pump 3.0 mm i.d. silicone tubing is used and is connected to the 1.0 mm i.d. PTFE tube with a flanged glass connector. From the nitrogen bubble introduction to the refractometer a 1 m long PTFE tube of 3 mm i.d. is employed. When the deoxygenator is in use, it is connected between the bubbler and the refractometer.

System Operation. Before an experiment is started, the control and data acquisition program reminds the operator to make the proper initial instrument settings, resets certain instrument functions, asks for instrument control parameters, e.g. sweep rate or sampling time, and other pertinent data, e.g. temperature or sample characteristics, computes the actual operating parameters that come closest to those desired, and asks if these are acceptable. When the operator makes the final selection of operating parameters, the program calculates and outputs the appropriate control codes.

Prior to an experiment, distilled water is used to flush the flow system while the sampling arm is in the "standby" position. Then air is pumped through the system. To start the experiment, the control program initializes the sample changer (the arm dips into sample 1) and goes into a waiting loop in which it polls the status of the refractometer signal. Five seconds after arrival of the first sample at the refractometer, the program rechecks the status of the refractometer to confirm the presence of the sample. This is done only for the first sample as a precautionary measure to avoid false arrival signals from the refractometer due to small segments of distilled water remaining from flushing the system. Such segments are rarely observed.

Once sample arrival is confirmed, the program starts a delay during which the cell is rinsed with the first several segments of the sample itself. This rinse time is the same for all samples and it is provided as one of the operating parameters. At the end of the rinse time, a mercury drop is grown and the flow is stopped. The potential sweep is started after a 1 s delay for settling by

sending a command to the potentiostat controller. At the end of the potential sweep the drop is knocked off and the flow restarted. If signal averaging is requested, the same procedure is repeated the desired number of times with a 3-s delay between each sweep.

At the end of each sample, the actual currents are calculated and the data are saved on disk. The program again goes into a waiting loop and polls the refractometer for the arrival of the next sample. When a new sample is detected, the previous voltammogram is plotted on the monitor, normally requiring about 4-7 s. At the end of the plot, the delay time is started and the same sequence of operations as for the previous sample is repeated for the new sample. Data plotting is autoscaled and no operator intervention is allowed. Displaying voltammograms on the screen is very useful since it provides visual assurance that the experiment is being carried out properly. If something appears to be wrong, the experiment can be aborted with the loss of only a few samples. At the end of the experiment the entire system is shut down.

The control program, written in H-P assembly language, is also provided with a nonflow mode which can analyze a single sample in a batch mode. Other utilities for data smoothing, analysis, and plotting are also available. All digital logic used was TTL LS series SSI and LSI integrated circuits. Much of this could be replaced to advantage with a microcontroller in a commercial instrument; however, construction of a prototype is often more easily accomplished with hard-wired logic. Program listings and detailed circuit diagrams are available from the authors on request.

Reagents and Chemical Tests. All solutions were prepared with doubly distilled water and reagent grade chemicals. Experiments were done at 23-25 $^{\circ}$ C in unbuffered solutions with either 1 M KCl or 1 M KNO_3 as the supporting electrolyte. All samples analyzed were 10.0 mL in volume and were prepared by dilution from stock solutions of 0.02 M $\text{Cd}(\text{NO}_3)_2 \cdot 4\text{H}_2\text{O}$ and $\text{Pb}(\text{NO}_3)_2$. In experiments in which samples were directly deoxygenated chemically, 0.2 mL of 1 M Na_2SO_3 was added to the sample (final $[\text{SO}_3^{2-}] = 0.02$ M). The other experiments were done by using the deoxygenator or sometimes by using only nitrogen segmentation.

The peristaltic pump speed was set for a flow rate of 5 mL/min. Sampling times between 35 s and 65 s were used, but most of the experiments were done with a 60-s sampling time and three-drop signal averaging. Although staircase voltammetry and normal pulse voltammetry were employed in some cases, square wave voltammetry was mainly used to test and evaluate the performance of the instrument.

RESULTS AND DISCUSSION

In any flow analyzer that uses a mercury drop electrode, the electrode characteristics will be very important in establishing the reproducibility of the analyses. A syringe-driven SMDE offers a wide variability in drop size for optimizing experimental conditions and provides freedom from capillary wall surface effects on drop size (7) since drops are grown by displacement rather than gravity. In addition our SMDE is free from problems such as the trapping of air in the valve system (7), shielding by a blunt capillary tip, high contact resistance, and the need to maintain a treated surface (26) commonly observed in commercial designs. A single unsilanized capillary was used in all experiments without any cleaning required during the testing period. The relative standard deviation of peak heights for Cd(II) samples of the same concentration was 0.5%, indicating excellent reproducibility of the drop surface area.

A major disadvantage of the syringe-driven SMDE is the limited volume of mercury available in the syringe. Experiments must be stopped during the refill time of the syringe, which is about 30 s. Alternatively, the SMDE controller logic and the computer program could be easily changed such that the syringe is refilled during a rinse time after every few samples. A second disadvantage is the sensitivity of drop volume to changes in temperature over time. This is not a drawback with this instrument since the life of each drop is very short.

The problems of flow noise, sample loss, and the carry-over of analyte between samples (memory effect) are common to all flow systems. To study sample loss and flow noise, samples were introduced directly into the electrochemical cell and the instrument was operated in the single sample mode. The peak heights obtained under these conditions were compared with those obtained with the flow system operating. When Tygon tubing was employed in the flow system during preliminary testing, significant sample loss at analyte concentrations below 5×10^{-6} M, as indicated by a rapid decay of peak current to zero, was observed. On replacement of Tygon with PTFE, voltammograms obtained under the two sets of conditions were identical indicating no sample loss and freedom from flow noise.

Memory effects, which can be a serious problem in SFA, are expected to arise in parts of the system in which there is no segmentation, e.g. the sampling arm or electrochemical cell, or in which the tubing is not hydrophobic, e.g. the refractometer. Cell design was found to be very important in this regard. The cell should be as small as possible and should not allow the flow stream to stagnate. Voltammetry should be performed as late in the sample life as possible, allowing each sample to rinse the cell thoroughly. With the system described above, the observed memory effect was 0.7%, as measured by comparing the peak height obtained for a 10^{-4} M Cd(II) solution with that obtained for a sequential blank solution. The memory effect was absent (the analyte concentration was below the detection limit) in the second of two sequential blank solutions following a solution of 5×10^{-4} M Cd(II). Problems arise when the concentration of a sample is lower than 10% of the previous sample. In this case, each sample can be alternated with a rinse solution, a larger sampling time can be used to rinse the system, or mathematical corrections can be applied (17).

Sampling time depends on the number of scans requested per sample and the rinse time. Each complete voltammogram takes about 5 s, which includes a 3-s delay between scans, drop growth time, a 1-s settling time, and the scan time. The 3-s delay between scans is required to open the flow control valve and fill the electrochemical cell with a new aliquot of sample for the next scan. If signal averaging is not employed, sampling times as low as 30 s can be used without significant memory effects.

The presence of dissolved oxygen is often a problem in reductive electrochemical detection. Square wave voltammetry is not particularly sensitive to oxygen, its reduction being irreversible, and the interference appears as an increase in base line, which is somewhat potential dependent, rather than a sharp peak. Thus less care is needed for oxygen removal than with other electrochemical techniques. Experiments on our system have shown that approximately 80% of the effect of dissolved oxygen can be removed simply by a combination of nitrogen segmentation and flowing nitrogen over the cell. About 90% of the effect is removed by non-exhaustive nitrogen purging in static experiments run under the same conditions. The most efficient removal of oxygen was effected by addition of sulfite plus use of the deoxygenator, followed by addition of sulfite only, use of the deoxygenator only, and nitrogen segmentation only. Although the addition of sulfite was most efficient for oxygen removal, it also lowered precision and produced an unexplained non-linearity in response at concentrations above 5×10^{-6} M in our experiments. Therefore sulfite was not used in further tests of the instrument. The deoxygenator by itself removed approximately 95% of the effect of oxygen.

Nitrogen segmentation alone was sufficient for determinations down to 10^{-7} M concentrations of Cd(II) and Pb(II). Other metal ions, which react at different potentials, might

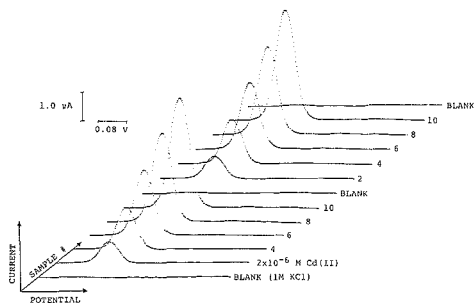


Figure 7. Square wave voltammograms of Cd(II) in 1 M KCl obtained by SFA.

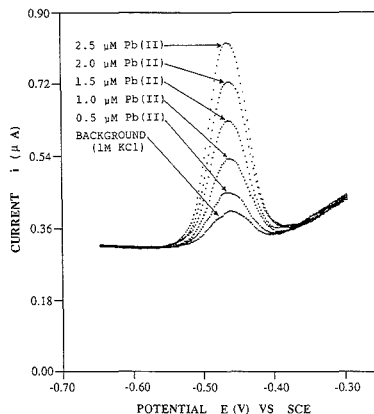


Figure 8. Square wave voltammograms of Pb(II) in 1 M KCl obtained by SFA. The concentrations listed are those added to the background KCl.

require more exhaustive oxygen removal for trace analysis. A smaller diameter flow tubing and finer segmentation with nitrogen would provide further oxygen removal from samples. In cases where sample matrices can be duplicated, background subtraction may prove useful for discrimination against dissolved oxygen since all samples are subjected to the same segmentation pattern and dwell time with nitrogen.

The linearity of response of the instrument was tested by analyzing series of samples with known concentrations of Cd(II) in the 2×10^{-6} to 5×10^{-4} M range. For example, Figure 7 shows 13 voltammograms in the concentration range of (2 to 10) $\times 10^{-6}$ M. These are identical with voltammograms obtained with a conventional static system. Linear regression analysis applied to the peak heights of these two sets resulted in a standard regression coefficient of 1.000 for both sets. The slopes of the sets were 0.376 ± 0.002 and 0.377 ± 0.003 A L mol⁻¹, respectively, indicating excellent linearity, sensitivity, and reproducibility. Similar experiments in the (2 to 10) $\times 10^{-5}$ and (1 to 5) $\times 10^{-4}$ M concentration ranges resulted in standard regression coefficients between 0.999 and 1.000 and slopes between 0.366 ± 0.002 and 0.370 ± 0.008 A L mol⁻¹. The standard regression coefficient, slope, and intercept over the entire concentration range (2×10^{-5} to 5×10^{-4} M) were 1.000, 0.3671 ± 0.008 A L mol⁻¹, $0.361 \mu\text{A}$, respectively. Comparable results were obtained with more than one electroactive species present (Pb(II) and Cd(II)) and without the use of the deoxygenator. The detection limits (2σ) obtained with the instrument were 5×10^{-8} M (6 ppb) and 4×10^{-8} M

(8 ppb) for Cd(II) and Pb(II), respectively.

Figure 8 shows the data from a standard addition experiment carried out to determine the Pb(II) concentration in BDH Analytical Grade KCl. The regression coefficient and slope for the peak heights are 0.999 and $0.388 \pm 0.008 \text{ A L mol}^{-1}$, respectively. The intercept of the graph, $5.81 \times 10^{-7} \text{ M}$, is the concentration of Pb(II) in the background (1 M KCl). This corresponds to 0.12 ppm Pb(II) in solution or 1.6 ppm of Pb(II) in solid KCl. In all of the above experiments oxygen was removed by flowing nitrogen over the cell, nitrogen segmentation, and use of the deoxygenator.

The analyzer described above could easily be modified to use solid electrodes in either the oxidative or reductive mode. Decreasing the volume of the electrochemical cell and increasing the flow rate could decrease the sample rinse time required to remove any memory effect and increase the sampling rate to over 200 samples/h. A smaller cell would also be needed to convert the system into an LC detector. In this case the column effluent would be introduced directly into the flow cell, an electrochemical scrubber such as that used by Hanekamp et al. (27) could be employed to remove the oxygen from the eluent, and a two-way valve used to divert the flow stream during the scan to reduce flow noise, if necessary.

ACKNOWLEDGMENT

The authors wish to thank David P. Surette for the mechanical design and construction of the SMDE.

LITERATURE CITED

- (1) Johnson, D. C.; Weber, S. G.; Bond, A. M.; Wightman, R. M.; Shoup, R. E.; Krull, I. S. *Anal. Chim. Acta* **1986**, *180*, 187-250.
- (2) Wang, J.; Ouziel, E.; Yarnitzky, C.; Ariel, M. *Anal. Chim. Acta* **1978**, *102*, 99-112.
- (3) Sarraueis, R.; O'Dea, J.; Osteryoung, J. *Anal. Chem.* **1980**, *52*, 2215-2216.
- (4) Thomas, M. B.; Msimanga, H.; Sturrock, P. E. *Anal. Chim. Acta* **1985**, *174*, 287-291.
- (5) Owens, D. S.; Sturrock, P. E. *Anal. Chim. Acta* **1986**, *188*, 269-274.
- (6) Thomas, M. B.; Sturrock, P. E. *J. Chromatogr.* **1986**, *357*, 318-324.
- (7) Scanlon, J. J.; Flaquer, P. A.; Robinson, G. W.; O'Brien, G. E.; Sturrock, P. E. *Anal. Chim. Acta* **1984**, *158*, 169-177.
- (8) Ploegmakers, H. H. J. L.; Van Oort, W. J. *Anal. Instrum.* **1987**, *16*, 467-486.
- (9) Janata, J.; Ruzicka, J. *Anal. Chim. Acta* **1982**, *139*, 105-115.
- (10) Kowalski, Z.; Kubiak, W. *Anal. Chim. Acta* **1984**, *159*, 129-137.
- (11) Lunte, C. E.; Wong, S.-Wen; Ridgway, T. H.; Heineman, W. R. *Anal. Chim. Acta* **1986**, *188*, 263-267.
- (12) Lunte, C. E.; Ridgway, T. H.; Heineman, W. R. *Anal. Chem.* **1987**, *59*, 761-766.
- (13) Wang, J.; Dewald, H. D. *Anal. Chim. Acta* **1983**, *153*, 325-330.
- (14) Wang, J.; Dewald, H. D. *Talanta* **1984**, *31*, 387-390.
- (15) Alexander, P. W.; Akapongkul, U. *Anal. Chim. Acta* **1984**, *166*, 119-127.
- (16) Scoari, C. A.; Brown, S. D. *Anal. Chim. Acta* **1985**, *178*, 239-246.
- (17) Yarnitzky, C. N. *Anal. Chem.* **1985**, *57*, 2011-2015.
- (18) Peled, D.; Yarnitzky, C.; Smyth, W. F. *Analyst* **1987**, *112*, 959-964.
- (19) Ramaley, L.; Wilson, G. S. *Anal. Chem.* **1970**, *42*, 606-611.
- (20) Jayaweera, P.; Ramaley, L. *Anal. Instrum.* **1988**, *17*, 365-384.
- (21) Jayaweera, P.; Ramaley, L. *Anal. Instrum.* **1986**, *15*, 259-277.
- (22) Jayaweera, P.; Ramaley, L. *Anal. Instrum.* **1986**, *15*, 241-257.
- (23) Superior Electric Co. *DC Stepping Motors*; Superior Electric Co.: Bristol, CT, 1976.
- (24) Sundem, T.; Cedergren, A.; Siemer, A. A. *Anal. Chem.* **1984**, *56*, 1085-1089.
- (25) Fraticelli, Y. M.; Meyerhoff, M. E. *Anal. Chem.* **1983**, *55*, 359-364.
- (26) Mairoza, P.; Johnson, D. C. *Anal. Chim. Acta* **1980**, *118*, 233-241.
- (27) Hanekamp, H. B.; Voogt, W. H.; Bos, P.; Frei, R. W. *Anal. Chim. Acta* **1980**, *118*, 81-86.

RECEIVED for review December 28, 1988. Accepted June 20, 1989. This work was supported in part by the Faculty of Graduate Studies, Dalhousie University. P.J. also wishes to acknowledge scholarship support from Dalhousie University.

Automated Titrations Using a Discontinuous Programmed Flow Analyzer

Dennis P. Arnold*

Centre for Analytical Science, Department of Chemistry, Queensland University of Technology, G.P.O. Box 2434, Brisbane, Queensland 4001, Australia

Russell M. Peachey, John D. Petty, and Denis R. Sweatman

Ionode Pty. Ltd., P.O. Box 52, Holland Park, Queensland 4121, Australia

The technique of automated discontinuous programmed flow analysis is described, together with a working prototype instrument employing syringe pumps driven by interchangeable cams. This technique relies on the cyclic generation of flow profiles for both a suction and a discharge pump, such that at various times sample only, reagent only, or a predefined combination of the two is conveyed via a mixing chamber to a detector. Different cam profiles allow a number of direct reading or reagent addition analysis methods, as well as both single and dual flow titrations. Results are presented for argentometric titrations of chloride in water using as detectors anodized silver microelectrodes contained in two alternative mixer/sensor assemblies. In the range of 60–160 mg/L, precision for analysis times of 30 s or less is typically better than 1%, with sample consumption of 0.9 mL. Accuracy for chloride determinations in city water samples is limited by the characteristics of the electrodes to ca. 2–3%. Cycle times for this instrument are selectable from 6 to 90 s. Carryover from sample to sample is negligible because of the incorporation of a sample flush step to commence each cycle. The operating characteristics of this analyzer were studied by using a conductivity detector, and pump displacement precision is better than 0.1%.

INTRODUCTION

In recent years, various automated methods of flow-based chemical analysis have been adopted enthusiastically. These have included continuous flow analysis (1–5), stopped flow analysis (6–8), and flow injection analysis (9–11). Almost universally, such methods have employed pumps (peristaltic or piston) operating in a discharge mode to convey samples, diluents, and reagents to detector systems, with or without active mixing. An alternative arrangement of pumps is possible, viz., one discharge and one suction pump. A difference between the suction and discharge flow rates allows aspiration of sample into the reagent or diluent stream. This principle has been applied to stopped flow analysis (12) and continuous flow analysis (13). A common feature of such schemes has been their operation with a constant flow rate differential between the pumps, thus maintaining a fixed ratio of sample to reagent volume. Constant flow rates were maintained, for example, by clock-driven stepper motors driving syringe pumps (12).

A conceptual advance on this simple "push-pull" pumping arrangement is to vary the flow rates of either or both pumps in a reproducible manner (14). By suitable programming of the flow rates, a wide variety of flow analysis methods becomes accessible, depending on the mixing, dispersion, and detection characteristics of the flow system (15). These include single or multiple reagent additions, as well as automated flow titrations (16–19). This arrangement is potentially compatible

with a range of detection methods.

One of several possible ways of generating known, variable flow rate differentials is to drive syringe pumps mechanically by using specifically profiled, interchangeable cams, linked to a common shaft. The operating principles and design of this instrument, as well as two self-contained mixer/sensor assemblies, are described below. The results of chloride determinations using two discontinuous flow argentometric titration techniques are presented. Analyses using reagent additions will be reported subsequently (20).

EXPERIMENTAL SECTION

Description of the Instrument. Pumping System. A schematic section view is shown in Figure 1. A rigid brass frame (A) with inset $3/8$ in. i.d. ball race bearings (B) supports the drive shaft (C), while the pump cylinders, valve block, and motor are fixed to the frame. The pistons (D) are identical $3/8$ -in. centerless ground and polished stainless steel rods with 1-mm center holes and concave ends to facilitate the elimination of bubbles. The stationary seals between the pistons and acrylic cylinders that make up the pump bodies consist of two adjacent compressed $1/16$ in. thickness Viton O-rings (E). Each cam profile is translated into linear piston movement by vertically sliding assemblies (F) comprising $3/8$ in. o.d. ball race cam followers, brass connecting rods, and spring returns (not shown). These assemblies are guided through holes in the top and bottom sections of the frame by the connecting rods. The cams (G) are made from $1/4$ in. plate stainless steel and are produced by wire cutting a 720-point computer-generated profile with linear interpolation between points on the circumference. The cams have minimum radii of 34.24 mm (suction pump) and 47.28 mm (discharge pump for single titration). The latter cam can be interchanged with that for a discharge pump for dual titrations with a minimum radius of 46.94 mm. The maximum radius for all cams is 60.00 mm. The corresponding displaced volumes are 1.83, 0.91, and 0.93 mL, respectively. The cams are press-fitted onto the square section steel shaft (C), which has been turned down at both ends to be an interference fit in the $3/8$ in. i.d. bearings.

A 30-V dc motor (Philips 4322-010-78010) with a 250:1 reduction gearbox (SAIA Series F) drives the shaft. Mounted on the motor shaft is a 25 pulse/revolution optical tachometer that is combined with a phase lock speed controller to enable precise speed control, with cycle times selectable from 6 to 90 s. Attached to the other end of the cam shaft is a 1000 pulse/revolution incremental encoder with marker pulse (Process Control and Automation 1A2B1A) for accurate determination of the angular position of the cams and thus the flow rates of the pumps. Teflon tubing of 1-mm i.d. connects the pumps to the acrylic valve block. The valves (H) are $1/8$ -in. stainless steel needles that slide through multiple $1/8 \times 1/4$ in. Viton O-rings and that are activated by common linkage to a third cam attached to the drive shaft. Fluid flows to and from the pumping/valve assembly are indicated by arrows in the figure. The operation of the valves is described in the Results and Discussion below.

Sensing System. Two chloride sensor cells and one conductivity cell have been used to obtain the present results, and these are referred to as cell 1, cell 2, and cell 3 below.

The sensor cells are made of acrylic blocks $70 \times 40 \times 25$ mm

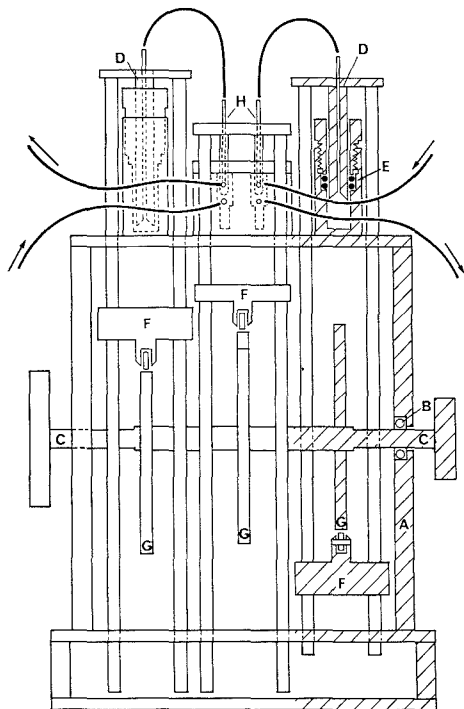


Figure 1. Vertical section view of the pumping and mechanical systems, the right-hand (discharge) syringe pump shown cut away (hatched), and fluid flow indicated by arrows, as follows: top left, to waste; top right, from titrant reservoir; bottom right, to mixer; bottom left, from detector. Lettering is the same as in the text. The motor is at the left-hand end of the shaft; the encoder is on the right.

having a common sample/titrant introduction and mixing configuration (Figure 2a), but differing in electrode arrangement (Figure 2b,c). A stainless steel sample tube (A) (0.8 mm i.d. \times 70 mm) extends into a vertical cavity (B) of 1.6-mm diameter and the titrant (C) enters this cavity 8 mm below the top of A. The sample and titrant streams unite coaxially before turning 90° into the horizontal mixing region (D) (1.6 mm \times ca. 40 mm to sensor). The mixing rod is an epoxy or glass encapsulated iron rod (overall diameter ca. 0.9 mm). The rod is positioned ca. 1 mm from the sensor for 30-s cycles. It was modified for 6-s cycles by adding a small right-angle arm at one end that detented in the entrance hole, thus preventing contact with the electrode surface at high flow rates. Plug (E) seals the hole used for insertion of the rod. The rod is vibrated laterally at frequencies up to 100 Hz by two 12-V electromagnets (F) (16-mm diameter) positioned in holes drilled in both sides of the block, with pole faces 3 mm apart (21).

In cell 1 (Figure 2a,b), the stream impinges on the surface of a flat 1 mm diameter Cl^- anodized Ag electrode set in a threaded poly(vinyl chloride) (PVC) body and then exits from the rear of the block at 80° to the mixer axis. A double-junction reference electrode (inner chamber Ag/AgCl/1 M KCl, outer electrolyte 0.1 M KNO_3 , ceramic constriction type) is isolated from the waste exit channel (1-mm diameter) by a vertical capillary (0.7 mm diameter \times 3 mm) that enters the waste exit channel ca. 2 mm downstream from the bend. The capillary is flushed with 0.1 M KNO_3 after 20–30 cycles to prevent AgCl from contacting the ceramic.

Cell 2 (Figure 2a,c) was designed primarily for derivative experiments. Two Cl^- anodized Ag wires (0.5 mm diameter \times 1.5 mm exposed length) in threaded PVC bodies are positioned perpendicular to the mixing channel and separated by 2.5 mm. This cell was also used for single sensor measurements, by re-

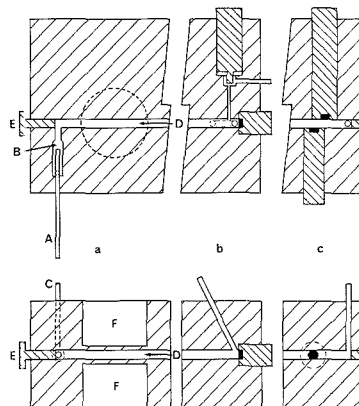


Figure 2. Schematic diagram of sensor cells (above, vertical section; below, horizontal section): (a) common sample and titrant introduction and mixing system; (b) cell 1 electrode configuration; (c) cell 2 electrode configuration. Threads have been omitted for clarity.

placing the downstream wire electrode with a double-junction reference electrode. Conductivity cell 3 is a variation of cell 2. In place of the threaded electrodes, two platinum rods (3-mm diameter, 3 mm apart) are pressed into slightly undersized vertical holes intersecting the flow path, with the mixing channel drilled through both platinum rods. The mixing rod extends through the holes in the platinum electrodes.

The potentiometric responses of all electrodes were measured by a dual high input impedance common mode rejecting amplifier (TPS 1852K) with the common potential taken from the brass frame of the instrument. Conductivity measurements were made with an analog meter of our own design. The respective outputs were further amplified and zero offset before digitizing (12-bit) and displaying on a personal computer with one data point recorded per pulse of the incremental encoder. Because of this variable amplification, sensor output graphs show an arbitrary y-axis scale. All measurements were carried out at room temperature (22–27 °C). Manual potentiometric titrations were carried out by the standard method (22).

Reagents. Chloride standards (60, 80, 100, 120, 140, 160 mg/L) were prepared by dilution of a 4000 mg/L stock solution prepared from dry NaCl (Ajax, A.R.). A 101.2 mg/L solution was used for discrimination tests. A single Brisbane water supply sample was used for all determinations. In all figures, the solutions mentioned above are represented by the letters a–f (calibration standards), g (101.2 mg/L), and h (city water), respectively. The titrant for ISE titrations was 2.82×10^{-3} M AgNO_3 (equivalent to 100 mg/L Cl^-) prepared by weighing AgNO_3 (Johnson-Matthey, A.R.) and containing 0.1 M KNO_3 as ionic strength adjuster (ISA). The titrant for conductivity titrations was ca. 1.5×10^{-2} M AgNO_3 . These solutions were stored in polypropylene bottles in the dark.

RESULTS AND DISCUSSION

Chloride was chosen as the analyte of interest because of the ease of fabrication of anodized silver microelectrodes in different configurations (e.g. flat surface, fine rod) and with the object of minimizing the sensor cell volume so that optimal comparisons between flow rate profiles and sensor response are possible. Moreover the AgCl electrode responds to both Ag^+ and Cl^- ions, and the precipitation of AgCl constitutes a stringent test of the capabilities of the analyzer. The conductivity cell was used because of that sensor's high stability and short response time. Results are reported here for the determination of Cl^- by both single and dual titrations.

The operation of the instrument is illustrated in schematic form in Figure 3. During the measurement cycle valves V1 and V2 connect the pump cylinders C1 and C2 to the sensor S; piston P1 expels liquid to the fluid junction J, while piston

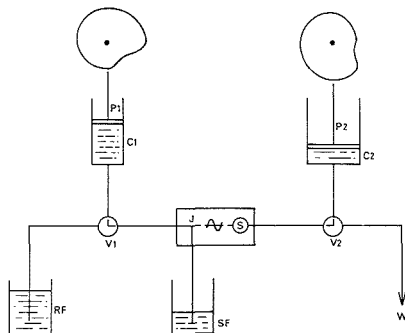


Figure 3. Schematic fluid flow diagram: C1, C2, pump cylinders; P1, P2, pump pistons; V1, V2, valves; SF, sample fluid reservoir; RF, reagent fluid reservoir; W, waste; J, fluid junction; S, sensor.

P2 withdraws at a greater rate so that sample fluid SF may be aspirated. No aspiration occurs if P1 and P2 generate equal flow rates; i.e. titrant only is pumped through the system. After agitation in the mixing chamber, the combined fluids pass sensor S and flow on to cylinder C2. At the end of the measurement cycle valves V1 and V2 are switched to the alternative positions and cylinder C1 refills with reagent fluid RF as cylinder C2 expels to waste W. The sensor response to the combined fluids is determined by the relative flow rates of pumps 1 and 2, the degree of mixing of the solutions, and the dispersion of the combined solutions during transport from the fluid junction to the sensor. In order to relate the sensor output directly to the flow rates, complete mixing and negligible dispersion are required. Such conditions are approached if the mixer volume is minimized, the sensor is located within the mixing region, and transverse mixing is thorough. For a step change in the flow rate of piston P1, the actual time response of sensor S is determined by parameters of the mixing/sensing cell such as fluid junction design, cell volume, and mixing efficiency as well as the sensor's inherent response time. For a change in sample fluid SF, the volume of the aspiration tube also affects the initial time response. In the present configuration cylinder C2 has an active volume of 1830 μL , while the cell volume with the rod in place is 60–70 μL and the aspirator tube volume is ca. 30 μL .

Single Titration. The cycle used in the present version of the instrument is shown in Figure 4. In Figure 4a,b, the cam profiles are plotted in millimeters relative to the minimum radius and flow rates as amplified cam slope displayed on the same scale. The cycle will be discussed in terms of the lettered regions A–E.

The cycle begins with a short, steep increase in suction pump cam radius to point A, while the discharge pump is stationary. This causes aspiration of sample and an initial flush of the system with new sample. The next short section of both cams establishes the flow rate ratio at the start of the titration at B as 4:1 sample:titrant, to allow the flow system to equilibrate and to allow any turbulence resulting from the sudden change of flow rates to subside. The suction pump cam profile then continues as a linear incremental spiral to point E. However, the titrant cam profile changes at B to a quadratic function ($r = (1.04907 \times 10^{-4})(x + 64)^2 + \text{constant}$, where x = degrees of cam rotation), whose constants are chosen to increase linearly the flow rate of titrant such as to generate flow rate ratios as shown in Figure 4d. The ratio of sample rate to titrant rate thus changes from 4:1 at B to 1:4 at C, so carrying out a single flow titration during this section. An end point will be reached provided that the sample concentration is not less than one-quarter nor more than 4 times

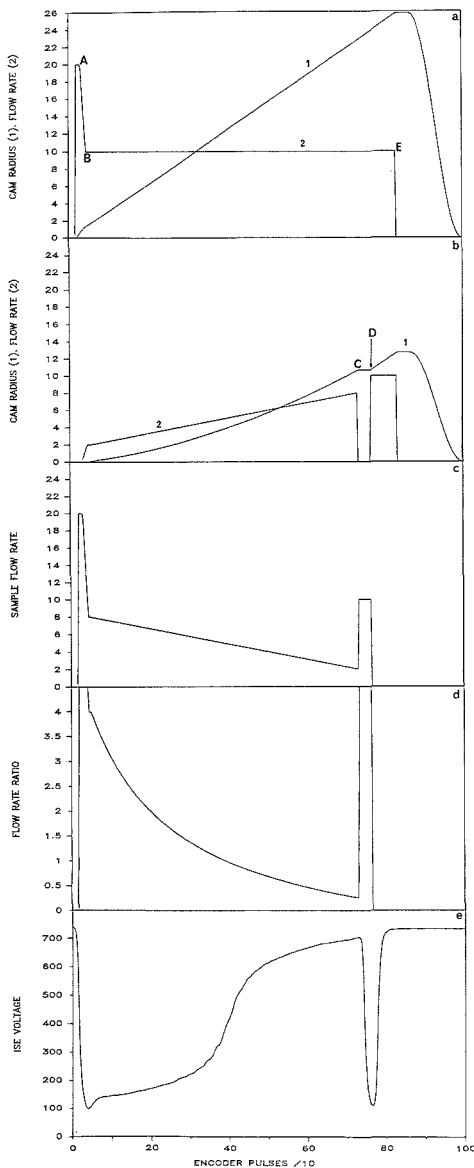


Figure 4. Cycle for single titration: (a) suction pump cam radius (1) and flow rate (2); (b) discharge pump cam radius (1) and flow rate (2); (c) sample flow rate; (d) ratio of sample flow rate to titrant flow rate; (e) output of ISE during measurement cycle. Arbitrary y-axis units (see text).

that of the titrant. For a 1:1 stoichiometry, the point where the flow rates are equal represents the end point of the titration of equimolar solutions, assuming instantaneous detector response. In practice, a time lag occurs, and the detected end point is shifted to the right.

At point C, the titrant cam becomes circular again for the section to D. Since the suction pump is still being withdrawn at constant rate, titrant flow is now zero, and the sensing

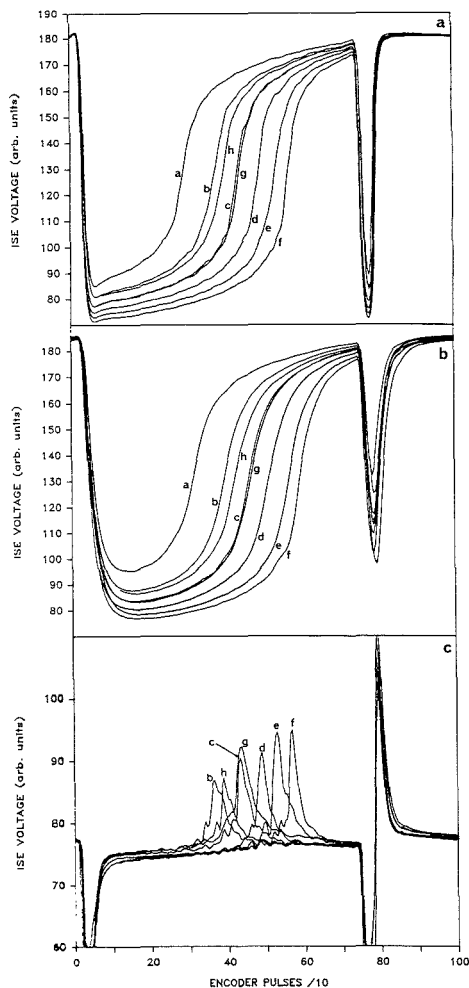


Figure 5. (a) Single titration curves for 30-s cycle. (b) Single titration curves for 6-s cycle. (c) Direct derivative single titration curves for 30-s cycle. Letters a-h correspond to calibration standards and samples as described in the text.

system is flushed with neat sample again up to point D. The length of this section (sample spike) in this version is too short to allow an ISE to reach equilibrium, but the reading at D is still of diagnostic value. For example, the height of the spike is sensitive to changes in sensor response time, any variations of which will affect the equivalence point in a flow titration. From D to E, the titrant cam profile becomes parallel to that of the suction pump, so that now sample is excluded, and the system is flushed with neat titrant. The detector now records a base-line value for titrant, which enables any drift to be detected. At point E, both cams briefly become circular while the valves change as described above, and then the radii of both cams contract rapidly to reset the system for the start of the next cycle.

Figure 4e, an actual response curve, illustrates (i) the zone at A corresponding to the Cl^- sample flush; (ii) the zone A-B, the lead-in to the start of the titration; (iii) the titration zone B-C where the ISE responds to the change from Cl^- sample

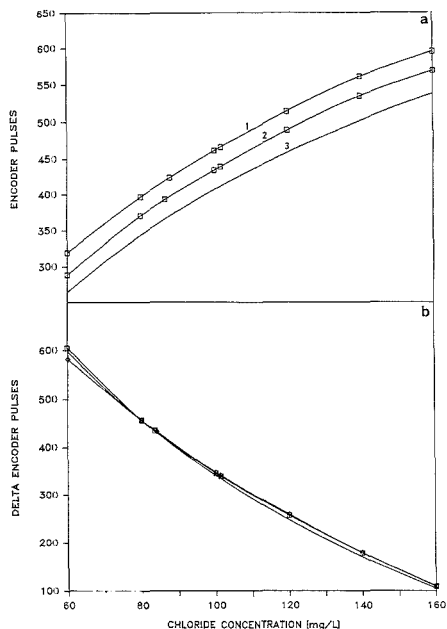


Figure 6. (a) Calibration curves for the data sets of Figure 5a,b: (1) 6-s cycle, (2) 30-s cycle, (3) calculated from flow rate ratios and titrant concentration. (b) Experimental (\square) 30-s cycle, (\diamond) 6-s cycle and calculated calibration curves for dual titrations.

in excess to Ag^+ titrant in excess; (iv) the zone C-D as Cl^- sample is again aspirated (where the response time of the mixer/sensor cell and the finite size of the cam follower distort the theoretically square peak); and (v) the zone at E where only titrant is pumped. The zone B-C of each curve is therefore similar to the potentiometric titration curve typical of a static titration. In this case the concentration of the product species depends on both the concentrations of the reactants and the relative quantities of the reactant species, i.e. the flow rate ratio. The curve of Figure 4e has been shifted to align the experimental response curve with Figure 4a-d.

Figure 5a shows the response curves for the Cl^- standards (60–160 mg/L) and that for city water, with a cycle time of 30 s, while Figure 5b displays results for a cycle time of 6 s, both obtained by using cell 1. The figures illustrate (i) the direct indication of Cl^- concentration in the sample-only A-B and D zones; (ii) the shift in inflection point with Cl^- concentration in the titration zone B-C; (iii) the stable AgNO_3 response in zone E; and (iv) the broadening of all features for the 6-s cycle time as the sensor response time becomes an appreciable fraction of the cycle.

The end point of the titration can be ascertained by taking the point of inflection. Because the noise level on the derivative of the raw 30-s titration curves prevented accurate estimation of the inflection points, a least-squares fit of a suitable function was performed on the original titration curves (Figure 5a,b). This function was derived from the modified Nernst equation

$$E = E'_0 + RT/F \ln ([\text{Ag}^+]/[\text{Cl}^-])$$

which applies to a solution of constant ionic strength (e.g. containing 0.1 M KNO_3), where the ratio of activity coefficients is constant. In the titration zone B-C, the concentration of KNO_3 increases by a factor of 4, but the variation in activity

coefficient ratio was considered small enough for it to be ignored in the fitting function. Calibration curves (Figure 6a) of inflection points for the standard samples (measured as the number of pulses from the encoder marker pulse) were used to determine the unknown concentrations. The predicted curve 3 is an x - y transformation of the flow rate ratio function (Figure 4d) with the 1:1 ratio scaled to 100 $\mu\text{g/L}$ Cl^- ("transformed curve"), which has then been y -axis shifted in an attempt to eliminate all but the sensor response time contribution. The encoder origin position, transfer of fluid from fluid junction to sensor, and sensor response time all shift the equivalence points so that the calibration curves are higher than the transformed curves. By addition of the encoder pulse difference between the sharply defined point C on the sample flow rate (curve 2, Figure 4b) and the average of the corresponding point for the experimental curves (Figure 5a) to the transformed curve, the encoder origin offset and fluid delay are incorporated, while the effect of sensor response time is largely excluded. Thus the ordinate differences between the two calibration curves and this y -shifted transformed curve reflect the sensor response time. Curves from measurements with longer cycle times should approach a limiting value nearer the y -shifted transformed curve. Although the curves are not coincident, the shapes are similar, so that an approximate calibration curve could be generated by further y -shifting to pass through one experimental point.

A significant advantage of this flow titration method is that the determination of the inflection point can be performed by measuring a response derivative directly. This is achieved by placing two sensors in the stream separated by a small linear displacement (cell 2) and removes the need for a reference electrode. The differential response curves for a 30-s cycle are displayed in Figure 5c. Results were also obtained with a 6-s cycle time and, as expected, display broadening of all features. End points of the titrations were estimated manually, using the centers of mass of the peaks rather than the peak maxima.

Conductometric titrations were also performed, and response curves are shown in Figure 7a. These curves illustrate (i) the concentration-dependent conductivities of the standards at point A and between C and D; (ii) the decrease in conductivity to the end point followed by an increase with excess AgNO_3 ; (iii) the stable AgNO_3 response after point E, and (iv) the abnormal behavior of the city water sample due to the other nonreacting ionic components. The dilution of these ions between B and C contributes a linearly decreasing conductivity component. End points were measured manually as the point of intersection of the linear sections. The figure also includes a trace (i) of the conductivity of distilled water, which defines the magnitude of the conductivity change as the AgCl precipitates.

Dual Titration. This method is analogous to the triangle programmed titration technique of Pungor et al. (23-25), as applied to continuous stream titrimetry, and demonstrates the versatility provided by the use of interchangeable discharge pump cams. The cam profiles relative to the minimum radius, flow rates, flow rate ratio, and actual response curves are shown in Figure 8a-e. The initial flush with new sample is followed by a short section that establishes a sample:titrant ratio of 2:1 and allows turbulence to subside. The constant withdrawal of the suction pump continues while the discharge pump cam profile describes a function whereby the flow rate changes linearly from 2:1 at B to 1:2 at C, and then inverts and the reverse titration is conducted to D, where the ratio again reaches 2:1. After D the discharge pump ramps up to point E where its rate is equal to that of the suction pump. Within section E-F, titrant only is flushed through the cell and the sensor records the voltage for pure titrant. At F, both

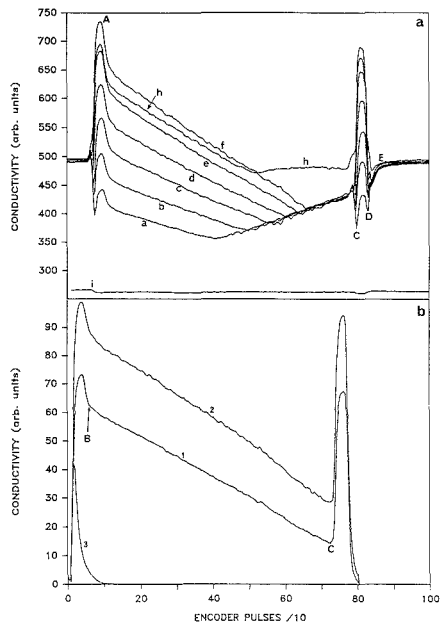


Figure 7. (a) Conductometric titration curves obtained with cell 3, samples coded as before, together with distilled water base line (i). (b) Dilution experiments: curve 1, dilution of 140 $\mu\text{g/L}$ Cl^- with water; curve 2, dilution of 0.1 M KCl with water; curve 3, first cycle with water only following 0.1 M KCl .

cams become circular for the valve changes, and then the syringes reverse to reset for the next cycle. The measured response curve (Figure 8e) illustrates (i) the sample flush zone A; (ii) zone A-B corresponding to flow stabilization; (iii) the dual titration zone B-D; and (iv) the zone after E where titrant only is pumped through the sensor cell. Zone B-D now consists of two sequential potentiometric titration curves, with the complication that for some ISE's the speed of response is dependent on the sign of change of the potential. This is not markedly the case for AgCl as can be seen from the sample spike (C-D) in Figure 5. The end points of the two titrations were obtained by locating the inflection points, using a least-squares fit of the individual halves of the curves, as described for the single titrations. The difference in these end points should be independent of the time response of the sensor as both are similarly delayed.

Figure 9a shows the response curves for the Cl^- standards (60-160 $\mu\text{g/L}$) and that for city water obtained by using cell 2 and a cycle time of 30 s. This figure shows (i) the shift in both end points with changing Cl^- concentration in the titration zone B-D and (ii) the variation of the response curve of the city water sample relative to those of the Cl^- standards. Results were also collected for a 6-s cycle, and as usual showed a broadening of all features. The differences in position of the two end points were used to calculate the calibration data (Figure 6b). The predicted curve is origin independent, and close correspondence between theoretical and experimental values is found because of the cancellation of the mixer/sensor response time (cf. Figure 6a). This emphasizes an advantage of the dual technique, namely that for moderate accuracy, no calibration is required. In this case concentrations of Cl^- can be determined within 3%, without calibration.

The direct derivative technique was also used to determine the inflection points using cell 2, as described for the single

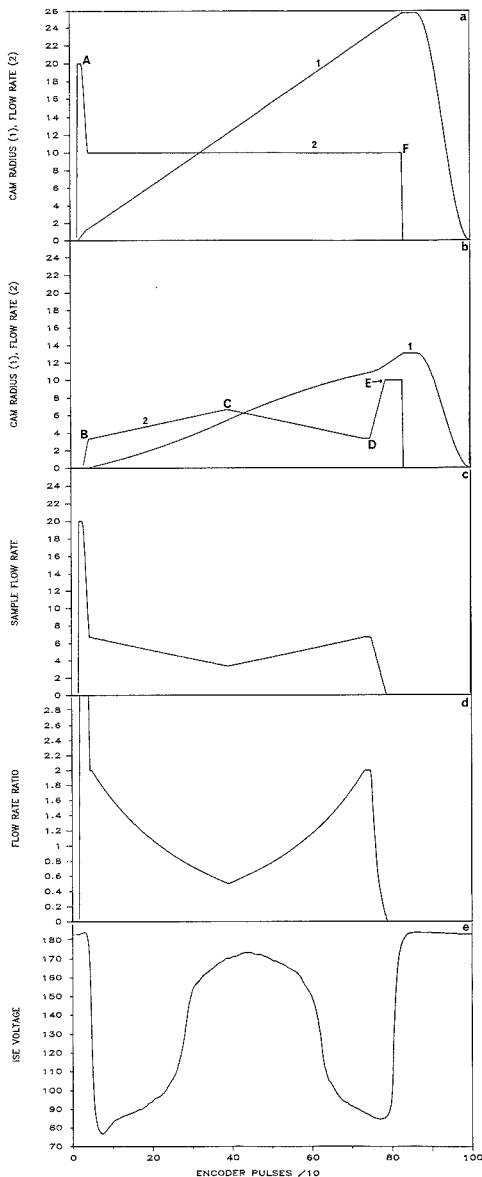


Figure 8. Cycle for dual titration: (a) suction pump cam radius (1) and flow rate (2); (b) discharge pump cam radius (1) and flow rate (2); (c) sample flow rate; (d) ratio of sample flow rate to titrant flow rate; (e) output of ISE during measurement cycle. Arbitrary y-axis units (see text).

titrations (Figure 9b). The time displacement of the inflection points for the city water is again apparent. Separate calibration curves for the forward and reverse halves of the titration yielded concentrations of 89 and 81 mg/L, respectively, whereas treatment using the usual difference method gave 85.2 mg/L. This may be explained by either an increase in the sensor response time or a modification of the response by other ionic components, as expected for the AgCl electrode (26).

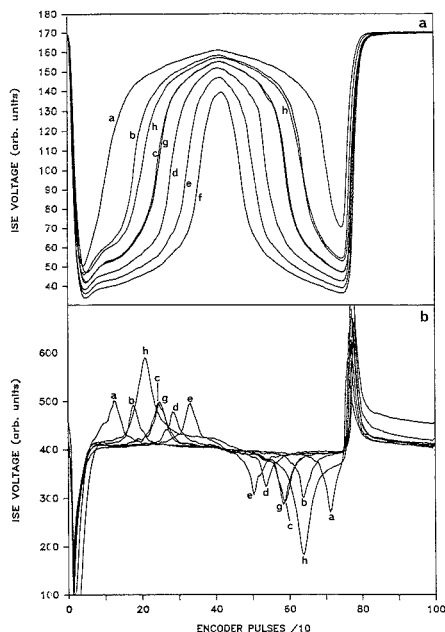


Figure 9. (a) Dual titration curves for 30-s cycle. (b) Direct derivative dual titration curves for 30-s cycle.

Evaluation of Instrument Parameters. An evaluation of parameters such as flow rate accuracy and reproducibility should ideally be undertaken using a flow rate sensor. In the absence of one with appropriate resolution, measurements were made using conductivity cell 3.

Flow rate ratio parameters were obtained by using the single titration cam, replacing the titrant with distilled water, and using the 140 mg/L Cl^- standard as sample. In this case the concentration of Cl^- in the sensed mixture is proportional to the sample flow rate divided by the suction pump flow rate if mixing is perfect and dispersion negligible. For the titration section B-C (Figure 4) this should be a 4-fold linearly decreasing concentration. The experimental curve 1 (Figure 7b) illustrates three features. Firstly, an approximately 4-fold decrease in conductivity occurs, which confirms that the measured curve closely resembles that expected from the cam profiles. This ratio, in conjunction with the reproducibility of sharp features in all curves, suggests that mixing is adequate. Secondly, the degree of dispersion is low, as can be seen from the shape of the sample spike (section C-D). All time and dispersion dependent phenomena contribute to the distortion of this spike, which amounts to an interval of ca. 15 pulses or only 2% of the titration section. Finally, deviations from linearity are small, considering several factors could contribute to errors, e.g. (i) the small deviation from a linear dependence of conductivity on concentration in the range measured, (ii) the characteristics of cell 3, and (iii) flow rate variations. These may arise from mechanical sources such as cam inaccuracies, shaft eccentricity, and bearing play and are probably responsible for the small irregularities on the curves in the titration section. It should be noted that it is the flow rate ratio that is measured by this method, not the individual flow rates, so features on the curve could arise from either or both pumps. A calibration curve for the titration of a number of standards generates points on the actual flow rate ratio curve. Variations of the ratio from theoretical are apparent in the calibration plots (Figure 6).

Table I. Results of Chloride Determinations (mg/L)

method	city water	101.2 mg/L standard
(1) single titratn		
(a) 30 s	86.6 ± 0.3	101.7 ± 0.3
(b) 6 s	87.9 ± 0.5	101.8 ± 0.5
(c) 30-s deriv	87.2 ± 0.3	100.3 ± 0.3
(d) 6-s deriv	87.6 ± 0.5	100.0 ± 0.5
(2) dual titratn		
(a) 30 s	83.6 ± 0.5	101.4 ± 0.5
(b) 6 s	84.1 ± 0.5	101.3 ± 0.5
(c) 30-s deriv	85.2 ± 1.0	101.7 ± 1.0
(3) single titratn (conductivity)		
(a) 30 s	84.1 ± 1.0	100.5 ± 1.0
(4) static macro titratn	86.3	

The reproducibility of the piston displacement of both pumps was also determined by conductivity measurements. The integral of a base-line-corrected conductivity curve for the dilution of a sample with distilled water is related to the displacement of the pistons. Integrations of four equal width zones within the titration section, and the total area, were obtained for seven 30-s cycles of the dilution of 0.1 M KCl with distilled water (e.g. curve 2, Figure 7b). The relative mean deviation of integrals for the quarter sections was less than 0.1%, and for the total integral was 0.03%. In terms of piston travel, this uncertainty corresponds to a mechanical error of less than 10 μm and represents the upper limit of the piston displacement reproducibility as it includes variations due to the sensor.

The reproducibility of the flow rate ratio can also be estimated from these data. The relative mean deviation of the conductivity profiles was calculated for the seven dilutions and ranged from 0.3% to 1.0% across the titration zone, with a value near the 1:1 point of 0.4%. Again this represents an upper limit on reproducibility and is similar to the error estimated from the variation of titration end points (Table I).

In Figure 7b, curve 1 (dilution of 140 mg/L Cl⁻) has been amplified to the same ordinate as curve 2 (dilution 0.1 M KCl), and the different responses illustrate the nonlinear dependence of conductivity on concentration in the latter solution.

Cell 3 was also used to monitor the rate at which liquid in the system from a previous sample cycle is flushed through the mixing and sensor region in the next cycle, i.e. sample carryover. Figure 7b illustrates the effects with two consecutive curves, one from the last of a series of samples of 0.1 M KCl (curve 2) followed by a sample of distilled water with the discharge pump containing distilled water. Curve 3 shows the decay in conductivity as the water sample flush removes the 0.1 M KCl in the probe/mixing/sensing conduit, and then the stabilization to the base line. The duration of the decay indicates that carryover from one sample to the next affects only the first 30 pulses of the total titration region of ca. 700 pulses.

Summary of Results. The Cl⁻ concentrations for the city water and the 101.2 mg/L discrimination sample determined from the calibration plots are presented in Table I. The values were obtained by averaging measurements of at least two complete sets of standards and samples, and the estimated errors were calculated as half of the range of intersections of the sample end points on the mean calibration curves. The discrimination sample was analyzed with an accuracy of better than 1.2%, with several methods giving better than 0.5%. The most inaccurate are the 6-s derivative and conductivity techniques. The former result can be explained by the sensor response time being a significant fraction (ca. 3%) of the cycle time. The conductivity titrations suffer from larger uncer-

tainties in end points because of the more gradual slope change. However, the reproducibility of the results from all methods is still good, suggesting that an acceptable level of accuracy can be achieved even with cycle times as low as 1 s.

These results may be compared with those obtained from the triangle programmed argentometric flow titration of Cl⁻ in wastewater, which yielded standard deviations for single samples of 1-2% (24, 27). A continuous flow two-point titrimetric method has been reported for Cl⁻ at levels below 18 mg/L (28). Precision of 0.9% and accuracy of 2% were found, results that are comparable to those reported here.

The results for the city water sample highlight problems inherent in the use of ion selective electrodes. Clearly the single titrations give high reproducibility and are internally consistent, but the results differ from those obtained with the dual system. While the dual titrations suffer less from effects due to system time lags, the inherent asymmetry of the Ag/AgCl ISE in the multicomponent city water sample still leaves a residual uncertainty in the absolute value for Cl⁻ concentration. Although precision for this application is apparently better than 1%, accuracy is likely to be in the range of 2-3%, as it is limited by the performance of the electrodes.

CONCLUSION

The reproducibility of these results is not the best performance anticipated for this instrument. For the case chosen, the precision is limited by the characteristics of the sensor, the eventual fouling of the flow lines and electrodes by precipitated AgCl, and the inherently broad end points in the concentration range studied. A stable fast detector and suitable titration reaction involving a sharp end point and no precipitation would better characterize the fundamental accuracy and precision of the instrument as a titrator. This study is in progress. The conductivity/dilution results indicate that averaged flow rates can be defined within 0.1% by using the principles embodied in the basic design. Discontinuous flow analysis will facilitate a wide variety of flow analyses by virtue of the flexibility provided by reproducible programmed flow rates.

ACKNOWLEDGMENT

We thank C. J. Moore for critically reading the manuscript and R. E. Pink of Electronic Innovations Pty. Ltd. for designing and constructing the motor power supply, and for providing general advice.

LITERATURE CITED

- Skeggs, L. J. *Anal. Chem.* **1966**, *38*, 31A.
- Mottola, H. A. *Anal. Chem.* **1981**, *53*, 1312A.
- Snyder, L. R. *Anal. Chim. Acta* **1980**, *114*, 3.
- Snyder, L. R.; Levine, J.; Stoy, R.; Conetta, A. *Anal. Chem.* **1976**, *48*, 942A.
- Patton, C. J.; Crouch, S. R. *Anal. Chim. Acta* **1966**, *179*, 189.
- Bartels, H.; Walsler, P. *Fresenius' Z. Anal. Chem.* **1983**, *315*, 6.
- Bartels, H.; Walsler, P. *Fresenius' Z. Anal. Chem.* **1983**, *315*, 109.
- Malmstadt, H. V. *Analyst* **1980**, *105*, 1018.
- Ruzicka, J.; Hansen, E. H. *Flow Injection Analysis*; Wiley: New York, 1981.
- Betteridge, D. *Anal. Chem.* **1978**, *50*, 832A.
- Riley, C.; Aslett, L. H.; Rocks, B. F.; Sherwood, R. A.; Watson, J. D.; Mergon, J. *Chin. Chem.* **1983**, *29*, 332.
- Bartels, H.; Mez, H.; Huber, W.; Stoiz, H. (Ciba-Geigy Corp., Ardsley, NY). U.S. Patent 4,333,356, 1982.
- Herron, R. E. (Technicon Instrument Corp., Tarrytown, NY). U.S. Patent 3,669,936, 1972.
- Petty, J. D.; Peachey, R. M.; Sweatman, D. R. (Ionode Pty. Ltd., Tenynson, Australia). Int. Patent Appl. PCT/AU86/00323, 1986.
- Poppe, H. *Anal. Chim. Acta* **1980**, *114*, 59.
- Fleet, B.; Ho, A. Y. W. *Anal. Chem.* **1974**, *46*, 9.
- Abicht, S. M. *Anal. Chim. Acta* **1980**, *114*, 247.
- Pungor, E.; Feher, Z.; Nagy, G.; Toth, K. *CRC Crit. Rev. Anal. Chem.* **1982**, *14*, 175.
- Blaedel, W. J.; Laessig, R. H. *Anal. Chem.* **1964**, *36*, 1617.
- Arnold, D. P.; Peachey, R. M.; Petty, J. D.; Sweatman, D. R., unpublished work, Ionode Pty. Ltd., 1988.
- Sweatman, D. R.; Petty, J. D.; Peachey, R. M. (Ionode Pty. Ltd., Tenynson, Australia). Int. Patent Appl. PCT/AU88/00054, 1988.

- (22) *Standard Methods for the Examination of Water and Wastewaters*, 16th ed.; American Public Health Association: Washington DC, 1985; pp 290-292.
- (23) Nagy, G.; Feher, Z. S.; Toth, K.; Pungor, E. *Anal. Chim. Acta* 1977, 91, 87.
- (24) Nagy, G.; Feher, Z. S.; Toth, K.; Pungor, E. *Anal. Chim. Acta* 1977, 91, 97.
- (25) Toth, K.; Nagy, G.; Feher, Z.; Horvai, G.; Pungor, E. *Anal. Chim. Acta* 1980, 114, 45.

- (26) Van Staden, J. F. *Anal. Chim. Acta* 1986, 179, 407.
- (27) Nagy, G.; Pungor, E.; Toth, K.; Havas, J.; Feher, Z. (EGYT, Budapest, Hungary). U.S. Patent 4,120,657, 1978.
- (28) Harai, H.; Waizaka, Y.; Okazaki, S. *Anal. Chem.* 1986, 58, 1502.

RECEIVED for review December 14, 1988. Accepted June 10, 1989.

CORRESPONDENCE

Exchange of Comments on Identification and Quantitation of Arsenic Species in a Dogfish Muscle Reference Material for Trace Elements

Sir: Marine organisms generally accumulate substantial amounts of arsenic, and information on the arsenic complex is quite important to evaluate the toxicological implications as well as to elucidate the cycling of the element in the marine environment. The ubiquitous nature of arsenobetaine in marine animals has been well documented (1, 2), but there is only limited information on the presence/absence of other arsenic species in the samples. Among the arsenic species, arsenocholine has attracted attention (3, 4). Arsenocholine is expected to be a precursor of arsenobetaine (3, 4). Furthermore, it was speculated to be a constituent of lipid-soluble arsenic (5), though the major lipid-soluble arsenic in a macroalga is recently identified as a diacylated derivative of arsenic-containing ribofuranoside (6). We have developed a combination of high-performance liquid chromatography (HPLC) with inductively coupled argon plasma atomic emission spectrometry (ICP-AES) for the chemical speciation of arsenic (7, 8) and analyzed arsenic species of various marine animals, including fish, crustaceans, and molluscs (9). We could not detect arsenocholine in any of them, but found a strong basic species identified as tetramethylarsonium ion in some of the samples (9).

Recently, Beauchemin et al. identified and quantified arsenic species in a dogfish muscle reference material, DORM-1, and reported the presence of trace amounts of arsenocholine (10). The detection of arsenocholine reported before their paper had been limited in shrimp samples (3, 11, 12). Therefore, we examined the reference material together with another one, DOLT-1, by using an HPLC/inductively coupled plasma mass spectrometry (ICP-MS) optimized for the speciation of arsenic (13).

EXPERIMENTAL SECTION

Sample. The reference materials DORM-1 (dogfish muscle) and DOLT-1 (dogfish liver) (14) were obtained from the National Research Council of Canada.

Reagents. Fifteen water-soluble arsenic compounds reported so far from the marine samples were used as the authentic standards (Table I). They were prepared as reported previously (9, 13). All the chemicals and solvents were the commercial products of reagent grade or special grade for LC but were selected carefully to keep the contaminated arsenic and chloride levels as low as possible. 1-Butanesulfonate sodium salt was used after being recrystallized twice from ethanol (95%).

Instrumentation. An ICP-MS, PMS100 (Yokogawa Electric Co. Ltd., Japan), was used as the arsenic-specific detector for HPLC. Quantitation of arsenic in the sample was done by an ICP-AES (JY-38; Seiko Electric Co. Ltd., Japan) after wet digestion by nitric acid. The operating conditions of the ICP-MS, the chromatographic conditions, and the construction of the

Table I. Structures of Arsenic Standards

(I) AsO_4^{3-} , (II) AsO_3^{2-} , (III) $\text{CH}_3\text{AsO}_3^{2-}$, (IV) $(\text{CH}_3)_2\text{AsO}_2^-$, (V) $(\text{CH}_3)_3\text{AsO}$, (VI) $(\text{CH}_3)_4\text{As}^+$, (VII) $(\text{CH}_3)_3\text{As}^+\text{CH}_2\text{CH}_2\text{OH}$, (VIII) $(\text{CH}_3)_3\text{As}^+\text{CH}_2\text{COO}^-$, (IX) $(\text{CH}_3)_2\text{As}(\text{O})\text{CH}_2\text{CH}_2\text{OH}$

	R ₁	R ₂	R ₃
X	$(\text{CH}_3)_2\text{As}(\text{O})-$	-OH	-OH
XI	$(\text{CH}_3)_2\text{As}(\text{O})-$	-OH	$-\text{OP}(\text{O})_2\text{OCH}_2\text{CH}(\text{OH})\text{CH}_2\text{OH}$
XII	$(\text{CH}_3)_2\text{As}(\text{O})-$	-OH	$-\text{SO}_3^-$
XIII	$(\text{CH}_3)_2\text{As}(\text{O})-$	$-\text{NH}_3^+$	$-\text{SO}_3^-$
XIV	$(\text{CH}_3)_2\text{As}(\text{O})-$	-OH	$-\text{SO}_4^-$
XV	$(\text{CH}_3)_3\text{As}^+$	-OH	$-\text{SO}_4^-$

system were same as those given in the previous report (13) except that Inertsil ODS-1 (4.6 × 250 mm; Gasukuro Kogyo, Japan) was used instead of Inertsil ODS-2 for ion-pair chromatographies. In accordance with this column change, the retention times of the arsenic species changed to some extent from those in the previous report (13). The elution buffer at pH 4.2 was prepared by the addition of ammonia to the pH 3.0 buffer.

Extraction and Chemical Speciation of Water-Soluble Arsenic Compounds from DORM-1 and DOLT-1. To the reference material (0.25 g) in a 10-mL centrifuge tube was added 5 mL of methanol/water (1:1, (v/v)), and the tube was sonicated for 15 min in an ultrasonic bath. The extract was collected after centrifugation. The extraction process was repeated 5 times, and the extracts were combined, evaporated to dryness, dissolved in 5 mL of water, and filtered through a membrane filter (Minisart NML, Sartorius GmbH, West Germany). An aliquot (typically 10 μL) for ion-pair chromatographies and 20 μL for gel permeation chromatography of the extract was injected into the HPLC, and the ion count at $m/z = 75$ was monitored. To check the interference by the molecular ion $^{40}\text{Ar}^{35}\text{Cl}$, the ion count at $m/z = 77$ (corresponding to $^{40}\text{Ar}^{37}\text{Cl}$) was monitored under the same condition.

RESULTS AND DISCUSSION

In addition to arsenobetaine, various kinds of water-soluble arsenic compounds have been reported from marine organisms (Table I). To identify these 15 arsenic species unambiguously, we have developed a combination of three HPLC conditions with different separation principles: i.e., gel permeation, ion-pair chromatography to separate anions (pH 6.8; pairing ion tetraethylammonium), and ion-pair chromatography to separate cations (pH 3.0; pairing ion 1-butanesulfonate) (13). In each case, the elution buffer was optimized to obtain a good

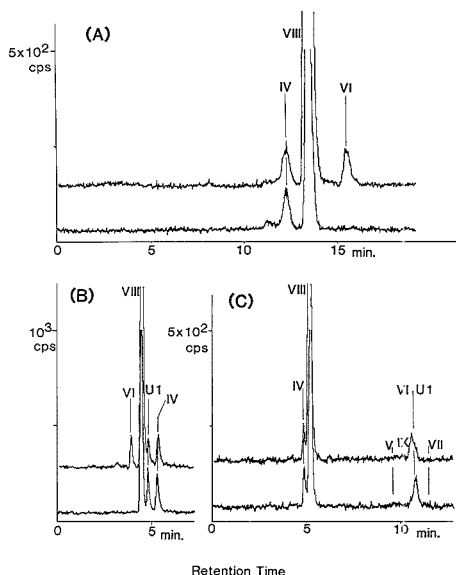


Figure 1. Chromatograms of the extracts of DORM-1 and DOLT-1 under three different column conditions: (A) GS220 (pH 6.8), (B) Inertsil ODS-1 (pH 6.8), (C) Inertsil ODS-1 (pH 3.0). The elution positions of some authentic standards (V, VII, and IX) are given in the figure (Figure 1C). In each figure, the chromatograms of DORM-1 and DOLT-1 are shown in the upper and lower lanes, respectively. See text for details.

separation within a reasonable time (within or around 15 min). Furthermore, the buffers were constructed by organic ions to prevent deposit of nonvolatile materials in the ICP-MS.

The chromatograms of arsenic species in the extracts of DORM-1 (dogfish muscle) and DOLT-1 (dogfish liver) are shown in Figure 1. As reported by Beauchemin et al. (10), arsenobetaine (VIII) was present as the dominant species in the extract of DORM-1 (Figure 1, upper chromatograms). It was dominant, too, in the extract of DOLT-1 (Figure 1, lower chromatograms). In addition to this, three minor arsenic species were detected in the extract of DORM-1. Based on the retention times under the three chromatographic conditions, two of them were identified as cacodylate (IV) and tetramethylarsonium ion (VI). DOLT-1 did not contain a detectable amount of tetramethylarsonium ion (Figure 1A,B). Contrary to the report of Beauchemin et al. (10), arsenocholine (VII) was not detected (Figure 1C, Figure 2). On the other hand, the other arsenic species present in both extracts did not fit any of the authentic standards (U1 in Figure 1B,C). U1 seems to be neutral at pH 6.8 (Figure 1B) but shows cationic nature at pH 3.0 (Figure 1C). The arsenic compounds with trialkylarsine oxide structure, such as V, IX, and X in Table I, generally behave in such a manner because the dimethylarsinoyl group, $(\text{CH}_3)_2\text{As}(\text{O})-$, protonates at around pH 4. In fact, U1 was eluted from the ODS column much earlier when the pH of the elution buffer changed from pH 3.0 to pH 4.2 (Figure 2). Among the authentic standards employed in the present study (Table I), trimethylarsine oxide (V) and dimethylarsinoylethanol (IX) showed similar retention times to U1. Coincidence of them with the extract clearly indicated, however, that U1 is different from them (Figure 2, Figure 1C). No arsenic peak to be assigned to U1 appeared on the chromatograms of the gel permeation column (Figure 1A). Probably the peak overlapped with that of arsenobetaine.

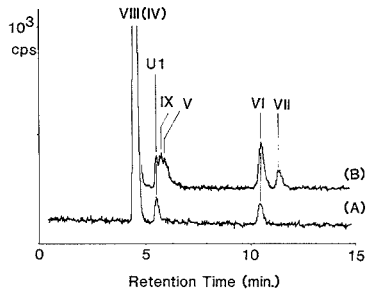


Figure 2. Chromatograms of DORM-1 extract (A) and that spiked with 200 µg of As each as trimethylarsine oxide (V), tetramethylarsonium ion (VI), arsenocholine (VII), and dimethylarsinoylethanol (IX) (B) on Inertsil ODS-1 at pH 4.2. In this condition, cacodylate (IV) has almost same retention time as arsenobetaine (VIII).

Chloride ion in the samples did not interfere under these conditions.

Total and water-soluble arsenic in DORM-1 were 18.4 ± 0.5 and 17.2 ± 0.9 µg/g, and those in DOLT-1 were 10.9 ± 0.5 and 7.3 ± 0.9 µg/g, respectively. These values are in accordance with previous reports (10, 14). Arsenobetaine accounted for 91% and 78% of the water-soluble fractions of DORM-1 and DOLT-1, respectively. Other arsenic species were cacodylate 3.5, tetramethylarsonium 2.7, and U1 2.4% in DORM-1 and cacodylate 10.7 and U1 10.9% in DOLT-1.

Tetramethylarsonium ion (VI) is a cationic arsenic compound similar to arsenocholine (VII), and the chromatographic conditions should be selected carefully for the unambiguous identification of them. Judging from the present data, it seems that the arsenic compound identified as arsenocholine by Beauchemin et al. is really tetramethylarsonium ion. Tetramethylarsonium ion was detected in bivalve, crab, sea cucumber, sea hare, sea anemone, and gastropod mollusc (9, 15-17). As far as we know, this is the first report of its presence in fishes. Trimethylarsine oxide (V), a possible intermediate between cacodylate and tetramethylarsonium ion, however, was not detected in the reference materials. It may be lost during the acetone treatment of these reference materials (14). Trimethylarsine oxide was detected in fish as a natural constituent (18, 19) and also as a metabolite of inorganic arsenic (19). It is also produced from arsenobetaine by the action of some bacteria (20). The structure of U1 is not clear at this stage. The same compound is present in a crab (Y. Shibata, et al., unpublished). U1 seems to have been overlooked in the previous report (10).

Our knowledge of arsenic in the natural environment is fragmentary, and the list of arsenic species is still growing, as shown in the present communication. In addition to the number of available standards, selection of the chromatographic conditions is quite important for the reliable identification. The HPLC conditions described in the present communication seem to be promising for the chemical speciation of arsenic in marine organisms.

ACKNOWLEDGMENT

We thank Drs. J. S. Edmonds and K. A. Francesconi (Western Australian Marine Research Laboratories) for supplying the standard (IX), Dr. K. Okamoto (NIES) for valuable discussions, and Mr. K. Sakata (Yokogawa Electric Co.) for technical support.

LITERATURE CITED

- Edmonds, J. S.; Francesconi, K. A.; Cannon, J. R.; Raston, C. L.; Skelton, B. W.; White, A. H. *Tetrahedron Lett.* **1977**, 1543-1546.
- Hanaoka, K.; Yamamoto, H.; Kawashima, K.; Tagawa, S.; Kaise, T. *Appl. Organomet. Chem.* **1988**, 2, 371-376, and references therein.

- (3) Norin, H.; Ryhage, R.; Christakopoulos, A.; Sandstrom, M. *Chemosphere* **1983**, *12*, 299-315.
- (4) Edmonds, J. S.; Francesconi, K. A. *Experientia* **1987**, *43*, 553-557.
- (5) Irgolic, K. J.; Woolson, E. A.; Stockton, R. A.; Newman, R. D.; Bottino, N. R.; Zingaro, R. A.; Kearney, P. C.; Pyles, R. A.; Maeda, S.; McShane, W. J.; Cox, E. R. *EHP, Environ. Health Perspect.* **1977**, *19*, 61-66.
- (6) Morita, M.; Shibata, Y. *Chemosphere* **1988**, *17*, 1147-1152.
- (7) Morita, M.; Uehiro, T.; Fuwa, K. *Anal. Chem.* **1981**, *53*, 1806-1808.
- (8) Kurosawa, S.; Taguchi, M.; Yamazaki, S.; Toda, S.; Morita, M.; Uehiro, T.; Fuwa, K. *Agric. Biol. Chem.* **1980**, *44*, 1993-1994.
- (9) Morita, M.; Shibata, Y. *Anal. Sci.* **1987**, *3*, 575-577.
- (10) Beauchemin, D.; Bednas, M. E.; Berman, S. S.; McLaren, J. W.; Siu, K. W. M.; Sturgeon, R. E. *Anal. Chem.* **1988**, *60*, 2209-2212.
- (11) Lawrence, J. F.; Michalik, P.; Tam, G.; Conacher, H. B. S. *J. Agric. Food Chem.* **1986**, *34*, 315-319.
- (12) Lau, B. P.-Y.; Michalik, P.; Porter, C. J.; Krollik, S. *Biomed. Environ. Mass Spectrom.* **1987**, *14*, 723-732.
- (13) Shibata, Y.; Morita, M. *Anal. Sci.* **1989**, *5*, 107-109.
- (14) Berman, S. S.; Sturgeon, R. E. *Fresenius' Z. Anal. Chem.* **1987**, *326*, 712-715.
- (15) Shiomi, K.; Kakehashi, Y.; Yamanaka, H.; Kikuchi, T. *Appl. Organomet. Chem.* **1987**, *1*, 177-183.
- (16) Shiomi, K.; Aoyama, M.; Yamanaka, H.; Kikuchi, T. *Comp. Biochem. Physiol., C: Comp. Pharmacol. Toxicol.* **1988**, *90C*, 361-365.
- (17) Francesconi, K. A.; Edmonds, J. S.; Hatcher, B. G. *Comp. Biochem. Physiol., C: Comp. Pharmacol. Toxicol.* **1988**, *90C*, 313-316.
- (18) Norin, H.; Christakopoulos, A.; Sandstrom, M.; Ryhage, R. *Chemosphere* **1985**, *14*, 313-323.
- (19) Edmonds, J. S.; Francesconi, K. A. *Sci. Total Environ.* **1987**, *64*, 317-323.
- (20) Kaisa, T.; Hanaoka, K.; Tagawa, S. *Chemosphere* **1987**, *16*, 255-2558.

Yasuyuki Shibata*
Masatoshi Morita

Chemistry and Physics Division
National Institute for Environmental Studies
16-2 Onogawa, Tsukuba
Ibaraki 305, Japan

RECEIVED for review February 23, 1989. Accepted June 8, 1989.

Sir: It is gratifying to know that experienced scientists using quite different procedures have largely confirmed our experimental results that arsenobetaine is the major arsenic species in DORM-1 (1). The discrepancy is on the assignment of an approximately 1% fraction that we attributed to arsenocholine. According to the authors, that fraction should have been assigned to tetramethylarsonium ion.

We have recently found that tetramethylarsonium ion has retention properties very similar to that of arsenocholine on a Dowex 50W-X8 column. Having been shown the authors' HPLC data, we have to agree that our assignment of arsenocholine is likely to be erroneous. We are grateful to the authors for bringing this to our attention.

ACKNOWLEDGMENT

We thank W. R. Cullen, Department of Chemistry, Univ-

ersity of British Columbia for a sample of tetramethylarsonium iodide.

LITERATURE CITED

- (1) Beauchemin, D.; Bednas, M. E.; Berman, S. S.; McLaren, J. W.; Siu, K. W. M.; Sturgeon, R. E. *Anal. Chem.* **1988**, *60*, 2209-2212.

K. W. M. Siu*
R. E. Sturgeon
J. W. McLaren
S. S. Berman

Division of Chemistry
National Research Council of Canada
Montreal Road
Ottawa, Ontario
Canada K1A 0R9

RECEIVED for review May 22, 1989. Accepted June 8, 1989.

Complex Mixture Analysis Using Differential Gas Chromatographic Mass Spectrometry

Sir: Commercial analytical laboratories routinely use gas chromatographic mass spectrometry (GCMS) to identify and quantitate a relatively small number of well-defined analytes in environmental or clinical samples. The components are most often priority pollutants, drugs, or metabolites whose chromatographic retention times and mass spectra are known. Increasingly, however, analysts are called upon to screen very complex samples and to identify unknown components that may be of environmental or clinical concern. This task is usually straightforward for components that are well separated by gas chromatography and are present in sufficient concentration to provide clean mass spectra. Complications invariably arise when, as is more often the case, the components are incompletely resolved, mass spectra overlap, and interpretation becomes problematic. A host of computer techniques have been proposed (1-8) for the deconvolution of overlapping peaks, providing cleaner mass spectra and allowing interpretation and even quantitation of the unknown analytes.

In all of the methods described to date, spectral deconvolution is performed after the data collection is over and the

raw mass spectra are stored in the data system. We recently proposed (8) "differential GCMS", a method that improves spectral quality by subtracting successive pairs of mass spectra and storing the result. As the concentration of a compound increases, the abundances of ions representing that compound increase and these ions appear with positive abundances in the differential mass spectrum. As the concentration decreases, ion abundances in the differential mass spectra become negative (8).

Several aspects of the method are unusual. Of all the mass spectral deconvolution techniques, differential GCMS is the only one capable of real-time operation. That is, the spectral cleanup could be performed as data are being collected. The processed spectra could be stored along with, or instead of, the raw mass spectra. When the differential mass spectra are summed into a total ion chromatogram, there is an increase in apparent chromatographic resolution (8). This improvement can be quantitatively estimated by using existing theory.

Davis and Giddings (9) have developed a theoretical model for a chromatographic system. The model uses Poisson sta-

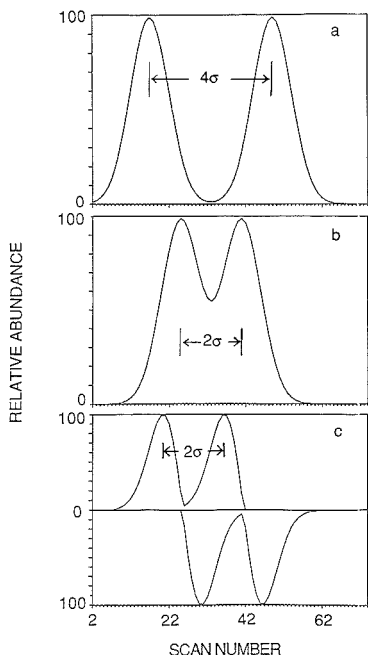


Figure 1. (a) Simulated GCMS data ($I(t)$) showing two Gaussian peaks separated by a distance of 4σ . (b) Same as a, but with peak separation of 2σ . (c) Differential GCMS total ion profile (θ) derived from the data set in b. Mass spectral overlap is reduced and apparent chromatographic resolution is improved.

tistics to describe the random elution of compounds in a system with finite peak capacity. For a mixture of m components in a system with a peak capacity of n_c , the model predicts that the number of components eluting as singlets is expressed as

$$p_1 = me^{-2\alpha}$$

where α is the ratio of the number of components to the peak capacity: $\alpha = m/n_c$. The hypothetical peak capacity is determined by dividing the entire chromatographic coordinate space, X , by the width of one chromatographic peak, x_0 (x_0 is, therefore, the minimum distance by which two components may be separated and still be considered chromatographically "resolved"):

$$n_c = X/x_0$$

The model goes on to predict the number of chromatographic peaks (p) eluted from the system to be

$$p = me^{-\alpha}$$

This model can be readily be adapted to the differential GCMS case. If a chromatographic peak is symmetrical, ion abundances in the differential mass spectra will be positive during the first half of the elution and negative during the second half. In terms of chromatographic overlap, the situation can be represented as in Figure 1. The resolution of two Gaussian peaks (Figure 1a) will be achieved when $R_s = 1$ or $x_0 = 4\sigma$, where σ represents the average standard deviation of the two peaks (9). In the case of differential GCMS (Figure 1b,c), the peaks achieve the same degree of overlap at a distance $x_0 = 2\sigma$. Because of the differentiation process, the effective "width" of a peak has been halved.

Davis and Giddings showed that for a 50-component mix-

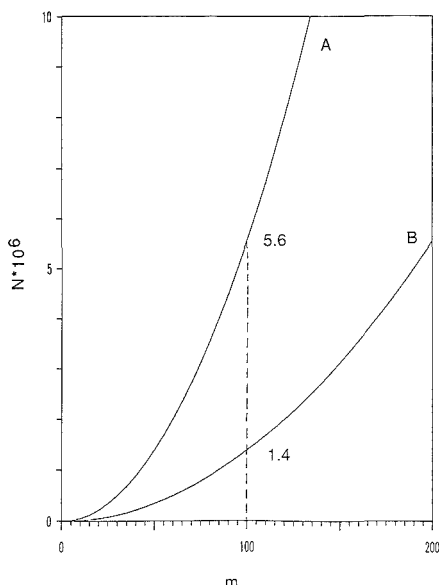


Figure 2. Number of theoretical plates required to form a singlet with a probability of 90% as a function of m : (A) standard GCMS experiment, $V_2/V_1 = 25$, $R_s = 1.0$; (B) differential GCMS experiment.

ture in a system with a peak capacity of 100, only 30 chromatographic peaks can be expected to elute ($p = me^{-m/n_c} = 50e^{-(50/100)} = 30$), and only 18 of these will represent pure components ($p_1 = me^{-2m/n_c} = 50e^{-2(50/100)} = 18$). Our differentiation has the effect of doubling the peak capacity (n_c) of the chromatographic system (by halving the peak width) without any change in other variables. This also has the effect of halving α . For the 50-component sample above, differential GCMS would produce 39 distinct chromatographic peaks ($p = 50e^{-50/200} = 39$), of which 30 would be pure components ($p_1 = 50e^{-2(50/200)} = 30$).

An alternative perspective for viewing the improvement in chromatographic resolution is to calculate the number of theoretical plates required to provide a high probability (90%) of forming a pure singlet ($p_1 = 0.9$) (9). Figure 2A shows a plot of such a calculation: The number of theoretical plates (N) is plotted as a function of the number of components (m). (A retention volume ratio, V_2/V_1 , of 25 and a resolution, R_s , of 1 are assumed for this plot as in ref 9.) In the differential GCMS data, components are "resolved" when the peak separation is 2σ , rather than 4σ (see Figure 1). In other words, peak resolution requires only $R_s = 0.5$. The peak capacity (9)

$$n_c = \frac{N^{1/2}}{4R_s} \ln \frac{V_2}{V_1}$$

is doubled when $R_s = 0.5$ compared to $R_s = 1.0$, consistent with the discussion above. To achieve a given probability of singlet formation, one would require only one-fourth the number of theoretical plates (Figure 2B). This means that an acceptable degree of separation can be achieved on a shorter GC column (lower N) or in a shorter period of time by using differential GCMS than would be necessary for the standard experiment.

Martin and Guiochon (11) have proposed a parameter they term γ , the extent of separation, to describe the quality of a chromatographic separation of a multicomponent mixture. The model is based on an analogy between the chromatographic separation process and a random depolymerization

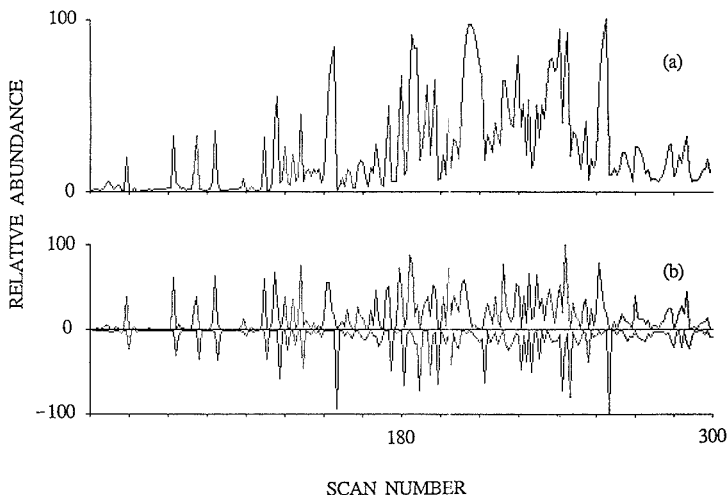


Figure 3. (a) Total ion profile and (b) differential GCMS profile from the analysis of the volatile organic compounds in a sample of indoor air. Compounds trapped on Tenax were thermally desorbed into a continuously scanning Hewlett-Packard 5985 B GCMS system. Electron ionization (70 eV) mass spectra were collected every 2.2 s from m/z 40 to 400.

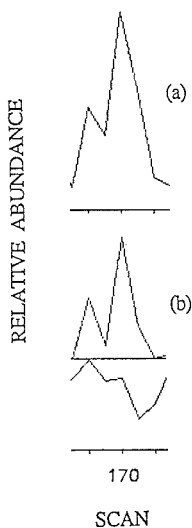


Figure 4. (a) Total ion profile and (b) differential GCMS profile for scans 167-173 of the data set in Figure 3.

process and results in mathematical expressions virtually identical with those of Davis and Giddings (9). The γ parameter ranges in value from 0 to 1, with 0 indicating no separation at all and 1 indicating perfect separation, analogous to the extent of chemical reaction (depolymerization). Mathematically, the relationship between the two models may be expressed (11) by

$$\gamma = e^{-\alpha} = e^{-m/n_c}$$

As before, the effect of differential GCMS is readily observed. For the same 50-component mixture in a 100-peak-capacity system, one calculates the extent of separation as $\gamma = e^{-50/100} = 0.61$ before differentiation. After differentiation, γ becomes $e^{-50/200} = 0.78$, closer to 1 and therefore a more complete separation.

The most efficient data collection mode for differential mass spectra would be to collect and store the difference spectra in place of the usual raw mass spectra. Some analysts are understandably uncomfortable with the notion of discarding the raw data. This need not be a cause for concern. (It should be noted, in passing, that the "raw" mass spectra being discussed are already extensively processed: digitized, amplified, filtered, centroided, mass assigned, etc., after which *real* raw data, i.e. the analogue signals from the electron multiplier, are discarded.) The differential mass spectra are the result of a subtraction of successive mass spectra. When the first mass spectrum in a data set is collected, it has no prior spectrum to subtract. If this first spectrum is stored intact (absolute abundances, as measured), and if each subsequent spectrum is stored as the difference between two adjacent spectra, the original mass spectra can be reassembled, post-run, by simply summing the first and second spectra, the second the third, etc. By starting at the first spectrum, stored with its measured abundances, one can "unzip" the differential mass spectra to recover what most analysts now consider to be the raw data. In time, we believe, the differential mass spectra will be shown to provide all of the same information as the raw data, and in a form, after some initial acustomization, that is perhaps more efficient and easier to use.

As an illustration of the chromatographic resolution enhancement, we include a data set from the analysis of the organic compounds in an air sample. This sample was collected in a local building after several employees complained of illnesses and unpleasant reactions, thought to be associated with the air inside the building. The organic compounds were trapped on a solid adsorbent and then thermally desorbed into the GCMS system. Figure 3a shows the total ion profile from the data set; the sample obviously represents a very complex mixture. Figure 3b shows the same data set after processing to generate a differential GCMS file. Successive pairs of mass spectra were subtracted, as we have described elsewhere (8). The positive and negative abundances of ions were summed separately and plotted against scan number (of the later scan) to produce the differential GCMS profile in Figure 3b. The improvement in chromatographic resolution is readily apparent, particularly in regions of the chromatogram that are complex, for example, between scans 180 and 250. The

background from chemical noise is also lower, as evidenced by a decreased base line. In effect, by differentiating the GCMS data set, one is subtracting a "local background" from every scan.

A small region of the chromatogram is expanded in Figure 4 (scans 167-173). A partially resolved doublet appears in Figure 4a, the total ion profile. The resolution of these two compounds can be estimated to be $0.6 (R_s = (t_2 - t_1) / [0.5(w_1 + w_2)])$, where t_2, t_1 are retention times and w_1, w_2 are peak widths for components 1 and 2). After differentiation (Figure 4b), the two components are resolved almost to base line; $R_s = 0.9$. The peak separation, $(t_2 - t_1)$, has not changed, but the peak width is substantially narrower, approaching the theoretical prediction discussed above. The mass spectra corresponding to these compounds are also improved. In the original data set, the mass spectra overlapped in many of the scans; in the differential data set, the spectra do not overlap and provide correspondingly easier interpretation. In fact, in this sample, we were able to demonstrate the presence of benzene only after differentiation. In the raw spectra, compounds eluting close to benzene produced many ions in the region where the m/z 78 of benzene was observed, making the identification of benzene somewhat tenuous. After differentiation, a clear mass spectrum of benzene was recovered that exactly matched the spectrum from the reference library (data not shown).

In summary, the technique of differential GCMS, although very simple to implement, provides a number of advantages

over conventional GCMS, including better chromatographic resolution, lower background, and cleaner mass spectra. Studies to demonstrate the utility of the method for quantitation of analytes are under way.

ACKNOWLEDGMENT

Stimulating discussions with Cliff Carlin, University of Maine, are gratefully acknowledged.

LITERATURE CITED

- (1) Biller, J. E.; Biemann, K. *Anal. Lett.* **1974**, *7*, 515-528.
- (2) Dromey, R. G.; Stefik, M. J.; Rindfleisch, T. C.; Duffield, A. M. *Anal. Chem.* **1976**, *48*, 1368-1375.
- (3) Knorr, F. J.; Futrell, J. H. *Anal. Chem.* **1979**, *51*, 1236-1241.
- (4) Sharaf, M. A.; Kowalski, B. R. *Anal. Chem.* **1982**, *54*, 1291-1296.
- (5) Knorr, F. J.; Thorsheim, H. R.; Harris, J. M. *Anal. Chem.* **1981**, *53*, 821-825.
- (6) King, M. D.; King, G. S. *Anal. Chem.* **1985**, *57*, 1049-1056.
- (7) Lacey, R. F. *Anal. Chem.* **1986**, *58*, 1404-1410.
- (8) Ghosh, A.; Anderegg, R. J. *Anal. Chem.* **1989**, *61*, 73-77.
- (9) Davis, J. M.; Giddings, J. C. *Anal. Chem.* **1983**, *55*, 418-424.
- (10) Ghosh, A.; Morison, D. S.; Anderegg, R. J. *J. Chem. Educ.* **1988**, *65*, A154-A156.
- (11) Martin, M.; Guiochon, G. *Anal. Chem.* **1985**, *57*, 289-295.

* Author to whom correspondence should be addressed.

Amit Ghosh
Robert J. Anderegg*

Department of Chemistry
University of Maine
Orono, Maine 04469

RECEIVED for review July 3, 1989. Accepted July 3, 1989.

TECHNICAL NOTES

Chiral Polysiloxanes Derived from (*R,R*)-Tartramide for the Gas Chromatographic Separation of Enantiomers

Kouji Nakamura*

Tanabe Seiyaku, 16-89, Kashima 3-chome, Yodogawa-ku, Osaka 532, Japan

Shoji Hara and Yasuo Dobashi

Tokyo College of Pharmacy, 1432-1 Horinouchi, Hachioji, Tokyo 192-03, Japan

The first chiral polysiloxane, termed Chirasil-Val, for the gas chromatographic separation of enantiomers was synthesized by coupling L-valine-*tert*-butylamide as a chiral moiety to a copolymer of (2-carboxypropyl)methylsiloxane and dimethylsiloxane in 1977 (1). It was found to be extensively applicable to the enantiomeric separation of optical antipodes of amino acid, hydroxy acid, amino alcohol, diol, alcohol, and halocarboxylic acid (2-7). It was possible to synthesize chiral polysiloxanes similar to Chirasil-Val by using commercially available polysiloxanes. Verzele et al. synthesized a chiral polysiloxane by coupling L-valine-*tert*-butylamide to commercial polysiloxane OV-225 followed by subsequent conversion to acid chloride in two steps (8). König et al. also synthesized chiral polysiloxane by coupling L-valine-(*S* or *R*)-phenylethylamide to modified commercial polysiloxane XE-60 with dicyclohexyl carbodiimide (DCC) (9). Glass and fused-silica capillary columns coated with these chiral polysiloxanes were used for the gas chromatographic separation of enantiomers. The enantiomeric separation of chiral polysiloxanes is based on differences in the stability of diastereomeric complexes in enantiomeric pairs and the chiral moiety on chiral polysiloxane via hydrogen bonding.

We recently reported (*R,R*)-*N,N'*-diisopropyltartramide to be broadly applicable as a chiral mobile phase additive in silica

gel chromatography and a chiral stationary phase derived from (*R,R*)-tartramide to have a considerable scope of application to the liquid chromatographic resolution of enantiomers (10-12). (*R,R*)-Tartramide was observed to have excellent resolving power in distinguishing enantiomers from each other via hydrogen bonding. The present study was carried out to prepare chiral polysiloxane derived from (*R,R*)-tartramide for the gas chromatographic separation of enantiomers.

EXPERIMENTAL SECTION

Apparatus. Gas chromatographic analysis was performed on a Shimadzu GC-9A equipped with a split injector and a flame ionization detector, using helium as the carrier gas at an inlet pressure of approximately 1.3 kg/cm². The chromatographic signal was recorded and processed by a Shimadzu C-R3A integrator.

¹H NMR spectra were obtained on a Varian EM-390 spectrometer and chemical shifts were expressed in parts per million (δ) relative to tetramethylsilane as the internal standard. IR spectra were obtained on a Hitachi 260-10 spectrometer. Optical rotation was measured on a Jasco DIP-360 polarimeter. Melting points were determined on a micro hot-plate melting point apparatus.

Reagent and Synthetic Preparations. *Synthesis of N-Isopropyltartramic Acid Monoamide* (2). *N*-Isopropylidiacetyl-tartramic acid monoamide (4.0 g, 14.5 mmol) was dissolved in 15

mL of 29% ammonia water. After the solution was gently stirred at room temperature for 6 h, 6 N hydrochloric acid was added to make the solution acidic followed by extraction 5 times with 300 mL of ethyl acetate. The ethyl acetate extracts were pooled, dried over anhydrous sodium sulfate, and evaporated under reduced pressure to afford crude products. Recrystallization from acetone gave 1.39 g (50%) of pure *N*-isopropyltartaric acid monoamide as colorless crystals: mp 178–179 °C; $[\alpha]_D^{25} +75.1^\circ$; IR (KBr) 3600–2600, 3380, 1745, 1640, 1545, 1320, 1120 cm^{-1} ; NMR ($\text{Me}_2\text{SO}-d_6$) δ 1.05 (d, 6 H), 3.65–3.95 (m, 1 H), 4.15 (d, 1 H), 4.30 (d, 1 H), 7.30 (d, 1 H).

Synthesis of the Activated Ester of *N*-Isopropyltartaric Acid Monoamide (3). *N*-Hydroxy-5-norbornene-2,3-dicarboximide (1.08 g, 6 mmol) and *N*-isopropyltartaric acid monoamide (1.15 g, 6 mmol) were dissolved in 50 mL of dry tetrahydrofuran and cooled in an ice bath. DCC (1.24 g, 6 mmol) was added to this solution with stirring, which was then continued at 0 °C for 10 h under an atmosphere of argon. The resulting mixture was filtered to remove dicyclohexylurea and evaporation of the filtrate under reduced pressure afforded crude products. Recrystallization from a mixture of hexane and acetone gave 1.56 g (73.6%) of the pure activated ester as colorless crystals: mp 155–156 °C; $[\alpha]_D^{25} +52.5^\circ$; IR (KBr) 3600–3100, 2980, 1735, 1660, 1540, 1210 cm^{-1} ; NMR [CDCl_3 - $\text{Me}_2\text{SO}-d_6$ (10:1)] δ 1.20 (d, 6 H), 1.70 (q, 2 H), 3.30–3.50 (m, 4 H), 3.85–4.30 (m, 1 H), 4.45 (q, 1 H), 4.95 (q, 1 H), 5.35 (d, 1 H), 5.45 (d, 1 H).

Synthesis of Aminobutyl Polysiloxanes (5). Aminobutyl polysiloxane derived from OV-225 was synthesized according to a modified procedure of König et al. (13).

Aminobutyl polysiloxane derived from OV-1701 was synthesized as follows: To a suspension of lithium aluminum hydride (130 mg, 3.43 mmol) in 20 mL of dry diethyl ether was slowly added a solution of 1.03 g of OV-1701 in 20 mL of dry diethyl ether at 0 °C followed by stirring at 0 °C for 5 h. The excess lithium aluminum hydride was carefully decomposed with saturated sodium sulfate solution, and the resulting white precipitate was separated by filtration. The filtrate was dried over anhydrous sodium sulfate and evaporated under reduced pressure. The residue was dissolved in chloroform followed by evaporation under reduced pressure to a colorless liquid: IR (neat) 2960, 1590, 1430, 1415, 1260, 1120–1000, 800 cm^{-1} .

Aminobutyl polysiloxane derived from OV-105 was synthesized in the same manner with OV-1701 except that the reaction temperature was –20 °C. IR (neat) 2960, 1600, 1430, 1410, 1260, 1120–1000, 800 cm^{-1} .

Synthesis of Chiral Polysiloxanes. The amount of amino functional groups in each aminobutylpolysiloxane obtained from OV-225, OV-1701, and OV-105 was determined by nonaqueous titration, and a small excess of the activated ester was condensed. Chiral polysiloxane derived from OV-1701 was synthesized according to the following procedure.

To a solution of aminobutyl polysiloxane (550 mg) in 10 mL of dichloromethane was added one of activated ester (374 mg, 1.06 mmol) in 12 mL of tetrahydrofuran at –30 °C. The mixture was stirred at –30 °C for 5 h and 100 mL of chloroform and 20 mL of 5% sodium hydrogen carbonate were then added. The organic layer was washed three times with 20 mL of water and dried over anhydrous sodium sulfate. The solvent was evaporated to afford a colorless gumlike material: $[\alpha]_D^{25} +14.6^\circ$; IR (neat) 3320, 2960, 1660, 1540, 1435, 1420, 1265, 1120, 800 cm^{-1} .

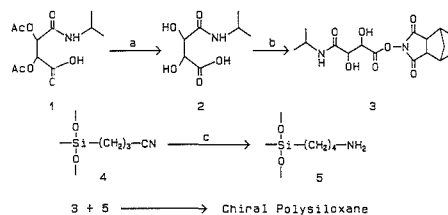
Column Preparation. A fused-silica capillary column (25 m \times 0.25 mm) was used without pretreatment. Column coating was performed according to the static procedure using 0.25% or 0.50% of the stationary phase in dichloromethane. The column was subsequently conditioned with helium gas at a temperature range from 40 to 150 °C at 0.5 °C min^{-1} .

Sample Preparation. A series of β -hydroxy acids as *tert*-butylamide derivatives from a previous study (11, 12) were used. *O*-Isopropylcarbamoyl-DL-lactic acid isopropyl ester was prepared according to the literature (14).

RESULTS AND DISCUSSION

The synthetic pathway of chiral polysiloxane is shown in Scheme 1. Diacetyltartaric acid monoamide (1) was synthesized as in our previous study (11, 12). *N*-Isopropyltartaric acid monoamide (2) was produced by the hydrolysis of 1 and

Scheme 1. Synthetic Pathway of Chiral Polysiloxane: (a) $\text{NH}_3\text{-H}_2\text{O}$; (b) *N*-Hydroxy-5-norbornene-2,3-dicarboximide, Dicyclohexyl Carbodiimide; (c) Lithium Aluminum Hydride



was then condensed with *N*-hydroxy-5-norbornene-2,3-dicarboximide by using DCC to obtain the activated ester 3. Commercial cyanopropyl polysiloxanes 4 such as OV-225, OV-1701, and OV-105 were reduced with lithium aluminum hydride (completion of reaction was confirmed by the disappearance of cyano stretching vibration as shown by IR). The resulting aminobutyl polysiloxanes 5 were condensed with a small excess of activated ester 3. Three chiral polysiloxanes each with a different tartramide binding ratio were synthesized. Their structures and properties are shown in Table I.

CSP-1 bound to tartramide at a high ratio was a solid while CSP-2 and CSP-3, bound at low ratios, were an advantageous gumlike material and a liquid, respectively, for capillary column preparation. Elemental analysis of nitrogen indicated almost complete binding of tartramide to polysiloxane. No CSP-2 showed loss of weight up to 200 °C, according to thermogravimetric analysis.

Chiral polysiloxanes for gas chromatography are characterized by high thermal stability and good wettability if the ratios of the binding of chiral substituents to polysiloxane are appropriate. Each chiral moiety in Chiralis-Val was separated from approximately seven siloxane units to prevent their interacting with neighboring chiral moieties by hydrogen bonding (15). By this separation, the percentage substitution of chiral moiety was 6.25%. Bradshaw et al. recently reported a new chiral polysiloxane containing 7% of the chiral substituents and also separated the enantiomers of amino acids (16). The CSP-2 containing 6.8% of the chiral substituents may thus be considered suitable for the gas chromatographic separation of enantiomers.

Each chiral polysiloxane was coated with film of 0.15 or 0.30 μm thickness in the fused-silica capillary column for assessment of chiral recognition. Figure 1 shows the optical resolution of 2-hydroxymethyl-3-methylbutanoic acid on each chiral polysiloxane.

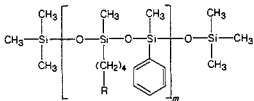
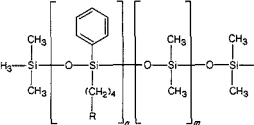
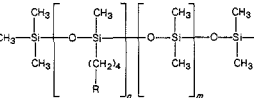
Although CSP-1 exhibited no enantioselectivity, CSP-2 and CSP-3 did so to a considerable degree. The separation factors of 2-hydroxymethyl-3-methylbutanoic acid on CSP-2 and CSP-3 were 1.075 and 1.061, respectively. The column efficiency of CSP-2 was superior to that of CSP-3, as shown in Figure 1. Table II gives chromatographic data for the separation factors of a series of β -hydroxy acids as *tert*-butylamide derivatives on CSP-2.

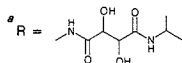
Separation factors indicate degrees of chiral recognition and directly reflect differences in the stability of diastereomeric complexes in enantiomeric pairs and the chiral moiety of chiral polysiloxane.

As shown in Table II, each separation factor was influenced by the steric bulkiness of the substituent at the asymmetric center. Separation factors of β -hydroxy acids with their asymmetric centers at the α -position were greater than those with their centers at the β -position.

CSP-2 also exhibited enantioselectivity for lactic acid derivative. Figure 2 shows the optical resolution of *O*-iso-

Table I. Structures and Properties of Chiral Polysiloxanes

	structure ^a	% of tartramide	appearance	$[\alpha]_D^{25}$, deg	anal. found
CSP-1		25	solid (mp 114-125 °C)	+26.6	% N 5.80 % C 51.02 % H 7.38
CSP-2		6.8	gumlike	+14.6	% N 3.38 % C 40.83 % H 7.69
CSP-3		5.0	liquid	+1.9	% N 2.72 % C 25.75 % H 8.63

**Table II. Optical Resolution of the Enantiomers of β -Hydroxy Acid Derivatives on CSP-2 (cf. Figure 1b conditions)**

R ₁	R ₂	col temp, °C	k ₁ ' ^a	k ₂ ' ^a	α^b
H	Et	120	10.16	10.79	1.062
H	<i>i</i> -Pr	120	11.97	12.87	1.075
H	phenyl	140	19.97	20.79	1.041
Et	H	120	9.15	9.53	1.042
<i>i</i> -Pr	H	120	10.24	10.72	1.047
phenyl	H	150	28.80	29.56	1.026

^a k₁' and k₂' are the capacity factors of the lesser retained enantiomer and the more retained enantiomer. ^b α (separation factor) = k₂'/k₁'.

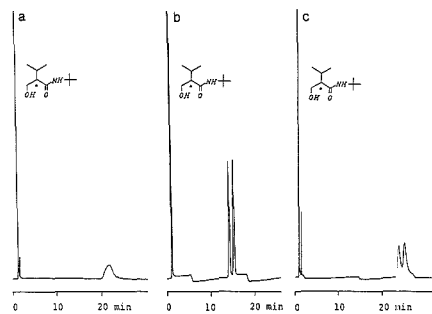


Figure 1. Optical resolution of a *tert*-butylamide derivative of 2-hydroxymethyl-3-methylbutanoic acid on a fused-silica capillary column (25 m × 0.25 mm) coated with each chiral polysiloxane: (a) with a 0.30 μ m thick film of CSP-1; 145 °C, 1.3 kg/cm² He; (b) with a 0.15 μ m thick film of CSP-2; 120 °C, 1.3 kg/cm² He; (c) with a 0.30 μ m thick film of CSP-3; 125 °C, 1.3 kg/cm² He.

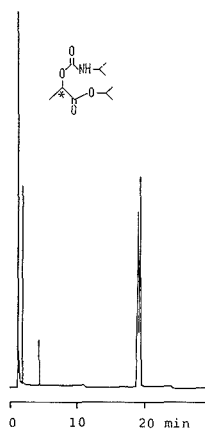


Figure 2. Optical resolution of *O*-isopropylcarbamoyl-DL-lactic acid isopropyl ester on CSP-2 (for conditions cf. Figure 1b, 120 °C).

Table III. McReynolds Constants of CSP-2

probe	ΔI^a	probe	ΔI^a
benzene	32	1-nitropropane	217
1-butanol	352	pyridine	219
2-pentanone	140		

^a Determined at 40 °C instead of 120 °C due to the low capacity factor of the capillary column.

propylcarbamoyl-DL-lactic acid isopropyl ester. The separation factor of this compound was 1.024.

Our method for achieving chiral recognition is based on the use of hydrogen bonding as the driving force for molecular association to bring about enantioselectivity.

The McReynolds constant of CSP-2 shown in Table III indicates CSP-2 to be moderately polar with a great ability

to form hydrogen bonds as evident from the high value of the 1-butanol probe.

The chiral polysiloxane derived from (*R,R*)-tartramide should find extensive application in chiral recognition.

LITERATURE CITED

- (1) Frank, H.; Nicholson, G. J.; Bayer, E. *J. Chromatogr. Sci.* **1977**, *52*, 174-176.
- (2) Nicholson, G. J.; Frank, H.; Bayer, E. *HRC CC, J. High Resolut. Chromatogr. Chromatogr. Commun.* **1979**, *2*, 411-415.
- (3) Koppenhoefer, B.; Allmendinger, H.; Nicholson, G. J.; Bayer, E. *J. Chromatogr.* **1983**, *260*, 63-73.
- (4) Frank, H.; Nicholson, G. J.; Bayer, E. *Angew. Chem., Int. Ed. Engl.* **1978**, *17*, 363-365.
- (5) Koppenhoefer, B.; Walser, M.; Bayer, E. *J. Chromatogr.* **1986**, *358*, 159-168.
- (6) Koppenhoefer, B.; Allmendinger, H. *Chromatographia* **1986**, *21*, 503-508.

- (7) Koch, E.; Nicholson, J.; Bayer, E. *HRC CC, J. High Resolut. Chromatogr. Chromatogr. Commun.* **1984**, *7*, 398-403.
- (8) Saëed, T.; Sandra, P.; Verzele, M. *J. Chromatogr.* **1979**, *186*, 611-618.
- (9) König, W. A.; Benecke, I.; Sievers, S. *J. Chromatogr.* **1981**, *217*, 71-79.
- (10) Debashi, Y.; Hara, S. *J. Am. Chem. Soc.* **1985**, *107*, 3406-3411.
- (11) Debashi, Y.; Hara, S. *Tetrahedron Lett.* **1985**, *26*, 4217-4220.
- (12) Debashi, Y.; Hara, S. *J. Org. Chem.* **1987**, *52*, 2490-2496.
- (13) König, W. A.; Benecke, I. *J. Chromatogr.* **1981**, *209*, 91-95.
- (14) König, W. A.; Benecke, I.; Sievers, S. *J. Chromatogr.* **1982**, *238*, 427-432.
- (15) Frank, H.; Nicholson, G. J.; Bayer, E. *J. Chromatogr.* **1978**, *146*, 197-206.
- (16) Bradshaw, J.; Aggarwal, S. K.; Rouse, C. A.; Tarbet, B. J.; Markieds, K. E.; Lee, M. L. *J. Chromatogr.* **1987**, *405*, 169-177.

RECEIVED for review May 1, 1989. Accepted June 1, 1989.

Fabrication and Characterization of Glassy Carbon Linear Array Electrodes

L. Joseph Magee, Jr., and Janet Osteryoung*

Department of Chemistry, State University of New York at Buffalo, Buffalo, New York 14214

Arrays of electrodes for use as electrochemical detectors in flowcells are the subject of many ongoing investigations. Originally developed to take advantage of the properties displayed by microelectrodes (i.e. enhanced current densities from nonplanar diffusional contributions to the net current, low *iR* drop characteristics, and a decreased dependence on convection) and to generate larger, more easily measured currents, arrays of electrodes have been fabricated from various materials and in different geometric configurations (1-9). However, because of the low dead volumes required of flowcell detectors, under conditions typical of liquid chromatography or flow injection analysis, the linear velocities of the fluids flowing through them are too high for nonplanar diffusion to be a factor. Only in extreme cases (very low flow rates and extremely small electrode size) will nonplanar diffusion affect the measured currents in these flowcell detectors.

Nevertheless, measured current densities of electrode arrays are almost always greater than those obtained for single electrodes of similar active electrode surface area under identical hydrodynamic conditions. This increase in current density is attributed to the reestablishment of the bulk concentration of the electroactive species as it travels across the insulating regions between electrode elements of the array (10-12). Consequently, each electrode element of the array "sees" bulk or near-bulk concentrations. This situation contrasts greatly with the depletion across the surface of a large electrode.

Electrode arrays have been fabricated in a number of geometries. The simplest geometry from the standpoint of fabrication is random. Random arrays can be made by combining powders or chips of electrode material with an insulator (e.g., plastic) (1, 2). Another type of random array is made by using a reticulated electrode material (e.g. reticulated vitreous carbon) with an insulator to fill the pores. Although difficult to characterize geometrically, random arrays are fairly simple to construct from readily available materials (3). Arrays of electrodes based on disks have also been fabricated (4). These arrays were constructed by sandwiching carbon fibers between glass microscope slides and sealing them in epoxy.

The most popular type of array geometry is the linear array. This electrode geometry is the most efficient in a flowcell when the lines are oriented opposed to the direction of flow, allowing one to obtain the highest current densities and net currents in the space allowed by flowcell dimensions. The most com-

mon method for fabricating linear arrays is by thin-film technology and lithography. Usually gold is vapor-deposited onto a substrate (5-8). The major drawbacks of these lithographically fabricated arrays arise from their three-dimensional nature. The gold lines are on top of the substrate and are on the order of 300-600 nm thick. Apparently no turbulence is caused by these lines in flowcells. However the layers tend to separate under voltammetric conditions in solution and are mechanically fragile. Thus their utility as something other than laboratory curiosities is limited, because they cannot be subjected to mechanical polishing, a routine procedure for the maintenance of electrodes. Another method involves etching a pattern in a Macor substrate and filling in the resulting grooves with a gold filler (9). The resulting inlaid electrode can be polished mechanically, but the etching procedure seems difficult to control.

Linear arrays based on carbon have not been described. Carbon electrodes, and especially glassy carbon electrodes, are probably the most common type in use today. They are used routinely as is or as the substrate for surface-modified and mercury-coated electrodes. Probably glassy carbon has not been used to make electrode arrays because of the nature of the material itself. Glassy carbon is a very hard, brittle material that shatters quite easily. Though the material is available in a number of shapes and sizes, including rods, plates, disks, tubes, cones, and crucibles, the only geometry that has had any extensive use as an electrode material has been the rod. Rods of glassy carbon, typically 3 mm in diameter, are readily sealed in Teflon, Kel-F, or some other insulating material to yield a disk electrode of 3-mm diameter. Machining techniques are available, however, that might allow one to fabricate electrode geometries other than a simple disk. This paper describes a method for fabricating linear arrays of electrodes for use in a flowcell detector.

EXPERIMENTAL SECTION

Electrode Fabrication. Electrodes were fabricated from glassy carbon plate treated to 2500 °C available from Atomergic Chemetals, Plainview, NY. The plate came in a 4 in. × 4 in. piece that was cut into 1 in. × 1 in. squares with a diamond saw. A series of grooves were cut in a 1 in. × 1 in. piece with a dicing saw (Tempress Model 602, Sola Basic Industries, Los Gatos, CA). Dicing saws are used routinely in the fabrication of microelectronic circuits to cut up silicon wafers. The cutting is done with a diamond impregnated wheel. This method worked quite well for

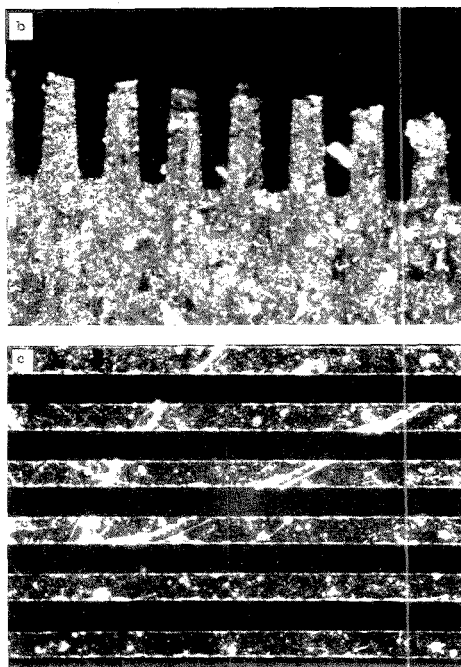
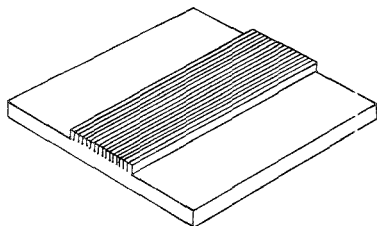


Figure 1. Grooves and ridges machined into a glassy carbon plate. (a) Drawing. (b) Photomicrograph of the end of a glassy carbon plate. Grooves are 90 μm wide and lines are 85 μm wide. (c) Photomicrograph of the top of a glassy carbon plate. Grooves are 65 μm wide (black) and lines are 60 μm wide (gray).

putting grooves in the glassy carbon plate.

The glassy carbon plate was mounted on the chuck, and the depth of cut was set to 0.010 in. A feed rate of about 3 in./min was used. Making a series of equally spaced grooves was greatly simplified by the fact that the saw has an automatic feed and jog setting. The saw will make a cut, return to the original position, move the workpiece a predetermined amount, and make another cut. This procedure runs continuously until the saw is turned off.

After a series of grooves was made in the center of the 1 in. \times 1 in. plate, the remaining surface was cut back, again by using the dicing saw, leaving a series of ridges in the middle of the plate (Figure 1). The dimensions in Figure 1b were obtained by using a calibrated grid on a microscope. This plate was then cut into three equally sized pieces, each of which could be used to make a flowcell detector.

The machined piece was cleaned in an ultrasonic bath to prepare the glassy carbon for sealing in an insulator and to remove any chips and particles remaining in the grooves from machining. A piece of this machined glassy carbon was potted in Maraglas epoxy (Acme Chemical and Insulation Co., New Haven, CT, No. 658 resin and No. 558 hardener) to fill the grooves and form the

Table I. Physical Characteristics of Two Linear Array Electrodes and a Single Disk Electrode

	line width, μm	gap width, μm	length, mm	no. of elements	total active surface area, mm^2
line I	60	65	4.5	24	6.48
line II	85	90	4.5	21	8.03
disk		$r = 1.5$ mm		1	7.10

Table II. Steady-State Response of a Series of Electrodes of Various Geometries^a

flow rate, mL/min	current density, nA/mm ²		
	disk	line I	line II
0.2	9.18	16.67	14.70
0.4	11.55	21.14	18.80
0.6	13.30	24.38	21.79
0.8	14.82	27.16	24.16
1.0	15.94	29.48	26.46
1.2	16.96	31.56	28.14
1.4	17.80	33.41	29.58
1.6	18.59	35.26	31.32
1.8	19.32	36.81	32.44
2.0	20.11	38.35	33.94

^a 4 μM solution of $\text{K}_4\text{Fe}(\text{CN})_6 \cdot 3\text{H}_2\text{O}$ in 0.05 M KCl.

body of the flowcell. Electrical contact was made from the bottom with a brass screw. The electrode assembly was prepared for use by first grinding off the excess epoxy coating the glassy carbon with 600-grit sandpaper. The surface was then polished with alumina/water slurries on a polishing cloth starting with 1- μm alumina and working down to 0.05 μm alumina for the final polishing.

Some difficulties with bubbles in the epoxy yielded imperfect seals with the carbon, resulting in a background current density roughly 10 times (7 nA/mm²) that for the commercial detector. Adequate seal between insulator and conductor is important for any embedded electrode. High background currents arising from imperfect seals might be expected to vary linearly with the perimeter of the seal. In this case the perimeter of the arrays is about 20 times the perimeter of the circular commercial electrode.

Equipment and Reagents. The flow system used to characterize these electrodes consisted of an LKB Model 2150 high-performance liquid chromatography pump and a BAS Model LC 17A electrochemical flowcell detector with a BAS Model LC 4A amperometric detector. The mobile phase was 0.1 M KCl (Mallinckrodt reagent grade) in deionized water. The analyte was $\text{K}_4\text{Fe}(\text{CN})_6 \cdot 3\text{H}_2\text{O}$ (Baker reagent grade).

RESULTS AND DISCUSSION

Two different glassy carbon line array electrodes were fabricated and characterized. The physical characteristics of these two electrodes, as well as the characteristics of the disk electrode with which they are compared, are given in Table I. An experiment was run to determine the current densities of these two electrodes under steady-state conditions and to compare the results with those obtained for the single disk electrode under similar conditions. This was done by continuously pumping a solution of analyte (4 μM $\text{Fe}(\text{CN})_6^{4-}$) in the mobile phase (0.1 M KCl) through the detector at a series of flow rates. The results of these experiments are given in Table II. As expected, the linear arrays of glassy carbon yielded higher current densities than the single disk. Plots of log current vs log flow rate using the data of Table II give slopes of 0.36 for the two arrays and 0.34 for the disk electrode. These slopes agree closely with the one-third power dependence on flow rate established for the channel flowcell (13, 14).

It is apparent from the photomicrographs that the dicing saw is capable of making very small, chip-free lines in the

glassy carbon. Line widths as small as 60 μm were obtained at a fairly high feed rate. It should be possible to make even narrower lines by using lower feed rates. Also worth pointing out is the versatility of the dicing saw for making cuts of different sizes. Changing the spacing between blade cuts merely requires the setting of a switch. In addition, gaps of different widths can be made by making multiple cuts with the blade or by using blades of different widths.

The success achieved with the dicing saw in making smooth lines of glassy carbon in micrometer dimensions in such an easy fashion makes the technique noteworthy. The range of application can probably be extended to other electrode materials such as gold or platinum and to other sealing materials such as other epoxies or Pyrex (15, 16).

ACKNOWLEDGMENT

We thank Mike Jackson and the Rochester Institute of Technology for the use of the dicing saw.

Registry No. $\text{Fe}(\text{CN})_6^{4-}$, 13408-63-4; carbon, 7440-44-0.

LITERATURE CITED

- (1) Weisshaar, D. E.; Tallman, D. E.; Anderson, J. L. *Anal. Chem.* **1981**, *53*, 1809.

- (2) Falat, L.; Cheng, H. Y. *Anal. Chem.* **1982**, *54*, 2109.
 (3) Wang, J.; Freiha, B. A. J. *Chromatogr.* **1984**, *298*, 79.
 (4) Casdill, W. L.; Howell, J. O.; Wightman, R. M. *Anal. Chem.* **1982**, *54*, 2531.
 (5) Bcnd, A. M.; Henderson, T. L. E.; Thorman, W. J. *Phys. Chem.* **1986**, *96*, 2911.
 (6) Thorman, W.; van den Bosch, P.; Bond, A. M. *Anal. Chem.* **1985**, *57*, 2764.
 (7) Fosdick, L. E.; Anderson, J. L. *Anal. Chem.* **1986**, *58*, 2481.
 (8) Fosdick, L. E.; Anderson, J. L.; Baginski, T. A.; Jaeger, R. C. *Anal. Chem.* **1986**, *58*, 2750.
 (9) DeAbreu, M.; Purdy, W. C. *Anal. Chem.* **1987**, *59*, 204.
 (10) Moldoveanu, S.; Anderson, J. L. *J. Electroanal. Chem. Interfacial Electrochem.* **1985**, *185*, 239.
 (11) Anderson, J. L.; Ou, T. S.; Moldoveanu, S. *J. Electroanal. Chem. Interfacial Electrochem.* **1985**, *198*, 213.
 (12) Cope, D. S.; Tallman, D. E. *J. Electroanal. Chem. Interfacial Electrochem.* **1986**, *205*, 101.
 (13) Sparrow, E. M. National Advisory Committee for Aeronautics TN 3331, 1555.
 (14) Weber, S. G.; Purdy, W. C. *Anal. Chim. Acta* **1978**, *100*, 531.
 (15) Sembell, R. A. J.; Bowen, D. H.; Phillips, D. C. *J. Mater. Sci.* **1972**, *7*, 663.
 (16) Sembell, R. A. J.; Briggs, A.; Phillips, D. C.; Bowen, D. H. *J. Mater. Sci.* **1972**, *7*, 676.

RECEIVED for review March 8, 1989. Accepted May 12, 1989. This work was supported in part by the National Science Foundation under Grant CHE 8521200.

Tuning and Calibration in Therospray Liquid Chromatography/Mass Spectrometry Using Trifluoroacetic Acid Cluster Ions

Steven J. Stout* and Adrian R. daCunha

American Cyanamid Company, Agricultural Research Division, P.O. Box 400, Princeton, New Jersey 08540

INTRODUCTION

Liquid chromatography/mass spectrometry (LC/MS) is a rapidly developing technique for the analysis of complex mixtures not amenable to gas chromatography/mass spectrometry (GC/MS) techniques (1). Of the several approaches for interfacing liquid chromatography with mass spectrometry, therospray (TSP) LC/MS appears to be the one best suited for the analysis of polar and labile organic compounds (2-6). One of the major drawbacks of TSP LC/MS is the need to install a separate ion volume which then must be tuned and calibrated. As discussed by Heeremans et al. (7), current methods of tuning TSP LC/MS suffer from serious shortcomings. Tuning on a solution of a particular analyte may not be applicable for the analysis of unknown compounds or when limited quantities of sample are available. Tuning solutions of poly(propylene glycol) (PPG), poly(ethylene glycol) (PEG) (8, 9), and sodium acetate (10) offer a more universal method of tuning but result in rapid contamination of the ion source and memory effects. To overcome these shortcomings, Heeremans et al. (7) reported adding volatile acetic acid to an ammonium acetate eluent. Tuning on acetic acid-ammonia cluster ions from m/z 100 to 1000 was achieved with no ion source contamination.

In this paper, we report on the use of trifluoroacetic acid to generate cluster ions for TSP LC/MS tuning and calibration to m/z 4000 (the upper mass limit of our instrumentation) without ion source contamination. Additionally, the same tuning solution can be used for tuning in the negative ion mode of operation.

EXPERIMENTAL SECTION

The experiments were performed with a TSQ-70 triple-stage quadrupole system equipped with a therospray interface

(Finnigan-MAT Corp., San Jose, CA). Operational parameters specific to the therospray interface included the following: vaporizer temperature, 90 °C; aerosol temperature, 230 °C; repeller voltage, 70 V; mass spectrometer high vacuum, 2.7×10^{-6} Torr. Solvent delivery was performed with an ABI Kratos Spectroflow Model 400 LC pump. The mobile phase was $\text{CH}_3\text{OH}/\text{H}_2\text{O}$ /trifluoroacetic acid (15/84.5/0.5, 0.1 M ammonium acetate), flowed at 1.5 mL/min, and gave a back pressure of approximately 30 bar. [^{15}N]Ammonium acetate (99% ^{15}N enriched) was obtained from ICON Services (Summit, NJ). Analytical reagent grade [^{14}N]-ammonium acetate was obtained from Mallinckrodt, Inc. (Paris, KY).

RESULTS AND DISCUSSION

Since Heeremans (7) demonstrated tuning and calibration of a TSP LC/MS ion source to m/z 1000 using acetic acid (HOAc)-ammonia cluster ions, we anticipated the greater mass of trifluoroacetic acid (TFA) would approximately double this mass range if TFA (molecular weight 114) exhibited the same level of cluster ion formation as acetic acid (molecular weight 60). As shown in Figure 1, this objective was achieved with cluster ions covering the mass range of m/z 100-2000. The predominant series of TFA-ammonia cluster ions corresponds to $(\text{TFA})_x(\text{NH}_3)_y(\text{NH}_4)^+$. This series starts with the $(\text{TFA})(\text{NH}_3)(\text{NH}_4)^+$ ion at m/z 149 and repeats in increments of 131 u (equivalent to TFA + NH_3). This pattern is especially evident above m/z 400. Several ions below m/z 400 correspond to additions of NH_3 to this series. Ions at m/z 192 (base peak) and m/z 175 correspond to $(\text{TFA})(\text{HOAc})(\text{NH}_4)^+$ and m/z 152 - NH_3 , respectively. The origins of the m/z 119 and 110 ions are uncertain at the present time. With switching to the high mass range of the instrument, the $(\text{TFA})_x(\text{NH}_3)_y(\text{NH}_4)^+$ series is found to extend to m/z 4000 (Figure 2), the upper mass limit of the instrument. Unfortunately, extending the mass range is also accompanied by a degradation in mass resolution.

* Author to whom correspondence should be addressed.

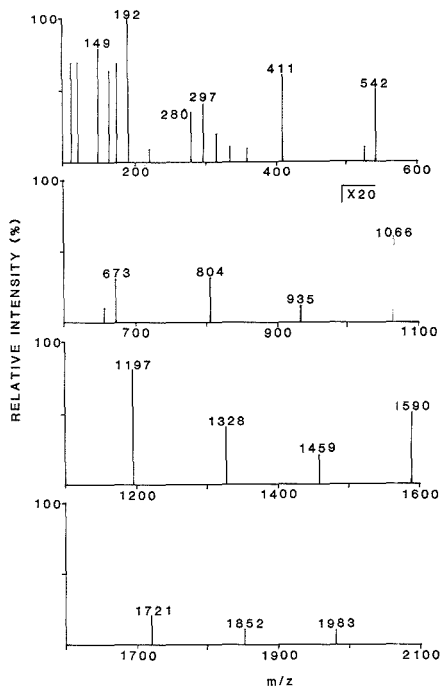


Figure 1. Positive ion mass spectrum of the thermospray LC/MS tuning solution in the low mass range mode (to m/z 2000).

The extent of NH_3 incorporation in the cluster ions was verified by using a mobile phase containing 0.1 M $^{15}\text{NH}_4\text{OAc}$ in place of the 0.1 M $^{14}\text{NH}_4\text{OAc}$. For every NH_3 (or NH_4^+) contained in a TFA-ammonia cluster ion, the cluster ion is shifted 1 u higher on going from $^{14}\text{NH}_4\text{OAc}$ to $^{15}\text{NH}_4\text{OAc}$ in the mobile phase. The results of this experiment show the cluster ion series now starting with $(\text{TFA})_1(^{15}\text{NH}_3)(^{15}\text{NH}_4)^+$ at m/z 151 and repeating every 132 u (equivalent to TFA + $^{15}\text{NH}_3$) and support the proposed compositions of the TFA-ammonia cluster ions.

Because of the electrophilic nature of the fluorine-containing TFA, the mobile phase was also evaluated for its potential for tuning TSP LC/MS in the negative ion mode. While being useful for negative ion tuning, the mobile phase did not work nearly as well as was found in the positive ion mode. As shown in Figure 3, approximately 90–95% of the ion current is carried by the $(\text{CF}_3\text{COO}^-)(\text{TFA})$ ion at m/z 227. This situation is dramatically different from the positive ion spectrum where no one ion carries the vast majority of the ion current. The cluster ions formed in the negative ion mode also do not follow as well-defined of a simple, repetitive pattern as found in the positive ion mode. As listed in Table I, after the $(\text{CF}_3\text{COO}^-)(\text{TFA})_2$ ion at m/z 341, higher mass cluster ions incorporate varying amounts of NH_3 with the TFA in the cluster. Finally, while negative ion clusters have been detected to m/z 2000, their responses diminish markedly above m/z 1000.

While no ion source contamination has been detected or TSP LC/MS performance impaired after pumping as much as liter volumes of the tuning solution through the instrument, a solid precipitate did deposit in the vacuum tubing external to the heated mass spectrometer manifold. The chemical ionization (CH_4) mass spectrum of this precipitate from the solid probe generated ions at m/z 18, NH_4^+ , and m/z 115, the

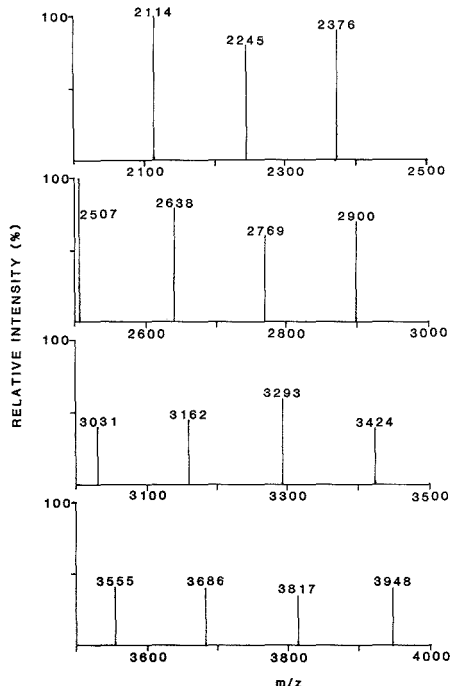


Figure 2. Positive ion mass spectrum of the thermospray LC/MS tuning solution in the high mass range mode (scanning from m/z 2000 to 4000).

Table I. Proposed Compositions of Major TFA- NH_3 Cluster Ions in the Negative Ion Mode

m/z with ^{14}N	m/z with ^{15}N	proposed composition
227	227	$(\text{CF}_3\text{COO}^-)(\text{TFA})$
341	341	$(\text{CF}_3\text{COO}^-)(\text{TFA})_2$
455	455	$(\text{CF}_3\text{COO}^-)(\text{TFA})_3$
472	473	$(\text{CF}_3\text{COO}^-)(\text{TFA})_3(\text{NH}_3)$
489	491	$(\text{CF}_3\text{COO}^-)(\text{TFA})_3(\text{NH}_3)_2$
603	605	$(\text{CF}_3\text{COO}^-)(\text{TFA})_4(\text{NH}_3)_2$
734	737	$(\text{CF}_3\text{COO}^-)(\text{TFA})_3(\text{NH}_3)_3$
865	869	$(\text{CF}_3\text{COO}^-)(\text{TFA})_6(\text{NH}_3)_4$
996	1001	$(\text{CF}_3\text{COO}^-)(\text{TFA})_7(\text{NH}_3)_5$
1127	1133	$(\text{CF}_3\text{COO}^-)(\text{TFA})_8(\text{NH}_3)_6$
1144	- ^a	$(\text{CF}_3\text{COO}^-)(\text{TFA})_8(\text{NH}_3)_7$
1161	1169	$(\text{CF}_3\text{COO}^-)(\text{TFA})_8(\text{NH}_3)_8$
1275	1283	$(\text{CF}_3\text{COO}^-)(\text{TFA})_9(\text{NH}_3)_8$
1292	1301	$(\text{CF}_3\text{COO}^-)(\text{TFA})_9(\text{NH}_3)_9$
1406	1415	$(\text{CF}_3\text{COO}^-)(\text{TFA})_{10}(\text{NH}_3)_9$
1423	1433	$(\text{CF}_3\text{COO}^-)(\text{TFA})_{10}(\text{NH}_3)_{10}$
1554	1565	$(\text{CF}_3\text{COO}^-)(\text{TFA})_{11}(\text{NH}_3)_{11}$
1685	1697	$(\text{CF}_3\text{COO}^-)(\text{TFA})_{12}(\text{NH}_3)_{12}$
1816	-	$(\text{CF}_3\text{COO}^-)(\text{TFA})_{13}(\text{NH}_3)_{13}$
1947	-	$(\text{CF}_3\text{COO}^-)(\text{TFA})_{14}(\text{NH}_3)_{14}$

^a Corresponding ion not detected in $^{15}\text{NH}_4\text{OAc}$ experiment.

(M + H) ion of TFA, indicative of ammonium trifluoroacetate. The salt began volatilizing immediately upon entry into the ion source, volatilized predominantly at 60 °C, and was completely vaporized by a solid probe temperature of 90 °C. The solid probe volatilization characteristics of ammonium trifluoroacetate explain why the material is volatile under vacuum in the heated ion source and mass spectrometer manifold but precipitates on reaching ambient temperatures in the

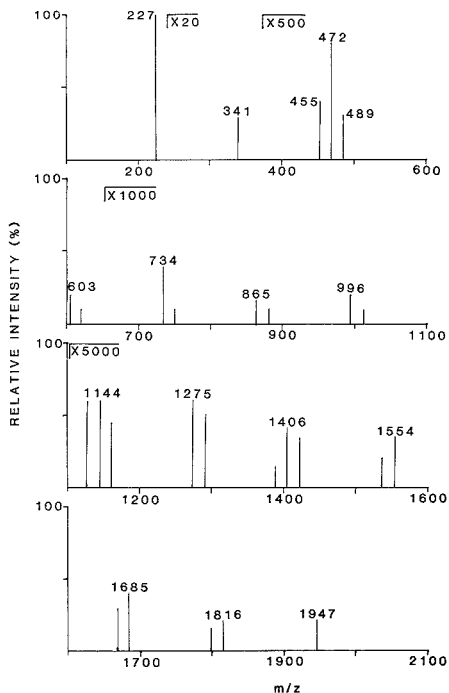


Figure 3. Negative ion mass spectrum of the thermospray LC/MS tuning solution.

vacuum tubing outside of the instrument. While giving an unsightly appearance in the vacuum tubing, the precipitate has never deposited in the ion source or metal pumpout lines connecting the ion source to the vacuum tubing and has never adversely affected subsequent TSP LC/MS performance. The precipitate can be readily removed by disconnecting the tubing and flushing with water when convenient. Although not tested, an alternative approach for eliminating the precipitate from the tubing would be to heat the tubing from the manifold to the rough pump isolation trap during TSP LC/MS operation. Reducing the concentrations of TFA and NH_4OAc in the mobile phase to 0.1% and 0.05 M, respectively, has been found to reduce the rate of precipitate deposition without adversely affecting the intensities of the ion clusters. A further reduction of the TFA concentration to 0.01% decreased the intensities of the cluster ions by more than an order of magnitude.

To test for potential memory effects caused by the tuning solution, the ion current was monitored after switching from

the tuning solution to a mobile phase of 18% H_2O in CH_3OH (0.1 M ammonium acetate). The tuning solution was monitored for 2 min after which the LC pump was switched to the new mobile phase. Following the drop accompanying the switchover, the response increased momentarily as residual tuning solution was pumped out of the connecting tubing between the thermospray interface and the LC pump. As the fresh mobile phase eluted, response to the tuning solution was eliminated over the next 2 min. The same pumpout characteristics were observed in both positive ion and negative ion modes.

In conclusion, a tuning and calibration solution for TSP LC/MS has been developed that generates TFA- NH_3 cluster ions to m/z 4000 in the positive ion mode. Not only is this mass range markedly higher than that provided by HOAc- NH_3 cluster ions (7), the predominant repetitive pattern of $(\text{TFA})_x(\text{NH}_3)_y\text{NH}_4^+$ is simpler than that for HOAc- NH_3 cluster ions where a fixed ratio of HOAc to NH_3 is not maintained. The same mobile phase can be used for tuning and calibration in the negative ion mode but, unfortunately, does not work as well as in the positive ion mode. While temperature effects are expected to have some influence on cluster ion formation, they are expected to be similar to those previously reported for sodium acetate (10). Although a precipitate, determined to be ammonium trifluoroacetate, deposits in the vacuum tubing external to the instrument, no contamination of the ion source has been observed, and no degradation of TSP LC/MS performance in subsequent analyses has been detected. Better instrumental response to the high mass cluster ions is anticipated with a recently introduced 20-kV conversion dynode multiplier kit (11). Finally, the use of fluorine to increase the mass of the cluster ions without increasing their positive mass affect may prove useful for obtaining exact mass measurements when coupling high-resolution mass spectrometry with TSP LC/MS.

LITERATURE CITED

- (1) Covey, T. R.; Lee, E. D.; Bruins, A. P.; Henion, J. D. *Anal. Chem.* **1986**, *58*, 1451A-1461A.
- (2) Blackley, C. R.; Vestal, M. L. *Anal. Chem.* **1983**, *55*, 750-754.
- (3) Liberato, D. J.; Fenselau, C. C.; Vestal, M. L.; Yergey, A. L. *Anal. Chem.* **1983**, *55*, 1741-1744.
- (4) Filicot, D.; Kim, H. Y.; Dykes, D. F.; Vestal, M. L. *Anal. Chem.* **1984**, *56*, 1236-1240.
- (5) Vestal, M. L.; Fergusson, G. J. *Anal. Chem.* **1985**, *57*, 2373-2378.
- (6) Covey, T. R.; Crowther, J. B.; Dewey, E. A.; Henion, J. D. *Anal. Chem.* **1985**, *57*, 474-481.
- (7) Heeremans, C. E. M.; van der Hoeven, R. A. M.; Niessen, W. M. A.; Tjaden, U. R.; van der Greef, J. *Org. Mass Spectrom.* **1989**, *24*, 109-112.
- (8) Yang, L.; Fergusson, G. J. *Annu. Conf. Mass Spectrom. Allied Top.*, **33rd** **1985**, 775-776.
- (9) *Thermospray Accessory Operation and Service Manual*, Finnigan-MAT Corp., San Jose, CA, June 1987.
- (10) Robins, R. H.; Crow, F. W. *Rapid Commun. Mass Spectrom.* **1989**, *2*, 30-34.
- (11) Schoen, A.; Syka, J. E. P. *Annu. Conf. Mass Spectrom. Allied Top.*, **36th** **1988**, 843-844.

RECEIVED for review March 31, 1989. Accepted June 22, 1989.

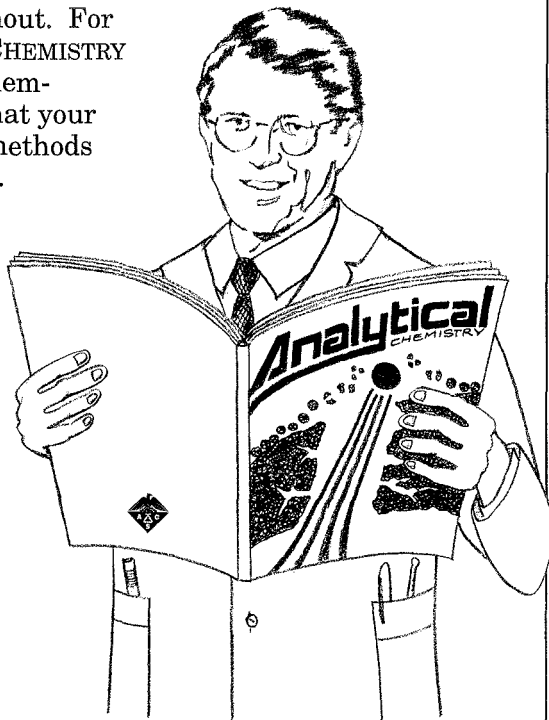
When you're confronted
with a specific "need to know"...

Analytical CHEMISTRY

Every chemist knows, having the most up to date information is essential for success. And, in the vital field of measurement science, ANALYTICAL CHEMISTRY is the one publication you cannot do without. For over sixty years, ANALYTICAL CHEMISTRY has proven to be a useful problem-solving resource, no matter what your specialty. And now, it covers methods used in the biotechnology field.

Publishing information that will help you deal more skillfully with problems such as sampling, data analysis and methodology—the papers in today's twice monthly ANALYTICAL CHEMISTRY cover real world problems involving trace analysis of air, water, soil, materials, drugs, and biopolymers.

Call now and reserve your own personal subscription.



Volume 61 (1989)

	U.S.	Canada and Mexico	Europe Air-Service Included	All Other Countries Air- Service Included
ACS Member - 1 year	\$ 27	\$ 56	\$ 83	\$120
2 years	\$ 45	\$103	\$157	\$231
Nonmember	\$ 49	\$ 78	\$155	\$192

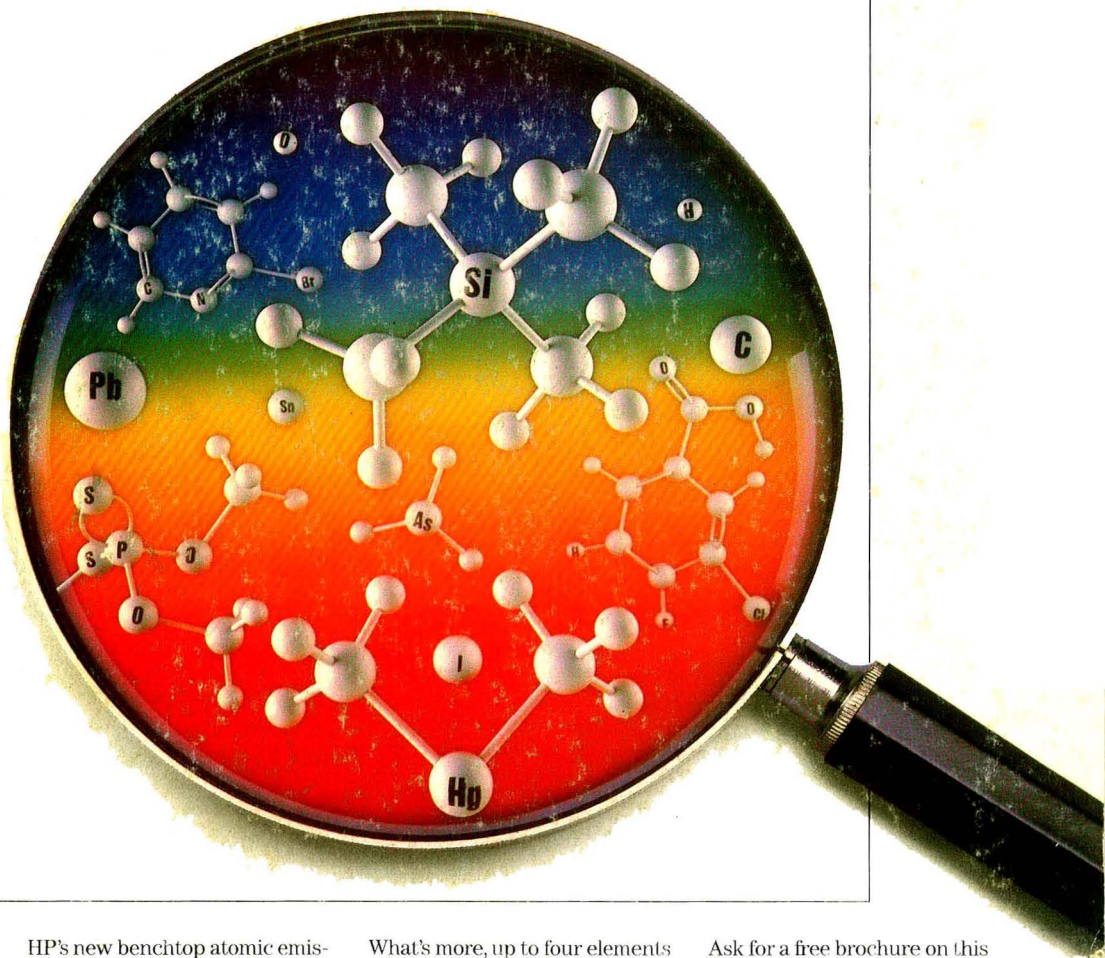
Member rates are for personal use only. Subscriptions may start any month of the year and expire one year later. Foreign payment must be made in U.S. currency by international money order, UNESCO coupons, or U.S. bank draft, or order through your subscription agency. For nonmember rates in Japan, contact Maruzen Co., Ltd. This publication is available on microfilm, microfiche, and the full text is available online on STN International.

**Call Toll-Free
1-800/227-5558
for credit card orders**

or write:

**American Chemical Society
Marketing Communication Dept.
1155 Sixteenth Street N.W.
Washington D.C. 20036**

Now GC detection is more elemental.



HP's new benchtop atomic emission detector enables you to selectively identify multiple elements in GC effluents. Even some that were previously difficult or impossible to detect. Like carbon. And organometallics. And it's the first GC detector to perform both qualitative *and* quantitative analysis of oxygen.

What's more, up to four elements may be simultaneously detected from a single injection. And sequencing through any number of elements is performed automatically. To confirm MSD or IRD library searches, HP's AED provides elemental information, with the convenience of single-instrument setup.

Ask for a free brochure on this exciting new product. Just call **1 800 556-1234, Ext. 10213**. In California, call **1 800 441-2345, Ext. 10213**.



**HEWLETT
PACKARD**

38702